ISSN 0042-8469
e-ISSN 2217-4753
UDC 623 + 355/359

Vol. 73, Issue 4
2025

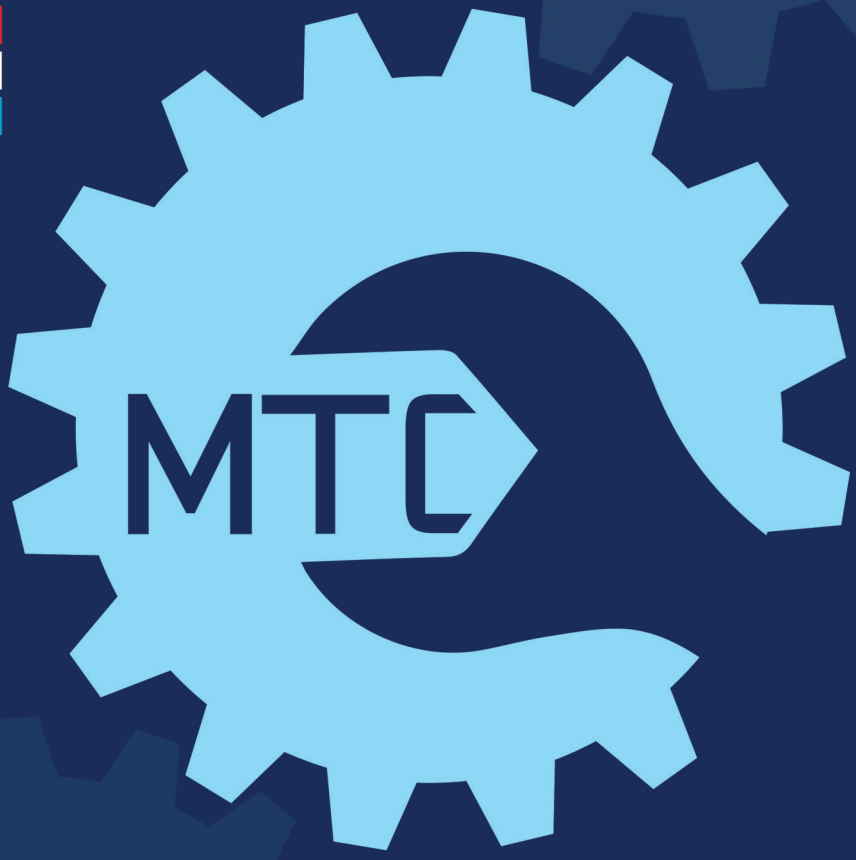

SCIENTIFIC JOURNAL OF THE MINISTRY OF DEFENCE AND THE SERBIAN ARMED FORCES

MILITARY TECHNICAL COURIER

MILITARY TECHNICAL COURIER
4 2025

ВТГ.МО.УПР.СРБ
www.vtg.mod.gov.rs

ISSN 0042-8469
e-ISSN 2217-4753
УДК 623 + 355/359

Вол. 73, бр. 4
2025

НАУЧНИ ЧАСОПИС МИНИСТАРСТВА ОДБРАНЕ И ВОЈСКЕ СРБИЈЕ

ВОЈНОТЕХНИЧКИ ГЛАСНИК

4 2025 ВОЈНОТЕХНИЧКИ ГЛАСНИК

втг.мо.упр.срб

www.vtg.mod.gov.rs

ISSN 0042-8469
e-ISSN 2217-4753
UDC 623 + 355/359

SCIENTIFIC JOURNAL OF THE MINISTRY OF DEFENCE AND SERBIAN ARMED FORCES

MILITARY TECHNICAL COURIER

VOLUME 73•ISSUE 4•OCTOBER – DECEMBER 2025

НАУЧНИ ЧАСОПИС МИНИСТАРСТВА ОДБРАНЕ И ВОЈСКЕ СРБИЈЕ

ВОЈНОТЕХНИЧКИ ГЛАСНИК

ВОЛУМЕН 73•БРОЈ 4• ОКТОБАР – ДЕЦЕМБАР 2025.

ВТГ.МО.УПР.СРБ
www.vtg.mod.gov.rs
COBISS.SR-ID 4423938
DOI: 10.5937/VojnotehnickiGlasnik

ВЛАСНИЦИ:
Министарство одбране и Војска Србије

ИЗДАВАЧ:
Универзитет одбране у Београду, Војна академија

УРЕДНИШТВО (странице чланова уредништва у ORCID iD-у, Google Scholar-у, Web of Science ResearcherID-у, Scopus Author ID-у и РИНЦ-у доступни су на http://www.vtg.mod.gov.rs/urednistvo.html):

ГЛАВНИ И ОДГОВОРНИ УРЕДНИК:
Др Драган Трифковић, Универзитет одбране у Београду, Војна академија, Београд, Србија,
e-mail: dragan.trifkovic@va.mod.gov.rs

УРЕДНИК:
Др Владан Анићијевић, Универзитет одбране у Београду, Војна академија, Београд, Србија,
e-mail: vladan.anicijevic@va.mod.gov.rs

Уредник за област математике и механике
Др Рале Николић, Универзитет одбране у Београду, Војна академија, Београд, Србија

Уредник за област електронике, телекомуникација и информационих технологија
Др Бобан Бонџулић, Универзитет одбране у Београду, Војна академија, Београд, Србија

Уредник за област машинства
Др Бранимир Крстић, Универзитет одбране у Београду, Војна академија, Београд, Србија

Уредник за област материјала и хемијских технологија
Др Михаел Бучко, Универзитет одбране у Београду, Војна академија, Београд, Србија

УРЕЂИВАЧКИ ОДБОР:
Др Градимир Миловановић, Српска академија наука и уметности, Београд, Србија,
Др Ђи-Хуан Хи, Универзитет Суџоу, Факултет за текстилну и одевну технику, Суџоу, Кина,
Др Мађид Тафана, Универзитет Ла Сал, Одељење за пословне системе и аналитику, Филаделфија, САД,
Др Шанкар Чакраборти, Универзитет Јадавпур, Одељење за производно машинство, Калкута, Индија,
Др Раду-Емил Прекуп, Универзитет Политехника у Темишвару, Темишвар, Румунија,
Др Јургита Антуцхевичи, Технички универзитет Гедиминас у Вилњусу, Грађевински факултет, Вилњус, Литванија,
Др Срећко Јоксимовић, Универзитет у Јужној Аустралији, Аделејд, Аустралија,
Др Мортеза Јаздани, Факултет за бизнис и маркетинг ESIC, Мадрид, Шпанија,
Др Прасенџит Чатерџи, Институт за инжењерство MCKV, Одељење за машинство, Ховрах, Индија,
Др Жељко Стевић, Универзитет у Источном Сарајеву, Саобраћајни факултет, Добој, Република Српска, БиХ,
Др Хамед Фазлолахтабар, Универзитет Дамган, Одељење за индустријско инжењерство, Дамган, Иран,
Др Јарослав Ватробски, Универзитет у Шчећину, Факултет за економију, финансије и менаџмент, Шчећин, Пољска,
Др Кристиано Фрагаса, Универзитет у Болоњи, Одељење за индустријско инжењерство, Болоња, Италија,
Др Војчех Салабун, Западнопоморански технолошки универзитет у Шчећину, Факултет рачунарских наука и информационих технологија, Шчећин, Пољска,
Др Иева Меидуте-Кавалиаускиене, Војна академија Литваније „Генерал Јонас Жемаитис“, Виљнус, Литванија,
Др Шарка Мајерова, Универзитет одбране у Брну, Одељење за математику и физику, Брно, Чешка Република,
Др Фатих Ецер, Универзитет Афион Кођатепе, Факултет за економију и административне науке, Афионкарахисар, Турска,
Др Ернесто Д.Р. Сантибанез Гонзалез, Универзитет у Талки, Талка, Чиле,
Др Драган Маринковић, Технички универзитет у Берлину, Факултет за машинске и транспортне системе, Берлин, Немачка,
Др Стефано Валвано, Универзитет Коре у Ени, Одељење за ваздухопловни инжењеринг, Ена, Италија,
Др Рафал Мадонски, Универзитет Ђинан, Центар за истраживање електричне енергије, Гуангџоу, Кина,
Др Миленко Андрић, Универзитет одбране у Београду, Војна академија, Београд, Србија,
Др Самарџит Кар, Национални институт за технологију, Одељење за математику, Дургапур, Индија,
Др Росен Митрев, Технички универзитет у Софији, Софија, Бугарска,
Др Бојан Милановић, Универзитет одбране у Београду, Војна академија, Београд, Србија,
Др Ирик Мухамедзјанов, Државни нафтни технолошки универзитет у Уфи, Уфа, Руска Федерација,
Др Павел Отрисал, Универзитет Палацки, Оломоуц, Чешка Република,
Др Радован Радовановић, Криминалистичко-полицијски универзитет, Београд, Србија,
Др Бошко Рашуо, Универзитет у Београду, Машински факултет, Београд, Србија,
Др Саад Аслам, Универзитет Сунваи, Куала Лумпур, Малезија,
Др Насрин Каусар, Технички универзитет Јилдиз, Факултет уметности и науке, Турска

C O N T E N T S / С А Д Р Ж А Ј

ORIGINAL SCIENTIFIC PAPERS / ОРИГИНАЛНИ НАУЧНИ РАДОВИ

ORIGINAL SCIENTIFIC PAPERS

Metaheuristic-based approach to optimizing the weights in the TOPSIS method for driver candidate performance assessment

Ivana M. Sarić[a], *Jasmina* Dž. Vujadinović[b], *Rale* M. Nikolić[c]

[a] University of Belgrade, Faculty of Technology and Metallurgy, Department of Mathematical Sciences, Belgrade, Republic of Serbia; e-mail: isaric@tmf.bg.ac.rs, ORCID iD: https://orcid.org/0000-0001-9141-8098

[b] University of Defence in Belgrade, Military Academy, Department of Natural and Mathematical Sciences, Belgrade, Republic of Serbia; e-mail: jasmina.fijuljanin@va.mod.gov.rs, **corresponding author**, ORCID iD: https://orcid.org/0000-0003-2479-9868

[c] University of Defence in Belgrade, Military Academy, Department of Natural and Mathematical Sciences, Belgrade, Republic of Serbia; e-mail: rale.nikolic@va.mod.gov.rs, ORCID iD: https://orcid.org/0000-0002-8703-3029

https://doi.org/10.5937/vojtehg73-62775

FIELD: mathematics, multi-criteria decision making, metaheuristic, cognitive assessment in driver evaluation

ARTICLE TYPE: original scientific paper

Abstract:

Introduction/purpose: Traffic safety and reliable driver selection are the key components of modern transport systems. The aim of this paper is to improve the evaluation process of candidates performance in driving tests by the applying multi-criteria decision-making and metaheuristic approach. Based on the results obtained using the Vienna Test System, a TOPSIS-based model with adaptive weighting of evaluation criteria is proposed.

Methods: The weights of the TOPSIS method were optimized using three metaheuristic algorithms: Genetic Algorithm (GA), Ant Colony Optimization (ACO), and Artificial Bee Colony (ABC) algorithm. Two objective

ACKNOWLEDGMENT: This paper is supported by the Ministry of Defence of the Republic of Serbia under the scientific research project (project name: Driver model in the transport units of the Serbian armed forces , project code: VA-TT/2/20-25).

The authors would like to thank the anonymous reviewers for their valuable comments and constructive suggestions, which significantly improved the quality of this paper.

functions were used during optimization — the AUC and the F1-score — to analyze their impact on model accuracy and stability. The experimental framework consisted of three parts: (1) comparison of GA, ACO, and ABC performance using the AUC as the objective function, (2) analogous comparison using the F1-score as the objective function, and (3) cross-comparison between AUC and F1-score optimized models.

Results: The obtained results indicate that both the choice of metaheuristic algorithm and the objective function significantly influence the performance of the TOPSIS method. AUC-based optimization resulted in more stable models and a better balance between successful and unsuccessful candidates, while F1-based optimization achieved higher sensitivity and better identification of successful candidates.

Conclusions: Applying metaheuristic algorithms for weight optimization within the TOPSIS framework enables adaptive and more reliable candidate ranking, contributing to the development of intelligent driver selection systems and improved traffic safety. The results confirm that an appropriate choice of an optimization algorithm and an objective function can significantly enhance model accuracy and robustness.

Key words: TOPSIS, multi-criteria decision making, metaheuristics, GA, ACO, ABC, Vienna Test System.

Introduction

Traffic safety represents one of the key challenges of modern societies, as road accidents continue to cause significant human, economic, and social consequences worldwide. According to international reports, the human factor remains the dominant cause of most traffic incidents, which emphasizes the importance of systematically assessing drivers abilities and readiness. Consequently, the process of selecting candidates for driving licenses plays a crucial role in improving overall traffic safety levels. In addition to theoretical and practical training, the evaluation of psychomotor, perceptual, and cognitive abilities constitutes an essential part of the driver selection process. In contemporary practice, standardized psychodiagnostic systems based on objective measurement instruments have become highly relevant. Among them, the Vienna Test System (VTS) (Schuhfried, 2013) is one of the most widely used and reliable tools, providing comprehensive assessments of numerous parameters important for safe vehicle operation — including attention, reaction speed, visual perception, risk-taking tendencies, and motor coordination. Such testing results offer valuable input for decision-making regarding candidates driving abili-

ties but simultaneously pose a multi-criteria decision problem, where numerous factors of unequal importance must be objectively combined. In such decision-making contexts, the use of multi-criteria decision-making (MCDM) methods are particularly justified. One of the most prominent among them is the Technique for Order Preference by Similarity to Ideal Solution (TOPSIS) (Hwang & Yoon, 1981), recognized for its interpretability and capability to rank alternatives according to their distance from the ideal and anti-ideal solutions (Ren et al., 2021; Huang et al., 2020). However, one of the key challenges in applying TOPSIS lies in determining the weights of criteria, since the final decision outcome depends directly on their distribution. Traditional approaches to assigning weights often rely on subjective expert judgment or predefined assumptions, which may limit the objectivity and accuracy of the model. With advances in computational intelligence, metaheuristic algorithms have emerged as a powerful alternative for optimizing weighting schemes based on empirical data and clearly defined objective functions. Among them, the Genetic Algorithm (GA) (Holland, 1975), Ant Colony Optimization (ACO) (Dorigo & Gambardella, 1997), and Artificial Bee Colony (ABC) (Karaboga, 2005; Pham et al., 2006) have demonstrated notable effectiveness in solving complex optimization tasks, especially those that are nonlinear, multidimensional, or lack analytical formulations. This paper explores the application of these three metaheuristic algorithms to optimize the weights of criteria within the TOPSIS method, using data obtained from the Vienna Test System applied to a group of candidates for the driving test. Furthermore, two distinct objective functions — the F1-score and the Area Under the Receiver Operating Characteristic Curve (AUC) — are introduced to analyze how different optimization goals affect model performance. A systematic comparison of GA, ACO and ABC efficiency for each objective function is performed, followed by an assessment of the differences between F1-score and AUC-optimized models. The results of this research contribute to enhancing the candidate evaluation process through adaptive weighting and intelligent optimization. By combining TOPSIS with metaheuristic approach, the proposed approach ensures higher accuracy and reliability of assessment, supporting the development of advanced decision-support systems applicable in both civilian and military contexts, where safe and precise vehicle operation is of critical importance.

Problem settings and data representation

The experimental data used in this research originate from a dataset collected through the *Vienna Test System (VTS)*, developed by Schuhfried GmbH. The VTS is a computer-based psychodiagnostic platform designed for standardized assessment of cognitive, psychomotor and perceptual abilities relevant to driving performance. It has been widely implemented in transport, aviation and occupational psychology for the selection and training of drivers and operators in safety-critical environments (Kubinger, 2007; Kaça et al., 2021; Tinella et al., 2021; Masoudi et al., 2022).

In the present study, the VTS was used to evaluate a sample of 583 candidates prior to practical driving examination. Each candidate completed a battery of tests measuring various psychological and motor skills associated with safe vehicle control, such as sustained attention, selective reaction, motor coordination, visual search and decision-making under stress. Table 1 summarizes the main VTS modules used for this study, covering cognitive, psychomotor, and emotional dimensions of performance.

The raw scores obtained from individual tests were normalized to a common scale and aggregated into a matrix $X \in \mathbb{R}^{n \times m}$, where n represents the number of candidates and m the number of considered criteria. Each row of X corresponds to a candidate, and each column to a specific ability index (e.g., reaction time or spatial orientation). For the purpose of evaluation, the target variable y is binary and indicated the final outcome of the driving test (1 – passed, 0 – failed). This setting naturally leads to a multi-criteria classification problem, where the goal is to combine multiple VTS-based criteria into a single composite index of driving ability.

The dataset consisted of percentile scores obtained from the VTS, covering multiple psychometric and cognitive performance criteria for each candidate. All records were complete, with no missing values or invalid entries.

Since VTS tests are expressed in percentiles that differ in scale and dispersion, a z-score normalization was applied to each criterion to ensure comparability and to eliminate potential scale effects in subsequent analysis. This transformation preserved the relative differences between candidates while standardizing all variables to have zero mean and unit variance.

All variables were benefit-type attributes (oriented so that higher values represented better performance), ensuring consistent interpretation across

the criteria. The resulting standardized dataset served as an input for evaluation, enabling objective aggregation of psychometric indicators into a single performance score for each candidate.

Table 1 – Classification of criteria in the Vienna Test System

Group	Criterion	Description
COG	COG	Recognition of visual patterns.
DT	DT	Reaction speed to various stimuli (psychomotor + attention).
PP-R	VF	Perception of objects in the peripheral visual field (visual perception).
	TD	Precision of position maintenance and tracking (psychomotor control).
RT	RS	Speed of motor response (psychomotor ability).
	MS	Motor execution speed (psychomotor ability).
ATAVT	ATAVT	Fast recognition of traffic scenes (visual perception).
IVPE	MST	Speed in performing motor tasks (psychomotor speed).
	RSB	Reaction time measured via key press (psychomotor speed).
	SC	Sustained attention and selective reaction to stimuli (attention + concentration).
	RA	Tendency towards risk-taking behavior (cognitive–psychological assessment).
RR	RR	Verbal fluency and attention (attention / verbal fluency).
VIP	SP	Spatial perception and orientation (cognitive ability).
	VIP	Processing and interpretation of visual information (cognitive ability).
	AI	Solving logical and abstract reasoning tasks (cognitive ability).
ED	ED	Decision-making in emotionally challenging situations (emotional and psychological assessment).

TOPSIS with learnable weights

TOPSIS was employed as an MCDM method. The underlying principle of TOPSIS assumes that the best alternative should have the shortest distance from the positive ideal solution (PIS) and the farthest distance from the negative ideal solution (NIS).

In this study, each candidate represents an alternative A_i, while the $m = 16$ criteria derived from the VTS represent quantitative indicators of cognitive and psychomotor performance relevant to driving ability. The decision matrix is defined as:

$$X = [x_{ij}]_{n\times m}, \quad i = 1, 2, \ldots, n,\ j = 1, 2, \ldots, m,$$

where x_{ij} denotes the observed value of criterion C_j for candidate A_i.

Unlike the classical TOPSIS, where weights are predefined or expert-assigned, in learnable weights approach, the weights are optimized using multiple strategies.

This enables the model to *learn* the most informative weighting configuration directly from the data. The resulting weighted normalized matrix, obtained after applying z-score standardization to all criteria, is used to compute the distances to PIS and NIS, yielding a ranking of all candidates. However, unlike traditional MCDM applications, the availability of ground-truth exam outcomes (pass/fail) allows TOPSIS to be evaluated in a classification setting. By comparing the computed preference scores with actual outcomes, we assess how well each weighting strategy discriminates between successful and unsuccessful candidates, using the AUC and the F1-score as performance metrics.

In this study, we focus on the metaheuristic approach of learnable weights within the TOPSIS framework, employing GA, ACO and ABC to discover the most discriminative weighting configurations. Other weighting strategies, including random initialization, regression-based optimization, and fixed (equal-weight) baseline, have been previously examined (Vujadinović et al., 2025).

The pseudocode of the TOPSIS for ranking and optional classification used in this study is given below.

Algorithm 1: TOPSIS for ranking and classification

Input: Criteria matrix X, weight vector w
Output: Ranking of alternatives, success prediction

```
Normalize the criteria matrix X;
Apply weights w to the criteria;
Determine PIS and NIS;
for each alternative do
    Compute the distance to PIS and NIS;
    Compute the TOPSIS score as the relative closeness to PIS;
end
Rank the alternatives according to their scores;
Determine the classification threshold τ on validation data;
for each alternative do
    if TOPSIS score ≥ τ then
        classify as successful;
    end
    else
        classify as unsuccessful;
    end
end
```

Validation procedure

To ensure robustness of the learned weights and to mitigate overfitting to a specific data split, a k-fold cross-validation scheme was employed during optimization. The dataset was partitioned into $k = 5$ disjoint folds, with four folds used for training and one for validation in each iteration.

Each metaheuristic algorithm (GA, ACO, ABC) optimized the weight vector w by maximizing the selected objective function (the AUC or the F1-score) averaged across all folds. The mean validation performance was used as the fitness value guiding the search process.

This procedure ensured that the resulting weights generalize well and that the optimization process reflects the model's stability across different data partitions.

Objective functions

A crucial component of the metaheuristic-based approach process is the *objective function*, which quantifies the quality of each candidate weight vector w during the search. In this study, two alternative objective functions were implemented and the model performance was compared. Each offers a different perspective on model performance — the AUC emphasizes discriminative ability, whereas the F1-score focuses on balanced classification.

AUC as an optimization objective function.

The AUC is a threshold-independent measure of model separability, quantifying how well the continuous TOPSIS scores $C_i(w)$ distinguish between successful and unsuccessful candidates (Hanley & McNeil, 1982; Fawcett, 2006). Mathematically, it can be expressed as:

$$AUC = P(C_+ > C_-),$$

representing the probability that a randomly chosen successful candidate (C_+) has a higher score than a randomly chosen unsuccessful one (C_-). By maximizing the AUC, the optimization process improves overall discriminative power, independent of any specific classification threshold.

F1-score as an optimization objective function.

The F1-score is defined as the harmonic mean of precision and recall, fundamental measures in binary classification problems (Powers, 2011; Sokolova & Lapalme, 2009). Given the confusion matrix components:

- True Positives (TP): correctly predicted successful candidates,
- True Negatives (TN): correctly predicted unsuccessful candidates,
- False Positives (FP): unsuccessful candidates incorrectly predicted as successful, and
- False Negatives (FN): successful candidates incorrectly predicted as unsuccessful.

Precision and recall are computed as:

$$Precision = \frac{TP}{TP + FP}, \quad Recall = \frac{TP}{TP + FN}.$$

The F1-score is then:

$$F1 = 2 \cdot \frac{Precision \cdot Recall}{Precision + Recall},$$

ranging from 0 (worst) to 1 (best). By maximizing F1, the model seeks to balance false positives and false negatives simultaneously.

When the F1-score is used as the objective function, the metaheuristic algorithm searches for a weight vector that maximizes the average F1-score across validation folds and returns the best solution found during the optimization process. The classification threshold is determined from the Receiver Operating Characteristic (ROC) curve, which represents the trade-off between the True Positive Rate and the False Positive Rate across all possible thresholds. The optimal threshold is selected using Youden's J statistic (Youden, 1950), ensuring the best possible separation between successful and unsuccessful candidates.

AUC-based optimization prioritizes global separability of candidate scores, enabling flexible thresholding for advisory decision-making. F1-score based optimization emphasizes balanced classification performance, minimizing both false approvals and rejections. In this study, both objective functions were applied independently to each metaheuristic (GA, ACO, ABC), yielding complementary insights into model behavior and stability of learned weights.

Each metaheuristic evaluates candidate weight vectors $w^{(k)}$ assigning them the corresponding fitness values. For each vector:

1. Compute TOPSIS scores $C_i(w^{(k)})$.
2. Evaluate the selected objective function (the AUC or the F1-score) on a validation subset.
3. Use the computed metric as the fitness value guiding the search (e.g., selection probability in GA, pheromone deposition in ACO, recruitment probability in ABC).

Optimization continues until convergence or exhaustion of the evaluation budget, with the best-performing weight vector w^* selected for testing on unseen data.

AUC optimized models enhance candidate ranking capability, useful in advisory systems where thresholds may be defined post-hoc. Models optimized for the F1-score reduce both false approvals and rejections, supporting operational decision-making in driver selection.

Metaheuristic

Metaheuristic algorithms represent a broad class of stochastic optimization methods, some of which are inspired by natural processes such as

evolution and swarm behavior. They are particularly effective in solving complex, nonlinear and multimodal optimization problems where analytical gradients are unavailable or the search space is discontinuous (Talbi, 2009).

In this study, metaheuristics are used to optimize the TOPSIS weight vector

$$w = (w_1, w_2, \ldots, w_m),$$

subject to the constraints:

$$w_j \geq 0, \quad \sum_{j=1}^{m} w_j = 1.$$

Each algorithm iteratively explores the search space, evaluates candidate weight vectors using the selected objective function (the AUC or the F1-score), and gradually improves them through stochastic operators such as recombination, mutation, and pheromone reinforcement. To ensure a fair comparison, all algorithms were configured with the same computational budget (number of fitness evaluations) and identical stopping criteria.

In this research, three metaheuristic algorithms (GA, ACO and ABC) were used and each of them was adapted to problems characteristics.

Genetic Algorithm (GA)

GA is a population-based stochastic optimization method inspired by biological evolution and Darwinian natural selection.

GA begins with a randomly generated population of weight vectors. Each vector is evaluated using a fitness function $f(w)$, corresponding to the chosen objective function (AUC or F1-score):

$$f(w) = \begin{cases} AUC(w), & \text{if AUC is the optimization objective function,} \\ F1(w), & \text{if F1-score is the optimization objective function.} \end{cases}$$

The evolutionary process consists of iterative application of three GA operators, together with fitness evaluation and a population replacement step:

- *Selection* – parent selection is performed using deterministic elitist rank selection, where the individuals are sorted according to their fitness values (rank-based elitist selection).

- *Crossover* – offsprings are generated using single-point crossover. For each offspring, a random crossover point is selected and the first segment of the weight vector is inherited from one parent, while the remaining segment is inherited from the other parent.
- *Mutation* – for each individual, a fixed percentage of genes is randomly selected and perturbed by adding Gaussian noise. For a selected gene j, the mutated value is given by

$$w_j^{\text{new}} = w_j + \epsilon_j, \qquad \epsilon_j \sim \mathcal{N}(0, \sigma^2).$$

  where $\sigma = 0.1$. After mutation, all weights are clipped to the interval $[0, 1]$ and the entire weight vector is normalized to satisfy

$$\sum_{j=1}^{m} w_j^{\text{new}} = 1.$$

Through repeated application of selection, crossover and mutation, the population gradually evolves towards better solutions. The algorithm terminates after a predefined maximum number of generations is reached. The final output is the best weight vector found during the optimization process according to the fitness function.

The pseudocode of the GA implementation used in this study is given below.

Algorithm 2: Genetic Algorithm for optimizing TOPSIS weights

Input: Criteria matrix X, ground truth labels y, GA parameters (max_generations, population size, number of parents, mutation rate)

Output: Best found vector w

```
Initialize population of random weight vectors
for generation = 1 to max_generations do
    Evaluate fitness function of each individual using TOPSIS + metric (AUC/F1-score)
    Select the best individuals (elitism + selection)
    Generate offspring using crossover
    Apply mutation to offspring
    Form new population from parents and offspring
end
return best found vector w
```

Ant Colony Optimization (ACO)

ACO is a population-based metaheuristic inspired by the collective foraging behavior of ants, where solution quality is reinforced through pheromone-mediated learning. In the considered formulation, ACO is adapted to a continuous optimization setting in order to determine optimal weight vectors for the TOPSIS method.

In each iteration, a population of n_{ants} ants constructs candidate solutions represented as a continuous weight vector.

The pheromone trail τ_j represents the learned importance of the criterion j and is initialized uniformly with a small random perturbation in order to avoid symmetry and premature bias:

$$\tau_j^{(0)} = 1 + \epsilon_j, \qquad \epsilon_j \sim \mathcal{U}(0, 0.01).$$

Candidate solutions are constructed by combining pheromone-driven exploitation with stochastic exploration of the continuous search space. Specifically, each ant generates a weight vector according to

$$w = \alpha \frac{\boldsymbol{\tau}}{\sum_j \tau_j} + \beta \frac{\boldsymbol{r}}{\sum_j r_j}, \qquad \boldsymbol{r} \sim \mathcal{U}(0,1)^m,$$

followed by an L_1 normalization step, thereby ensuring feasibility of the constructed solution. Here, $\boldsymbol{\tau}$ denotes the pheromone vector, while $\boldsymbol{r}$ is a random vector introducing exploration. The parameters $\alpha \geq 0$ and $\beta \geq 0$ control the balance between pheromone-based exploitation and random exploration. These parameters are kept constant within each ACO run, but are varied across experiments using a predefined parameter grid, with $\alpha \in \{0.8, 1.0\}$ and $\beta \in \{0.1, 0.2\}$.

Each constructed solution is evaluated using a fitness function

$$f(w) \in \{AUC(w),\, F1(w)\},$$

obtained from the TOPSIS-based classifier.

The algorithm employs an *offline pheromone update* mechanism. After all ants construct and evaluate their solutions in a given iteration, pheromone levels are updated in two steps. First, evaporation is applied:

$$\boldsymbol{\tau} \leftarrow (1-\rho)\boldsymbol{\tau},$$

where $\rho \in (0, 1)$ denotes the pheromone evaporation rate. Subsequently, pheromone is reinforced using only a subset of elite solutions from the current iteration. Let $\mathcal{E}$ denote the set of top-performing ants, defined as a fixed fraction of the population. The pheromone update is then given by

$$\boldsymbol{\tau} \leftarrow \boldsymbol{\tau} + \rho \sum_{i \in \mathcal{E}} f(w^{(i)})\, w^{(i)},$$

where $f(w^{(i)})$ denotes the fitness value of the solution $w^{(i)}$ generated in the current iteration.

The algorithm maintains the best found solution across all iterations for reporting purposes. The optimization process is repeated for a fixed number of iterations n_{iter}, which serves as the stopping criterion.

The pseudocode of the ACO implementation used in this study is given below.

Algorithm 3: Ant Colony Optimization for optimizing TOPSIS weights

Input: Criteria matrix X, ground truth labels y, ACO parameters (number_of_ants, max_iterations, α, β, ρ)
Output: Best found vector w

Initialize pheromone vector $\boldsymbol{\tau}$ for all criteria (small random perturbation)
Initialize best found solution w^* and best score
for *iteration* $= 1$ **to** *max_iterations* **do**
    for *each ant* $i = 1, \ldots, number\_of\_ants$ **do**
        Draw random vector $\boldsymbol{r} \sim \mathcal{U}(0,1)^m$ and normalize it
        Construct solution $w^{(i)}$
        Evaluate fitness $f(w^{(i)})$ using TOPSIS + metric (AUC/F1)
        Update (w^*, f^*) if $f(w^{(i)}) > f^*$
    end
    Evaporate pheromone
    Select elite set $\mathcal{E}$ (top n_{elite} ants in the current iteration)
    Offline pheromone update using elite solutions
end
return *best found vector* w

Artificial Bee Colony (ABC)

ABC is a swarm intelligence metaheuristic inspired by the collective foraging behavior of honey bees. The algorithm simulates how bees search for food sources, communicate solution quality, and recruit other bees to promising areas. In ABC, each bee represents a candidate solution encoded as a continuous weight vector.

Each iteration of ABC consists of two complementary phases:

1. *Exploration (scout phase):* scout bees randomly generate new solutions to explore unexplored regions of the search space,
2. *Exploitation (recruitment phase):* non-scout bees follow the best solutions found so far and refine them through local search.

The recruitment probability of the bee i is defined as:

$$P_i = \frac{f(w_i)}{\sum_{k=1}^{N} f(w_k)},$$

where $f(w_i) \in \{AUC(w),\ F1(w)\}$ denotes the fitness of the weight vector generated by the bee i. Better solutions attract more bees, increasing exploitation pressure on high-quality areas of the search space.

During local exploitation, the weight vector is refined using a stochastic update followed by normalization:

$$w_j = \frac{w_j + \epsilon}{\sum_{k=1}^{m}(w_k + \epsilon)}, \qquad \epsilon \sim \mathcal{N}(0, \sigma^2).$$

The pseudocode of the ABC implementation used in this study is given below.

Algorithm 4: Artificial Bee Colony for optimizing TOPSIS weights

Input: Criteria matrix X, ground truth labels y, ABC parameters (number of bees, max_iterations, ρ, e_frac, sco_str)
Output: Best found vector w

```
Initialize population of bees with random candidate solutions
for iteration = 1 to max_iterations do
    Evaluate fitness of all bees using TOPSIS + metric (AUC/F1-score)
    Select elite bees with best solutions
    Redirect non-elite bees towards elite solutions (exploitation)
    Scout bees explore new random solutions (exploration)
end
return best found vector w
```

Results

Experiments were conducted on a dataset consisting of 583 candidates evaluated through VTS tests which includes 16 evaluation criteria (Table 1) and the binary outcome representing pass or fail on the driving exam. All algorithms were implemented in Python and evaluated using 5-fold cross-validation. Each algorithm was executed five times, and the average results were recorded. The performance metrics included Accuracy, the AUC and the F1-score as well as time (s) which represents the internal fitness evaluation time. Precision and Recall were also calculated, although not shown in the tables, since they are required for computing the F1-score. Additionally, execution time and algorithmic complexity were recorded for

each optimization approach. The experiments were performed on a standard workstation equipped with an AMD Ryzen 3 processor, 4 GB of RAM, and running Windows 10.

The results of GA metaheuristic

When the optimization objective function is the AUC, GA achieved consistent and interpretable performance across the tested parameter settings. The best results were observed for the configuration of 20 generations (n_gens), 10 individuals (n_pop), 10 parents (n_par), where GA reached an **AUC of 0.7234** and an **accuracy of 0.6585–0.7271**. Increasing the generations number from 10 to 20, the accuracy was improved, indicating that a longer evolutionary process allowed better exploration of the search space and refinement of promising solutions. A mutation rate between 5% and 10% (mut (%)) had a minimal impact on the final AUC, confirming that the algorithm evolved in a stable manner and was not overly sensitive to stochastic variations.

In some configurations, overall accuracy increased while the AUC slightly decreased. This indicates that although the model correctly classified a higher proportion of samples, its ability to consistently rank positive versus negative cases was slightly reduced. Such behavior reflects the inherent difference between the accuracy and the AUC as evaluation metrics.

Table 2 – Best 5 GA results for objective functions AUC and F1-score

Obj	n_gens	n_pop	n_par	mut (%)	Accuracy	AUC/F1	time (s)
AUC	20	10	10	5	0.6585	0.7234	1.79
AUC	20	10	10	10	0.6585	0.7234	1.96
AUC	20	20	10	5	0.7271	0.7233	3.82
AUC	20	20	10	10	0.7271	0.7233	3.66
AUC	30	20	10	5	0.7308	0.7227	5.78
F1	30	10	5	5	0.7737	0.8468	2.82
F1	30	10	5	10	0.7737	0.8468	2.84
F1	20	10	5	5	0.7326	0.8039	1.94
F1	20	10	5	10	0.7326	0.8039	1.91
F1	20	20	10	5	0.7017	0.7765	3.76

When the optimization objective function was shifted to the F1-score, the GA adapted its search behavior accordingly. The top-performing configuration 30 generations, 10 individuals, 5 parents, 5% mutation achieved an

F1-score of 0.8468 with an **accuracy of 0.7737**. Unlike the AUC-based runs, no trade-off between accuracy and the F1-score was observed in this case. Other configurations with slightly different mutation rates (5–10%) yielded identical performance, reflecting stable convergence behavior. Overall, GA demonstrated high robustness and adaptability to different objective function formulations, maintaining solid performance and minimal sensitivity to parameter tuning.

Table 2 presents the five best-performing results for both objective functions, the AUC and the F1-score.

The results of ACO metaheuristic

When optimized for the AUC-based fitness function, the ACO algorithm demonstrated consistent convergence and solid discriminative performance. The best configuration was achieved with $\alpha = 1.0$, $\beta = 0.1$, $\rho = 0.2$ and a colony size of 20 ants (n_ants) and 50 iterations (n_iter). This setup resulted in an **AUC of 0.7528** with an **accuracy of 0.7479**. The relatively high heuristic importance (β) guided ants towards more promising regions in the search space, while a moderate pheromone evaporation rate (ρ) maintained useful historical information without premature stagnation. The algorithm achieved a strong balance between exploration and exploitation, as evidenced by a stable convergence curve and low variance across folds. Overall, ACO optimized for the AUC favored global ranking consistency and maintained well-balanced classification metrics across classes.

Table 3 – Best 5 ACO results for objective functions AUC and F1-score

Obj	n_ants	n_iter	ρ	α	β	Accuracy	AUC/F1	time (s)
AUC	20	50	0.2	1.0	0.1	0.7479	0.7528	9.39
AUC	40	50	0.1	0.8	0.1	0.7393	0.7527	17.94
AUC	20	50	0.2	0.8	0.1	0.7565	0.7525	9.12
AUC	20	50	0.1	1.0	0.2	0.7065	0.7519	9.19
AUC	40	100	0.1	1.0	0.1	0.7530	0.7519	35.87
F1	20	100	0.1	1.0	0.2	0.7134	0.7780	18.02
F1	40	100	0.1	0.8	0.1	0.7168	0.7699	36.48
F1	40	50	0.2	1.0	0.2	0.7098	0.7640	18.17
F1	20	50	0.2	0.8	0.1	0.7081	0.7640	9.35
F1	20	100	0.2	0.8	0.2	0.7064	0.7638	18.24

When the F1-score is used as the objective function, ACO shifts its search towards solutions that prioritize the correct identification of successful candidates. This leads to a higher **F1-score of 0.7780** obtained

at $\alpha = 1.0$, $\beta = 0.2$, $\rho = 0.1$, 20 ants and 100 iterations but with a noticeably lower **accuracy of 0.7134**. This indicates that F1-based optimization pushes ACO to favor sensitivity towards the majority class, even at the cost of overall classification balance. Compared to AUC optimization, the F1-score optimized configurations show greater variability, meaning the search space is less smooth and more sensitive to hyperparameter settings.

The five best results obtained using the AUC and the F1-score as objective functions are shown in Table 3.

The results of ABC metaheuristic

In the AUC-optimized mode, the ABC algorithm achieved its best performance with a population of 20 bees (n_bees), 50 iterations (n_iter), an evaporation rate of $\rho = 0.2$, elite fraction of 0.2 (e_frac), and scout strength (sco_str) of 0.05. This configuration produced an **AUC of 0.7455** with an **accuracy of 0.7598**. The balance between exploration and exploitation was effectively maintained through moderate elitism and controlled scout activity, enabling the algorithm to refine high-quality solutions without excessive random wandering. The strong AUC performance indicates that ABC successfully ranked candidates in alignment with the target classification boundaries. Stability across multiple runs confirms that these parameter values provide a robust trade-off between convergence speed and solution quality.

Table 4 – Best 5 ABC results for objective functions AUC and F1-score

Obj	n_bees	n_iter	ρ	e_frac	sco_str	Accuracy	AUC/F1	time (s)
AUC	20	50	0.2	0.2	0.05	0.7598	0.7455	8.99
AUC	20	100	0.1	0.2	0.1	0.7271	0.7453	18.52
AUC	40	50	0.2	0.2	0.05	0.7340	0.7445	18.43
AUC	40	100	0.2	0.2	0.1	0.7340	0.7445	36.29
AUC	20	100	0.2	0.1	0.05	0.7597	0.7445	18.41
F1	20	50	0.1	0.1	0.1	0.7598	0.8346	8.99
F1	20	50	0.1	0.2	0.1	0.7547	0.8316	9.01
F1	40	50	0.2	0.1	0.1	0.7410	0.8149	18.14
F1	20	50	0.1	0.1	0.05	0.7204	0.7861	9.09
F1	20	50	0.2	0.1	0.1	0.7102	0.7854	9.20

When optimizing for the F1-score, ABC exhibited more aggressive exploitation behavior, focusing on reducing false negatives. The best-performing setup used 20 bees, 50 iterations, an evaporation rate of $\rho =$

0.1, elite fraction of 0.1, and scout strength of 0.1, resulting in an **F1-score of 0.8346** with an **accuracy of 0.7598**. Compared to the AUC-oriented version, this configuration converged faster but with higher variability across runs. The increased scout activity improved the exploration of new candidate regions, yet introduced minor instability in fitness progression. Despite this, the F1-score based optimization was particularly effective in identifying successful candidates, achieving strong class sensitivity performance and competitive classification accuracy.

Table 4 presents the five best-performing results for both objective functions, the AUC and the F1-score.

Comparison between the AUC and F1-score objective functions

A direct comparison between the two optimization objective functions reveals that the AUC-based optimization yields more stable and generalizable models, while the F1-score based optimization prioritizes performance on the dominant class. The difference in overall accuracy was minor, yet the class-wise behavior diverged significantly: The AUC optimization maintained better overall class balance, whereas the F1-score optimization improved detection of successful candidates but at the cost of false negatives. This highlights the importance of selecting an appropriate objective function according to the intended application—whether balanced discrimination or maximal recognition of a specific class is desired.

When the AUC is used as the optimization objective function, all three metaheuristic algorithms (GA, ACO, ABC) tend to converge towards weight vectors that improve the global discriminative power of the TOPSIS model. In this setting, the algorithms search for solutions that maximize the separation between successful and unsuccessful candidates across the entire scoring scale, rather than focusing on the performance of a specific class. As a result, the AUC-based optimization produces more balanced and stable models, with relatively low variability between executions and smoother convergence. This behavior is particularly suited for ranking problems, where the goal is to ensure that higher-ranked candidates are consistently better than lower-ranked ones according to all criteria.

In contrast, when the objective function is the F1-score, the optimization becomes strongly oriented towards correct identification of the positive class, i.e., candidates who successfully pass the driving exam. The

search focuses on solutions that increase sensitivity and improve detection of successful candidates, even if this leads to slightly lower overall ranking precision or weaker class separation. In this mode, the metaheuristic tends to emphasize exploitation of the search space, producing higher F1-score values but also greater variability across parameter configurations. This makes F1-score optimized solutions particularly suitable when false negatives (misclassifying successful candidates as unsuccessful) are considered more costly than false positives.

In summary, the AUC-oriented optimization yields stable, globally discriminative models suitable for ranking, whereas the F1-oriented optimization yields sensitive, class-focused models suitable for decision-making and risk detection. The choice of the objective function should therefore follow the practical requirements of the evaluation system: whether the goal is to build an accurate ranking of candidates or to minimize the risk of approving an unfit driver.

Time-budget comparison of metaheuristic-based weight optimization methods

To enable a fair comparison between metaheuristics with different convergence speeds, all algorithms are evaluated under the same fixed time budget of 300 seconds, using their previously optimized parameter settings.

Table 5 summarizes the best-found results obtained by GA, ACO, and ABC under a fixed time budget. The reported best-target value represents the best average cross-validation performance obtained within the allotted time budget.

Table 5 – Best-found performance of GA, ACO, and ABC under a fixed time budget

Variant	Target	Best target	Precision	Recall	F1	AUC
GA	AUC	0.748	0.896	0.661	0.758	0.748
ACO	AUC	0.765	0.898	0.740	0.802	0.765
BCO	AUC	0.761	0.903	0.746	0.805	0.761
GA	F1	0.837	0.853	0.828	0.837	0.692
ACO	F1	0.807	0.900	0.740	0.807	0.743
BCO	F1	0.800	0.878	0.747	0.800	0.713

Under these conditions, the evaluated metaheuristics exhibit distinct and complementary strengths depending on the optimization objective

function. When the AUC is used as the objective function, ACO and ABC consistently achieve higher best-found AUC values than GA, indicating a stronger ability to optimize the global ranking of candidates across the entire score distribution. This behavior can be attributed to pheromone-based information sharing, which promotes collective exploration of promising regions and leads to smoother and more stable ranking structures. In contrast, when the F1-score is directly optimized, GA attains the highest F1-score values, reflecting its effectiveness in fine-grained adjustment of weight configurations that balance precision and recall at a specific decision threshold. The evolutionary operators of GA, particularly mutation and elitist selection, enable more aggressive local refinements that are beneficial for threshold-dependent metrics. As a result, improvements in the F1-score are achieved even when global ranking quality, as measured by the AUC, is not maximized. These findings confirm that no single metaheuristic dominates across objective functions and emphasize that the selection of the optimization algorithm should be aligned with the intended evaluation criterion and decision-making requirements.

Computational complexity

The computational cost of the proposed approach consists of two parts: (1) evaluation of the TOPSIS method for a given weight vector, and (2) iterative optimization performed by a metaheuristic algorithm (GA, ACO or ABC).

For a decision matrix $X \in \mathbb{R}^{n \times m}$ containing n candidates and m criteria, one evaluation of TOPSIS requires: normalization of the matrix, weighting of the criteria, computing distances to PIS and NIS and calculating the closeness coefficient. This results in a computational complexity of:

$$\mathcal{O}(nm + n \log n),$$

where the first term corresponds to matrix operations and the second term to sorting performed during evaluation of performance metrics.

Each metaheuristic performs a number of TOPSIS evaluations. If E denotes the number of candidate solutions generated during optimization, then the total complexity of the optimization process is:

$$\mathcal{O}(E \cdot (nm + n \log n)).$$

Since E depends only on the algorithm parameters (population size, number of generations/iterations) and not on the data itself, the complexity grows linearly with the number of fitness evaluations. Therefore, all three algorithms (GA, ACO, ABC) exhibit the same asymptotic behavior, differing only in the value of E.

In practice, the execution time is dominated by the number of fitness evaluations, since each evaluation requires running TOPSIS and computing classification metrics. Because TOPSIS operates on relatively small matrices (a fixed number of criteria), the metaheuristic approach remains computationally efficient and can be executed on a standard workstation without parallelization.

Although all three metaheuristic algorithms operate under the same asymptotic computational complexity, their execution time differs in practice due to the way each algorithm generates and evaluates candidate solutions.

GA maintains a fixed-size population and produces a limited number of new solutions per generation through crossover and mutation operators. Consequently, the number of fitness evaluations E grows proportionally to the number of generations and the population size. Since GA typically converges quickly towards promising regions of the search space, fewer candidate weights are evaluated overall.

In contrast, ACO and ABC are based on swarm-search mechanisms, where a significantly larger number of solutions is generated during each iteration. In ACO, every ant probabilistically constructs a new solution using pheromone trails, which results in many more candidate weight vectors evaluated in each step. Similarly, in ABC, both recruited bees and scout bees explore the search space simultaneously, leading to multiple parallel solution updates per iteration.

Because each newly generated solution requires a complete execution of TOPSIS, followed by evaluation of classification metrics (the F1-score or the AUC), the total execution time increases proportionally to the number of solutions explored. Therefore, ACO and ABC require more computational time than GA, not because their per-iteration complexity is higher, but because they evaluate a substantially larger number of candidate weight vectors during the optimization process.

Conclusion

This paper presented a metaheuristic-based optimization framework for improving the weight determination process in the TOPSIS method when evaluating the performance of driver candidates based on psychomotor and cognitive abilities measured by the VTS. Unlike traditional TOPSIS implementations that rely on fixed or subjectively assigned weights, the proposed approach automatically learns the optimal weight configuration by using three population-based optimization algorithms: GA, ACO, and ABC.

Two optimization objective functions were analyzed — the AUC and the F1-score. The AUC encouraged the algorithm to improve the overall separability of candidates, resulting in stable and balanced ranking performance. In contrast, the F1-score optimization directed the search towards maximizing correct identification of successful candidates, emphasizing sensitivity of the classification process. This makes the F1-score an objective function particularly suitable when the decision system prioritizes reducing classification errors in determining whether a candidate is ready to proceed to practical driving examination.

Among the evaluated metaheuristics, ACO achieved the highest mean AUC value, indicating superior capability in separating successful from unsuccessful candidates, whereas ABC reached the highest mean F1-score. GA demonstrated competitive performance with a significantly lower computational cost, making it suitable for applications with limited execution time.

The findings confirm that introducing the metaheuristic approach into TOPSIS substantially improves decision accuracy and removes the need for subjective weight assignment. This contributes to the development of data-driven, objective function, and scalable evaluation tools for candidate assessment in transportation safety domains. Future research may extend this work by incorporating additional machine learning models, testing hybrid optimization strategies, or validating the approach on larger datasets and real-world licensing processes.

References

Dorigo, M. & Gambardella, L.M. 1997. Ant colony system: a cooperative learning approach to the traveling salesman problem, *IEEE Transactions on Evolution-*

ary Computation, 1(1), pp. 53–66. Available at: https://doi.org/10.1109/4235.585892

Fawcett, T. 2006. An introduction to ROC analysis, Available at: https://doi.org/10.1016/j.patrec.2005.10.010

Hanley, J.A. & McNeil, B.J. 1982. The meaning and use of the area under a receiver operating characteristic (ROC) curve, *Radiology*, 143(1), pp. 29–36. Available at: https://doi.org/10.1148/radiology.143.1.7063747

Holland, J.H. 1975. Adaptation in Natural and Artificial Systems, *Ann Arbor: University of Michigan Press.*

Huang, S., Guo, Y., Zhang, X. & Li, J. 2020. Comprehensive evaluation of expressway safety based on AHP–TOPSIS–RSR. *Physica A: Statistical Mechanics and its Applications*, 551, 124–134.

Hwang, C.L. & Yoon, K. 1981. *Multiple Attribute Decision Making: Methods and Applications*. Berlin: Springer.

Kaça, G., Izmitligil, T., Koyuncu, M. & Amado, S. 2021. How well do the traffic psychological assessment systems predict on-road driving behaviour?, *Applied Cognitive Psychology*, 35(5), pp.1321–1337. Available at: https://doi.org/10.1002/acp.3867

Karaboga, D. 2005. An idea based on honey bee swarm for numerical optimization, *Technical Report TR06*, Erciyes University, Turkey.

Kubinger, K.D. 2007. Psychological test calibration using the Rasch model: some critical remarks. *Psychology Science*, 49(1), pp.49–56. Available at: https://doi.org/10.1207/s15327574ijt0504_3

Masoudi, N., Rezaei, M., Farahbakhsh, M., Zamani-Sani, H., Abdi, S. & Sadeghi-Bazargani, H. 2022. Evaluating the risk of road traffic accidents (RTAs) and the reaction time of individuals with attention deficit disorder (ADD) in the virtual environment: A study protocol using the Sahand driving simulator and the Vienna test system, *Medical Journal of Tabriz University of Medical Sciences*, 44(5), pp.367–379. Available at: https://doi.org/10.34172/mj.2022.041

Pham, D.T., Ghanbarzadeh, A., Koc, E., Otri, S., Rahim, S. & Zaidi, M. 2006. The bees algorithm — A novel tool for complex optimization problems, in: *Proceedings of the 2nd Virtual International Conference on Intelligent Production Machines and Systems (IPROMS 2006)*, pp. 454–459. Available at: https://doi.org/10.1016/B978-008045157-2/50081-X

Powers, D.M.W. 2011. Evaluation: From precision, recall and F-measure to ROC, informedness, markedness & correlation, *Journal of Machine Learning Technologies*, 2(1), pp. 37–63. Available at: https://doi.org/10.9735/2229-3981

Ren, W., Zhang, X. & Zhao, M. (2021). A comprehensive traffic risk assessment model for urban roads based on entropy–TOPSIS. *Safety Science*, 138, 105236.

Schuhfried GmbH. 2013. *Vienna Test System: User Manual*. Mödling, Austria: Schuhfried GmbH. Available at: https://www.schuhfried.com/en/

Sokolova, M. & Lapalme, G. 2009. A systematic analysis of performance measures for classification tasks, *Information Processing & Management*, 45(4), pp. 427–437. Available at: https://doi.org/10.1016/j.ipm.2009.03.002

Talbi, E.G. 2009. Metaheuristics: From Design to Implementation, *Hoboken*, New Jersey: Wiley. Available at: https://www.wiley.com/

Tinella, L., Caffò, A.O., Lopez, A., Nardulli, F., Grattagliano, I. & Bosco, A. 2021. Reassessing fitness-to-drive in drinker drivers: The role of cognition and personality, *International Journal of Environmental Research and Public Health*, 18(23), 12828. Available at: https://doi.org/10.3390/ijerph182312828

Vujadinović, J., Sarić, I. & Nikolić, R. 2025. Assessment of candidates performance in the driving test using the TOPSIS method and its modifications, in: *Proceedings of the International Symposium on Operational Research – SIMOPIS 2025*, Palić, 7–10. September 2025, pp. 225–230 (in Serbian). Available at: https://www.symopis2025.fon.bg.ac.rs/

Youden, W.J. 1950. Index for rating diagnostic tests, *Cancer*, 3(1), pp. 32–35. Available at: https://doi.org/10.1002/1097-0142(1950)3:1<32::aid-cncr2820030106>3.0.co;2-3

Метахеуристички приступ оптимизацији тежина у методи TOPSIS за процену успеха кандидата на возачком испиту

Ивана М. Сарић[а], *Јасмина* Ц. Вујадиновић[б], *Рале* М. Николић[в]

[а] Универзитет у Београду, Технолошко-металуршки Факултет, Катедра за Математичке науке, Београд, Република Србија

[б] Универзитет одбране у Београду, Војна академија, Катедра Природно-математичких наука, Београд, Република Србија
аутор за преписку

[в] Универзитет одбране у Београду, Војна академија, Катедра Природно-математичких наука, Београд, Република Србија

ОБЛАСТ: математика, вишекритеријумско одлучивање, когнитивна процена у евалуацији кандидата за возача
КАТЕГОРИЈА (ТИП) ЧЛАНКА: оригинални научни рад

Сажетак:

Увод/циљ: Безбедност у саобраћају и поуздана селекција возача представљају важан сегмент савременог друштва. Циљ овог рада је унапређење поступка процене успешности кандидата на возачком испиту применом вишекритеријумских метода одлучивања и метахеуристичке оптимизације. На основу резултата добијених тестом Vienna Test System, предложена је примена методе TOPSIS са адаптивним одређивањем тежина критеријума.

Методе: Тежински коефицијенти методе TOPSIS оптимизовани су помоћу три метахеуристичка алгоритма – генетског алгоритма (GA), алгоритма мрављих колонија (ACO) и алгоритма пчелињих колонија (ABC). Током оптимизације коришћене су две различите функције циља: AUC и F1-score, како би се испитало њихово дејство на тачност и стабилност модела. Експериментални оквир обухвата три сегмента: (1) поређење перформанси GA, ACO и ABC метахеуристика за AUC функцију циља, (2) аналогно поређење за F1-score функцију циља и (3) међусобну анализу AUC и F1-score оптимизованих модела.

Резултати: Указано је да избор метахеуристичког алгоритма и функције циља знатно утичу на перформансе методе TOPSIS. Оптимизација са AUC функцијом циља довела је до стабилнијих модела и бољег баланса између успешних и неуспешних кандидата, док је оптимизација са F1-score функцијом циља постигла већу осетљивост и бољу идентификацију успешних кандидата.

Закључак: Увођење метахеуристичких алгоритама у оптимизацију тежина методе TOPSIS омогућава адаптивно и поузданије рангирање кандидата, чиме се доприноси развоју интелигентних система за селекцију возача и унапређењу безбедности у саобраћају. Добијени резултати потврђују да се правилним избором функције циља и алгоритма оптимизације мсже постићи знатно побољшање тачности модела.

Кључне речи: TOPSIS, метахеуристике, GA, ACO, ABC, F1-score, AUC, Vienna Test System, вишекритеријумско одлучивање.

Paper received on: 13.11.2025.
Manuscript corrections submitted on: 05.12.2025.
Paper accepted for publishing on: 26.12.2025.

VOJNOTEHNIČKI GLASNIK / MILITARY TECHNICAL COURIER, 2025, Vol. 73, Issue 4

ORIGINAL SCIENTIFIC PAPERS

On modified enriched versions of the Browder-Göhde-Kirk fixed point theorem

Divyanshu Chamoli[a], *Shivam* Rawat[b], *Monika* Bisht[c], *R.C.* Dimri[d]

[a] H.N.B. Garhwal University, Srinagar (Garhwal), Uttarakhand 246174, India,
e-mail: divyanshuchamoli@gmail.com,
ORCID iD: https://orcid.org/0009-0006-0226-0078

[b] Department of Mathematics, Graphic Era (Deemed to be University), Dehradun, Uttarakhand, 248002, India,
e-mail: rawat.shivam09@gmail.com, **corresponding author**,
ORCID iD: https://orcid.org/0000-0002-5927-2524

[c] Department of Mathematics, Graphic Era Hill University, Dehradun, Uttarakhand, 248001, India,
e-mail: monikabisht391@gmail.com,
ORCID iD: https://orcid.org/0000-0003-4688-4342

[d] H.N.B. Garhwal University, Srinagar (Garhwal), Uttarakhand 246174, India,
e-mail: dimrirc@gmail.com,
ORCID iD: https://orcid.org/0000-0001-5392-9428

https://doi.org/10.5937/vojtehgxx-56938

FIELD: mathematics
ARTICLE TYPE: original scientific paper

Abstract:

Introduction/Purpose: In this paper, a modified enriched version of the classical Browder-Göhde-Kirk fixed point theorem in the setting of uniformly convex Banach spaces was proposed. This work aimed to extend fundamental fixed-point results to broader classes of mappings, contributing to the ongoing development of fixed-point theory and its applications in nonlinear analysis.

Methods: A modified enriched asymptotically nonexpansive mappings was introduced and analytical techniques from functional analysis and metric fixed-point theory were employed. This study leverages the geometric properties of uniformly convex Banach spaces to establish new existence and convergence results.

Results: Several key theorems extending the Goebel–Kirk fixed point theorem for modified enriched asymptotically nonexpansive mappings were proved. The results demonstrated the existence of fixed points under weaker assumptions, generalizing classical outcomes in this framework.

Conclusions: The findings provided a significant advancement in fixed-point theory, particularly for enriched mappings in uniformly convex Banach spaces. These results have potential applications in nonlinear analysis.

Key words: uniformly convex Banach spaces, nonexpansive map, convex set, fixed point

Introduction

As a fundamental principle of nonlinear analysis, fixed point theory finds remarkable applicability in mathematics and its applications, including optimization, game theory, and differential equations. A classical result in this topic is the Browder-Göhde-Kirk fixed point theorem which guarantees existence of fixed points of nonexpansive mappings on uniformly convex Banach spaces. This theorem has been improved and extended by weakening its assumptions or generalizing its range of applicability to larger classes of mappings over the years.

Several researchers have expanded upon the idea that a continuous mapping on a convex set that fulfills a restricted Lipschitz condition must also be Lipschitz continuous (see (Matkowski, 2007)). Many generalizations of the Browder-Göhde-Kirk theorem have been established on the basis of this observation (Browder: (Browder, 1965), Göhde: (Göhde, 1965), Kirk: (Kirk, 1965), and see also (Granas & Dugundji, 1982), (Goebel & Reich, 1984), (Reich, 1976), (Reich, 1980)).

Two extensions of the Browder-Göhde-Kirk theorem were shown in (Matkowski, 2022). The first one says that if a mapping T satisfies a nonlinear Lipschitz-type inequality, there is a fixed point. The second result claims that if T is continuous and there exists a positive sequence (t_n) of real numbers converging to zero and such that this implication holds for every $n \in \mathbb{N}$ and $u, v \in C$, then there exists a fixed point of T. This work helps to highlight the link between contractive mappings and fixed point theorems.

Recently, Berinde (Berinde, 2019, 2020) has extended the literature related to Banach space by introducing enrichments to mappings of con-

tractive types. Enriched contractions (Berinde & Pacurar, 2020) refer to self-mappings T on the structure U of a normed linear space $(U, \| \ . \ \|)$. These mappings adhere to a symmetric contraction condition, expressed as $\| b(u-v) + Tu - Tv \| \leq \theta \| u - v \|$, where $\theta \in [0, b+1)$ and $b \in [0, \infty)$, for each $u, v \in U$. Undoubtedly, the category of enriched contractions is more extensive, encompassing not only the conventional Banach contractions (where $b = 0$) but also incorporating Lipschitz-type and nonexpansive mappings. The broader scope of the enriched contraction, which is an extension of Banach contractions, reinforces the assertion that within the Banach space context, a fixed point x^* is guaranteed to exist, and the Krasnoselskij iteration offers an approach to approximate the fixed point. This assertion has been substantiated by Berinde and Păcurar (Berinde & Pacurar, 2020). Recent years have seen an increasing interest in expanding the theory of enriched type contractions (Rawat et al., 2023).

Recently, Anjum and Abbas (Anjum & Abbas, 2024) analysed it and concluded that the idea of enriched nonexpansive mappings needs further reconsideration, because it coincides with the concept of nonexpansive mappings. Working in this direction, they defined a modified class of enriched nonexpansive mappings, and gave some fixed point results.

These developments emphasize how important it is to expand the scope of classical fixed point theorems to include more extensive contractive conditions. Our study expands on these discoveries by putting forth a brand-new enriched contractive framework that consolidates and generalizes a number of earlier findings, strengthening our knowledge of fixed point theory and its uses.

In this paper, we will generalize the Browder-Göhde-Kirk theorem by providing an enriched version of the contractive condition. Our generalization increases the usefulness of the theorem without overhauling its core structure. In particular, fixed point results are obtained under enriched Lipschitz-type conditions, which allows us to provide a much broader setting to examine nonexpansive and related classes of operators. This refinement is motivated by recent progress in the theory of metric fixed points, where more general and powerful results have been obtained by relaxing strict contractive assumptions.

Preliminaries

In this section, we give some preliminary results for subsequent use.

DEFINITION 1. *Let $(U, \|.\|)$ be a real normed vector space. It is called uniformly convex, if there is some $\delta > 0$ for every $\epsilon \in (0, 2]$, such that $\|x - y\| \geq \epsilon$ implies that $\|\frac{u+v}{2}\| \leq 1 - \delta$ for any two vectors $u, v \in U$ with $\|u\| = \|v\| = 1$.*

The fixed point theorem given by Browder, Göhde and Kirk is stated as follows.

THEOREM 1. *Let U be a uniformly convex Banach space and $T : C \to C$ be a nonexpansive mapping, where C is a non-empty, bounded, convex and closed subset of U. Then T has at least one fixed point in C.*

In (Berinde, 2019), Berinde generalized the scope of nonexpansive mappings by introducing and analysing a new set of mappings called the set of enriched nonexpansive mappings.

DEFINITION 2. *Let $(U, \|.\|)$ be a normed linear space and $T : U \to U$ be a mapping. If there exists $b \in [0, \infty)$ so that*

$$\|b(u - v) + Tu - Tv\| \leq (b + 1)\|u - v\|, \forall\, u, v \in U, \tag{1}$$

then T is known as an enriched nonexpansive mapping.

The set of enriched nonexpansive mappings is strictly bigger than the set of nonexpansive mappings, according to (Berinde, 2019). In fact, the concept of a nonexpansive mapping is obtained when $b = 0$ is specified in (1).

EXAMPLE 1. Consider a self-mapping T on $\mathbb{R}$ such that

$$T(u) = \frac{u}{2} + \frac{1}{2}.$$

For $b = 1$, we get

$$\|b(u - v) + Tu - Tv\| = \|u - v + \frac{u}{2} - \frac{v}{2}\| = \frac{3}{2}\|u - v\|.$$

Thus, T satisfies (1) with $b = 1$ and is an enriched nonexpansive mapping, but not necessarily nonexpansive.

REMARK 1. (Berinde & Pacurar, 2020) Let U be a normed space space and T be a self-mapping on U, then an averaged mapping T_λ for any $\lambda \in (0, 1)$

is obtained by

$$T_\lambda u = (1-\lambda)u + \lambda Tu, \forall u \in U. \tag{2}$$

Moreover,

$$Fix(T_\lambda) = \{u \in U : T_\lambda u = u\} = \{u \in U : Tu = u\} = Fix(T). \tag{3}$$

The b-enriched nonexpansive condition can be reformulated as a nonexpansive mapping condition, as demonstrated by the authors in (Anjum & Abbas, 2024). Thus, the writers made the following changes to the definition.

DEFINITION 3. *Consider a normed space $(U, \|.\|)$ and a mapping $T : U \to U$. If for some $b \in [0, +\infty)$ the following condition holds*

$$\|b(u-v) + Tu - Tv\| \leq \|u - v\|, \forall\, u, v \in U,$$

then T is called a b-modified enriched nonexpansive or modified enriched nonexpansive mapping.

This refined condition ensures a stronger form of contraction, leading to the next fixed point theorem.

THEOREM 2. *Let $T : U \to U$ be a modified enriched nonexpansive mapping with $b \neq 0$, where $(U, \|.\|)$ is a Banach space. Then*

1. *$Fix(T) = \{u^*\}$.*
2. *$\lambda \in (0, 1)$ exists such that, for any initial guess $u_0 \in U$, the Krasnoselskii iteration related to T, namely the sequence $\{u_n\}_{n=0}^{\infty}$, provided by $u_{n+1} = (1-\lambda)u_n + \lambda Tu_n, n \geq 0$, converges to u^*.*

DEFINITION 4. *Let U be a Banach space and $C \subset U$. A transformation $T : C \to C$ is known as an asymptotically nonexpansive if for every $u, v \in C$,*

$$\|T^i u - T^i v\| \leq L_i \|u - v\|, \quad u, v \in C,$$

where $\{L_i\}$ is a sequence of real numbers satisfying $\lim_{i\to\infty} L_i = 1$.

In (Kirk, 1965), Goebel and Kirk proved the following result.

THEOREM 3. *Let U be a uniformly convex Banach space and T be an asymptotically nonexpansive self-mapping on C, where $C \subset U$ is a nonempty, convex, bounded and closed set. Then T has a fixed point.*

Main results

LEMMA 1. *Let U, V be normed spaces, $T : C \to V$ be a mapping where $C \subset U$ is a convex set, $b \in [0, \infty)$ and a real function $\beta : (0, \infty) \to [0, \infty)$ such that*

$$\|b(u - v) + Tu - Tv\| \leq \beta(\|u - v\|), \tag{4}$$

for all $u, v \in C$ and $u \neq v$. If

$$\limsup_{t \to 0^+} \frac{\beta(t)}{t} < +\infty, \tag{5}$$

then

$$\|b(u - v) + Tu - Tv\| \leq L\|u - v\|, \ u, v \in C, \tag{6}$$

where $\liminf_{t \to 0^+} \frac{\beta(t)}{t} = L$.

Proof. Taking $\lambda = \frac{1}{b+1}$, we get $b = \frac{1-\lambda}{\lambda}$, using which (4) reduces to

$$\|(1 - \lambda)(u - v) + \lambda Tu - \lambda Tv\| \leq \lambda\beta(\|u - v\|),$$

that is,

$$\|T_\lambda u - T_\lambda v\| \leq \lambda\beta(\|u - v\|), \tag{7}$$

where $T_\lambda u = (1 - \lambda)u + \lambda Tu$.

Clearly, T_λ is continuous from equations (5) and (7). Also, from equation (5), for fixed $x, y \in C$ with $x \neq y$ and $\epsilon > 0$, there exists $t_\epsilon > 0$ such that

$$\frac{\beta(t)}{t} \leq L + \epsilon, \text{ for all } t \in (0, t_\epsilon] \tag{3}$$

and define $n(\epsilon) = \left\lfloor \frac{\|u-v\|}{t_\epsilon} \right\rfloor$.

Now, define the sequence $\{z_k\}$ as follows:

$$z_k = \left(1 - \frac{k}{n(\epsilon)}\right) u + \frac{k}{n(\epsilon)} v, \quad k = 0, 1, \ldots, n(\epsilon).$$

Since C is convex, there exists $z_k \in C$ for all k. Moreover,

$$\|z_{k+1} - z_k\| = \frac{1}{n(\epsilon)}\|u - v\| \in (0, t_\epsilon], \quad \text{for all } k = 0, \ldots, n(\epsilon) - 1.$$

Chamoli, D. et al., On modified enriched versions of the Browder-Göhde-Kirk fixed point theorem, pp.1222–1238

Also $z_0 = u, z_{n(\epsilon)} = v$, and

$$\|u - v\| = \sum_{k=0}^{n(\epsilon)-1} \|z_{k+1} - z_k\|.$$

Using the triangle inequality and condition (7), one obtains

$$\begin{aligned}
\|T_\lambda u - T_\lambda v\| &= \left\| \sum_{k=0}^{n(\epsilon)-1} (T_\lambda z_k - T_\lambda z_{k+1}) \right\| \\
&\leq \sum_{k=0}^{n(\epsilon)-1} \|T_\lambda z_k - T_\lambda z_{k+1}\| \\
&\leq \sum_{k=0}^{n(\epsilon)-1} \beta(\|z_k - z_{k+1}\|) \\
&\leq \lambda \sum_{k=0}^{n(\epsilon)-1} \beta\left(\frac{\|u - v\|}{n(\epsilon)}\right) \\
&\leq \lambda n(\epsilon) \beta\left(\frac{\|u - v\|}{n(\epsilon)}\right) \\
&\leq \lambda n(\epsilon)(L + \epsilon)\left(\frac{\|u - v\|}{n(\epsilon)}\right) \\
&= \lambda(L + \epsilon)\|u - v\|.
\end{aligned}$$

Taking $\epsilon \to 0$ in the inequality above, one obtains

$$\|T_\lambda u - T_\lambda v\| \leq \lambda L \|u - v\|.$$

This further implies

$$\begin{aligned}
\|(1 - \lambda)(u - v) + \lambda T u - \lambda T v\| &\leq \lambda L \|u - v\| \\
\|b(u - v) + T u - T v\| &\leq L \|u - v\|.
\end{aligned}$$

This concludes the proof. □

LEMMA 2. *Let U, V be real normed spaces and $T : C \to V$ be a continuous mapping, where $C \subset U$ is a bounded convex set. If there exists some*

$b \in [0, \infty)$, *a non-negative real* L *and two positive sequences* $(c_n), (t_n)$ *satisfying*

$$\lim_{n\to\infty} c_n = L \text{ and } \lim_{n\to\infty} t_n = 0,$$

so that for all $u, v \in C$ *and* $n \in \mathbb{N}$,

$$\|u - v\| \leq t_n \implies \|b(u - v) + T(u) - T(v)\| \leq c_n t_n, \tag{8}$$

then T *satisfies*

$$\|b(u - v) + Tu - Tv\| \leq L\|u - v\|, u, v \in C.$$

Proof. Taking $\lambda = \frac{1}{b+1}$, we get $b = \frac{1-\lambda}{\lambda}$, using which (8) reduces to

$$\|(1 - \lambda)(u - v) + \lambda Tu - \lambda Tv\| \leq \lambda c_n t_n,$$

that is,

$$\|u - v\| \leq t_n \implies \|T_\lambda u - T_\lambda v\| \leq \lambda c_n t_n, \tag{9}$$

where $T_\lambda u = (1 - \lambda)u + \lambda Tu$.

Let $u, v \in C$ such that $u \neq v$. Since C is convex and bounded, for any $n \in \mathbb{N}$, define an integer $k_n \in \mathbb{N}$ such that

$$(k_n - 1)t_n < \|u - v\| \leq k_n t_n.$$

Now define a partition of the segment from u to v into k_n equal parts

$$z_k = (1 - \frac{k}{k_n})u + \frac{k}{k_n}v, \text{ for } k = 0, 1, 2, ..., k_n.$$

Then each $z_k \in C$ by convexity, and $\|z_{k+1} - z_k\| = \frac{1}{k_n}\|u - v\| \leq t_n$, equation (9) implies that $\|T_\lambda z_{k+1} - T_\lambda z_k\| \leq \lambda c_n t_n$.
Also $z_0 = u, z_{k_n} = v$, and

$$\begin{aligned} \|z_{k_n-1} - v\| &= \left\| \left(1 - \frac{k_n - 1}{k_n}\right) u + \frac{k_n - 1}{k_n} v - v \right\| \\ &= \frac{1}{k_n} \|u - v\| < t_n. \end{aligned} \tag{10}$$

Using the triangle inequality and condition (9), one obtains

$$\|T_\lambda u - T_\lambda v\| = \left\| \sum_{k=0}^{k_n-2} (T_\lambda z_k - T_\lambda z_{k+1}) + (T_\lambda z_{k_n-1} - T_\lambda v) \right\|$$

$$\leq \sum_{k=0}^{k_n-2} \|T_\lambda z_k - T_\lambda z_{k+1}\| + \|T_\lambda z_{k_n-1} - T_\lambda v\|$$
$$\leq \sum_{k=0}^{k_n-2} \lambda c_n t_n + \|T_\lambda z_{k_n-1} - T_\lambda v\|$$
$$= \lambda c_n t_n (k_n - 1) + \|T_\lambda z_{k_n-1} - T_\lambda v\|. \tag{11}$$

Now, from (10), we obtain $\|z_{k_n-1} - v\| < t_n$. Therefore, we have $\lim_{n\to\infty} \|z_{k_n-1} - v\| = 0$ and, in view of the continuity of T_λ, $\lim_{n\to\infty} \|T_\lambda z_{k_n-1} - T_\lambda v\| = 0$. Also, taking into account that $(k_n - 1)t_n \leq \|u - v\|$, from (11) on taking $n \to \infty$, one obtains

$$\|T_\lambda u - T_\lambda v\| \leq \lambda L \|u - v\|.$$

This further implies

$$\|(1-\lambda)(u-v) + \lambda T u - \lambda T v\| \leq \lambda L \|u - v\|$$
$$\|b(u-v) + Tu - Tv\| \leq L\|u - v\|.$$

This concludes the proof. □

LEMMA 3. *Let U, V be real normed spaces and $T : C \to V$ be a continuous mapping, where $C \subset U$ is a bounded convex set. If there exist a non-negative real L, some $b \in [0, \infty)$, a function $\beta : (0, \infty) \to [0, \infty)$, and a positive sequence (t_n) of real numbers with $\lim_{n\to\infty} t_n = 0$ and satisfying*

$$\lim_{n\to\infty} \frac{\beta(t_n)}{t_n} = L,$$

so that for all $u, v \in C$ and $n \in \mathbb{N}$,

$$\|u - v\| = t_n \implies \|b(u-v) + Tu - Tv\| \leq \beta(\|u - v\|),$$

then T satisfies

$$\|b(u-v) + Tu - Tv\| \leq L\|u - v\|, u, v \in C.$$

Proof. Taking $c_n = \frac{\beta(t_n)}{t_n}$, we obtain $\lim_{n\to\infty} c_n = L$. As for every $n \in \mathbb{N}$ and $u, v \in C$, $\|b(u-v) + Tu - Tv\| \leq \beta(t_n) = c_n t_n$ if $\|u - v\| = t_n$, so the result follows from Lemma 2. □

THEOREM 4. *Let U be a uniformly convex Banach space and T be a self-mapping on C, where $C \subset U$ is a nonempty, convex, bounded and closed set. If there exists $b \in [0, \infty)$ and a function $\beta : (0, \infty) \to [0, \infty)$ for which*

$$\|b(u - v) + Tu - Tv\| \leq \beta(\|u - v\|), u, v \in C, u \neq v,$$

and

$$\limsup_{t \to 0^+} \frac{\beta(t)}{t} < +\infty, \ \liminf_{t \to 0^+} \frac{\beta(t)}{t} = 1,$$

then,

1. $Fix(T) \neq \emptyset$.
2. *For $b \in (0, \infty)$ the fixed point is uniquely determined. Moreover, $\lambda \in (0, 1)$ exists such that, for any initial guess $u_0 \in U$, the Krasnoselskii iteration related to T, namely the sequence $\{u_n\}_{n=0}^{\infty}$, provided by*

$$u_{n+1} = (1 - \lambda)u_n + \lambda T u_n, n \geq 0, \tag{12}$$

converges to u^*.

Proof. Applying Lemma 1 with $L = 1$, we get

$$\|b(u - v) + Tu - Tv\| \leq \|u - v\|, \quad u, v \in C.$$

Setting $\lambda = \frac{1}{b+1}$, we derive $b = \frac{1-\lambda}{\lambda}$, which leads to

$$\|T_\lambda u - T_\lambda y\| \leq \lambda \|u - v\|, \quad u, v \in C.$$

If $b \in (0, \infty)$, i.e. $\lambda < 1$, then this indicates that the averaged operator T_λ satisfies the Banach contraction principle. The Krasnoselskij iterative sequence $\{u_n\}_{n=0}^{\infty}$, defined by (12), coincides with the Picard iteration for T_λ, i.e.,

$$u_{n+1} = T_\lambda u_n, \quad n \geq 0. \tag{13}$$

Since T_λ is a Banach contraction mapping on U, where U is a Banach space, the Banach fixed-point theorem guarantees that T_λ has a unique fixed point, denoted by $u^* \in U$, and the Picard iteration related with T_λ, as defined in (13), converges to u^*. Also, if $\lambda = 1$, then T_λ is a nonexpansive mapping, so from the Browder-Göhde-Kirk fixed point theorem T_λ has a fixed point. Furthermore, from equation (3), we conclude that T also has a fixed point. □

EXAMPLE 2. Let the sets $U = V = \mathbb{R}$ with the norm $\|.\|$, $C = [0, 1]$ and $b = \frac{1}{2}$. Define a function $T : C \to C$ as follows

$$T(u) = \frac{u}{2},$$

where $u \in C$. Now, for any two $u, v \in C$, $T(u) = \frac{u}{2}$ and $T(v) = \frac{v}{2}$. So,

$$\begin{aligned} \|b(u-v) + Tu - Tv\| &= \left\| \frac{1}{2}(u-v) + \frac{u}{2} - \frac{v}{2} \right\| \\ &= \|(u-v)\| \end{aligned}$$

Now, on defining $\beta(t) = t$, we obtain

$$\|b(u-v) + T(u) - T(v)\| \leq \beta(\|u-v\|).$$

Also, $\limsup_{t\to 0+} \frac{\beta(t)}{t} = 1$, and $\liminf_{t\to 0+} \frac{\beta(t)}{t} = 1$. Clearly, all the assumptions of the theorem are satisfied and therefore, $u = 0$ is a unique fixed point of T.

THEOREM 5. *Let U be a uniformly convex Banach space and T be a continuous self-mapping on C, where $C \subset U$ is a nonempty, convex, bounded and closed set. If there exists some $b \in [0, \infty)$, a function $\beta : (0, \infty) \to [0, \infty)$ and a sequence of positive real (t_n), $\lim_{n\to\infty} t_n = 0$ satisfying the condition*

$$\lim_{n\to\infty} \frac{\beta(t_n)}{t_n} = 1,$$

so that for all $u, v \in C$ and for every $n \in \mathbb{N}$,

$$\|u-v\| = t_n \implies \|b(u-v) + T(u) - T(v)\| \leq \beta(\|u-v\|),$$

then,

1. *$Fix(T) \neq \emptyset$.*
2. *for $b \in (0, \infty)$ the fixed point is uniquely determined. Moreover, $\lambda \in (0, 1)$ exists such that, for any initial guess $u_0 \in U$, the Krasnoselskii iteration related to T, namely the sequence $\{u_n\}_{n=0}^{\infty}$, provided by*

$$u_{n+1} = (1-\lambda)u_n + \lambda T u_n, n \geq 0, \tag{14}$$

converges to u^*.

Proof. Applying Lemma 2 with $L = 1$, we get

$$\|b(u - v) + Tu - Tv\| \leq \|u - v\|, \quad u, v \in C.$$

Setting $\lambda = \frac{1}{b+1}$, we derive $b = \frac{1-\lambda}{\lambda}$, which leads to

$$\|T_\lambda u - T_\lambda v\| \leq \lambda \|u - v\|, \quad u, v \in C.$$

If $b \in (0, \infty)$, i.e. $\lambda < 1$ it indicates that the averaged operator T_λ satisfies the Banach contraction principle. If $\lambda = 1$, then T_λ is a nonexpansive mapping. The rest of the reasoning is same as of Theorem 4. □

Now, we define modified enriched asymptotically nonexpansive mapping in a Banach space U.

DEFINITION 5. *Let C be a subset of a Banach space U. A transformation $T : C \to C$ is said to be modified enriched asymptotically nonexpansive if for some $b \in [0, \infty)$ and for each $u, v \in C$,*

$$\|b(u - v) + T^i u - T^i v\| \leq L_i \|u - v\|, \quad u, v \in C,$$

where $\{L_i\}$ is a sequence of real numbers satisfying $\lim_{i\to\infty} L_i = 1$.

THEOREM 6. *Let C be a nonempty, convex, closed and bounded subset of a uniformly convex Banach space U, and $T : C \to C$ be a modified enriched asymptotically nonexpansive. Then*

1. *$Fix(T) \neq \emptyset$.*
2. *for $b \in (0, \infty)$ the fixed point is uniquely determined. Moreover, $\lambda \in (0, 1)$ exists such that, for any initial guess $u_0 \in U$, the Krasnoselskii iteration related to T, namely the sequence $\{u_n\}_{n=0}^{\infty}$, provided by*

$$u_{n+1} = (1 - \lambda)u_n + \lambda T u_n, n \geq 0, \tag{15}$$

converges to u^*.

Proof. Setting $\lambda = \frac{1}{b+1}$, we derive $b = \frac{1-\lambda}{\lambda}$. So the modified enriched asymptotically nonexpansive condition reduces to

$$\|(1 - \lambda)(u - v) + \lambda T^i u - \lambda T^i v\| \leq \lambda L_i \|u - v\|,$$

i.e.,

$$\|T_\lambda^i u - T_\lambda^i v\| \leq \lambda L_i \|u - v\|, \quad u, v \in C.$$

Now, since $\lim_{i\to\infty} L_i = 1$, therefore $\lim_{i\to\infty} \lambda L_i = \lambda \leq 1$. If $b \in (0,\infty)$, then $\lambda < 1$ which indicates that for i large enough, the averaged operator T_λ^i satisfies the Banach contraction principle. If $b = 0$, then $\lambda = 1$ which indicates that for i large enough, the averaged operator T_λ^i satisfies the Browder-Göhde-Kirk fixed point theorem. The rest of the reasoning is the same as of Theorem 4. □

REMARK 2. Also note that if $\lim_{i\to\infty} L_i < 1$, then also T_λ^i satisfies the Banach contraction principle, i.e. T_λ has a unique fixed point. Furthermore, from (3), we conclude that T also has a unique fixed point.

THEOREM 7. *Let U be a uniformly convex Banach space and T be a self-mapping on C, where $C \subset U$ is a nonempty, convex, bounded and closed set. Assume that T is a modified enriched nonlinear asymptotically nonexpansive mapping, i.e., for all $i \in \mathbb{N}$, a function $\beta_i : (0,\infty) \to (0,\infty)$ exists, such that*

$$\|b(u-v) + T^i u - T^i v\| \leq \beta_i(\|u-v\|), u, v \in C, u \neq v,$$

and

$$\limsup_{t\to 0^+} \frac{\beta_i(t)}{t} < +\infty \text{ and } \liminf_{t\to 0^+} \frac{\beta_i(t)}{t} = L_i, i \in \mathbb{N},$$

where the sequence (L_i) converges with $\lim_{i\to\infty} L_i \leq 1$. Then

1. *$Fix(T) \neq \emptyset$.*
2. *for $b \in (0,\infty)$ the fixed point is uniquely determined. Moreover, $\lambda \in (0,1)$ exists such that, for any initial guess $u_0 \in U$, the Krasnoselskii iteration related to T, namely the sequence $\{u_n\}_{n=0}^{\infty}$, provided by*

$$u_{n+1} = (1-\lambda)u_n + \lambda T u_n, n \geq 0, \tag{16}$$

converges to u^*.

Proof. Using Lemma 1 with T^i in place of T, and L_i in place of L, for every $i \in \mathbb{N}$, we get

$$\|b(u-v) + T^i u - T^i v\| \leq L_i \|u-v\|, \ u, v \in C. \tag{17}$$

Now if $\lim_{i\to\infty} L_i = 1$, then clearly T is a modified enriched asymptotically nonexpansive mapping as given in Definition 5. So, from Theorem 6 the results follow. If $\lim_{i\to\infty} L_i < 1$ then from Remark 3.7, the results follow. □

THEOREM 8. *Let U be a uniformly convex Banach space and T be a continuous self-mapping on C, where $C \subset U$ is a nonempty, convex, bounded and closed set. Suppose, for all $i \in \mathbb{N}$ a function $\beta_i : (0,\infty) \to (0,\infty)$ and a sequence $(t_{i,n} : n \in \mathbb{N})$ with $\lim_{n\to\infty} t_{i,n} = 0$ exists, satisfying the condition*

$$\lim_{n\to\infty} \frac{\beta(t_{i,n})}{t_{i,n}} = L_i,$$

so that for all $x, y \in C$ and for every $n \in \mathbb{N}$,

$$\|u - v\| = t_{i,n} \implies \|b(u - v) + T^i(u) - T^i(v)\| \leq \beta_i(\|u - v\|),\ i \in \mathbb{N}.$$

If $L = \lim_{i\to\infty} L_i \leq 1$, then

1. *$Fix(T) \neq \emptyset$.*
2. *for $b \in (0,\infty)$ the fixed point is uniquely determined. Moreover, $\lambda \in (0,1)$ exists such that, for any initial guess $u_0 \in U$, the Krasnoselskii iteration related to T, namely the sequence $\{u_n\}_{n=0}^{\infty}$, provided by*

$$u_{n+1} = (1 - \lambda)u_n + \lambda T u_n, n \geq 0, \tag{18}$$

converges to u^*.

Proof. Based on Lemma 3, the mapping T^i satisfies

$$\|b(u - v) + T^i u - T^i v\| \leq L_i \|u - v\|, \text{ for all } i \in \mathbb{N} \text{ and } u, v \in C. \tag{19}$$

Now if $\lim_{i\to\infty} L_i = 1$, then clearly T is a modified enriched asymptotically nonexpansive mapping as given in Definition 5. So, from Theorem 6 the results follow. If $\lim_{i\to\infty} L_i < 1$ then from Remark 3.7, the results follow. □

References

Anjum, R., & Abbas, M. 2024. Remarks on b-enriched nonexpansive mappings, arXiv preprint arXiv:2405.07999. Available at: https://doi.org/10.48550/arXiv.2405.07999

Berinde, V. 2019. Approximating fixed points of enriched nonexpansive mappings by Krasnoselskii iteration in Hilbert spaces, *Carpathian Journal of Mathematics*, 35(3), pp.293-304. Available at: https://www.jstor.org/stable/26905206

Berinde, V., & Pacurar, M. 2020. Approximating fixed points of enriched contractions in Banach spaces, *Journal of Fixed Point Theory and Applications*, 22, 10. Available at: https://doi.org/10.1007/s11784-020-0769-9

Berinde, V. 2020. Approximating fixed points of enriched nonexpansive mappings in Banach spaces by using a retraction-displacement condition, *Carpathian Journal of Mathematics*, 36, pp.27-34. Available at: https://www.jstor.org/stable/26898779

Browder, F.E. 1965. Nonexpansive nonlinear operators in a Banach space, *Proceedings of the National Academy of Sciences of the USA*, 54, pp.1041-1044. Available at: https://doi.org/10.1073/pnas.54.4.104

Goebel, K., & Kirk, W. A. 1972. A fixed point theorem for asymptotically nonexpansive mappings, *Proceedings of the American Mathematical Society*, 35(1), pp.171-174. Available at: https://doi.org/10.1090/S0002-9939-1972-0298500-3

Goebel, K., & Reich, S. 1984. Uniform Convexity, Hyperbolic Geometry and Nonexpansive Mappings, *Series of Monographs and Textbooks in Pure and Applied Mathematics*, Dekker, New York. ISBN: 0824772237.

Göhde, D. 1965. Zum Prinzip der kontraktiven Abbildung, *Mathematische Nachrichten*, 28, pp.251-258. Available at: https://doi.org/10.1002/mana.19650300312

Granas, A., & Dugundji, J. 1982. Fixed Point Theory, *Monografie Matematyczne, Polska Akademia Nauk, War-szawa*, 1. ISBN: 0387001735, 9780387001739. Available at: https://archive.org/details/fixed-point-theory/mode/2up

Kirk, W. A. 1965. A fixed point theorem for mappings which do not increase distances, *American Mathematical Monthly*, 72, pp.1004-1006. Available at: https://doi.org/10.2307/2313345

Matkowski, J. 2007. Remarks on Lipschitzian mappings and some fixed point theorems, *Banach Journal of Mathematical Analysis*, 2, pp.237-244. Available at: 10.15352/bjma/1240336222

Matkowski, J. 2022. A refinement of the Browder–Göhde–Kirk fixed point theorem and some applications, *Journal of Fixed Point Theory and Applications*, 24, 70. Available at: https://doi.org/10.1007/s11784-022-00985-2

Rawat, S., Bartwal, A. & Dimri, R.C. 2023. Approximation and existence of fixed points via interpolative enriched contractions, *Filomat*, 37(16), pp.5455-5467. Available at: https://doiserbia.nb.rs/img/doi/0354-5180/2023/0354-5180231645 5R.pdf

Reich, S. 1976. The fixed point property for nonexpansive mappings, I, *American Mathematical Monthly*, 83(4), pp.266-268. Available at: https://www.tandfonline.com/doi/pdf/10.1080/00029890.1976.11994096

Reich, S. 1980. The fixed point property for nonexpansive mappings, II, *American Mathematical Monthly*, 87, pp.292-294. Available at: https://www.tandfonline.com/doi/pdf/10.1080/00029890.1980.11995019

О модификованим обогаћеним верзијама Browder-Göhde-Kirk теореме непокретне тачке

Дивјаншу Чамоли[а], *Шивам* Рават[б] **аутор за преписку**, *Моника* Бишт[ц],
Р.С. Димри[а]

[а] Универзитет H.N.B. Гарвал, Шринагар Гарвал, Утаракханд 246174, Индија

[б] Катедра за математику, Универзитет Graphic Era (са статусом „Deemed to be“), Дехрадун, Утаракханд, 248002, Индија.

[ц] Катедра за математику, Универзитет Graphic Era Hill, Дехрадун, Утаракханд, 248001, Индија.

ОБЛАСТ: математика
КАТЕГОРИЈА (ТИП) ЧЛАНКА: оригинални научни рад

Сажетак:

Увод/циљ: У раду се предлаже модификована обогаћена верзија класичне Browder-Göhde-Kirk теореме непокретне тачке у оквиру униформно конвексних Банахових простора. Циљ рада је проширење основних резултата о непокретним тачкама на шире класе пресликавања чиме се доприноси континуираном развоју теорије непокретне тачке и њеним применама у нелинарној анализи.

Методе: Уведена су модификована обогаћена асимптотски неекспанзивна пресликавања, а коришћене су аналитичке технике функционалне анализе и метричке теорије непокретне тачке. Ово истраживање користи геометријске особине униформно конвексних Банахових простора за успостављање нових резултата о постојању и конвергенцији.

Резултати: Доказано је неколико кључних теорема које проширују Goebel–Kirk теорему непокретне тачке за модификована обогаћена асимптотски неекспанзивна пресликавања. Резултати показују постојање непокрентних тачака под слабијим претпоставкама, генерализујући класичне исходе у овом оквиру.

Закључци: Добијени резултати представљају значајан напредак у теорији непокретне тачке, нарочито када је реч о обогаћеним пресликавањима у униформно конвексним Банаховим просторима. Ови резултати могу се применити у нелинеарној анализи.

Кључне речи: униформно конвексни Банахови простори, неекспанзивно пресликавање, конвексни скуп, непокретна тачка

Paper received on: 21.02.2025.
Manuscript corrections submitted on: 29.05.2025.
Paper accepted for publishing on: 30.05.2025.

Topological indices and structural properties of ideal-based unit graphs in commutative rings

Veerappan Rajkumar [a], *Balasubramanian* Sivakumar [b]

[a] Rajalakshmi Engineering College, Department of Mathematics Chennai, Tamilnadu, India,
e-mail: rajkumar.v@rajalakshmi.edu.in, **corresponding author**,
ORCID iD: https://orcid.org/0000-0002-3026-4109

[b] Sri Sivasubramaniya Nadar College of Engineering, Department of Mathematics, Chennai, Tamilnadu, India,
e-mail:sivakumarb@ssn.edu.in,
ORCID iD: https://orcid.org/0000-0002-3612-6241

https://doi.org/10.5937/vojtehg73-57888

FIELD: mathematics
ARTICLE TYPE: original scientific paper

Abstract:

Introduction/Purpose: This study introduced the concept of a prime ideal-based unit graph associated with a commutative ring R. In this graph, the vertices consisted of units of R that were not contained in a chosen prime ideal I, and two such vertices were considered adjacent if their difference belonged to I. The aim was to investigate the structural, algebraic, and topological properties of this graph and examine the algebraic implications of various graph-theoretic invariants.

Methods: The construction of ideal-based unit graphs was carried out using the ring $\mathbb{Z}_n$, where units excluded from the chosen prime ideal formed the vertex set. The adjacency between two vertices was determined by whether their difference lay in the ideal. The analysis involved computing several topological indices including the Zagreb indices, Wiener index, Arithmetic-Geometric index, Harmonic index, Estrada index, and graph energy. Adjacency matrices and graphical visualizations were employed to understand structural complexity and connectivity.

Results: It was observed that the structure of the resulting graph depended significantly on both the modulus n and the nature of the selected ideal. Smaller ideals produced graphs with higher connectivity, while larger ideals led to sparser or disconnected graphs. The calculated indices reflected patterns in symmetry, degree distribution, and distances, revealing deeper algebraic characteristics.

Conclusions: Prime ideal-based unit graphs provided a novel approach to studying the interaction between ring-theoretic and graph-theoretic

concepts. The findings contributed to potential applications in mathematical chemistry, secure communications, and theoretical computer science.

Keywords: units, ideals, topological indices, commutative ring.

Introduction

Graph theory serves as a powerful tool to model and analyse relationships between algebraic structures, providing a visual and structural framework that bridges abstract mathematics with concrete representations. Among its numerous applications, the study of graph representations of commutative rings has garnered significant interest. These representations including zero-divisor graphs introduced by Anderson and Livingston (Anderson et al., 2011, pp. 23-45) and unit graphs studied by Sharma and Bhatwadekar (Sharma & Bhatwadekar, 2009, pp. 124 -127). Since then, various graphs such as annihilating-ideal graphs (Behboodi and Rakeei, 2011, pp.741-753), Cayley graphs (Abdollahi, 2008; Akhtar et al., 2009) total graphs (Akbari et al., 2009, pp.2224-2228; Asir & Chelvam, 2013, pp. 3820-3835), and unit graphs (Ashrafi, 2010, pp.2851-2871; Ramaswamy & Veena, 2009, pp.N24-N24) have been extensively studied.

Building on this foundation, this paper focuses on a novel graph construction known as the ideal-based unit graph, denoted as $G_I(R)$. This graph is built using the set of units of a commutative ring R and a chosen ideal I. Unlike the zero-divisor graph which emphasizes the multiplicative annihilation of elements, or the unit graph which focuses on the additive properties of all units, the ideal-based unit graph incorporates the influence of ideals to define adjacency. This approach opens new avenues for exploring the interplay between ideals and the unit structure of a ring.

Motivation and context

The ideal-based unit graph $G_I(R)$ captures the interplay between the additive and multiplicative structures of a ring through a chosen ideal *I*, highlighting how units interact modulo *I*. This framework enables the application of graph-theoretic invariants for computational analysis of ring-theoretic properties.

Objectives of the study

The ideal-based unit graph $G_I(R)$ is rigorously defined by its vertex set and adjacency relation, reflecting how elements of a ring interact modulo an ideal *I*. Its structural features such as connectivity, diameter,

and girth are analyzed, along with topological indices to quantify the graph's properties numerically.

The study of $G_I(R)$ incorporates the computation and analysis of topological indices, numerical invariants that reflect the graph's structural characteristics, specifically indices such as the Zagreb indices introduced by Gutman and Trinajstić in (Gutman & Trinajstić,1972, pp.535-538) the Wiener index extensively researched within chemical graph theory (Wiener, 1947, pp.17-20) and the Estrada index developed by Estrada (Estrada, 2000, pp.713-718). Through this analysis, quantitative acumens into the graph's complexity, symmetry, and connectivity are obtained.

In the subsequent sections, $G_I(R)$ is rigorously defined, its properties are explored, and meaningful topological indices are computed, thereby showcasing the intricate interplay between algebraic and graph-theoretic concepts.

Materials and methods

The ideal-based unit graph $G_I(R)$ uses the units of R as its vertices but excludes those lying within the ideal I. Two vertices are considered adjacent if their difference lies in the ideal I. This definition captures the interaction of units with respect to I, yielding a graph that is sensitive to the algebraic properties of R and the structural role of I. To interpret this definition and its implications, a formal construction and an illustrative example using the ring Z_n and the integers modulo n is provided. The ring Z_n serves as a particularly instructive example due to its finite nature and a well-defined unit group.

DEFINITION 1. Let R be a commutative ring with unity, and let I be an ideal of R. The ideal-based unit graph is a graph constructed using the algebraic structure of R filtered through its unit group $U(R)$ and the chosen ideal I. This graph provides a novel way to study the interplay between the ring's unit structure and its ideal. The vertices of $\mathrm{G_I(R)}$ are defined as the units of R that do not lie in the ideal I.

That is, $V(G_I(R)) = \{u \in U(R) \mid u \notin I\}$, where $U(R)$ represents the set of all units (invertible elements) in R. This restriction ensures that the graph reflects the relationship between units under the influence of I, excluding any units directly contained within I.

Two distinct vertices $u, v \in V(G_I(R))$ are adjacent if and only if their difference belongs to the ideal I. That is, $\{u, v\} \in E(G_I(R)) \iff u - v \in I$. This adjacency condition establishes a connection between the units based on the additive structure of R as mediated by I.

Theoretical significance

The choice of an ideal I is vital because ideals have unique properties that influence the graph structure. An ideal restricts the differences $u - v$ to a subset of R, providing a combinatorial perspective on the ring's additive relationships (Lambek, 2009; Stanley, 2007). Since I is , it avoids trivial containment of non-units, ensuring that the graph captures meaningful connections between distinct units. This construction connects the algebraic properties of R with graph-theoretic structures, creating a bridge between commutative algebra and combinatorics (Yap, 2000).

Construction for Z_n

To illustrate the concept of $G_I(R)$, consider the specific case where $R = Z_n$, the ring of integers modulo n, and I is an ideal of Z_n. The units $U(Z_n)$ are the integers $a \in Z_n$ that are co- to n. These elements satisfy $gcd(a, n) = 1$ and have multiplicative inverses modulo n. For Z_n, an ideal $I = (d)$ is generated by a divisor d of n. If d is, $I = (d) = \{0, d, 2d, \ldots, (n/d - 1)d\}$.

The vertices are the units of Z_n that are not in I. That is $V(G_I(Z_n)) = \{u \in U(Zn) \mid u \notin I\}$. Two distinct units $u, v \in V(G_I(Z_n))$ are adjacent if $u - v \in I$. This means $u - v$ is a multiple of d. For example, the graphs of $G_2(Z_{90})$ and $G_6(Z_{128})$ are depicted in the following figures, Figure 1 and Figure 2, respectively.

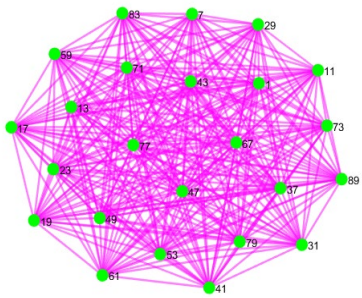

Figure 1 – Graph for $G_2(Z_{90})$

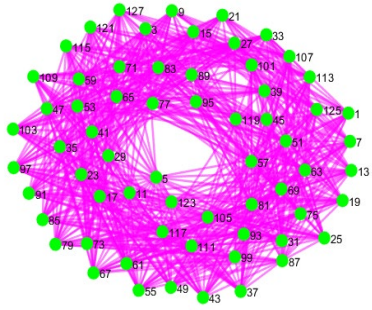

Figure 2 – Graph for $G_6(Z_{128})$

Main results

In this section, the key structural and graph-theoretic properties of the ideal-based unit graph $G_I(R)$, including its finiteness, connectivity, diameter, and girth, are investigated.

PROPOSITION 1. If R/I is finite, then the graph $G_I(R)$ has a finite number of vertices. Specifically, the size of the vertex set is given by

$$| V(G_I(R)) | = | U(R) | - | U(R) \cap I |.$$

Proof. To establish this result, recall that the vertex set $V(G_I(R))$consists of all units of R that do not belong to the ideal I. That is, $V(G_I(R)) = \{u \in U(R) \mid u \notin I\}$.

Here, $U(R)$ represents the set of all units in R, and $U(R) \cap I$ represents the subset of these units that also belong to the ideal I. Since R/I is assumed to be finite, the set $U(R)$ must also be finite, as it is a subset of the ring R. Consequently, $U(R) \cap I$ is finite as well.

The number of vertices in the graph is simply the total number of units in R minus the number of units that belong to I. This gives the result,

$|V(G_I(R)) | = | U(R) | - | U(R) \cap I |$.

Thus, the finiteness of R/I ensures the finiteness of $G_I(R)$, completing the proof.

EXAMPLE 1. Consider the ring $Z_6 = \{0,1,2,3,4,5\}$ units of Z_6, which are the elements with multiplicative inverses, are $\{1,5\}$. The ideal $I = (2)$ consists of the multiples of 2 in Z_6, which are $\{0,2,4\}$. Notably, there are no units within the ideal I. Using the above proposition 3.1, the size of the vertex set of the graph $G_2(Z_6)$ as $2 - 0 = 2$.

THEOREM 1.The graph $G_I(R)$ is connected if and only if, for any two vertices $u, v \in V(G_I(R))$, there exists a finite sequence of vertices $u = u_0, u_1, \dots, u_k = v$ such that $u_i - u_{i+1} \in I$ for all i.

Proof. To prove this result, it is necessary to show that the existence of such a sequence is sufficient for connectivity. By the definition of adjacency in $G_I(R)$, two vertices u and v are directly connected by an edge if $u - v \in I$. For the vertices u, v that are not directly adjacent, the existence of a sequence $u = u_0, u_1, \dots, u_k = v$, where $u_i - u_{i+1} \in I$ for all i, ensures a path connecting u and v. Therefore, if such sequences exist for all pairs of vertices, the graph is connected.

Conversely, assume that $G_I(R)$ is connected. This implies that for any $u, v \in V(G_I(R))$, there must exist a path between them. A path is a sequence of vertices $u = u_0, u_1, \dots, u_k = v$ such that u_i is adjacent to $u_i + 1$ for all i. By the definition of adjacency, this implies $u_i - u_{i+1} \in I$ for all i.

Hence, the existence of such a sequence is a necessary condition for connectivity.

Thus, $G_I(R)$ is connected if and only if every pair of vertices can be connected by a sequence satisfying the stated condition, completing the proof.

EXAMPLE 2. Consider the ring $Z_{20} = \{0,1,2,\dots,19\}$ The units of Z_{20} which are the elements coprime to 20, are $\{1,3,7,9,11,13,17,19\}$.The ideal $I = (5)$ consists of the multiples of 5, specifically $\{0,5,10,15\}$. Thus, the vertex set of the graph $G_5(Z_{20})$ is $V(G_5(Z_{20})) = \{1,3,7,9,11,13,17,19\}$, as these are the units not in the ideal I. To determine connectivity, consider the vertices $u = 1$ and $v = 19$. A possible sequence connecting them is $(1,11,19)$ where the differences satisfy $1 - 11 = -10 \in I$, but $11 - 19 = -8 \notin I$. Since no complete path exists connecting $u = 1$ and $v = 19$ such that all differences belong to I, the graph $G_5(Z_{20})$ is not connected. This lack of connectivity extends to other pairs of vertices, as similar interruptions occur in potential paths. This example illustrates how the structure of $G_I(R)$ depends on the interplay between the units and the ideal in higher-order rings.

THEOREM 2. If $I \neq (0)$, the diameter of $G_I(R)$, denoted $diam(G_I(R))$ satisfies the inequality $diam(G_I(R)) \leq 3$.

Proof. The diameter of a graph is the maximum distance between any two vertices, where the distance $d(u,v)$ is the length of the shortest path connecting u and v. In $G_I(R)$, adjacency is defined by the condition $u - v \in I$.

If $u, v \in V(G_I(R))$ are directly adjacent (i.e., $u - v \in I$), then $d(u,v) = 1$. For the vertices u, v that are not directly adjacent, there exists a vertex $w \in V(G_I(R))$ such that $u - w \in I$. In this case, the path $u \to w \to v$ has length 2, implying $d(u,v) = 2$.

In certain configurations, a third vertex x may be required to connect u and v, resulting in a path $u \to x \to w \to v$ of length 3. Hence, the maximum distance between any two vertices in $G_I(R)$ is at most 3. This establishes the result that $diam(G_I(R)) \leq 3$.

EXAMPLE 3. In the ring $Z_{36} = \{0,1,2,\dots,35\}$ the units are $\{1,5,7,11,13,17,19,23,25,29,31,35\}$, as these elements are co-prime to 36. The ideal $I = (4)$ consists of multiples of 4. The graph $G_4(Z_{36})$ has the vertex set $V(G_4(Z_{36})) = \{1,5,7,11,13,17,19,23,25,29,31,35\}$, which excludes the units contained in I. To verify the diameter, consider the vertices 1 and 29. These are not directly connected, but a path can be formed through intermediate vertices. For example, $1 \to 7 \to 19 \to 29$ is a

valid path where the differences $1-7=-6 \in I, 7-19=-12 \in I$, and $19-29=-10 \in I$. This path has a length of 3, and since no shorter path exists between 1 and 29, the graph's diameter is $diam(G_4(Z_{36}))=3$. It can be seen in Figure 3.

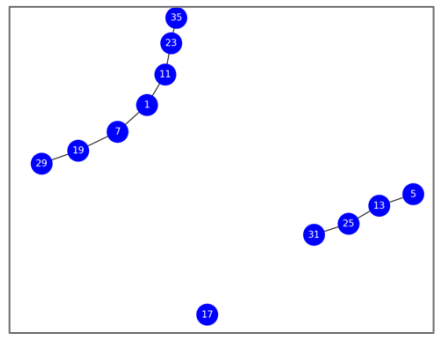

Figure 3 – *A path of length 3 in* $G_4(Z_{36})$

THEOREM 3. The girth of $G_I(R)$, defined as the length of its shortest cycle, is at least 3. If $G_I(R)$contains no cycles, its girth is infinite.

Proof. A cycle in $G_I(R)$ is a sequence of vertices $u_1, u_2, \ldots, u_k$ such that $u_1 = u_k$ and $u_i - u_i + 1 \in I$ for $i = 1,2,\ldots,k-1$. The length of the cycle is k. By definition, a cycle must involve at least three distinct vertices, as a two-vertex cycle would violate the condition that the vertices are distinct.

If $G_I(R)$ contains no cycles, then by convention, its girth is infinite. Otherwise, the shortest cycle must have a length of at least 3. This establishes the result.

EXAMPLE 4. Consider the ring $Z_8 = \{0,1,2,3,4,5,6,7\}$ where the units are $\{1,3,5,7\}$ with $I = (2)$. The vertex set of $V(\mathrm{G_I}(Z_8)) = \{1,3,5,7\}$. A cycle of length 3 is formed with the vertices $1 \to 3 \to 5 \to 1$, where each difference between connected vertices belongs to I. For instance, $1-3=-2 \in I, 3-5=-2 \in I$, and $5-1=4 \in I$. This confirms the girth of the graph is 3.

THEOREM 4. The vertex set of $G_I(Z_n)$ is a subset of the unit group $U(Z_n)$. That is, $V(G_I(Z_n)) \subseteq U(Z_n)$.

Proof. The unit group $U(Z_n)$ consists of all integers in $\{1,2,\ldots,n-1\}$ that are co- to n. The vertices of $G_I(Z_n)$ are chosen from Z_n such that their adjacency depends on membership in the ideal (d). Particularly, a vertex $u \in Z_n$ can only be included if it is a unit, as non-units cannot

satisfy the adjacency condition $u - v \in (d)$. Since only units $u \in U(Z_n)$ are to be vertices in $G_I(Z_n)$, it follows the result.

EXAMPLE 5. Consider $Z_{18} = \{0,1,2,\ldots,17\}$The unit group $U(Z_{18})$ consists of all integers coprime to 18: $\{1,5,7,11,13,17\}$. The ideal $I = (2)$ includes $\{0,2,4,6,8,10,12,14,16\}$. The vertex set of $G_2(Z_{18})$ is $\{1,5,7,11,13,17\}$ as all vertices must be units. Adjacency depends on the ideal I, and vertices like 1,7,13 satisfy adjacency conditions $1 - 7 = -6 \in I, 7 - 13 = -6 \in I$. Hence, the graph demonstrates that only units form the vertex set, consistent with the above theorem.

THEOREM 5. The number of vertices in $G_I(Z_n)$ is given by $| V(G_I(Z_n)) | = \phi(n) - | U(Z_n) \cap (d) |$,where $\phi(n)$ is Euler's totient function, and $| U(Z_n) \cap (d) |$ represents the number of units in Z_n that belong to the ideal (d).

Proof. The number of units in Z_n is given by $\phi(n)$. The ideal $(d) \subseteq Z_n$ contains elements $\{kd \mid k \in Z_n\}$. The intersection $U(Z_n) \cap (d)$ contains units that are also multiples of d. The vertices in $G_I(Z_n)$ are the units $u \in U(Z_n)$ that are not in $U(Z_n) \cap (d)$. This follows the result.

EXAMPLE 6. For the ring Z_{42}, the unit group is$U(Z_{42}) = \{1,5,11,13,17,19,23,25,29,31,37,41\}$, containing 12 elements. Euler's totient function gives $\phi(42)=12$. The ideal (7) in Z_{42} consists of the elements $\{0,7,14,21,28,35\}$. As none of these elements are units, the intersection $U(Z_{42}) \cap (7)$ is empty, and $| U(Z_{42}) \cap (7) | = 0$. Using the theorem, $| V((G_7(Z_{42})) | = \phi(42) - | U(Z_{42}) \cap (7) |$, the number of vertices is $12-0=12$. Consequently, the vertex set of $G_7(Z_{42})$ is $\{1,5,11,13,17,19,23,25,29,31,37,41\}$, and the graph has 12 vertices.

THEOREM 6. Two vertices $u, v \in V(G_I(Z_n))$ are adjacent if and only if $u - v \in (d)$, that is, the difference $u - v$ is divisible by d.

Proof. By the definition of the graph $G_I(Z_n)$ two vertices $u, v \in V(G_I(Z_n))$ are adjacent if their difference $u - v$ belongs to the ideal (d). The ideal (d) consists of all multiples of d. That is, $(d) = \{kd \mid k \in Z_n\}$. Hence, $u - v \in (d)$ implies that there exists an integer k such that $u - v = kd$. Therefore, two vertices u and v are adjacent if and only if $u - v$ is divisible by d, which establishes the adjacency condition.

EXAMPLE 7. In the ring $Z_{15} = \{0,1,2,\ldots,14\}$ and $I = (5)$ the vertex set of $G_5(Z_{15})$ is {1,2,4,7,8,11,13,14} which includes the units of Z_{15}. The ideal (5) contains the multiples of 5, specifically $\{0,5,10\}$. For adjacency verification, consider $u = 1$ and $v = 1$. Their difference is $1 - 11 = -10$, and since $-10 \in (5)$, 1 and 11 are adjacent. Similarly, for $u = 4$ and $v = 14$, the difference is $4 - 14 = -10$, and $-10 \in (5)$, so 4 and 14 are

adjacent. However, u =1 and $v = 4$ are not adjacent because $1 - 4 = -3 \notin (5)$. This illustrates that adjacency depends on the divisibility of the difference by 5, aligning with the theorem.

THEOREM 7. The graph $G_I(Z_n)$ is undirected. That is, if u is adjacent to v, then v is adjacent to u.

Proof. The adjacency condition $u - v \in (d)$ implies that $u - v = kd$ for some $k \in Z_n$. If $u - v = kd$, then $v - u = -kd$. Since $-kd \in (d)$ (as (d) is closed under multiplication by integers), it follows that $v - u \in (d)$. Thus, if u is adjacent to v, then v is also adjacent to u, making $G_I(Z_n)$ an undirected graph.

EXAMPLE 8. In the ring $Z_{20} = \{0,1,2,\ldots,19\}$ the unit group is $U(Z_{20}) = \{1,3,7,9,11,13,17,19\}$. The ideal $I = (4)$ consists of the multiples of 4, $\{0,4,8,12,16\}$. For the graph $G_4(Z_{20})$, the adjacency between two vertices u and v is determined by whether their difference $u - v$ lies in (4).

Consider the vertices $u = 1$ and $v = 9$. The difference $u - v = 1 - 9 = -8$, and since $-8 \in (4)$, u is adjacent to v. To check symmetry, calculate $v - u = 9 - 1 = 8$, which also belongs to (4). Hence, v is adjacent to u, demonstrating that adjacency is mutual. This symmetry holds for all pairs of vertices in $G_I(Z_{20})$, confirming that the graph is undirected, as per the statement of the theorem.

THEOREM 8. The connectivity of the graph $G_I(Z_n)$ depends on the properties of the ideal (d) in Z_n.If $(d) = (0)$, the graph $G_I(Z_n)$ is a complete graph with $\phi(n)$ vertices.

For $d > 0$, the graph $G_I(Z_n)$ may decompose into connected components, with the structure determined by the interaction of d with the units in Z_n.

Proof. Case 1: $(d) = (0)$

When $(d) = (0)$ the ideal consists only of 0 in Z_n, meaning $u - v \in (d)$ implies $u = v$. For all pairs $u, v \in V(G_I(Z_n))$ the adjacency condition $u - v \in (d)$ is always satisfied, since $0 \in (d)$. This implies that every pair of the vertices u, v is connected by an edge. As a result, $G_I(Z_n)$ is a complete graph with $\phi(n)$ vertices, because the vertex set is precisely $U(Z_n)$ and $| U(Z_n) | = \phi(n)$.

Case 2: $d > 0$

When $d > 0$, the ideal (d) consists of all multiples of d. That is, $(d) = \{kd \mid k \in Z_n\}$. Two vertices $u, v \in V(G_I(Z_n))$ are adjacent if $u - v \in (d)$. The divisibility condition creates a partition of the vertex set into equivalence classes, where u and v are in the same equivalence class if $u - v$ is divisible by d. The number of connected components and their

size depend on the interaction of d with $U(Zn)$. If d divides many differences $u-v$, the graph is more connected. If d divides fewer differences, the graph decomposes into multiple connected components. The connectivity of $G_I(Z_n)$ is directly influenced by the ideal (d). That is, $(d)=(0)$ results in a complete graph with $\phi(n)$ vertices. $d>0$ leads to a graph whose connectivity and component structure depend on the divisibility properties of d in Z_n.

EXAMPLE 9. In the ring $Z_{10}=\{0,1,2,\ldots,9\}$ the unit group is $U(Z_{10})=\{1,3,7,9\}$, consisting of 4 elements. When $I=(0)$, the ideal contains only 0, meaning that for any two vertices $u,v \in V(G_4(Z_{10}))$ the adjacency condition $u-v \in (0)$ is always satisfied. Consequently, every pair of vertices is connected by an edge, and the graph becomes a complete graph. The graph has $|U(Z_{10})|=\phi(10)=4$ vertices. In this case, $G_4(Z_{10})$ is a fully connected graph where all vertices form a single component, demonstrating the scenario when the ideal (d) is trivial.

Topological indices for ideal-based unit graphs

Topological indices are numerical descriptors that capture the structural properties of graphs. They provide critical insights into graph complexity, connectivity, and topology, with applications in fields such as algebraic graph theory, chemistry, and network analysis.

DEFINITION 2. The first Zagreb index (M_1) and the second Zagreb index (M_2) provide information about vertex degrees and their interactions. These indices of a graph G are defined as follows, $M_1(G)=\sum_{v\in V(G)} deg(v)^2$ and
$M_2(G)=\sum_{\{u,v\}\in E(G)} deg(u).deg(v)$, where $\{u,v\}$ denotes an edge in the graph G.

DEFINITION 3. The Wiener Index captures the overall closeness of vertices in the graph. It is defined as follows $W(G)=\sum_{\{u,v\}\subseteq V(G)} d(u,v)$ where $d(u,v)$ is the shortest-path distance between the vertices u and v.

DEFINITION 4. The Randić Index reflects graph branching and is defined as

$$R(G)=\sum_{\{u,v\}\subseteq E(G)} \frac{1}{\sqrt{deg(u).deg(v)}}.$$

DEFINITION 5. The Estrada Index is based on eigenvalues of the adjacency matrix $A(G)$. It is defined as

$EE(G)=\sum_{i=1}^{n} e^{\lambda_i}$, where λ_i are the eigenvalues of $A(G)$.

DEFINITION 6. (Ramaswamy & Veena, 2009, pp.N24-N24) The graph energy (E) measures graph irregularity based on eigenvalues. It is defined as $E(G) = \sum_{i=1}^{n} |\lambda_i|$, where λ_i are the eigenvalues of the adjacency matrix.

DEFINITION 7. (Vukičević & Furtula, 2009, pp.1369-1376) The Arithmetic-Geometric Index (AG) evaluates the interactions of adjacent vertices' degrees using an arithmetic-geometric mean. It is defined as

$$AG(G) = \sum_{\{u,v\} \in E(G)} \frac{2\, deg(u).deg(v)}{deg(u)+deg(v)}.$$

DEFINITION 8. (Zhou & Trinajstić, 2009, pp.1252-1270; Deng et al.,2013, pp.2740-2744) The Harmonic Index (HI) measures connectivity using inverse degree sums. It is defined as

$$HI(G) = \sum_{\{u,v\} \in E(G)} \frac{2}{deg(u)+deg(v)}.$$

Calculated values of topological indices

The calculated values of topological index for various values of n and the corresponding ideal structures for unit graphs on Z_n are presented in Table 1. These indices include the first and second Zagreb indices, Wiener index, Randić index, Estrada index, Graph energy, Arithmetic-Geometric index, and Harmonic index.

Table 1 - Calculated values of selected topological indices for some graphs

$G_I(Z_n)$	M_1	M_2	Wiener Index	Randić Index	Estrada Index	Graph Energy	AG	HI
$G_2(Z_6)$	8	4	1	0.5	3.086	2	2	0.5
$G_2(Z_8)$	18	12	2	0.5	6.502	4	4.5	1.0
$G_2(Z_{10})$	32	22	4	0.4	12.248	6	6.2	1.25
$G_3(Z_{12})$	50	36	6	0.4	19.292	8	9	1.5
$G_3(Z_{15})$	72	50	10	0.35	24.532	10	12	1.75
$G_4(Z_{16})$	96	72	12	0.3	30.456	12	16	2.0
$G_3(Z_{18})$	128	90	15	0.28	35.127	14	20	2.25
$G_5(Z_{20})$	160	110	20	0.25	41.052	16	25	2.5
$G_4(Z_{24})$	288	204	30	0.2	58.728	18	40	3.0
$G_5(Z_{25})$	400	280	40	0.18	63.456	20	50	3.25
$G_6(Z_{30})$	750	550	60	0.15	83.452	24	75	3.5
$G_6(Z_{36})$	1152	816	90	0.12	112.892	28	112	4.0

$G_8(Z_{40})$	1600	1120	120	0.1	125.532	30	150	4.25
$G_9(Z_{45})$	2025	1410	150	0.09	150.412	32	225	4.5
$G_{10}(Z_{50})$	2500	1750	200	0.08	175.236	34	300	4.75

The comparative graphs which provide a clear visualization of how different topological indices evolve with increasing n in the unit graphs $G_I(Z_n)$ can be seen in Figures 4 and 5. The first Zagreb Index (M_1) and the second Zagreb Index (M_2) demonstrate a steady growth, correlating with the increasing vertex degrees and their interactions, while the Wiener Index reflects the growing average distances between vertices in larger graphs. The Estrada Index, with its exponential-like rise, highlights the influence of spectral contributions as graph complexity increases. Conversely, the Randić Index shows a slight decline, indicating reduced branching as the graphs become denser. In contrast, the Harmonic Index (HI) grows gradually, signalling enhanced vertex connectivity. Together, these graphs reveal how different aspects of graph topology such as degree distribution, connectivity, and spectral characteristics respond to changes in n, offering a comprehensive perspective on structural dynamics.

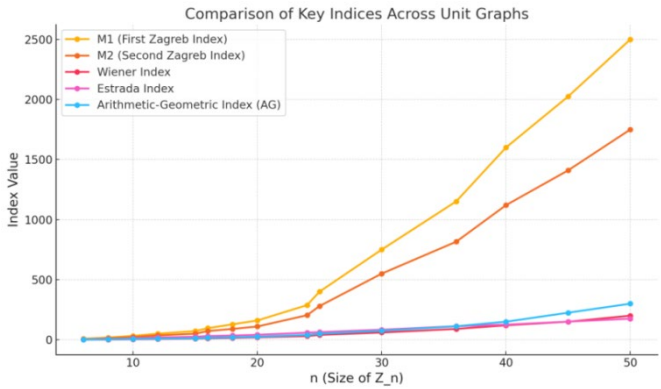

Figure 4 - Comparison of the key indices across unit graphs

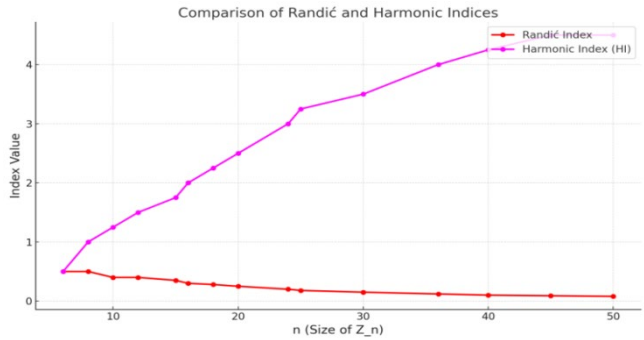

Figure 5 - Comparison of Randić and Harmonic indices

Algebraic properties and graph indices

This section explores the elaborate relationship between the algebraic properties of commutative rings Z_n and the topological indices derived from their associated unit graphs. These indices, computed for various ideals and values of n, are analyzed to uncover their dependence on the ring structure and the selected ideal. The algebraic structure of Z_n profoundly impacts the topology of its associated unit graph $G_I(Z_n)$.

The unit graph $G_I(Z_n)$ serves as a bridge between algebraic structures and graph theory. Its topology is inherently influenced by the properties of Z_n, particularly the chosen ideal $I = (d)$. The divisor d and its relationship with n shape the graph's connectivity, symmetry, and vertex interactions. The ideal $I = (d)$ is defined as the set of all multiples of d modulo n. Since d must divide n, the size of I is determined by the quotient n/d. This quotient reflects how many elements are part of the ideal, with significant implications for graph adjacency and structure. When d is small, I contains a larger number of elements, making adjacency conditions more relaxed and resulting in a denser graph. For example, if $n = 12$ and $d = 1$, the ideal contains all elements of Z_{12}, making the graph complete. Conversely, larger d values, such as $d = 6$ in Z_{12}, produce a smaller ideal, reducing adjacency and potentially causing the graph to become fragmented or disconnected.

Impact on connectivity

The divisor d determines how elements of Z_n interact within the graph. When $d = 1$, the ideal $I = (1)$ spans the entire ring, ensuring every pair of vertices is connected and forming a complete graph. However, as d increases, the connectivity diminishes because fewer

differences $u - v$ fall within I. For larger values of d, the graph may split into disconnected components, corresponding to different residue classes modulo d.

The adjacency matrix of the graph provides a clear representation of the connections between vertices. For $G_I(Z_{12})$, the matrix below highlights how the adjacency condition $u - v \in \{0,3,6,9\}$ results in limited connectivity.

The size of each connected component depends on the overlap between the cosets of I and the set of units $U(Z_n)$. For example, in Z_8 with $d = 2$, the ideal $I = \{0,2,4,6\}$ splits the graph into two components, one containing the units $\{1,3,5,7\}$ and another with non-units overlapping with I. $G_3(Z_{12})$ can be see visually in Figure 6. The unit graphs of $G_2(Z_8)$ and $G_3(Z_{12})$ can be seen in Figure 7.

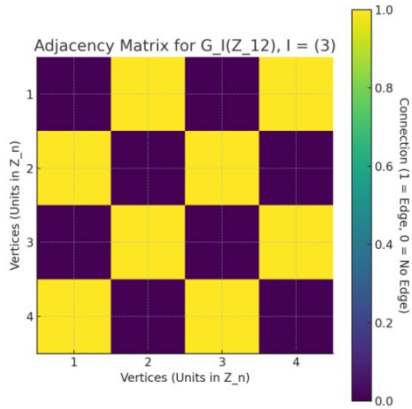

Figure 6 - Heat map of the adjacency matrix for $G_3(Z_{12})$

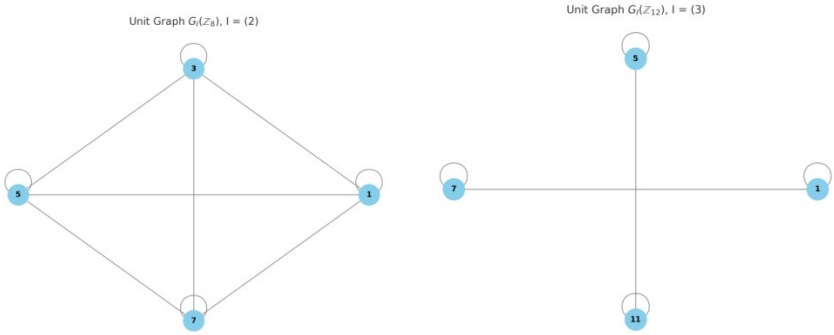

Figure 7 - Unit graphs of $G_2(Z_8)$ *and* $G_3(Z_{12})$

Cyclic structure of Z_n

The additive group of Z_n is cyclic, meaning all elements can be generated by repeated addition of a single element g. This cyclicity introduces periodicity in the graph's structure. The ideal I partitions Z_n into cosets, where each coset is of the form $a + I$ for some representative a. These cosets form disjoint subsets, and adjacency in the graph depends on whether the difference between the vertices u and v lies within I.

For smaller d, the cosets are larger, and many elements are connected, creating denser graphs. For larger d, the cosets are smaller, leading to sparser connections. This modular partitioning of Z_n ensures that the graph reflects the periodic and symmetric nature of the ring. For example, Figure 8 depicts the cyclic structure of $G_3(Z_{15})$.

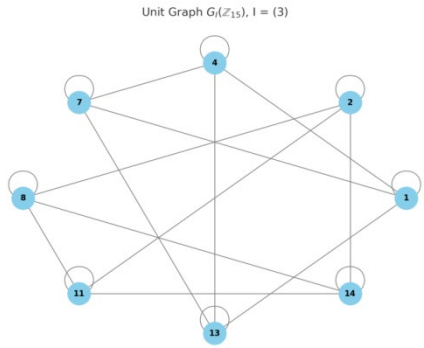

Figure 8 - Unit graph of $G_3(Z_{15})$

The ideal I forms a subgroup of Z_n under addition modulo n. Each coset of I contains n/d elements, and the graph structure depends on how these cosets interact with the units $U(Zn)$. Residue classes play a crucial role in determining the adjacency of vertices. If two vertices u and v belong to the same coset, their difference $u - v$ is in I, making them adjacent. Connections between cosets depend on their representatives. For example, in Z_{10} with $d = 5$, the ideal $I = \{0,5\}$ divides Z_{10} into two cosets $\{0,5\}$ and $\{1,2,3,4,6,7,8,9\}$. The resulting graph is sparse, with limited adjacency between these cosets.

The adjacency matrix for $G_I(Z_{10})$, where $I = \{0,5\}$, reveals the sparsity of connections caused by the ideal's partitioning into cosets. The matrix below highlights the restricted adjacency between vertices. It can be seen in Figure 9.

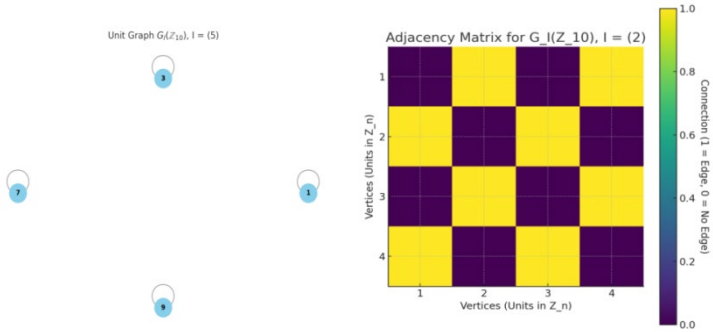

Figure 9 -Unit graph and the heat map of the adjacency matrix of $G_5(Z_{10})$

Interaction with units and degree distribution

The multiplicative group of units $U(Z_n)$ interacts with the additive structure of I. Units correspond to vertices with potentially higher degrees, as they are more likely to form edges based on the adjacency condition $u - v \in I$. Non-units, on the other hand, often contribute to sparsity, particularly when they overlap with I. Degree distributions in the graph are shaped by this interaction. In highly connected graphs (e.g., small d), most vertices have similar degrees, resulting in symmetric degree distributions. In sparse graphs (e.g., large d), the degrees vary significantly, reflecting irregular adjacency patterns.

For $G_I(Z_{15})$, the adjacency matrix below reflects how the ideal $I = \{0,3,6,9,12\}$ influences the degree distribution. Vertices within the same coset show higher connectivity, as seen in the matrix. This can be seen in Figure 10.

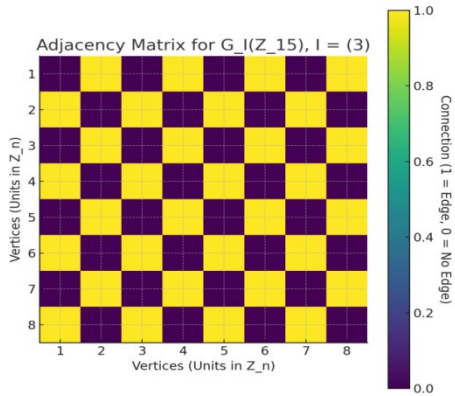

Figure 10 - Heat map of the adjacency matrix for $G_3(Z_{15})$

Graph symmetry and algebraic properties

The symmetry of Z_n is particularly evident when n is please include 15. In such cases, all non-zero elements of Z_n are units, and the graph exhibits uniformity. For composite n, the presence of zero-divisors and varying interactions between units and non-units introduce asymmetry, leading to diverse graph structures.

The algebraic properties of Z_n, including its cyclic nature, residue classes, and ideal structure, are vividly reflected in the topology of $G_I(Z_n)$. These properties influence vertex connectivity, graph symmetry, and degree distribution, highlighting the interplay between ring theory and graph topology.

Applications

The applications of ideal-based unit graphs span structural, algebraic, and comparative domains. By leveraging topological indices and their correlation with ring properties, these graphs serve as a powerful tool for analyzing the underlying algebraic structures. Their ability to unify graph-theoretic and ring-theoretic perspectives makes them a promising framework for future research in algebraic graph theory and related fields.

Structural insights

The study of topological indices in ideal-based unit graphs $G_I(R)$ provides valuable structural insights into graph complexity and connectivity. Indices such as the First Zagreb Index (M_1) and the Second Zagreb Index (M_2) quantify vertex degree interactions, offering a measure of graph density and edge distribution. Higher values of M_1 and M_2 correlate with dense connectivity, typically observed when the ideal $I = (d)$ has smaller d, allowing for more relaxed adjacency conditions. Conversely, sparse graphs with lower values of these indices emerge when d is larger, limiting connections.

The Wiener Index captures the average pairwise distances between vertices, providing a measure of graph compactness. Dense graphs with small d exhibit lower Wiener Index values, reflecting shorter paths between vertices, while sparse graphs with larger d show increased distances. Similarly, the Estrada Index reveals spectral characteristics, with exponential growth indicating the influence of eigenvalues on connectivity. The Randić Index and the Harmonic Index further enrich the analysis, highlighting how branching and connectivity vary with the ideal's size. These indices collectively allow researchers to classify graphs,

identify patterns, and predict structural properties based on the choice of R and I.

Ring-theoretic implications

The topology of $G_I(R)$ directly correlates with the algebraic properties of the ring R and its ideal I. The adjacency condition $u - v \in I$ reflects the additive subgroup structure of R, and the resulting graph connectivity encapsulates how the ideal I partitions R. For instance, smaller ideals encompass more differences $u - v$, leading to connected graphs, while larger ideals, containing fewer elements, can fragment the graph into disconnected components.

The interaction of the multiplicative group of units $U(R)$ with the additive structure of I further highlights ring-theoretic nuances. For example, the distribution of units and non-units within R determines vertex degrees and edge formation in $G_I(R)$. The analysis of these graphs provides insights into ring symmetry, residue class structures, and the relationship between ring elements and their cosets modulo I. This bridge between graph topology and ring theory can uncover properties such as the presence of zero divisors, the nature of subgroups, and the behaviour of R under different ideal selections.

Comparisons

The ideal-based unit graph $G_I(R)$ offers a new perspective for comparing standard unit graphs and zero-divisor graphs (Ashrafi et al.,2010, pp.2851-2871; Anderson et al.,2011, pp.23-45). Unlike standard unit graphs, where adjacency is based solely on the sum of units being invertible, $G_I(R)$ introduces an additional layer of complexity by restricting adjacency via the ideal I. This leads to a richer variety of graph structures, ranging from dense to sparse, based on the ideal's size and position within R.

In contrast to zero-divisor graphs, which focus on the multiplicative behaviour of non-units, $G_I(R)$ emphasizes additive properties. While zero-divisor graphs reveal information about ring annihilators and zero-divisors, $G_I(R)$ highlights the distribution of units and their differences modulo I. Comparing these graphs provides a comprehensive view of the interplay between additive and multiplicative structures within R. Such comparisons can guide applications in algebraic graph theory, where understanding the balance between addition and multiplication in ring structures is critical.

Properties of ideal-based unit graphs

The study of graph-theoretical representations of algebraic structures has gained significant attention in recent years, particularly through the exploration of ideal-based zero-divisor graphs. Mallika, Kala, and Selvakumar developed foundational properties of zero-divisor graphs where the adjacency of vertices is influenced by an ideal of the ring (Mallika et al., 2017, pp.177-187). These graphs have proven to be powerful tools for understanding the interplay between ring-theoretic properties and graph invariants, such as chromatic number, clique number, and girth. Inspired by their approach, this section extends similar concepts to ideal-based unit graphs which focus on the additive difference relationship among the units of a ring, constrained by an ideal. By adapting and generalizing the results from zero-divisor graphs, this section aims to provide a deeper structural understanding of ideal-based unit graphs and their chromatic, connectivity, and regularity properties.

THEOREM 9. The girth of the graph $G_I(R)$, denoted by $girth\ (\ G_I(R))$, satisfies the following properties:

If $G_I(R)$ contains cycles, then $girth\ (\ G_I(R)) \geq 3$ as the cycles in $G_I(R)$ must involve at least three distinct vertices due to the additive adjacency condition.

If $G_I(R)$ is acyclic, then $girth(\ G_I(R)) = \infty$.

Proof. The graph $G_I(R)$ is constructed with vertices as $u, v, w, \ldots \in U(R) \setminus I$, the set of units of R excluding those in the ideal I. Two vertices u and v are adjacent if $u - v \in I$. To determine the girth of $G_I(R)$, the cycle structure of the graph is analysed.

For a cycle to exist in $G_I(R)$, there must be a sequence of vertices $u_1, u_2, \ldots, u_k$ such that $u_i - u_{i+1} \in I$ for $1 \leq i < k$, and $u_k - u_1 \in I$. This sequence forms a closed loop where each adjacent pair satisfies the additive adjacency rule $u - v \in I$. The girth of $G_I(R)$, defined as the length of the shortest cycle, is determined by the minimum k for which such a sequence exists. Due to the additive nature of adjacency and the exclusion of self-loops ($u - u = 0$) and two-vertex cycles, the minimum cycle length is $k \geq 3$ if cycles exist.

If $G_I(R)$ does not contain any cycles, it is considered acyclic. In this case, the girth of the graph is defined as ∞, reflecting the absence of closed paths. This situation arises when no sequence of vertices $u_1, u_2, \ldots, u_k$ satisfies the adjacency rule for a complete cycle.

The proof assurances that if cycles exist in $G_I(R)$, the girth is at least 3, as cycles must involve at least three vertices due to the exclusion

of self-loops and two-vertex cycles. Otherwise, the graph is acyclic, and the girth is ∞. This completes the proof.

EXAMPLE 10. Ring: $R = Z_{18}$, Ideal: $I = (3) = \{0,3,6,9,12,15\}$, the vertices set is $U(R)\backslash I = \{1,5,7,11,13,17\}$. Edges : the vertices u, v are adjacent if $u - v \in I$. There exists the cycle 1→7→11→1. Graph Properties: A single large cycle involving all 8 vertices.

THEOREM 10. Let R be a commutative ring and I an ideal of R. The graph $G_I(R)$ contains a cycle if and only if there exist distinct $u, v, w \in U(R) \setminus I$ such that $(u - v), (v - w), (w - u) \in I$.

Proof. To prove the theorem, both the necessity and sufficiency of the stated condition for the presence of a cycle in $G_I(R)$ are established.

Necessity. A cycle in $G_I(R)$ implies the existence of vertices $u, v, w \in U(R)$ such that $u \to v \to w \to u$. By the definition of adjacency in G $G_I(R)$, two vertices $x, y \in U(R) \setminus I$ are adjacent if and only if their difference $x - y \in I$. For the cycle $u \to v \to w \to u$ in $G_I(R)$, the adjacency conditions are satisfied because $u - v \in I$, and $w - u \in I$. These adjacency relations demonstrate that the differences between the consecutive vertices u, v, w are contained in the ideal I. Hence, the existence of a cycle in $G_I(R)$ necessitates the presence of distinct vertices $u, v, w \in U(R) \setminus I$ such that $(u - v), (v - w), (w - u) \in I$.

Sufficiency. Conversely, assume there exist distinct vertices $u, v, w \in U(R) \setminus I$ such that $u - v \in I, v - w \in I$, and $w - u \in I$. These conditions ensure that u and v are adjacent, v and w are adjacent, and w and u are adjacent in $G_I(R)$. As a result, the edges $u \to v \to w \to u$ form a cycle in $G_I(R)$. Thus, the presence of such u, v, w is sufficient to guarantee a cycle in the graph.

EXAMPLE 11. Let $R = Z_9 = \{0,1,2,3,4,5,6,7,8\}$ and $I = (3) = \{0,3,6\}$. The units $U(R) = \{1,2,4,5,7,8\}$. The vertices of $G_I(R)$ are $U(R) \setminus I = \{1,2,4,5,7,8\}$, as I contains no units. Two vertices $u, v \in U(R) \setminus I$ are adjacent if $u - v \in I$. The adjacency relations, $1 - 4 = -3 \equiv 6\ mod\ 9 \in I, 4 - 7 = -3 \equiv 6\ mod\ 9 \in I, 7 - 1 = -6 \equiv 3\ mod\ 9 \in I$. This forms a cycle $1 \to 4 \to 7 \to 1$.

THEOREM 11. Let R be a commutative ring and I an ideal. If $G(R/I)$ is disconnected, $G_I(R)$ is regular only if all connected components of $G(R/I)$ are regular, and cosets contribute uniformly to $G_I(R)$.

Proof. To establish the regularity conditions for $G_I(R)$, the relationships between $G_I(R)$ and $G(R/I)$ and the uniform contribution of cosets has to be analysed. If $G(R/I)$ is regular with the degree k, each vertex in $G(R/I)$ has exactly k adjacent vertices. This regularity arises from the structure of R/I, where vertices (cosets of I) are connected if

their difference lies in I. The adjacency relations in $G_I(R)$ are inherited from $G(R/I)$, as the vertices of $G_I(R)$ (units in $R \setminus I$) are distributed among the cosets $a+I$. For the regularity to propagate from $G(R/I)$ to $G_I(R)$, it is necessary that each coset $a+I$ contributes uniformly to the vertex set of $G_I(R)$.

Uniform contribution means that all cosets $a+I$ in R/I contribute an equal number of vertices to $G_I(R)$. Specifically, the number of vertices contributed by each coset $a+I$ is $|U(R) \setminus I|/|R/I|$, where $|U(R) \setminus I|$ represents the total number of units not in I and $|R/I|$ is the number of cosets in R/I. If this contribution is uniform, the adjacency relations between the vertices of $G_I(R)$ mirror the regular structure of $G(R/I)$, ensuring consistent vertex degrees in $G_I(R)$.

The graph $G_I(R)$ is regular if $G(R/I)$ is regular and all cosets contribute uniformly to the vertex set of $G_I(R)$. The uniform contribution ensures that the vertex degrees in $G_I(R)$ remain consistent across all vertices, thereby propagating the regularity of $G(R/I)$ to $G_I(R)$. This concludes the proof.

EXAMPLE 12. The ring Z_{24} consists of the elements $\{0,1,2,\ldots,23\}$. The ideal $I=(3)$ includes $\{0,3,6,9,12,15,18,21\}$. The units are $U(Z_{24}) = \{1,5,7,11,13,17,19,23\}$. The vertex set of $G_I(R)$ is $U(Z_{24})\setminus I = \{1,5,7,11,13,17,19,23\}$.

Adjacency relations as follows, 1−5 = −4 ≡ 20 mod 24 ∈ I, 5−7 = −2 ≡22 mod 24 ∈ I, 7−11 = −4 ≡ 20 mod 24 ∈ I, 11−1 = −10 ≡ 14 mod 24 ∈ I (forming cycle 1). Similarly, 13→17→19→23→13 forms cycle 2.

Comparision of unit graphs and chemical graphs

Graphs are powerful tools for representing both algebraic and chemical structures. Unit graphs $G_I(R)$ from algebraic ring theory and molecular graphs from chemistry share deep structural similarities. This section explores these similarities, focusing on regularity, symmetry, and cyclic properties. By comparing ideal-based unit graphs of commutative rings with well-known chemical graphs, the study bridges abstract algebra with real-world molecular systems.

DEFINITION 9. For the unit graph $G_I(R)$, the vertices are units of R, $U(R)$ excluding those in the ideal I. The edges are defined as two vertices u and v which are adjacent if $u-v \in I$.Topology depends on the structure of the ring R and the ideal I.

For the chemical graphs, the vertices are atoms in the molecule (e.g., carbon, hydrogen, oxygen). The edges are covalent bonds (single,

double, triple) connecting atoms. Topology reflects the molecular structure and bond distribution.

Case studies and comparisons

EXAMPLE 13. Benzene **(**C_6H_6**)** vs. $G_I(Z_9), I = (3)$. Unit graph $G_I(Z_9)$, $I = (3)$; vertices: $\{1,2,4,5,7,8\}$; edges: two disjoint triangles: 1→4→7→1 ; 2→5→8→2. It is 2-regular (each vertex connects to 2 neighbours). Chemical graph (benzene): vertices: six carbon atoms arranged cyclically. Edges: alternating single and double bonds. It is 2-regular (each carbon connects to 2 neighbours).

Observation: Both graphs exhibit cyclic symmetry, with benzene's molecular structure reflecting the disjoint triangles of $G_I(Z_9)$. Figure 12 depicts this example.

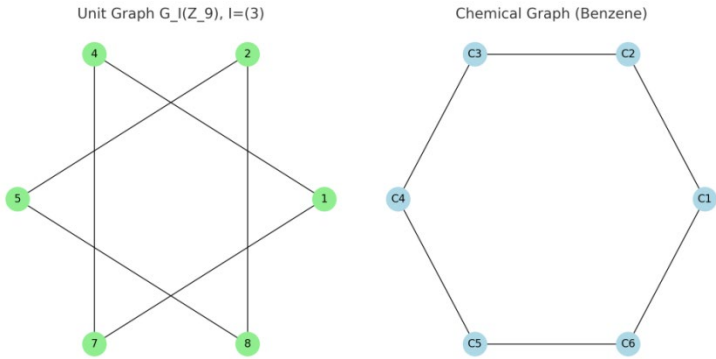

Figure 12 - Unit graph of $G_3(Z_9)$ *and the chemical graph of benzene*

EXAMPLE 14. Cyclooctane (C_8H_{16}) vs. $G_I(Z_{24}), I = (3)$. Unit graph $G_I(Z_{24}), I = (3)$: vertices: $\{1,5,7,11,13,17,19,23\}$. Edges: single cycle: 1→5→7→11→13→17→19→23→1.Regularity:2-regular.
Chemical graph (cyclooctane): vertices: eight carbon atoms in a cyclic structure. Edges: single bonds between consecutive atoms. Regularity: 2-regular.

Observation: The large cyclic structure of cyclooctane parallels the single cycle in $G_I(Z_{24})$. The following figure (Figure 13) depicts this example.

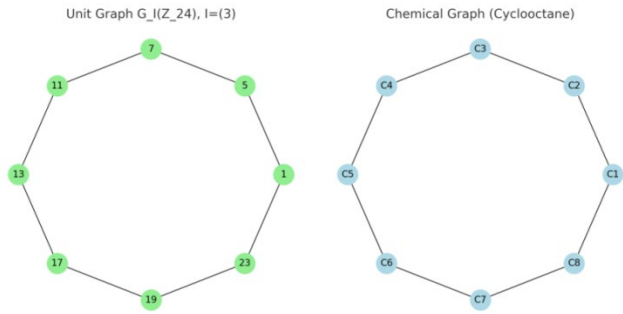

Figure 13- Unit graph of $G_3(Z_{24})$ and the chemical graph of cyclooctane

This comparative study reveals the versatility of graph theory in linking algebraic and chemical systems. The symmetry, regularity, and cyclic properties of unit graphs and chemical graphs illustrate how abstract algebra can model real-world molecular systems. Future work can explore further connections, enhancing interdisciplinary understanding and applications.

Conclusion

The study of ideal-based unit graphs $G_I(Z_n)$ provides a fascinating intersection of algebraic structures and graph theory, revealing deep connections between the properties of Z_n, the choice of ideals, and the resulting graph topology. By analysing these graphs, it is observed that the divisor d of n, which generates the ideal $I = (d)$, plays a pivotal role in determining the connectivity, symmetry, and sparsity of the graph. Smaller values of d lead to dense, highly connected graphs, often complete, while larger d values result in sparse graphs that may fragment into disconnected components. This interplay is further enriched by the cyclic structure of Z_n, where adjacency is influenced by residue classes and coset interactions. The interaction between the additive subgroup I and the multiplicative group of units $U(Z_n)$ highlights the algebraic properties shaping vertex connectivity and degree distributions.

The evaluation of topological indices on these graphs such as the Zagreb indices, Wiener Index, Estrada Index, Randić Index, and others provides a numerical lens to quantify their structural and spectral characteristics. The key insights include the steady growth of the first and second Zagreb Indices with increasing n, reflecting enhanced degree interactions, and the exponential rise of the Estrada index, indicating the growing influence of spectral contributions. Conversely, the Randić index

declines slightly, showcasing reduced branching, while the Harmonic index increases, emphasizing improved connectivity in denser graphs. These indices, when considered collectively, reveal the dynamic interplay between algebraic properties and graph topology, offering a comprehensive framework for analysing unit graphs of commutative rings.

The comparison of these unit graphs with chemical graphs not only highlights structural parallels but also opens pathways for interdisciplinary applications in mathematical chemistry and cryptography. Future work could extend this framework to weighted graphs, modular systems, or higher algebraic structures, further broadening the scope of ideal-based unit graph research.

References

Abdollahi, A., 2008. Commuting graphs of full matrix rings over finite fields. *Linear algebra and its applications*, 428(11-12), pp.2947-2954. Available at: https://doi.org/10.1016/j.laa.2008.01.036

Akbari, S., Kiani, D., Mohammadi, F. & Moradi, S., 2009. The total graph and regular graph of a commutative ring. *Journal of pure and applied algebra*, 213(12),pp.2224-2228. Available at: https://doi.org/10.1016/j.jpaa.2009.03.013

Akhtar, R., Boggess, M., Jackson-Henderson, T., Jiménez, I., Karpman, R., Kinzel, A. & Pritikin, D., 2009. On the unitary Cayley graph of a finite ring. *the electronic journal of combinatorics*, pp.R117-R117. Available at: https://doi.org/10.37236/206

Anderson, D.F., Axtell, M.C. & Stickles, J.A., 2011. Zero-divisor graphs in commutative rings. *Commutative algebra: Noetherian and non-Noetherian perspectives*, pp.23-45. Available at: https://doi.org/10.1007/978-1-4419-6990-3_2

Ashrafi, N., Maimani, H.R., Pournaki, M.R. & Yassemi, S., 2010. Unit graphs associated with rings. *Communications in Algebra*, 38(8), pp.2851-2871.Available at: https://doi.org/10.1080/00927870903095574

Asir, T. & Chelvam, T.T., 2013. On the total graph and its complement of a commutative ring. *Communications in algebra*, 41(10), pp.3820-3835. Available at: https://doi.org/10.1080/00927872.2012.678956

Behboodi, M. & Rakeei, Z., 2011. The annihilating-ideal graph of commutative rings II. *Journal of Algebra and its Applications*, 10(04), pp.741-753.Available at: https://doi.org/10.1142/S0219498811004902

Deng, H., Balachandran, S., Ayyaswamy, S.K. & Venkatakrishnan, Y.B., 2013. On the harmonic index and the chromatic number of a graph. *Discrete Applied Mathematics*, 161(16-17), pp.2740-2744. Available at: https://doi.org/10.1016/j.dam.2013.04.003

Estrada, E., 2000. Characterization of 3D molecular structure. *Chemical Physics Letters*, *319*(5-6), pp.713-718. Available at: https://doi.org/10.1016/S0009-2614(00)00158-5

Gutman, I. & Trinajstić, N., 1972. Graph theory and molecular orbitals. Total φ-electron energy of alternant hydrocarbons. *Chemical physics letters*, 17(4), pp.535-538. Available at: https://doi.org/10.1016/0009-2614(72)85099-1

Gutman, I. & Zhou, B., 2006. Laplacian energy of a graph. *Linear Algebra and its applications*, 414(1), pp.29-37. Available at: https://doi.org/10.1016/j.laa.2005.09.008

Lambek, J., 2009. Lectures on rings and modules, vol. 283. *American Mathematical Soc*.

Mallika, A., Kala, R. & Selvakumar, K., 2017. A note on ideal based zero-divisor graph of a commutative ring. *Discussiones Mathematicae-General Algebra and Applications*, 37(2), pp.177-187. Available at: http://dx.doi.org/10.7151/dmgaa.1273

Ramaswamy, H.N. & Veena, C.R., 2009. On the energy of unitary Cayley graphs. *the electronic journal of combinatorics*, pp.N24-N24. Available at: https://doi.org/10.37236/262

Sharma, P.K. & Bhatwadekar, S.M., 1995. A note on graphical representation of rings. *Journal of Algebra*, 176(1), pp.124-127. Available at: https://doi.org/10.1006/jabr.1995.1236

Stanley, R.P., 2007. *Combinatorics and commutative algebra* (Vol. 41). Springer Science & Business Media.

Vukičević, D. & Furtula, B., 2009. Topological index based on the ratios of geometrical and arithmetical means of end-vertex degrees of edges. *Journal of mathematical chemistry*, 46, pp.1369-1376. Available at: https://doi.org/10.1007/s10910-009-9520-x

Wiener, H., 1947. Structural determination of paraffin boiling points. *Journal of the American chemical society*, 69(1), pp.17-20. Available at: https://doi.org/10.1021/ja01193a005

Yap, C.K., 2000. *Fundamental problems of algorithmic algebra* (Vol. 49). Oxford: Oxford University Press.

Zhou, B. & Trinajstić, N., 2009. On a novel connectivity index. *Journal of mathematical chemistry*, 46, pp.1252-1270. Available at: https://doi.org/10.1007/s10910-008-9515-z

Тополошки индекси и структурне особине јединичних графова заснованих на идеалима у комутативним прстеновима

Вирапан Раджкумар[а], Баласубраманијан Сивакумар[б]

[а] Инжењерски колеџ Раджалакшми, Катедра за математику, Ченај, Тамил Наду, Индија, аутор за кореспонденцију.

[б] Инжењерски колеџ Шри Сивасубраманија Надара, Катедра за математику, Ченај, Тамил Наду, Индија.

ОБЛАСТ: математика
КАТЕГОРИЈА (ТИП) ЧЛАНКА: оригинални научни рад

Сажетак:

Увод/сврха: У овом раду уводи се појам јединичних графова заснован на простом идеалу који је повезан са комутативним прстеном R. Чворови овог графа јесу јединице R које не припадају изабраном простом идеалу I, а два таква чвора сматрају се суседним ако њихова разлика припада идеалу I. Циљ је да се истраже структурна, алгебарска и тополошка својства овог графа, као и да се испитају алгебарске импликације различитих граф-теоријских инваријанти.

Методе: Јединични графови засновани на идеалима конструишу се коришћењем прстена $\mathbb{Z}_n$ где јединице искључене из изабраног простог идеала формирају скуп чворова. Суседност између два чвора одређује се по томе да ли се њихова разлика налази у идеалу. Приликом анализе израчунато је неколико тополошких индекса, укључујући Загребачке индексе, Винеров индекс, аритметичко-геометријски индекс, хармонијски индекс, Естрадинов индекс, и енергију графа. Геометријске визуализације и матрице суседства користе се за тумачење комплексности и повезаности графова.

Резултати: Резултати показују да структура добијеног графа у знатној мери зависи од модулуса n и природе изабраног идеала. Мањи идеали доводе до графова са великом повезаношћу, док већи идеали дају ређе или неповезане графове. Израчунати индекси одражавају обрасце у симетрији, расподели степена и растојању, указујући тако на суштинске алгебарске карактеристике.

Закључци: Јединични графови засновани на идеалима представљају нови оквир за проучавање интеракције између алгебарских својстава прстена и структурних особина графова. Добијени резултати доприносе развоју алгебарских алата применљивих у математичкој хемији, безбедној комуникацији и теоријској рачунарској науци.

Кључне речи: јединице, идеали, тополошки индекси, комутативни прстен.

Paper received on: 31.03.2025.
Manuscript corrections submitted on:11.04.2025.
Paper accepted for publishing on: 10.06.2025.

Fixed-circle and fixed-disc problems in metric spaces

Vineeta Chandra[a], *Uma Devi* Patel[b]

[a] Guru Ghasidas Vishwavidyalaya, Department of Mathematics, Bilaspur, India,
e-mail: vineetachandra4@gmail.com,
ORCID iD: https://orcid.org/0009-0007-8615-2695

[b] Guru Ghasidas Vishwavidyalaya, Department of Mathematics, Bilaspur, India,
e-mail: umadevipatel@yahoo.co.in, **corresponding author**
ORCID iD: https://orcid.org/0000-0003-2853-5501,

https://doi.org/10.5937/vojtehg73-55778

FIELD: mathematics
ARTICLE TYPE: original scientific paper

Abstract:

Introduction/purpose: The purpose of this paper is to establish existence theorems for fixed circles and fixed discs in metric spaces using different types of contractive conditions. By considering self-mappings on metric spaces, classical fixed point results are extended to these geometric fixed structures. Several examples are provided to illustrate and validate the theoretical results.

Methods: Self-mappings defined on metric spaces are considered and various types of contractive conditions introduced. Analytical techniques from fixed point theory are used to derive sufficient conditions for the existence of ϕ-fixed circles and ϕ-fixed discs. The theoretical results are supported by carefully constructed examples that satisfy the proposed contractions and demonstrate the applicability of the obtained theorems.

Results: The study successfully establishes ϕ-fixed circles and ϕ-fixed disc results for Caristi-type contractions and another class of contractions within the framework of metric spaces. Additionally, supportive examples are provided.

Conclusion: This paper establishes new existence theorems for ϕ-fixed circles and ϕ-fixed discs in metric spaces using Caristi-type and related contractive conditions. These results extend classical fixed point theory beyond single fixed points to broader geometric fixed structures, thereby enriching the theory of metric fixed points. The provided examples demonstrate the applicability and effectiveness of the proposed results and indicate their potential for further generalizations.

Key words: Fixed circle, fixed disc, metric space, Caristi contraction

Introduction

The study of fixed point theory has been a fundamental area in mathematical analysis, with applications spanning across various branches of mathematics. In metric spaces, the investigation of fixed points has led to numerous significant results, beginning with Banach's contraction principle in 1922. "While traditional fixed point theory focuses on single points, recent developments have expanded to include the study of fixed sets, particularly fixed circles and fixed discs. A fixed circle of a self-mapping T on a metric space X is a circle C such that $T(C) = C$. Similarly, a fixed disc is a disc D where $T(D) = D$." Several researchers have contributed to this area. Özgür, & Taş (2019) established the first results on fixed circles using Caristi-type contractions in metric spaces. Later, Özgür, & Taş (2021) extended these results to more general spaces. Recent work by [Mlaiki et al. (2023), Taş (2018)] has introduced new techniques for studying fixed disc properties. However, the existence of fixed circles and fixed discs under certain types of contractive conditions remains unexplored. Moreover, the relationship between different contractive conditions and their impact on the existence of fixed sets needs further investigation. The fixed-circle problem was also studied in the setting of S-metric spaces in [Özgür et al. (2017), Özgür et al. (2018)]. In recent years, the fixed-disc problem have been studied with this perspective on metric and some generalized metric spaces (see [Özgür (2019), Taş et al. (2021)] for more details). This paper presents new existence theorems for fixed circles and fixed discs using various contractive conditions. The obtained results extend previous work by considering [Özgür, & Taş (2021), Taş (2018)]. Examples are also provided demonstrating that the conditions given here are optimal. This paper is organized as follows: Section 1 presents preliminary and definitions. Section 2 establishes the main results on fixed circles, which contain theorems related to fixed discs, and provides illustrative examples. The definition of the fixed circle has been generalized by replacing the radius r of the circle with the function $\phi(r)$ where $\phi : \mathbb{R}^+ \to \mathbb{R}^+$. The results have been also generalized by using a Caristi-type contraction in metric spaces, and Section 3 concludes the paper with some remarks and future directions.

DEFINITION 1. *Özgür, & Taş (2019) Let (X,d) be a metric space and $C_{x_0,r} = \{x \in X : d(x_0,x) = r\}$ be a circle, for a self-mapping $T : X \to X$, if $Tx = x$ for every $x \in C_{x_0,r}$ then the circle is a fixed circle of T.*

THEOREM 1. *Özgür, & Taş (2019) Let (X,d) be a metric space and $C_{x_0,r}$ be any circle on X. Let us define the mapping $\psi : X \to [0,\infty)$*

$$\psi(x) = d(x,x_0) \tag{1}$$

for all $x \in X$. If there exists a self-mapping $T : X \to X$ satisfying

1. $d(x,Tx) \leq \psi(x) - \psi(Tx)$
2. $d(Tx,x_0) \geq r$

for each $x \in C_{x_0,r}$ then the circle $C_{x_0,r}$ is a fixed circle of T.

THEOREM 2. *Özgür, & Taş (2019) Let (X,d) be a metric space and $C_{x_0,r}$ be any circle on X. Let the mapping ψ be defined as equation (1) for all $x \in X$. If there exists a self-mapping $T : X \to X$ satisfying*

(1)* $d(x,Tx) \leq \psi(x) + \psi(Tx) - 2r$

(2)* $d(Tx,x_0) \leq r$

for each $x \in C_{x_0,r}$ then the circle $C_{x_0,r}$ is a fixed circle of T.

THEOREM 3. *Özgür, & Taş (2019) Let (X,d) be a metric space and $C_{x_0,r}$ be any circle on X. Let the mapping ψ be defined as equation (1) for all $x \in X$. If there exists a self-mapping $T : X \to X$ satisfying:*

*(1**)* $d(x,Tx) \leq \psi(x) - \psi(Tx)$

*(2**)* $hd(x,Tx) + d(Tx,x_0) \leq r$

for each $x \in C_{x_0,r}$ then the circle $C_{x_0,r}$ is a fixed circle of T.

In 2019, Özgür (2019) defined a new contractive type mapping on metric spaces, and that includes fixed disc results via a simulation function on metric spaces.

DEFINITION 2. *Taş et al. (2021) Let (X,d) be a metric space, $D_{x_0,r} = \{x \in X : d(x_0,x) \leq r\}$ $(r \in \mathbb{R}^+ \cup \{0\})$ a disc and a self-mapping $T : X \to X$, if $Tx = x$ for every $x \in D_{x_0,r}$ then the disc is called a fixed disc of T.*

DEFINITION 3. *Özgür (2019) Let $\zeta \in \mathcal{Z}$ be any simulation function. T is said to be a $\mathcal{Z}_c$-contraction with respect to ζ if there exists an $x_0 \in X$ such that*

the following condition holds for all $x \in X$*:*

$$d(Tx, x) > 0 \Rightarrow \zeta(d(Tx, x), d(Tx, x_0)) \geq 0.$$

If T *is a* $\mathcal{Z}_c$*-contraction with respect to* ζ*, then there exists*

$$d(Tx, x) < d(Tx, x_0), \tag{2}$$

for all $x \in X$ *with* $Tx = x$*. Indeed, if* $Tx = x$ *then inequality (2) is satisfied . If* $Tx \neq x$ *then* $d(Tx, x) > 0$*. By the definition of a* $\mathcal{Z}_c$*-contraction and the condition of* ζ*, we get*

$$0 \geq \zeta(d(Tx, x), d(Tx, x_0)) < d(Tx, x_0) - d(Tx, x)$$

and so equation (2) is satisfied. In all fixed disc results, they use the number $r \in \mathbb{R}^+ \cup \{0\}$ *defined by*

$$r = \inf_{x \in X} \{d(x, Tx) | Tx \neq x\}.$$

THEOREM 4. *Özgür (2019) If* T *is a* $\mathcal{Z}_c$*-contraction with respect to* ζ *with* $x_0 \in X$ *and the condition* $0 < d(Tx, x_0) \leq r$ *holds for all* $x \in D_{x_0,r} - \{x_0\}$ *then the* $D_{x_0,r}$ *is a fixed disc of* T*.*

DEFINITION 4. *Özgür (2019) Let* (X, d) *be a metric space and* $T : X \to X$ *be a self-mapping and* $\zeta \in \mathcal{Z}$*.* T *is said to be a Ćirić-type* $\mathcal{Z}_c$*-contraction with respect to* ζ *if there exists an* $x_0 \in X$ *such that the following condition holds for all* $x \in X$*;*

$$d(x, Tx) > 0 \Rightarrow \zeta(d(Tx, x), m^*(x, x_0)) \geq 0$$

where $m^*(x, x_0) = max\{d(x, x_0), d(x, Tx), d(x_0, Tx_0), \frac{d(x,Tx_0)+d(x_0,Tx)}{2}\}$*.*

THEOREM 5. *Özgür (2019) Let* (X, d) *be a metric space and* $T : X \to X$ *a Ćirić-type* $\mathcal{Z}_c$*-contraction with respect to* ζ *with* $x_0 \in X$*, If the condition* $0 < d(Tx, x_0) \leq r$ *holds for all* $x \in D_{x_0,r} - \{x_0\}$ *then* $D_{x_0,r}$ *is a fixed disc of* T*.*

Main results

In this section, we have generalized the definition of the fixed circle by replacing the radius r of the circle with the function $\phi(r)$ where $\phi : \mathbb{R}^+ \to \mathbb{R}^+$. We have also generalized theorem (1) by using the Caristi-type contraction in metric spaces.

DEFINITION 5. *Let (X,d) be a metric space and $C_{x_0,\phi(r)} = \{x \in X : d(x_0,x) = \phi(r)\}$ where $\phi : \mathbb{R}^+ \to \mathbb{R}^+$ be a circle, for a self-mapping $T : X \to X$, if $Tx = x$ for every $x \in C_{x_0,\phi(r)}$ then the circle is a ϕ-fixed circle of T.*

THEOREM 6. *Let (X,d) be a metric space and $C_{x_0,\phi(r)}$ be any circle on X. Let us define the mapping $\psi : X \to [0,+\infty)$*

$$\psi(x) = d(x,x_0) \tag{3}$$

and $\phi : \mathbb{R}^+ \to \mathbb{R}^+$ for all $x \in X$. If there exists a self-mapping $T : X \to X$ satisfying

1. $d(x,Tx) \leq \psi(x) - \psi(Tx)$
2. $d(Tx,x_0) \geq \phi(r)$

for each $x \in C_{x_0,\phi(r)}$ then the circle $C_{x_0,\phi(r)}$ is a ϕ-fixed circle of T.

Proof. Let us assume that the mapping ψ is defined by $\psi : X \to [0,+\infty)$ and $\psi(x) = d(x,x_0)$. Let $x \in C_{x_0,\phi(r)}$ be any arbitrary point. We show that $Tx = x$, whenever $x \in C_{x_0,\phi(r)}$ using condition (1)

$$\begin{aligned} d(x,Tx) \leq\ & \psi(x) - \psi(Tx) \\ =\ & d(x,x_0) - d(Tx,x_0) \\ =& \phi(r) - d(Tx,x_0) \end{aligned} \tag{4}$$

because of condition(2), the point Tx should be lying on the exterior of the circle $C_{x_0,\phi(r)}$. Then there are two cases. If $d(Tx,x_0) > \phi(r)$ then using (4) is a contradiction. Now therefore it should be $d(Tx,x_0) = \phi(r)$. In this case, by using (4) we get

$$\begin{aligned} d(x,Tx) &\leq \phi(r) - \phi(r) \\ &= 0. \end{aligned}$$

Hence, we obtain $Tx = x$ for all $x \in C_{x_0,\phi(r)}$. Consequently, $C_{x_0,\phi(r)}$ is a ϕ-fixed circle of T. □

EXAMPLE 1. Let $X = [\frac{1}{2},\infty]$, (X,d) be a metric space and let us consider a circle $C_{x_0,\phi(r)}$ and define the mapping $T : X \to X$

$$T(x) = \begin{cases} x; & x \in C_{x_0,\phi(r)} \\ 2x; & otherwise \end{cases}$$

and $\phi : \mathbb{R}^+ \to \mathbb{R}^+$ is defined by

$$\phi(r) = \frac{1}{r}.$$

Solution: If $x \in C_{x_0,\phi(r)}$ then $Tx = x$.

1. $d(x, Tx) \leq \psi(x) - \psi(Tx)$,

$$\begin{aligned} d(x,Tx) &\leq \psi(x) - \psi(Tx) \\ d(x,Tx) &= d(x,x) = 0 \\ \psi(x) - \psi(Tx) &= d(x,x_0) - d(Tx,x_0) \\ &= d(x,x_0) - d(x,x_0) \\ &= 0. \end{aligned}$$

2. $d(Tx, x_0) = d(x, x_0) = \phi(r)$.

holds for each $x \in X$ and for all $r \geq 1$.
Then it can be easily seen that conditions (1) and (2) are satisfied. Clearly $C_{x_0,\phi(r)}$ is a ϕ-fixed circle of T.

EXAMPLE 2. Let $X = \mathbb{R}^+$ and (X, d) be a metric space and let us consider a circle $C_{x_0,\phi(r)}$ and let $\phi : \mathbb{R}^+ \to \mathbb{R}^+$ define as

$$\phi(r) = \begin{cases} \frac{1}{r}; & \text{if } r \geq 2 \\ \frac{1}{5}; & \text{otherwise} \end{cases}$$

and define the mapping $T : X \to X$ as

$$Tx = \begin{cases} \frac{1}{2}; & \text{if } x \in C_{x_0,\phi(r)} \\ 5; & otherwise \end{cases}$$

if $x \in C_{x_0,\phi(r)}$ then $Tx = \frac{1}{2}$ and if $r \geq 2$ and $x_0 = 0$ then

1. $d(x, Tx) \leq \psi(x) - \psi(Tx)$

$$\begin{aligned} d(x,Tx) &\leq \psi(x) - \psi(Tx) \\ d(x,\frac{1}{2}) &\leq d(x,0) - d(Tx,0) \\ &= x - \frac{1}{2} \end{aligned}$$

2. $d(Tx, x_0) = d(\frac{1}{2}, 0) = \frac{1}{2} \geq \frac{1}{r}$.

for $x_0 = 0$ and for each $x \in C_{x_0,\frac{1}{r}}$, hence T satisfies conditions (1) and (2). Clearly $C_{x_0,\frac{1}{r}}$ is a ϕ-fixed circle of T. But it does not satisfy condition (2) in theorem (1).

EXAMPLE 3. Let $X = [0, 2]$ and (X, d) be a metric space and let us consider a circle $C_{x_0,\phi(r)}$ and let $\phi : \mathbb{R}^+ \to \mathbb{R}^+$ defined as

$$\phi(r) = \begin{cases} \frac{1}{2r-1}; \text{ if } r \geq 1 \\ \frac{1}{3}; \text{ otherwise} \end{cases}$$

and define the mapping $T : X \to X$ as

$$Tx = \begin{cases} \frac{x}{10}; \text{ if } x \in C_{x_0,\phi(r)} \\ \frac{1}{2}; \quad otherwise. \end{cases}$$

If $x \in C_{1,\frac{1}{2r-1}}$ then $Tx = \frac{x}{10}$,

1. $d(x, Tx) \leq \psi(x) - \psi(Tx)$

$$d(x, \frac{x}{10}) \leq d(x, 1) - d(\frac{x}{10}, 1)$$
$$\frac{9x}{10} = \frac{9x}{10}.$$

2. $d(Tx, x_0) = d(\frac{x}{10}, 1) = \frac{x}{10} - 1 \not\geq \frac{1}{2r-1}$.

Hence, T satisfies condition (1) but does not satisfy condition (2). Clearly, T does not have a ϕ-fixed circle.

EXAMPLE 4. Let $X = \mathbb{R}^+$ and (X, d) be a metric space and let us consider a circle $C_{x_0,\phi(r)}$ and let $\phi : \mathbb{R}^+ \to \mathbb{R}^+$ defined as

$$\phi(r) = \begin{cases} \frac{1}{r}; \text{ if } r \geq 1 \\ \frac{2}{3}; \text{ otherwise} \end{cases}$$

and define the self-mapping $T : X \to X$ as

$$Tx = \begin{cases} 2; \text{ if } x \in C_{x_0,\phi(r)} \\ \frac{12}{5}; \quad otherwise. \end{cases}$$

If $x \in C_{x_0,\phi(r)}$ then $Tx = 2$, $r \geq 1$.

1. $d(x,Tx) \leq \psi(x) - \psi(Tx)$

$$\begin{aligned} 1. \quad d(x,Tx) &\leq \psi(x) - \psi(Tx) \\ d(x,2) &\leq \frac{1}{r} - d(Tx,x_0) \\ x &\nleq \frac{1}{r}, \quad \forall \ r > 1 \end{aligned}$$

2. $d(Tx,x_0) = d(2,0) = 2 \geq \frac{1}{r} = \phi(r)$
   $d(Tx,x_0) \geq \phi(r), \quad \forall \quad r \geq 1.$

Hence, the self-mapping T satisfies condition (2) but does not satisfy condition (1). Then, clearly T does not have a ϕ-fixed circle.

THEOREM 7. *Let (X,d) be a metric space and $C_{x_0,\phi(r)}$ be any circle on X. Let the mapping ψ be defined as equation (3) and $\phi : \mathbb{R}^+ \to \mathbb{R}^+$ for all $x \in X$. If there exists a self-mapping $T : X \to X$ satisfying*

(1)* $d(x,Tx) \leq \psi(x) + \psi(Tx) - 2\phi(r)$

(2)* $d(Tx,x_0) \leq \phi(r)$

for each $x \in C_{x_0,\phi(r)}$ then the circle $C_{x_0,\phi(r)}$ is a ϕ-fixed circle of T.

Proof. Let us assume that the mapping ψ is defined as $\psi : X \to [0,\infty)$ and let $x \in C_{x_0,\phi(r)}$ be any arbitrary point.
Now, using condition (1^*), we get

$$\begin{aligned} d(x,Tx) &\leq \psi(x) + \psi(Tx) - 2\phi(r) \\ &= d(x,x_0) + d(Tx,x_0) - 2\phi(r) \\ &= \phi(r) + d(Tx,x_0) - 2\phi(r) \\ &= d(Tx,x_0) - \phi(r) \end{aligned} \tag{5}$$

Because of condition (2*), the point Tx should be lying on or be interior of the circle $C_{x_0,\phi(r)}$. Then there are two cases. If $d(Tx,x_0) < \phi(r)$ then by using (5) we get a contradiction. It should be $d(Tx,x_0) = \phi(r)$. If $d(Tx,x_0) = \phi(r)$ then by using (5), we get

$$\begin{aligned} d(x,Tx) &\leq d(Tx,x_0) - \phi(r) \\ &\leq \phi(r) - \phi(r) \\ &= 0 \end{aligned} \tag{6}$$

Hence, $Tx = x$. Consequently, $C_{x_0,\phi(r)}$ is a ϕ-fixed circle of T. □

EXAMPLE 5. Let (X, d) be a metric space. Let us consider a circle $C_{x_0,\phi(r)}$ where $\phi(r)$ is defined as

$$\phi(r) = \begin{cases} \frac{1}{2r-1}; & r \in \{1, 2, 3\} \\ \frac{1}{3}; & \text{otherwise} \end{cases}$$

and define the self-mapping $T : X \to X$ as

$$Tx = \begin{cases} x; & \text{if } x \in C_{x_0,\phi(r)} \\ \frac{1}{5}; & \text{otherwise} \end{cases}$$

for all $x \in X$.

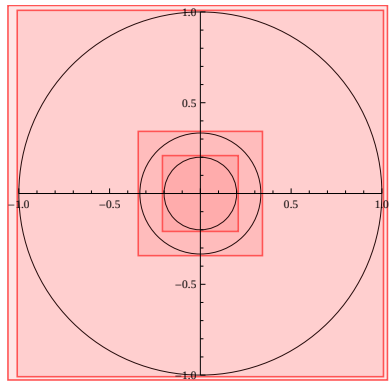

Figure 1

Figure 1 represents the circle $C_{0,\phi(r)}$ where $r \in \{1, 2, 3\}$. If $x \in C_{x_0,\phi(r)}$ then $Tx = x$. Then it is easily seen that conditions (1*) and (2*) are satisfied. Hence, clearly $C_{x_0,\phi(r)}$ is a ϕ-fixed circle of T.

EXAMPLE 6. Let$X = \mathbb{R}^+$ and (X, d) be a metric space. Let us consider a circle $C_{x_0,\phi(r)}$ where $\phi(r)$ is defined as

$$\phi(r) = \begin{cases} \frac{1}{2r-1}; & r \in \{1, 2, 3\} \\ \frac{1}{3}; & \text{otherwise} \end{cases}$$

and define the self-mapping $T : X \to X$ as

$$Tx = \begin{cases} \frac{1}{6}; & \text{if } x \in C_{x_0,\phi(r)} \\ 5; & \text{otherwise} \end{cases}$$

for all $x \in X$. If $x \in C_{x_0,\phi(r)}$ then $Tx = \frac{1}{6}$ and $x_0 = 0$.

1. $d(x,Tx) \leq \psi(x) + \psi(Tx) - 2\phi(r)$

$$\begin{aligned} d(x,Tx) &\leq \psi(x) + \psi(Tx) - 2\phi(r) \\ \psi(x) + \psi(Tx) - 2\phi(r) &= d(x,x_0) + d(Tx,x_0) - 2\phi(r) \\ &= \phi(r) + d(\frac{1}{6},0) - 2\phi(r) \\ &= \frac{1}{6} - \frac{1}{2r-1} \\ &\not\geq d(x,\frac{1}{6}). \end{aligned}$$

2. $d(Tx,x_0) = d(\frac{1}{6},0) = \frac{1}{6} \leq \frac{1}{2r-1} = \phi(r)$.

Then the self-mapping T satisfies condition (2*) but does not satisfy condition (1*). Clearly, T does not ϕ-fix the circle $C_{0,\phi(r)}$.

EXAMPLE 7. Let $X = [0, \frac{3}{2}]$ and (X,d) be the usual metric space with $d(x,y) = |x-y|$ and define the self-mapping $T : X \to X$ as

$$T(x) = \begin{cases} 2; \text{ if } x \in C_{0,\phi(r)} \\ \frac{5}{2}; \text{ otherwise} \end{cases}$$

where $\phi : \mathbb{R}^+ \to \mathbb{R}^+$ is defined as

$$\phi(r) = \begin{cases} \frac{1}{2r-1}; \text{ if } r \geq 1 \\ \frac{1}{3}; \text{ otherwise .} \end{cases}$$

If $x \in C_{0,\phi(r)}$ then $T(x) = 2$ for $r \geq 1$

1. $d(x,Tx) \leq \psi(x) + \psi(Tx) - 2\phi(r)$

$$\begin{aligned} d(x,Tx) &\leq \psi(x) + \psi(Tx) - 2\phi(r) \\ d(x,2) &\leq d(x,x_0) + d(Tx,x_0) - 2\phi(r) \\ |x-2| &\leq \phi(r) + d(2,0) - 2\phi(r) \\ &\leq 2 - \frac{1}{2r-1} \\ &\leq \frac{4r-3}{2r-1} \quad for \quad r \geq 1. \end{aligned}$$

2. $d(Tx,x_0) = d(2,0) = 2 \not\leq \frac{1}{2r-1} = \phi(r), \quad for \quad r \geq 1.$

Hence, the self-mapping T satisfies condition (1*) but does not satisfy condition (2*). Then, clearly T does not ϕ-fix the circle $C_{0,\phi(r)}$.

THEOREM 8. *Let (X,d) be a metric space and $C_{x_0,\phi(r)}$ be any circle on X. Let the mapping ψ be defined as equation (3) and $\phi : \mathbb{R}^+ \to \mathbb{R}^+$ for all $x \in X$. If there exists a self-mapping $T : X \to X$ satisfying*

*(1**)* $d(x,Tx) \leq \psi(x) - \psi(Tx)$

*(2**)* $hd(x,Tx) + d(Tx,x_0) \geq \phi(r)$

for each $x \in C_{x_0,\phi(r)}$ and some $h \in [0,1)$, then $C_{x_0,\phi(r)}$ is a ϕ-fixed circle of T.

Proof. We consider the mapping $\psi : X \to [0,+\infty)$ and $\psi(x) = d(x,x_0)$. Assume that $x \in C_{x_0,\phi(r)}$ and $Tx = x$ then using conditions (1**) and (2**). Now we obtain

$$\begin{aligned} d(x,Tx) &\leq \psi(x) - \psi(Tx) \\ &= d(x,x_0) - d(Tx,x_0) \\ &= \phi(r) - d(Tx,x_0) \\ &\leq hd(x,Tx) + d(Tx,x_0) - d(Tx,x_0) \\ &= hd(x,Tx), \end{aligned}$$

which is a contradiction with our assumption since $h \in [0,1)$. Therefore we get $Tx = x$ and $C_{x_0,\phi(r)}$ is a ϕ-fixed circle of T. □

EXAMPLE 8. Let $X = [0,1]$ and (X,d) be the usual metric space. Let us consider the circle $C_{\frac{1}{2},\frac{1}{2}} = \{0,1\}$ where $\phi(r) = \frac{1}{2}$, $x_0 = \frac{1}{2}$ and define the self-mapping $T : X \to X$ as

$$Tx = \begin{cases} \frac{1}{2}; \text{ if } x \in C_{\frac{1}{2},\frac{1}{2}} \\ 1; \text{ otherwise} \end{cases}$$

for all $x \in X$. If $x \in C_{\frac{1}{2},\frac{1}{2}}$ then $Tx = \frac{1}{2}$.

1. $d(x,Tx) \leq \psi(x) - \psi(Tx)$

$$\begin{aligned} d(x,Tx) &\leq \psi(x) - \psi(Tx) \\ \psi(x) - \psi(Tx) &= d(x,x_0) - d(x,Tx_0) \\ &= d(x,\frac{1}{2}) - d(\frac{1}{2},\frac{1}{2}) \end{aligned}$$

$$\Rightarrow d(x, \frac{1}{2}) \geq d(x, \frac{1}{2}).$$

2. $hd(x, Tx) + d(Tx, x_0) \geq \phi(r)$

$$h \cdot d(x, Tx) + d(Tx, x_0) = h \cdot d(x, \frac{1}{2}) + d(\frac{1}{2}, \frac{1}{2})$$
$$\ngeq \frac{1}{2}.$$

Hence, the self-mapping T satisfies condition (1**) where $h \in [0, 1)$, but does not satisfy condition (2**). Clearly T does not ϕ-fix the circle $C_{\frac{1}{2}, \frac{1}{2}}$.

Now, we generalize the definition of fixed discs and the results of fixed disc.

DEFINITION 6. *Let (X, d) be a metric space, $D_{x_0, \phi(r)} = \{x \in X : d(x_0, x) \leq \phi(r)\}$ where $\phi : \mathbb{R}^+ \to \mathbb{R}^+$ be a disc and T be a self-mapping on X, if $Tx = x$ for every $x \in D_{x_0, \phi(r)}$ then the disc is called a ϕ-fixed disc of T.*

THEOREM 9. *If T is a $\mathcal{Z}_c$-contraction with respect to ζ with $x_0 \in X$ and the condition $0 < d(Tx, x_0) \leq \phi(r)$ where $\phi : \mathbb{R}^+ \to \mathbb{R}^+$ holds for all $x \in D_{x_0, \phi(r)} - \{x_0\}$ then the disc $D_{x_0, \phi(r)}$ is a ϕ-fixed disc of T.*

Proof. Let $\phi(r) = 0$. In this case $x \in D_{x_0, \phi(r)} = \{x_0\}$. I f $Tx_0 \neq x_0$ then $d(Tx_0, x_0) > 0$ and using the definition of $\mathcal{Z}_c$ -contraction we get

$$\zeta(d(Tx_0, x_0), d(Tx_0, x_0)) \geq 0.$$

This is a contradiction by the condition of ζ, $(\zeta(t, s) < s - t)$ for all $s, t > 0$. Hence, $Tx_0 = x_0$.
Now, assume $\phi(r) \neq 0$. Let $x \in D_{x_0, \phi(r)}$ be such that $Tx \neq x$. By the definition of $\phi(r)$ we have $0 < \phi(r) \leq d(x, Tx)$ and using the condition of ζ, we obtain

$$\begin{aligned} \zeta(d(Tx, x), d(Tx, x_0)) &< d(Tx, x_0) - d(Tx, x) \\ &\leq \phi(r) - d(Tx, x) \\ &\leq \phi(r) - \phi(r) \\ &= 0 \end{aligned}$$

which is a contradiction with the property of T. It should be $Tx = x$, so T ϕ-fixes the disc $D_{x_0, \phi(r)}$. □

EXAMPLE 9. Let $X = \mathbb{R}$ and (X, d) be the usual metric space with $d(x, y) = |x - y|$. Let us define the self-mapping $T : X \to X$ as

$$Tx = \begin{cases} x; & x \in [-1, 1] \\ x^2 + 1 & otherwise \end{cases}$$

for all $x \in \mathbb{R}$ and define the mapping $\phi : \mathbb{R}^+ \to \mathbb{R}^+$ as $\phi(r) = \frac{1}{\sqrt{r}}$ where $\phi(r)$ is a disc radius. The function $\zeta : [0, \infty)^2 \to \mathbb{R}$ defined as $\zeta(t, s) = \frac{2}{3}s - t$. Indeed, it is clear that

$$0 < d(Tx, x_0) = d(x, 0) = |x| \leq \frac{1}{\sqrt{r}} = \phi(r)$$

hence $0 < d(Tx, x_0) \leq \phi(r)$, holds for all $x \in D_{x_0,[-1,1]} - \{0\}$ and $r \in [\frac{1}{9}, 1]$, we have

$$\begin{aligned} \zeta(d(Tx, x), d(Tx, x_0)) &= \zeta(d(x^2 + 1, x), d(x^2 + 1, 0)) \\ &= \zeta(|x^2 + 1 - x|, |x^2 + 1 - 0|) \\ &= \frac{2}{3}|x^2 + 1| - |x^2 + 1 - x| \\ &\leq \frac{1}{3}|3x - x^2 - 1|. \end{aligned}$$

for all $x \in \mathbb{R}$ such that $d(Tx, x) > 0$. Hence T is a $\mathcal{Z}_c$-contraction with the radius $\phi(r) = \frac{1}{\sqrt{r}}$ and the center is 0. Consequently, T is a ϕ-fixed disc $D_{x_0,\phi(r)} = [-1, 1]$, but does not hold theorem (4) in the condition $(0 < d(Tx, x_0) \leq r)$.

THEOREM 10. *Let (X, d) be a metric space and $T : X \to X$ a Ćirić-type $\mathcal{Z}_c$-contraction with respect to ζ with $x_0 \in X$, If the condition $0 < d(Tx, x_0) \leq \phi(r)$ holds for all $x \in D_{x_0,\phi(r)} - \{x_0\}$ then $D_{x_0,\phi(r)}$ is a ϕ-fixed disc of T.*

Proof. Let $\phi(r) = 0$. In this case, $x \in D_{x_0,\phi(r)} = \{x_0\}$ and the Ćirić-type $\mathcal{Z}_c$-contraction theory produces $Tx_0 = x$. Indeed, If $Tx_0 \neq x$ then we have $d(x_0, Tx_0) > 0$. By the definition of the Ćirić-type $\mathcal{Z}_c$-contraction, we get

$$\zeta(d(x_0, Tx_0), m^*(x_0, x_0) \geq 0 \tag{7}$$

Since

$$m^*(x_0, x_0) = max\{d(x_0, x_0), d(x_0, Tx_0), d(x_0, Tx_0), \frac{d(x_0, Tx_0) + d(x_0, Tx_0)}{2}\}$$

$$= max\{d(x,x_0), d(x_0,Tx_0), d(x_0,Tx_0), d(x_0,Tx_0)\}$$
$$= d(x_0,Tx_0).$$

Now, we find

$$\zeta(d(x_0,Tx_0), m^*(x_0,x_0)) = \zeta(d(x_0,Tx_0), d(x_0,Tx_0)) < 0$$

by the condition of ζ such that $\zeta(t,s) < s-t$. This is a contradiction to equation (7). Hence, it should be $Tx_0 = x_0$. Assume that $\phi(r) \neq 0$. Let $x \in D_{x_0,\phi(r)}$ be such that $Tx \neq x$. Then we have

$$m^*(x,x_0) = max\{d(x,x_0), d(x,Tx), d(x_0,Tx_0), \frac{d(x,Tx_0)+d(x_0,Tx)}{2}\}$$
$$= max\{d(x,x_0), d(x,Tx), \frac{d(x,Tx_0)+d(x_0,Tx)}{2}\}$$

By the assumption, we have

$$\zeta(d(Tx,x), m^*(x,x_0)) \geq 0$$

and

$$\zeta(d(Tx,x), max\{d(x,x_0), d(x,Tx), \frac{d(x,x_0)+d(x_0,Tx)}{2}\} \geq 0 \qquad (8)$$

Now, we have the following three cases:
Case 1. Let $max\{d(x,x_0), d(x,Tx), \frac{d(x,x_0)+d(x_0,Tx)}{2}\} = d(x,x_0)$ from equation (8) we get

$$\zeta(d(Tx,x), d(x,x_0)) \geq 0.$$

Using the condition ζ s.t. $(\zeta(t,s) < s-t)$ and consider the definition of $\phi(r)$, we find

$$\zeta(d(Tx,x), d(x,x_0)) < d(x,x_0) - d(Tx,x) < \phi(r) - \phi(r) = 0$$

which is a contradiction.
Case 2. Let $max\{d(x,x_0), d(x,Tx), \frac{d(x,x_0)+d(x_0,Tx)}{2}\} = d(x,Tx)$ from equation (8) we get

$$\zeta(d(Tx,x), d(x,Tx)) \geq 0.$$

Using the condition ζ s.t. $(\zeta(t,s) < s - t)$, again we obtain a contradiction.
Case 3. Let $max\{d(x,x_0), d(x,Tx), \frac{d(x,x_0)+d(x_0,Tx)}{2}\} = \frac{d(x,x_0)+d(x_0,Tx)}{2}$ from equation (8) we get

$$\zeta(d(Tx,x), \frac{d(x,x_0) + d(x_0,Tx)}{2}) \geq 0.$$

Using the condition ζ s.t. $(\zeta(t,s) < s - t)$, we obtain

$$\begin{aligned}\zeta(d(Tx,x), \frac{d(x,x_0) + d(x_0,Tx)}{2}) &< \frac{d(x,x_0) + d(x_0,Tx)}{2} - d(Tx,x) \\ &\leq \phi(r) - d(Tx,x) \leq \phi(r) - \phi(r) = 0.\end{aligned}$$

Again this is a contradiction with the *Ćirić*-type $\mathcal{Z}_c$-contractive property of T. In all the above cases, we have a contradiction. Hence, it should be $Tx = x$ and consequently, T ϕ-fixes the disc $D_{x_0,\phi(r)}$. □

Conclusion and future work

This study contributes to the field by broadening the scope of fixed point theory to include fixed circles and discs, incorporating a more flexible definition via the function $\phi(r)$. The use of Caristi-type contractions further enhances the applicability of the results within metric spaces. These advancements provide a robust framework for exploring geometric properties in fixed point theory. Future work may focus on extending these ideas to fuzzy metric spaces and probabilistic metric spaces, as well as investigating applications in dynamic systems and optimization problems.

References

Özgür, N. Y. & Taş, N. 2019. Some fixed-circle theorems on metric spaces, *Bulletin of the Malaysian Mathematical Sciences Society*, 42(4), pp. 1433-1449. Available at: https://doi.org/10.1007/s40840-017-0555-z.

Özgür, N. & Taş, N. 2021. On The Geometry of ϕ-Fixed Points. *Conference Proceedings Of Science And Technology*, 4(2), pp. 226-231.

Özgür, N. & Taş, N. 2021. Geometric properties of fixed points and simulation functions, *arXiv preprint arXiv:2102.05417*, Feb 10. Available at: https://doi.org/10.48550/arXiv.2102.05417.

Karapınar E. 2016. Fixed points results via simulation functions. *Filomat*, 30(8), pp. 2343-2350. Available at: https://www.jstor.org/stable/24899250.

Özgür, N. 2019. Fixed-disc results via simulation functions. *Turkish J. Math.*, 43(6), pp. 2794-2805. Available at: https://www.jstor.org/stable/24899250.

Taş, N. Mlaiki N., Aydi H.,Özgür N. 2021. Fixed-disc results on metric spaces, *Filomat*, 35(2), pp. 447-457. Available at: https://doi.org/10.2298/FIL2102447T.

Taş, N., Özgür, N. Y., & Mlaiki, N. 2018. New types of Fc-contractions and the fixed-circle problem, *Mathematics*, 10(6), pp. 188. Available at: https://doi.org/10.3390/math6100188.

Mlaiki, N., Özgür, N., Taş, N., & Santina, D. 2023. On the Fixed Circle Problem on Metric Spaces and Related Results. *Axioms*, 12(4), pp. 401. Available at: https://doi.org/10.3390/axioms12040401.

Taş N. 2018. Various types of fixed-point theorems on S-metric spaces. *BAUN Fen. Bil. Enst. Dergisi.*, December 20(2), pp. 211-223. Available at: doi:10.25092/baunfbed.426665.

Özgür, N.Y. Taş, N., & Çelik, U. 2017. New fixed-circle results on S-metric spaces. *Bull. Math. Anal. Appl.*, 9, pp. 10-23. Available at: https://hdl.handle.net/20.500.12462/6665.

Özgür, N.Y., Taş, N. 2018. Fixed-circle problem on S-metric spaces with a geometric viewpoint. *Facta Univ. (NIS) Ser. Math. Inform.*, 34, pp. 459-472. Available at: https://doi.org/10.48550/arXiv.1704.08838.

Проблеми фиксне тачке и фиксног диска у метричким просторима

Винеета Чандра[a], Ума Деви Пател[b],
аутор за кореспонденцију

[a] Гуру Гасидас Вишвавидјалаја, Одељење за математику, Биласпур, Чатисгарх, Индија,

[b] Гуру Гасидас Вишвавидјалаја, Одељење за математику, Биласпур, Чатисгарх, Индија,

ОБЛАСТ: математика
КАТЕГОРИЈА ЧЛАНКА (ТИП): оригинални научни рад

Сажетак:

Увод/циљ: Циљ овог рада јесте да се установе теореме постојања за непокретне кругове и непокретне дискове у метричким просторима коришћењем различитих врста услова за контракцију. Применом пресликавања у самог себе на метричким просторима, резултати класичне непокретне тачке проширују се на ове фиксне геометријске структуре. Наведено је неколико примера за илустрацију и потврду теоријских резултата.

Методе: Разматрају се пресликавања у самог себе на ме-

тричким просторима и уводе различите врсте услова за контракцију. Аналитичке технике из теорије непокретне тачке користе се за извођење довољних услова за постојање ϕ-непокретних кругова и ϕ-непокретних дискова. Теоријски резултати су поткрепљени пажљиво конструисаним примерима који задовољавају предложене контракције и потврђују применљивост добијених теорема.

Резултати: Успешно су увдени резултаи ϕ-непокретних кругова и ϕ-непокретних дискова за Каристијеве контракције, као и друга класуа контракција у оквиру метричких простора. Наводе се и одговарајући примери.

Закључак: Овај рад уводи нове теореме постојања за ϕ-непокретне кругове и ϕ-непокретне дискове у метричким просторима помоћу Каристијевих и одговарајућих услова за контракцију. Његови резултати проширују класичну теорију непокретне тачке са појединачних непокретних тачака на шире геометријске непокретне структуре и на тај начин обогаћују теорију метричких непокретних тачака. Наведени примери указују на применљивост и ефикасност предложених резултата, као и на њихов потенцијал за будућа уопштавања.

Кључне речи: непокретни круг, непокретни диск, метрички простор, Каристијева контракција

Paper received on: 31.12.2024.
Manuscript corrections submitted on: 13.01.2025.
Paper accepted for publishing on: 30.01.2025.

Strategic framework for selecting advanced air defence systems: insights from a developing country

Yousaf Ali

College of Business & Management, Fahad Bin Sultan University, Tabuk, Saudi Arabia
Email: yali@fbsu.edu.sa
ORCID: https://orcid.org/0000-0002-7612-497X

https://doi.org/10.5937/vojtehg73-48407

FIELD: operations research, decision sciences, defense studies, military system analysis
ARTICLE TYPE: original scientific paper

Abstract

Introduction/Purpose: In this modern world, every country is trying to improve its defense system by acquiring new technologies. One of the main components of a defense system is the Air Defense System (ADS), which further includes fighter aircraft, drones, 3D radar, fighter command vehicles, and missile systems. The missile system has become the most important component of air defense systems around the globe. Due to the limited resources and weak economy, it is a challenge for a developing country to acquire an ADS that suits its resources and economic capabilities. This research paper aims to study the needs and goals of the defense system of the Pakistan Air Force (PAF) and to select the best missile system to improve its existing air defense system.

Methods: A hybrid Multi-Criteria Decision Making (MCDM) methodology, Decision-Making Trial and Evaluation Laboratory (DEMATEL), and Analytical Hierarchy Process (AHP) are used to evaluate the factors affecting the missile system as well as to select the best missile system for Pakistan.

Results: The results depict that the S-400 missile system is the most feasible for Pakistan's air defense, followed by THAAD and S-300, which can meet the country's current security needs.

Conclusion: The research concludes that precision target capability, range, and maneuverability are the prominent factors that play a greater role in the ADS sector of Pakistan. This research is the first of its kind to use the DEMATEL-AHP approach for the evaluation of air defense systems in the case of a developing country such as Pakistan.

Keywords: Pakistan, ADS, missile system, MCDM, DEMATEL-AHP

Introduction

In today's modern technology-driven world, a nation's Air-Defense System (ADS) forms the backbone of its overall security. The importance it carries can be justified by the fact that no matter how advanced or numerous the nation's aircraft may be, a weaker ADS would make that nation vulnerable to modern threats (Aljohani, 2024). That is the reason that the major European powers and North America have equipped their key cities with the most sophisticated and robust ADS networks, an approach that highlights the growing importance of strengthening such systems in various developing countries (Tytarenko and Pavlenko, 2024). Furthermore, many states across the region have been strengthening their layered air-defense systems to meet evolving threats, such as in the case of India, having signed the contract with Russia back in 2018 for the S-400 Triumf system and began receiving and deploying the system from the year 2021 onwards, with original deliveries that are still under the schedule to be delivered in the coming years as we speak towards the end of 2025 (Yaqub, Ali and Kumar, 2025). Taken together, these acquisitions by various nations paint a picture of a wider regional move towards a multi-band, multi-layered air-defense coverage.

Comparatively, in the case of Pakistan, the requirement under consideration for an effective air-defense and strike system (ADS) must be understood in relation to its own strategic environment. The system's suitability is usually shaped by the state's threat perceptions, geography, and its operational doctrine, rather than by the comparisons of the missile range alone (Eslami and Borges, 2025). Considering the territorial size of Pakistan, a missile with a range of 400 km can provide many target points to an external factor within its territory; however, in the case of a country like Pakistan, to achieve similar reach against external factors that has a much larger territorial size, it would require systems with significantly longer ranges (Kristensen *et al.*, 2025). Similarly, sometimes the technical specifications of a missile system can involve inherent trade-offs, such as the enhancement of range, etc., that will need an adequate fueling system and structural reinforcement that can result in an increase in the overall weight. This can, in turn, reduce its mobility and even result in complicated deployment options (Zou, Liu and Teng, 2025). An ADS in such cases requires a balanced competing requirement for a country like Pakistan, which can constitute a strategically suitable and effective missile capability.

With the advancement in technology and rapidly changing world affairs, the nature of warfare between countries is changing. The huge

number of armies cannot win wars in this era of modern technology. Instead of a full-scale war, a new trend of attacks has been developed called a "Surgical Strike" in which the enemies do not launch a full-scale war, but rather enter the targeted country's territory and neutralize the target. Even if the targeted country is nuclear-powered, the one being attacked cannot respond to the attacker with nuclear weapons. In that scenario, a timely response is needed to counterbalance the threat, and such a response is only possible through a complete air defense shield known as an ADS. These systems ensure that no intruder can carry out an intrusion without being intercepted or detected (Kizza, 2024).

In the case of developing countries such as Pakistan, the nation operates within a complex regional and internal environment, having to manage ever-growing economic difficulties, and broader geopolitical dynamics. The location of the concerned country naturally results in shaping its approach and strategic considerations to national security (Adhikari, 2024). Similarly, speaking of Pakistan, the nation has also stepped-in towards modernization of its air-defense posture with the Chinese systems: the LY-80 (HQ-16), which is a low-to-medium altitude air-defense system formally inducted in 2017, and later on, it signed another agreement with the Chinese government for the acquisition of the long-range HQ-9/P surface-to-air missile system, thus providing and extended layer and range to its integrated air-defense network (Hartley and Belin, 2019). While these acquisitions have supposedly improved Pakistan's layered coverage at low to long altitudes, it is widely noted that high-altitude/exo-atmospheric coverage and wider ballistic-missile-defense layers remain the area of concern and something that carries potential capability deployment (Haider, 2025a). Given this evolving context, the current research aims to identify and select the ADS system solution that can best fit Pakistan's operational requirements, economic constraints, and industrial capacity, via a hybrid Multi-Criteria Decision-Making (MCDM) methodology, i.e., Decision-Making Trial and Evaluation Laboratory (DEMATEL), and Analytical Hierarchy Process (AHP), to recommend options that provide realistic, sustainable improvements to the country's air-defense position.

Research questions

Based on the aforementioned discussion, the current research aims to find the answers to the following research questions.

1. What key factors influence the selection of an appropriate ADS system within a country's evolving regional security environment?
2. Which Air-Defense System emerges as the most suitable option for a country like Pakistan when evaluated against multiple factors using the MCDM methodologies?

This paper is divided into five sections. The introduction is followed by a literature review, methodology, results, discussion, and conclusion of the whole research study.

Literature review

A stronger defense system is essential for any state or nation, whether it is developed or developing, as it reduces vulnerabilities and limits external interference. As modern threats keep on becoming more sophisticated, countries increasingly rely on integrated and technologically advanced defense architectures to help protect their strategic interest and their territory (Wasi *et al.*, 2025). In this era, even the countries that have nuclear weapons prefer to be in a defensive mode because it may cause a very dangerous war that may lead to the loss of humans, plants, animals, the nation's economy, natural resources, climate change, etc. (Mynuddin *et al.*, 2024). Despite the dangers that it might pose to the sustainability of the economies, environment, and society, almost every country tries to protect itself from any type of potential adventure from its rivals or enemies (Streeck, 2025).

In such cases, many of the countries have armed themselves with various advanced weaponry, tactical armed systems, improved satellites, aerial and ground artillery, and even the latest air defense systems (ADSs). To do so, the previous literature highlights some of the scenarios in which nuclear and non-nuclear countries have armed themselves with the latest weaponry and ADSs to ensure that they are well protected and can also keep an eye on any potential attack from their rivals. They have also armed themselves to ensure that they can meet the minimal requirements for their protection, as well as to counter any encounters that might arise as a repercussion (Park, 2024). One such example is the United States, which is developing Next-Generation Interceptors (NGIs) to replace the Ground-Based Midcourse Defense (GMD) systems so that it can address aerial vulnerabilities such as hypersonic maneuvering threats (Moric and Kadyshev, 2025). Similarly, in April 2024, the U.S. Missile Defense Agency (MDA) selected Lockheed Martin to build NGIs to protect the homeland against long-range ballistic-missile threats and future advances. In this

case, the NGI represents an effort to stay ahead of such threats by replacing older technologies with a more resilient architecture (Raser, 2025). Similarly, the installation of the NATO Integrated Air and Missile Defence (IAMD by the NATO allies against the recent escalations in the Russia-Ukraine conflict is also an example of the country's importance to its ADS (Passbach, 2024). It is also important to mention that countries like China and Russia are also taking it seriously to implement advanced systems, such as China's HQ-9 Series to engage long-range ballistic missiles (Jones, 2024) and Russia's S-400/S-500 systems to engage targets at a distance of 400km (Sagild and Hsiung, 2024). Such designs ensure that they can integrate multi-layered radar systems while also ensuring their stealth capabilities. These countries are much in line with the improvement of their military business, and in accordance with that fact, two additional S-400 units are in line to be delivered to a South-Asian country by the year 2026-27, a contract comprising delivering 5 regiments (Haider, 2025b). Similarly, Algeria also became part of the list of countries to have adopted the use of the latest S-400 ADS, confirming reliance on the Russian modern technology (Sanef and Trouzine, 2025). Reportedly, Turkey is also in line for the acquisition of the modern S-400s, adding further to the ever-increasing list of nations adopting the modern ADS, further acknowledging the superiority of such systems (Analytica, 2024). Knowing the importance of the latest ADS and its adoption around the globe, its visual representation of installations across various locations can give a much better idea of the trend of adopting advanced security systems for a resilient strategic position, as depicted in Figure 1.

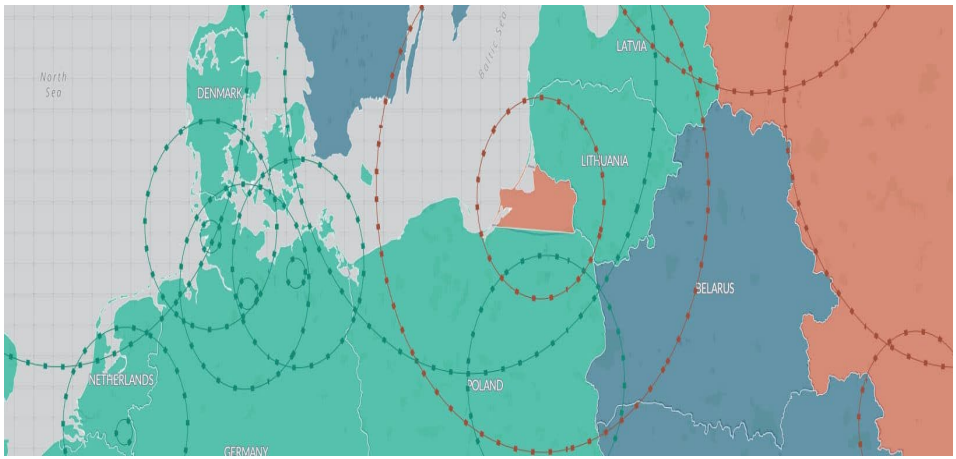

Figure 1. Visualization of long-range ADSs across various locations (Source: Missile Defence Project, 2024)

Furthermore, in the case of a developing country such as Pakistan, the ADS of Pakistan is one of the main components of its defense system, and over the past several years, the country has incorporated Chinese-made (LOMADS) LY-80 in its ADS, which is built by China Aerospace Science and Technology Corps (CASC). This technology hits the target up to an altitude of 400-1000 meters. This missile weighs around 70 kg and can hit a flying aircraft at a maximum altitude of 18 km, while having a horizontal engagement range of nearly 40 km (Khurshid and Zaman, 2024). Similarly, to strengthen longer-range coverage, the nation has also inducted the HQ-9P surface-to-air missile system, alongside related variants such as FD-2000 and HQ-9BE. The HQ-9P is capable of providing high-to-medium altitude defense, thus extending the country's capability of layered air-defense requirements. Together, these systems form part of Pakistan's move to acquire the latest ADS systems initiatives, designed to address threats across different altitude bands and aerial threat types. Given the country's position in the region, it still requires exploration to further integrate the latest systems to enhance both the medium and long-range defense coverage. To address that, the current research aims to assist policymakers and stakeholders in opting for a much better and well-suited ADS to further strengthen the country's ADS.

Furthermore, Pakistan's pursuit of the acquisition of the latest air defense system is molded by a combination of various entities such as evolving regional threats, economic limitations, and technological dependencies. A challenge that a country like Pakistan faces is the technological and operational gap which poses legacy system limitations and integration challenges along with the shortage of skilled and trained personnel (Muhammad Usman, 2024). Internal security, protection of the infrastructure, and geopolitical dependencies and risks are also key challenges that Pakistan faces (Anwar and Atif, 2025). Similarly, the economic constraint is another major issue for a country like Pakistan being already burdened by inflation and reliance on foreign loans, and together with these external issues, it poses a bigger challenging picture for the protection of the country's sovereignty (Hanif and Sultan, 2024). Such challenges can become even bigger to handle when a country is up against rival countries especially having to deal with them when they are already armed with modern weaponry. Such a task requires effective assessment and resilient evaluation of the options that a developing country such as Pakistan can have to effectively counter such a challenge. Recent literature often overlooks the range of external pressures and internal constraints shaping Pakistan's security environment. A clearer understanding of these combined factors is important for assessing the

country's air-defense needs and future system requirements. The current research focuses on providing a novel assessment to assist policymakers in defining strategic investments in cost-effective, layered ADSs to ensure a viable and effective path to stability and deterrence. In such a way, the country can offset its weaker economy as well as secure its airspace in an imbalanced region.

Multi-criteria decision-making (MCDM) models are useful in assessing complex problems such as decision scenarios that require input from various experts in the form of primary or secondary data. It is an essential tool to evaluate conflicting criteria and assess diverse alternatives. MCDM models are useful when it comes to handling the interdependencies between the criteria as well as the large sets of alternatives, proving to be effective in handling complex decision scenarios (Kumar, 2025). Furthermore, they assist in balancing the conflicting objectives such as revealing optimal compromises or in the quantification of subjective preferences (Kizielewicz and Salabun, 2024). Similarly, the MCDM models are effective in handling both qualitative and quantitative data sets and in helping towards reproducibility and transparency, along with the resilient operations management of uncertainty and subjectivity when it comes to fuzzy logic (Pham *et al.*, 2024). Such factors enable the importance of MCDM models without which decision makers might risk making biased choices and ignoring critical factors. Based on such importance, the current study utilizes a combination of MCDM methodologies out of many available choices in terms of various techniques such as ANP, FUCOM, TOPSIS, VIKOR, etc. Various applications of MCDM models can be observed in the current literature that highlight the all-around applications in various complex decision scenarios. One such example of the MCDM model comprises a hybrid assessment, carried out for the supplier selection in public manufacturing and involves the application of Fuzzy DEMATEL, Best-Worst Method (BWM), COCOSO, MOORA, and TOPSIS (Kolour et al., 2026). Similarly, another application can be observed in the case of optimization of leadership strategies, where the application of the Delphi method along with the Analytic Hierarchy Process (AHP) technique contributes to the prioritization of the key influencing factors that can enable transformational change at the workplace (Malmir, 2026). A unique application of TODIM, i.e., an interactive and multicriteria decision-making technique, can be found for the assessment of robust ranking of criteria weights (Zhang and Gao, 2026). An application of DEMATEL also involves the assessment of cause-and-effect relationships among factors that affect transgender people, a study being carried out under uncertain circumstances

(Appasamy, 2026). Another study involved the application towards the enhancement of the cold supply chain resilience by implementing FUCOM in a hybrid combination with the Fuzzy QFD method (Khan and Ali, 2023). Similarly, the selection of the sustainable supply for the cold supply chain also comes under the domain of MCDM applications, i.e., Interpretive Structural Modelling (ISM), along with the fuzzy VIKOR technique (Khan and Ali, 2021). Also, the risk assessment and mitigation comprise the diverse MCDM applications such as FMEA-RPN and FUCOM techniques (Khan *et al.*, 2022). It is safe to consider MCDM an ultimate choice for the current decision scenario, and therefore, the current research implies a DEMATEL-AHP approach to help with the selection of the air defense system for a developing country such as Pakistan. The choice of these methods is in comparison to others in the sense that the DEMATEL approach is helpful in the identification of the interdependencies among the criteria and can distinguish the cause from the effect, which can be extremely fruitful when it comes to timely decision making. Similarly, the application of the AHP method proves to be helpful when complex problems are to be narrowed down in terms of hierarchical structures to identify the goal, criteria, and alternatives. It thus enables pairwise comparisons and proves worthy in critical scenarios such as defense systems and safety (Khan *et al.*, 2022). Therefore, in a scenario where hierarchy and interdependencies are critical, DEMATEL and AHP can prove to be a top choice for studies of a similar nature.

In the current research, the study utilizes two Multi-Criteria Decision Making (MCDM) methodologies, i.e., Decision-Making Trial and Evaluation Laboratory (DEMATEL) and Analytical Hierarchy Process (AHP). The DEMATEL is a useful method that can convert the relations and "cause and effect" of criteria into a visual structural model. It can also be used for handling inner dependencies within a set of criteria. One such example states the application of the Fuzzy DEMATEL approach in the case of main battle tanks (MBTs), analyzing various concerned factors for better assessment results (Kharola *et al.*, 2024). Similarly, another application involves the use of a hybrid methodological model, i.e., Fuzzy AHP, DEMATEL, & TOPSIS to enhance the protection of airplanes from crashing (Sharma *et al.*, 2025). The DEMATEL method was used for data processing and criteria and attributes determination to eliminate less significant criteria and attributes. For each criterion and attribute, the weight values were determined by the AHP method. The eigenvector for prioritization was used to determine reliability and the consistency ratio for each result (Ahmad Al-Rawashdeh, Al'Azzeh, and Al-Tarawneh, 2025). Similarly, another research applied the ANP and DEMATEL approach for

the selection of knowledge management strategies. The study assessed such models to enhance the development of the organizational culture (Vatan, Raissi Ardali, and Shahin, 2024). Recent research has incorporated a novel fuzzy decision-making model to pinpoint appropriate policies for the transition to renewable energy (Dincer et al., 2023). Another research delved into the Financial Performance Evaluation of Energy Companies (Dagistanli, 2023). Furthermore, AHP is a technique used for the selection of the best alternative. It was introduced by Thomas Saaty in 1980, and it sets the priorities and helps the decision maker to make the best decision (Saaty, 1994). AHP, apart from making a decision, also talks about the consistency of data to minimize biases (De Felice and Petrillo, 2024). AHP works by considering a set of criteria and possible alternatives among which a decision is to be made, and it is not necessary for the AHP method that all criteria should be optimized. In AHP, weights are assigned to each criterion (Khan & Ali, 2020). AHP is used in every industry and organization, from a simple problem like bicycle features to the manufacturing of an aircraft. It can also be used in an environment where the exact numerical values for weight are not possible to collect. In that case, the linguistic terms need to be transformed into numerical values. The same approach is used for renewable energy planning in Istanbul. In this case, the best alternative for renewable energy is obtained by using VIKOR-AHP. Similarly, in the same project, the same method is used in a fuzzy environment for the selection of the best site for renewable energy (Ma *et al.*, 2025). Similarly, a hybrid MCDM approach, i.e., fuzzy AHP-Fuzzy TOPSIS, is incorporated in the context of fighter aircraft selection in the case of the Algerian Air Force (Kaanit, Mouss, and Berghout, 2025). The scenario requires a regular check on changes in the criteria that may lead to some interdependency casually; in that case, AHP and DEMATEL were integrated as a top choice (Singh and Sharma, 2024). Moreover, the advantage of the AHP integration is that it can easily improve the supplier performance and is implemented in determining the success factors associated with the spare parts supply chain (Zaid, Saleh, and Tomeh, 2025). AHP is also used for setting the priorities, while DEMATEL is used for the evaluation of success factors, as AHP and DEMATEL both work well even in a fuzzy environment. The studies were done for the evaluation of human resources for science, in which fuzzy AHP is used to weigh each criterion, after which fuzzy DEMATEL is used for the evaluation of the criteria and the alternatives (Lin and Wang, 2024).

Research gap

The current research comprises an idea that concerns developing countries as a whole and Pakistan in particular, as it is designed in such a way that highlights the factors affecting the ADS, as well as evaluating the best missile system based on various factors. Since there is no other study that highlights this topic on such grounds, and similarly, there is no study involved in the previous literature that has carried out a diverse decision scenario in the ADS sector of Pakistan, based on a hybrid DEMATEL-AHP approach, this forms a novel study. Furthermore, the motivation of the current research can also be extracted from the fact that the timing of the study is such that currently Pakistan faces both internal and external threats, and such arrangements are of extreme importance for the country's sovereignty. Therefore, the study is the need of the hour and thus a major motivation and importance for the current research.

Methodology

The DEMATEL approach was first used by the Science and Human Affairs Program of the Battelle Memorial Institute of Geneva in 1972-1976. This approach was designed to determine the complex problems and transform them into a solvable form. Since then, the methodology has been applied by different researchers to find interrelationships among different criteria in multi-criteria decision-making scenarios. The DEMATEL helps capture the logical relationship between different elements of the system and helps frame the strength of the interrelationship as well. DEMATEL classifies the factors of cause and effect while illustrating their relationship through a diagram. It determines the relationship among the factors while prioritizing the criteria according to the relationship and effect on each other. DEMATEL filters out the unnecessary criteria and sub-criteria, which are less important for an alternative selection, and guarantees the important criteria to be included in the selection process (Shafaei *et al.*, 2025). The whole methodology is displayed in the flow chart in Figure 2.

From different literature and sources, the criteria affecting the selection of an air defense system are collected. A 19x19 matrix is formed from the shortlisted criteria which were distributed among experts to get their review on the relative importance of each criterion. In this way, a total of 40 responses were collected from various commissioned and non-commissioned officers of the Pakistan Air Force. Each respondent gave judgment about each criterion and its interdependence with other criteria. This step was done using the DEMATEL approach. The pairwise

comparison is performed according to a scale of 0-4 (0 for No Influence, 1 for Low Influence, 2 for Middle Influence, 3 for High Influence, and 4 for Very High Influence).

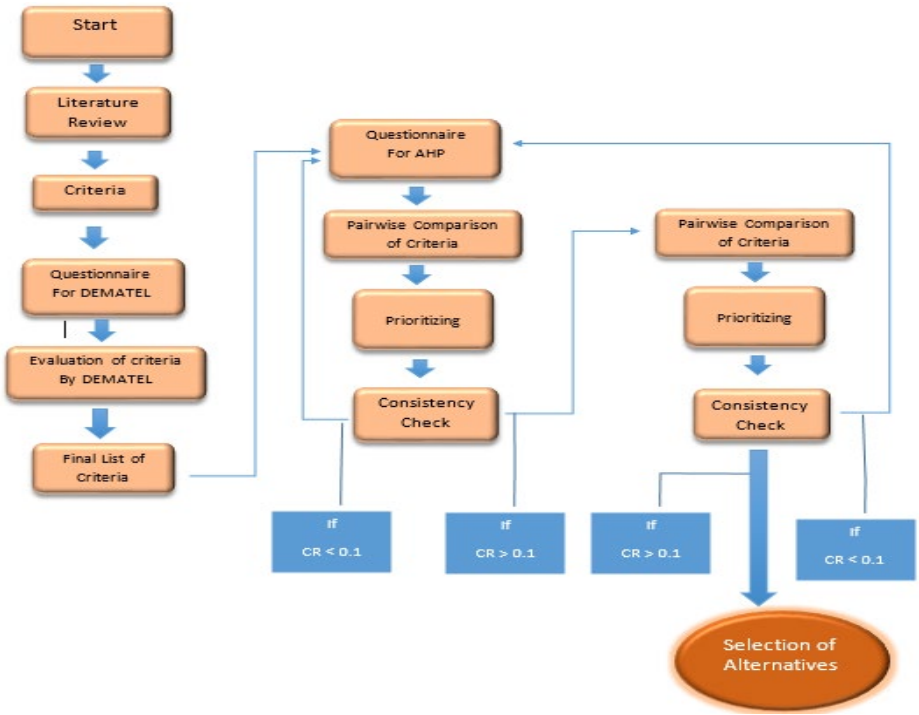

Figure 2. Flow chart showing the methodology

The following are the steps followed in the DEMATEL:

1. The first step in DEMATEL is to study the literature and find the factors affecting the selection of the air defense system. In this case, the expert review is very important for shortlisting the criteria and factors that are very relevant to the selection of the air defense system. The shortlisted criteria are shown in Table 1.
2. The second step in the DEMATEL process is to make an initial matrix that identifies the relationship between any two criteria. This matrix is reviewed by experts who grade the influence of one criterion over another criterion on a scale of 0 to 4. The notation that is used for this influence is X_{ij}, where X_{ij} is the expert judgment on the influence of i over j. When i and j are equal, it means that they do not influence each other. In that case, the

value will be zero. For each respondent, a 19x19 matrix was created in an Excel sheet; as a result, the total number of matrices is equal to the total number of respondents, which is denoted by H in this research. $X_1, X_2, X_3 - - - - X_n$

Table 1. List of the criteria

Life Cycle Cost	Durability	Maintenance	Time Of Response
Acquisition Cost	Payload	Reliability	Maneuverability
Versatility	Air Speed	Radar And Other Sensors	Flight Control System
Data Processing Time	Rate Of Fire	Maintainability	Number Of Targets It Can Engage at A Time
Infrastructure	Precision Target Capability	Range	

3. To integrate the responses of all the respondents, all the responses were added to get their average value. All the corresponding elements of the matrices are added, and their sum is divided by the number of responses. The resultant matrix is called the Average Matrix, denoted by A. This step can be summarized in equation 1 as

$$A_{ij} = \frac{1}{H}\sum_{k=1}^{H} X_{ij}^{k} \quad (1)$$

4. In this step, the Normalized Initial Direct Relation matrix is determined. Each element gets a value between zero and one. Equations 2 and 3 are used for this step.

$$D = A \times S \quad (2)$$

where

$$S = \frac{1}{max_{1<i<n}\sum_{j=1}^{n} A_{ij}} \quad (3)$$

5. In this step, the Total Relation Matrix T is constructed by using Equation 4 as

$$T = D\ x\ \left(I - D\right)^{-1} \quad (4)$$

In the Total Relation Matrix, I is the identity matrix. Next, the summation of the rows and columns of the matrices is calculated in the total matrix. R_i represents the sum of rows; C_j represents the sum of columns, while $R_i - C_j$ and $R_i + C_j$ show the sum and difference of R_i and C_i.

The second method used in this research for the evaluation of alternatives is the Analytical Hierarchy Process (AHP). AHP is a very powerful decision-making tool that was introduced by Saaty in 1990. It uses a pairwise comparison between criteria to convert the scale of the comparison between criteria into a number. In AHP, each criterion is weighted against another by weight from (1, 3, 5, 7, and 9). The higher-ranking number indicates the importance of one criterion over another criterion (Huang *et al.*, 2025). Thus, AHP reduces complex decision making to a comparison of criteria, where AHP not only chooses the best alternative but also talks about the consistency of the data.

In this research, AHP is used to evaluate the shortlisted criteria for a missile and then to look for the available alternatives to see which one satisfies the needs of Pakistan's current air defense. To select the best missile system for Pakistan Air Defense (PAD), a set of criteria is chosen with the help of DEMATEL, upon which all the alternatives will be weighted equally. The criteria upon which the selection of the missile system will be evaluated are Payload, versatility, Fire Rate, Reliability, Precision Target Capability, Range, Cruising Speed, Maneuverability, Acquisition Cost, Operation Cost, Maintainability, and Availability. One of the most important criteria is Availability, and this criterion includes the trade embargo and the sanctions that can be placed against a country by the international community or a specific country. The importance of this criterion can be understood well from the cold relations between Pakistan and the US for so many years.

For this project, a total of five options are shortlisted, among which one optimum option will be chosen. The shortlisted alternatives for PAD are shown in Table 2.

Table 2. List of the alternatives

THAAD	S-400	S-300	PATRIOT	LY80

For a comparison of each air defense system against the criteria in the matrices, a detailed review is done from different forums and experts. The required specifications were used against different air defense systems with weights of 1, 3, 5, 7, and 9 for pairwise comparison. All the

matrix calculations are done in Microsoft Excel. From these matrices, the normalized matrix, consistency ratio, and priority vector are calculated.

The following are the steps followed in the Analytical Hierarchy Process (AHP).

1. In the first step, all the criteria and decision alternatives are listed.
2. In this step, a rate is assigned to each criterion based on relative importance. The sum of each column will be used for the normalization of the matrix.
3. The next step is to normalize the matrix by dividing each element of every column by the respective sum of the column. The normalized matrix 'N' with the weighted vector 'W' on the right of the matrix, which indicates the average of each row.
4. The next step is to check the consistency of the matrix by first calculating the weighted sum vector 'W_s' using the multiplication of the matrix 'C' with the vector 'W'. This step is summarized in Equation 5.

$$\{Ws\} = [C] \tag{5}$$

After determining the weighted sum vector, the consistency vector is calculated using Equation 6 as

$$\{Cons\} = \{Ws\} / \{W\} \tag{6}$$

The average A of the consistency vector {Cons} is used in Equation 9 to calculate the consistency index CI.

$$CI = (A - n) / (n - 1) \tag{7}$$

Finally, a random index value is used to calculate the consistency ratio CR using Equation 8.

$$CR = CI / RI \tag{8}$$

If this value is lower than 0.10, the matrix is consistent; otherwise, an adjustment in the 'C' matrix entries is necessary to repeat step 4.

5. The same steps from step 1 to step 4 are applied this time for the evaluation of the alternatives which are shown in Table 2. The priority vector of each matrix is compiled in a matrix. This matrix is called the Final Rating matrix. After taking the transpose of the Final Rating matrix, it is multiplied by the vector 'W' using Equation 9.

$$[FRating]T \; x\{W\} = \{Alternative\ Value\} \tag{9}$$

Results and discussion

The criteria chosen had a complex relationship among them; without the application of a sophisticated technique, it was hard to comprehend the meaning and relation of the criteria. Therefore, DEMATEL-AHP was used to determine the interaction among them, the steps of which are shown in the methodology.

Table 3. R_i and C_j values were obtained for the assessment. (Source: Author's creation)

Criteria	Ri	Cj
Precision Target Capability	2.4926	2.7520
Range	2.6399	2.5009
Manoeuvrability	2.6928	2.4299
Versatility	2.3928	2.6575
Maintainability	2.4501	2.4081
Data Processing Time	2.5969	2.2300
Radar And Other Sensors	2.3524	2.3950
Time Of Response	2.4385	2.3021
Reliability	2.5958	2.1019
Rate Of Fire	2.3806	2.1447
Flight Control System	2.4185	2.0772
Number Of Targets It Can Engage at A Time	2.4268	2.0536
Payload	0.0012	0.2515
Durability	1.8837	2.3120
Air Speed	1.9007	2.2473
Infrastructure	-0.2766	0.0264
Maintenance	1.6561	1.8472
Life Cycle Cost	1.4289	1.9873
Acquisition Cost	1.4854	1.7884

The sum of the R_i and C_j shows the total impact and importance of ‘i' as compared to 'j'. The difference R_i-C_j is called the relation, which represents the net effect of ‘i’ over the system. If the difference is positive, it indicates that the factor ‘i’ is the cause, while the factor will be the receiver if the difference comes out to be negative. The individual values obtained for R_i and C_j are listed in Table 3. Table 4 shows the ranking of the criteria based on the values of R_i+C_j and R_i-C_j. The value of R_i+C_j for the criterion ‘Precision Target Capability' is the highest, i.e., 5.2446, and its corresponding value of R_i-C_j is positive, which means that the Precision Target Capability is the most important factor that should be considered for the selection of an ADS for Pakistan. Moreover, the 'Range' of hitting

the target and the 'Maneuverability' are the second and third most important factors based on which the missile system should be selected. The other criteria that should be considered for the selection of ADS are prioritized as shown in Table 4.

Table 4. Ranking of the criteria

Criteria	R_i+Cj	R_i-Cj	Rank
Precision Target Capability	5.2446	-0.25941	1
Range	5.140833	0.138936	2
Maneuverability	5.122678	0.262827	3
Versatility	5.050276	-0.26464	4
Maintainability	4.858191	0.04208	5
Data Processing Time	4.826916	0.366989	6
Radar And Other Sensors	4.747371	-0.04255	7
Time Of Response	4.740586	0.136442	8
Reliability	4.697649	0.493929	9
Rate Of Fire	4.525268	0.235876	10
Flight Control System	4.495664	0.341241	11
Number Of Targets It Can Engage at A Time	4.480463	0.373168	12
Payload	0.252751	-0.25026	13
Durability	4.195692	-0.42825	14
Air Speed	4.148004	-0.34659	15
Infrastructure	-0.25026	-0.30303	16
Maintenance	3.503309	-0.19107	17
Life Cycle Cost	3.416167	-0.55845	18
Acquisition Cost	3.273806	-0.30303	19

These criteria are then used for the evaluation of the alternatives using AHP. After constructing the Normalized Matrix in Table 5, the consistency of the data has been checked, where the Consistency Index (CI) can be depicted as 0.10528. The matrix is consistent with the consistency ratio CR i.e.,

$$CR = \frac{CI}{RI} = \frac{0.10528}{1.12} = 0.094$$

As indicated by Equation 9, the product of the transpose of the Final Rating Matrix and the W vector gives the alternative value. All the

alternatives are ranked according to these values. The larger value indicates that the alternative is the best one among all. Therefore, it is concluded from Table 6 that the S-400 Triumf is the best solution for Pakistan Air Defense with the highest value of 0.29, followed by THAAD, S-300, LY 80, and PATRIOT.

Table 5. Construction of the Pairwise Comparison Matrix

	S-400	THAAD	S-300	LY 80	PATRIOT
S-400	1.000	1.0506	1.536	2.394	3.083
THAAD	0.952	1.000	1.462	2.279	2.935
S-300	0.651	0.684	1.000	1.559	2.007
LY 80	0.417	0.439	0.641	1.000	1.287
PATRIOT	0.324	0.341	0.498	0.776	1.000

Table 6. Ranking of the alternatives based on AHP

Missile System	$A_t x W_c$	Rank
S-400	0.29896063	1
THAAD	0.28459462	2
S-300	0.1946512	3
LY 80	0.12483901	4
PATRIOT	0.09695455	5

Based on all the criteria, especially the top three, i.e., Precision Target Capability, Range, and Maneuverability, the best air defense system for Pakistan is the S-400. It is more favorable for Pakistan to purchase the S-400 missile system from Russia, as it possesses the radar system and can hit the target precisely. The S-400 is also easy to maintain, and its cost is more suitable according to the economic situation of Pakistan. The validity of the results obtained can be compared in such a way that it comprises consistency with global studies such as (Sari, et al., 2024), which ranks the S-400 as the most powerful defense system in the world by assessing it based on active sensors for anti-aircraft missiles. Keeping in mind that Pakistan already has the Chinese HQ-9, the outcome from the analysis depicting the S-400 as a better choice paints the picture of the latter offering significantly greater engagement range, along with interception at

higher altitudes and flexibility in more missile-type options in comparison to the HQ-9 family, thus enabling wider and more defensible air-defense zones around the critical assets. When the S-400 is added to Pakistan's existing HQ-9 coverage, it would strengthen the outermost layer of defense, complicating enemy strike planning along with improvements in deterrence. It must be kept in mind that the overall success would depend on the robust integration, including radar support, mobility, command-and-control, and maintenance infrastructure to ensure effective operations beyond mere technical specifications (Bronk, 2018). Furthermore, techniques like AHP have been used either alone or in hybrid combination with others, such as TOPSIS, to assess weapon selection. In short, the current research aligns closely in terms of performance with the global studies but diverges in a regional context. The comparative studies validate our choice of methodologies as well as the outcome and therefore prove to be an effective outcome for the country and the region.

Research implications & future recommendations

The current research focuses on the regional context to support and evaluate the assessment of the best and most effective air defense system by considering a hybrid approach of DEMATEL and AHP methodologies. It enforces and supports technical performance and ensures that similar results can be obtained with such efficiency and effectiveness. The current research proves to be timely, especially in the case of heightened tensions in the country's internal and external environment, serving the need for a reliable and effective air-defense system (ADS) which has become more critical for Pakistan's overall security planning. Similarly, in the future context, a similar study can be extended to the combination of more hybrid methodologies to ensure effective comparisons of the results and also to account for the factors qualitatively. Future research can also include factors such as electronic warfare resistance or strategic mobility in a global or developing country(s) context.

Conclusion

Air defense systems (ADSs) are very important for any country, whether developed or developing. The ADS helps a country or a nation to defend its sovereignty. This research paper aims to identify the factors and criteria for the selection of the ADS which is preferable for Pakistan. For this purpose, the criteria, i.e. precision target capability, range, maneuverability, versatility, maintainability, data processing time, radar and other sensors, time of response, reliability, rate of fire, flight control

system, number of targets it can engage at a time, payload, durability, airspeed, infrastructure, maintenance, life cycle cost, and acquisition cost, are considered. Moreover, the five missile systems (alternatives), i.e., S-400, S-300, THAAD, LY-80, and PATRIOT, are considered. Two hybrid MCDM methodologies, called DEMATEL and AHP, are integrated to identify and rank the criteria and then select the alternatives based on the criteria. DEMATEL is used for the evaluation of criteria and finding their relative importance to determine the most important criteria. Using AHP, after performing all the necessary steps and checking for consistency, the alternatives were evaluated against each criterion, which generated a ranking vector shown in Table 4. It is concluded that the precision target capability, range, and maneuverability are the prominent criteria based on which ADSs are to be selected for Pakistan. The S-400 Triumf emerged as the highest-ranked option after the AHP assessment application, indicating the most suitable ADS for Pakistan's current needs, based on the concerned distinct criteria.

Limitations

The current research considers various criteria to evaluate alternatives via DEMATEL-AHP methods. The overall boundary of the research scope is limited to Pakistan, and one of the limitations is that it does not cover almost all the developing countries. Only those who face similar crises will be able to benefit from this research . Similarly, the time constraint proves to be another limitation for the research since it is the need of the hour, and it was done to ensure that it is completed within the current time frame. Similarly, the limitation of finding the right experts is another major issue, especially in a country like Pakistan, where most of the experts are not easily available and access to the data is rather difficult. Such limitations, although they did not create any obstacle, could have improved the study by a much greater margin.

References

Adhikari, L.D. (2024) “Exploring the Relationship between National Security Risks and Economic Factors: A Nepalese Perspective,” *Journal of Political Science*, pp. 39–56. Available at: https://doi.org/10.3126/jps.v24i1.62853.

Ahmad Al-Rawashdeh, T., Al’Azzeh, F. and Al-Tarawneh, F. (2025) “An Analytical Hierarchy Process-Based Technique for Software Requirements Prioritization,” *IEEE Access*, 13, pp. 50603–50610. Available at: https://doi.org/10.1109/ACCESS.2025.3552490.

Aljohani, T.M. (2024) “Cyberattacks on Energy Infrastructures as Modern War Weapons—Part I: Analysis and Motives,” *IEEE Technology and Society Magazine*, 43(2), pp. 59–69. Available at: https://doi.org/10.1109/MTS.2024.3395688.

Analytica, O. (2024) *Emerald Expert Briefings*. Emerald Expert Briefings. Available at: https://doi.org/10.1108/OXAN-DB283554

Anwar, U. and Atif, M. (2025) ‘“CPEC & BRI regional game changers: security and geopolitical implications in Pakistan”’, *Australian Journal of Maritime & Ocean Affairs*, pp. 1–17. Available at: https://doi.org/10.1080/18366503.2025.2480945.

Appasamy, S. (2026) ‘A Study on DEMATEL Approach Under Uncertainty Environments’, *Spectrum of Operational Research*, 3(1), pp. 29–39. Available at: https://doi.org/10.31181/sor31202628.

Bronk, J. (2018) “The RAF’s Force Structure Plan and Future Threat Scenarios,” *The RUSI Journal*, 163(3), pp. 52–57. Available at: https://doi.org/10.1080/03071847.2018.1495806.

De Felice, F. and Petrillo, A. (eds.) (2024) *The Art of Decision Making - Applying AHP in Practice*. IntechOpen (Business, Management and Economics). Available at: https://doi.org/10.5772/intechopen.1003360.

Dincer, H., Yuksel, S. and Eti, S. (2023) ‘Identifying the right policies for decision-making model’, *Journal of Soft Computing and Decision Analytics*, 1(1), pp. 50–62. Available at: https://10.31181/jscda1120234

Eslami, M. and Borges, L. (2025) “Military Drones and the Offense–Defense Balance in Future Wars,” in Eslami, M. and Borges, L., *The Drones Race and International Security*. Cham: Springer Nature Switzerland (Contributions to Security and Defence Studies), pp. 137–154. Available at: https://doi.org/10.1007/978-3-032-05921-5_7.

Haider, U. (2025a) “India’s Evolving Air Defence Capabilities and Options for Pakistan,” *Journal of Security & Strategic Analyses*, 11(1), pp. 88–109. Available at: https://doi.org/10.57169/jssa.0011.01.0380.

Haider, U. (2025b) “India’s Evolving Air Defence Capabilities and Options for Pakistan,” *Journal of Security & Strategic Analyses*, 11(1), pp. 88–109. Available at: https://doi.org/10.57169/jssa.0011.01.0380.

Hanif, R. and Sultan, I. (2024) ‘The Economic Dependency of Pakistan: Reasons, Challenges and Prospects’, *Pakistan Journal of Social Sciences* [Preprint]. Available at: https://doi.org/10.5281/ZENODO.11471595.

Hartley, K. and Belin, J. (2019). *The Economics of the Global Defence Industry*. 1st ed. Edited by K. Hartley and J. Belin. Milton Park, Abingdon, Oxon; New York: Routledge, 2020.: Routledge. Available at: https://doi.org/10.4324/9780429466793.

Huang, J. *et al.* (2025) “Hybrid FAHP-FTOPSIS methodology for objective football player selection and ranking,” *Scientific Reports*, 15(1), p. 27913. Available at: https://doi.org/10.1038/s41598-025-13973-6.

Jones, S.G. (2024) *Rebuilding the arsenal of democracy: the U.S. and Chinese defense industrial bases in an era of great power competition*. 1st edn. Blue Ridge Summit: Center for Strategic & International Studies. ISBN: 9781538170779

Kaanit, A., Mouss, K.N. and Berghout, T. (2025). "A Hybrid Fuzzy Multicriteria Decision-Making Approach for Fighter Aircraft Selection: Application to the Algerian Air Force," *International Journal of Aerospace Engineering*. Edited by R. Zhang, 2025(1), p. 9958630. Available at: https://doi.org/10.1155/ijae/9958630.

Khan, A.U. and Ali, Y. (2020) 'Analytical hierarchy process (AHP) and analytic network process methods and their applications: A twenty-year review from 2000–2

0 Khan, A.U. and Ali, Y. (2021) 'Sustainable supplier selection for the cold supply chain (CSC) in the context of a developing country', *Environment, Development and Sustainability*, 23(9), pp. 13135–13164. Available at: https://doi.org/10.1007/s10668-020-01203-0.

h Khan, A.U. and Ali, Y. (2023) 'Enhancement of resilience and quality of cold supply chain under the disruptions caused by COVID-19: A case of a developing country', *Australian Journal of Management*, 48(2), pp. 341–365. Available at: https://doi.org/10.1177/03128962221095596.

s Khan, A.U. *et al.* (2022) 'Risk Management for Cold Supply Chain: Case of a Developing Country', *Acta Polytechnica Hungarica*, 19(8), pp. 161–185. Available at: https://doi.org/10.12700/APH.19.8.2022.8.10.

/ Kharola, A. *et al.* (2024) "Fuzzy canonical approach based on delphi technique for effective decision making: A case of main battle tanks (MBTs)," in. *INTERNATIONAL CONFERENCE ON RECENT TRENDS IN COMPOSITE SCIENCES WITH COMPUTATIONAL ANALYSIS*, Dehradun, India, p. 040006. Available at: https://doi.org/10.1063/5.0182937.

1 Khurshid, T. and Zaman, H. (2024) 'AI INTEGRATION IN INDIAN MILITARY: APPRAISAL OF SECURITY APPREHENSIONS FOR SOUTH ASIA', *NDU Journal*, pp. 1–15. Available at: https://doi.org/10.54690/ndujournal.38.179.

1 Kizielewicz, B. and Salabun, W. (2024) 'A Robust Framework for Renewable Energy Policy Evaluation Using MCDA and Compromise Ranking with Stochastic Weight Identification', *Journal of Intelligent Management Decision*, 3(4), pp. 213–223. Available at: https://doi.org/10.56578/jimd030402.

3 Kizza, J.M. (2024) "System Intrusion Detection and Prevention," in Kizza, J. M., *Guide to Computer Network Security*. Cham: Springer International Publishing (Texts in Computer Science), pp. 295–323. Available at: https://doi.org/10.1007/978-3-031-47549-8_13.

a Kolour, H.R., Momayezi, V. and Momayezi, F. (2026) 'Enhancing supplier selection in public manufacturing: A hybrid multi-criteria decision-making approach', *Spectrum of Decision Making and Applications*, 3(1), pp. 1–20.

Kristensen, H.M. *et al.* (2025) “Pakistan nuclear weapons, 2025,” *Bulletin of the Atomic Scientists*, 81(5), pp. 386–408. Available at: https://doi.org/10.1080/00963402.2025.2543685.

Kumar, R. (2025) ‘A Comprehensive Review of MCDM Methods, Applications, and Emerging Trends’, *Decision Making Advances*, 3(1), pp. 185–199. Available at: https://doi.org/10.31181/dma31202569.

Lin, L.-H. and Wang, K.-J. (2024) ‘Enhancing Talent Retention in Work 4.0 Era: An Improved Fuzzy Analytical Hierarchy Process and Fuzzy Decision-Making Trial and Evaluation Laboratory Methodology’, *International Journal of Fuzzy Systems* [Preprint]. Available at: https://doi.org/10.1007/s40815-024-01844-7.

Ma, Y. *et al.* (2025) “Hybrid AHP-VIKOR methodology for multi-criteria decision-making in marine renewable energy systems: Optimizing DC-DC buck converters for sustainable offshore applications,” *Marine Pollution Bulletin*, 214, p. 117809. Available at: https://doi.org/10.1016/j.marpolbul.2025.117809.

Malmir, A. (2026) ‘Ranking of Factors Affecting Transformational Leadership in Organizations: Application of AHP Method in Optimizing Leadership Strategies’, *Spectrum of Decision Making and Applications*, 3(1), pp. 62–69. Available at: https://doi.org/10.31181/sdmap31202627.

Missile Defence Project (2024). "Missile Maps and Data Visualizations," *Missile Threat*. Available at: https://missilethreat.csis.org/missile-maps-infographics/.

Moric, I. and Kadyshev, T. (2025) ‘Forecasting Costs of U.S. Ballistic Missile Defense Against a Major Nuclear Strike’, *Defence and Peace Economics*, 36(2), pp. 141–166. Available at: https://doi.org/10.1080/10242694.2024.2396415.

Muhammad Usman, Dr.S. (2024) ‘Pakistan in the Crosshairs and the Rising Stakes of Strategic Information Warfare’, *Journal of Research in Social Sciences*, 12(1), pp. 25–47. Available at: https://doi.org/10.52015/jrss.12i1.235.

Mynuddin, M. *et al.* (2024) ‘Trojan Attack and Defense for Deep Learning-Based Navigation Systems of Unmanned Aerial Vehicles’, *IEEE Access*, 12, pp. 89887–89907. Available at: https://doi.org/10.1109/ACCESS.2024.3419800.

Park, H.-R. (2024) ‘A non-nuclear US ally’s nuclear preparedness dilemma: South Korea’s “Three-Axis System”’, *Defence Studies*, 24(2), pp. 257–276. Available at: https://doi.org/10.1080/14702436.2024.2303412.

Passbach, D. (2024) ‘National and International Perspectives of the Hungarian Ground-Based Air Defence Forces (1): Strategic Environment and First Glimpse of Multinational Capability Development Options’, *Academic and Applied Research in Military and Public Management Science*, 23(2), pp. 39–50. Available at: https://doi.org/10.32565/aarms.2024.2.3.

Pham, T.Y. *et al.* (2024) ‘The fuzzy MCDM for container terminal choice in Vietnam from shipping lines’ perspective based on cumulative prospect theory’, *The Asian Journal of Shipping and Logistics*, 40(3), pp. 147–156. Available at: https://doi.org/10.1016/j.ajsl.2024.06.003.

Raser, J. (2025) “Strategic Safety Time-Lags: AGI-Driven CPA Reversal in U.S. Missile Defense, 2027-2032 -Part I.” SSRN. Available at: https://doi.org/10.2139/ssrn.5565558.

Saaty, T.L. (1994) 'Highlights and critical points in the theory and application of the Analytic Hierarchy Process', *European Journal of Operational Research*, 74(3), pp. 426–447. Available at: https://doi.org/10.1016/0377-2217(94)90222-4.

Sagild, R.Å. and Hsiung, C.W. (2024) 'Chinese Re-Examinations of Russia? The Strategic Partnership in the Wake of Russia's War Against Ukraine', *Journal of Contemporary China*, pp. 1–16. Available at: https://doi.org/10.1080/10670564.2024.2358876.

Sanef, A.C. and Trouzine, B. (2025) "Response to Incitement: Call for Algeria Sanctions (International Legal Analysis)," *Law and World*, 11(2), pp. 97–111. Available at: https://doi.org/10.36475/11.2.9.

Sari, R.E., Melamedika, C., Hartati, T. and Iljannah, C. (2024) 'Active sensor working system on anti-aircraft missiles', *Journal of Frontier Research in Science*,

Shafaei, A. *et al.* (2025) "An integrated decision-making approach for identifying sustainable tier-1 suppliers: Fuzzy Delphi-Borda-SWARA," *Annals of Operations Research* [Preprint]. Available at: https://doi.org/10.1007/s10479-025-06923-y.

Sharma, S.K. *et al.* (2025) "A fuzzy multi-criteria decision-making framework for assessing the impact of multi-agent technology in preventing the probabilities of airplane crashing," *Aircraft Engineering and Aerospace Technology*, 97(10), pp. 1320–1332. Available at: https://doi.org/10.1108/AEAT-04-2025-0154.

Singh, V. and Sharma, S.K. (2024) 'Critical factors of multi-agent technology influencing manufacturing organizations: an AHP and DEMATEL-oriented analysis', *International Journal of Computer Integrated Manufacturing*, 37(3), pp. 243–265. Available at: https://doi.org/10.1080/0951192X.2023.2209857.

Streeck, W. (2025) 'Notes on the political economy of war', in R. Giammetti and T. Palley (eds) *The Political Economy of War, Peace, and the Military–Industrial Complex*. Edward Elgar Publishing, pp. 19–33. Available at: https://doi.org/10.4337/9781035357178.00007.

Tytarenko, I. and Pavlenko, I. (2024) "An Approach for Modeling City Defense Means: Sumy Region Case Study," in V. Ivanov et al. (eds.) *Advances in Design, Simulation and Manufacturing VII*. Cham: Springer Nature Switzerland (Lecture Notes in Mechanical Engineering), pp. 96–106. Available at: https://doi.org/10.1007/978-3-031-63720-9_9.

Vatan, E., Raissi Ardali, G.A. and Shahin, A. (2024) 'Selecting information systems development models based on organizational culture: an integrated approach of DEMATEL and ANP', *VINE Journal of Information and Knowledge Management Systems*, 54(3), pp. 531–560. Available at: https://doi.org/10.1108/VJIKMS-08-2021-0164.

Wasi, A.T. *et al.* (2025) "Generative AI as a Geopolitical Factor in Industry 5.0: Sovereignty, Access, and Control." arXiv. Available at: https://doi.org/10.48550/ARXIV.2508.00973.

Yaqub, M., Ali, J. and Kumar, J. (2025) "The new arms race: analyzing Sino-US geo-strategic dynamics and implications for global security," *Asian Journal of*

Political Science, 33(2), pp. 198–223. Available at: https://doi.org/10.1080/02185377.2024.2424749.

Zaid, A.A., Saleh, Y. and Tomeh, A.J. (2025) “Identifying the success factors for TQM implementation among automotive spare parts companies using analytic hierarchy process (AHP): evidence from Palestine,” *International Journal of Organizational Analysis*, 33(4), pp. 743–762. Available at: https://doi.org/10.1108/IJOA-02-2024-4252.

Zhang, W. and Gao, H. (2026) ‘Interpretable Robust Multicriteria Ranking with TODIM in Generalized Orthopair Fuzzy Settings’, *Spectrum of Operational Research*, 3(1), pp. 14–28. Available at: https://doi.org/10.31181/sor31202632.

Zou, D., Liu, Y. and Teng, Z. (2025). "Study on the impact resistance of reinforced concrete protective structures for energy facilities subjected to tube-type missile impacts," *Structures*, 79, p. 109445. Available at: https://doi.org/10.1016/j.istruc.2025.109445.

Стратешки оквир за избор напредних ПВО система: увиди из земље у развоју

Јусуф Али
Факултет за бизнис и менаџмент, Универзитет „Фахад Бин Султан”, Табук, Саудијска Арабија

ОБЛАСТ: операциона истраживања, науке о одлучивању, студије одбране, анализа војних система
КАТЕГОРИЈА (ТИП) ЧЛАНКА: оригинални научни рад

Сажетак:

Увод/циљ:Данас свака држава покушава да унапреди свој систем одбране набавком нових технологија. Једну од најважнијих компоненти система одбране представља систем противваздухопловне одбране (ПВО) који обухвата ловачке авионе, беспилотне летелице, 3Д радаре, борбена командна возила и ракетне системе. Ракетни систем је постао најважнија компонента система ПВО широм света. Услед ограничених средстава и слабе економије, земље у развоју имају потешкоће да набаве ПВО систем који одговара њиховим ресурсима и економским могућностима. Сврха овог истраживачког рада јесте да проучи потребе и циљеве система одбране ваздухопловних снага Пакистана, као и да предложи најбољи ракетни систем који би побољшао постојећи ПВО систем.

Методе: Хибридна методологија вишекритеријумског одлучивања (MCDM), метода DEMATEL и метода аналитичког хијерархијског процеса (AHP) коришћене су за процену фактора који утичу на ракетни систем, као и за избор најбољег ракетног система за Пакистан.

Резултати: Указано је да је за ПВО Пакистана најпогоднији ракетни систем С-400, а затим ТХААД и С-300, који могу да задовоље тренутне безбедносне потребе земље.

Закључак: Закључено је да способност прецизног гађања циљева, домет и маневарске способности представљају водеће факторе који имају значајнију улогу у систему ПВО Пакистана. Ово истраживање је прво такве врсте које користи приступ DEMATEL-AHP за процену система ПВО у земљи у развоју као што је Пакистан.

Кључне речи: Пакистан, ПВО, ракетни систем, MCDM, DEMATEL-AHP.

Paper received on: 25.12.2023.
Manuscript corrections submitted on:09.01.2024.
Paper accepted for publishing on: 11.05.2025.

A computational study on the drag reduction effectiveness of a spinning projectile with different afterbody configurations at supersonic speeds

Quang Tuan Nguyen

Le Quy Don Technical University, Faculty of Special Equipment, Hanoi, Socialist Republic of Vietnam

e-mail: tuannguyenmta28@gmail.com, **corresponding author**,
ORCID iD: https://orcid.org/0000-0002-7741-8232

https://doi.org/10.5937/vojtehg73-57712

FIELD: mechanical engineering, fluid dynamics, exterior ballistics
ARTICLE TYPE: original scientific paper

Abstract:

Introduction/purpose: In this paper, five Army-Navy Spinner Rocket configurations with different afterbodies were numerically evaluated on drag reduction effectiveness at supersonic speeds.

Methods: Reynolds-Averaged Navier-Stokes equations with the SST k-ω turbulence model were employed for numerical simulations. Mesh sensitivity studies were undertaken to ensure the independence of simulation results on the mesh size. The simulation results were validated against archival experimental data. A comparison of aerodynamic drag coefficients for baseline and modified afterbodies was carried out. The flow fields around different afterbody configurations were visualized and analyzed.

Results: The research results have indicated that a conical boattail or a combination of a conical boattail with a base cavity are the most effective methods showing on the average 10.99% and 11.96% in drag reduction, respectively. The base cavity configuration alone is the least effective method showing an average drag reduction of only 1.33% compared to the baseline configuration. The multi-step afterbody configuration can come up with an average drag reduction of 2.15% compared to the baseline configuration.

Conclusion: Afterbody configurations significantly affect the aerodynamic drag of a spinning projectile. Out of the considered afterbody configurations, the combination of a conical boattail and a base cavity is the most effective way to reduce a projectile drag. The findings presented in this study have provided significant insights into better understanding of passive methods for aerodynamic drag reduction.

Key words: numerical simulation, aerodynamic characteristics, drag reduction, conical boattail, base cavity.

Introduction

Aerodynamic drag is a crucial factor affecting the performance of projectiles such as missiles, rockets, artillery shells, and bullets. Reducing aerodynamic drag not only improves the effectiveness and precision of projectiles but also enhances their operational efficiency by extending their range and reducing the energy required for propulsion. Over the past decades, a wide range of methods have been developed to reduce projectile aerodynamic drag, each method being suitable for specific types of projectiles and their operational conditions. There are several means applied to reduce total drag acting on projectiles during their flight. Among them, the most practical and effective method is to lower projectile base drag by using a conventional axisymmetric conical boattail afterbody and other unconventional afterbodies such as a triangular afterbody, a square afterbody, a multi-step afterbody or a base cavity, slot cavity afterbodies, etc.

In recent years, there is a renewed interest in drag reduction research for missiles and projectiles. Platou (1975) conducted a series of experiments with unconventional projectile boattails and concluded that these unconventional projectile boattails have improved aerodynamic performance over the standard conical boattail. These boattails have equal or lower drag and an improved gyroscopic stability. Mathur and Viswanath (2004) experimentally investigated the effect of square-based afterbodies at high speeds on drag and concluded that, compared to conventional axisymmetric boattails with conical and circular-arc profiles, square-based afterbodies have the lowest total drag in the Mach number range of 0.95–1.60. El-Awwad et al. (2020) have investigated the aerodynamic characteristics and ballistic performance of projectiles with a triangular base and came to the conclusion that the triangular boattial has a base drag reduction of approximately 5% at $M > 1.0$ compared to the conventional conical boattail with the same length and the angle of inclination; also, the triangular boattail projectile has better performance from the stability point of view. The studies on the effectiveness of base cavities, ventilated cavities, locked vortex afterbodies, and multi-step afterbodies by Viswanath and Patil (1997) have indicated that base drag and total drag have been significantly reduced with unconventional boattail configurations. Lunghi et al. (2024) investigated the potential of multiple grooves to lower the aerodynamic drag on a boat-tailed bluff body. The work has revealed that the presence of two consecutive transverse grooves results in a maximum boat-tail drag reduction of 23.2%. Ibrahim and Filipone (2010) performed experimental and computational studies on the effect of streamwise slots applied to the

boattail on the total drag coefficient. Guidos and Sturek (1987) conducted a study on the aerodynamics of a 25mm diameter practice round with a triangular afterbody using a thin-layer Parabolized Navier-Stokes computational technique. Kumar et al. (2014) numerically studied the flow around a conical nose with a rounded tail projectile of 120mm caliber at three flow regimes and stated that the rounded tail is a better option than the boattail in terms of drag reduction. Lu and Zhang (2022) investigated the effect of the base cavity shape and dimensions on drag reduction of a slender body. Viswanath (2001) performed an investigation to analyse the aerodynamics of the flow around a multi-step afterbody and compared the drag of multi-step afterbodies with that of the blunt afterbody. The obtained result showed that the multi-step afterbody has smaller total drag than the baseline model. Viswanath and Patil (1990) conducted an experimental investigation into the effect of several base modifications, namely, base cavities, ventilated cavities, and two vortex suppression devices, on the reduction of total drag and base drag. The main conclusion drawn from his work is that, while several devices can provide appreciable base drag reduction, the net total drag reduction is relatively lower, possibly due to additional losses related to the devices. Fu and Liang (1994) carried out a numerical study on optimal drag reduction for a spinning projectile at transonic speeds with a passive control device. Mariotti et al. (2017) conducted numerical and experimental investigations to assess the efficiency and performance of a control method to delay boundary layer separation consisting of the introduction on the surface of contoured transverse grooves. Mahdi and Al-Atabi (2008) predicted the impact of forebody and afterbody geometries on the aerodynamic performance of several projectile bodies at supersonic speeds using analytical methods. The results of this work have shown that the lowest drag was obtained with a cone-cylinder configuration for the forebody and drag can be reduced by boattailing the afterbody. Ma et al. (2020) carried out a comparative study of the aerodynamic characteristics of a spinning projectile with cylindrical and boattailed afterbodies.

The research studies conducted so far have mostly focused on investigating the effect of a separate afterbody configuration on the drag reduction magnitude and the main research method is through experiments. In addition, the research objects of these studies are of different calibers and shapes; hence, it is impossible to summarize and generalize the obtained results. Moreover, of all components of the aerodynamic drag coefficient, the zero-lift drag coefficient is the most interesting parameter to be studied. It indicates the drag that a flying body experiences when no lift is generated. This coefficient provides deep

insights into the efficiency and performance of the flying object. Therefore, the primary objective of this paper is to compare the zero-lift drag reduction effectiveness of several most widely used afterbody configurations by determining the drags of projectiles with the same caliber and the same forebody configurations using the modern numerical simulation technique.

Computational methodology

Computational geometry

In this paper, five Army-Navy Spinner Rocket (ANSR) models with different afterbody configurations were evaluated on drag reduction effectiveness. These ANSR models with the corresponding afterbodies are presented in Figure 1, including the baseline, conical boattail, base cavity, multi-step, and a combination of conical boattail and base cavity afterbodies.

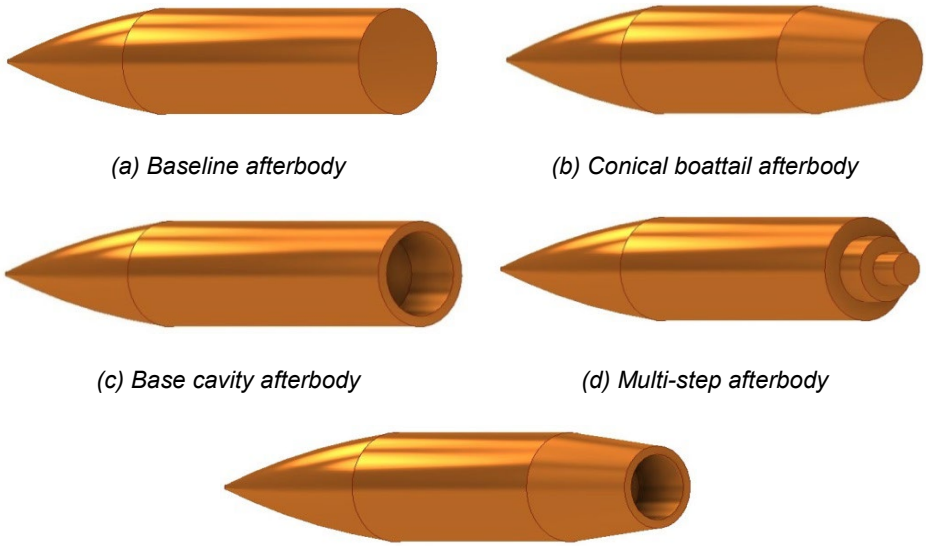

(a) Baseline afterbody

(b) Conical boattail afterbody

(c) Base cavity afterbody

(d) Multi-step afterbody

(e) Combination of a boattail and a base cavity

Figure 1 - Different ANSR afterbody configurations: (a) baseline afterbody; (b) conical boattail afterbody; (c) base cavity afterbody; (d) multi-step afterbody; and (e) conical boattail + base cavity afterbody

These configurations have the same total length of 5 calibers (1 caliber is 20mm) and the same 2-caliber secant ogive nose followed by a cylindrical bearing part of different length. The first configuration has the most simple afterbody and is used for baseline configuration. The second afterbody configuration consists of a conical boattail of 1-caliber length and a 7^0

inclination angle (Figure 2). The third afterbody configuration is a cylindrical base cavity with 0.8-caliber diameter and 1-caliber height. The fourth afterbody configuration consists of two steps with the same 0.5-caliber height; the first step diameter is 1/3-caliber and the second step diameter is 2/3-caliber. The fifth afterbody configuration is a combination of the second configuration with a cylindrical base cavity of 0.6-caliber diameter and 1-caliber height.

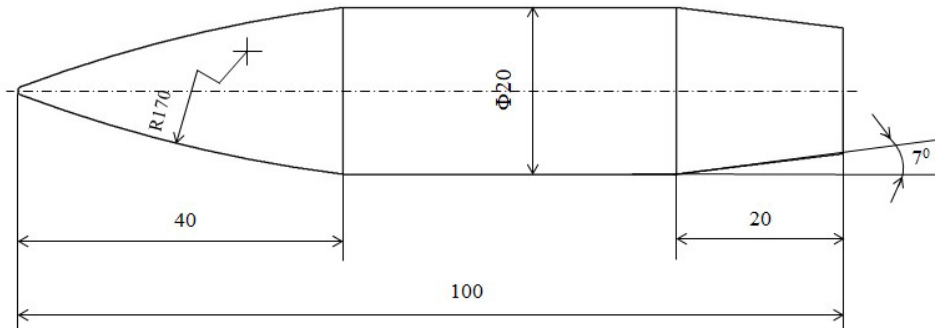

Figure 2 - Computational domain

Computational domain

Computational domains with the same dimensions were created for all model configurations in a cuboid form with 40L of length, 10L of width, and 10L of height (L is the total length of the computational model). This computational domain was created with dimensions large enough to accurately capture the aerodynamic phenomena taking place at the boundary layer and in the wake region behind the projectile base. The computational model was placed on the symmetrical longitudinal axis of the fluid domain and was 15L and 24L away from the Inlet and Outlet boundary respectively, as displayed in Figure 3.

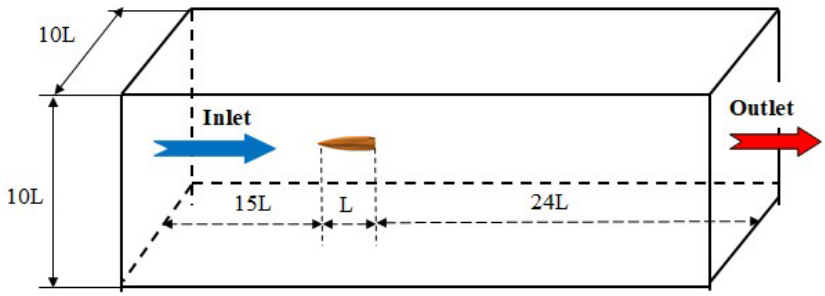

Figure 3 - Computational domain

Turbulence model

In order to simulate the flow around the models investigated in this work, the SST k-ω turbulence model were adopted. This is a two-equation eddy-viscosity turbulence model developed and improved by Menter (1994). This turbulence model blends the Standard *k-ε* and the Standard *k-ω* models to combine their advantages for enhancing the simulation accuracy and robustness. Near the wall region, it behaves like the *k-ω* model. In the free-stream region, it transitions to the *k-ε* model. This model provides more accurate predictions of flow separation than most RANS models and shows good performance in regions with adverse pressure gradients (Menter, 1994; Ameri et al., 2019). The two transport equations of the SST k-ω turbulence model are defined as follows (Menter, 1994):

$$\frac{\partial}{\partial t}(\rho k)+\frac{\partial}{\partial x_i}(\rho k u_i)=\frac{\partial}{\partial x_j}\left(\Gamma_k \frac{\partial k}{\partial x_j}\right)+G_k-Y_k+S_k, \tag{1}$$

$$\frac{\partial}{\partial t}(\rho \omega)+\frac{\partial}{\partial x_i}(\rho \omega u_i)=\frac{\partial}{\partial x_j}\left(\Gamma_\omega \frac{\partial \omega}{\partial x_j}\right)+G_\omega-Y_\omega+D_\omega+S_\omega, \tag{2}$$

where G_k is the turbulence kinetic energy due to the mean velocity gradients; G_ω is the generation of ω; Γ_k and Γ_ω are, respectively, the effective diffusivity of k and ω; Y_k and Y_ω are, respectively, the dissipations of k and ω due to the turbulence; S_k and S_ω are the user-defined source terms; D_ω is the the cross-diffusion term; and D_ω is the cross-diffusion term. The turbulent viscosity μ_t is defined as follows:

$$\mu_t=\frac{\rho k}{\omega}\frac{1}{max\left[1/\alpha^*, SF_2/\alpha_1\omega\right]}, \tag{3}$$

where α_1 is a constant of the turbulence model, S is the strain rate magnitude, and F_2 is a blending function. In the SST k-ω model, the turbulent Prandtl numbers σ_k and σ_ω are given as:

$$\sigma_k=\frac{1}{\frac{F_1}{\sigma_{k,1}}+\frac{1-F_1}{\sigma_{k,2}}},\ \sigma_\omega=\frac{1}{\frac{F_1}{\sigma_{\omega,1}}+\frac{1-F_1}{\sigma_{\omega,2}}}, \tag{4}$$

where F_1 is a blending function and $\sigma_{k,1}$, $\sigma_{k,2}$, $\sigma_{\omega,1}$, and $\sigma_{\omega,2}$ are constants.

The parameters G_k and G_ω are defined as:

$$G_k = min\left(G_k, 10\rho\beta^* k\omega\right),\ G_\omega = \frac{\alpha}{\upsilon_t} G_k, \tag{5}$$

The cross-diffusion term D_ω is determined as follows:

$$D_\omega = 2\left(1 - F_1\right)\rho\sigma_{\omega,2}\frac{1}{\omega}\frac{\partial k}{\partial x_j}\frac{\partial \omega}{\partial x_j}. \tag{6}$$

The model constants are given as follows: $\sigma_{k,1}$ = 1.176, $\sigma_{\omega,1}$ = 2.0, $\sigma_{k,2}$ = 1.0, $\sigma_{\omega,2}$ = 1.168, $\beta_{i,1}$ = 0.075, $\beta_{i,2}$ = 0.0828, β^* = 0.09, k = 0.41.

Solver and setup

In this study, the commercially available CFD software Ansys Fluent 2021 was used to evaluate the drag reduction of each afterbody configuration. A pressure-based solver with the Couple algorithm was chosen due to its robustness and accuracy. The air was set as an ideal gas. For the air viscosity model, the three-component Sutherland model were selected. The Inlet flow was defined as the Pressure far field and the Outlet flow was set as the Pressure outlet. On the body surface, the stationary, adiabatic and no-slip conditions were imposed. According to the ICAO atmosphere, the conditions for the atmosphere parameters were defined as follows: p_0 = 101325*Pa* and T_0 = 288.16*K* (ICAO, 1993). The simulations were considered converged once the flow residuals had reduced at least 5 orders in magnitude and the drag coefficient varied less than 1% over the last 100 iterations.

Mesh sensitivity study and result validation

It is well known that meshing is one of the factors affecting the simulation results. In this paper, a mesh sensitivity study was conducted to ensure the independence of the simulation results from the mesh resolutions. Firstly, the mesh sensitivity study was performed for the configuration with the baseline afterbody. To do that, six unstructured meshes with different resolutions were created by adjusting the size of the elements on the model surface as well as in the fluid domain to gradually refine the mesh while maintaining the dimensionless distance y+ less than 1 along the way. Numerical simulations were performed at the Mach number of 1.5 with the zero angle of attack under the same boundary conditions and the solver setup as presented above. The effect of the mesh resolutions on the simulated drag coefficient was presented in Table 1 and Figure 4.

Table 1 - Influence of the mesh resolutions on the simulation results

Mesh	Number of cells (x10^6)	C_{D0}	Deviation from the result of the previous mesh (%)
Mesh 1	0.734	0.536	-
Mesh 2	1.508	0.471	12.13
Mesh 3	2.492	0.422	10.40
Mesh 4	4.901	0.405	4.03
Mesh 5	7.553	0.404	0.25
Mesh 6	11.672	0.404	0

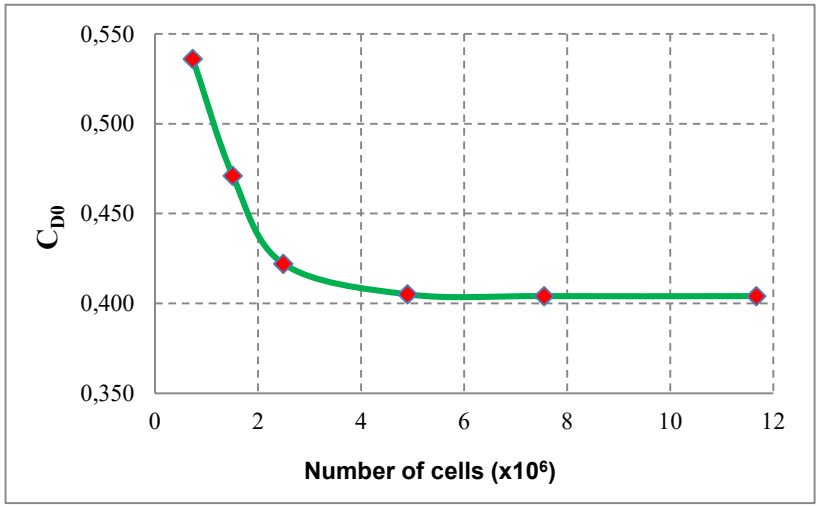

Figure 4 - Effect of the mesh resolutions on the total drag coefficient

Clearly, from the mesh size of 7.553 million of cells (Mesh 5), the subsequent mesh refinement practically will not affect the simulation results. For that reason, Mesh 5 was applied in this study for the ANSR baseline configuration taking into account a compromise between good accuracy and reasonable computation time. The adopted mesh was the finest on the projectile surface with the maximum cell size of 0.25mm and gets coarser from the region near the projectile surface to the fluid boundaries with the maximum cell size of 5mm. In order to maintain the dimensionless distance y+ less than 1, an additional 15-layer inflation with the first cell height of $5x10^{-4}$mm and a growth rate of 1.15 was added for better capturing the aerodynamics phenomena taking place in the vicinity of the projectile surface

and in the region directly behind the projectile base. The mesh structure used for the ANSR baseline afterbody configuration in this research is shown in Figure 5.

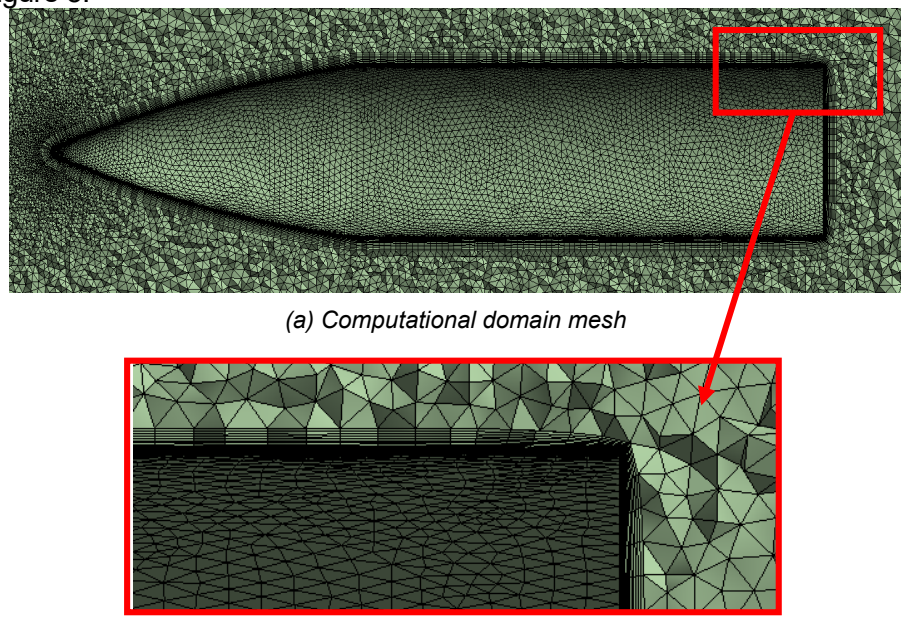

(a) Computational domain mesh

(b) A close-up view of the refined mesh near the afterbody surface

Figure 5 - Unstructured mesh used for the ANSR baseline configuration: (a) computational domain mesh; (b) a close-up view of the refined mesh near the afterbody surface

Next, the meshes for the remaining ANSR configurations were created based on the mesh structure used for the baseline ANSR after conducting an additional mesh sensitivity study for each case. Specifically, two meshes were created for each remaining ANSR configuration: the first mesh is based on the mesh configuration used for the baseline ANSR, while the second mesh has twice as many cells as the first mesh. The numerical simulations were then performed for these two meshes. In all cases, the numerical simulations have shown the same results. This has indicated that there is no need for further refinement of the meshes. Therefore, the meshes created for the remaining ANSR configurations based on the mesh structure used for the baseline ANSR were employed in this study. As a result, the meshes for the ANSRs with a conical boattail afterbody, a base cavity afterbody, a multi-step afterbody, and a combination of a conical boattail and a base cavity afterbody consist of 7.281, 7.781, 7.207 and 7.341 million of cells, respectively. The

close-up views of the meshes near the surface of the computational models for each ANSR configuration are displayed in Figure 6.

Eventually, the simulated total drag coefficient of the ANSR with a baseline afterbody was employed to validate the adopted computational methodology. The total drag coefficient obtained for the ANSR with a baseline afterbody through numerical simulation at the Mach number of 1.5 is 0.404, while the corresponding value obtained by Platou (1975) through experiments is 0.409. The relative deviation is only 1.22% demonstrating that the created meshes can be used with high confidence in this study.

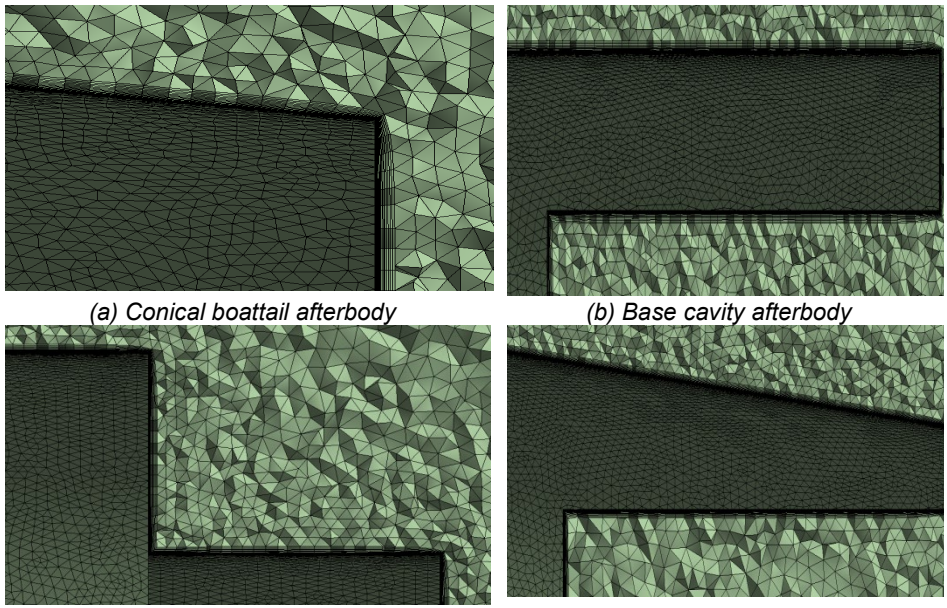

(a) Conical boattail afterbody *(b) Base cavity afterbody*

(c) Multi-step afterbody *(d) Boattail + Base cavity afterbody*

Figure 6 - Close-up views of the refined mesh near the afterbody surface:

a) conical boattail (top left); b) vase cavity afterbody (top right); c) multi-step afterbody (bottom left); and d) boattail + Base cavity (bottom right)

Results and discussion

Drag reduction effectiveness of different afterbody configurations

In this paper, to evaluate the drag reduction effectiveness of afterbody configurations at supersonic speeds, numerical simulations

were carried out for each configuration at Mach numbers ranging from 1.5 to 4.0 with an increment of 0.5. The obtained total drag coefficients C_{D0} are listed in Table 2. The relative drag reduction of each configuration compared to the baseline configuration was also calculated and presented in Table 2.

Based on the obtained results, several remarks can be derived. First of all, if not taking into account the combination of a conical boattail and a base cavity, then the conical boattail is the most effective configuration for drag reduction showing a drag reduction of up to 12.46% and the average drag reduction of the conical boattail configuration is 10.99% for the Mach number interval from 1.5 to 4.0. Meanwhile, the base cavity afterbody seems to be the least effective configuration with the maximum drag reduction of only 1.73% and the average drag reduction for the entire Mach number interval is 1.33%. However, adding a base cavity to the conical boattail configuration can provide additional drag reduction with the maximum drag reduction of up to 13.48%. Although the multi-step configuration is a better alternative for drag reduction than the base cavity configuration, the drag reduction provided by this configuration is still small compared to the conical boattail configuration. Overall, the multi-step configuration can provide a total drag reduction of 2.15% on the average. Generally speaking, the most effective afterbody configuration in terms of total drag reduction is the combination of a conical boattail and a base cavity showing an average drag reduction of 11.96%. The second most effective configuration is the conical boattail providing a total drag reduction of 10.99% on the average. Additionally, the least effective configuration is the base cavity afterbody with the average drag reduction of only 1.33%.

The results obtained in this study have shown a very good agreement with other simulations. Namely, Suliman et al. (2009) pointed out that for a 155mm M549 artillery shell, the case of using a base cavity alone has shown the smallest reduction in the drag coefficient of only 1-2%, while having a boattail afterbody can reduce the total drag coefficient by about 12%. An experimental investigation conducted by Kidd et al. (1990) for a spin-stabilized and a fin- stabilized projectiles also revealed that the multi-stepped afterbody does not

significantly reduce the total drag at supersonic flight regimes compared to the flat baseline afterbody.

Table 2 - Total drag coefficient and relative drag reduction for different afterbody configurations

	Total drag coefficient C_{D0}					Drag reduction compared to the baseline configuration (%)			
M	Baseline	Conical boattail	Base Cavity	Multi-step	Boattail + Cavity	Conical boattail	Base Cavity	Multi-step	Boattail + Cavity
1.5	0.404	0.355	0.397	0.391	0.351	12.13	1.73	3.22	13.12
2.0	0.356	0.312	0.351	0.347	0.308	12.36	1.40	2.53	13.48
2.5	0.313	0.274	0.309	0.307	0.271	12.46	1.28	1.92	13.42
3.0	0.275	0.245	0.271	0.270	0.242	10.91	1.45	1.82	12.00
3.5	0.243	0.220	0.240	0.238	0.217	9.47	1.23	2.06	10.70
4.0	0.221	0.202	0.219	0.218	0.201	8.60	0.90	1.36	9.05
Average						10.99	1.33	2.15	11.96

The total drag coefficients obtained for each afterbody configuration as functions of the Mach number are presented in Figure 7. Obviously, the curves of the total drag coefficients follow the same fluctuation trend showing a constant decrease with the increase in Mach numbers. The curve of the baseline configuration is the highest followed by the curves of the base cavity and the multi-step configurations. The lowest curves are those of the conical boattail and the combined configurations. However, the curves of the base cavity and the multi-step configurations are situated very close to the curve of the baseline configuration. That means the drag reductions provided by these two afterbody configurations are insubstantial. Conversely, the curves of the conical boattail and the combined configurations located far below the curve of the baseline configuration show a significant drag reduction for all Mach numbers of interest.

Apart from the total drag coefficients, it is interesting to see how the base drag changes in each case of configurations. The base drag coefficients C_{DB} of the investigated afterbody configurations as functions of the Mach number are presented in Figure 8.

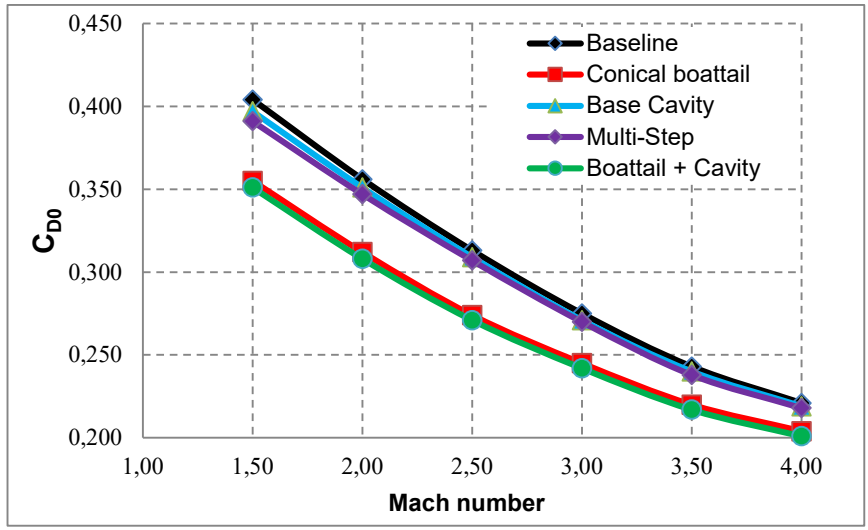

Figure 7 - Total drag coefficient for different afterbody configurations versus Mach

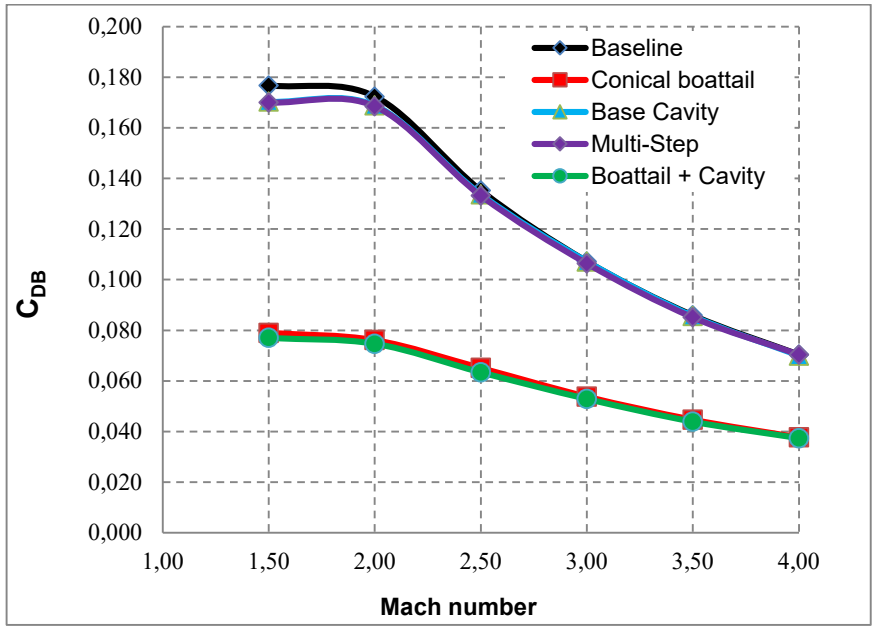

Figure 8 - Base drag coefficient for different afterbody configurations versus Mach

Clearly, as in the case of the total drag coefficients, the base drag coefficients of the studied configurations also follow the same

fluctuation trend. The relative positions between the curves of the base drag coefficients follow the same manner as the curves of the total drag coefficients. The conical boattail configuration and the combined configuration provide the most significant reduction in base drag. The base cavity configuration and the multi-step configurations are the least effective for base drag reduction for the entire interval of the Mach numbers of interest.

Flow field visualization

One of the main advantages of numerical simulation methods is the ability to visualize the flow field around a flying object. In this study, the flow Mach number profiles obtained at Mach 2.0 are presented in Figures 9 to 13.

The presence of the phenomena such as normal and oblique shock waves which characterize the supersonic flow regime can be clearly seen in all cases. Moreover, the flow separation takes place at the projectile base edge leading to the formation of a recirculation flow behind the projectile base. However, the near-wake regions for the conical boattail and the combined configurations are significantly smaller than those of the remaining configurations. That flow behavior has led to a significant change in the pressure distribution on the projectile base surface resulting in appreciable total drag reduction as expected.

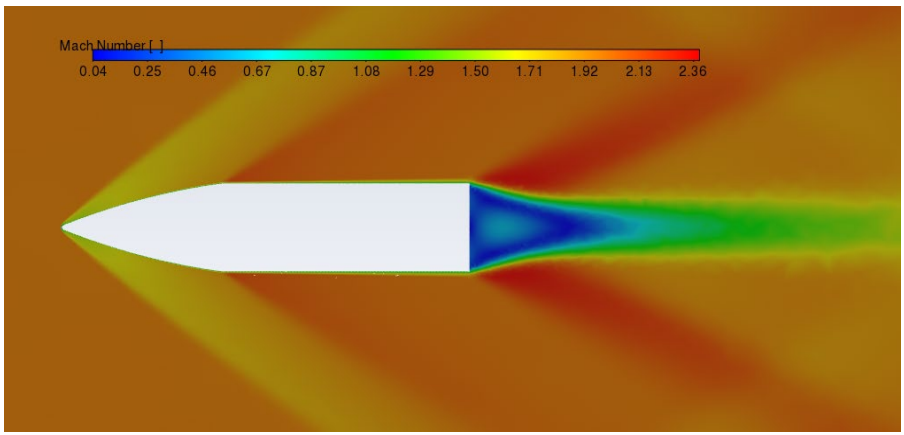

Figure 9 – Mach number profile around the projectile with the baseline afterbody at Mach 2.0

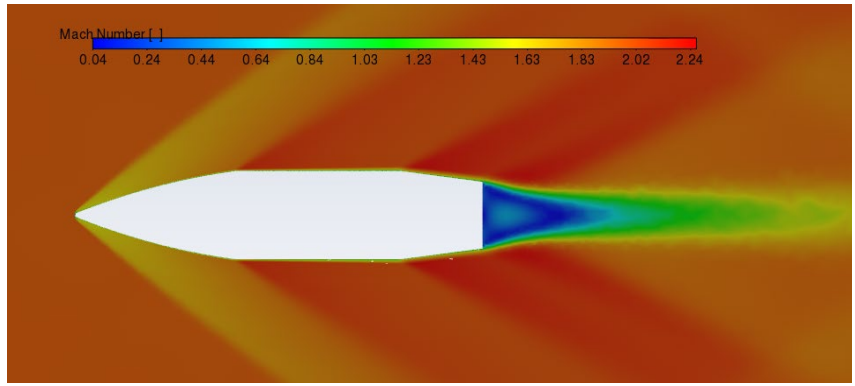

Figure 10 - Mach number profile around the projectile with the conical boattail afterbody at Mach 2.0

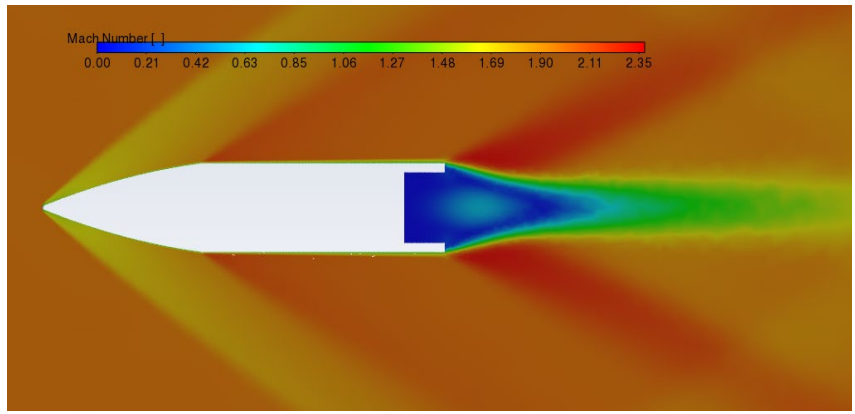

Figure 11 - Mach number profile around the projectile with the base cavity afterbody at Mach 2.0

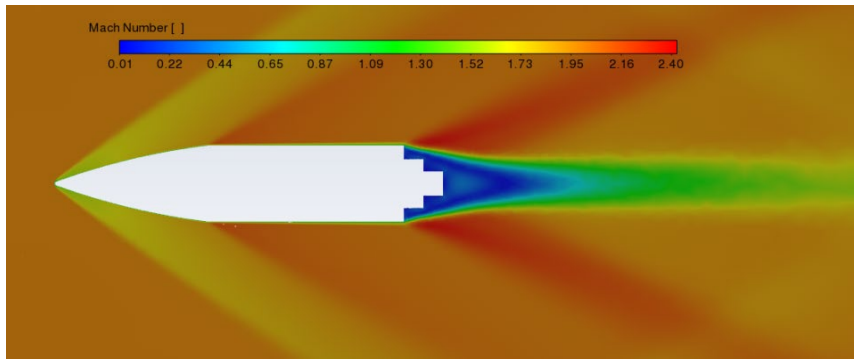

Figure 12 - Mach number profile around the projectile with the multi-step afterbody at Mach 2.0

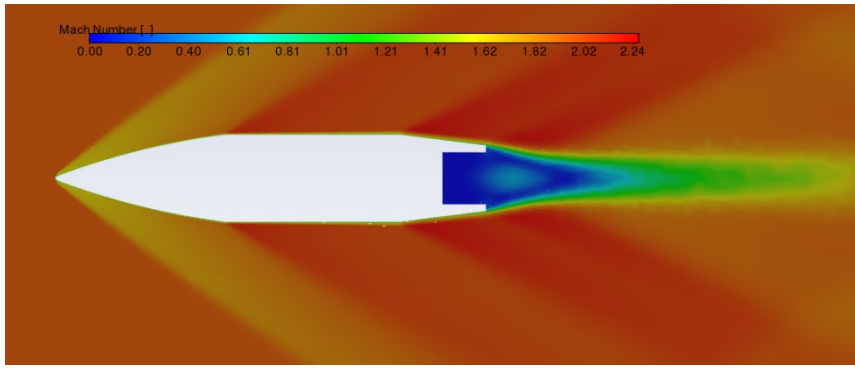

Figure 13 - Mach number profile around the projectile with a combination of the conical boattail and the base cavity at Mach 2.0

Conclusion

In this paper, numerical simulations were performed for ANSRs with five different afterbody configurations to investigate their effect on the aerodynamics and flow structure around the afterbody region. Based on the research results, several important insights can be gained. Firstly, the conical boattail afterbody is the most effective passive device to lower the total drag acting on the projectile, reducing it by up to 12.46 % of the total drag. A combination of the conical boattail and a base cavity can potentially reduce the total drag coefficient by up to 13.48%. For the 5-caliber ANSR, a base cavity alone as well as a multi-step afterbody alone can reduce the total drag coefficient but not significantly, by 1.33% and 2.15%, respectively. These simulation results agree well with other experimental and simulation data for larger caliber projectiles. Secondly, the afterbody modifications greatly affect the structure of the flow field around the projectile base, changing the recirculation region and the base pressure. The findings of this research are significant contributions to a better understanding of the effectiveness of different passive drag reduction devices for small caliber spinning projectiles in particular, and to a broadening knowledge about aerodynamics of slender bodies in general. The results obtained in the present study can be applied for selecting appropriate means for drag reduction of small caliber projectiles.

Future work

The presented study has clarified certain questions about the performance of different afterbody configurations regarding the zero-lift drag reduction of a small caliber projectile. However, further works need

to be done to quantify their efficiency of drag reduction with a varying angle of attack, as well as to evaluate their effect on the dynamic characteristics, namely, roll damping moment, pitch damping moment, and Magnus force and moment to assess their overall aerodynamic performance. Therefore, further analysis of the aerodynamic performance of these afterbody configurations would be recommended for a deeper understanding of effects that each of them have on the general aerodynamic performance of a projectile.

References

Ameri, M.J., Heidari, M.R., Nowruzi, H. & Najafi, A. 2019. Analysis of different turbulence models in simulation of hypersonic flow in the wind tunnel. *American Journal of Mechanical Engineering*, 7(4), pp. 172-180. Available at: http://pubs.sciepub.com/ajme/7/4/3 [Accessed: 22 January 2025].

El-Awwad, E., Ibrahim, A.Z., El-Sebae, A.M. & Riad, A.M. 2020. Flow computations past a triangular boattailed projectile. *Defence Technology*, 16(3), pp. 712-719. Available at: https://doi.org/10.1016/j.dt.2019.08.009

Fu, J. & Liang, S. A. 1994. Numerical study of optimal drag reduction for turbulent transonic projectiles using a passive control. *International Journal of Computational Fluid Dynamics*, 3(3-4), pp. 251-264. Available at: https://doi.org/10.1080/10618569408904510

Guidos, B. & Sturek, W. 1987. *Computational aerodynamic analysis for a range-limited 25mm training round*. US Army Ballistic Research Laboratory, Aberdeen Proving Ground, Maryland, Technical Report BRL-TR-2833. Available at: https://apps.dtic.mil/sti/citations/ADA185270 [Accessed: 22 January 2025].

ICAO. 1993. *Manual of the ICAO standard atmosphere extended to 80 kilometres (262 500 feet). International Civil Aviation Organization, Doc 7488/3*. Available at: https://aiac.ma/wp-content/uploads/2018/01/Manuel-de-l%E2%80%99atmosph%C3%A8re-Type-OACI-Doc7488-1.pdf [Accessed: 22 January 2025].

Ibrahim, A. & Filippone, A. 2010. Supersonic aerodynamics of a projectile with slot cavities. *The Aeronautical Journal*, 114(1151), pp. 15-24. Available at: https://doi.org/10.1017/S0001924000003493

Kidd, J.A., Wikoff, D. & Cottrell, C. J. 1990. Drag reduction by controlling flow separation using stepped afterbodies. *Journal of Aircraft*, *27*(6), pp. 564-566. Available at: https://doi.org/10.2514/3.25320

Kumar, A., Panda, H.S., Biswal, T.K. & Appavuraj, R. 2014. Flow around a conical nose with rounded tail projectile for subsonic, transonic, and supersonic flow regimes: A numerical study. *Defence Science Journal*, 64(6), pp. 509-516. Available at: https://doi.org/10.14429/dsj.64.8111

Lu, H. & Zhang, Q. 2022. Numerical investigation on aerodynamic drag reducing of slender body with non-cylindrical base cavity. In: *Proceedings of the*

2022 International Conference on Smart Manufacturing and Material Processing, pp. 227-234. Available at: https://doi.org/10.3233/ATDE220838

Lunghi, G., Pasqualetto, E., Mariotti, A. & Salvetti, M.V. 2024. Drag reduction in a spanwise-infinite boat-tailed body through multiple transverse grooves. *Computers & Fluids*, *275*, 106250. Available at: https://doi.org/10.1016/j.compfluid.2024.106250

Ma, J., Chen, Z., Xue, D. & Sun, X. 2020. Influences of boattail structures on aerodynamic characteristics of supersonic spinning projectiles. *Theoretical and Computational Fluid Dynamics*, 34, pp. 249-270. Available at: https://doi.org/10.1007/s00162-020-00532-0

Mahdi, A.S. & Al-Atabi, M. 2008. Effect of body shape on the aerodynamics of projectiles at supersonic speeds. *Journal of Engineering Science and Technology*, 3(3), pp .278-292. Available at: https://jestec.taylors.edu.my/Vol%203%20Issue%203%20December%2008/Vol_3_3_278-292_abdulkareem_mushtak.pdf [Accessed: 22 January 2025].

Mariotti, A., Buresti, G., Gaggini, G. & Salvetti, M.V. 2017. Separation control and drag reduction for boat-tailed axisymmetric bodies through contoured transverse grooves. *Journal of Fluid Mechanics*, 832, pp. 514-549. Available at: https://doi.org/10.1017/jfm.2017.676

Mathur, N.B. & Viswanath, P.R. 2004. Drag reduction from square base afterbodies at high speeds. *Journal of aircraft*, 41(4), pp. 811-820. Available at: https://doi.org/10.2514/1.532

Menter, F.R. 1994. Two-equation eddy-viscosity turbulence models for engineering applications. *AIAA Journal*, 32(8), pp. 1598-1605. Available at: https://doi.org/10.2514/3.12149

Platou, A.S. 1975. Improved projectile boattail. *Journal of Spacecraft and Rockets*, 12(12), pp. 727-732. Available at: https://doi.org/10.2514/3.57040

Suliman, M.A., Mahmoud, O.K., Al-Sanabawy, M.A. & Abdel-Hamid, O. E. 2009. Computational investigation of base drag reduction for a projectile at different flight regimes. In: *International Conference on Aerospace Sciences and Aviation Technology*, 13, No. Aerospace sciences & Aviation technology, ASAT-13, pp. 1-13. The Military Technical College. Available at: https://www.researchgate.net/publication/298353323_Computational_investigation_of_base_drag_reduction_for_a_projectile_at_different_flight_regimes [Accessed: 22 January 2025].

Viswanath, P.R. 2001. Drag reduction of afterbodies by controlled separated flows. *Journal of aircraft*, 39(1), pp. 73-78. Available at: https://doi.org/10.2514/2.1272

Viswanath, P.R. & Patil, S.R. 1990. Effectiveness of passive devices for axisymmetric base drag reduction at Mach 2. *Journal of Spacecraft and Rockets*, 27(3), pp. 234-237. Available at: https://doi.org/10.2514/3.26130

Viswanath, P.R. & Patil, S.R. 1997. Zero-lift drag characteristics of afterbodies with a square base. *Journal of spacecraft and rockets*, 34(3), pp.290-293. Available at: https://doi.org/10.2514/2.3231

Рачунарска студија о ефикасности смањења отпора ротирајућих пројектила са различитим конфигурацијама задњег тела при суперсоничним брзинама

Кван Туан Нуиен, **аутор за преписку**

Државни технички универзитет „Ле Куи Дон", Факултет специјалног машинства, Ханој, Социјалистичка Република Вијетнам

ОБЛАСТ: машинство, динамика флуида
КАТЕГОРИЈА (ТИП) ЧЛАНКА: оригинални научни рад

Сажетак:

Увод/циљ: У овом раду нумерички је процењена ефикасност смањења отпора при надзвучним брзинама пет конфигурација са различитим задњим телом ракета „спинер" које поседује војска и морнарица.

Методе: Једначине Реинолдс-Аверагед Навиер-Стокес са SST к-ω моделом турбуленције коришћене су за нумеричке симулације. Студије осетљивости мреже предузете су како би се осигурала независност резултата симулације од величине мреже. Резултати симулације су потврђени на основу архивских експерименталних података. Извршено је поређење коефицијената аеродинамичког отпора за основну линију и модификована задња тела. Визуализована су и анализирана поља струјања око различитих конфигурација накнадног тела.

Резултати: Резултати истраживања су показали да су конусни чамац или комбинација конусног чамца са базном шупљином најефикасније методе које показују у просеку 10,99%, односно 11,96% смањење отпора. Сама конфигурација базне шупљине је најмање ефикасан метод који показује просечно смањење отпора од само 1,33% у поређењу са основном конфигурацијом. Вишестепена конфигурација накнадног тела може да оствари просечно смањење отпора од 2,15% у поређењу са основном конфигурацијом.

Закључак: Конфигурације задњег тела знатно утичу на аеродинамички отпор пројектила који се окреће. Од разматраних конфигурација задњег тела комбинација конусног репа и базне шупљине је најефикаснији начин да се смањи отпор пројектила. Налази представљени у овој студији пружили су значајан увид у боље разумевање пасивних метода за смањење аеродинамичког отпора.

Кључне речи: нумеричка симулација, аеродинамичке карактеристике, смањење отпора, конусни боатаил, базна шупљина.

Nguyen, Q. T. , A computational study on the drag reduction effectiveness of a spinning projectile with different afterbody configurations at supersonic speeds. pp.1307-1326

Paper received on: 22.03.2025.
Manuscript corrections submitted on:11.04.2025.
Paper accepted for publishing on: 27.05.2025.

Reliability of artificial intelligence in civilian and military applications

Slavko J. Pokorni
Information Technology School, Belgrade, Republic of Serbia,
e-mail: slavko.pokorni@its.edu.rs,
ORCID iD: https://orcid.org/0000-0002-3173-597X

FIELD: Information technology
ARTICLE TYPE: Review paper

https://doi.org/10.5937/vojtehg73-56016

Abstract:

Introduction/purpose: The goal of this paper is to show the importance of reliability and availability regarding artificial intelligence (AI) which is nowadays applied in almost every area of human life, both civilian and military. Everything can fail, including AI as any other product or device. AI also needs to be reliable. It is mainly realized as software, but also involves hardware, data and the human factor, so it is complex for building in and for reliability assessment.

Methods: This study has used the published articles of this author as well as some other papers and documents.

Results: The research has resulted in brief definitions of reliability, availability, artificial intelligence, reliability of hardware, software, data, the human factor, and AI as well as in a brief analysis of some reasons for the unreliability of AI, such as data quality, a small or insufficient amount of training and test data, training on unreal data, the nature of learning algorithms and user incompetence.

Conclusion: The reliability of artificial intelligence is very complex and due to its importance it must be considered during AI design and application.

Key words: artificial intelligence, reliability, availability, hardware, software, human factor, data.

This paper, under a similar title, was presented at the *11th International Scientific Conference on Defensive Technologies OTEH 2024*, 09-11 October 2024.

Introduction

Everything can fail, and artificial intelligence (AI) is not an exception. If AI is an attempt to replace human intelligence with machine intelligence, and human reasoning can sometimes fail, so AI can fail in a similar way

(Pokorni, 2021, Pokorni, 2024). In the sense of AI reliability, failure can mean that, when needed, it will not react, or it will not react as expected. Artificial intelligence is mainly realized as software, but it involves hardware, data and the human factor - and software, hardware, and people can also fail. If something can fail, one speaks about reliability, and if something can be repaired, one speaks about maintenance.

Reliability is related to failures, and failures can cause consequences from minor to major ones, for example, material and financial ones, and sometimes they can lead to the loss of human life. Reliability is thus important, and sometimes critical, depending on the area where AI is applied (airplanes and autonomous vehicles both civilian and military, medical devices, products and services based on people's interest, etc.). It implies that the reliability of AI is important in order to use it with confidence and safety for the benefit of all people, without its misuse.

As mentioned before, artificial intelligence is mainly realized as software, but it also involves hardware, data and the human factor. Therefore, when AI reliability is concerned, it obviously includes hardware, software, data and the human factor reliability.

The importance of reliability can be illustrated by the following statement from a well-known book of (Kececioglu, 2002): "No industry in any country can progress effectively without the knowledge and implementation of reliability engineering". This also applies to AI.

Definition of reliability and availability

In general, reliability is defined as the ability of an item to perform a required (expected) function under stated conditions for a stated period of time (Pokorni, 2021b). Instead of the term *item*, this paper will use the term *product* as a general term, and this will include a device, an element or a system realized in hardware, software or both. AI can also be treated as a product, so the reliability of AI can be defined in a similar way as the reliability of a product.

Quantitatively, reliability is expressed as a probability, and it is very important in reducing downtime and both operational and maintenance costs of a product. Reliability and maintenance are mutually connected. Higher reliability means less costly maintenance. There are many factors which can influence reliability. For example, reliability of hardware can change if the environment changes (temperature, mechanical stresses, etc). Similarly, the reliability of AI changes if data and user behaviour change.

High reliability is of high importance, especially in professional equipment such as military, medical or driverless cars, and it comprises hardware reliability, software reliability, and human reliability (Pokorni, 2021a); it can also include AI, so the reliability of AI is significant as well.

In calculating reliability, prognostic reliability is essentially calculated. That is why one does not talk about determination, but about reliability assessment or reliability prognostic. Reliability prognostic has been done since the sixties of the last century using MIL-HDBK-217, mostly for electronic hardware (Pokorni, 2016), but it has not been updated since the nineties of the last century.

Reliability is built in during the product design phase, provided in production and supported in use. It is also connected with cost. A more reliable product is more expensive, but a more reliable product is also cheaper for maintenance.

Artificial intelligence is, in essence, software but it also involves hardware, data and humans. Having this in mind, one can define the reliability of AI starting from the definition in (Pokorni, 2023): “reliability is the probability that a product will meet the intended standards of performance and deliver the desired results within a specified period of time under specified (environmental) conditions”.

Availability is a metric used to assess the performance of repairable systems, incorporating both the reliability and maintainability properties of a component or a system. There are different definitions of availability and different ways to calculate it (Pokorni, 2021a).

Unlike reliability, availability is a probability whether a product is ready to perform its function when it is required, and represents a characteristic of repaired devices.

Reliability of hardware

AI as software runs on hardware, so the reliability of AI depends on the reliability of that hardware. As said in (Pokorni, 2021a), up to now, hardware reliability has been calculated mostly using MIL-HDBK-217 military manual for the calculation of the reliability of electronic devices.

Hardware usually comprises different components concerning quality and reliability: very often of a commercial type, without established reliability, and very often without any data about the failure rate or the mean time to failure (MTTF), or the mean time between failures (MTBF), thus making precise reliability calculation very difficult.

Since the sixties of the previous century, hardware reliability has been calculated mostly using MIL-HDBK-217 military manual. However, MIL-

HDBK-217 has its limitations and has not been updated since 1995. RIAC's 217Plus™ methodology and a software tool is a replacement for MIL-HDBK-217, but it is not free (Pokorni, 2021a).

Reliability of software

Since AI is predominantly a type of software, it is connected with software reliability. Software errors are the dominant cause of software unreliability. Software can contain errors, and errors can produce faults. Errors in software are produced by programmers, so it is important to be familiar with these errors.

Software reliability is an important attribute determining the quality of the software as a product. There are many models of software reliability assessment, but none of them is generally accepted (Pokorni, 2016, Pokorni, 2021a). The problem is that the requirements for the reliability of software are often not adequately specified, if specified at all, and the problem is in the different nature of software compared to hardware.

Reliability assessment of software is more complicated than hardware reliability. The problem also lies in the different natures of software and hardware.

Reliability of the human factor

AI can learn from humans, and human knowledge can be erroneous, so it is connected with human reliability.

There are different approaches and models to human reliability assesment (Pokorni, 2016).

Procedures, rules, codes, standards and laws cannot completely prevent system failures, but, in this author's experience, they can reduce system failures.

Humans can be and are involved in the artificial intelligence system. A human action can influence the reliability or unreliability of the artificial intelligence system.

This author has considered human reliability important from the beginning of his work in reliability; hence, human reliability is included in his textbooks published in the Military Academy and the Information Technology School in Belgrade, Serbia.

Reliability of data

Data reliability means that data is complete and accurate, and it is a crucial foundation for building data trust across any organization. Ensuring

data reliability is one of the main objectives of data integrity initiatives, which are also used to maintain data security, data quality, and regulatory compliance (Pokorni, 2023).

Data is crucial for AI. AI uses data and can learn from data, and data can be accidentally or intentionally corrupted, so AI can fail. Consequently, AI reliability is connected with data reliability.

Data is also very important in calculating reliability of hardware. Reliability is not easy to calculate or evaluate. In calculation reliability of hardware, input data is the biggest problem. Not because there is too much data, but because sometimes there is too little data or no data at all. When dealing with maintenance, the problem is very often that there is not enough data.

How much data does one have about AI reliability, especially if they deal with a new application?

Definition of artificial intelligence

There is no generally accepted definition of artificial intelligence (Government of the Republic of Serbia, 2019). According to the Encyclopaedia Britannica Dictionary (Pokorni, 2024), artificial intelligence is the ability of a digital computer or computer-controlled robot to perform tasks commonly associated with intelligent beings.

According to the Merriam-Webster Dictionary, AI is a branch of computer science dealing with the simulation of intelligent behaviour in computers, or the capability of a machine to imitate intelligent human behaviour.

The Government of the Republic of Serbia (Government of the Republic of Serbia, 2019, Sl. glasnik RS, 2023) has accepted the following definition of AI, also used in (European Commission, 2019): “Artificial intelligence (AI) refers to systems that display intelligent behaviour by analysing their environment and taking actions – with some degree of autonomy – to achieve specific goals.”

Artificial intelligence-based systems can be purely software-based and operate in a virtual world (for example: virtual assistants, photo analysis software, web browsers, recommendation systems, speech and face recognition systems) or they can be embedded in devices - hardware (for example: advanced robots, autonomous vehicles, drones, etc.) (Government of the Republic of Serbia. National AI Platform, 2023, European Commission, 2019).

Artificial intelligence was founded as an academic and scientific discipline in the middle of the fifties of the last century, and since then its

development has gone in different directions, being divided in sub-fields. Therefore, it is not a surprise that the definition of AI has been changed during time.

In the history of AI, there have been ups and downs, starting with the logic-based approach (during the 1950s and 1960s), the knowledge-based expert systems approach (1970s and 1980s), and the data-based approach (since 2000) years onwards - with periods of disappointment and reduced investment (Government of the Republic of Serbia, 2019). In the last decades, AI has been defined as a study of intelligent agents - any device that perceives its environment and takes actions (by learning or using knowledge) to achieve its goals (Pokorni, 2021b).

Essentially, the use of AI is an attempt to replace human intelligence with machine intelligence. Because of that, AI is sometimes called machine intelligence. However, it does not mean that AI learns just by copying humans. Nowadays, AI can learn in its own way, and it, maybe, gives it a potential to outperform the human (brain).

Reliability of artificial intelligence

As mentioned before, everything can fail, and artificial intelligence is not an exception. If AI is an attempt to replace human intelligence with machine intelligence, and human reasoning can sometimes fail, so can AI fail in a similar way. Therefore, does this happen because of erroneous reasoning (erroneous concluding, decision making) or wrong learning? Having that in mind, can we raise the question about the reliability of AI, or how to avoid AI to fail? (Pokorni, 2021b).

If AI fails, this means it is unreliable – ergo, can we trust it?

In (University of Cambridge, 2016) under the title “Enhancing the reliability of artificial intelligence“, it is stated that “computers that learn for themselves are with us now. As they become more common in 'high-stakes' applications like robotic surgery, terrorism detection and driverless cars, researchers ask what can be done to make sure we can trust them.“ So, are they reliable? Or, can they fail? Or can we fool them?

Deep learning AI can easily be fooled. An example is in a self-driving car application in a real situation. But it can happen in a case of sabotage as well.

There are examples of erroneous AI. From these examples, we can derive some reasons for AI to fail, such as: quality of data, a small or insufficient amount of training and test data, training on unreal data, the nature of learning algorithms, and user incompetence.

Definition of the reliability of artificial intelligence

In the document entitled “Ethical Guidelines for Development, Implementation and Use of Robust and Accountable AI” (Government of the Republic of Serbia, National AI Platform), so-called technical reliability means that “systems are developed under constant risk assessment and prevention, and that they behave reliably and as intended, while minimising possible unintended and unforeseen damage”.

The reliability of an artificial intelligence system is defined as the probability, at a certain level of confidence, that the system will successfully, without failure, perform the function for which it is intended, within the specified performance limits, during the specified duration of the tasks, when it is used in the prescribed manner and for the purpose for which it is intended, under defined load levels, taking into account the previous system usage time.

In [NIST, nd], reliability is defined in the same standard as the “ability of an item to perform as required, without failure, for a given time interval, under given conditions” (Source: iso/iec ts 5723:2022). Reliability is a goal for the overall correctness of AI system operation under the conditions of expected use and over a given period of time, including the entire lifetime of the system.

A wider term is *trustworthy*. According to (NIST, nd), for AI systems to be trustworthy, they often need to be responsive to a multiplicity of criteria that are of value to interested parties. Approaches which enhance AI trustworthiness can reduce negative AI risks. This framework articulates the following characteristics of trustworthy AI and offers guidance for addressing them. Trustworthy AI systems are: valid and reliable, safe, secure and resilient, accountable and transparent, explainable and interpretable, privacy-enhanced, and fair with harmful bias managed. Creating trustworthy AI requires balancing each of these characteristics based on the AI system’s context of use. While all characteristics are socio-technical system attributes, accountability and transparency also relate to the processes and activities internal to an AI system and its external setting. Neglecting these characteristics can increase the probability and magnitude of negative consequences.

Trustworthiness can be considered important because it attracted the attention of ISO/IEC. In (ISO, 2020), there are surveys of topics related to the so-called trustworthiness in AI systems, including the following: (1) approaches to establish trust in AI systems through transparency, explainability, controllability, etc.; (2) engineering pitfalls and typical associated threats and risks to AI systems, along with possible mitigation

techniques and methods; and (3) approaches to assess and achieve availability, resiliency, reliability, accuracy, safety, security, and privacy of AI systems. In that document, trustworthiness is defined as an ability to meet stakeholders' expectations in a verifiable way, including the characteristics of trustworthiness such as reliability, availability, resilience, security, privacy, safety, accountability, transparency, integrity, authenticity, quality, and usability.

Because of the complexity of AI as a system, and since AI includes hardware, software, data and sometimes humans, which can be treated as subystems, and if all of the subsystems must function in order for an AI system to function, then the reliability block diagram is as in Figure 1 while the reliability of an AI system can be calculated by the formula based on (Pokorni, 2021a)

$$R_{AI} = R_{HW}\, R_{SF/HW}\, R_{D/HW,SF}\, R_{H/HW,SF,D} \tag{1}$$

where R_{HW}, R_{SF}, R_D and R_H are hardware reliability, software reliability, data reliability and human reliability, respectively, and $R_{SF/HW}$ is conditional reliability that software will function reliably if hardware is functioning reliably, $R_{D/HW,SF}$ is conditional reliability that the data subsystem will function reliably if hardware and software are functioning reliably, and $R_{H/HW,SF,D}$ is conditional reliability that the human subsystem will function reliably if hardware, software and data subsystems are functioning reliably.

If one can consider that failures of hardware, software and humans are mutually exclusive, then equation (1) can be rewritten as

$$R_{AI} = R_{HW}\, R_{SF}\, R_D\, R_H \tag{2}$$

This is not always the case, but this formula is simpler for caculation, and can show an indication of the whole reliability, which is better than not to do any calculation.

In all cases, relaibilities are usually time dependent.

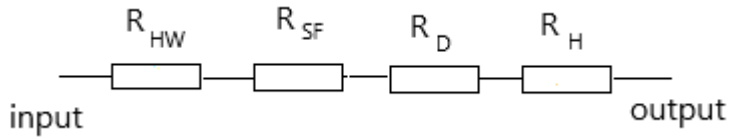

Figure 1 – Reliability block diagram of an artificial intelligence system

Let us discuss some reasons for unreliability such as the quality of data, a small or insufficient amount of training and test data, training on unreal data, the nature of learning algorithms and user incompetence.

Impact of data on reliability

As stated before, reliability has always been data-driven (if being data-driven means that all decisions and processes are based on data), and valid and relevant data has always been the main problem.

Quality of data

Quality of data can have a significant impact on the reliability of AI. What if AI learns from corrupted data or data which are corrupted on purpose (for example by an enemy)? The consequences can be different, from insignificant to catastrophic. Therefore, we need some kind of control on the data which AI uses to learn from. This problem does not imply not to use AI, or not to allow AI to learn from data, but to be aware of the problem in order to prevent serious consequences.

Some examples can be found in (Bathaee, 2018) about AI failures from IBM, Microsoft, Apple, and Amazon. The example from IBM happened in 2013, when IBM partnered with the University of Texas MD Anderson Cancer Center which developed a new “Oncology Expert Advisor” system with the goal to cure cancer (Pokorni, 2024).

Obviously, data quality influences reliability. That is the reason to speak of data reliability. Data reliability refers to the completeness and accuracy of data as a measure of how well it can be counted on to be consistent and free from errors across time and sources. The more reliable data is, the more trustworthy it becomes (IBM, 2023).

There are authors who ask questions about potential risks such as whether AI will pose an existential threat to humanity, or whether AI technology will be concentrated in the hands of the few (Bathaee, 2018). It is not only the question of reliability, though.

Amount and the nature of data

One of the important questions is whether AI can work on a small amount of data, for example, the number of failures of a product. In (Pokorni, 2024), it is concluded that model's predictive accuracy depends on the relevancy, sufficiency, and quality of the training and test data. Two questions are commonly asked with regard to failure history data: (1) How many failure events are required to train a model? And (2) how many records is considered as "enough"?

In July 2018, StatNews reviewed internal IBM documents and found that IBM's Watson was giving erroneous, downright dangerous cancer treatment advice. In (Heaven, 2019), it was concluded that a probable reason was the fact that the software had been trained on a small number of hypothetical cancer patients, rather than on real patient data.

Reliability is also important for the security of AI (for example, protection of unauthorized access).

Nature of the algorithm

There is also a question raised whether AI can fail to function as expected, and the reason is because of the nature of the machine-learning algorithms on which modern AI techniques are commonly built. These algorithms are capable of learning from massive amounts of data, and once that data is internalized, they are capable of making decisions experientially or intuitively like humans. This means that for the first time, computers are no longer merely executing detailed pre-written instructions but are capable of arriving at dynamic solutions to problems based on patterns in data that humans may not even be able to perceive. This new approach comes at a price, because many of these algorithms can be black boxes, even to their creators (Bathaee, 2018). An algorithm of AI is good if data from which this algorithm learns is good. So, again we can speak about data reliability.

User competence

It seems that user competence or incompetence in using AI can also be a reason for inadequate results which AI can deliver. An important question is whether humans can control AI.

As a conclusion for AI reliability, or trustworthiness (which is a broader term), let us use the statement from (European Commission, 2018): "Having the capability to generate tremendous benefits for individuals and society, AI also gives rise to certain risks that should be properly managed" and "It is known that humans are biased in their decision making. Since AI systems are designed by humans, it is possible that humans inject their bias into them, even in an unintended way".

Analysing AI failures can help to improve AI reliability. On the other hand, the use of AI can help to improve its reliability, and evaluate other products, and also improve maintenance (methodology and training).

AI and human reliability

As stated before, AI can learn from humans, and human knowledge can be erroneous. Since humans are involved in AI, obviously AI reliability is connected with human reliability and, consequently, human actions can influence the reliability of AI.

This author has considered human reliability important from the beginning of his work in reliability, so human reliability is included in his textbooks and lectures for students in the Military Academy and the Information Technology School in Belgrade, Serbia.

Artificial intelligence in military applications

The theory and practice of reliability arose from the problems of malfunction in military equipment in the middle of the previous century.

Artificial intelligence is also applied in the military area across different branches and types (army, navy, space forces) of the military, and the unreliability of AI can have more severe consequences than in other areas.

The problem of the reliability of AI is not only in that it will not function, but also, or more importantly, in that it can produce unwanted actions.

We cannot be sure if we can trust humans who are to decide to start nuclear weapons, but can we trust AI?

AI has been used in the military long before its today's use in civilian aplications. AI can benefit the military in numerous areas, just to mention a few such as autonomuos vehicles, use of drones, decision making, etc.

The study (Hunter et al. 2023) examined how AI technology is applied in the militaries in the US, China, and Russia and analysed the implications for the future of AI, global military competition, and international security. This study is based on previous research and expert interviews and reinforce the pivotal role that AI will play in shaping international security in the near future.

In this study, it is concluded that currently the US and China are applying AI across numerous sectors within their economies, societies, and militaries. This trend is likely to accelerate at a rapid pace in the years ahead as AI technology becomes more powerful and efficient. Russia’s AI related command-and-control developments have been split between more traditional intelligence collection formats and innovative monitoring and various facial recognition programmes for both civilian and military applications. China may be more inclined to rely on strategies calculated by AI programmes that have been trained through wargaming scenarios in potential conflicts.

In (Oluyemi, O.A. 2024), it is stated that recent developments in the field of AI have demonstrated that this emerging technology would have a deterministic and potentially transformative influence on the military power, strategic competition, and international security in general. It is argued in this research that there are various military uses of AI technologies and that national interests of powerful states are to endlessly pursue these advanced technologies as preliminary for future warfare in order to gain strategic advantages over potential emerging adversaries. It is also concluded that AI can be integrated into diverse applications, which is an improvement to the "Internet of Things" whereby different devices can be networked together for optimization of performance, and that another attribute of AI is the dual-use of many of its applications which means AI applications are useful in both military and civilian domains.

Drones are now very often used in civilian and military applications. In (Deebak & Hwang, 2023), it is stated that drone applications have gained prominence for various military observations including surveillance, medical transport, aerial photography, and medical transport.

In (Marasco & Bourlai 2025), Large Language Models (LLMs) are examined. It is stated that LLMs have the potential to enhance decision making significantly in core military operational contexts that support training, readiness, and mission execution under low-risk conditions, but still, their implementation must be approached carefully, considering the associated risks. This paper examines the integration of LLMs into military decision making, emphasizing the LLM's ability to improve intelligence analysis, enhance situational awareness, support strategic planning, predict threats, optimize logistics, and strengthen cybersecurity. This paper also considers misinterpretation, bias, misinformation, or overreliance on AI-generated suggestions, potentially leading to errors in routine but critical decision-making processes.

(Roberson et al. 2022) described a case study based on the question what it means to be responsible and responsive when developing and deploying trusted autonomous systems in defense. The lessons from this case study are: the value and impact of embedding responsible research and innovation-aligned, ethics-by-design approaches and principles throughout the development of technology at high translation readiness levels.

(Abaimov & Martellini, 2020) explored cyber vulnerabilities in autonomous technologies, highlighted critical issues of the AI use in autonomous weapons systems, incorporation of ethical principles into development of technologies, revealed legal complications and consequences of AI arms race, forecast future challenges, and

argumented that generated neural networks and machine learning algorithms, being of a complex nature, still remain unpredictable, unreliable and even dangerous when fully autonomous.

(Schwarz, E. 2021) explored the (im)possibility of human control and questioned the presupposition that humans can be morally adequately or meaningfully in control over AI-supported lethal autonomous weapons systems.

Standardization and certification are also imortant. In (Jurado et al. 2024), an overview of the current state of development regarding certification and standardization efforts for Artificial Intelligence systems in military aviation is given.

From the previously mentioned, it can be concluded that nowadays military applications of AI have become a prominent topic of interest in the field of artificial intelligence, which holds a significant potential to support the military in their missions. In the past several years, the use of AI has made tremendous leaps forward in both capability and availability, such as in the field of generative AI.

As the general public has gained access to AI, this means that it can be a treat to the military, so the military must adapt to the changing threat. The military needs to keep pace with these developments in order to maintain security and a technological edge. With new ways of using AI constantly developing, it can be challenging to keep up with ways in which it can aid military operations. As AI becomes more essential, military dominance will not be defined by the size of an army, but by the performance of its algorithms, so it deserves examination of how the military currently uses AI and how it may use AI in the future.

This means that military applications of AI can give advance to small countries. For example, AI's algorithms are able to collect and process data from numerous different sources to aid in decision making, especially in high-stress situations.

Conclusion

Artificial intelligence (AI) is nowadays applied in almost every area of human life, and can have a big impact. Everything can fail to function properly or as expected, and AI is not an exception; therefore, as any other product, AI must be reliable.

Some reasons why AI is not reliable are inadequate quality of data used for learning, a small or insufficient amount of training and test data, training with unreal data, change of data, the nature of learning algorithms, and changes of user behaviour.

It must be kept in mind that AI is mainly software and uses data to learn.

In order to avoid situations when AI becomes unreliable, it is important to be familiar with causes of its unreliability.

To build successful AI, there is a need to be familiar with cases when AI failed in order not to make the same mistakes. But if AI can learn itself, it is not easy to predict mistakes it can done. Analysing AI failures can help to improve AI reliability. Designers who want to apply AI must have in mind its reliability.

If humans are biased in their decision making, this can happen also with AI since AI learns from humans.

AI is predominantly software, but can involve hardware and humans, and of course data, so the reliability of AI is related to software reliability, hardware reliability, human reliability and data reliability. Software reliability is usually a more complex problem than hardware reliability, and AI reliability is more complex than any of these including human and data reliability.

Obviously, the reliability of AI is very complex and must be considered during its design and usage.

References

Abaimov, S. & Martellini, M. 2020. *Artificial Intelligence in Autonomous Weapon Systems*. In: Martellini, M., Trapp, R. (eds) 21st Century Prometheus. Springer, Cham. https://doi.org/10.1007/978-3-030-28285-1_8

Bathaee, Y. 2018. The Artificial Intelligence Black Box and the Failure of Intent and Causation. *Harvard Journal of Law & Technology*. Volume 31, Number 2 Spring 2018. [online]. Available at: https://jolt.law.harvard.edu/assets/articlePDFs/v31/The-Artificial-Intelligence-Black-Box-and-the-Failure-of-Intent-and-Causation-Yavar-Bathaee.pdf

Deebak, B.D. & Hwang, O. S. 2023. Intelligent drone-assisted robust lightweight multi-factor authentication for military zone surveillance in the 6G era. *Computer Networks.* Volume 225, April 2023. https://doi.org/10.1016/j.comnet.2023.109664

European Commission. 2018. *Draft Ethics Guidelines for Trustworthy AI*. Available at: https://digital-strategy.ec.europa.eu/en/library/draft-ethics-guidelines-trustworthy-ai [Accessed: 21 July 2024]

European Commission. 2019. *A definition of AI: Main capabilities and scientific disciplines.* Brussels: European Commission Independent High-Level Expert Group on Artificial Intelligence [online]. Available at: https://digital-strategy.ec.europa.eu/en/library/definition-artificial-intelligence-main-capabilities-and-scientific-disciplines

Government of the Republic of Serbia. 2019. *Strategy for the Development of Artificial Intelligence in the Republic of Serbia for the period 2020-2025*. [online]. Available at: https://www.srbija.gov.rs/tekst/en/149169/strategy-for-the-development-of-artificial-intelligence-in-the-republic-of-serbia-for-the-period-2020-2025.php

Government of the Republic of Serbia. National AI Platform, 2023. Ethical guidelines for development, implementation and use of robust and accountable AI [online]. February 2023. (ai.gov.rs) Available at https://www.ai.gov.rs/tekst/en/459/ethical-guidelines.php [Accessed: 11 March 2025]

Hunter, Y. L., Albert, D. C., Henningan, C. & Rutland, J. 2023. The military application of artificial intelligence technology in the United States, China, and Russia and the implications for global security. *Defense and Security Analysis* 39(2) May 2023. https://doi.org/10.1080/14751798.2023.2210367 Available at: https://www.researchgate.net/publication/370694042_The_military_application_of_artificial_intelligence_technology_in_the_United_States_China_and_Russia_and_the_implications_for_global_security

IBM What is data reliability? Available at: https://www.ibm.com/topics/data-reliability. [Accessed: 15 March 2023]

ISO. 2020. ISO/IEC TR 24028:2020 *Information technology — Artificial intelligence — Overview of trustworthiness in artificial intelligence*. [online]. Available at: https://www.iso.org/standard/77608.html?browse=tc

Jurado, R. D. A., Ye, X., Plaza, O. V., Suárez Z. M., Moreno, P. F. & Valdés, A. M. R. 2024. An introduction to the current state of standardization and certification on military AI applications. *Journal of Air Transport Management* Volume 121, November 2024, https://doi.org/10.1016/j.jairtraman.2024.102685

Kececioglu-B. D. 2002. Reliability Engineering Handbook, volume 1. DEStech Publications. Lancaster. Pennsylvania. USA. ISBN No. 1-932078-00-2. Available at: https://ndesoneandik.wordpress.com/wp-content/uploads/2012/04/dimitri-kececioglu-reliability-engineering-handbook-vol-1.pdf

Marasco, E. & Bourlai, T. 2025. Enhancing trust in Large Language Models for streamlined decision-making in military operations. *Image and Vision Computing.* Available online 18 March 2025. https://doi.org/10.1016/j.imavis.2025.105489

-NIST National Institute of Standard and Tehnology. US Department of Commerce. [online]. Available at: https://airc.nist.gov/AI_RMF_Knowledge_Base/AI_RMF/Foundational_Information/3-sec-characteristics [Accessed: 25 December 2024]

Oluyemi, O.A. 2024. The Military Uses of Artificial Intelligence (AI) and Their Implications on International Security, *The International Journal of Research and Innovation in Social Science (IJRISS)*. June 2024. Available at: https://dx.doi.org/10.47772/IJRISS.2024.803075S

Pokorni, S. 2016. Reliability prediction of electronic equipment: problems and experience. In: *7th International Scientific Conference on Defensive Technologies*

OTEH 2016, Belgrade, pp.695-700, 6-7 October. ISBN 978-86-81123-82-9. http://www.vti.mod.gov.rs/oteh16/elementi/rad/020.html

Pokorni, S. 2021a. The Reliability of Data-driven Internet of Things Systems. *Annals of Spiru Haret University. Economic Series*, 21(4), pp.43-52 [online]. Available at: https://doi.org/10.26458/2141

Pokorni, S. 2021b. Current State of the application of Artificial Intelligence in Reliability and Maintainability. *Vojnotehnički glasnik/Military Technical Courier*, Vol. 69, Issue 3, pp. 578-593. Available at: https://doi.org/10.5937/vojtehg69-30434

Pokorni, S. 2023. Data-driven reliability and availability of electronic equipment. *Vojnotehnički glasnik/Military Technical Courier*. Vol. 71, Issue 3, pp. 769-782. Available at: https://doi.org/10.5937/vojtehg71-43474

Pokorni, S. 2024. Reliability of artificial intelligence. In: *11th International Scientific Conference on Defensive Technologies OTEH 2024*, Belgrade, 09-11 October 2024, pp. 643-646. Available at: https://doi.org/10.5937/OTEH24118

Roberson, T., Bornstein, S., Liivoja, R., Ng, S., Scholz, J., Devitt, K. 2022. A method for ethical AI in defence: A case study on developing trustworthy autonomous systems. *Journal of Responsible Technology*. Volume 11, October 2022. Available at: https://doi.org/10.1016/j.jrt.2022.100036

Schwarz, E. 2021. Autonomous Weapons Systems, Artificial Intelligence, and the Problem of Meaningful Human Control. *Philosophical Journal of Conflict and Violence.* 5(1):53-72, May 2021. Available at: https://doi.org/10.22618/TP.PJCV.20215.1.139004

-University of Cambridge. 2016. Enhancing the reliability of artificial intelligence. [online]. Available at: https://phys.org/news/2016-10-reliability-artificial-intelligence.html

Поузданост вештачке интелигенције у цивилним и војним применама

Славко Ј. Покорни
Школа информационих технологија, Београд, Република Србија

ОБЛАСТ: информационе технологије
КАТЕГОРИЈА (ТИП) ЧЛАНКА: прегледни рад

Сажетак:

Увод/циљ: Циљ овог рада јесте да покаже значај поузданости и расположивости вештачке интелигенције, која се данас примењује у готово свим областима живота. Као и било који производ или уређај, тако и вештачка интелигенција може да откаже. Ипак, она треба да буде поуздана. Углавном се реализује као софтвер, али укључује хардвер, податке и корисника, па је сложена за уградњу и процену поузданости.

Методе: Ово истраживање је рађено углавном коришћењем објављених чланака аутора овог рада, као и неких других радова и докумената.

Резултати: Резултат истраживања јесу кратке дефиниције поузданости, доступности, вештачке интелигенције, поузданости хардвера, софтвера, података и корисника, као и поузданости вештачке интелигенције. Поред тога, укратко су анализирани неки разлози непоузданости вештачке интелигенције, као што су квалитет података, мали или недовољан број података за обуку и тестирање, обука на нереалним подацима, природа алгоритама учења и некомпетентност корисника.

Закључак: Поузданост вештачке интелигенције је веома важна, што се мора узети у обзир приликом њеног пројектовања и употребе.

Кључне речи: вештачка интелигенција, поузданост, расположивост, хардвер, софтвер, корисник, подаци.

Paper received on: 14.01.2025.
Manuscript corrections submitted on: 25.05.2025.
Paper accepted for publishing on: 27.05.2025.

Conception and application of machine learning for inductance prediction in multilayer rectangular spiral micro coils

Younes Benazzouz[a], *Djilalia* Guendouz[b]

University of Oran 2 Mohamed Ben Ahmed,Industrial Maintenance and Safety Institute (IMSI), Department of instrumentation maintenance,Laboratory of Production Engineering and Industrial Maintenance (LGPMI),Oran, People's Democratic Republic of of Algeria

[a] e-mail: benazzouzyounes14@gmail.com, **corresponding author**,
ORCID iD: https://orcid.org/0009-0004-8736-7610

[b] e-mail: lila.guen@yahoo.fr,
ORCID iD: https://orcid.org/0009-0006-7129-5960

https://doi.org/10.5937/vojtehg73-56224

FIELD: computer sciences, electronics
ARTICLE TYPE: original scientific paper

Abstract:

Introduction/purpose: This research introduces a novel approach for designing a dataset of multilayer rectangular planar coils by the integration of a complementary software tools. MATLAB works as a high-level design environment, facilitating the creation of complex geometries and FastHenry acts as a computational engine to solve Maxwell's equations and extract inductance values. Two diverse synthetic datasets are generated using advanced sampling techniques, including Latin hypercube sampling, for different configurations. These datasets are then processed and trained using machine learning algorithms to predict inductance values based on the derived geometric parameters.

Methods: Initially, MATLAB is used to generate extensive synthetic datasets, comprising 20000 rows for 2-layer coil configurations and 15000 rows for 3-layer configurations. After the generation process, the datasets are checked for the readiness for training. Six machine learning models (Gaussian Process Regressor (GPR), KNeighborsRegressor (KNN), BayesianRidge, ElasticNetCV, GammaRegressor, and Bagging Regressor) are trained and evaluated using metrics such as R^2 and RMSE. The models are further tested on unseen test data and validated using the cross-validation technique to check how much the models can generalize.

Results: The datasets were generated successfully, and the models KNeighborsRegressor, Gaussian Process Regressor (GPR), and Bagging Regressor performed the best and showed a high accuracy and low error.

Conclusion: The results show that machine learning is a practical and effective method for predicting inductance in multilayer rectangular planar coils based on the geometry.

Key words: rectangular planar micro-coil, multilayer planar coil, inductance, machine learning, synthetic dataset

Introduction

Multilayer planar coils combine superior inductance and energy efficiency properties with efficient space utilization making them ideal for compact electronic applications using a parallel architecture alignment of layers. They offer an enhanced efficiency and performance in such systems, which makes them vital for advanced applications in power transmission and high-precision energy management in modern applications (Alghrairi et al., 2022). Flexible multilayer microelectromechanical systems (MEMS) coils further improve energy efficiency and space utilization and demonstrate high integration capability in arbitrary spaces, significantly enhancing the utilization of the space magnetic field and output performance in energy harvesters; their vibration energy harvesters achieve up to a 43% increase in open-circuit voltage and compact dimensions suitable for small electronics in constrained environments (Zhang et al., 2024). Furthermore, planar on-silicon multilayer inductors have proven highly beneficial in clinical applications, particularly in electromagnetic tracking (EMT) systems. These inductors achieve a stringent requirement for precise tracking in medical environments (Sidun et al., 2023). These technologies also enable the development of wireless intracranial pressure (ICP) monitoring systems, where carefully designed spiral planar coils improve the coupling factor and detection range of miniature implanted sensors, enhancing wireless power transfer efficiency and sensor performance (Wang et al., 2018). Recent designs of wireless resistive analog passive sensors have demonstrated the feasibility of bio-signal monitoring using optimized planar spiral coil pairs which are critical for long-term body signal monitoring. By employing inductive coupling and coil design optimization with genetic algorithms, these sensors achieve high sensitivity and reliable performance (Noroozi & Morshed, 2024).

Higher inductance can be achieved by increasing the number of parallel layers. However, estimating inductance remains a challenge, as directly solving Maxwell's equations for complex shapes is impractical. To address this, a versatile analytical tool has been developed for calculating the self-inductance of planar coils with general geometries. Based on Grover's equations, this method aims to combine speed, precision, intuitive use, and geometric flexibility (Faria et al., 2021). Additionally, inductance behavior in printed-circuit rectangular spiral coils, especially in

eddy-current testing applications, can be effectively modeled using analytical methods that simplify multi-turn geometries and account for practical PCB constraints, aiding in accurate mutual inductance prediction and design optimization without relying on coil thickness (Wu et al., 2023). In superconducting circuits, mutual coupling decreases exponentially with distance between striplines, while microstrips exhibit long-range coupling, limiting scalability for large-scale integration. In addition, analytical expressions provide inductance estimations (Tolpygo et al., 2022). Another method for calculating mutual inductance between planar spiral coils with arbitrary geometries has been proposed, using a partial inductance approach that simplifies the coils into polygonal segments, allowing accurate and generalizable analysis validated by simulations and measurements (Tavakkoli et al., 2019). All these techniques are based on equation estimation and require a precise coupling factor to determine inductance.

The integration of supervised learning has demonstrated great promise in planar coil applications. Deep learning has been applied to model complex polyphase inductive coils in wireless power transfer systems, significantly reducing computational effort while maintaining high accuracy in predicting mutual inductance, with a normalized root mean square error (NRMSE) of 3.3% and a coefficient of determination of 0.985 (Gastineau et al., 2024). In magnetic resonance imaging (MRI), deep learning has shown promise for quickly predicting RF-induced heating of conductive implants based on their geometry and position, offering a faster alternative to traditional phantom experiments (Chen et al., 2023). In single-layer planar coils, a machine learning-based method has been proposed for calculating self- and mutual inductance and multiple linear regression with polynomial features achieved near-reference precision while being orders of magnitude faster(Stillig et al., 2023). Additionally, machine learning techniques have been applied to accelerate the design of magnetic couplers for wireless power transfer systems; by training on synthetic datasets from ANSYS Maxwell, these models can efficiently predict optimal coil parameters such as inner radius and number of turns while accounting for constraints like inductance and core materials (Ding et al., 2025). After recognizing the potential of machine learning in predicting the planar coil behavior and addressing the challenges of deriving precise empirical equations, we propose a machine learning-based methodology for multilayer rectangular spiral micro-coil inductance estimation.

Diving into specific algorithms, GPR proven effective for inductance estimation under magnetic saturation, significantly reduces prediction errors from 9.6% to 4.7% by improving training datasets. Its ability to minimize computational costs while maintaining accuracy highlights its potential in inductance prediction tasks (Bayazıt et al., 2023). Furthermore, inductance modeling for planar meander structures using the Restricted Boltzmann Machine (RBM) and KNN demonstrated good performance with analytical and simulation datasets and showcase the potential of these algorithms for compact inductor designs (Ansari & Agarwal, 2024). Among those using ML, none have specifically addressed the inductance of multilayer rectangular planar coils using supervised data-driven models. The primary contributions of this work are twofold:
1- The development of a systematic methodology for designing multilayer rectangular planar coils and generating a comprehensive synthetic dataset through simulations, capturing diverse coil geometries and inductance behaviors.
2- The implementation of supervised machine learning models to predict inductance values, bypassing the computational complexity of traditional coupling factor calculations and empirical formulations. This approach offers a scalable framework for rapid and accurate inductance estimation in multilayer configurations.

Methodology flowchart

The following flowchart, shown in Figure 1, illustrates the proposed methodology for the design and inductance prediction of multilayer rectangular planar coils. This structured approach integrates all key stages, including coil conception, simulation, dataset generation, and machine learning model deployment. The process begins with geometry modeling in MATLAB, where user-defined coil specifications (e.g., turns, layer alignment, trace dimensions) are translated into precise configurations. The geometries are then discretized into nodes and segments compatible with FastHenry, an open-source field solver software used to compute inductance values through electromagnetic simulations. The resulting data combining geometric parameters and simulated inductance is preprocessed to normalize features and split into training and validation sets. Supervised machine learning models are subsequently trained to map geometric inputs to inductance outputs, with performance rigorously evaluated using metrics like RMSE and MAE. The finalized model is tested on unseen configurations to validate generalizability before deployment and that enable an accurate inductance

prediction for new designs. This structured approach bridges physical simulations with data driven modeling, which eliminates reliance on complex analytical derivations.

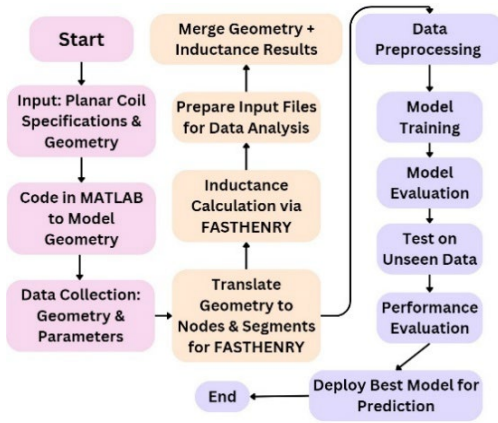

Figure 1 – Methodology flowchart for designing and predicting inductance of multilayer rectangular planar coils

Single-layer design framework for planar coils as a foundation

Before delving into the complexity of multilayer rectangular planar coils, it is essential to first understand the characteristics and behavior of a single-layer design, as it forms the basis of the multilayer coil. In the conception of planar coils for inductance estimation, a lot of estimation formulas are available such as Wheeler Expression, Modified Wheeler Expression, and Current Sheet Expression, shown in Equations 1, 2, and 3 (Wheeler, 1928) (Mohan et al., 1999), respectively. However, by analyzing these formulas, it shows that the geometry of the planar coil plays an important role in determining the inductance.

$$L_{wh} = \frac{N^2 r^2}{8r+11\Delta} \tag{1}$$

$$L_{mwh} = k_1 N_0 \frac{\mu^2 davg}{1+\rho k_2} \tag{2}$$

$$L = \frac{\mu_0 n^2 d_{avg} C_1}{2} (ln(C_2/\rho)+C_3\rho+C_4\rho^2) \tag{3}$$

In these equations, N represents the number of turns of the coil, and r is the radius of the planar coil. The parameter Δ is defined as half the difference between the outer and inner diameters, i.e., $\Delta = \frac{d_{out}-d_{in}}{2}$, while d_{avg} denotes the average diameter, given by $d_{avg} = \frac{d_{out}+d_{in}}{2}$. The term ρ is the fill factor, expressed as $\rho = \frac{d_{out}-d_{in}}{d_{out}+d_{in}}$. The constants k_1, k_2, C_1, C_2, C_3 and C_4 are empirical coefficients that depend on the specific geometry of the coil and μ_0 represents the permeability of free space.

By consequence, our design approach for the planar coil layer focuses on deconstructing the concept into multiple geometric variations to generate a substantial and diverse dataset for analysis, as Figure 2 shows.

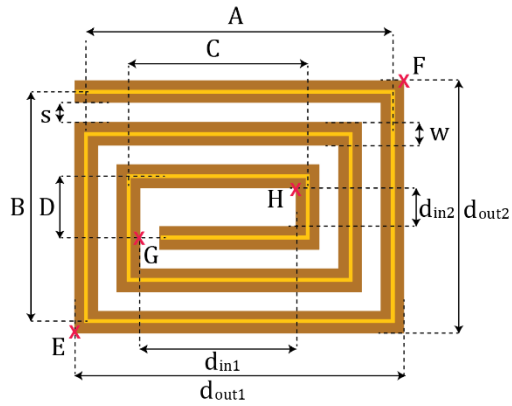

Figure 2 –2D representation of a single layer rectangular planar coil geometry with the labeled parameters

Geometric variables such as s the spacing between traces, w the trace width , n the number of turns and the inner and outer diameters d_{in1}, d_{in2} , d_{out1} and d_{out2} are commonly used and can be derived from established equations like the Wheeler's formula but these equations assume symmetrical shapes using only two diameters d_{in} and d_{out} instead of four and that reflect the symmetrical nature of the geometry. We introduced additional geometric parameters such as distances A , B , C and D in our approach of design and geometric data. Collecting these distances represents the bone diameters of the spiral shape excluding the trace width. We added hypothenuses EF and GH which are also variable distances incorporated into the design data to provide a broader range of

input parameters and to enable exploring a wider variety of geometric patterns and maximizing design versatility.,specifically $EF^2 = {d_{out1}}^2 + {d_{out2}}^2$ and $GH^2 = {d_{in1}}^2 + {d_{in2}}^2$.

Extending the single layer concept to a multilayer concept

The advantage of multilayer planar coils is their ability to increase inductance while minimizing space, making them ideal for miniaturized electronic applications. The modeling of a single layer is extended into multilayer configurations, connected in parallel through via connections that ensure seamless current flow between layers. To achieve real-world applicability, a height of 1 oz (28.35 grams) of copper material is incorporated, transforming the design into a 3D structure. Then, a FastHenry compatible input file is generated, encompassing node definitions and segment connections with material properties. This enables precise simulation of the coil's inductance and resistance, facilitating the systematic design and optimization of compact, high-inductance planar coils for advanced electronic systems. Figure 3 illustrates 3D representations of multilayer rectangular planar coils with spiral segments and via connections plotted.

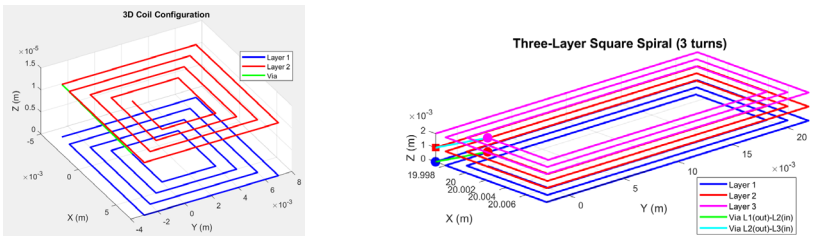

(a) 2-layer rectangular planar coil *(b) 3-layer rectangular planar coil*

Figure 3 –3D representation of a 2-layer and 3-layer rectangular planar coil with spiral segments and via connections

For multilayer planar coils, the total inductance L_T can be approximated by the sum of the self-inductances L_1, L_2 of each layer and the mutual inductance M between them (Zhao, J .2010), which is given by

$$L_T = L_1 + L_2 \pm M \tag{4}$$

$$M = 2\sqrt{L_1 L_2}\,\frac{n^2}{0.64[(0.184z^3 - 0.525z^2 + 1.038z + 1.001)(1.67n^2 - 5.84n + 65)]} \tag{5}$$

where n is the number of coil's turns, and z the distance between the layers.However, these formulas are typically valid for coils with 5 to 20 turns, and layer distances between 0.75 mm and 2 mm, are not suitable for rectangular shapes. Additionally, as the number of turns increases, the formula changes so our model will use a range of 3 to 30 turns, with wire widths varying from 40 µm to 180 µm. Unlike these analytical methods, we propose using ML to predict inductance values, which will allow us to bypass the need for these analytical formulas.

Dataset generation

After establishing the logical concept of creating multilayer planar coils, we delve into generating a dataset for training machine learning models. The dataset focuses on two configurations: two-layer and three-layer planar coils, containing 20000 rows and 15000 rows, respectively. Each row in the dataset represents a single data entry which includes multiple geometric input variables, with the output being the inductance value for each configuration.

The geometric variables include those mentioned earlier, such as the A, B, C and D segment lengths, the inner diameters and the outer diameters d_{in1}, d_{in2} , d_{out1} and d_{out2}, the spacing s, the trace width w, and the diagonals (EF, GH). In addition, the loop creation variables (i, j) are used, representing the incremental steps of the spiral design along the vertical and horizontal directions, respectively. These are defined as $i = first\ segment\ distance/\Delta x$ and $j = second\ segment\ distance/\Delta x$ where Δx is a fixed step size as shown in Figure 4.

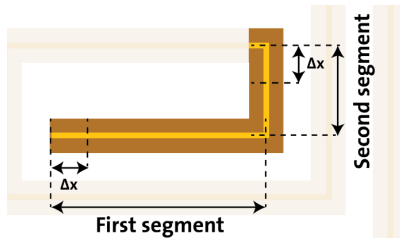

Figure 4 – Initial segments and design steps in the spiral creation

The vertical spacing between the layers, Z, represents the via distance, and that completes the foundational geometry. To enhance the dataset, feature engineering variables are introduced, such as d_{in_r} and

d_{out_r} defined as $d_{in\_r} = \sqrt{d_{in1}d_{in2}}$ and $d_{out\_r} = \sqrt{d_{out1}d_{out2}}$ respectively, These equations are adapted from the formulas used for elliptical shapes (Farooq et al. 2023) and modified for rectangular geometries by applying the area equality method, the average diameter $d_{avg} = \frac{d_{out\_r}+d_{in\_r}}{2}$, the fill ratio $\rho = \frac{d_{out\_r}-d_{in\_r}}{d_{out\_r}+d_{in\_r}}$.

These features engineered variables are commonly used in inductance estimation equations (Asadi Et all. 2023) (Wheeler, 1928). It will significantly enhance the robustness of our models and the predictive power of the dataset. This comprehensive approach ensures that the dataset captures all critical factors influencing the inductance of multilayer planar coils, making it suitable for supervised machine learning models, after defining all input parameters. A structured parameter sampling approach was implemented to generate two datasets for two and three layers planar coils. The physical and geometric parameters of the coils, along with their respective ranges, are summarized in Table 1. These ranges were chosen to cover a broad spectrum of coil designs that balance the manufacturability and performance requirements.

Table 1 – Design parameters and ranges

	Minimum Value	Maximum Value
n	3	30
i	1	15
j	1	15
w	20 μm	200 μm
s	30 μm	250 μm
z	40 μm	180 μm

To ensure a diverse and representative dataset, we combine three techniques, i.e., Latin Hypercube Sampling (LHS), parameter mapping, and physical validation and that leads us to explore a wide design space while ensuring practical manufacturability constraints were met. The main idea of LHS is dividing the range of each parameter into equally spaced intervals and it guarantees that one sample is drawn from each interval to minimize redundance in variables and clustering in the sample space. In addition, small perturbations with a value of 2% were introduced to each sampled value to simulate real word variability. Parameterization involves mapping normalized values generated through Latin Hypercube Sampling (LHS) to real-world ranges relevant to the coil design; for example, the

number of turns was mapped to [3–30], wire width to [20–200µm], and spacing to [30–250µm], while physical validation ensures that the generated coil configurations are physically feasible and adhere to manufacturability constraints with a minimum wire spacing of 30 µm to prevent electrical shorts. A layer separations [40–180µm] is compatible with standard fabrication processes.

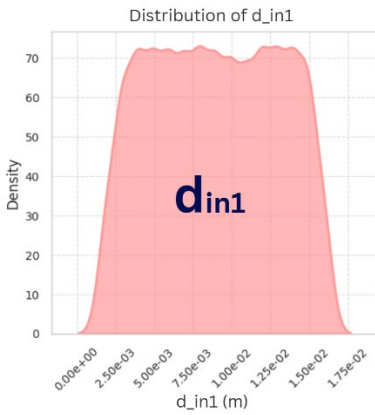

(a) Destitution of d_{in1}

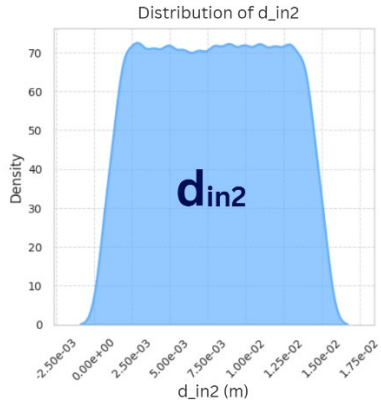

(b) Destitution of d_{in2}

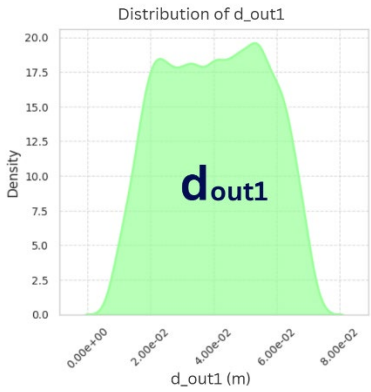

(c) Destitution of d_{out1}

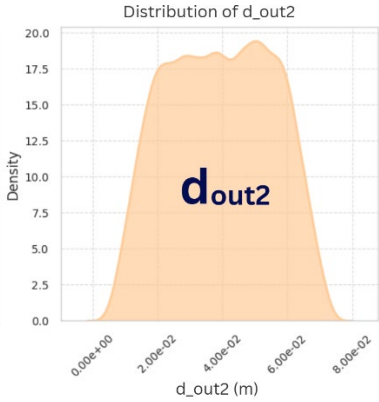

(d) Destitution of d_{out2}

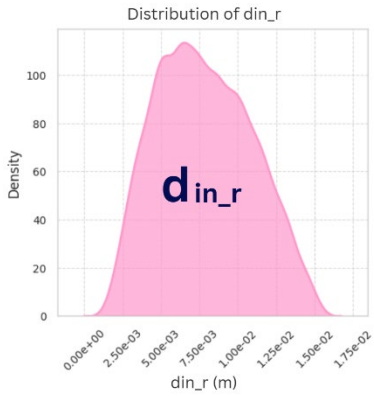

(e) Destitution of d_{in_r}

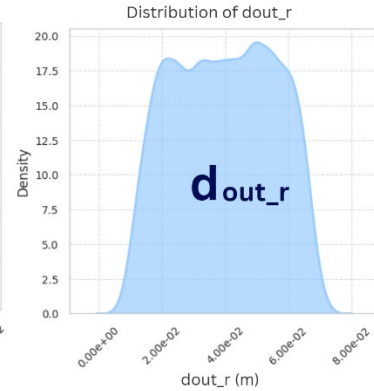

(f) Destitution of d_{in_r}

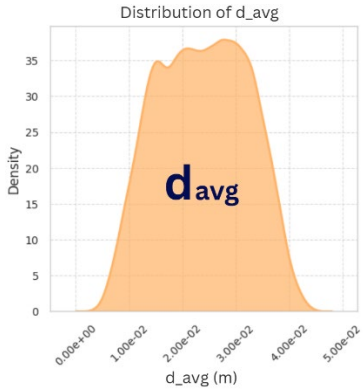

(g) Destitution of d_{avg}

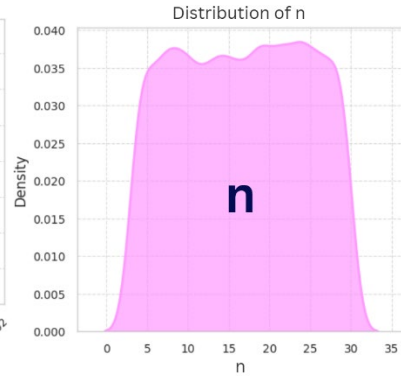

(h) Destitution of d_n

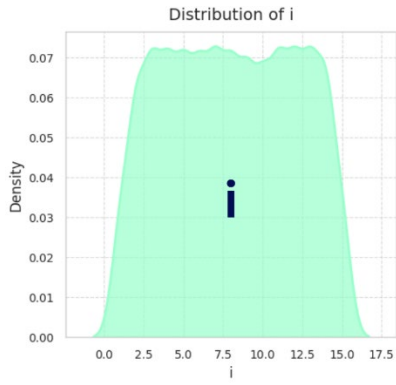

(i) Destitution of i

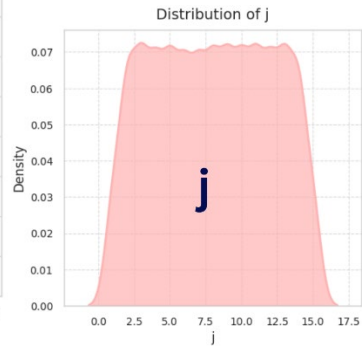

(j) Destitution of j

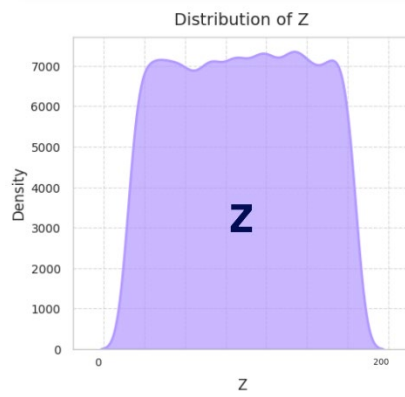

(k) Destitution of z

Figure 5 – Distribution of the geometric parameters in the 2-layer planar coil design

Figure 5 shows the density distributions of the key geometric parameters for the two-layer planar coil design and it demonstrates the effectiveness of our Latin hypercube sampling approach for multiple dimensional parameters. The inner and outer d_{in1}, d_{in2} , d_{out1} and d_{out2} diameters of the two layers show uniform distributions within their respective ranges and that indicates complete coverage of possible coil configurations. Feature engineering variables such as d_{in_r} and d_{out_r} show slightly asymmetrical distributions and the average diameter d_{avg} follows a bell-shaped distribution, suggesting a natural convergence towards optimal intermediate values. The rotation parameters n , i and j show uniform distributions in their discrete ranges, validating the efficiency of the LHS in sampling the design space. The distribution of the separation distance z guarantees adequate spacing between the layers while respecting manufacturing constraints. These distributions collectively confirm that our sampling strategy successfully explores the design space while maintaining physical feasibility, as shown by the smooth, well-defined boundaries of each parameter distribution.

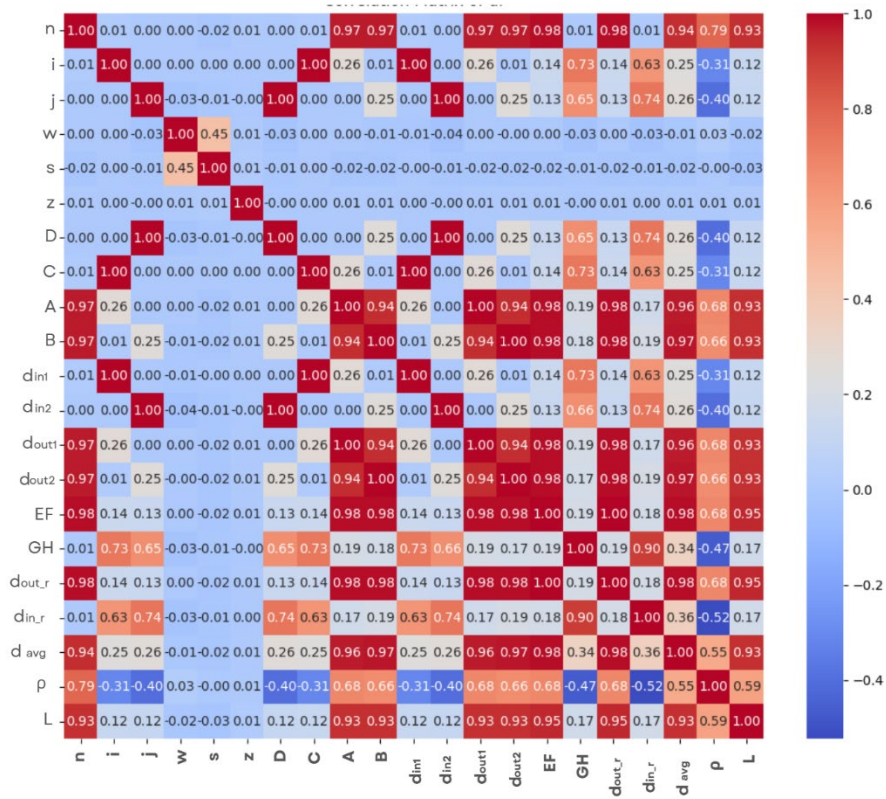

Figure 6 – Correlation matrix of the geometric variables and the inductance (L) for the two layers planar coil dataset

To gain deeper insights into the relationships among geometric variables and their influence on inductance prediction, a correlation analysis was conducted, as shown in Figure 6. The purpose of this analysis is to assess the interdependencies between the design parameters and to identify the key predictors of inductance prior to training machine learning models. The correlation matrix reveals several notable trends and positive correlations were observed between the inductance L and the parameters such as n number of turns, d_{avg} average diameter and the engineered features d_{in_r} and d_{out_r} showing a direct impact on inductance. The geometric A, B, C and D also demonstrate high correlations with L and that reflects their role in defining the overall dimensions of the coil. On the other hand, the parameters such as the (w) trace width, the spacing s, and the z vertical separation show less

correlation with L . However, even variables with weak linear correlation may contribute through non-linear interactions, especially when using models like the GPR and BaggingRegressor that can capture such complex relationships.The motivation for including both directly measured and engineered geometric variables d_{avg} , ρ d_{in_r} and d_{out_r} is based on their relevance in well-established inductance calculation equations, including those proposed in (Wheeler, 1928) (Mohan et al., 1999) and more recently in (Farooq et al. 2023). This correlation analysis serves as a foundational step to the dataset to ensure the inclusion of critical features like d_{avg} and ρ fill ratio, which give an enhancement and a predictive power of the data driven models. Furthermore, retaining a broad set of features allows machine learning models with internal feature selection mechanisms to determine their usefulness automatically.

Machine learning models selection

The data generated for inductance estimation was evaluated using various machine learning models which can be classified according to their methodologies. All models were implemented using Scikit-learn, a widely used open-source Python library that provides a consistent interface and efficient implementations for a wide range of machine learning algorithms. Unless otherwise stated, all models were used with their default parameters as defined in Scikit-learn version 1.5.2. Probabilistic models include the GaussianProcessRegressor (GPR), which assumes that the data follows a Gaussian process. As described by Rasmussen and Williams (Williams & Rasmussen, 2006), GPR predictions at a new point x^* are given by

$$f^*(x^*) = k^{*T}(K + \sigma^2 I)^{-1} y \tag{6}$$

where k^* represents the vector of covariances between x^* and the training points, K is the covariance matrix between the training points, σ^2 denotes the noise variance, I is the identity matrix and y is the vector of the training outputs.

In the category of instance-based learning, KNeighborsRegressor (KNN) was employed, a non-parametric model that predicts on the basis of nearest neighbors, thus capturing local relationships in the dataset (Altman, 1992). KNN uses the Euclidean, Manhattan and Minkowski distance metrics presented respectively:

$$d(x, X_i) = \sqrt{\sum_{i=1}^{d} \left(x_j - X_{ij}\right)^2} \quad (7)$$

$$d(x, y) = \sum_{i=1}^{n} |x_i - y_i| \quad (8)$$

$$d(x, y) = \left(\sum_{i=1}^{n} (x_i - y_i)^p\right)^{1/p} \quad (9)$$

Only one distance metric is used during model training. KNN does not use multiple distance functions simultaneously, while Euclidean measures straight-line distance in a d-dimensional space, Manhattan sums absolute differences for total travel distance, and Minkowski generalizes both, adapting to diverse data structures with the parameter p (e.g, p =2 for Euclidean, p =1 for Manhattan).

We also used linear and regularized models, such as BayesianRidge and ElasticNetCV. BayesianRidge applies Bayesian inference to linear regression, balancing bias and variance (MacKay, 1992). The model assumes

$$f(x) = \beta_0 + \beta_1 x_1^1 + \beta_2 x_2^2 + \ldots + \beta_2 x_n^n + \varepsilon \quad (10)$$

where β_i represents the coefficient and ε is the measurement error.

ElasticNetCV combines Lasso and Ridge penalties to manage multicollinearity and perform feature selection. We applied 5-fold cross-validation to automatically select the optimal values for the regularization parameters, including the overall penalty strength and the mixing ratio between the two techniques.

The BaggingRegressor model is used to combine the predictions of several instances of KNeighborsRegressor, with a total of 10 estimators in the set, each trained on different bootstrap samples of the dataset as indicated by setting (bootstrap = True).

Finally, a distribution-specific model, the GammaRegressor, has been included, designed for target variables with a Gamma distribution. The model was implemented using the default settings: alpha = 1.0 which controls regularization to balance bias and variance; link = 'log', ensuring that the predicted values remain strictly positive, suitable for Gamma-distributed targets; and solver = 'lbfgs', a quasi-Newton optimization algorithm known for efficient convergence.

To assess the performance of the machine learning models developed to estimate the inductance of multilayer planar coil designs, we employed multiple evaluation metrics. They were chosen for their ability to provide insights into the prediction capabilities of the models from different perspectives like accuracy, robustness and generalization to unseen data. By comparing these models based on these criteria, we can evaluate their suitability for inductance estimation. The metrics used for model evaluation includes the coefficient of determination R^2 and the root mean square error RMSE, which are defined by Equations (11) and (12), respectively:

$$\mathrm{R}^2 = 1 - \frac{\sum_{\mathrm{i}=1}^{\mathrm{N}} (\mathrm{y}_{\mathrm{obs,i}} - \mathrm{y}_{\mathrm{pre,i}})^2}{\sum_{\mathrm{i}=1}^{\mathrm{N}} (\mathrm{y}_{\mathrm{obs,i}} - \overline{y_{obs}})^2} \qquad (11)$$

$$\mathrm{RMSE} = \sqrt{\frac{1}{\mathrm{N}} \sum_{\mathrm{i}=1}^{\mathrm{N}} (\mathrm{y}_{\mathrm{obs,i}} - \mathrm{y}_{\mathrm{pre,i}})^2} \qquad (12)$$

where $\mathrm{y}_{\mathrm{obs,i}}$ is the observed inductance value, $\mathrm{y}_{\mathrm{pre,i}}$ is the corresponding predicted value, and $\overline{y_{obs}}$) is the mean of the observed inductance values. The variable n represents the total number of samples in the dataset.

Dataset splitting and models training results

All geometric variables were considered for experiment training of the selected models. The data was split into training and testing datasets with 80% used for training and 20% for testing. For the 2-layer dataset, there were 16000 samples for training and 4000 samples for testing. For the 3-layer dataset, it resulted in 12000 samples for training and 3000 samples for testing. All data was thoroughly checked for missing values, and the health of the data was verified before training to ensure that everything is perfect and all rows value are in a healthy condition.

The performance of the selected machine learning models was assessed on both training and testing datasets and through cross-validation. By this evaluation, we ensure the model's ability to generalize unseen data and avoid overfitted and underfitted models and to identify the most suitable methods for inductance prediction. Table 2 summarizes the results.

Table. 2 – Performance on train and test sets for the 2-layer planar coil

	Train set		Test set	
	R^2	RMSE	R^2	RMSE
GPR	0.999	$4.4 \cdot 10^{-9}$	0.993	$7.9 \cdot 10^{-7}$
BaggingRegressor	0.999	$3 \cdot 10^{-7}$	0.997	$4.7 \cdot 10^{-7}$
KNN	0.998	$3.2 \cdot 10^{-7}$	0.997	$5.2 \cdot 10^{-7}$
BayesianRidge	0.945	$2.3 \cdot 10^{-6}$	0.943	$2.3 \cdot 10^{-6}$
ElasticNetCV	0.922	$2.7 \cdot 10^{-6}$	0.922	$2.7 \cdot 10^{-6}$
GammaRegressor	0.760	$4.7 \cdot 10^{-6}$	0.736	$5.1 \cdot 10^{-6}$

As shown in Table 2, the Gaussian Process Regressor (GPR) demonstrated exceptional performance, achieving an R^2 of 0.999 on the training set and 0.993 on the testing set with a low RMSE, making it the top performing model. Bagging Regressor and KNN also performed well, maintaining high R^2 values on both training and testing sets and that indicates a strong predictive capability too. Linear models like Bayesian Ridge and ElasticNetCV showed moderate performance, achieving values around 0.94. The Gamma Regressor, however, displayed significantly lower R^2 square and higher RMSE values.

Table. 3 – Performance on the train and test sets for the 3-layer planar coil

	Train set		Test set	
	R^2	RMSE	R^2	RMSE
GPR	0.999	$4 \cdot 10^{-9}$	0.998	$3.2 \cdot 10^{-7}$
BaggingRegressor	0.998	$3.3 \cdot 10^{-7}$	0.998	$4 \cdot 10^{-7}$
KNN	0.998	$3.6 \cdot 10^{-7}$	0.997	$4.5 \cdot 10^{-7}$
BayesianRidge	0.943	$2.3 \cdot 10^{-6}$	0.946	$2.2 \cdot 10^{-6}$
ElasticNetCV	0.922	$2.7 \cdot 10^{-6}$	0.926	$2.6 \cdot 10^{-6}$
GammaRegressor	0.747	$4.9 \cdot 10^{-6}$	0.765	$4.7 \cdot 10^{-6}$

A similar pattern was observed for the 3-layer dataset as shown in Table 3. The GPR model again demonstrated the best performance, achieving an R of 0.999 on the training set and 0.998 on the testing set. Bagging Regressor and KNN closely followed, with minimal discrepancies between training and testing metrics. Linear models, including Bayesian Ridge and ElasticNetCV, performed consistently achieving a moderate accuracy, while the Gamma Regressor once again showed low results.

The cross-validation was applied to validate the models. This technique evaluates model performance by splitting the dataset into multiple folds and then compute the existed metrics for each fold. Table 4 summarizes the results of the cross-validation

Table. 4 – Cross-validation results using the k-fold method (k=5)

	2layers		3layers	
	R^2	RMSE	R^2	RMSE
GPR	0.998	$3.3 \cdot 10^{-7}$	0.998	$3.7 \cdot 10^{-9}$
BaggingRegressor	0.998	$3.8 \cdot 10^{-7}$	0.998	$4.1 \cdot 10^{-7}$
KNN	0.998	$4.2 \cdot 10^{-7}$	0.997	$4.5 \cdot 10^{-7}$
BayesianRidge	0.945	$2.3 \cdot 10^{-6}$	0.944	$2.2 \cdot 10^{-6}$
ElasticNetCV	0.922	$2.7 \cdot 10^{-6}$	0.923	$2.7 \cdot 10^{-6}$
GammaRegressor	0.760	$4.7 \cdot 10^{-6}$	0.754	$4.8 \cdot 10^{-6}$

The cross-validation results for both datasets confirmed the trends from experiment training and testing. In this context, the cross-validation (k=5) was applied on the training data only, in order to assess the model's robustness and consistency without involving the held-out test set. For the two-layer dataset, the GPR achieved the best performance with an R^2 of 0.998 and the lowest RMSE of $3.3 \cdot 10^{-7}$, followed by Bagging Regressor and KNN. the linear models, such as Bayesian Ridge and ElasticNetCV, showed moderate performance R around 0.94, while the Gamma Regressor struggled with the highest RMSE. Similar results were observed for the three-layer dataset, with the GPR again leading R^2 of 0.998, followed by Bagging Regressor and KNN, while the linear models performed moderately and the Gamma Regressor lagged.

Table. 6 – Monte Carlo cross-validation through 50 iterations

	2layers		3layers	
	R^2	RMSE	R^2	RMSE
GPR	0.998	$3.9 \cdot 10^{-7}$	0.998	$3.8 \cdot 10^{-9}$
BaggingRegressor	0.998	$3.8 \cdot 10^{-7}$	0.998	$4.2 \cdot 10^{-7}$
KNN	0.998	$2.24 \cdot 10^{-7}$	0.997	$4.6 \cdot 10^{-7}$
BayesianRidge	0.945	$2.27 \cdot 10^{-6}$	0.943	$2.3 \cdot 10^{-6}$
ElasticNetCV	0.922	$2.7 \cdot 10^{-6}$	0.922	$2.6 \cdot 10^{-6}$
GammaRegressor	0.760	$4.7 \cdot 10^{-6}$	0.753	$4.8 \cdot 10^{-6}$

To further validate model performance and assess robustness against data splits, Monte Carlo cross-validation through 50 iterations of randomized subsampling was applied on both 2-layer and 3-layer datasets. This method randomly splits the dataset into training (80%) and testing (20%) subsets across multiple iterations. The procedure yields distributions of performance metrics across all splits. Table 5 summarizes the performance of the models using this approach.

The Monte Carlo cross-validation results presented in Table 6 are consistent with the findings from the k-fold cross-validation presented inTable 4 and that reenforces the reliability of the models. In both the 2-layer and 3-layer datasets, the GPR consistently delivered the highest R^2 values of 0.998 and the lowest RMSE and that confirms its superior performance and robustness to data splits. Bagging Regressor and KNN also maintained strong and stable performance across all iterations. The linear models such as Bayesian Ridge and ElasticNetCV demonstrated moderate accuracy, while the Gamma Regressor exhibited the weakest results, with the highest RMSE and lowest R^2 values.

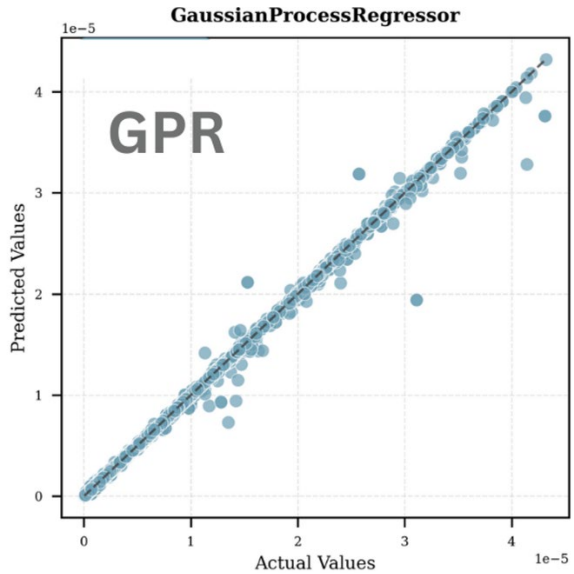

(a) Gaussian Process Regressor (GPR) – predicted vs actual values

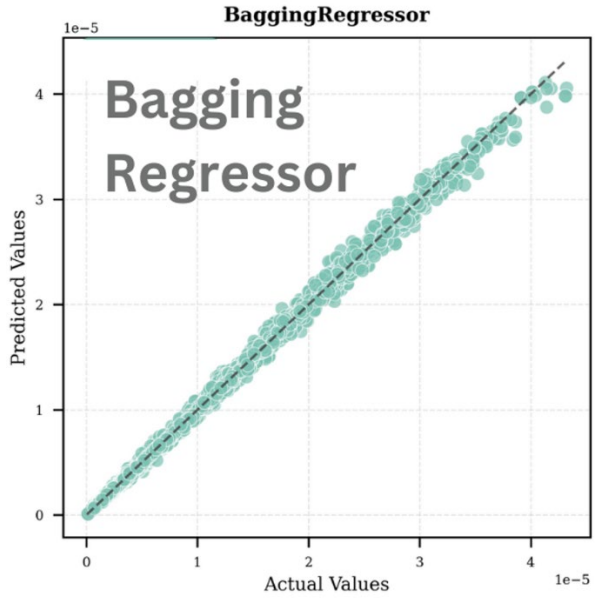

(b) *Bagging Regressor – predicted vs actual values*

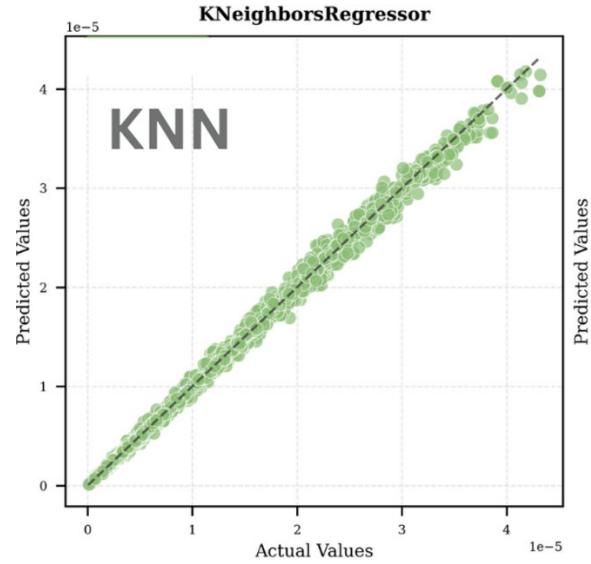

(c) K-Nearest Neighbors (KNN) – predicted vs actual values

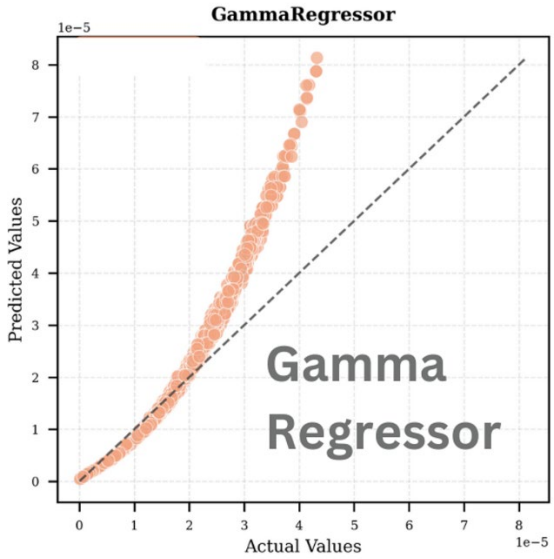

(f) Gamma Regressor – predicted vs actual values

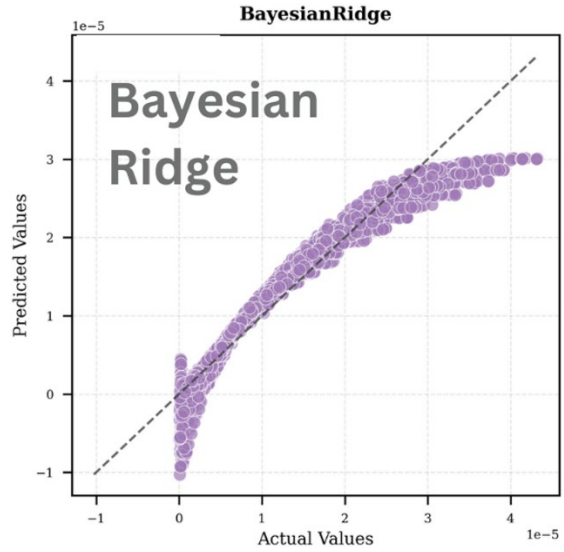

(d) Bayesian Ridge – predicted vs actual values

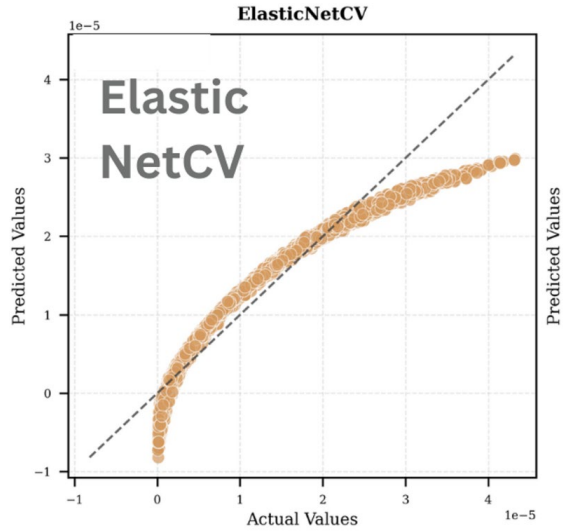

(e) ElasticNetCV – predicted vs actual values

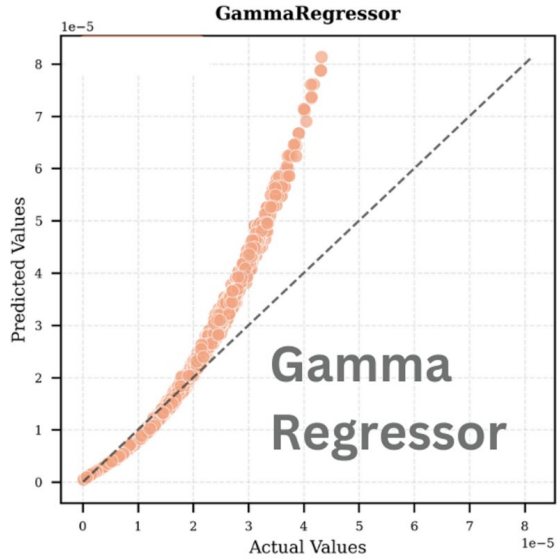

(f) Gamma Regressor – predicted vs actual values

Figure 7 – Scatter plot of predicted vs. actual values for 2-layer configurations

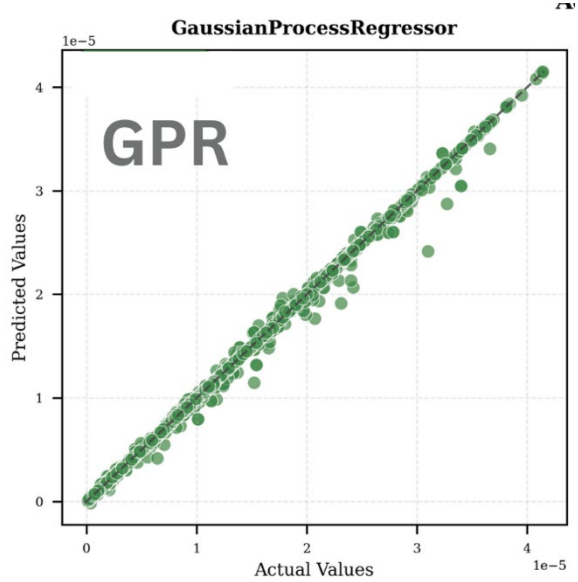

(a) Gaussian Process Regressor (GPR) – predicted vs actual values

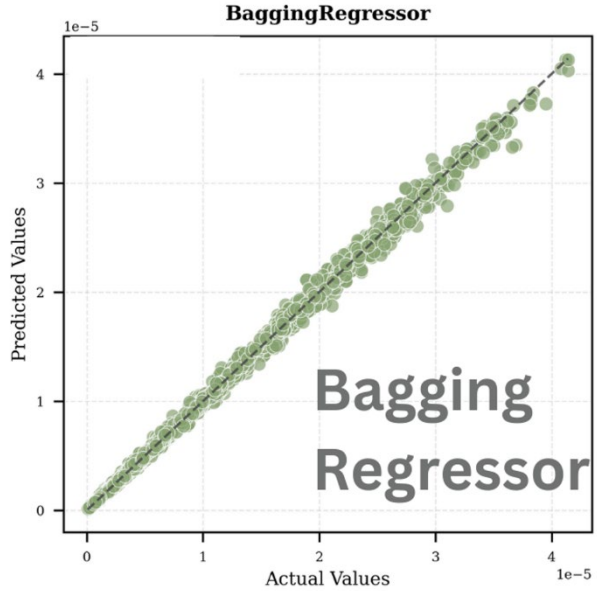

(b) Bagging Regressor – predicted vs actual values

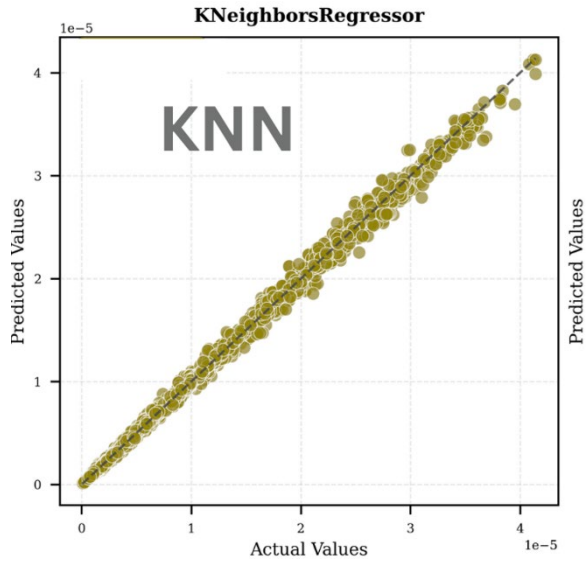

(c) K-Nearest Neighbors (KNN) – predicted vs actual values

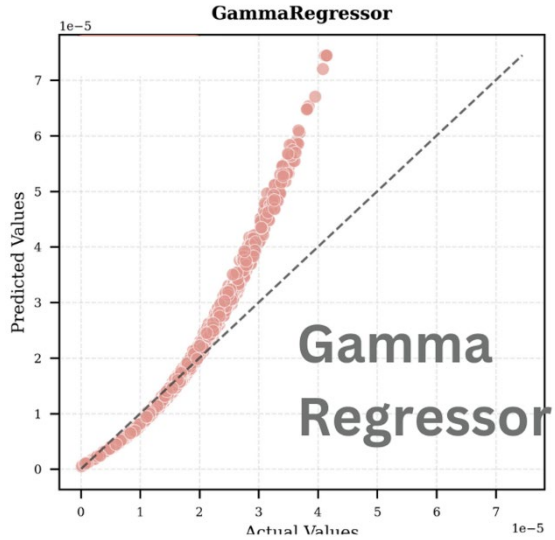

(f) Gamma Regressor – predicted vs actual values

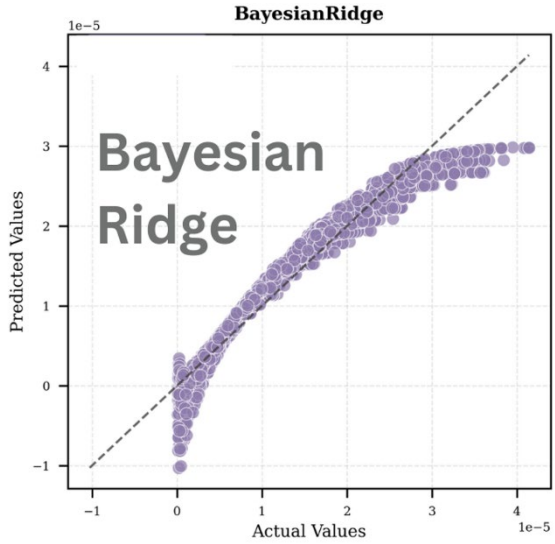

(d) Bayesian Ridge – predicted vs actual values

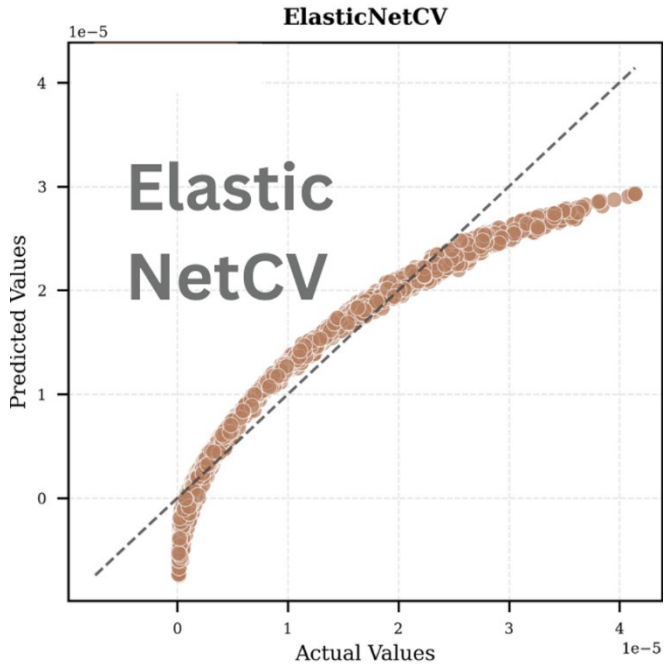

(e) ElasticNetCV – predicted vs actual values

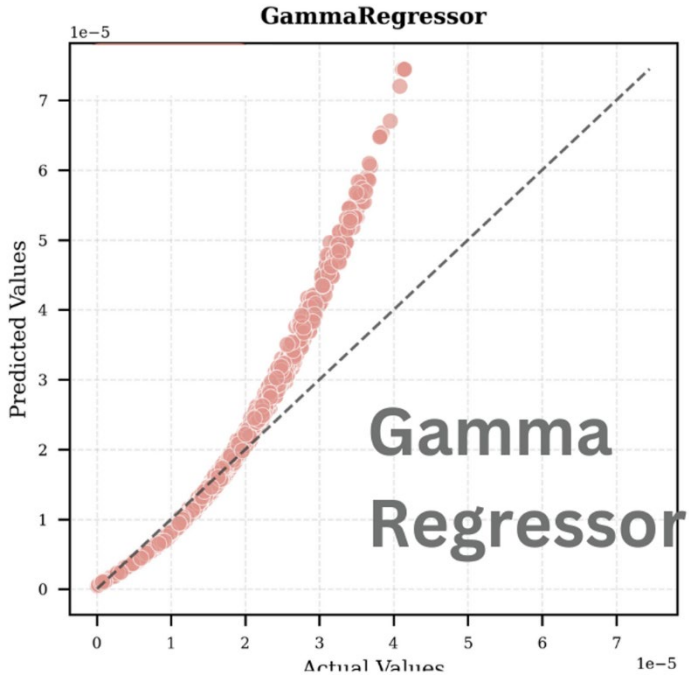

(f) Gamma Regressor – predicted vs actual values
Figure 8 – Scatter plot of predicted vs. actual values for 3-layer configurations

Figures 7 and 8 present the scatter plots of predicted versus actual values for all models across both two-layer and three-layer configurations and they provide a visual confirmation of the quantitative metrics previously discussed. The diagonal dashed line represents a perfect prediction (y=x), allowing for a direct assessment of the model performance through deviation patterns.

The GPR model exhibits remarkably tight clustering along the diagonal line in both configurations, with minimal scatter and virtually no systematic deviation, corroborating its superior R^2 value. The plot demonstrates exceptional predictive accuracy across the entire range of inductance values, with only occasional minor deviations at higher values in the three-layer configuration. The KNN and Bagging Regressor plots display similarly strong adherence to the diagonal, though with slightly more visible scatter than that of the GPR, particularly at higher inductance values. The consistency of the scatter patterns between the two-layer and three-layer configurations supports their robust generalization capabilities. In contrast, the Bayesian Ridge and ElasticNetCV models exhibit

noteworthy systematic deviations from the diagonal, particularly evident in their curvilinear patterns. These models occasionally produce negative inductance values due to their linear nature and lack of constraint mechanisms, which makes them inadequate for capturing the highly non-linear and strictly positive behavior of inductance. This behavior suggests these linear models struggle to capture the inherent non-linearities in the inductance relationships and it is manifested as a systematic underprediction at higher inductance values.

The Gamma Regressor demonstrates the most significant departure from the ideal behavior, with a distinct non-linear pattern and substantial scatter. The graph shape reveals systematic overprediction pronounced at higher inductance values and that explains the lower R^2 value. This visual evidence reinforces its inferior performance metrics and suggests fundamental limitations in capturing the underlying physical relationships.

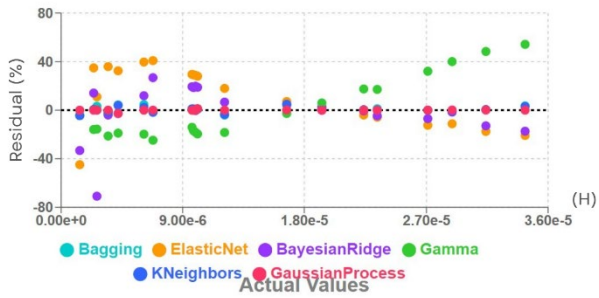

Figure 9 - Residual plot for various models of 2-layer planar coils

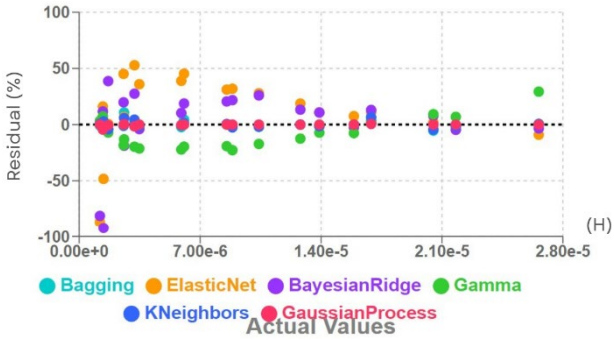

Figure 10 - Residual plot for various models of 3-layer planar coils

Testing 20 micro-planar coils with known actual inductance values, chosen randomly to ensure unbiased analysis, was visualized in Figures 9 and 10 for two-layer and three-layer configurations, respectively, and it provides evidence of model performance stability. These plots are zoomed to focus on 20 samples, allowing better visualization of variations, which is why this sample size was chosen. The plots reveal distinct error distribution patterns across different models, with the GPR, KNeighbors, and Bagging Regressor demonstrating superior prediction stability as evidenced by their tight clustering around the zero-error line, with residuals predominantly contained within a small range. This contrasts markedly with the more erratic behavior observed in the ElasticNet and Bayesian Ridge linear models, and the systematic deviations displayed by the Gamma Regressor, particularly at higher inductance values. The three-layer configuration exhibits similar patterns, though with a slight increase in residual spread, reflecting the enhanced complexity of the prediction task. Based on the comprehensive evaluation of quantitative metrics, scatter plots, and residual analyses, the GPR emerges as the optimal model for inductance prediction, followed in a close way by Bagging Regressor and KNeighbors, all demonstrating robust generalization capabilities and reliable performance on unseen data across both geometric configurations.

Conclusion

The study demonstrates a new approach based on supervised learning models to achieve high accuracy in estimating the inductance of multilayer rectangular planar coils. The methodology utilized geometric parameters to train machine learning models, with the Gaussian Process Regressor achieving superior performance, demonstrating R^2 values exceeding 0.99 for both configurations. This approach eliminates the need for complex empirical equations compared to traditional analytical methods. The proposed data-driven framework provides higher precision and adaptability to diverse rectangular multilayer coil configurations. The simulation results validated the accuracy of the machine learning models, highlighting the significant role of the parameters such as the number of turns, the average diameter, and the fill ratio in predicting inductance. As future work, the methodology can be extended to include more complex coil configurations and explore alternative shapes using other machine learning models or even using deep learning techniques to further enhance its accuracy and versatility.

References

Alghrairi, M., Sulaiman, N., Mutashar, S., Wan Hasan, W. Z., Jaafar, H., & Algriree, W. (2022). Designing and analyzing multi-coil multi-layers for wireless power transmission in stent restenosis coronary artery. *AIP Advances, 12*(12). Available at: https://doi.org/10.1063/5.0121532

Altman, N. S. (1992). An Introduction to Kernel and Nearest-Neighbor Nonparametric Regression. *The American Statistician, 46*(3), 175–185. Available at: https://doi.org/10.1080/00031305.1992.10475879

Ansari, M.A., & Agarwal, P. (2024). Inductance Modelling of Planar Meander Structure Using RBM and kNN. *SN Computational Sciences, 5*, 1169. Available at: https://doi.org/10.1007/s42979-024-03516-7

Asadi, M., Rezaei, A., & Abazari, A. M. (2023, December). Calculation of Mutual Inductance between Two Planar Coils with Custom Specifications and Positions Using a Machine Learning Approach. In *Proceedings of the International Conference on New Trends in Applied Sciences* (Vol. 1, pp. 20-30). Available at: https://doi.org/10.58190/icontas.2023.50

Bayazıt, G. H., Caarls, E. I., & Lomonova, E. A. (2023). Inductance Map Regression of Doubly Excited Electrical Machines Considering Cross-Saturation. *IEEE Transactions on Magnetics, 59*(11), 1-5. Available at: https://doi.org/10.1109/TMAG.2023.3292500

Chen, X., Zheng, C., & Golestanirad, L. (2023). Application of Machine learning to predict RF heating of cardiac leads during magnetic resonance imaging at 1.5 T and 3 T: A simulation study. *Journal of Magnetic Resonance*, *349*, 107384. Available at: https://doi.org/10.1016/j.jmr.2023.107384

Ding, W., Wang, Y., Chen, T., Lu, Z., You, Y., Wang, J., & Huang, Z. (2025). A stacking machine-learning based method for accelerating magnetic coupler design with ferrite cores in inductive power transfer applications. International Journal of Circuit Theory and Applications, 53(1), 67-80. Available at: https://doi.org/10.1002/cta.4096

Farooq, M., Amin, B., Elahi, A., Wijns, W., & Shahzad, A. (2023). Planar Elliptical Inductor Design for Wireless Implantable Medical Devices. *Bioengineering, 10*(2), 151. Available at: https://doi.org/10.3390/bioengineering10020151

Faria, A. R. S., Marques, L. S., Gaspar, J., Alves, F. S., & Cabral, J. M. N. (2021, March). High precision, geometry independent analytical method for self-inductance calculation in planar coils. In *2021 22nd IEEE International Conference on Industrial Technology (ICIT)* (Vol. 1, pp. 1234-1239). IEEE. Available at: http://doi.org/10.1109/ICIT46573.2021.9453559

Gastineau, L. A., Lewis, D. D., & Ionel, D. M. (2024, November). Combined 3D FEA and Machine Learning Design of Inductive Polyphase Coils for Wireless EV Charging. In *2024 13th International Conference on*

Renewable Energy Research and Applications (ICRERA) (pp. 1811-1816). IEEE. Available at: https://doi.org/10.1109/ICRERA62673.2024.10815533

MacKay, D. J. (1992). Bayesian interpolation. *Neural Computation, 4*(3), 415-447. Available at: https://doi.org/10.1162/neco.1992.4.3.415

Noroozi, B., & Morshed, B. I. (2021). Design and optimization of printed spiral coils for wireless passive sensors. *IET Wireless Sensor Systems*, *11*(4), 169-178. Available at: https://doi.org/10.1049/wss2.12019

Sidun, Aleksandr, SRIVASTAVA, Manish, O'DONOGHUE, Kilian, et al. Planar On-Silicon Inductor Design for Electromagnetic Tracking. *IEEE Sensors Journal, 2023*. Available at: https://doi.org/10.1109/JSEN.2023.3296471

Stillig, J., Parspour, N., Ewert, D., & Jung, T. J. (2022, July). Feasibility Study on Machine Learning-based Method for Determining Self-and Mutual Inductance. In *2022 International Seminar on Intelligent Technology and Its Applications (ISITIA)* (pp. 193-198). IEEE. Available at: https://doi.org/10.1109/ISITIA56226.2022.9855321

Tolpygo, S. K., Golden, E. B., Weir, T. J., & Bolkhovsky, V. (2022). Mutual and self-inductance in planarized multilayered superconductor integrated circuits: Microstrips, striplines, bends, meanders, ground plane perforations. *IEEE Transactions on Applied Superconductivity, 32*(5), 1-31. Available at: https://doi.org/10.1109/TASC.2022.3162758

Wang, F., Zhang, X., Shokoueinejad, M., Iskandar, B. J., Webster, J. G., & Medow, J. E. (2018). Spiral planar coil design for the intracranial pressure sensor. Medical Devices & Sensors, 1(3), e10012. Available at: https://doi.org/10.1002/mds3.10012

Wheeler, H. A. (1928). Simple inductance formulas for radio coils. *Proceedings of the Institute of Radio Engineers, 16*(10), 1398-1400. Available at: https://doi.org/10.1109/JRPROC.1928.221309

Williams, C. K., & Rasmussen, C. E. (2006). Gaussian processes for machine learning (Vol. 2, No. 3, p. 4). Cambridge, MA: MIT press.

Wu, D., Lin, S., Chen, H., & Wang, X. (2023). Mutual inductance model of double printed circuit board-based coplanar rectangular spiral coils for eddy-current testing. International Journal of Numerical Modelling: Electronic Networks, Devices and Fields, 36(1), e3038. Available at: https://doi.org/10.1002/jnm.3038

Zhang, J., Hou, X., Qian, S., Bi, X., Hu, D., Liu, J., ... & Chou, X. (2024). Flexible multilayer MEMS coils and their application in energy harvesters. *Science China Technological Sciences, 67*(4), 1282-1293. Available at: https://doi.org/10.1007/s11431-023-2474-9

Zhao, J. (2010). A new calculation for designing multilayer planar spiral inductors. *EDN (Electrical Design News, 55*(14), 37.

Концепт и примена машинског учења у предвиђању индуктивности у вишеслојним правоугаоним спиралним микрозавојницама

Јунес Беназуз, **аутор за преписку**, *Џилалија* Гендуз
Универзитет у Орану 2 Мохамед Бен Ахмед, Институт за индустријско одржавање и безбедност (IMSI), Одељење за одржавање инструмената, Лабораторија за производно инжењерство и индустријско одржавање (LGPMI), Оран, Народна Демократска Република Алжир

ОБЛАСТ: рачунарске науке, електроника
КАТЕГОРИЈА (ТИП) ЧЛАНКА: оригинални научни рад

Сажетак:

Увод/циљ: Овим истраживањем уводи се нов приступ пројектовању скупа података правоугаоних планарних завојница помоћу комплементарних софтверских алата. МАТЛАБ функционише као окружење за пројектовање високог нивоа, а FastHenry делује као рачунарски оквир за решавање Максвелових једначина и добијање вредности индуктивности. Генеришу се два различита синтетичка скупа података помоћу напредних техника узорковања за различите конфигурације, укључујући методу узорковања латинске хиперкоцке. Ови скупови података се затим обрађују и обучавају помоћу алгоритама машинског учења за предвиђање вредности индуктивности на основу добијених геометријских параметара.

Методе: За генерисање екстензивних синтетичких скупова података који садрже 20 000 редова за двослојне конфигурације завојница и 15 000 редова за трослојне конфигурације прво се користи МАТЛАБ. Након процеса генерисања, проверава се да ли су скупови података спремни за обуку. Шест модела машинског учења: Gaussian Process Regressor (GPR), KNeighborsRegressor (KNN), BayesianRidge, ElasticNetCV, GammaRegressor, као и Bagging Regressor обучено је и процењено помоћу метрика као што су R^2 и RMSE. Модели се затим испитују на непознатим подацима за испитивање и оцењују помоћу технике унакрсне валидације како би се утврдило колико могу да генерализују.

Резултати: Скупови података су успешно генерисани, а модели KNeighborsRegressor, Gaussian Process Regressor (GPR) и Bagging Regressor остварили су најбоље резултате, исказали су велику тачност и малу грешку.

Закључак: Резултати показују да је машинско учење практичан и ефикасан метод за предвиђање индуктивности у вишеслојним правоугаоним планарним завојницама на основу геометрије.

Кључне речи: правоугаона планарна микрозавојница, вишеслојна планарна завојница, индуктивност, машинско учење, синтетички скуп података

Paper received on: 22.01.2025.
Manuscript corrections submitted on:22.04.2025.
Paper accepted for publishing on: 04.06.2025.

A four-unknown higher-order shear deformation theory for the analysis of bending in sigmoid-FGM plates

Fatima Zohra Djidar[a], *Habib* Hebali[b]

[a.] Mustapha Stambouli University,Departement of Civil Engineering,Mascara,People's Democratic Republic of Algeria, e-mail: fatima.djidar@univ-mascara.dz. ORCID iD: https://orcid.org/0009-0006-6361-073X

[b.] Mustapha Stamnouli University, Departement of Civil Engineering,Mascara,People's Democratic Republic of Algeria,e-mail: habib.hebali@univ-mascara.dz ,**corresponding author**.ORCID iD: https://orcid.org/0009-0001-1309-2595

https://doi.org/10.5937/vojtehg73-57862

FIELD: civil engineering
ARTICLE TYPE: original scientific paper

Abstract:

In this paper, the analysis of bending of sigmoid functionally graded materials (S-FGM) plates is presented using a four-variable high-order shear deformation theory.This theory reduces the number of unknown functions simply from five to four compared to other shear deformation theories; it does not require shear correction factors, and it satisfies the conditions of zero shear stresses for the top and bottom surface of the plate since the variation of shear stresses is parabolic through the thickness. The equilibrium equations of this theory are derived from the principle of virtual work, and the Navier solution is used to solve these equations. For this S-FGM plate, according to the power law, the materials are distributed in terms of volume fractions of the constituents, and their properties are gradually varied in the thickness direction. This analytical study gave very satisfactory results, and the comparison between the numerical results obtained from the presented theory and those obtained from the classical plate theory (CPT) and high-order shear deformation theories (HSDTs) demonstrated the simplicity, accuracy, and reliability of this presented theory in analyzing the static bending behavior of thick S-FGM plates.

Methods:This study presents a four-variable shear deformation theory that determines the stresses and displacements of a simply supported functionally graded (S-FGM)plate. The equilibrium equations and boundary conditions were obtained from the principle of virtual work. Navier's method was then used to solve the equilibrium equations. The comparison of the results of this new theory with other solutions using the CPT and HSDTs was presented in this work.

Results:The comparison between the presented refined theory and the HSDT(Reddy's theory) also showed that the deformations and stresses of these theories are almost identical, while the classical plate theory underestimates the deflection of these plates.

Conclusion:The calculated different stresses and dimensionless displacements clearly demonstrated the effectiveness and accuracy of the presented theory in studying the static behaviors of simply supported S-FGM plates.

Key words:S-FGM plates, classical plate theory, higher-order theory, powerlaw, bending.

Introduction

In recent years, Functionally Graded Materials (FGMs) have seen wide applications in several diverse engineering and industrial fields such as civil, mechanical, electronic, automotive, aerospace, etc., due to their attractive and distinctive properties, which are high wear resistance, significant reduction in residual stresses and high resistance to temperature gradients (Reddy, 2000; Eltaher et al., 2013; Kar & Panda, 2015; Ahmed et al., 2019; Karami & Karami, 2019; Selmi, 2020; Abdulrazzaq et al., 2020; Dehshahri et al., 2020).

FGMs are used in these important fields in the form of plates, characterized by a gradual variation in the volume fraction of their constituent materials, which leads to a continuous and smooth change in the properties of these materials from one surface to another (Birman et al., 2013; Dai et al., 2016). This technology contributes to reducing thermal stress concentrations and effectively eliminating interface problems for devices using FGM plates, such as environmental sensors, biomedical industry, and fast computers (Avcar, 2015; Boukhari et al., 2016).

In order to effectively investigate the behavior of these FGM plates, many modern scientific studies have been conducted,leading to the development of different plates theories. Among these theories is the classical plate theory (CPT) which is considered the simplest theory because it does not take into account the effects of transverse shear of these plates. However, it gives very satisfactory analytical results withregard to isotropic and thin plates (Mechab et al., 2010; Taczała et al., 2022).

Since these transverse shear effects cause instability and failure of plates structures, especially composite plates, the First-order Shear Deformation Theory (FSDT), proposed by Mindlin (1951) and Reissner (1945), has been relied upon to conduct an effective study of FGM plates because they take these effects into account. However, it requires a

correction coefficient often set at 5/6 (Hosseini-Hashemi et al., 2010; Hosseini-Hashemi et al., 2011). The violation of equilibrium conditions at both the bottom and top surfaces of the FGM plate is considered the most significant drawback of the FSDT (Fallah et al., 2013), which necessitated the development of the Higher-order Shear Deformation Theory (HSDT). This theory takes into account the transverse shear effect and ensures the state of zero shear stresses in the top and bottom surfaces of the plate without the correction factor (Thai & Choi, 2012; Thai & Kim, 2013; Sobhy, 2013; Pandey et al., 2020).

Recently, plates based on Sigmoid Functionally Graded Materials (S-FGM plates) have been studied in a very precise analytical manner by (Beldjelili et al., 2016; Duc, 2017; Singh, Harsha, 2019; Singh, Harsha, 2020; Tao & Dai, 2021; Karakoti et al., 2022; Kurpa et al., 2023; Kumar & Pandey, 2024).

The aim of this work is to study the bending behavior of S-FGM plates using the present high-order theory with a sinusoidal shear function. The results obtained have been compared with those calculated using Reddy's shear function and the classical plate theory (CPT). To carry out an efficient and precise analytical study, the influence of the powerlaw index **p** on the deflection and different non-dimensional stresses of S-FGM plates made of aluminum/alumina mixture has been investigated for various values of the dimension ratios (a/h and a/b).

Refined FGM plate theory

Geometric configuration

Figure 1 presents a rectangular S-FGM plate with the dimensions a and b in the plane, as well as with a uniform thickness h. This S-FGM plate is made of a material with a property gradient that varies in the thickness direction, as shown in Figure 1, and is subjected to a transverse load q(x,y). TheCartesian coordinate system is used such that the x, y plane coincides with the median plane of the plate.

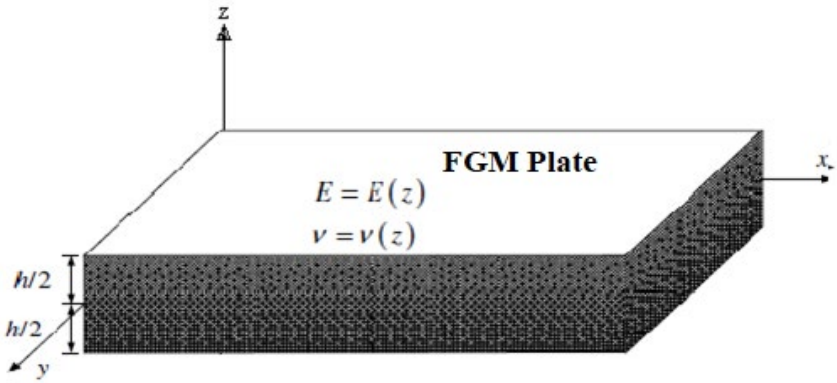

Figure 1 – Geometry of an FGM plate(Chi, Chung, 2006)

The S-FGM plate studied in this work is delimited by the planes at the coordinates x=0,a and y=0,b. The middle surface, defined by z=0, serves as the reference surface of this plate, where z represents the thickness coordinate measured from this undeformed middle surface. For an S-FGM plate with a ceramic-metal mixture, the functional relationship between E and z can be given as:

$$g_1(z) = 1 - \frac{1}{2}\left(\frac{h/2 - z}{h/2}\right)^p \text{ for } 0 \le z \le h/2$$

$$g_2(z) = \frac{1}{2}\left(\frac{h/2 + z}{h/2}\right)^p \text{ for } -h/2 \le z \le 0 \quad (1)$$

$$E(z) = g_1(z).E_c + [1 - g_1(z)].E_m \text{ for } 0 \le z \le h/2$$

$$E(z) = g_2(z).E_c + [1 - g_2(z)].E_m \text{ for } -h/2 \le z \le 0$$

where p is the volume fraction exponent, and the properties of the ceramic and metal materials are represented by Ec and Em, respectively.

To determine the different effective characteristics of metal-ceramic plates, the power law hypothesis is used as a simple rule regarding mixtures. As shown in equation (1), the top surface (z= h/2) of the S-FGM plate is ceramic, while the bottom surface (z= -h/2) is metal-rich. This explains that the metal and ceramic volume fractions are high near the bottom and top surfaces of the plate, respectively.To simplify thestudy of the S-FGM plate, Poisson's ratio v is assumed to be constant across the thickness of this plate.

Figure 2 shows the distribution of the volume fraction across the thickness of the S-FGM plate for different values of the power law index **p**. From this figure, for p=1, the composition of the ceramic and the metal varies linearly, while the p values of zero and infinity represent an all-ceramic and all-metal plate, respectively.

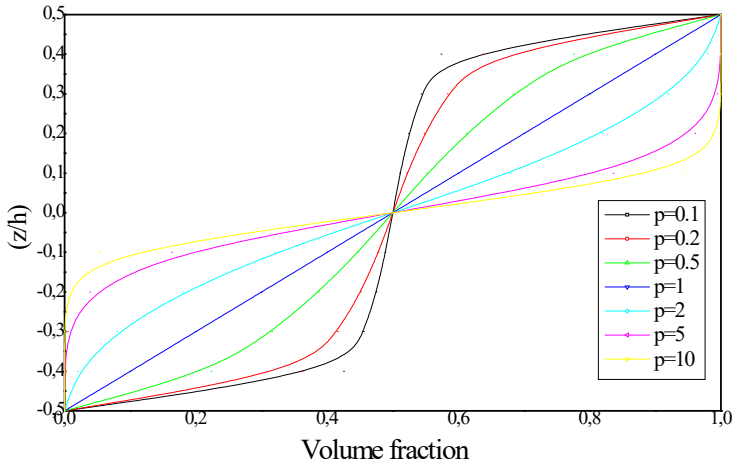

Figure 2 – Volume fraction distribution across the thickness of the S-FGM plate

Refined theory assumptions

The RPT theory is based on the following four important assumptions:

1. The strains involved are infinitesimal since the displacements are small compared to the thickness of the plate.
2. The transverse displacement W is decomposed into two components: bending w_b and shear w_s, which depend only on the x and y coordinates.

$$W(x,y,z) = w_b(x,y) + w_s(x,y) \quad (2)$$

3. The transverse normal stress σ_z is negligible compared to the other stresses σ_x and σ_y.
4. The U and V displacements in the x and y directions respectively consist of bending, shear components, and extension.

$$u = u_0 + u_b + u_s, \qquad v = v_0 + v_b + v_s \quad (3)$$

The bending components u_b and v_b are assumed to be similar to the displacements described by the classical plate theory (CPT). Therefore,

the expressions for these components can be formulated as follows:

$$u_b = -z\frac{\partial w_b}{\partial x}, v_b = -z\frac{\partial w_b}{\partial y} \qquad (4a)$$

The strain components γ_{xz} and $\gamma_{yz}$are derived component displacement state u(x,y,z) and v(x,y,z) respectively, together with the transverse displacement w(x,y,z), as shown in equation 5.These strains vary parabolically across the thickness of the S-FGM plate, while satisfying the condition of zero shear stress τ_{xz} and τ_{yz} at the top and bottom surfaces of this plate. Therefore, the expressions for u_s and $v_s$can be formulated as:

$u_{s=}f(z)\frac{\partial w_s}{\partial x}, v_{s=}f(z)\frac{\partial w_s}{\partial y}$(4.b)

Constitutive equations and kinematics

The displacement field of the S-FGM plate can be found by exploiting the assumptions of the refined theory and using the following equations:

$$\begin{gathered} u(x,y,z) = u_0(x,y) - z\frac{\partial w_b(x,y)}{\partial x} - f(z)\frac{\partial w_s(x,y)}{\partial x} \\ v(x,y,z) = v_0(x,y) - z\frac{\partial w_b(x,y)}{\partial y} - f(z)\frac{\partial w_s(x,y)}{\partial y} \qquad (5) \\ w(x,y,z) = w_b(x,y) + w_s(x,y) \\ f(z) = z - \left(\frac{h}{\pi}\right) * sin(\pi * z/h) \end{gathered}$$

where f(z) is Touratier's shear function. The deformations associated with the displacements in equation 5 are:

$$\begin{Bmatrix} \varepsilon_x \\ \varepsilon_y \\ \gamma_{xy} \end{Bmatrix} = \begin{Bmatrix} \varepsilon_x^0 \\ \varepsilon_y^0 \\ \gamma_{xy}^0 \end{Bmatrix} + z\begin{Bmatrix} k_x^b \\ k_y^b \\ k_{xy}^b \end{Bmatrix} + f(z)\begin{Bmatrix} k_x^s \\ k_y^s \\ k_{xy}^s \end{Bmatrix}; \begin{Bmatrix} \gamma_{yz} \\ \gamma_{xz} \end{Bmatrix} = g(z)\begin{Bmatrix} \gamma_{yz}^0 \\ \gamma_{xz}^0 \end{Bmatrix}; \varepsilon_z = 0 \quad (6)$$

where $\begin{Bmatrix} \varepsilon_x^0 \\ \varepsilon_y^0 \\ \gamma_{xy}^0 \end{Bmatrix} = \begin{Bmatrix} \frac{\partial u_0}{\partial x} \\ \frac{\partial v_0}{\partial x} \\ \frac{\partial u_0}{\partial y} + \frac{\partial v_0}{\partial x} \end{Bmatrix}, \begin{Bmatrix} k_x^b \\ k_y^b \\ k_{xy}^b \end{Bmatrix} = \begin{Bmatrix} -\frac{\partial^2 w_b}{\partial x^2} \\ -\frac{\partial^2 w_b}{\partial y^2} \\ -2\frac{\partial^2 w_b}{\partial x \partial y} \end{Bmatrix}, \begin{Bmatrix} k_x^s \\ k_y^s \\ k_{xy}^s \end{Bmatrix} = \begin{Bmatrix} -\frac{\partial^2 w_s}{\partial x^2} \\ -\frac{\partial^2 w_s}{\partial y^2} \\ -2\frac{\partial^2 w_s}{\partial x \partial y} \end{Bmatrix}$ and

$$\begin{Bmatrix}\gamma_{yz}^{0}\\ \gamma_{xz}^{0}\end{Bmatrix}=\begin{Bmatrix}\dfrac{\partial w_s}{\partial y}\\ \dfrac{\partial w_s}{\partial x}\end{Bmatrix} \quad (7)$$

$$g(z)=1-f^{'}(z)$$

The stress-strain relationships of an S-FGM plate can be expressed as:

$$\begin{Bmatrix}\sigma_x\\ \sigma_y\\ \tau_{xy}\\ \tau_{yz}\\ \tau_{xz}\end{Bmatrix}=\begin{bmatrix}Q_{11} & Q_{12} & 0 & 0 & 0\\ Q_{12} & Q_{22} & 0 & 0 & 0\\ 0 & 0 & Q_{66} & 0 & 0\\ 0 & 0 & 0 & Q_{44} & 0\\ 0 & 0 & 0 & 0 & Q_{55}\end{bmatrix}\begin{Bmatrix}\varepsilon_x\\ \varepsilon_y\\ \gamma_{xy}\\ \gamma_{yz}\\ \gamma_{xz}\end{Bmatrix} \quad (8)$$

where ε_x , ε_y, γ_{xy}, γ_{yz}, γ_{xz} are the strain components, and σ_x ,σ_y, τ_{xy}, τ_{yz}, τ_{xz} are the stress components. In accordance withdifferent properties of metal and ceramic materials specified in equation (1), the expressions of the stiffness coefficients Q_{ij} can be given as:

$$Q_{11}=Q_{22}=\frac{E(z)}{1-\nu^2};\quad Q_{12}=\frac{\nu\,E(z)}{1-\nu^2};Q_{44}=Q_{55}=Q_{66}=\frac{E(z)}{2(1+\nu)} \quad (9)$$

Equilibrium equations

The principle of virtual displacements can be used to derive the equilibrium equations, and in the present case, the principle of virtual

$$\int_{-h/2}^{h/2}\int_{\Omega}\left[\sigma_x\delta\varepsilon_x+\sigma_y\delta\varepsilon_y+\tau_{xy}\delta\gamma_{xy}+\tau_{yz}\delta\gamma_{yz}+\tau_{xz}\delta\gamma_{xz}\right]d\Omega\,dz-\int_{\Omega}q\,\delta w\,d\Omega=0 \quad (10)$$

where Ω is the top surface of the S-FGM plate.
By substituting equations (5), (6), and (8) into equation (10) and integrating it through the plate thickness, equation (11) can be written as:

$$\int_{\Omega}(N_x\delta\varepsilon_x^0+N_y\delta\varepsilon_y^0+N_{xy}\delta\varepsilon_{xy}^0+M_x^b\delta k_x^b+M_y^b\delta k_y^b+M_{xy}^b\delta k_{xy}^b+M_x^s\delta k_x^s+M_y^s\delta k_y^s+M_{xy}^s\delta k_{xy}^s$$
$$+S_{yz}^s\delta\gamma_{yz}+S_{xz}^s\delta\gamma_{xz})d\Omega-\int_{\Omega}q(\delta w_b+\delta w_s)d\Omega=0 \quad (11)$$

$$\left(N_x,N_yN_{xy}\right)=\int_{-h/2}^{h/2}(\sigma_x,\sigma_y\,\tau_{xy})\,dz\;;\;\left(M_x^b,M_y^b,M_{xy}^b\right)=\int_{-h/2}^{h/2}(\sigma_x,\sigma_y\,\tau_{xy})z\,dz$$

$$\left(M_x^s, M_y^s, M_{xy}^s\right) = \int_{-h/2}^{h/2} (\sigma_x, \sigma_y\, \tau_{xy}) f(z)\, dz;$$

$$\left(S_{xz}^s, S_{yz}^s\right) = \int_{-\frac{h}{2}}^{\frac{h}{2}} (\tau_{xz}\,,\, \tau_{yz}) g(z) dz \quad (12)$$

By substituting equation (8) into equation (12) and then integrating equation (12) through the thickness of the plate, equation (13) can be written as follows:

$$\begin{Bmatrix} N_x \\ N_y \\ M_x^b \\ M_y^b \\ M_x^s \\ M_y^s \end{Bmatrix} = \begin{bmatrix} A_{11} & A_{12} & B_{11}\, B_{12} & B_{11}^s & B_{12}^s \\ A_{12} & A_{22} & B_{12}\, B_{22} & B_{12}^s & B_{22}^s \\ B_{11} & B_{12} & D_{11}\, D_{12} & D_{11}^s & D_{12}^s \\ B_{12} & B_{22} & D_{12}\, D_{22} & D_{12}^s & D_{22}^s \\ B_{11}^s & B_{12}^s & D_{11}^s\, D_{12}^s & H_{11}^s & H_{12}^s \\ B_{12}^s & B_{22}^s & D_{12}^s\, D_{22}^s & H_{12}^s & H_{22}^s \end{bmatrix} \begin{Bmatrix} \varepsilon_x^0 \\ \varepsilon_y^0 \\ k_x^b \\ k_y^b \\ k_x^s \\ k_y^s \end{Bmatrix};$$

$$\begin{Bmatrix} N_{xy} \\ M_{xy}^b \\ M_{xy}^s \end{Bmatrix} = \begin{bmatrix} A_{66} & B_{66} & B_{66}^s \\ B_{66} & D_{66} & D_{66}^S \\ B_{66}^s & D_{66}^S & H_{66}^s \end{bmatrix} \begin{Bmatrix} \gamma_{xy}^0 \\ k_{xy}^b \\ k_{xy}^s \end{Bmatrix}; \begin{Bmatrix} S_{yz}^s \\ S_{xz}^s \end{Bmatrix} = \begin{bmatrix} A_{44}^s & 0 \\ 0 & A_{55}^s \end{bmatrix} \begin{Bmatrix} \gamma_{yz} \\ \gamma_{zx} \end{Bmatrix} \quad (13)$$

$$\left(A_{ij}, B_{ij}, D_{ij}, B_{ij}^s, D_{ij}^s, H_{ij}^s\right) = \int_{-h/2}^{h/2} (1, z, z^2, f(z), zf(z), f^2(z)) Q_{ij} dz \quad (14)$$

And $A_{ij}^s = \int_{-h/2}^{h/2} g(z)^2 * Q_{ij} dz$

By integrating equation (11) by parts, and setting the coefficients $\delta u_0; \delta v_0; \delta w_b$ and δw_s to zero separately, the resulting equilibrium equations for this FGM plate are:

$$\begin{aligned} &\delta u_0 : \ \frac{\partial N_x}{\partial x} + \frac{\partial N_{xy}}{\partial y} = 0 \\ &\delta v_0 : \ \frac{\partial N_{xy}}{\partial x} + \frac{\partial N_y}{\partial y} = 0 \\ &\delta w_b : \ \frac{\partial^2 M_x^b}{\partial x^2} + 2\frac{\partial^2 M_{xy}^b}{\partial x \partial y} + \frac{\partial^2 M_y^b}{\partial y^2} + q = 0 \\ &\delta w_s : \ \frac{\partial^2 M_x^s}{\partial x^2} + 2\frac{\partial^2 M_{xy}^s}{\partial x \partial y} + \frac{\partial^2 M_y^s}{\partial y^2} + \frac{\partial S_{xz}^s}{\partial x} + \frac{\partial S_{yz}^s}{\partial y} + q = 0 \end{aligned} \quad (15)$$

Analytical solutions for S-FGM plates

Navier presented the external force in the form of a double trigonometric series in order to solve this problem:

$$q(x,y) = \sum_{m=1}^{\infty}\sum_{n=1}^{\infty} q_{mn} sin\left(\frac{m\pi}{a}x\right) sin\left(\frac{n\pi}{b}y\right) \quad (16)$$

In the case of application of a distributed sinusoidal load, m and q_{11} are the following:

m=n=1 and $q_{11} = q_0$; $\lambda = \frac{m\pi}{a}$; $\mu = \frac{n\pi}{b}$ (17)

where q0 is the intensity of the charge in the center of this S-FGM plate.

By satisfying the boundary conditions and from Navier's solution, the displacements u_0, v_0, w_b and w_s can be written in the form of double Fourier series.

$$\begin{Bmatrix} u_0 \\ v_0 \\ w_b \\ w_s \end{Bmatrix} = \sum_{m=1}^{\infty}\sum_{n=1}^{\infty} \begin{Bmatrix} U_{mn}\cos(\lambda x)\sin(\mu y) \\ V_{mn}\sin(\lambda x)\cos(\mu y) \\ W_{bmn}\sin(\lambda x)\sin(\mu y) \\ W_{smn}\sin(\lambda x)\sin(\mu y) \end{Bmatrix} \quad (18)$$

where U_{mn} , V_{mn}, W_{bmn} , and W_{smn} are considered as arbitrary parameters to be determined.

After substitution and simplification, the following operator equation is obtained:

$$[K]\{\Delta\}^T = \{F\} \quad (19)$$

$\{\Delta\} = \{U_{mn}, V_{mn}, W_{bmn}, W_{smn}\}$; $[K]$ is the symmetric matrix given by:

$$[K] = \begin{bmatrix} a_{11} & a_{12} & a_{13} & a_{14} \\ a_{12} & a_{22} & a_{23} & a_{24} \\ a_{13} & a_{23} & a_{33} & a_{34} \\ a_{14} & a_{24} & a_{34} & a_{44} \end{bmatrix} \quad \text{And} \quad \{F^T\} = \{0,0,-q_{mn},-q_{mn}\} \quad (20)$$

for which

$$a_{11} = -\left(A_{11}\lambda^2 + A_{66}\mu^2\right)$$

$$a_{12} = -\lambda\,\mu\left(A_{12} + A_{66}\right)$$

$$a_{13} = +\lambda\left[B_{11}\lambda^2 + \left(B_{12} + 2B_{66}\right)\mu^2\right]$$

$$a_{14} = \lambda\,[B_{11}^{s}\lambda^{2} + (B_{12}^{s} + 2B_{66}^{s})\,\mu^{2}]$$

$$a_{22} = -A_{66}\lambda^{2} - A_{22}\mu^{2}$$

$$a_{23} = \mu\left[(B_{12} + 2B_{66})\lambda^{2} + B_{22}\mu^{2}\right]$$

$$a_{24} = \mu\left[(B^{s}{}_{12} + 2B^{s}{}_{66})\lambda^{2} + B^{s}{}_{22}\mu^{2}\right] \qquad (21)$$

$$a_{33} = -D_{11}\lambda^{4} - 2(D_{12} + 2D_{66})\lambda^{2}\mu^{2} + D_{22}\mu^{4}$$

$$a_{34} = -D_{11}^{s}\lambda^{4} - 2(D_{12}^{s} + 2D_{66}^{s})\lambda^{2}\mu^{2} - D_{22}^{s}\mu^{4}$$

$$a_{44} = -H_{11}^{s}\lambda^{4} - 2(H_{11}^{s} + 2H_{66}^{s})\lambda^{2}\mu^{2} - H_{22}^{s}\mu^{4} - A_{55}^{s}\lambda^{2} - A_{44}^{s}\mu^{2}$$

Numerical results and discussions

The results were obtained for S-FGM plates and compared withthose determined by the classical plate theory (CPT) and the high-order shear deformation theory (HSDT) (Reddy, 1984) to validate the presented theory.

$f(z) = z - \frac{h}{\pi}\sin\left(\frac{z}{h}\right)$[Touratier 1991](22.a)

$f(z) = z - z\left(1 - \frac{4z^{2}}{3h^{2}}\right)$[Reddy1984](22.b)

To carry out this analytical study on the S-FGM plate by applying the presented method, aluminum (Al) and alumina (Al_2O_3) were used as metal and ceramic, respectively, for this plate. These materials possess the following properties: aluminum metal ($E_m = 70GPa$, $\nu = 0.3$) and alumina ceramic ($E_c = 380GPa$, $\nu = 0.3$). In addition, the following different dimensionless parameters were used:

$$\bar{w} = \frac{10h^{3}E_{c}}{q_{0}a^{4}}w\left(\frac{a}{2},\frac{b}{2}\right),\ \overline{\sigma_{x}} = \frac{h}{q_{0}a}\sigma_{x}\left(\frac{a}{2},\frac{b}{2},\frac{h}{2}\right),\ \bar{\sigma}_{y} = \frac{h}{q_{0}a}\sigma_{y}\left(\frac{a}{2},\frac{b}{2},\frac{h}{3}\right),$$

$$\bar{\tau}_{xy} = \frac{h}{q_{0}a}\tau_{xy}\left(0,0,-\frac{h}{3}\right),\quad \bar{\tau}_{yz} = \frac{h}{q_{0}a}\tau_{yz}\left(\frac{a}{2},0,\frac{h}{6}\right),\quad \bar{\tau}_{xz} = \frac{h}{q_{0}a}\tau_{xz}\left(0,\frac{b}{2},0\right),$$

Table 1 – Dimensionless deflections and stresses for a square S-FGM plate, subjected to a sinusoidal load (a/h=10), obtained by the presented theory and the HSDT

P	$\bar{w}$		$\bar{\sigma}_x$		$\bar{\sigma}_y$		$\bar{\tau}_{yz}$	
	HSDT	Present	HSDT	Present	HSDT	Present	HSDT	Present
Ceramic	0.2960	0.2960	1.9943	1.9955	1.3124	1.3121	0.2121	0.2132
1	0.5890	0.5889	3.0850	3.0870	1.4898	1.4894	0.2608	0.2622
2	0.6551	0.6550	3.1915	3.1935	1.5992	1.5988	0.2916	0.2930
3	0.6912	0.6911	3.2663	3.2682	1.6398	1.6395	0.3117	0.3129
4	0.7120	0.7119	3.3126	3.3145	1.6540	1.6537	0.3249	0.3261
5	0.7248	0.7247	3.3421	3.3440	1.6589	1.6586	0.3336	0.3347
6	0.7332	0.7331	3.3617	3.3636	1.6606	1.6603	0.3394	0.3404
7	0.7390	0.7388	3.3754	3.3773	1.6613	1.6610	0.3432	0.3442
8	0.7431	0.7430	3.3852	3.3871	1.6616	1.6613	0.3457	0.3466
9	0.7462	0.7460	3.3925	3.3944	1.6618	1.6615	0.3473	0.3483
10	0.7485	0.7483	3.3980	3.3999	1.6619	1.6616	0.3484	0.3493
Metal	1.6071	1.6070	1.9943	1.9955	1.3124	1.3121	0.2121	0.2132

P	$\bar{\tau}_{xz}$		$\bar{\tau}_{xy}$	
	HSDT	Present	HSDT	Present
Ceramic	0.2386	0.2462	0.7067	0.7065
1	0.2386	0.2462	0.6111	0.6110
2	0.2373	0.2447	0.5212	0.5211
3	0.2361	0.2434	0.4902	0.4902
4	0.2354	0.2425	0.4857	0.4856
5	0.2348	0.2418	0.4893	0.4892
6	0.2345	0.2414	0.4943	0.4942
7	0.2342	0.2411	0.4987	0.4986
8	0.2340	0.2408	0.5022	0.5021
9	0.2338	0.2407	0.5050	0.5048
10	0.2337	0.2405	0.5071	0.5070
Metal	0.2386	0.2462	0.7067	0.7065

Table 1 illustrates different dimensionless deflections and stresses of a square S-FGM plate, subjected to a sinusoidal load with a ratio a/h=10, for different values of the power law index **p**, obtained by the present refined plate theory (RPT) and the HSDT. As shown in this table, and since both theories take into account the transverse shear effect, the results obtained by the present theory, both for deflection and stresses, are in agreement with those obtained by Reddy's high-order shear deformation

theory. In addition, the dimensionless deflection $\overline{w}$ and the longitudinal stresses $\overline{\sigma}_x$,$\overline{\sigma}_y$ in the plane are directly proportional to the increase in the power law index **p**. It should also be noted that the stresses for the ceramic plate are identical to those for the metal plate, since this S-FGM plate in both cases is completely homogeneous and these stresses are independent of the modulus of elasticity.

Table 2 – Dimensionless deflections and transverse shear stresses of the square S-FGM plate calculated by the present theory, HSDTand CPT

a/h	***p***	$(wE_c)/(q_0h)$			$\tau_{xz}(0, b/2)/q_0$	
		CPT	HSDT	Present	HSDT	Present
	0.25	0.3049	0.3715	0.3714	0.1191	0.1228
	0.5	0.3207	0.3874	0.3873	0.1192	0.1230
5	1	0.3514	0.4180	0.4178	0.1190	0.1228
	4	0.4288	0.4936	0.4932	0.1175	0.1209
	10	0.4518	0.5157	0.5152	0.2387	0.2463
	0.25	4.8782	5.1453	5.1450	0.2386	0.2462
	0.5	5.1310	5.3985	5.3981	0.2389	0.2465
10	1	5.6228	5.8895	5.8891	0.2386	0.2462
	4	6.8604	7.1200	7.1187	0.2354	0.2425
	10	7.2289	7.4849	7.4831	0.2337	0.2405

Table 2 shows a comparative study of the deflections and transverse shear stresses of a simply supported square S-FGM functionally graded plate, subjected to a sinusoidal load with two ratios (a/h=5 and a/h=10) for five values of the power law exponent **p**, calculated by the present, HSDT and CPT theories. According to these results, it can be confirmed that there is an excellent agreement between the values of deflection and transverse shear stress obtained by the present theory and HSDTs, for all values of the power law exponent **p** and the two ratios a/h. On the other hand, the classical platetheory (CPT) underestimates transverse plate displacement because it does not take into account the impacts of transverse shear deformation, which is the biggest disadvantage of this theory.

The analytical values illustrated in Tables 1 and 2 demonstrate the effectiveness of this present theory in the study of S-FGM plates because its results are in high agreement with theHSDTand better than the CPT.

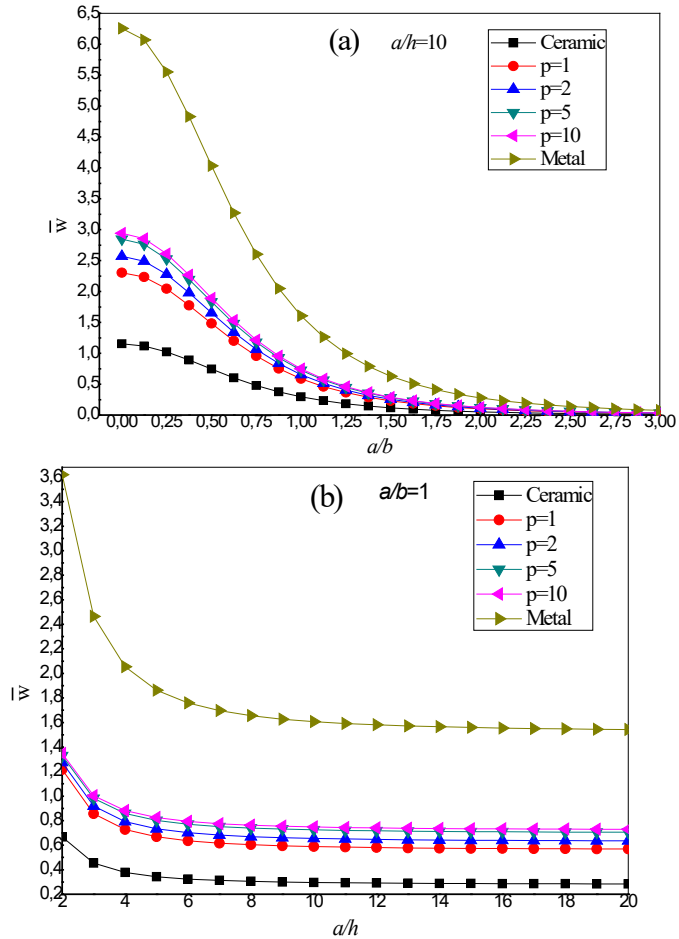

Figure 3 – $\bar{w}$ vs ratios: (a) - a/b, (b) - a/h, of an S-FGM plate

Figures 3-a and 3-b show the evolution of the dimensionless deflection $\bar{w}$ as a function of the thickness ratios a/b and a/h of an S-FGM plate, respectively, for different values of the power law index **p**using the present theory. The present theory shows that the dimensionless deflection of the S-FGM plate decreases sharply within the ranges of 0 to 1.5 and 2 to 8 for the ratios a/b and a/h, respectively; after that, it becomes less affected by these ratios.

According to these results, the deflection values of the metal plate are higher than those of the ceramic plate. They increase with the power law index **p** and remain almost constant when going from a moderately thick to a very thick plate. This indicates that the response of the S-FGM

plate lies between those of isotropic plates, i.e., between the ceramic-rich plate and the metal-rich plate.

In this section of our analytical study, the distribution of different shear stresses of the S-FGM plate under a sinusoidal load was investigated, where the exponent of the volume fraction of this plate is p=2.

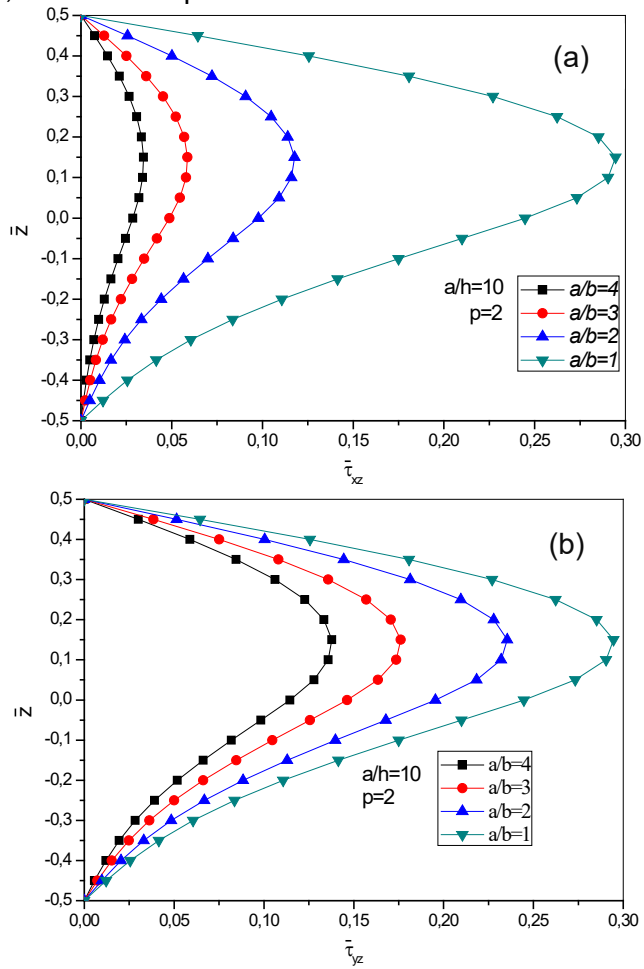

Figure 4 – Distribution of stresses: (a) - $\bar{\tau}_{xz}$, (b) - $\bar{\tau}_{yz}$, across the thickness of the S-FGM plate

Figures 4-a and 4-b respectively represent the variation of the transverse tangential stresses $\bar{\tau}_{xz}$ and $\bar{\tau}_{yz}$ across the thickness of an S-FGM plate for different a/b ratios. These shear stress values are zero at the two top and bottom edges of the plate and then gradually increase with decreasing the a/b ratio, reaching the maximum values at $\bar{z} = 0.154$, which

represents the inhomogeneous case. Moreover, the maximum values of $\overline{\tau}_{yz}$ stresses are larger compared to those of $\overline{\tau}_{xz}$ at the ratios a/b=2, 3, and 4.

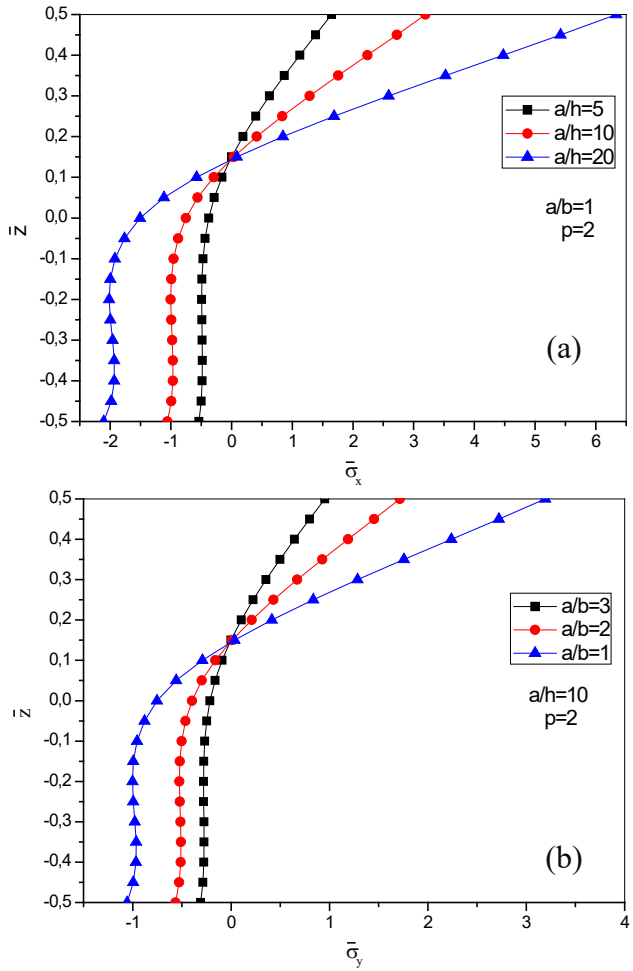

Figure 5 – Distribution of normal stresses: (a) - $\overline{\sigma}_x$, (b) - $\overline{\sigma}_y$, across the thickness of the S-FGM plate

Figures 5-a and 5-b show the variation of the normal stresses $\overline{\sigma}_x$ and $\overline{\sigma}_y$ according to the thickness of an S-FGM plate for different values of the ratios a/b and a/h, respectively. As shown in these figures, the normal stresses are in compressive throughout the S-FGM plate up to $\overline{z} = 0.154$, then in tensile beyond this value. Furthermore, the maximum compressive and tensile values of these stresses are produced respectively at points

located on the bottom surface and the top surface of this plate. In addition, for the normal stresses $\overline{\sigma}_x$, and when the a/h ratio increases, the tensile stress at the top surface increases, while the compressive stress at the bottom surface decreases for this S-FGM plate. On theother hand, and for normal stresses $\overline{\sigma}_y$, the tensile and compressive stresses decrease and increase respectively as a function of the increase in the ratio a/b, as shown in Figures 5-a and 5-b.

According to the results of the variation of the transverse tangential stress $\overline{\tau}_{xy}$ across the thickness of the S-FGM plate for the three values of a/b ratio, presented in Figure 6, the tensile and compressive stresses occur on the bottom and top surfaces of this plate, respectively, and this is inconsistent with what was found for the normal stresses $\overline{\sigma}_x$ and $\overline{\sigma}_y$. Furthermore, the zero value of this transverse tangential stress corresponds to $\bar{z} = 0.154$.

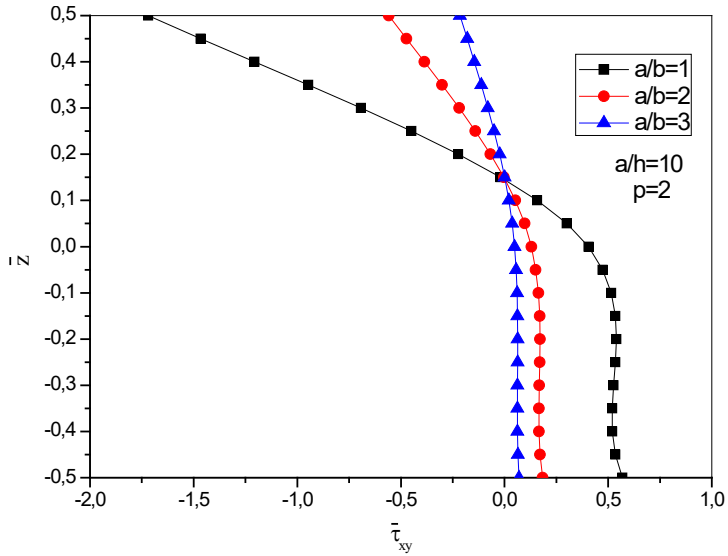

Figure 6 – Distribution of the transverse tangential stress $\overline{\tau}_{xy}$ across the thickness of the S-FGM plate

Figure 7 shows the effect of the moduli ratios Em/Ec on the dimensionless deflection $\overline{w}$ of S-FGM plates with various ceramic-metal mixtures p studied at a thickness of a/h = 10. As shown in these results, the dimensionless deflection is strongly affected by the moduli ratios, as it decreases significantly with these ratios up to the value Em/Ec = 0.25, after which this effect diminishes. In addition, the dimensionless deflection

increases with the increase in the percentage of metal (aluminum) in the plate made of a mixture of metal and ceramic.

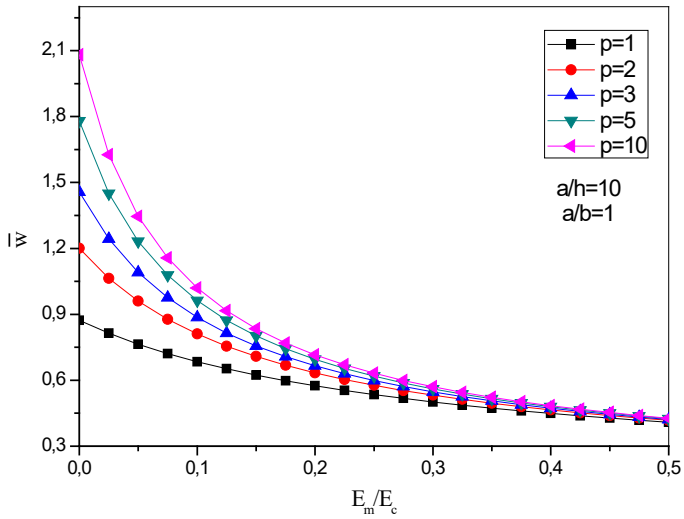

Figure 7 – $\bar{w}$ vs E_m/E_c ratio of the S-FGM plate

Conclusion

In this work, a refined two-variable theory was presented for the bending analysis of S-FGMs plates with ceramic-metal mixture and under sinusoidal load distribution. Although no shear correction factors were used, this theory satisfied the conditions of zero shear stresses on the plate surfaces and gave a parabolic distribution of transverse shear stresses. The calculated different stresses and dimensionless displacements clearly demonstrated the effectiveness and accuracy of the present theory to study the static behaviors of simply supported S-FGM plates.The comparison between the present refined theory and the HSDT (Reddy's theory) also showed that the deformations and stresses of these theories are almost identical, while the classical plate theory underestimates the deflection of these plates. It was observed from the results obtained that there is an excellent agreement between the deflections of ceramic plates and those rich in metals, while the deflection value is directly proportional to the power law index **p**, which proves the importance of gradients in material properties in determining the response of S-FGM plates.

References

Abdulrazzaq, M., A., Fenjan, R., M., Ahmed, R., A., Faleh, N., M. 2020. Thermal buckling of nonlocal clamped exponentially graded plate according to a

secant function based refined theory. *Steel Compos Struct,* 35(1),pp.147-157. Available at: https//doi.org/10.12989/scs.2020.35.1.147

Ahmed, R., A., Fenjan, R., M., Faleh, N., M. 2019. Analyzing post-buckling behavior of continuously graded FG nanobeams with geometrical imperfections. *Geomechanics and Engineering*, 17(2), pp.175-180. Available at: https//doi.org/10.12989/gae.2019.17.2.175

Avcar, M. 2015. Effects of rotary inertia shear deformation and non-homogeneity on frequencies of beam. *Struct. Eng. Mech,*55(4), pp.871-884. Available at: https//doi.org/10.12989/sem.2015.55.4.871

Beldjelili, Y., Tounsi, A., Mahmoud, S., R. 2016.Hygro-thermo-mechanical bending of S-FGM plates resting on variable elastic foundations using a four-variable trigonometric plate theory. *Smart Structures and Systems,* 18(4), pp.755-786. Available at: https//doi.org/10.12989/sss.2016.18.4.755

Birman, V., Keil, T., Hosder, S. 2013. Functionally graded materials in engineering. In: S Thomopoulus, V Birman and GM Genin (eds) Structural interfaces and attachments in biology. *New York: Springer,*pp.19–41. Available at: https//doi.org/10.1007/978-1-4614-3317-0_2

Boukhari, A., Ait Atmane, H., Houari, M., S., A., Tounsi, A., AddBedia, E., A., Mahmoud, S., R. 2016.An efficient sheadeformation theory for wave propagation of functionally gradedmaterial plates. *Struct. Eng. Mech,* 57(5), pp.837-859. Available at: https//doi.org/10.12989/sem.2016.57.5.837

Chi, S., H. Chung, Y., L. 2006. Mechanical behavior of functionally graded material plates under transverse load—Part I: Analysis. International Journal of Solids and Structures, 43(13), pp.3657-3674. Available at: https//doi.org/10.1016/j.ijsolstr.2005.04.011

Dai, H., L., Rao, Y., N., Dai, T. 2016. A review of recent researches on FGM cylindrical structures under coupled physical interactions. *Compos Struct,*152, pp.199–225. Available at: https//doi.org/10.1016/j.compstruct.2016.05.042

Dehshahri, K., Nejad, M., Z., Ziaee, S., Niknejad, A., Hadi, A. 2020. Free vibrations analysis of arbitrary threedimensionally FGM nanoplates. *Adv. Nano Res,* 8(2), pp.115-134. Available at: https//doi.org/10.12989/anr.2020.8.2.115

Duc, N., D., Quang, V., D., Anh, V., T., T. 2017. The nonlinear dynamic and vibration of the S-FGM shallow spherical shells resting on an elastic foundations including temperature effects. *Int. J. Mech. Sci,* 123,pp. 54–63. Available at: https//doi.org/10.1016/j.ijmecsci.2017.01.043

Eltaher, M., A., Alshorbagy, A., E., Mahmoud, F., F. 2013.Determination of neutral axis position and its effect on natural frequencies of functionally graded macro/nanobeams. *Composite Structures*, 99, pp.193-201. Available at: https//doi.org/10.1016/j.compstruct.2012.11.039

Fallah, A., Aghdam, M., M., Kargarnovin, M., H. 2013. Free vibration analysis of moderately thick functionally graded plates on elastic foundation using the extended Kantorovich method. *Arch. Appl. Mech,* 83(2), pp.177-191. Available at: https//doi.org/10.1007/s00419-012-0645-1

Hosseini-Hashemi, S., Rokni Damavandi Taher, H., Akhavan, H., Omidi, M. 2010. Free vibration of functionally graded rectangular plates using first-order

shear deformation plate theory. *Appl. Math. Model,* 34(5), pp.1276-1291. Available at: https//doi.org/10.1016/j.apm.2009.08.008

Hosseini-Hashemi, S., Fadaee, M., Atashipour, S., R. 2011. A new exact analytical approach for free vibration of ReissnerMindlin functionally graded rectangular plates. *Int. J. Mech.Sci,*53(1), pp.11-22. Available at: https//doi.org/10.1016/j.ijmecsci.2010.10.002

Kar, V., R., Panda, S., K. 2015.Nonlinear flexural vibration of shear deformable functionally graded spherical shell panel. *Steel Compos. Struct, Int. J.*, 18(3), pp.693-709. Available at: https//doi.org/10.12989/scs.2015.18.3.693

Karakoti, A., Pandey, S., Kar, V., R. 2022. Nonlinear transient analysis of porous P-FGM and S-FGM sandwich plates and shell panels under blast loading and thermal environment. *Thin-Walled Structures,*173, 108985. Available at: https//doi.org/10.1016/j.tws.2022.108985

Karami, B., Karami, S. 2019. Buckling analysis of nanoplate-type temperature-dependent heterogeneous materials. *Advances in Nano Research*, 7(1), pp.51-61. Available at: https//doi.org/10.12989/anr.2019.7.1.051

Kumar, A., Pandey, S. 2024. Transient analysis of size-dependent S-FGM micro-folded plates based on exact shear correction factor in the thermal environment. *Arch Appl Mech*, 94, pp.1335–1357. Available at: https//doi.org/10.1007/s00419-024-02578-6

Kurpa, L., Shmatko, T., Awrejcewicz, J., Timchenko, G., Morachkovska, I. 2023, Analysis of Free Vibration of Porous Power-law and Sigmoid Functionally Graded Sandwich Plates by the R-functions Method. *Journal of Applied and Computational Mechanics,*9(4), pp.1144-1155. Available at: https//doi.org/10.22055/jacm.2023.43435.4082

Mechab, I., Ait Atmane, H., Tounsi, A., Belhadj, H., A., Adda Bedia, El-A. 2010. A two variable refined plate theory for the bending analysis of functionally graded plates. *Acta Mech Sin*, 26, pp.941–949. Available at: https//doi.org/10.1007/s10409-010-0372-1

Pandey, H., K., Agrawal, H., Panda, S., K., Hirwani, C., K., Katariya, P., V., Dewangan, H., C. 2020. Experimental and numerical bending deflection of cenosphere filled hybrid (Glass/Cenosphere/Epoxy) composite. *Struct. Eng.Mech,*73(6),pp.715-724. Available at: https//doi.org/10.12989/sem.2020.73.6.715

Reddy, J., N.2000. Analysis of functionally graded plates. *Int. J. Numer. Method. Eng*, 47(1-3), pp.663-684. Available at: https//doi.org/10.1002/(SICI)1097-0207(20000110/30)47:1/3<663::AID-NME787>3.0.CO;2-8

Reddy, J., N. 1984. A simple higher-order theory for laminated composite plates. *J Appl Mech,*51, pp.745–52. Available at: https//doi.org/10.1115/1.3167719

Selmi, A.2020. Dynamic behavior of axially functionally graded simply supported beams. *Smart Struct. Syst,* 25(6), pp.669-678. Available at: https//doi.org/10.12989/sss.2020.25.6.669

Singh, S., J., Harsha, S., P.2019. Nonlinear dynamic analysis of sandwich S-FGM plate resting on pasternak foundation under thermal environment. *European*

*Journal of Mechanics - A/Solids,*76, pp.155-179. Available at: https//doi.org/10.1016/j.euromechsol.2019.04.005

Singh, S., J., Harsha, S., P.2020.Thermo-mechanical analysis of porous sandwich S-FGM plate for different boundary conditions using Galerkin Vlasov's method: A semi-analytical approach. *Thin-Walled Structures,* 150, 106668. Available at: https//doi.org/10.1016/j.tws.2020.106668

Sobhy, M. 2013. Buckling and free vibration of exponentially graded sandwich plates resting on elastic foundations under various boundary conditions. *Compos. Struct,* 99, pp.76-87. Available at: https//doi.org/10.1016/j.compstruct.2012.11.018

Taczała, M., Buczkowski, R., Kleiber, M. 2022. Analysis of FGM plates based on physical neutral surface using general third-order plate theory. *Composite Structures,*301, 116218. Available at: https//doi.org/10.1016/j.compstruct.2022.116218

Tao, C., Dai, T. 2021. Analyses of thermal buckling and secondary instability of post-buckled S-FGM plates with porosities based on a meshfree method. *Applied Mathematical Modelling,* 89, pp.268-284. Available at: https//doi.org/10.1016/j.apm.2020.07.032

Thai, H., T., Choi, D., H.2012.A refined shear deformation theory for free vibration of functionally graded plates on elastic foundation. *Compos. Part B: Eng,* 43(5), pp.2335-2347. Available at: https//doi.org/10.1016/j.compositesb.2011.11.062

Thai, H., T., Kim, S., E. 2013. A simple quasi-3D sinusoidal shear deformation theory for functionally graded plates. *Compos. Struct,* 99, pp.172-180. Available at: https//doi.org/10.1016/j.compstruct.2012.11.030

Touratier, M. 1991. An efficient standard plate theory. *Int J Eng Sci.* 29(8): 901–16. Available at: https//doi.org/10.1016/0020-7225(91)90165-Y

Теорија смицајне деформације вишег реда са четири непознате за анализу савијања S-FGM плоча

Фатима Зохра Џидар, *Хабиб* Хебали, **аутор за преписку**
Универзитет „Мустафа Стамболи", Одсек за грађевинарство, Маскара, Народна Демократска Република Алжир

ОБЛАСТ:грађевинарство
КАТЕГОРИЈА (ТИП) ЧЛАНКА:оригинални научни рад

Сажетак:

Увод/циљ: Плоче од сигмоидно функционално градијентно распоређених материјала (S-FGM) испитане су на савијање помоћу теорије смицајне деформације вишег реда са четири променљиве.
Представљена теорија једноставно смањује број непознатих функција са пет на четири у односу на друге теорије које се баве смицајном деформацијом. Такође, не захтева факторе корекције

смицања и задовољава услов да не постоје смицајни напони на горњој и доњој површини плоче, будући да смицање варира у облику параболе кроз дебљину плоче. Једначине равнотеже ове теорије изведене су из принципа виртуелног рада и решавају се помоћу Навијеовог решења. На основу закона снаге, материјали ове S-FGM плоче распоређени су по запреминским уделима конституената, а њихова својства се постепено мењају по дубини. Ова аналитичка студија дала је веома задовољавајуће резултате, а поређење њених нумеричких резултата и оних добијених помоћу класичне теорије плоча (CPT) и теорија смицајне деформације вишег реда (HSDTs) указало је на једноставност, тачност и поузданост ове теорије у анализи понашања дебелих S-FGM плоча при статичком савијању.

Методе: Представљена је теорија смицајне деформације са четири променљиве којом се одређују напони и померања у једноставно ослоњеној плочи од функционално градијентно распоређених материјала (S-FGM). Једначине равнотеже и граничних услова добијене су из принципа виртуелног рада. Навијеов метод је затим примењен у решавању једначина равнотеже. Резултати ове нове теорије поређени су са решењима других теорија (CPT, HSDT).

Резултати: Поређење ове прерађене теорије и Редијеве теорије (HSDT) такође је показало да су деформације и напони ових теорија готово идентични, док класична теорија плоча потцењује дефлексију оваквих плоча.

Закључак: Израчунати различити напони и бездимензионална померања јасно показују ефикасност и тачност представљене теорије при проучавању статичких понашања једноставно ослоњених S-FGM плоча.

Кључне речи: S-FGM плоче, класична теорија плоча, теорија вишег реда, закон снаге, савијање

Paperreceivedon: 29.03.2025.
Manuscriptcorrectionssubmittedon:29.04.2025.
Paperacceptedfor publishingon: 28.05

Sustainable self-compacting concrete: effect of combined marble waste as fine and coarse aggregates

Belgacem Mohamed El Ghazali[a], *Ouldkhaoua* Younes[b], *Herihiri* Ouided[c], *Sadoudi* Lyacia[d], *Arroudj* Karima[e]
[a] University of Sciences and Technology Houari Boumediene
e-mail: ghazali2017@gmail.com, **corresponding author**
ORCID iD: https://orcid.org/0000-0001-8515-8568
[b] University of Sciences and Technology Houari Boumediene
e-mail: younes.ouldkhaoua@usthb.edu.dz
ORCID iD: https://orcid.org/0009-0001-8334-812X
[c] University Yahia Fares of Medea
e-mail: heri.widalg@gmail.com
ORCID iD: https://orcid.org/0000-0002-8787-029X
[d] University of Sciences and Technology Houari Boumediene
e-mail: sadoudi29@yahoo.com
ORCID iD: https://orcid.org/0000-0002-5071-7267
[e] University of Sciences and Technology Houari Boumediene
e-mail: karroudj@gmail.com
ORCID iD: https://orcid.org/0000-0003-2852-0836

https://doi.org/10.5937/vojtehg73-58717

FIELD: construction materials in civil engineering
ARTICLE TYPE: original scientific paper

Abstract:

Introduction/purpose: Environmental protection through waste recycling is one of the major challenges of our time. Inert waste, mainly generated by industry, makes up a significant portion that harms the environment due to its accumulation in nature.

Methods: The primary objective of this study is to examine the influence of marble waste valorization as sand and gravel on the rheological and mechanical properties of self-compacting concrete (SCC). For this study, marble was used as fine aggregate sand (MAS) at rates of 10%, 20%, and 30%, and as coarse aggregate gravel (MAG) at a rate of 100%.

Results: The results of this study demonstrate that the introduction of marble waste (MW) as aggregate positively influenced the rheological characteristics, notably reducing the need for superplasticizer dosage.

ACKNOWLEDGMENT: The authors gratefully acknowledge the Directorate-General of Scientific Research and Technological Development of Algeria (DGRSDT) for its valuable support.

Conclusions: Additionally, in terms of mechanical outcomes, the use of MAG led to improved mechanical strengths.
Key words: self-compacting concrete, marble waste, rheological behavior, superplasticizer dosage, mechanical strength, environment

Introduction

In the construction industry, technological advancements in concrete aim not only to enhance its performance but also to reduce its environmental impact. Concrete, an essential material in most modern infrastructures, has a significant environmental impact, particularly due to the extraction of its components, such as aggregates. Natural aggregates represent about 80% of the total volume of concrete (Yu *et al.*, 2024), and their extraction from natural areas such as rivers and mountains causes numerous ecological issues. The excessive exploitation of these resources can lead to the degradation of local ecosystems, loss of biodiversity, and disruption of natural cycles (Mathodi *et al.*, 2022). Therefore, it is crucial to seek ecological alternatives to traditional aggregates in order to minimize the negative effects of their extraction and promote more sustainable construction practices (Makul, Fediuk, Amran, Zeyad, Azevedo, *et al.*, 2021).

One of the most promising solutions lies in the use of recycled materials, such as marble, to replace natural aggregates in concrete (Kore and Vyas, 2016). Marble is an abundant material, and when recycled, it can offer significant environmental benefits. It helps reduce the amount of waste produced by the construction industry, while alleviating the pressure on natural resources (Thakur, Pappu and Thakur, 2018). However, recycling marble is not without its challenges. Although the recycling process offers ecological advantages, it also requires energy consumption for crushing and transforming the material into reusable aggregates. This energy consumption must be taken into account to fully evaluate the environmental benefits of recycled marble. If this energy can be minimized or offset by the reduction in carbon footprint generated by the extraction of natural aggregates, then recycling marble could represent an environmentally and economically viable solution (Gazi, Skevis and Founti, 2012).

Recent studies have highlighted the positive effects of recycled marble on concrete properties. For example, the incorporation of marble as coarse or fine aggregates can improve the workability of concrete due to its low water absorption and the smooth surface of its aggregates (Kore and Vyas, 2016). Furthermore, research has shown that partially replacing natural sand with marble sand can increase the compressive strength of

concrete, although this effect is limited to certain replacement rates (Demirel, 2010; Alyamaç and Aydin, 2015; Houria *et al.*, 2020). This opens up new possibilities for optimizing concrete formulations, taking into account not only mechanical performance but also the environmental benefits of recycling materials.

In this context, self-compacting concrete (SCC) emerges as a particularly valuable innovation due to its exceptional fluidity and its ability to flow effortlessly into complex formworks, even when dense reinforcement is present. The rheological behavior of SCC plays a critical role in its performance, especially when incorporating recycled aggregates (Ouldkhaoua *et al.*, 2019). However, the use of recycled materials poses specific challenges, as their variable characteristics such as water absorption and surface roughness can negatively affect the mix's flowability and stability (Silva, Brito and Dhir, 2018).

Despite these challenges, recent advancements in mix design techniques and the application of chemical admixtures, such as superplasticizers and stabilizers, have made it possible to overcome these limitations. These innovations allow for improved workability and consistency, even when recycled aggregates are used (Makul, Fediuk, Amran, Zeyad, Murali, *et al.*, 2021).

As a result, SCC incorporating recycled materials proves highly advantageous for placement in heavily reinforced or difficult-to-access areas, ensuring uniform filling without defects. Moreover, this approach contributes to environmental sustainability by reducing construction waste and the reliance on natural resources, all while maintaining the structural performance and durability of concrete (Rich, 2014). Ultimately, the development of SCC with recycled aggregates offers a promising solution to current environmental and technical challenges in the construction industry (Khairi *et al.*, 2020).

This study aims to investigate the enhancement of the properties of self-compacting concrete (SCC) through the incorporation of recycled marble aggregates, both fine and coarse. Specifically, the goal is to assess how the addition of recycled marble aggregates affects the workability, stability, and long-term durability of SCC. Furthermore, the study will explore the potential of recycled marble to offer an environmentally sustainable solution in concrete production by reducing dependence on natural resources. The ultimate objective is to contribute to a circular economy in the construction industry, where recycled materials not only improve performance but also help mitigate the environmental impact of traditional construction practices.

Materials and methods

Materials

The cement utilized in this study is CEM II/B, a type of ordinary Portland cement produced by GICA. This cement has a minimum compressive strength of 42.5 MPa at 28 days, making it suitable for various applications in construction.

For this study, the sand utilized is sourced from the Oued Souf region, located approximately 500 km south of Algiers.

Two types of aggregates, G 3/8 and G 8/15, derived from the crushing of limestone rocks, were used in this study. These aggregates were selected for their specific size gradation and mechanical properties, which are essential for achieving the desired performance characteristics in the concrete mixtures.

Marble waste was obtained through a crushing process using a jaw crusher, which produced a material with particle sizes ranging from 0 to 5 mm for the sand fraction, and two granular classes for the aggregates. This processed marble waste serves as a supplementary material in the concrete mixtures, contributing to their overall properties and performance.

In this research, a third-generation superplasticizer (SP) with high water-reducing capabilities was employed. This superplasticizer, supplied by Granitex-NP and marketed under the name Medaflow 30, is a yellowish liquid with a pH of 6 and a density of 1.07.

Formulation

The formulation of self-compacting concrete (SCC) is a delicate process that requires finding a balance among various seemingly contradictory characteristics. An SCC mixture must possess high fluidity, allowing it to flow solely under the influence of gravity, while minimizing the risks of segregation (both static and dynamic) and instability, without compromising mechanical strength. Therefore, SCC must meet three essential criteria: fluidity, homogeneity, and robustness. In this study, we selected three relevant tests to quantify the following properties:

- Confined flowability,
- Stability and homogeneity, and
- Resistance to segregation and bleeding.

The different components of the SCM studied are presented in Table 1.

Table1 – Different components of the SCC studied (source author)

Mixture	Cement (kg/m^3)	Sand (kg/m^3)	SM (kg/m^3)	Gravel (kg/m^3)	GM (Kg/m^3)	W/C	SP (%)
Control SCC	469.59	906.22	0	536.04+ 266.10	0	0,4	0.8
SCCG M	469.59	906.22	0	0	536.04+ 266.10	0,4	0.7
SCCG M10%S M	469.59	815.52	90.7	0	536.04+ 266.10	0,4	0.7
SCCG M10%S M	469.59	724.92	181.3	0	536.04+ 266.10	0,4	0.7
SCCG M30%S M	469.59	634.32	271.9	0	536.04+ 266.10	0,4	0.6

Testing

Fresh properties

To evaluate and characterize fresh self-compacting concrete (SCC), the following tests were conducted:

- Slump flow diameter test,
- V-funnel test,
- L-Box test, and
- Sieve stability test for segregation.

Hardened properties

The compressive strengthwas measured at 7, 14, and 28 days using square specimens 15x15x15 (cm). In our case, the compression test was performed on six pieces from three specimens. Each specimen was subjected to a progressively increasing load until failure, using a hydraulic press with a capacity of 2000 kN.

The measurement of wave propagation velocity was conducted using a sonic monitoring device (ultrasonic tester). The device generates electrical pulses that travel through the concrete sample from a transmitting transducer applied to a flat surface. The pulse is captured by

a receiving transducer, which is also applied to a flat surface, positioned opposite and parallel to the first. When the pulse is detected by the receiver, the instrument displays the propagation time. Knowing the distance 'd' between the two transducers, the velocity of sound in the concrete (VAS) is calculated using the following formula:

$$VAS = \frac{\mathrm{d}}{\mathrm{t}}$$

where **d** is the distance between the transducers and **t** is the time taken for the pulse to travel through the concrete.

The test was conducted in accordance with ASTM C642-97 Standard. The method involves drying prismatic specimens in an oven at 105 ± 5°C for 72 hours. After drying, the specimens are removed from the oven, allowed to cool, and then weighed (M1). They are subsequently fully immersed in water at 21°C for 72 hours. After this period, the specimens are removed, wiped with a towel to remove excess surface water, and then weighed again (M2). The absorption rate is calculated using the following formula:

$$Ab\ (\%) = \frac{\mathrm{M1} - \mathrm{M2}}{\mathrm{M1}} * 100$$

where **M1** is the initial weight of the specimen and **M2** is the weight after immersion.

The dynamic modulus of elasticity was determined using non-destructive testing methods. A sonic testing device was employed to measure the velocity of ultrasonic waves propagating through the concrete specimens. The dynamic modulus of elasticity (Ed) can be calculated using the following formula:

$$Ed=\rho \cdot V^2$$

where **ρ** is the density of the concrete and **V** is the velocity of the ultrasonic waves measured in the specimens.

Results and discussion

Optimization of G/S and SP/L ratios

For the selection of SCC, we utilized the AFGC method. The superplasticizer/binder (SP/L) and sand/mortar (G/S) ratios were adjusted to achieve highly fluid concrete with a slump flow between 750 and 850 mm (SF3) and a suitable viscosity, with a flow time of less than 5 seconds, as well as high resistance to segregation and no visual signs of bleeding. Optimizing the SP percentage aims to develop the best fresh-state characteristics of the concrete, ensuring optimal hardened performance.

In this study, we tested four compositions with varying SP percentages, from 0.6% to 0.8%. We fixed G/S ratios at 0.9 and 1% and maintained a water/cement (W/C) ratio of 0.40. Table 2 illustrates the spread test results and flow times for selecting the optimal SP percentage and the S/M ratio.

Table 2 – Different components of the SCC studied (source author)

Composition of SCC					
MIXTURES		SCC1	SCC2	SCC3	SCC4
SP %		0,6	0.7	0,75	0.8
G/S		0.9	0.9	0.9	0.9
		0.95	0.95	0.95	0.95
		1	1	1	1
Slump Flow	G/S=0.90	500	570	650	700
	G/S=0.95	520	595	692	730
	G/S=1	580	620	725	780
Flow Time	G/S=0.90	8	6.25	5.19	4.49
	G/S=0.95	7.5	5.36	4.20	4
	G/S=1	7	5	4.05	3.5
Visual Observation	G/S=0.90	Mixture outside recommendation	Mixture within recommendation SF1 Less fluid	Fluid mixture SF1	Fluid mixture, no signs of bleeding or segregation (SF2)
	G/S=0.95	Mixture outside recommendation	Mixture within recommendation limit SF1	Fluid mixture SF2	Fluid mixture, no signs of bleeding or segregation (SF2)
	G/S=1	Mixture within recommendation limit SF1	Mixture within recommendation limit SF2	Fluid mixture SF3	Very Fluid mixture, no signs of bleeding or segregation (SF3)

Table 2 shows that increasing the percentage of SP improves the flowability of concrete. With a dosage of 0.6%, the slump flow was 500 mm. An increase of 0.1% in the SP dosage leads to an increase of 700 mm in the diameter of concrete.

At a dosage of 0.8%, the concrete exhibited good flowability with a slump flow of 700-780 mm. A G/S ratio of 1 with an SP dosage of 1% is adequate for achieving very fluid (SF3) and homogeneous concretes that can flow through the most congested areas. Numerous studies have shown that a G/S ratio of 1 is the optimal ratio for obtaining very fluid self-compacting concrete.

Effect of marble aggregate on fresh self-compacting concrete

To better understand the effect of recycled marble aggregates, the dosage of SP is fixed in the reference mixture.

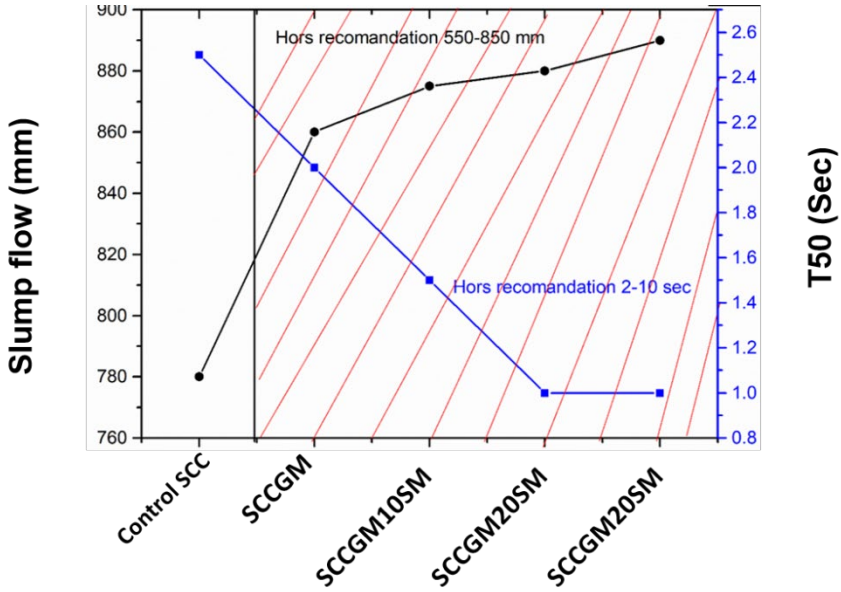

Figure 1 – Slump flow and T50 as a function of RMA for the SCC mix (source author)

The effect of substituting recycled marble aggregates (RMA) on the slump properties and the flow time of SCC is illustrated in Figure 1. From the figure, it is observed that the use and increase in the substitution rates of RMA enhance the slump diameter of SCC while decreasing the flow time, with values exceeding the recommended limits by (EFNARC, 2005) and showing significant signs of segregation and bleeding (Figure 2).

(Uygunoğlu, Topçu and Celik, 2014) studied the properties of SCC with marble aggregate and noted that flowability increased as the quantity of marble aggregate increased, particularly with a higher substitution rate SP. (Vaidevi, Kala and Kalaiyarrasi, 2019) investigated the effect of incorporating marble aggregate as fine aggregate on the properties of SCC.

The results indicate that flowability and filling ability are improved when natural sand is partially replaced with marble aggregate.

In summary, the introduction of marble aggregate into SCC mixtures at significant levels enhances fluidity, necessitating a reduction in SP to achieve values according to the required standards. This reduction in SP has minimized the negative impact of SCC on the total cost of 1 m³ of concrete.

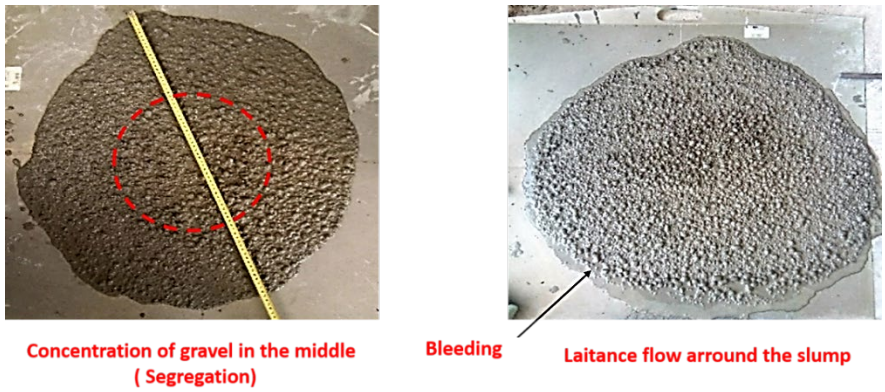

Figure 2 – Visual control of SCC with 30% RM as sand and 100% RM as gravel (source author)

Effect of marble aggregate on the dosage of superplasticizer in SCC

Figure 3 illustrates the variation of SP dosage based on the content of recycled marble aggregates (RMA) used in SCC mixtures. The data presented in this figure indicates a clear proportional relationship between the dosage of SP and the percentage of RMA incorporated into the mixtures. As the amount of RMA increases, it becomes necessary to reduce the SP dosage to achieve the desired fluidity and viscosity in accordance with the specified recommendations. This adjustment is crucial for maintaining the workability and performance of concrete, especially in applications where flowability is essential for effective placement and consolidation.

Specifically, the incorporation of 10%, 20%, and 30% of marble aggregate as a fine aggregate, while fully substituting 100% of natural gravel with marble gravel, results in significant reductions in the SP dosage. The reductions are approximately 14%, 31%, and 50%, respectively, for each level of marble aggregate substitution. This trend suggests that higher proportions of RMA not only enhance the fluidity of SCC but also reduce the reliance on chemical admixtures to achieve the necessary performance characteristics.

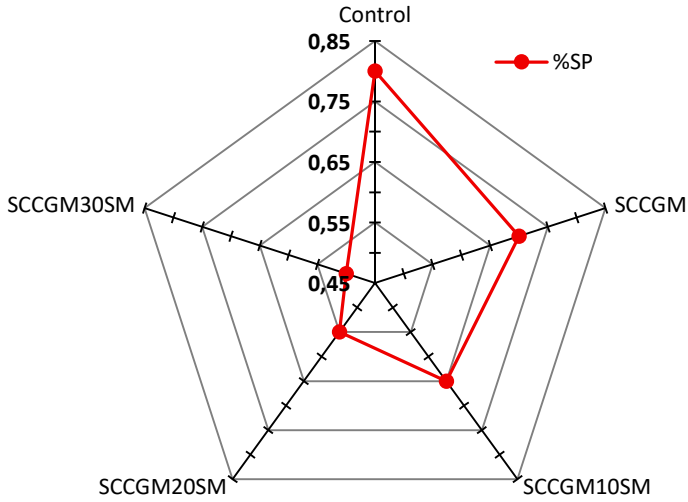

Figure 3 – Effect of marble aggregate on the dosage of superplasticizer in SCC (source author)

These findings underscore the importance of optimizing the mix design when utilizing recycled materials in concrete production. By effectively managing the dosage of SP in relation to the amount of RMA, it is possible to maintain high performance in terms of flowability while also minimizing the overall costs associated with the use of chemical additives in the concrete mix.

Slump flow with desired superplasticizer

The results for the slump of various SCC mixtures utilizing recycled marble aggregates (RMA) are illustrated in Figure 4. The figure indicates that the slump diameters for all SCC mixtures fall within the range of 760 mm to 810 mm. This range signifies a notable level of deformability in SCC, which is essential for ensuring effective flow and filling in complex forms without the need for mechanical vibration. These slump flow values are in compliance with the guidelines set forth by EFNARC (EFNARC, 2005), placing them within the category of (SF3). This classification denotes a high level of fluidity and workability, indicating that concrete can effectively fill molds and reach tight spaces, a crucial characteristic for modern construction practices.

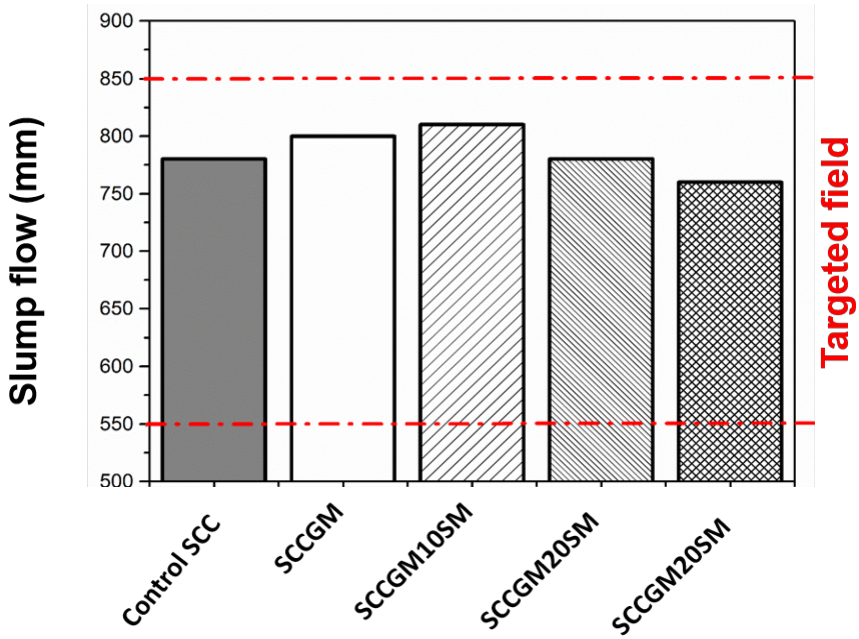

Figure 4 – Slump flow as a function of RMA with a desired superplasticizer (source author)

The observed improvement in diameter can be primarily attributed to the unique texture and properties of marble aggregate. Specifically, the low water absorption capacity of marble aggregates contributes to enhanced fluidity in the mixture, allowing for a more uniform distribution of the components and reducing the risk of segregation during placement.

Additionally, a study conducted by (Belaidi et al., 2012) explored how substituting natural aggregates with marble aggregates affects the properties of SCC. Their research highlighted that the inclusion of RMA not only enhances workability but also positively influences other mechanical properties of concrete. The improvements in workability facilitate easier handling and placement, making the construction process more efficient and reducing labor costs.

Flow time using the V-funnel test

Figure 5 illustrates the variation in flow time for the different SCC mixtures studied. According to the results obtained from the V-funnel test, all SCC mixtures exhibited high stability, as their flow times were below the values recommended by EFNARC (EFNARC, 2005). This indicates

favorable viscosity characteristics and resistance to segregation within the mixtures.

From Figure 5, it can be observed that the addition of recycled marble aggregates (RMA) increases the flow time of SCC compared to the reference mixture without RMA.

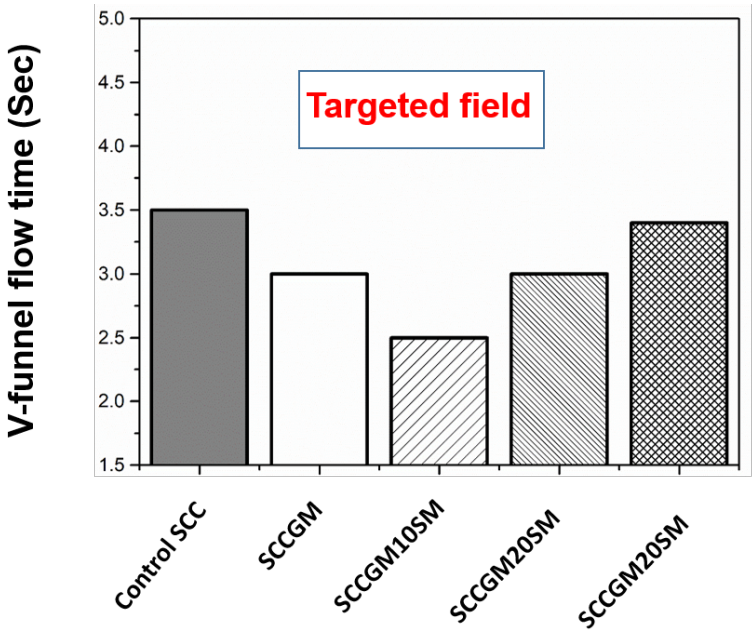

Figure 5 – V-funnel flow time as a function of RMA with a desired superplasticizer (source author)

However, the recorded flow times remain within acceptable limits, demonstrating that the properties of SCC can still be maintained despite a reduction in SP dosage. Even with moderate dosages of RMA, the measured flow times indicate that the incorporation of RMA contributes to reducing the SCC viscosity.

In research conducted by (Ofuyatan *et al.*, 2021), the fresh properties of SCC incorporating marble waste were examined. The study found that the flow time decreased as the quantity of marble aggregate increased, particularly with a lower dosage of SP. Optimal flow times were achieved when 30% marble aggregate was added to the mixture, which resulted in reduced viscosity and improved pumpability of concrete in confined areas. This suggests that the inclusion of RMA not only enhances the flow characteristics but also facilitates easier placement in challenging construction scenarios.

L-box Test

The variation of the H2/H1 ratio as a function of the percentage of marble aggregates used as sand and gravel is depicted in Figure 6. Regarding the filling capacity estimated by the H2/H1 ratio measured through the L-box test, all groups of self-compacting concrete (SCC) exhibited excellent filling capacity, mobility, and the ability to pass through highly confined areas.

It is observed that substituting sand with marble and introducing marble as 100% gravel positively influences both the passing ability and filling capacity of the mixtures. Consequently, the H2/H1 ratio varies between 90% and 100%. This variation indicates a significant advantage in achieving rapid flow through the reinforcement bars in the L-box test, which converges more quickly toward the upper threshold. As a result, the values of the H2/H1 ratios increase, reaching up to 100%.

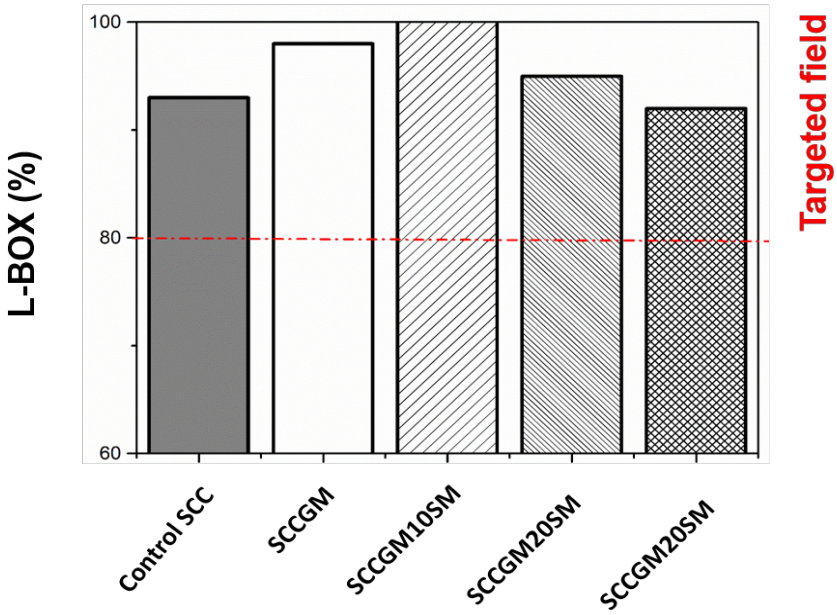

Figure 6 – L-BOX as a function of RMA with a desired superplasticizer (source author)

The high H2/H1 ratios demonstrate that SCC mixtures containing marble aggregates can effectively fill complex geometries and pass-through tight spaces, which is crucial for ensuring uniformity and

performance in concrete applications. These enhanced flowability and filling capacity are essential for optimizing the placement of concrete in intricate designs, thereby contributing to overall structural integrity and durability.

Results of the sieve stability analysis

The stability of the mixtures was evaluated using a sieve stability test, and the results are illustrated in the histogram form in Figure 7. The percentages of laitance passing through the sieve were observed to range from 5% to 15%. This variation indicates a relatively low amount of laitance, suggesting that all the powder-based SCC produced exhibit commendable resistance to both segregation and bleeding.

Visual inspections of the SCC samples further corroborate these findings, revealing that the mixtures maintain a consistent and homogeneous appearance throughout, as shown in Figure 8. This homogeneity is critical, as it implies a well-dispersed particle distribution, which contributes to the overall stability and performance of concrete in practical applications.

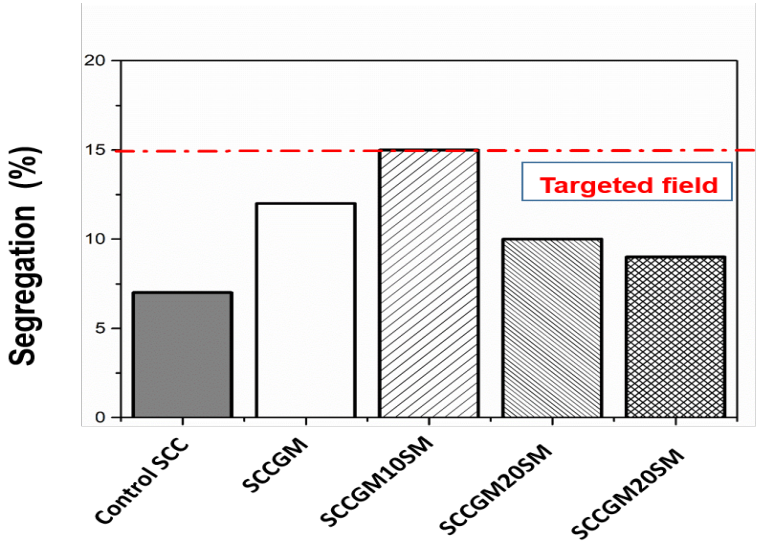

Figure 7– Segregation as a function of RMA with a desired superplasticizer (source author)

(Safawi, Iwaki and Miura, 2005) have established that the flow time measured in the V-funnel is an effective tool for assessing the potential for

segregation in concrete mixtures. Specifically, they observed that flow times below 2 seconds are indicative of a high susceptibility to segregation, highlighting that lower viscosity mixtures are more prone to separation of components. Our results align with these observations, reinforcing the notion that the measured flow times in our study correspond directly with the sieve stability results.

Figure.8 – Visual control of segregation and bleeding of RMA of different SCC mixtures (source author)

Furthermore, a direct correlation between concrete viscosity and stability were investigated, indicating that reductions in viscosity are associated with decreased stability. This relationship is critical for understanding the behavior of self-compacting concrete mixtures. Our findings, which will be further supported by the data collected on flow times, suggest that maintaining an optimal viscosity is essential for achieving the desired performance characteristics in SCC.

In conclusion, the results of our study indicate that the SCC mixtures tested demonstrate robust resistance to segregation, confirmed by both sieve stability tests and visual assessments. The flow time data further support these findings, suggesting that careful control of viscosity is key to optimizing the performance of self-compacting concrete.

Effect of marble aggregate on the compressive strength

Figure 9 presents the compressive strength development of different SCC mixtures at 7, 14, and 28 days. The results indicate a noticeable increase in compressive strength with the replacement of natural gravel by marble aggregate. For instance, the reference SCC exhibits a compressive strength of 32 MPa at 28 days. With a full 100% substitution of natural gravel by marble aggregate, the strength improves significantly to 43 MPa. This enhancement is attributed to the superior hardness of

marble waste compared to natural gravel, which contributes to a denser, stronger concrete matrix.

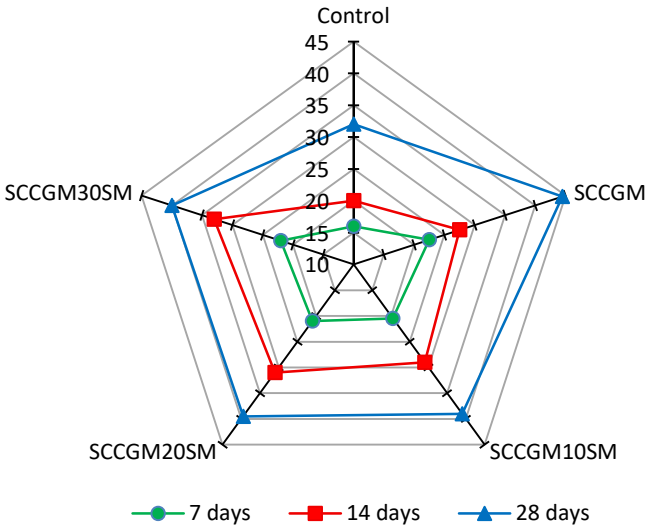

Figure 9 – Compressive strength of RMA of different SCC mixtures (source author)

Additionally, the compressive strength of SCC incorporating marble as a fine aggregate (denoted as SCC-MA) reaches 43 MPa at 28 days. However, when 30% of fine natural sand is replaced by marble sand, the compressive strength decreases slightly to 40 MPa. Despite this reduction, the SCC containing marble aggregate still demonstrates higher strength than conventional SCC without any recycled or alternative aggregates.

This observation aligns with findings from (Choudhary et al., 2021), who investigated the impact of marble aggregate on the mechanical properties of self-compacting concrete. Their study reported that adding marble aggregate at substitution levels of 20% and 30% reduced the compressive strength compared to the reference concrete without marble, suggesting that the optimal marble content for enhancing strength may vary depending on its role as coarse or fine aggregate in the concrete mix.

Effect of marble aggregate on the sonic pulse velocity

Figure 10 shows the effect of using 100% GMR as coarse aggregate on the sonic pulse velocity (SPV) test results after a 28-day curing period. The data indicate a steady decrease in SPV values with an increasing proportion of GMR, both as coarse aggregate and in cases where 20% to 30% of natural sand is substituted with marble-based sand.

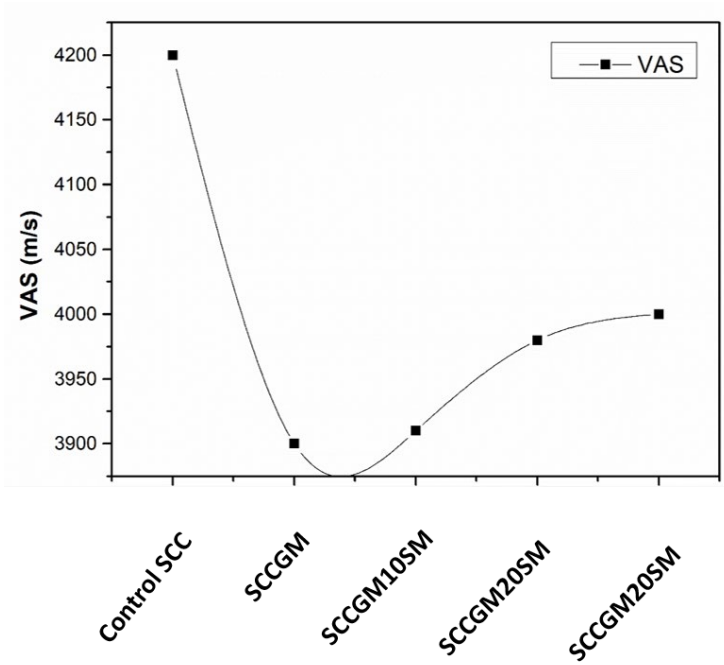

Figure 10 – VAS as a function of SCC with RMA ((source author)

SPV, or the velocity of sound waves through concrete, is an indicator of the material's quality and integrity. Higher SPV values generally correspond to denser, more homogeneous concrete with fewer pores, voids, or microcracks that might impede the wave path. When concrete contains recycled marble aggregate, however, several factors come into play that impact SPV:

1 **Density**: The presence of GMR tends to reduce the overall density of the concrete matrix. This is because GMR particles often have a mortar coating from previous use, which is less dense than natural aggregates. This lower density material slows down ultrasonic waves, contributing to lower SPV readings.
2 **Porosity and voids**: The residual mortar on GMR particles introduces additional pore space within concrete, creating more voids. This porous structure increases the distance ultrasonic waves need to travel through non-solid areas, thus reducing the overall pulse velocity.
3 **Homogeneity**: In standard SCC, natural aggregates contribute to a uniform, compact matrix that allows sound waves to travel quickly. However, the variability introduced by the GMR's residual mortar can

disrupt this uniformity, causing inconsistencies that further delay wave transmission.

4 **Wave path length**: With higher porosity and greater discontinuity due to residual mortar, the sonic wave encounters more obstacles, which effectively lengthens the path it has to travel. As a result, the wave takes longer to pass through concrete, resulting in lower SPV values.

Effect of RMA on capillary water absorption

The impact of RMA on capillary water absorption in hardened concrete is shown in Figure 11, where a clear trend of reduced water absorption is observed with increasing RMA content.

The reference concrete mix, which contains only natural aggregates, shows the highest absorption coefficient, suggesting a greater porosity and capillary network that can absorb more water. By contrast, as GMR content increases, the absorption coefficient decreases significantly.

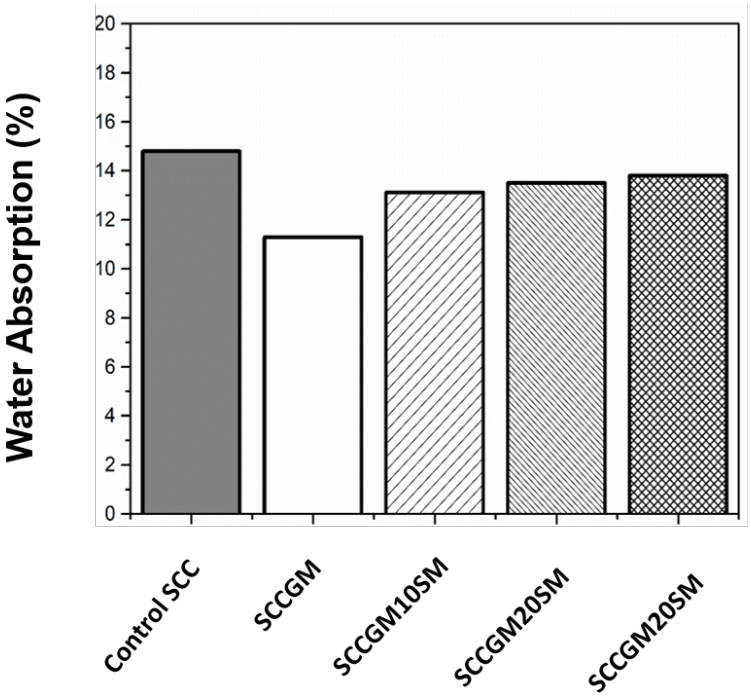

Figure 11 – Water absorption as a function of SCC with RMA (source author)

This reduction can be attributed to several key factors:

Low Water Absorption of GMR Particles: Marble-based aggregates are less porous than natural aggregates, meaning they absorb less water.

This characteristic inherently reduces the overall capillary action in the concrete, limiting how much water the material can absorb.

Reduced Connectivity of Capillary Pores: GMR's coarse particles (typically in the 0-5 mm range) help disrupt the capillary network within the concrete matrix. Larger particles reduce the overall connectivity between pores, effectively blocking some pathways that water would normally travel through, leading to a lower capillary absorption rate.

Dense Microstructure: GMR's low porosity leads to a denser concrete microstructure, minimizing the spaces through which water can penetrate. As a result, concrete with GMR exhibits improved resistance to water infiltration and, consequently, greater durability under exposure to moisture cycles.

Enhanced Durability against Cyclic Moisture Exposure: With a reduced absorption rate, concrete is better able to resist the expansion and contraction stresses associated with cyclic wetting and drying. This stability under moisture fluctuations helps prevent internal micro-cracking, which can otherwise weaken concrete over time.

When GMR content reaches around 30%, these benefits become particularly pronounced. The combination of GMR's low water absorption coefficient and its larger particle size means that concrete is less susceptible to capillary water absorption. This makes GMR an effective material for enhancing the durability and lifespan of concrete structures exposed to environments with frequent moisture variation, as the lower capillary absorption limits water-related damage mechanisms.

Dynamic elastic modulus of SCC with RMA

According to Figure 12, the dynamic elastic modulus of self-compacting concrete (SCC) with recycled marble aggregates follows a similar trend to the sonic pulse velocity (SPV) results. Additionally, SCC containing marble aggregates as both sand and gravel shows high elastic modulus values, likely due to the high compressive strength of these mixtures. The dynamic elastic modulus is highly influenced by the type of aggregate, as well as the material's compressive strength and density.

Replacing natural gravel with 100% marble gravel reduces the elastic modulus by approximately 30% compared to the reference concrete. Similarly, substituting natural sand with marble sand at 10%, 20%, and 30% decreases the elastic modulus by 21%, 11%, and 5%, respectively, relative to the reference SCC.

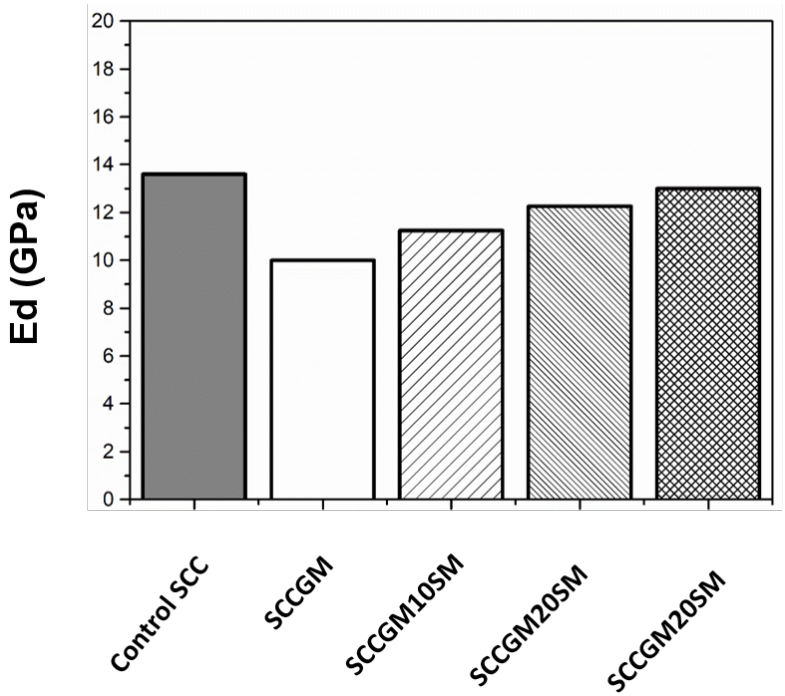

Figure.12 – Dynamic elastic modulus as a function of SCC with RMA (source author)

The reduction in the elastic modulus can be attributed to increased porosity, which influences how ultrasonic waves travel through the material. Higher porosity results in more wave absorption and a lower elastic modulus. Consequently, while recycled marble aggregates contribute to a high initial compressive strength, their influence on porosity and the dynamic elastic modulus must be considered in applications requiring high material stiffness.

Conclusion

The primary objective of this study was to evaluate the impact of recycled marble waste (RMW), utilized at various percentages as both sand and gravel, on the performance of self-compacting concrete (SCC). Based on the comprehensive analysis of the results, the following conclusions can be drawn.

The investigation revealed that for the effective formulation of SCC using local materials, an optimal water-to-cement (W/C) ratio of 0.4 and a

gravel-to-sand (G/S) ratio of 1 were necessary. Additionally, incorporating 0.8% superplasticizer (SP) was essential to achieve the desired workability and mechanical properties. These parameters are crucial for ensuring that SCC meets the required performance standards while maintaining cost efficiency.

The introduction of RMW as both fine and coarse aggregates led to a significant reduction in the demand for SP, approximately by 60%. This reduction not only highlights the effectiveness of RMW in enhancing the flow characteristics of concrete but also contributes to lower overall material costs, making SCC more economically viable.

The presence of RMW demonstrated a marked improvement in the flowability and filling ability of SCC. This characteristic is vital for ensuring that concrete can adequately fill complex forms and achieve a high level of homogeneity, which is essential for structural integrity.

An increase in the percentage of marble used as coarse aggregate resulted in a substantial enhancement of compressive strength, with an increase of approximately 26% compared to traditional self-compacting concrete (TSCC). This improvement indicates that RMW can effectively contribute to the structural performance of concrete, potentially leading to more durable and resilient construction materials.

Notably, a decrease in compressive strength was observed when marble was used as sand, compared to its application as gravel. However, it is important to highlight that the compressive strength of SCC with marble as sand remained superior to that of TSCC. This finding suggests that while the choice of aggregate type influences strength characteristics, RMW continues to offer viable performance.

The total immersion water absorption of SCC decreased with an increasing proportion of marble, whether used as sand or gravel. This reduction in water absorption is indicative of improved impermeability and durability, which are critical factors for the longevity of concrete structures.

The addition of RMW also led to a significant enhancement in the elastic modulus of the SCC studied. A higher elastic modulus is associated with improved stiffness and stability, contributing positively to the overall performance of the concrete under load.

In conclusion, this study underscores the promising potential of recycled marble waste as a sustainable alternative in the formulation of self-compacting concrete. By utilizing RMW, the construction industry can achieve enhanced performance characteristics while simultaneously addressing environmental concerns related to waste management. These findings pave the way for future research aimed at optimizing the use of

recycled materials in concrete applications, ultimately contributing to more sustainable construction practices.

References

Alyamaç, K. and Aydin, A. (2015) 'Concrete properties containing fine aggregate marble powder', *KSCE Journal of Civil Engineering*, 19. Available at: https://doi.org/10.1007/s12205-015-0327-y.

Belaidi, A.S.E. *et al.* (2012) 'Effect of natural pozzolana and marble powder on the properties of self-compacting concrete', *Construction and Building Materials*, 31, pp. 251–257. Available at: https://doi.org/10.1016/j.conbuildmat.2011.12.109.

Choudhary, R. *et al.* (2021) 'Permeation, corrosion, and drying shrinkage assessment of self-compacting high strength concrete comprising waste marble slurry and fly ash, with silica fume', *Structures*, 33, pp. 971–985. Available at: https://doi.org/10.1016/j.istruc.2021.05.008.

Demirel, B. (2010) 'The effect of the using waste marble dust as fine sand on the mechanical properties of the concrete', *International Journal of the Physical Sciences*, 5, pp. 1372–1380, ISSN 1992 - 1950.

EFNARC (2005) *EFNARC, M. The European Federation of Specialist Construction and Concrete System: The European Guidelines for Self-Compacting Concrete. Specification, Production and Use, 2005. - Recherche Google*. Available at: https://www.theconcreteinitiative.eu/images/ECP_Documents/EuropeanGuidelinesSelfCompactingConcrete.pdf.

Gazi, A., Skevis, G. and Founti, M. (2012) 'Energy efficiency and environmental assessment of a typical marble quarry and processing plant', *Journal of Cleaner Production*, 32, pp. 10–21. Available at: https://doi.org/10.1016/j.jclepro.2012.03.007.

Houria, H. *et al.* (2020) 'Introduction of Marble Waste Sand in the Composition of Mortar', in. Available at: https://doi.org/10.5772/intechopen.91254.

Khairi, W. *et al.* (2020) 'Relation between rheological and mechanical properties on behaviour of self-compacting concrete (SCC) containing recycled plastic fibres: a review', *European Journal of Environmental and Civil Engineering*, 26. Available at: https://doi.org/10.1080/19648189.2020.1868344.

Kore, S. and Vyas, A. (2016) 'Impact of Marble Waste as Coarse Aggregate on properties of lean cement concrete', *Case Studies in Construction Materials*, 4. Available at: https://doi.org/10.1016/j.cscm.2016.01.002.

Makul, N., Fediuk, R., Amran, M., Zeyad, A., Azevedo, A., *et al.* (2021) 'Capacity to Develop Recycled Aggregate Concrete in South East Asia', *Buildings*, 11, p. 234. Available at: https://doi.org/10.3390/buildings11060234.

Makul, N., Fediuk, R., Amran, M., Zeyad, A., Murali, G., *et al.* (2021) 'Use of Recycled Concrete Aggregates in Production of Green Cement-Based Concrete

Composites: A Review'. Available at: https://hdl.handle.net/10877/14139 (Accessed: 16 June 2025).

Mathodi, V. *et al.* (2022) 'Environmental impact assessment of laterite quarrying from Netravati–Gurpur river basin, South West Coast of India', *Environment, Development and Sustainability*, 26, pp. 1–22. Available at: https://doi.org/10.1007/s10668-022-02741-5.

Ofuyatan, O. *et al.* (2021) 'Marble waste and recycled concrete aggregates in self compacting concrete (SSC): an evaluation of fresh and hardened properties', *Australian Journal of Civil Engineering*, 20, pp. 1–13. Available at: https://doi.org/10.1080/14488353.2021.1921342.

Ouldkhaoua, Y. *et al.* (2019) 'Experimental study on the reuse of cathode ray tubes funnel glass as fine aggregate for developing an ecological self-compacting mortar incorporating metakaolin', *Journal of Building Engineering*, 27, p. 100951. Available at: https://doi.org/10.1016/j.jobe.2019.100951.

Rich, D. (2014) *On-site application of self-compacting concrete (SCC)*. thesis. Loughborough University. Available at: https://repository.lboro.ac.uk/articles/thesis/On-site_application_of_self-compacting_concrete_SCC_/9579296/1.

Safawi, M., Iwaki, I. and Miura, T. (2005) 'A study on the applicability of vibration in fresh high fluidity concrete', *Cement and Concrete Research*, 35, pp. 1834–1845. Available at: https://doi.org/10.1016/j.cemconres.2004.10.031.

Silva, R.V., Brito, J. and Dhir, R. (2018) 'Fresh-state performance of recycled aggregate concrete: A review', *Construction and Building Materials*, 178, pp. 19–31. Available at: https://doi.org/10.1016/j.conbuildmat.2018.05.149.

Thakur, A.K., Pappu, A. and Thakur, V.K. (2018) 'Resource efficiency impact on marble waste recycling towards sustainable green construction materials', *Reuse and Recycling / UN SGDs: How can Sustainable Chemistry Contribute? / Green Chemistry in Education*, 13, pp. 91–101. Available at: https://doi.org/10.1016/j.cogsc.2018.06.005.

Uygunoğlu, T., Topçu, İ. and Celik, A. (2014) 'Use of waste marble and recycled aggregates in self-compacting concrete for environmental sustainability', *Journal of Cleaner Production*, 84, pp. 691–700. Available at: https://doi.org/10.1016/j.jclepro.2014.06.019.

Vaidevi, C., Kala, D. and Kalaiyarrasi, A.R.R. (2019) 'Mechanical and durability properties of self-compacting concrete with marble fine aggregate', *Materials Today: Proceedings*, 22. Available at: https://doi.org/10.1016/j.matpr.2019.11.019.

Yu, Y. *et al.* (2024) 'Investigating specimen size and shape effects on compressive mechanical behaviors of recycled aggregate concrete using discrete element mesoscale modeling', *Construction and Building Materials*, 438, p. 137196. Available at: https://doi.org/10.1016/j.conbuildmat.2024.137196.

Одрживи самозбијајући бетон: утицај комбинованог мермерног отпада у облику финог и крупног агрегата

Белгасем Мохамед Ел Газали, **аутор за преписку,** *Оулдкауа* Јунес, *Херихири* Оуидед, *Садуди* Љасија, *Аруџ* Карима
Универзитет наука и технологије Хуари Бумедјен

ОБЛАСТ: материјали
КАТЕГОРИЈА (ТИП) ЧЛАНКА: оригинални научни рад

Сажетак:

Увод/циљ: Заштита животне средине путем рециклирања отпада један је од највећих изазова данашњице. Инертни отпад, настао углавном у индустрији, представља знатан удео који штети животној средини јер се акумулира у природи.

Методе: Испитиван је утицај валоризације мермерног отпада у облику песка и шљунка на реолошка и механичка својства самозбијајућег бетона (SCC). За потребе истраживања мермер је коришћен као фини агрегатни песак (MAS) у количинама од 10%, 20%, и 30%, а као крупни агрегатни шљунак (MAG) у количини од 100%.

Резултати: Показано је да је увођење мермерног отпада (MW) као агрегата имало позитиван утицај на реолошке карактеристике, знатно смањујући потребу за дозирањем суперпластификатора.

Закључак: Имајући у виду механичке моменте, коришћење крупног агрегатног шљунка довело је до побољшања механичке чврстоће.

Кључне речи: самозбијајући бетон, мермерни отпад, реолошко понашање, дозирање суперпластификатора, механичка чврстоћа, животна средина

Paper received on: 07.05.2025.
Manuscript corrections submitted on:23.05.2025.
Paper accepted for publishing on: 20.06.2025.

Chemical composition and toxicity of effluents from unhairing baths: case study of the Batna Unit, Algeria

Selma Ben Brahim[a]*; Sabrina* Tamersit[b] *; Afaf* Lalmi[c]*; Chahrazad* Amrane[d]*; Fatima* Chemlal[e]

[a] University of Batna 1, Laboratory of Chemistry and Environmental Chemistry LCCE, University of Batna 1, Algeria, Batna,
e-mail: selma.benbrahim@univ-batna.dz,
ORCID iD: https://orcid.org/0009-0001- 6346-940X
[b] University of Batna 1, Laboratory of Chemistry and Environmental Chemistry LCCE, University of Batna 1, Algeria, Batna,
e-mail: sabrina.tamersit@univ-batna.dz,
ORCID iD: https://orcid.org/0000-0002-5874-6281
[c] University of Batna 1, Laboratory of Chemistry and Environmental Chemistry LCCE, University of Batna 1, Algeria, Batna,
e-mail: afaf.lalmi@univ-batna.dz,
ORCID iD: https://orcid.org/0009-0004-2868-5774, **corresponding author**
[d] University of Batna 1, Laboratory of Chemistry and Environmental Chemistry LCCE, University of Batna 1, Algeria, Batna,
e-mail: chahrazad.amrane@univ-batna.dz,
ORCID iD: https://orcid.org/0000-0002-5874-6281
[e] University of Batna 1, Laboratory of Chemistry and Environmental Chemistry LCCE, University of Batna 1, Algeria, Batna,
e-mail: fatima.chemlal@univ-batna.dz,
ORCID iD: https://orcid.org/0000-0001-6298-0372

https://doi.org/10.5937/vojtehg73-58266

FIELD: environmental chemistry
ARTICLE TYPE: original scientific paper

Abstract:

Introduction/Purpose: The leather industry in Algeria contributes significantly to the economy, but its unhairing process generates highly polluted wastewater. This study aimed to characterize the chemical composition of unhairing bath effluents and assess their environmental toxicity.

Methods: The study focused on wastewater samples from the Batna tannery unit, where sheep and goat skins were processed. Thirteen samples were collected manually over 35 days (April 5–May 10, 2022), and

ACKNOWLEDGMENT: The authors gratefully acknowledge the support of the DGRSDT (Algerian Ministry of Higher Education and Scientific Research, MESRS).

standard chemical analyses were conducted to evaluate parameters such as pH, conductivity, total suspended solids (TSS), sulfides, ammonia ions, and proteins.

Results: The results showed that the wastewater had a high pH (12.47 on average), high conductivity (13.38 mS/cm), and significant levels of pollutants: sulfides (1120–1650 mg/L), TSS (862–2220 mg/L), and chemical oxygen demand (10.422–43.747 mg/L). Additionally, the wastewater contained free amino acids and proteins, products of partially hydrolyzed skin proteins, increasing its toxicity.

Conclusions:The study highlighted the severe environmental risks of untreated unhairing wastewater, underscoring the need for effective treatment solutions to mitigate pollution. The findings provide important insights into the environmental challenges of the leather industry and stress the importance of sustainable wastewater management.

Key words: leather industry, pollution, unhairing effluent, characterization, wastewater, toxicity

Introduction

In Algeria, the leather industry has a significant contribution to the economy and is represented by 6 units specializing in "wet blue" leather tanning operations. Tanning activities involve transforming animal skin into leather by removing lipids and hair. Several processes are used in this transformation, including unhairing, deliming, and tanning (Tamersit and Bouhidel, 2020). As a result, tanning industries consume a large amount of water (30 to 40 liters per kilogram of treated skin) and produce significant amounts of wastewater and solid waste (Benhadji et al., 2018). The unhairing process is the first and most pollutant-intensive operation (Hasan et al., 2024) which results in a partial hydrolysis of the animal skin (Morera et al., 2016). Consequently, the produced wastewater is dark brownish, malodorous, and characterized by very high pH, conductivity, and COD. It is also loaded with sulfides, total suspended solids, and by-products of hydrolyzed skin proteins (keratin) (Tamersit et al., 2018).

In leather production, only approximately 20% of the chemicals used are retained within the final leather product, while the remaining 80% are discharged into the resulting wastewater. Notably, around 40% of the sulphide applied in industrial liming processes is released into wastewater effluents. According to literature, tannery wastewater ranks among the most hazardous forms of industrial effluents, posing serious environmental and health risks.

Tannery wastewater constitutes a serious threat to the environment due to the high concentration and non-biodegradability of the majority of

pollutants present (Durai and Rajasimman, 2011). In addition, the final quality of unhairing effluent depends mainly on the nature and number of raw materials as well as the production operations applied (Mendoza-Roca et al., 2010). Thus, it is judicious to treat the tannery wastewater and in particular, the unhairing bath effluent before its discharge into the receiving medium (Hashem et al., 2021). In this context, wastewaters from unhairing baths should be evaluated and characterized in order to highlight their toxicity and to propose an adequate treatment technique according to the studied case (Zhao et al., 2022).

The objective of this study is to characterize the wastewater generated by the unhairing bath of an industrial tannery unit located in Batna, Algeria and to assess the impact of these discharges on the surrounding environment. This tannery discharges its wastewater into the nearby Oued El Gourzi River, which flows through the city and passes by the villages of FISDIS and EL-MADHER, areas known for their agricultural lands. As a result, the unhairing wastewater is either directly or indirectly used by local farmers for irrigation purposes.

The characterization and evaluation of unhairing tannery wastewater are conducted through a comprehensive analysis of 10 samples. Additionally, the number and type of animal skins processed, whether cattle, goat, or sheep, are clearly specified. The results obtained from this analysis are thoroughly interpreted, providing insights into the toxicity profile of these effluents.

Materials and methods

Industrial unhairing wastewater

In this study, the samples were collected from unhairing wastewater discharged by the Batna Unit, an industrial tannery unit located in the city of Batna.

The Batna Unit factory, the subject of this study, consumes enormous quantities of water, exceeding 500 m^3/d; 28.8 m^3/d is the volume of concentrated wastewater from the unhairing operation. This consumption varies depending on the quality and quantity of the raw material.

In all countries, these effluents must meet discharge standards.

Unhairing bath wastewater sampling was carried out manually in the morning after the first discharges from 6 AM. to 8 AM. The samples were collected according to the collection and storage standards and processes. The samples were stored in polyethylene containers of two-liter volume and carefully labeled. The collection of 13 samples of unhairing wastewater was spread over a period of 35 days (April 5 – May 10, 2022).

The volumes of daily discharges are not regular, rather peaks are observed. During the early hours of the morning, there is usually a peak of 250% compared to the hourly average. At this time of the day, different wastewaters present extreme analytical characteristics. During the other hours of the day, wastewater production represents 50% of the hourly average.

Analysis methods

Temperature, pH and conductivity measurements were carried out in situ. For other analyses (COD and BOD5), the samples were stored at 4 °C until the time of analysis to avoid any modification. Various analyses were carried out after decanting the samples. For certain analyses, dilution and/or filtration had to be carried out beforehand.

The pH and conductivity of the samples were determined by using a pH meter, Model 720 WTW and a Hanna Instruments conductivity meter, Model EC 215, respectively.

Tha analyses of chemical oxygen demand (COD), biological oxygen demand (BOD5) , total suspended solids (TSS), ammonia ($N\text{-}NH_3$), sulfide (S^{2-}), chloride (Cl^-), and phosphate ($P\text{-}PO_4^{3-}$) were carried out in accordance with the standard methods (Rodier et al., 1996).

Results and discussion

Number of treated skins

In the tannery, the consumption of both water and chemicals as well as the final quality of the wastewater from each stage depend on the quality and quantity of the treated hides. In this work, each sample was characterized previously by their number and type of treated skins.

According to the information provided by the workers, sheep skins have been the most used ones in recent years. Through the following histogram in Figure 1, which represents the number of skins treated in the bath of each sample, it is clear that the number of skins treated is between 600 to 900. However, the number and type of skins used vary depending on availability.

In comparison with the nineties, there is a drop in the number of skins treated (more than 1000 skins per bath) as well as a relative decrease in the availability of goatskins.

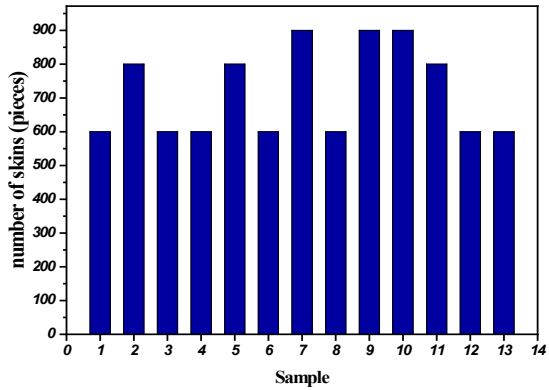

Figure 1 – Histogram of the number of treated skins from different samples, the Batna Unit

Using the results obtained, we can subsequently see whether the number and nature of the treated skins influence the quality of the final wastewater or not.

Analysis of the physicochemical parameters

The physicochemical quality of wastewater can be evaluated based on the values of several parameters:

• The pH is a pollution indicator with excellence; it varies depending on the nature of the basic or acidic effluents.

• Temperature is a parameter that influences the kinetics of metabolism, the distribution of species, and the dissolution of gases dissolved in water.

• Conductivity makes it possible to quickly and approximately assess the mineralization of wastewater and to monitor its evolution.

The pH, temperature, and conductivity significantly influence the fate of various contaminants in the receiving environment. These parameters play a crucial role in controlling the behavior and mobility of contaminants across different environmental compartments.

Determination of temperature

Temperature is one of the most important parameters determining the efficiency of the process.Figure 2 shows the evolution of the temperature values of the wastewater from the unhairing bath. These values ranged between 11-18 °C, so these values were *below* the discharge limit values (40 °C)(Sawadogo et al., 2012).

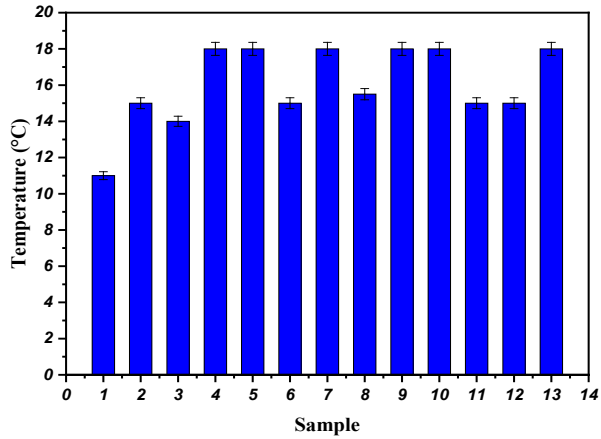

Figure 2 – Histogram of the temperature monitoring of the unhairing wastewater from the tannery, the Batna Unit

Determination of the pH

The evolution of the pH of different samples from the unhairing bath showed that these wastewaters are relatively alkaline with an average value of 12.47 and extreme values of 12.04 to 13 (Figure 3).

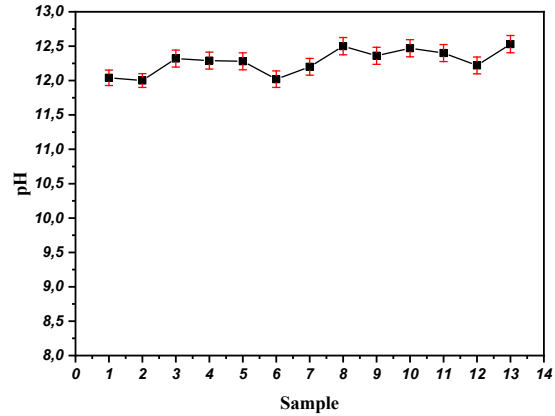

Figure 3 – Curve of the pH monitoring of the unhairing wastewater from the tannery at 20°C, the Batna Unit

This high pH is due to the presence of alkaline substances, S^{2-}, HS^{-} and $Ca(OH)_2$. The pH of the obtained results does not meet the general standards recommended for wastewater disposal (Islam, B.I. et al., 2014). In this case, neutralization of these wastewaters is necessary before their

discharge into the receiving environment. However, there is the risk of emission of H_2S gas release at pH 7.

Electrical conductivity (EC)

The salinity level, expressed in average electrical conductivity, is 13.38 mS/cm (Figure 4). The conductivity varies depending on the quantity of chemicals used during the operation (or the conservation stage). The dominant salt in these effluents is sodium chloride due to the high concentration of sodium and chloride in the studied environment. Salty skins release large amounts of NaCl.

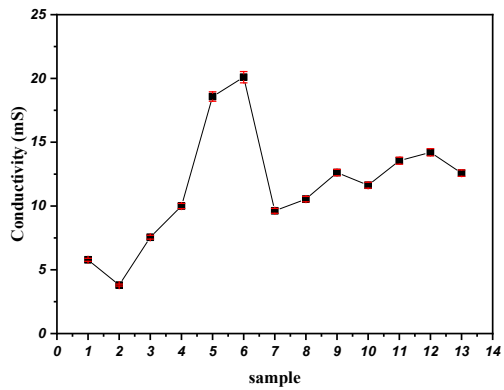

Figure 4 – Curve of the conductivity monitoring of the unhairing wastewater from the tannery at 20 °C, the Batna Unit

Above 2500 µS, salinity inhibits the proliferation of microorganisms and therefore reduces its purifying power; this is the major problem encountered with biological treatment. On the other hand, the presence of a high level of some ions such as chlorides and sulfates can cause the solubilization of a metal slurry through complexation reactions.

Determination of total suspended solids (TSS)

Suspended matter (TSS) represents the suspended mineral and organic particles contained in the effluent. These values are from 862.5 to 2220.8 mg/L with an average of 1804.22 mg/L (see Figure 5).

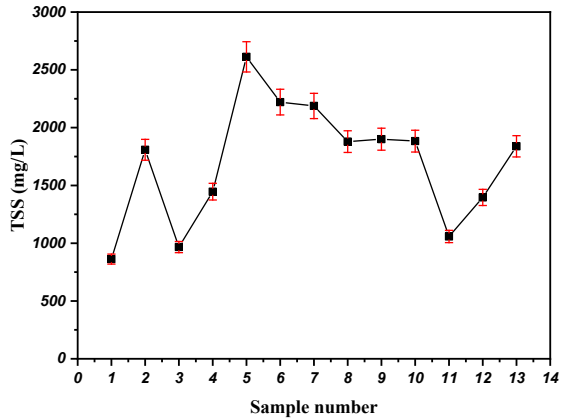

Figure 5 – Curve of the TSS monitoring of the unhairing wastewater from the tannery at 20 °C, the Batna Unit

High MES values are higher than the norm; they are directly linked to the nature and quality of the raw material processed in this industry (animal skins) in relation to the quantities of water used. These MES values come from hair, debris, skin fibers and any material attached to the used skin.

Analysis of cations and anions

Cations

Several cations were analyzed in the unhairing wastewater bath, such as those of calcium, magnesium, sodium, and potassium.

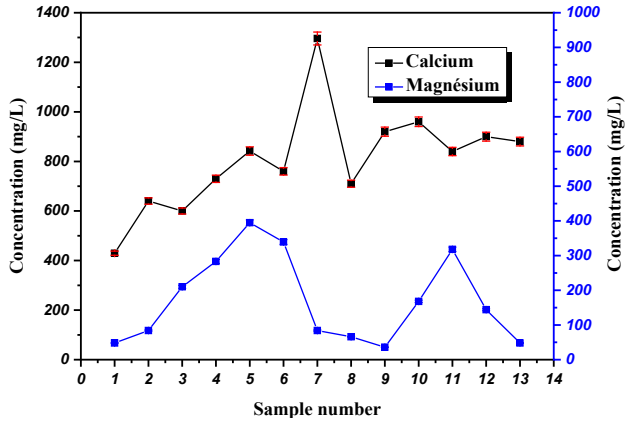

Figure 6 – Curve of the calcium and magnesium ions content monitoring in the unhairing wastewater from the tannery, the Batna Unit

Figure 6 represents the evolution of calcium and magnesium; the average magnesium content is around 171 mg/L. Calcium reaches an average value of 808.27 mg/L; this high value is essentially due to the use of lime ($Ca(OH)_2$) during this unhairing operation.

Sodium (Figure 7) is present in the effluents at an average content of around 4659.92 mg/L. This relatively high value is due both to the use of sodium chloride for the preservation of raw hides and to its presence in Na2S, the main reagent for hair removal.

For potassium, its concentration varies between 184.89 and 1393 mg/L; the average value is around 561.55 mg/L.

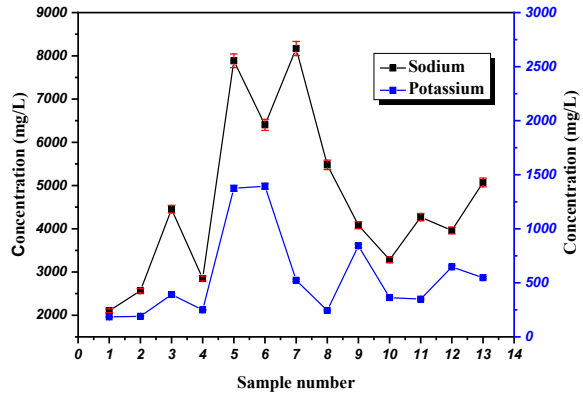

Figure 7 – Curve of the sodium and potassium ion content monitoring in the unhairing wastewater from the tannery, the Batna Unit

Anions

The anions analyzed in the unhairing wastewater bath were chlorides and sulfides.

The chloride ion content (Figure 8) was in the range of 720 and 1212 mg/L with an average value of around 906.91 mg/L.

In fact, inorganic sulfides (NaHS or Na_2S) and lime treatment were used in the unhairing process. The determination of sulfide (Figure 9) in all samples shows that their values vary between 1120 and 1650 mg/L. These values are rather comparable to those reported by other works. The presence of high concentrations of sulphides in wastewater causes a serious problem of odor and corrosion in sanitation canals. Dissolved sulfide is found in the form of a mixture of hydrosulfide ions and hydrogen sulfide (H_2S). The high toxicity of sulfides comes from the H_2S released (Floqi, T. et al., 2007), the content of which depends on the pH value. After evacuation, the effluents were diluted and neutralized in the natural

environment releasing H_2S gas into the atmosphere, thus causing serious olfactory nuisances (Floqi et al., 2007).

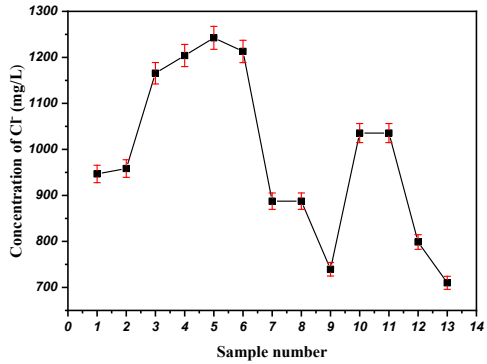

Figure 8 – Curve of the chloride ion content monitoring in the unhairing wastewater from the tannery, the Batna Unit

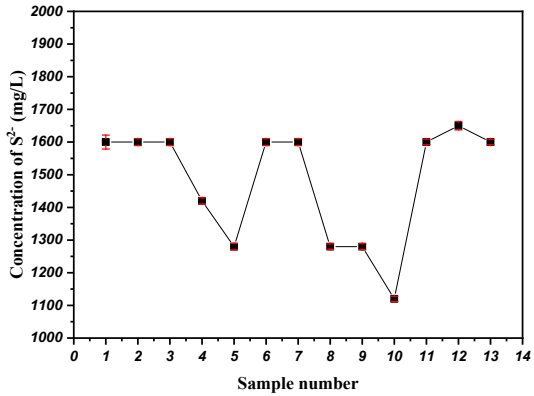

Figure 9 – Curve of the sulphide ion content monitoring in the unhairing wastewater from the tannery, the Batna Unit

Phosphorus analysis

Figure 10 shows the evolution of phosphates which vary between 44.66 and 736 mg/L with an average value of around 258.35 mg/L. These values are higher than the standard (1 mg/L); the presence of phosphates may be due to the use of detergents for rinsing the skin.

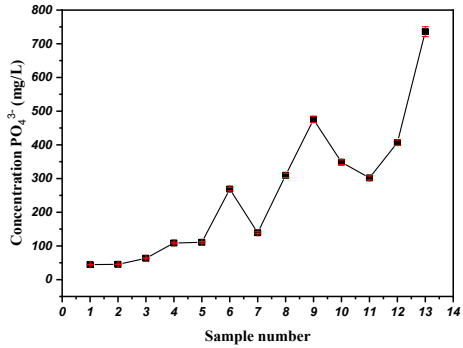

Figure 10 – Curve of the phosphate ion content monitoring in the unhairing wastewater from the tannery, the Batna Unit

Nitrogen analysis

From Figure 11, the ammonium ion concentration average was 16.3 mg/L with extreme values of 2 and 25 mg/L; these values are lower than the standard of the World Health Organization WHO (80 mg/L). As for the oxidized forms (nitrites and nitrates), the analyses indicate an average nitrite concentration of around 0.306 mg/L. However, for nitrates, the concentrations were more significant with an average value of around 28.8 mg/L (Figure 12) - this value is higher than the standard set by the WHO (1 mg/L). A high quantity of nitrate can contaminate underground water by infiltration, especially in cases where the soil is permeable.

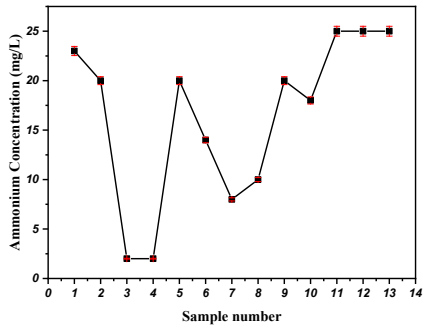

Figure 11 – Curve of the ammonium ion content monitoring in the unhairing wastewater from the tannery, the Batna Unit

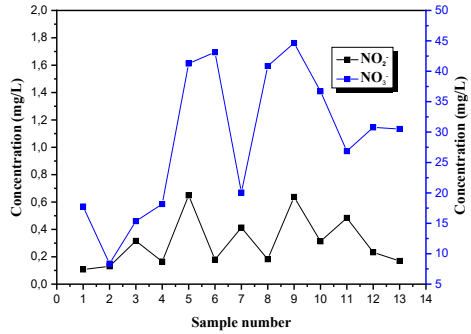

Figure 12 – Curve of the nitrite and nitrate ions content monitoring in the unhairing wastewater from the tannery, the Batna Unit

Analysis of organic pollution parameters (COD and BOD5)

For the studied samples, the COD values are between 23289 and 40000 mgO2/L with an average value of 30696 mg O_2/L (Figure 13); these values exceed the Algerian standard which is 1000 mg/L. As for BOD5, the values are 1150 to 2650 mg/l with an average of 1644.61 mg/L (Figure 14). In the tannery, around 75% of the organic load (measured as BOD5 or COD) is produced in the unhairing process. This high load of organic matter is mainly due to the biogenic material of hides and some used chemicals.

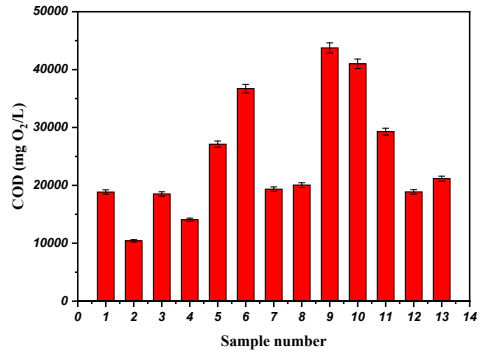

Figure 13 – Curve of the chemical oxygen demand monitoring in the unhairing wastewater from the tannery, the Batna Unit

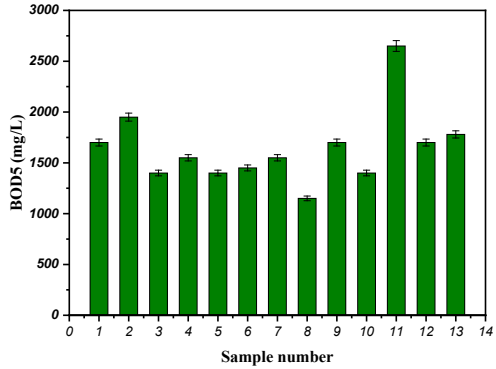

Figure 14 – Curve of the biochemical oxygen demand monitoring in the unhairing wastewater from the tannery, the Batna Unit

Calculation of the COD/BOD5 ratio

In this analysis, we calculated the COD/BOD5 ratio to assess the biodegradability (K coefficient) of the organic matter present in the unhairing wastewater from the tannery.

Table 1 – Values of the K coefficient for the studied samples

N° sample	1	2	3	4	5	6	7	8	9	10	11	12	13
K	6.6	3.2	7.9	5.4	11.6	15.1	7.4	10.4	15.4	17.5	6.6	6.62	7.1

The results shown in Table 1 indicate a high value of the K coefficient. These results suggest that the wastewater from the tannery's unhairing bath is not biodegradable. The primary cause of this is the presence of salts which inhibit bacterial growth. Therefore, biological treatment can be effective if combined with another treatment technique to reduce salinity.

Summary of the obtained results

The obtained results are summarized in Table 2.

Table 2 – Extreme and average values of the studied parameters

Parameter	Range	Average value
Temperature, °C	11-18	16
pH	12.04 – 13	12.47
Conductivity, mS	3.8 – 20.1	13.38
Turbidity, NTU	42 - 1000	416.3
TSS, mg/L	862.5 - 2220.8	1804.22
Calcium, mg/L	429.6 - 1296	808.27
Magnesium, mg/L	36 – 394.8	171
Sodium, mg/L	2103.82 – 8168.51	4659.92
Potassium, mg/L	184.89 - 1393	561.55
Chloride, mg/L	710 - 1212	906.91
Sulfide, mg/L	1120 - 1650	1479.23
Ortho phosphate, mg/L	44.66 - 736	258.35
Nitrate, mg/L	8.37 – 44.65	28.8
Nitrite, mg/L	0.107 – 0.649	0.306
Ammonium, mg/L	2 – 25	16.30
COD, mg O_2/L	10422.32 – 43747.97	30696
BOD5, mg O_2/L	1150 – 2650	1644.61

Conclusion

The results obtained from the comprehensive analysis of the unhairing bath wastewater indicate that the majority of the measured parameters exceed both national and European discharge standards. These findings highlight the substantial environmental impact of untreated tannery wastewater, reinforcing its role as a major source of pollution. The data gathered in this study provide essential baseline information that is critical for evaluating and developing effective wastewater treatment strategies.

The wastewater from the unhairing process exhibited a highly alkaline pH (12), elevated conductivity (13 mS), and significant concentrations of suspended solids (1800 mg/L) and sulfides (1500 mg/L). Additionally, the effluent contained excessive organic matter and demonstrated a high Chemical Oxygen Demand (30000 mg/L). The hair removal process was found to generate highly toxic and alkaline wastewater, enriched with

valuable organic compounds such as proteins, polypeptides, and free amino acids, resulting from the partial alkaline hydrolysis of skin proteins, including collagen and keratin.

While the leather industry plays a crucial role in utilizing slaughterhouse by-products to produce leather, its environmental impact remains considerable. The tanning process generates large volumes of contaminated wastewater, posing severe ecological risks. Despite its socio-economic contributions, such as job creation and income generation, the industry continues to face negative public perception due to its environmental footprint. Therefore, implementing sustainable wastewater management and treatment solutions is essential to mitigate pollution and enhance the industry's environmental sustainability.

References

Benhadji, A., Taleb Ahmed, M., Djelal, H. and Maachi, R. (2018) 'Electrochemical treatment of spent tan bath solution for reuse', Journal of Water Reuse and Desalination, 8, pp. 123–134. https://doi.org/10.2166/wrd.2016.123

Durai, G. and Rajasimman, M. (2011) 'Biological treatment of tannery wastewater – A review', Journal of Environmental Science and Technology, 1–17. Available at: http://scialert.net/fulltext/?doi=jest.2011.1.17&org=11

Floqi, T., Vezi, D. and Malollari, I. (2007) 'Identification and evaluation of water pollution from Albanian tanneries', Desalination, 213, pp. 56–64. https://doi.org/10.1016/j.desal.2006.03.603

Hasan, M.J., Alam, M.S., Mim, S., Haque, P. and Rahman, M.M. (2024) 'Pre-tanning of goatskin by minimizing chemical usage using crude protease enzyme for crust leather preparation', preprint, https://doi.org/10.21203/rs.3.rs-4196553/v1

Hashem, M.A., Khan, M.N.Z., Roy, P. and Hasan, M.A. (2021) 'Effect of oxidizers on sulphide removal from hair dissolving liming wastewater in tannery', Journal of Engineering Science, 12, pp. 67–72. https://doi.org/10.3329/jes.v12i3.57480

Mendoza-Roca, J., Galiana-Aleixandre, M., Lora-García, J. and Bes-Piá, A. (2010) 'Purification of tannery effluents by ultrafiltration in view of permeate reuse', Separation and Purification Technology, 70, pp. 296–301. https://doi.org/10.1016/j.seppur.2009.10.010

Morera, J.M., Bartolí, E. and Gavilanes, R.M. (2016) 'Hide unhairing: achieving lower pollution loads, decreased wastewater toxicity and solid waste reduction', Journal of Cleaner Production, 112, pp. 3040–3047. https://doi.org/10.1016/j.jclepro.2015.11.028

Rodier, J., Geoffray, C. and Rodi, L. (1996) L'analyse de l'eau: eaux naturelles, eaux résiduaires, eau de mer : chimie, physico-chimie, bactériologie, biologie. Paris: Dunod. ISBN: 2040014667.

Sawadogo, R., Guiguemde, I., Diendere, F., Diarra, J. and Bary, A. (2012) 'Caractérisation physico-chimique des eaux résiduaires de tannerie : cas de l'usine TANALIZ à Ouagadougou (Burkina Faso)', International Journal of Biological and Chemical Sciences, 6, pp. 7087–7095. https://doi.org/10.4314/ijbcs.v6i6.43

Tamersit, S. and Bouhidel, K.-E. (2020) 'Treatment of tannery unhairing wastewater using carbon dioxide and zinc cations for greenhouse gas capture, pollution removal and water recycling', Journal of Water Process Engineering, 34, 101120. https://doi.org/10.1016/j.jwpe.2019.101120

Tamersit, S., Bouhidel, K.-E. and Zidani, Z. (2018) 'Investigation of electrodialysis anti-fouling configuration for desalting and treating tannery unhairing wastewater: Feasibility of by-products recovery and water recycling', Journal of Environmental Management, 207, pp. 334–340. https://doi.org/10.1016/j.jenvman.2017.11.058

Zhao, J., Wu, Q., Tang, Y., Zhou, J. and Guo, H. (2022) 'Tannery wastewater treatment: conventional and promising processes, an updated 20-year review', Journal of Leather Science and Engineering, 4, 10. https://doi.org/10.1186/s42825-022-00082-7

Хемијски састав и токсичност отпадних вода из каде за уклањање длака при обради сирове коже: студија случаја штавионице у Батни, Алжир

Селма Бен Брахим, *Сабрина* Тамерсит, *Афаф Лалми,* **аутор за преписку***; Чахразад* Амране; *Фатима* Чемлал
Универзитет у Батни 1, Лабораторија за хемију и хемију животне средине, Универзитет у Батни 1, Алжир, Батна,

ОБЛАСТ: хемија животне средине
КАТЕГОРИЈА (ТИП) ЧЛАНКА: оригинални научни рад

Сажетак:

Увод/циљ: Индустрија коже у Алжиру значајно доприноси њеној економији, али се током процеса штављења стварају отпадне воде високог степена загађености. Циљ студије јесте да утврди хемијски састав отпадних вода из каде за уклањање длака при штављењу, као и да процени њихову токсичност на животну средину.

Методе: Анализирани су узорци отпадних вода из штавионице у Батни где су се прерађивале овчије и козје коже. Тринаест узорака је ручно прикупљено током 35 дана (од 5. априла до 10. маја 2022), а затим су извршене стандардне хемијске анализе за процену параметара попут pH вредности, проводљивости, укупних суспендованих материја (ТСС), сулфида, јона амонијака, као и протеина.

Резултати: Показано је да отпадне воде имају високу pH вредност (12,47 у просеку), високу проводљивост (13,38 mS/cm), као и знатно високе нивое загађивача: сулфида (1120–1650 mg/L), TSS (862–2220 mg/L) и хемијске потрошње кисеоника (10,422–43,747 mg/L). Отпадне воде су садржале и слободне аминокиселине и протеине, производе делимично хидролизованих протеина коже, што је повећавало њихову токсичност.

Закључак: Услед непречишћених отпадних вода пореклом из када за скидање длака при штављењу долази до великих ризика по животну средину. Стога се, ради смањења загађивања, наглашава потреба за ефикасним решењима за пречишћавање . Резултати пружају важан увид у еколошке изазове индустрије коже и истичу важност одрживог управљања отпадним водама.

Кључне речи: индустрија коже, загађивање, отпадне воде од скидања длака, карактеризација, отпадне воде, токсичност

Paper received on: 16.04.2025.
Manuscript corrections submitted on:12.05.2025.
Paper accepted for publishing on: 04.06.2025.

Enhancing the thermo-mechanical properties of the interface in composite materials based on the polysulfone polymer matrix

Khaled Bendahane[a], *Mohamed* Alami[b], *Allel* Mokaddem[c], *Mohammed* Belkheir[d], *Mehdi* Rouissat[e], *Bendouma* Doumi[f]

[a] Instrumentation and advanced materials laboratory, Institute of Science, University Center of Bayadh, 32000, Algeria
e-mail: k.bendahane@cu-elbayadh.dz , **corresponding author,**
ORCID iD: https://orcid.org/0009-0009-8408-9666
[b] Instrumentation and advanced materials laboratory, Institute of Science, University Center of Bayadh, Algeria
e-mail: alami.mohdz@gmail.com ,
ORCID iD: https://orcid.org/0000-0002-2106-2126
[c] Instrumentation and advanced materials laboratory, Institute of Science, University Center of Bayadh, Algeria
e-mail: a.mokaddem@cu-elbayadh.dz,
ORCID iD: https://orcid.org/0000-0002-2874-5923
[d] Instrumentation and advanced materials laboratory, Institute of Science, University Center of Bayadh, Algeria
e-mail: belkheir_m@yahoo.fr,
ORCID iD: https://orcid.org/0000-0003-1258-3656
[e] Instrumentation and advanced materials laboratory, Institute of Science, University Center of Bayadh, Algeria
e-mail: mehdi.m.rouissat@gmail.com,
ORCID iD: https://orcid.org/0000-0002-4444-2754
[f] Faculté des Sciences. Université Dr Tahar Moulay. Saida, Algérie
e-mail: bdoumma@gmail.com ,
ORCID iD: https://orcid.org/0000-0003-1563-8587
[g] Laboratoire STIC (Université de Tlemcen), Tlemcen, Algeria.

https://doi.org/10.5937/vojtehg73-53376

FIELD: materials sciences
ARTICLE TYPE:original scientific paper

Abstract

Introduction/purpose: Extensively engaged nanocomposite and biocomposite polymers reinforced with natural fibers as fillers possess the capability to not only augment material properties but also actively tackle challenges within green ecosystems. This versatile application underscored the dual benefits of improved material performance and a proactive commitment to environmental sustainability. The purpose of the present study was to investigate the temperature-induced damage to the fiber-matrix interface in various composite materials.

Methods: The study examined carbon/polysulfone, glass/polysulfone, and alfa/polysulfone biocomposite materials. A genetic approach based on the probabilistic formalism of Weibull was employed to model and analyze the interface damage caused by temperature variations.

Results: Notably, the alfa/polysulfone biocomposite emerged as a compelling alternative, showcasing cost-effectiveness and minimal environmental impact. Its fiber-matrix interface behavior closely paralleled that of carbon/polysulfone. The results revealed the remarkable resilience of the carbon/polysulfone composite's fiber-matrix interface to temperature impacts, distinguishing it from its counterparts.

Conclusions: This nuanced understanding provided valuable insights into the distinct responses of composite materials to temperature variations. It also underscored the advantageous characteristics of the alfa/polysulfone biocomposite, positioning it as a sustainable and efficient option in the field of reinforced polymers for modern applications.

Keywords: polysulfone, carbon, alfa, glass, interface, temperature

Introduction

The remarkable attributes of composite and biocomposite polymers have spurred researchers and manufacturers to delve deeper into this field (Manu et al., 2022; Agustiany et al., 2022; Chichane et al., 2023). The pursuit is centred on not only augmenting their existing properties but also innovating to introduce new materials suitable for a diverse array of contemporary applications. This exploration reflects a dynamic quest for advancements, aiming to continually broaden the scope of materials available for various present-day uses (Akhil et al., 2023; Mann et al., 2023). Composite materials are designed and produced through the arrangement of diverse components, including fibers (whether synthetic or natural), matrices (either thermoset or thermoplastic), fillers, and more (Sharma et al., 2023; Akter et al., 2024; Elfalehet al., 2023; Seydibeyoğlu et al., 2023). These constituents, initially immiscible, undergo a transformative process, resulting in the creation of new materials endowed with superior mechanical, thermal, and physicochemical properties (Rajeshkumar et al., 2023). These composites often exhibit superior strength (Syduzzaman et al., 2023), durability (Zuccarello et al., 2023), and resistance to environmental factors compared to their individual constituents (Nagalakshmaiah et al., 2019; Das Lala et al., 2018). Moreover, the advent of biocomposite polymers, where natural fibers or fillers are incorporated into a polymer matrix, reflects a conscious effort toward sustainability and eco-friendliness in material design (Lee & Jai, 2009; AL-Oqla & Omari, 2017). The applications of these advanced

materials are far-reaching, from aerospace to automotive industries (Asyraf et al., 2022; Al Maadeed & Ponnamma, 2023), in construction to offer novel solutions for durable and sustainable building materials (Alam et al., 2021). Additionally, the medical field benefits from biocomposite polymers, where their biodegradability and compatibility with biological systems open avenues for innovative biomedical devices and implants (Sivaraman et al., 2012; Teoh et al., 2016). In this study, we focus on a detailed examination of the influence of three specific fiber types: carbon fiber, glass fiber, and alfa fibers on the properties and performance of polysulfone (UPS). PSU is an amorphous matrix with an amber-colored transparency that resembles in its properties. This type of plastic with very good performance has a balanced ratio between high thermal stability, rigidity, toughness and high creep resistance. Due to its long-term strength and limited tendency to creep, PSU is predestined for long-term exposures. The primary objective is to gain a comprehensive understanding of how these reinforcing materials impact the polymer matrix. In the literature, numerous recent research studies have delved into the multifaceted impact of polysulfone across an array of practical and innovative applications. In (Nica et al., 2023), Nica et al. have characterized high-performance nanocomposite materials based on modified polysulfone using various amounts of modified carbon nanotube fillers for electronic applications. The study's findings unveiled a substantial improvement in the electrical conductivity of composite materials. This enhancement was particularly pronounced at higher filler loadings, suggesting promising prospects for the development of advanced electronic applications using these modified polysulfone nanocomposites. In another study (Stepashkin et al., 2023), Stepashkin et al. have investigated the impact of carbon fiber type, polymer mass fraction, and loading rate on tensile strength of polysulfone polymer using a polymer solution method. Scanning Electron Microscopy (SEM) analysis provided further insights, revealing that at low loading rates, elementary filaments within the impregnated fiber could align themselves along the applied load axis. This alignment, facilitated by the flow of the thermoplastic matrix under tensile stresses, led to more effective realization of the fiber's strength properties in thermoplastic-based composites compared to analogous composites with an epoxy matrix. In (Li et al., 2022), Li et al. studied the repercussions of hydrothermal aging on the long-term durability, specifically focusing on stress relaxation and creep properties, for both virgin and recycled PSU, where specimens of virgin and recycled polysulfone PSU were subjected to exposure to pure hot water at temperatures of 98 °C for varying durations ranging from 1 to

12 months. The findings of the study reveal that virgin PSU demonstrates exceptional resistance to hydrothermal aging across various mechanical parameters, including tensile, flexural, impact, and fracture toughness properties, as well as stress relaxation and creep resistance, even after a year of aging in 98 °C hot water. Additionally, the investigation establishes that the activation energy required for stress relaxation in PSU is consistent with that needed for creep. In another recent study (Lim et al., 2022), the authors have investigated the separation characteristics of polysulfone hollow fiber membranes for the removal of carbon dioxide and sulfur compounds from biogas. The research offers valuable insights into the impact of various operating conditions on the membrane's separation performance. Their findings revealed that the polysulfone membrane exhibited robust removal efficiency for sulfur compounds, ranging between 70% and 80%, within a feed pressure range of 2.3-2.6 bar. Importantly, the presence of sulfur compounds was observed to have a negligible effect on the separation performance of the polysulfone membrane. Building upon recent studies, this investigation focuses on probing the temperature-induced damage to the fiber-matrix interface in carbon/polysulfone and glass/polysulfone composite materials, as well as in alfa/polysulfone biocomposite material. The interesting mechanical properties of alfa fibers show that they can present an interesting alternative for the reinforcement of different polymer matrices.The study of morphological, physical and mechanical properties showed that alfa fibers present promising properties for use as reinforcement in composite materials. Its potential as reinforcement in composites requires the understanding of its microstructure, its mechanical properties, adequate control of fiber extraction as well as the transformation process (Brahim & Cheikh, 2007 ; Paiva et al., 2007; Bessadok et al., 2007; Bessadok et al., 2009; Arrakhiz et al., 2012; Marrakchi et al., 2012; Hamza et al., 2013; Mounir et al., 2014; Helaili & Chafra, 2014 ; Ghali et al., 2006).Traditional material characterization methods are efficient, but to characterize the behavior of a new material requires numerous physical tests (fracture, shear, bending, buckling, torsion, relaxation, etc.). These problems can be solved by adopting a more powerful AI-based strategy. This offers speed and precision in the development of new materials.

Artificial Intelligence (AI) tools, in our case, the approach employed is a genetic one, grounded in the probabilistic formalism of Weibull, can exploit and analyze large quantities of data to predict the properties of these materials, reducing the need for expensive and time-consuming physical testing. The obtained results revealed that the fiber-matrix interface of the carbon/polysulfone composite remained relatively

unaffected by temperature variations when contrasted with the interfaces of the alfa/polysulfone and glass/polysulfone composite and biocomposite materials. This insight contributes to a nuanced understanding of the diverse responses of different composite materials to temperature-induced stress, emphasizing the unique advantages and characteristics of the alfa/polysulfone biocomposite in this context.

Materials, models and methods

Polysulfone matrix (PSU)

Polysulfone (PSU) has one of the highest service temperatures of all high-performance melt-processable polymers. The high temperature nature of PSUs allows them to be used in demanding applications that other polymer materials cannot satisfy. PSU is highly resistant to acids, alkalis and electrolytes, oxidizing agents, surfactants and hydrocarbon oils. PSU is one of the so-called thermostable technical thermoplastic polymers. Indeed, the systematic presence, on the main chain, of aromatic nuclei, explains in particular the high thermal resistance of this polymer. Mechanical properties are retained by PSU over a wide range of temperatures. In addition, PSU is resistant to temperature, UV, gamma and X-ray radiation (De Leon et al., 2016; Mujika et al., 2002; Chukov et al., 2019; Solodilov et al., 2015; Yao et al., 2018; Anne, 2019).

Fibres

Carbon fiber (CF)

A number of carbon fiber reinforced composites based on thermoplastic have been developed and studied. Among thermoplastics, high-performance polymers are of particular interest due to their thermal stability and high mechanical properties. Carbon fiber composite materials are very popular for their lightness and strength, especially compared to steel, aluminum and even titanium. Aeronautics, for example, uses them extensively: in fact, the main cost of operating an aircraft is fuel and we reduce fuel consumption by reducing the weight of the plane. Carbon fiber is obtained by spinning a precursor prepolymer, generally polyacrylonitrile (or PAN). It is an unhardened plastic material that is made into a very fine wire. The latter is treated at high temperature in order to eliminate anything that is not pure carbon. This is carbonization: a process close to pyrolysis and similar to that which transforms wood into charcoal. The use of carbon rather than metals reduces weight without compromising the mechanical strength of the device. Motor racing, luxury cars, or manual devices also

use it, mainly for its lightness coupled with its resistance. Carbon is also used in luxury areas, for its beautiful appearance despite its high cost (Chukov et al., 2018). Figure 1 presents the structure of the composites reinforced with carbon fibers (a) initial and (b) oxidized at 500 °C (Chukov et al., 2018).

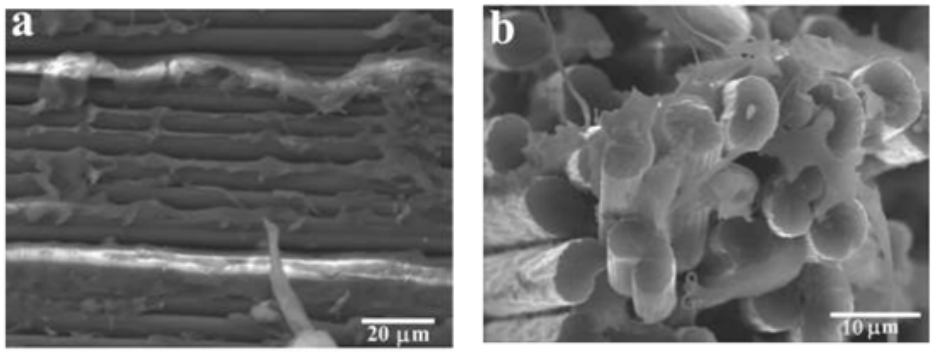

Figure 1– Structure of the composites reinforced with carbon fibers: (a) initial and (b) oxidized at 500 °C (Chukov et al., 2018).

Alfa fiber

Alfa plant fibers, also called lignocellulosic fibers, are rigid micro-fibrillar structures mainly composed of cellulose, hemicelluloses and lignin and in relatively small proportions of extractables and mineral materials. These natural fibers are low cost and low density fibers; they have specific properties, biodegradable and non-abrasive fibers (Saad, 2013). It has been studied from the point of view of chemical composition, evolution of the structure with the biological cycle, possibility of developing composites, surface modification by physico-chemical treatments, grafting, bleaching and production of paper with a study of the impact of various actions undergone by this fiber.

Glass fiber

As opposed to glass in massive forms, fiber glass with a diameter not exceeding a few microns loses its fragility and its sensitivity to cracking. Glass fibers show good mechanical characteristics. Depending on their composition, there are five types of glass fibers: E glasses which are for general use and which have good electrical properties, D glasses which have high dielectric properties, A glasses which have a high alkali content, C glasses which have good chemical resistance, and R and S glasses which have good mechanical resistance. Glass fibers are made up of

silica, alumina, lime, magnesia, boron oxide, fluorine, iron oxide, titanium oxide, sodium oxide, and oxide of potassium. The composition in percentage by mass of each chemical component varies from one type of fiber glass to another. (Hamlaoui, 2022).

Different physical properties of the constituents of the composite and biocomposite materials used in the genetic program have been mentioned in Table 1.

Table 1 – Physical properties of the constituents of the composite and biocomposite materials used in the genetic program.(Anne, 2019 ; Hamlaoui, 2022 ; Bourahli & Osmani, 2013 ; Biagiotti et al., 2004 ; Rowell, 2008; Moghaddam et al., 2016 ; Rao et al., 2007 ; Monteiro, 2011 ; Berthelot, 2005

Materials	Young's modulus (GPa)	Deformation at break (%)	Density (g/cm3)	Stress to break (MPa)
Carbon	230	4	1.7	4000
Alfa	21.5	2.4	1.4	247
Glass	73	4.4	2.6	3400
Polysulfone	3.1	4	1.24	80

Analytical models and genetic simulation

Thermal stress

Equation (1) is used to represent the thermal stresses that arise from the differential expansion of fibers and matrices. This occurs during the cooling process after the composite has been prepared at elevated temperatures (Weibull, 1939).

$$\sigma_f^T = E_f \frac{a}{a+1}(M_2 - M_0) \quad (1)$$

with:

$$M_0(T) = \int_{T_0}^{T_e} (\alpha_m - \alpha_f) dT$$

$$M_2(T) = \int_{T_e}^{T} (\alpha_m - \alpha_f) dT$$

- T_0: room temperature;
- T_e: temperature during the development process;
- T : test temperature; and

- α_f and α_m :expansion coefficients of the fiber and matrix, respectively. ($\alpha_{f\text{-}Carbon}$=1.2*10^{-6}/°C, $\alpha_{f\text{-}Glass}$= 1.2*10^{-6}/°C, and α_m=82*10^{-6} /°C)

Weibull approach

Weibull's statistical method has been utilized in the analysis of composite materials, assuming a uniform distribution of applied stress. The expressions for matrix and fiber damage are denoted by equations (2) and (3), respectively, and are elaborated upon in detail in reference (Lebrun, 1996). This approach involves using Weibull statistics to model stress distribution in composite materials, with equations (2) and (3) offering a quantitative representation of the damage to the matrix and fibers, guided by this statistical framework.

$$\boldsymbol{D_m = 1 - exp\left\{-\frac{V_{eff}}{V_0}\left(\frac{\sigma_f}{\sigma_0}\right)^m\right\}} \quad (2)$$

with :

- σ_f: applied stress;
- V_{eff}: matrix volume;
- $mand\sigma_0$: Weibull parameters; and
- V_0: initial volume of the matrix.

$$\mathbf{D_f = 1 - exp\left\{-A_f * L_{equi} * \left(\frac{\sigma^f_{max}}{\sigma_{of}}\right)^{m_f}\right\}} \quad (1)$$

with:

- σ^f_{max}: maximum stress applied to the fiber;
- σ_{0f}: initial stress applied to the fiber;
- m_f: Weibull parameters;
- A_f = π*a²; and
- L_{equi} : length of the fiber at equilibrium.

Genetic model

In this study, we will investigate the effect of temperature on the resistance and behavior of the fiber-matrix interface of composite materials (carbon/polysulfone and glass/polysulfone) and Alfa-polysulfone biocomposite material. The final performance of a composite material strongly depends on the quality of the fiber-matrix interface. This interfacial bond is quite difficult to model using deterministic models; in our case, we

chose genetic modeling based on the two Weibull equations (2 and 3) determining the damage of the fiber and that of the matrix. Our objective is to calculate the damage of the interface using the two aforementioned damage cases by the crossing operator (see the flowchart presented in Figure 2) (Lebrun, 1996; Belhadj et al., 2022; Belkheir et al., 2023; Mokaddem et al., 2012; Mokaddem et al., 2014; Benyamina et al., 2021).

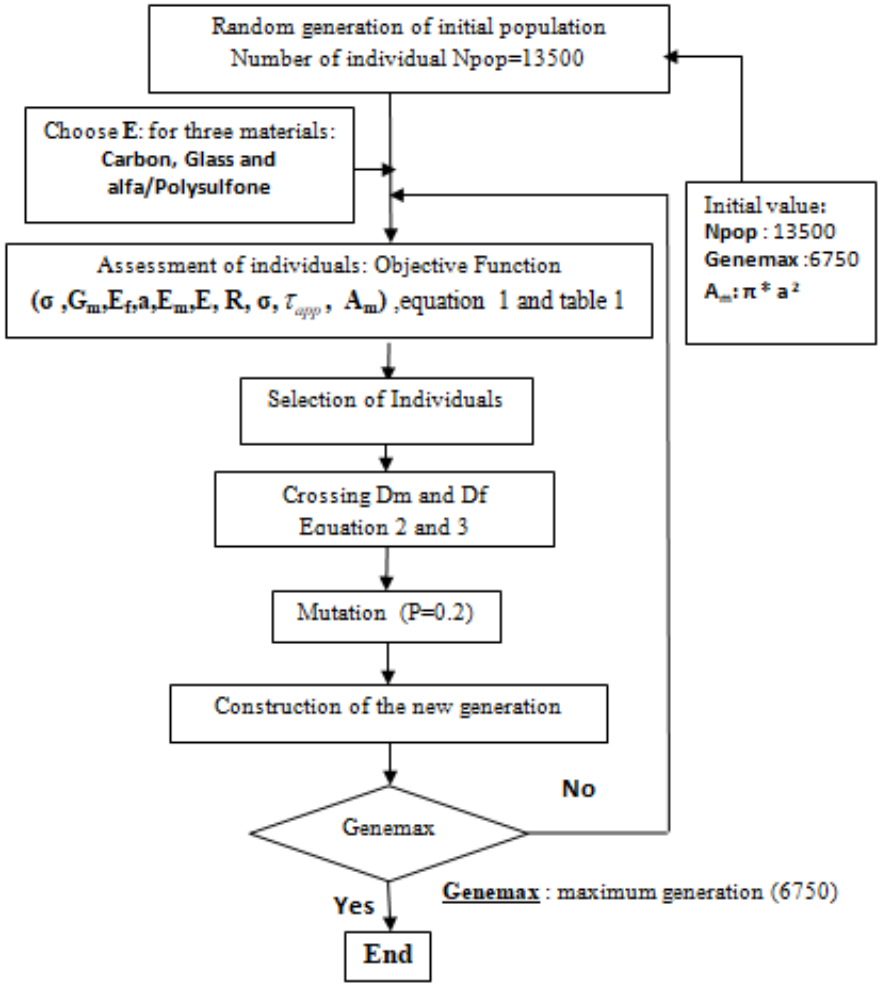

Figure 2– Genetic program flowchart

Results and discussion

In this work, the effect of temperature on damage to the fiber-matrix interface of carbon/polysulfone and glass/polysulfone composite materials, and alfa/polysulfone biocomposite material was investigated using a genetic approach based on the probabilistic formalism of Weibull (equations 2 and 3) (Belkheir et al., 2022; Belkheir et al., 2023). The damage at the interface was calculated by the genetic operator (crossover) using the two damage cases, one of the matrix and the other of the fiber given by equations (2) and (3), respectively. The random variables of the population consist of chromosomal genes representing the following variables: tensile stress (σ=600, 750, 900, 1050 and 1200MPa), Young's modulus, shear modulus of the matrix, fiber diameter, length of each fiber, and the half-distance R. This initial generated population is composed of 13500 individuals, which will be improved each time by the genetic operator mutation with a mutation probability of 0.2 (Mokaddem et al., 2020; Mokaddem et al., 2014). In each case, we used different values of the Young's modulus of each fiber and the Polysulfone matrix (Table1).The temperature variation for the five values of the mechanical stress and its influence on the damage of the interface was calculated and verified by equation (1). The results presented in Figures 3 to 5 refer to the level of interfacial damage as a function of temperature to the three composite and biocomposite materials studied (see the program flowchart in Figure 2).

Figures (3-5) show that the interface damage is strongly linked to the damage of the matrix which has the weakest constituent compared to the reinforcements (fibers), and show that the different temperature values applied to the three composite and biocomposite materials caused fiber-matrix interface damage which was lower for carbon/PSU, medium for Alfa/PSU and higher for glass/PSU. The fiber-matrix interface of the carbon/PSU composite was not influenced by temperature compared to the other interfaces of Alfa/PSU biocomposite material and glass/PSU composite material. The effect of temperature on the interface damage of the three studied composite and biocomposite materials shows almost the same results as those found by Dilyus Chukov et al.(Chukov et al., 2019). It should be noted that the alfa/polysulfone biocomposite material remains an interesting alternative given its very low environmental impact, a very low cost compared to other composite materials and that its fiber-matrix interface has a value that is close to the carbon/polysulfone interface. In this theoretical study, the fiber-matrix interface of the carbon/PSU composite was not influenced by the temperature compared to other interfaces of the Alfa/PSU and glass/PSU composite and biocomposite

materials. The results found, in particular those relating to the carbon/polysulfone interface, are in good agreement with the results found by Dilyus Chukov et al.(Chukov et al., 2019).

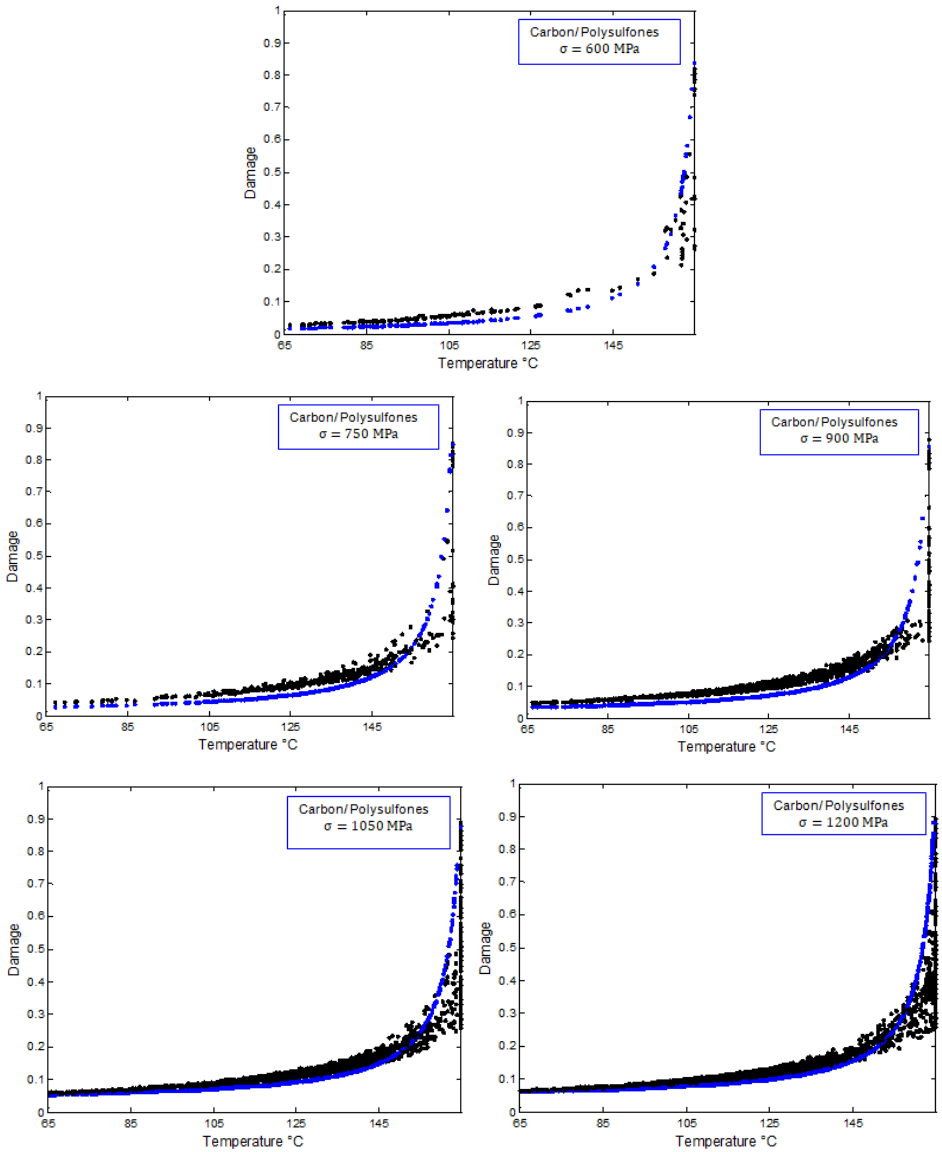

Figure 3– Temperature effect on the fiber matrix interface of the carbon/polysulfone composite

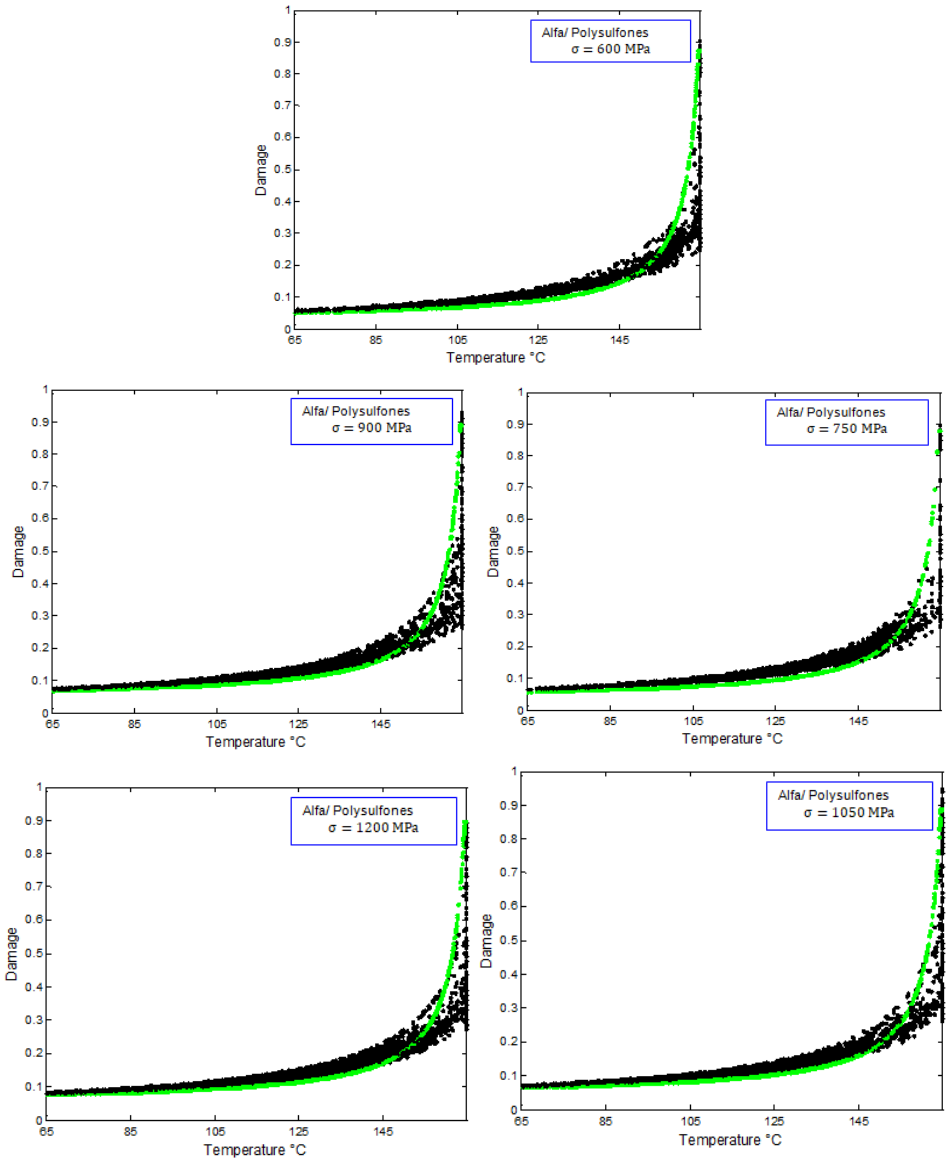

Figure 4– Temperature effect on the fiber matrix interface of the alfa/polysulfone biocomposite

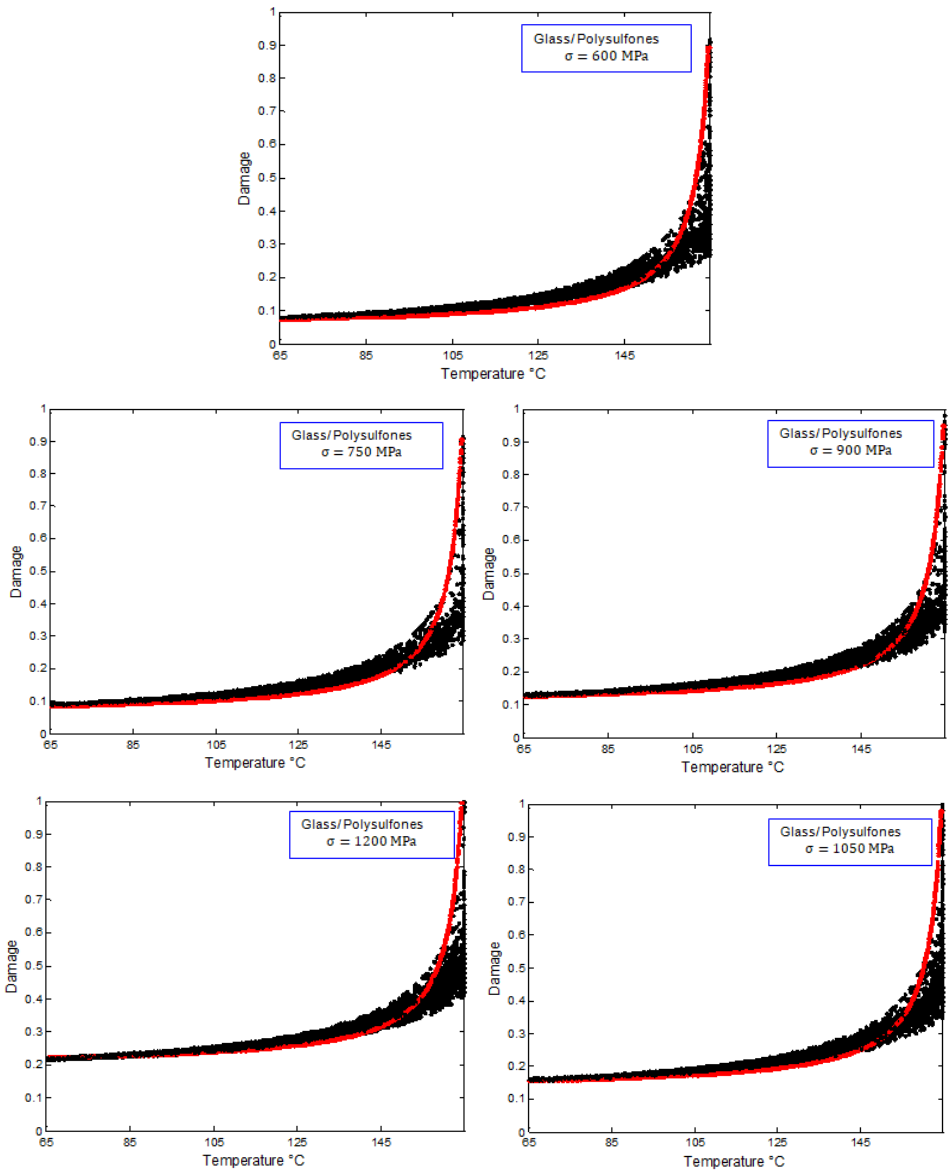

Figure 5– Temperature effect on the fiber matrix interface of the glass/polysulfone composite

In various studies carried out on composite materials, the fiber has a direct influence on the behavior of the fiber-matrix interface in relation to the matrix because fibers transmit their mechanical properties to the matrix

and this in terms of rigidity, resistance to breakage, hardness, etc. The reinforcements also confer their physical properties to the resin. Among these properties, we can cite Young's modulus, mechanical behavior, fire resistance, and abrasion resistance (Prakash et al., 2021; Pan, 2022; Ramesh et al., 2021).

Conclusions

The present study focuses on the influence wielded by three distinct fiber types (carbon fiber, glass fiber, and alfa fibers) on the properties and performance of polysulfone. The overarching objective is to attain a comprehensive understanding of how these reinforcing materials exert their influence on the polymer matrix, based on a genetic approach. In the theoretical exploration conducted, it was observed that the fiber-matrix interface of the carbon/PSU composite exhibited a notable resistance to temperature effects in contrast to the interfaces of the Alfa/PSU and glass/PSU composite and biocomposite materials. This finding emphasizes the distinct thermal behavior exhibited by these composite interfaces, highlighting the relative stability of the carbon/PSU composite's fiber-matrix interface under varying temperature conditions. This insight contributes to refining the understanding of how different composite materials respond to temperature-induced stress on their fiber-matrix interfaces.

References

Agustiany, E.A., Rasyidur Ridho, M., Rahmi D.N., M., Madyaratri, E.W., Falah, F., Lubis, M.A.R., Solihat, N.N., Syamani, F.A., Karungamye, P., Sohail, A., Nawawi, D.S., Prianto, A.H., Iswanto, A.H., Ghozali, M., Restu, W.K., Juliana, I., Antov, P., Kristak, L., Fatriasari, W., & Fudholi, A. 2022. Recent developments in lignin modification and its application in lignin-based green composites: A review. *Polymer Composites*, 43(8), pp.4848-4865. Available at: https://doi.org/10.1002/pc.26824

Akhil, U. V., Radhika, N., Saleh, B., Aravind Krishna, S., Noble, N., & Rajeshkumar, L. 2023. A comprehensive review on plant-based natural fiber reinforced polymer composites: Fabrication, properties, and applications. *Polymer Composites*, 44(5), pp.2598-2633. Available at: https://doi.org/10.1002/pc.27274

Akter, M., Uddin, M.H. & Anik, H.R. 2024. Plant fiber-reinforced polymer composites: A review on modification, fabrication, properties, and applications. *Polymer Bulletin (Berlin, Germany)*, 81(1), pp.1-85. Available at: https://doi.org/10.1007/s00289-023-04733-5

Al Maadeed, M.A.A. & Ponnamma, D. 2023. Fiber chemistry and technology: Their contributions to shaping Society 5.0. *Discover Nano*, 18(115). Available at: https://doi.org/10.1186/s11671-023-03888-4

Alam, M.A., Sapuan, S.M., Ya, H.H., Hussain, P.B., Azeem, M. & Ilyas, R.A. 2021. Application of biocomposites in automotive components: A review. In *Biocomposite and Synthetic Composites for Automotive Applications*. Elsevier, Amsterdam, The Netherlands, pp.1-17. Available at: https://doi.org/10.1016/B978-0-12-820559-4.00001-8

AL-Oqla, F.M. & Omari, M.A. 2017. Sustainable biocomposites: Challenges, potential and barriers for development. in *Green Energy and Technology*. Cham: Springer International Publishing, pp. 13–29. Available at: https://doi.org/10.1007/978-3-319-46610-1_2

Anne M. 2019. *Polymères - VI. Propriétés mécaniques*. *PHYS0904 : Physique des Matériaux, Liège Université*, 02/04/2019. Available at: http://www.metaux.ulg.ac.be/Fichierpourtelech/Pol-VI-2019.pdf

Arrakhiz, F.Z., El Achaby, M., Malha, M., Bensalah, M.O., Fassi-Fehri, O., Bouhfid, R. & Qaiss, A. 2012. Mechanical and thermal properties of polypropylene reinforced with Alfa fiber under different chemical treatment. *Materials in Engineering*, 35, pp. 318–322. Available at: https://doi.org/10.1016/j.matdes.2011.09.023

Asyraf, M.R. M., Ilyas, R.A., Sapuan, S.M., Harussani, M. M., Hariz, H. M., Aiman, J.M., Baitaba, D.M., Sanjay, M. R., Ishak, M. R., Norkhairunnisa, M., Sharma, S., Alam, M. A. & Asrofi, M. 2022. Advanced composite in aerospace applications: Opportunities, challenges, and future perspective. *Advanced Composites in Aerospace Engineering Applications*, Cham: Springer International Publishing, pp. 471–498. Available at: https://doi.org/10.1007/978-3-030-88192-4_24

Belhadj, F. A., Belkheir, M., Mokaddem, A., Doumi, B. & Boutaous, A. 2022. Numerical characterization of the humidity effect on the fiber-matrix interface damage of hybrid composite material based on vinyl ester polymer matrix for engineering applications. *Emergent Materials*, 5(2), pp. 591–600. Available at: https://doi.org/10.1007/s42247-022-00353-3

Belkheir, M., Alami, M., Mokaddem, A., Doumi, B. & Boutaous, A. 2022. An investigation on the effect of humidity on the mechanical properties of composite materials based on polymethyl methacrylate polymer optical fibers (POFs). *Fibers and Polymers*, 23(10), pp. 2897–2906. Available at: https://doi.org/10.1007/s12221-022-4164-6

Belkheir, M., Boutaleb, M., Mokaddem, A. & Doumi, B. 2023. Predicting the effect of coconut natural fibers for improving the performance of biocomposite materials based on the poly (methyl methacrylate)-PMMA polymer for engineering applications. *Polymer Bulletin (Berlin, Germany)*, 80(2), pp. 1975–1996. Available at: https://doi.org/10.1007/s00289-022-04166-6

Belkheir, M., Rouissat, M., Mokaddem, A. & Boutaous, A. 2023. Effect of carbon nanotube (CNT)-reinforced polymers and biopolymer matrix on interface

damage of nanocomposite materials. *Emergent Materials*, 6(5), pp. 1589–1602. Available at: https://doi.org/10.1007/s42247-023-00547-3

Benyamina, B., Mokaddem, A., Doumi, B., Belkheir, M. & Elkeurti, M. 2021. Study and modeling of thermomechanical properties of jute and Alfa fiber-reinforced polymer matrix hybrid biocomposite materials. *Polymer Bulletin (Berlin, Germany)*, 78(4), pp. 1771–1795. Available at: https://doi.org/10.1007/s00289-020-03183-7

Berthelot, J.M. 2005. *Matériaux composites : comportement mécanique et analyse des structures*. 4e édition. Paris Londres New York : Tec et Doc. ISBN 978-2-7430-0771-3. Available at: https://books.google.dz/books?id=wN7uAQAACAAJ

Bessadok, A., Marais, S., Gouanvé, F., Colasse, L., Zimmerlin, I., Roudesli, S. & Métayer, M. 2007. Effect of chemical treatments of Alfa (Stipa tenacissima) fibres on water-sorption properties. *Composites Science and Technology*, 67(3–4), pp. 685–697. Available at: https://doi.org/10.1016/j.compscitech.2006.04.013

Bessadok, A., Roudesli, S., Marais, S., Follain, N. & Lebrun, L. 2009. Alfa fibres for unsaturated polyester composites reinforcement: Effects of chemical treatments on mechanical and permeation properties. *Composites Part A: Applied Science and Manufacturing*, 40(2), pp. 184–195. Available at: https://doi.org/10.1016/j.compositesa.2008.10.018

Biagiotti, J., Puglia, D. & Kenny, J.M. 2004. A review on natural fibre-based composites-part I: Structure, processing and properties of vegetable fibres. *Journal of Natural Fibers*, 1(2), pp.37–68. Available at: https://doi.org/10.1300/j395v01n02_04

Bourahli, M.E.H. & Osmani, H. 2013. Chemical and mechanical properties of Diss (*Ampelodesmos mauritanicus*) fibers. *Journal of Natural Fibers*, 10(3), pp.219–232. Available at: https://doi.org/10.1080/15440478.2012.761115

Brahim, S.B. & Cheikh, R.B. 2007. Influence of fibre orientation and volume fraction on the tensile properties of unidirectional Alfa-polyester composite. *Composites Science and Technology*, 67(1), pp.140–147. Available at: https://doi.org/10.1016/j.compscitech.2005.10.006

Chichane, A., Boujmal, R. & El Barkany, A. 2023. Bio-composites and bio-hybrid composites reinforced with natural fibers: Review. *Materials Today: Proceedings*, 72, pp.3471–3479. Available at: https://doi.org/10.1016/j.matpr.2022.08.132

Chukov, D.I., Nematulloev, S.G., Tcherdyntsev, V.V., Torokhov, V.G., Stepashkin, A.A., Zadorozhnyy, M.Y., Zherebtsov, D.D. & Sherif, G. 2019. Structure and properties of polysulfone filled with modified twill weave carbon fabrics. *Polymers*, 12(1), 50. Available at: https://doi.org/10.3390/polym12010050

Chukov, D.I., Nematulloev, S.G., Stepashkin, A., Maksimkin, A., Zherebtsov, D. & Tcherdyntsev, V.V. 2018. Novel carbon fibers reinforced composites based on polysulfone matrix. *MATEC Web of Conferences*, 242, pp.01004. Available at: https://doi.org/10.1051/matecconf/201824201004

Chukov, D.I., Nematulloev, S.G., Torokhov, V., Stepashkin, A., Sherif, G. & Tcherdyntsev, V. 2019. Effect of carbon fiber surface modification on their

interfacial interaction with polysulfone. *Results in Physics*, 15, 102634. Available at: https://doi.org/10.1016/j.rinp.2019.102634

Das Lala, S., Deoghare, A. B. & Chatterjee, S. 2018. Effect of reinforcements on polymer matrix bio-composites – an overview. *Science and Engineering of Composite Materials*, 25(6), p.1039–1058. Available at: https://doi.org/10.1515/secm-2017-0281

de Leon, A. C., Chen, Q., Palaganas, N. B., Palaganas, J. O., Manapat, J. & Advincula, R. C. 2016. High performance polymer nanocomposites for additive manufacturing applications. *Reactive et Functional Polymers*, 103, pp.141–155. Available at: https://doi.org/10.1016/j.reactfunctpolym.2016.04.010

Elfaleh, I., Abbassi, F., Habibi, M., Ahmad, F., Guedri, M., Nasri, M. et Garnier, C. 2023. A comprehensive review of natural fibers and their composites: An eco-friendly alternative to conventional materials. *Results in Engineering*, 19, 101271. Available at: https://doi.org/10.1016/j.rineng.2023.101271

Ghali, L., Zidi, M. & Roudesli, S. 2006. Physical and mechanical characterization of technical Esparto (Alfa) fibres. *Journal of Applied Sciences (Faisalabad, Pakistan)*, 6(11), pp.2450–2455. Available at: https://doi.org/10.3923/jas.2006.2450.2455

Hamlaoui, O. 2022. *Étude de l'endommagement d'un composite de fibres de verres : application à une opération de rivetage par compression*. Ph.D. thesis, CY Cergy Paris Université. Available at: https://theses.fr/api/v1/document/2022CYUN1114

Hamza, S., Saad, H., Charrier, B., Ayed, N. & Charrier-El Bouhtoury, F. 2013. Physico-chemical characterization of Tunisian plant fibers and its utilization as reinforcement for plaster-based composites. *Industrial Crops and Products*, 49, pp.357–365. Available at: https://doi.org/10.1016/j.indcrop.2013.04.052

Helaili, S. & Chafra, M. 2014. Anisotropic visco-elastic properties identification of a natural biodegradable ALFA fiber composite. *Journal of Composite Materials*, 48(13), pp.1645–1658. Available at: https://doi.org/10.1177/0021998313488811

Lebrun, G.A. 1996. *Ph.D. Dissertation*. Université de Bordeaux. Available at: https://hal.science/tel-03616963/

Lee, L. S. & Jain, R. 2009. The role of FRP composites in a sustainable world. *Clean Technologies and Environmental Policy*, 11(3), pp.247–249. Available at: https://doi.org/10.1007/s10098-009-0253-0

Li, Z., Yu, L. & Yan, Z. 2022. Effect of hydrothermal aging on mechanical properties and long-term durability of recycled polysulfone. *Journal of Polymers and the Environment*, 30(1), pp.92–101. Available at: https://doi.org/10.1007/s10924-021-02182-7

Lim, Y.-G., Bak, C.-U. & Kim, Y.-D. 2022. Comprehensive experimental and theoretical insights into the performance of polysulfone hollow-fiber membrane modules in biogas purification process. *Chemical Engineering Journal (Lausanne, Switzerland: 1996)*, 433, 134616. Available at: https://doi.org/10.1016/j.cej.2022.134616

Mann, G. S., Azum, N., Khan, A., Rub, M. A., Hassan, M. I., Fatima, K. & Asiri, A. M. 2023. Green composites based on animal fiber and their applications for a sustainable future. *Polymers*, 15(3), pp.601. Available at: https://doi.org/10.3390/polym15030601

Manu, T., Nazmi, A.R., Shahri, B., Emerson, N. & Huber, T. 2022. Biocomposites: A review of materials and perception. *Materials Today: Communications*, 31, 103308. Available at: https://doi.org/10.1016/j.mtcomm.2022.103308

Marrakchi, Z., Oueslati, H., Belgacem, M. N., Mhenni, F. & Mauret, E. 2012. Biocomposites based on polycaprolactone reinforced with alfa fibre mats. *Composites Part A: Applied Science and Manufacturing*, 43(4), pp.742–747. Available at: https://doi.org/10.1016/j.compositesa.2011.12.027

Moghaddam, M. K., Safi, S., Hassanzadeh, S. & Mortazavi, S. M. 2016. Sound absorption characteristics of needle-punched sustainable Typha/polypropylene non-woven. *Journal of the Textile Institute*, 107(2), pp.145–153. Available at: https://doi.org/10.1080/00405000.2015.1016346

Mokaddem, A., Alami, M., Doumi, B. & Boutaous, A. 2012. A study by a genetic algorithm for optimizing the arrangement of the fibers on the damage to the fiber–matrix interface of a composite material. *Journal of the Textile Institute*, 103(12), pp.1376–1382. Available at: https://doi.org/10.1080/00405000.2012.727587

Mokaddem, A., Alami, M., Doumi, B. & Boutaous, A. 2014. Prediction by a genetic algorithm of the fiber–matrix interface damage for composite material. Part 1. Study of shear damage in two composites T300/914 and PEEK/APC2. *Strength of Materials*, 46(4), pp.543–547. Available at: https://doi.org/10.1007/s11223-014-9580-4

Mokaddem, A., Alami, M., Ziani, N., Beldjoudi, N. & Boutaous, A. 2014. Prediction by a genetic algorithm of the fiber–matrix interface damage for composite material. Part 2. Study of shear damage in graphite/epoxy nanocomposites. *Strength of Materials*, 46(4), pp.548–552. Available at: https://doi.org/10.1007/s11223-014-9581-3

Mokaddem, A., Doumi, B., Belkheir, M. & Touimi, A. 2020. Comparative analysis on the elastic behavior of composite materials based on plant fibers: Bamboo/Epoxy and coconut/Epoxy. *Current Materials Science*, 12(2), pp.127–135. Available at: https://doi.org/10.2174/2666145412666191106111630

Monteiro, S.N., Lopes, F.P.D., Barbosa, A.P., Bevitori, A.B., Silva, I.L.A.D. & Costa, L.L.D. 2011. Natural lignocellulosic fibers as engineering materials—an overview. *Metallurgical and Materials Transactions A*, 42(10), pp.2963–2974. Available at: https://doi.org/10.1007/s11661-011-0789-6

Mounir, J., Slah, W. B. M. & Mohamed, B. 2014. Characterization of mechanical extracted alfa fibres. *International Journal of Fiber and Textile Research*, 4(1), pp.1-4 [online]. Available at:https://fr.scribd.com/document/505101989/Fibres-Alfa-Article [Accessed: 28.November 2023.].

Mujika, F., De Benito, A., Fernández, B., Vázquez, A., Llano-Ponte, R. & Mondragon, I. 2002. Mechanical properties of carbon woven reinforced epoxy matrix composites. A study on the influence of matrix modification with polysulfone. *Polymer Composites*, 23(3), pp.372–382. Available at: https://doi.org/10.1002/pc.10439

Nagalakshmaiah, M., Afrin, S., Malladi, R. P., Elkoun, S., Robert, M., Ansari, M. A., Svedberg, A. & Karim, Z. 2019. Biocomposites. In: *Green Composites for Automotive Applications*. Elsevier, pp.197–215. Available at: https://doi.org/10.1016/B978-0-08-102177-4.00009-4

Nica, S. L., Asandulesa, M., Stoica, I., Varganici, C.-D., Ursu, E.-L., Gaina, C., Timpu, D. & Albu, R.M. 2023. Tailoring the features of modified polysulfone/carbon filler nanocomposites to enhance physical properties for electronic applications. *Materials Today Chemistry*, 33, 101711. Available at: https://doi.org/10.1016/j.mtchem.2023.101711

Paiva, M., Ammar, I., Campos, A., Cheikh, R. & Cunha, A. 2007. Alfa fibres: Mechanical, morphological and interfacial characterization. *Composites Science and Technology*, 67(6), pp. 1132–1138. Available at: https://doi.org/10.1016/j.compscitech.2006.05.019

Pan, Y. 2022. Mechanical and microstructural characteristics of the fiber-reinforced composite materials. *Journal of Minerals and Materials Characterization and Engineering*, 10(06), pp. 477–488. Available at: https://doi.org/10.4236/jmmce.2022.106034

Prakash, K. B., Fageehi, Y. A., Saminathan, R., Manoj Kumar, P., Saravanakumar, S., Subbiah, R., Arulmurugan, B. & Rajkumar, S. 2021. Influence of fiber volume and fiber length on thermal and flexural properties of a hybrid natural polymer composite prepared with banana stem, pineapple leaf, and S-glass. *Advances in Materials Science and Engineering*, 2021(1), pp. 1–11. Available at: https://doi.org/10.1155/2021/6329400

Rajeshkumar, L., Ramesh, M., Bhuvaneswari, V., Balaji, D. & Deepa, C. 2023. Synthesis and thermomechanical properties of bioplastics and biocomposites: a systematic review', *Journal of Materials Chemistry B*, 11(15), pp. 3307–3337. Available at: https://doi.org/10.1039/d2tb02221d

Ramesh, M., Rajeshkumar, L. & Balaji, D. 2021. Influence of process parameters on the properties of additively manufactured fiber-reinforced polymer composite materials: A review. *Journal of Materials Engineering and Performance*, 30(7), pp. 4792–4807. Available at: https://doi.org/10.1007/s11665-021-05832-y

Rao, K.M.M., Prasad, A.V.R., Babu, M.N.V.R., Rao, K. M. & Gupta, A.V.S.S.K.S. 2007. Tensile properties of elephant grass fiber reinforced polyester composites. *Journal of Materials Science*, 42(9), pp.3266–3272. Available at: https://doi.org/10.1007/s10853-006-0657-8

Rowell, R.M. 2008. Natural fibres: types and properties. *Properties and Performance of Natural-Fibre Composites*. Elsevier, pp. 3–66. Available at: https://doi.org/10.1533/9781845694593.1.3

Saad, H. 2013. Développement *de bio-composites à base de fibres végétales et de colles écologiques*. PhD thesis. Université de Pau.

Seydibeyoğlu, M.Ö., Dogru, A., Wang, J., Rencheck, M., Han, Y., Wang, L., Seydibeyoğlu, E.A., Zhao, X., Ong, K., Shatkin, J.A., Shams Es-haghi, S., Bhandari, S., Ozcan, S. & Gardner, D.J. 2023. Review on hybrid reinforced polymer matrix composites with nanocellulose, nanomaterials, and other fibers', *Polymers*, 15(4), p. 984. Available at: https://doi.org/10.3390/polym15040984

Sharma, H., Kumar, A., Rana, S., Sahoo, N.G., Jamil, M., Kumar, R., Sharma, S., Li, C., Kumar, A., Eldin, S.M. & Abbas, M. 2023. Critical review on advancements on the fiber-reinforced composites: Role of fiber/matrix modification on the performance of the fibrous composites', *Journal of Materials Research and Technology*, 26, pp. 2975–3002. Available at: https://doi.org/10.1016/j.jmrt.2023.08.036

Sivaraman, K.M., Kellenberger, C., Pané, S., Ergeneman, O., Lühmann, T., Luechinger, N. A., Hall, H., Stark, W.J. & Nelson, B.J. 2012. Porous polysulfone coatings for enhanced drug delivery. *Biomedical Microdevices*, 14(3), pp. 603–612. Available at: https://doi.org/10.1007/s10544-012-9639-6

Solodilov, V.I., Korokhin, R.A., Gorbatkina, Y.A. & Kuperman, A.M., 2015. Comparison of fracture energies of epoxy-polysulfone matrices and unidirectional composites based on the. *Mechanics of Composite Materials*, 51(2), pp. 177–190. Available at: https://doi.org/10.1007/s11029-015-9488-5

Stepashkin, A.A., Mohammad, H., Makarova, E.D., Odintsova, Y.V., Laptev, A.I. & Tcherdyntsev, V.V. 2023. Deformation behavior of single carbon fibers impregnated with polysulfone by polymer solution method. *Polymers*, 15(3), p. 570. Available at: https://doi.org/10.3390/polym15030570

Syduzzaman, M., Sultana Rumi, S., Faiza Fahmi, F., Akter, M. & Begum Dina, R. 2023. Mapping the recent advancements in bast fiber reinforced biocomposites: A review on fiber modifications, mechanical properties, and their applications. *Results in Materials*, 20, 100448. Available at: https://doi.org/10.1016/j.rinma.2023.100448

Teoh, S.H., Tang, Z.G. & Hastings, G.W. 2016. Chapter 3 thermoplastic polymers in biomedical applications: Structures, properties and processing. *Handbook of Biomaterial Properties*. New York, NY: Springer New York, pp. 261–290. https://doi.org/10.1007/978-1-4939-3305-1_19

Weibull, W. 1939. A statistical theory of the strength of materials', *Royal Swedish Academy of Engineering Sciences Proceedings*, 151, pp. 1–45.

Yao, S.-S., Jin, F.-L., Rhee, K. Y., Hui, D. & Park, S.-J., 2018. Recent advances in carbon-fiber-reinforced thermoplastic composites: A review. *Composites Part B: Engineering*, 142, pp. 241–250. Available at: https://doi.org/10.1016/j.compositesb.2017.12.007

Zuccarello, B., Militello, C. & Bongiorno, F. 2023. Environmental aging effects on high-performance biocomposites reinforced by sisal fibers. *Polymer Degradation and Stability*, 211, 110319. Available at: https://doi.org/10.1016/j.polymdegradstab.2023.110319..

Побољшавање термомеханичких својстава интерфејса код композитних материјала на бази полисулфонске полимерне матрице

Калед Бендахане[а], **аутор за преписку**, Мохамед Алами[а], *Алел* Мокадем[а], *Мохамед* Белкеир[а], *Меди* Роуисат[а], *Бендума* Думи[б]
[а] Лабораторија за инструментацију и напредне материјале, Институт за науку, Универзитетски центар Бајад, Алжир
[б] Природно-математички факултет. Универзитет др Тахар Мулеј. Саида, Алжир

ОБЛАСТ: материјали
КАТЕГОРИЈА (ТИП) ЧЛАНКА: оригинални научни рад

Сажетак:

Увод/циљ: Универзално употребљавани нанокомпозитни и биокомпозитни полимери ојачани природним влакнима као пунилима имају способност не само да побољшавају својства материјала него и активно решавају изазове у зеленим екосистемима. Овом разноврсношћу употребе наглашава се двострука корист – побољшане перформансе материјала, као и проактивна посвећеност еколошкој одрживости. Циљ ове студије био је испитивање оштећења проузрокованог температуром на интерфејсу влакно-матрица у различитим композитним материјалима.

Методе: Испитивани су карбон-полисулфонски, стакло-полисулфонски и алфа-полисулфонски биокомпозитни материјали. Генетички приступ заснован на пробабилистичком формализму Вејбула примењен је за моделовање и анализу оштећења интерфејса услед температурних варијација.

Резултати: Алфа-полисулфон биокомпозит показао се као одлична алтернатива захваљујући исплативости и минималном утицају на животну средину. Понашање његовог интерфејса влакно-матрица веома је слично понашању интерфејса карбон-полисулфон. Резултати су показали изузетну отпорност интерфејса влакно-матрица код карбон-полисулфонског композита на утицај температуре, што га издваја од осталих.

Закључак: Представљени су драгоцени увиди у различите одговоре композитних материјала на температурне варијације. Такође, наглашене су карактеристике алфа-полисулфонског биокомпозита које му, као одрживом и ефикасном решењу, дају предност у области ојачаних полимера за модерне примене.

Кључне речи: полисулфон, карбон, алфа, стакло, интерфејс, температура

Paper received on: 11.09.2024.
Manuscript corrections submitted on:10.12.2024.
Paper accepted for publishing on: 22.01.2025.

Impact of electrolytic hydrogen charging on the mechanical properties and microstructure of AISI 304 austenitic stainless steel

Amar Abboub[a], *Ahmed* Aboura[b], *Khaled* Benmahdi[c], *Mohamed* Sadoun[d], *Mohamed* Boukhelef[e]

[a] Mustapha Stambouli University, Faculty of Sciences and Technology, Department of Mechanical Engineering, Mascara, People's Democratic Republic of Algeria, e-mail: abboub.amar@yahoo.com, **corresponding author**, ORCID iD: https://orcid.org/0009-0004-0158-5837

[b] Ahmed Zabana University, Faculty of Sciences and Technology, Department of Mechanical Engineering, Relizane, People's Democratic Republic of Algeria, e-mail: ahmed.aboura@univ-relizane.dz, ORCID iD: https://orcid.org/0009-0005-3509-2026

[c] Mustapha Stambouli University, Faculty of Sciences and Technology, Department of Civil Engineering, Laboratory for the Study of Structures and Mechanics of Materials, Mascara, People's Democratic Republic of Algeria, e-mail: k.benmahdi@univ-mascara.dz, ORCID iD: https://orcid.org/0000-0002-8244-5817

[d] Mustapha Stambouli University, Faculty of Sciences and Technology, Department of Civil Engineering, Laboratory for the Study of Structures and Mechanics of Materials, Mascara, People's Democratic Republic of Algeria, e-mail: m.sadoun@univ-mascara.dz, ORCID iD: https://orcid.org/0009-0008-2314-9402

[e] Mustapha Stambouli University, Faculty of Sciences and Technology, Department of Mechanical Engineering, Mascara, People's Democratic Republic of Algeria, e-mail: mohamed.boukhelef@univ-mascara.dz, ORCID iD: https://orcid.org/0009-0003-1897-9536

https://doi.org/10.5937/vojtehg73-56087

FIELD: materials
ARTICLE TYPE: original scientific paper

Abstract:

Introduction/purpose: Hydrogen embrittlement (HE) substantially decreases the mechanical properties of austenitic stainless steels, constraining their efficacy in diverse applications. This study examines the impact of electrolytic hydrogen charging on the mechanical characteristics and microstructure of AISI304 stainless steel, a commonly utilized grade.

Methods: Tensile specimens measuring 8 mm in diameter were produced through machining and subjected to hydrogen loading electrolytically at different times in a glass chamber containing sulfuric acid (H_2SO_4) at 0.05M. The mechanical tests were conducted using a Karl Frank GMBH tensile testing universal machine, type 83431. The samples underwent microscopic analysis by means of optical microscopy (OM), X-ray diffraction (XRD), and scanning electron microscopy (SEM). The experimental characterization involved producing cylindrical specimens which underwent heat treatments (austenization) ranging from quenching to tempering, followed by immersion in a cold heat treatment cycle at -196°C for 35 minutes. Hydrogen preloading was carried out through electrochemical hydrogen charged for different loading times in hours.

Results: The results showed that the effects of hydrogen embrittlement (HE) on AISI304 stainless steel are characterized by a decrease in ductility, sometimes undergoing sudden embrittlement. This phenomenon is consistently recognized by other authors who have demonstrated a loss of ductility due to the martensitic transformation of austenite caused by deformation and hydrogen diffusion.

Conclusion: Inclusions such as second-phase particles, carbide precipitates, inclusions of small, medium, or large size, interfaces, and interphases, can be considered inclusions. Their mechanical properties and hydrogen transport and segregation mechanisms differ from those of the matrix, particularly in martensitic structures. The observation of the optical dark area (ODA) and black spots indicates that hydrogen is concentrated either in the molecular form H_2 or combined with sulphur in the form of H_2S.

Key words: AISI304 stainless steel, heat treatment, mechanical properties, hydrogen charged, hydrogen embrittlement, microstructure

Introduction

Hydrogen embrittlement (HE) substantially decreases the mechanical properties of austenitic stainless steels, constraining their efficacy in diverse applications (Cauwels et al., 2019; Amar Abboub et al., 2024). This study examines the impact of electrolytic hydrogen charging on the mechanical characteristics and microstructure of AISI304 stainless steel, a commonly utilized grade. Austenitic stainless steels, especially AISI304, are extensively utilized across several industries owing to their superior mechanical qualities, corrosion resistance, and high ductility. These characteristics render them suitable for use in demanding environments, including chemical, petrochemical, and nuclear sectors. The performance of AISI304 stainless steel can be substantially compromised by hydrogen embrittlement, a significant concern for materials subjected to hydrogen-rich environments.

Chrome nickel stainless steels are steels with excellent corrosion resistance which allows them to be chosen as a material intended for application in the energy industry (Cunat, 2000; Colombié, 2008). During their operations, often in aggressive hydrogenated environments, these steels undergo degradation of their mechanical strength and ductility - this is the phenomenon of hydrogen embrittlement called the (HE) phenomenon (Brass et al., 2000). Hydrogen, diffusing in atomic (H) or molecular H_2 form in the crystal lattice of the metallic material, weakens the atomic bonds (Lynch, 2012), which results macroscopically in a change in the mechanical properties and premature cracking at a stress below the elastic limit and by the loss of ductility during mechanical stresses (Frappart et al., 2011; Creus, 2013.; Chêne, 2009). Generally, the sensitivity of stainless steels to the (HE) phenomenon is influenced by their microstructure (Brass et al., 2000; Frappart et al., 2011; Lynch, 2012). The ferritic (α) phase of iron has a hydrogen conduction coefficient greater than that of the austenitic (γ) phase; for the case of solubility, it is the opposite - the austenitic (γ) phase has a higher hydrogen solubility than that of the ferritic (α) phase (Brass et al., 2000; Chêne, 2009).

The mechanisms of hydrogen embritllement (HE) are influenced by several factors, including the materials involved and specific experimental conditions (Grimault et al., 2012; Bach, 2018; Blanchard et al., 1960; El Hilali et al., 1999; Ly, 2009; Hamissi et al., 2016; Iacoviello, 1995; Sales, 2015) such as temperature, loading speed, hydrogen content, and duration of loading (Brass et al., 2000; Chêne, 2009). Numerous studies have established that hydrogen poses a significant risk to the mechanical properties of metallic materials, particularly affecting ductility, toughness, and strength (He et al., 1999; Depover et al., 2014; Laureys et al., 2018; Cauwels et al., 2019; Robertson et al., 2015). This phenomenon is primarily linked to the interaction between existing defects in the metal and hydrogen (Brass et al., 2000; Chêne, 2009; Lynch, 2012). Research has identified various mechanisms, including the rapid diffusion of hydrogen and its quick adsorption on defects (Chêne, 2009), which adversely impact material performance. The key interactions of hydrogen with intrinsic trapping sites, such as dislocations, micro-voids, pores, grain boundaries, inclusions, and oxide-matrix interfaces (Lee & Lee, 1987; He et al., 1999; Jin et al., 2010; Murakami et al., 2013, Laureys et al., 2018), are the critical factors contributing to the degradation of mechanical characteristics. These detrimental effects are especially pronounced during mechanical tensile fracture tests (Depover et al., 2014), where the presence of hydrogen can lead to a substantial reduction in material performance. The X-ray analysis of hydrogen-loaded material revealed a pseudo-martensitic

transformation, which accounts for the observed loss of ductility in the material. Scanning electron microscope (SEM) observations indicated that hydrogen interacts with non-metallic inclusions (Murakami et al., 2013), manifesting as dark areas, referred to as observation of the optic dark area (ODA). The experimental work was essential in elucidating the hydrogen embrittlement (HE) phenomenon and its impact on the mechanical properties of the material. The study utilized AISI304 stainless steel which was an electrochemically-hydrogen preloaded process at room temperature, as referenced in multiple studies (Murakami & Matsunaga, 2006; Robertson et al., 2015; Aurélie Laureys et al., 2020; El Hilali et al., 1999; Hamissi et al., 2016; Amar, 2023).

This research work focused on studying the influence of quenching and tempering heat treatments on the (HE) phenomenon, and utilized various observation techniques including optical microscopy and scanning electron microscopy.

Experimental work

Materials

Chemical composition

The material used in this experimental study is AISI304 austenitic stainless steel with the chemical composition given in Table 1 below.

Table 1 – Chemical composition (Wt. %) of the AISI304 steel studied

Chemical composition (Wt. %)					
Fe%	C%	Cr%	Ni%	Si%	Mn%
69.35	0.0632	17.98	9.64	0.0114	1.65
P%	S%	NB%	Mo%	Al%	Co%
<0,00030	0.028	0.0491	0.365	0.0074	0.0991
B%	V%	Ti%	Cu%	W%	Pb%
0.0152	0.0864	0.0052	0.174	0.0316	0.0045

Specimen geometry

The experimental part involves using standardised DIN50125 tensile specimens with the cylindrical shape and dimensions shown in Figure 1. These specimens are machined on a semi-automatic lathe TRENS, a.s. Suvoz 91132 Slovakia, type EN 50 C.

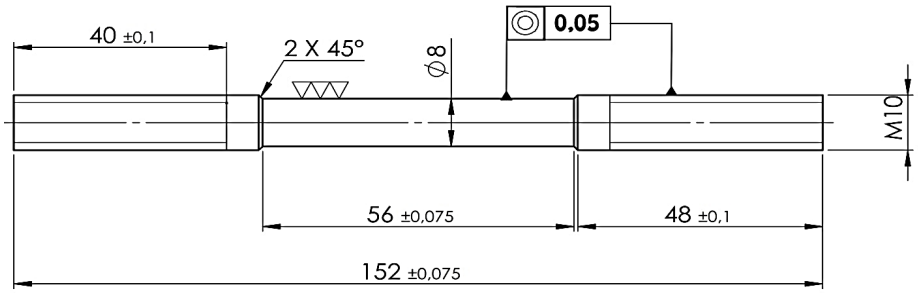

Figure 1 – Dimensions of the tensile specimens according to the standard (DIN TASCHENBUCH 19, 1975) (all dimensions are in mm)

Mechanical properties

The initial mechanical properties of the material in its raw state without heat treatment (as-delivered condition) are shown in Table 2 below.

Table 2 – Initial mechanical characteristics of the AISI304 steel

Initial mechanical properties							
Material	Rm, [TS], (Air) (MPa)	Re, [YS], (Air) (MPa)	Rr, [FS], (Air) (MPa)	A, (Air) (%)	Z, (Air) (%)	E (MPa)	υ
AISI304 As-delivered condition	686±7.03	589±1.79	414±0.12	78.5	41.5	200 000	0.27

Heat treatments

Following the fabrication of the specimens, an austenizing procedure was performed using the thermal cycle shown in Figure 2. It involves heating at 1050°C for 30 minutes and then quenching in the water.

Step two was to apply a temperature of 700°C for 35 minutes, then cool the specimens at room temperature to obtain a homogeneous and stable austenite structure. This results in a relaxation of residual stresses and an increase in the mechanical strength by micro-plasticity (BARRALIS et al., 1999; Grimault et al., 2012; Amar, 2023).

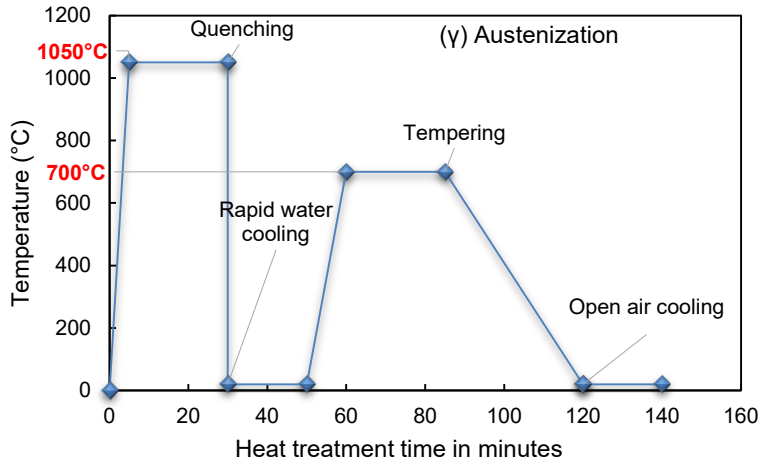

Figure 2 – Heat treatment cycle used (Amar, 2023)

Tempering at 700°C after solution quenching has several important objectives. Firstly, it aims to stabilise the austenitic microstructure by reducing the residual internal stresses caused by rapid quenching, which could otherwise promote martensite formation on subsequent stressing. Secondly, although treatment at this temperature can lead to sensitisation, particularly in AISI304 steel, a controlled short holding time at 700°C can maximise the stress stabilisation effect while minimising the risk of chromium carbide precipitation at grain boundaries, which could compromise intergranular corrosion resistance. Finally, this tempering also helps to reduce the density of residual crystalline defects. The main challenge is therefore to strike a balance between stabilising the austenite and maintaining good corrosion resistance.

Cryogenic heat treatment at -196°C

After austenitization, the tensile specimens underwent cold quenching (with N_2 liquid nitrogen bubbling) (El Hilali et al., 1999) following the thermal cycle illustrated in Figure 3 (G. Prieto et al. 2017). This type of treatment was carried out following a succession of immersions for 35 minutes and heating in the ambient air (ambient warm-up: 45 minutes). The cold quenching cycle is repeated with twenty (20) cycles.

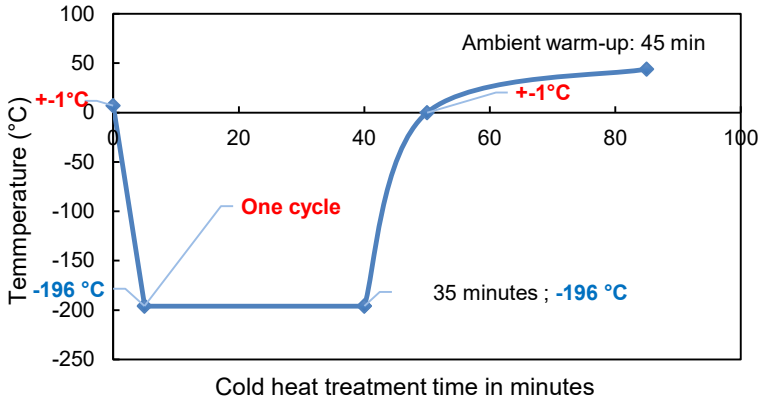

Figure 3 – Cold quenching cycle applied at -196°C (Prieto & Tuckart, 2017)

A cryogenic treatment at -196°C is presented as a method of obtaining a 'near perfect' material, based on the concept of zero entropy at 0 K. This treatment offers several potential benefits. Firstly, it can promote the transformation of residual martensite that can form as a result of internal stresses after quenching. Although a complete transformation is rare in AISI304 steel, the cryogenic treatment can contribute to this development. In addition, atomic diffusion is severely restricted at cryogenic temperatures, reducing the likelihood of significant chromium carbide formation while allowing the formation of very fine nanoprecipitates.

Cryogenic quenching can also help to reduce internal stresses through thermal cycling, which can relieve microscopic stresses. However, it is important to note that it can paradoxically increase the density of dislocations due to thermal shocks and induced stresses. These dislocations, although more numerous, could have different characteristics from those generated by machining, thus affecting hydrogen trapping. Finally, the cryogenic treatment could improve microstructural homogeneity by inducing very fine transformations or precipitates, thus contributing to a more uniform microstructure.

Conditions of electrochemically-hydrogen charged specimens

After the cyclic treatment, the specimens are electrolytically pre-charged with hydrogen. The method consists of using an enclosure containing a 0.05M (H_2SO_4) aqueous solution of sulfuric acid equipped with two electrodes, an unattackable platinum anode and a cathode connected to

the specimen, as illustrated in Figure 4 (a) and (b). Charging was carried out at room temperature with a current density equal to 100 mA/cm^2 for different durations, similarly to the author's work (Depover et al., 2014; Aurélie Laureys et al., 2020; Cauwels et al., 2019; Hamissi et al., 2016; Amar, 2023).

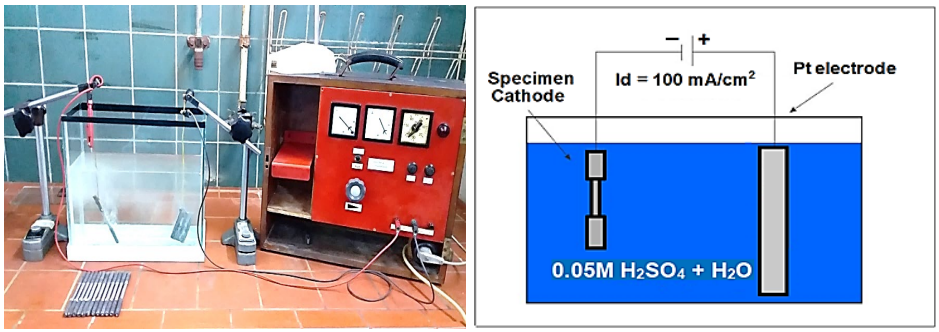

(a) (b)

Figure 4 – (a) Hydrogen-loaded specimens in 0.05M (H_2SO_4) (pH=1.32) and (b) schematic of the experimental cathodic hydrogen charging (Depover et al., 2014)

Mechanical tensile test

This experimental section describes the use of a universal (tension/compression) testing machine manufactured by Frank Karl GMBH to perform mechanical fracture tests on specimens preloaded with hydrogen. The tests were performed at a displacement speed of 20 mm/min, chosen according to the calibration of the laboratory machine. This equipment has an accuracy criterion of class 0.5, with a total measurement uncertainty of between 0.1% and 0.25%. These specifications correspond to those on the machine's nameplate and comply with DIN 50125 (DIN TASCHENBUCH 19, 1975).

Immediately after the loading process, the samples were characterized mechanically at room temperature using a tensile testing machine supplied by Karl Frank GMBH (He et al., 1999; Hamissi et al., 2016) with a maximum load capacity of 400 kN and a nominal speed of (ἑ= 20 mm/min) equipped with a table to plot experimental tensile curves (stress/strain), in order to calculate the different mechanical properties and study the hydrogen embrittlement (HE) of the steel studied, presented in Figure 5 (a), (b), and (c) and described in detail in Table 3.

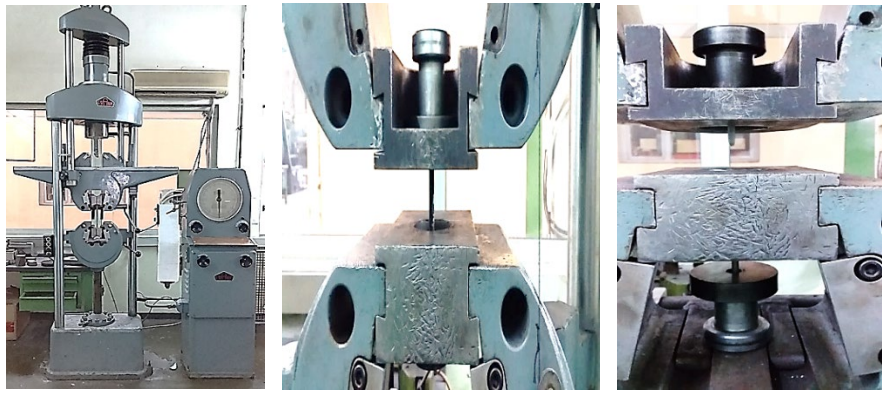

(a) (b) (c)

Figure 5 – Tensile machine Karl Frank GMBH used: (a) universal testing machine, (b) the specimen before tensile fracture, and (c) the specimen after tensile fracture (Amar, 2023)

Results and discussions

Mechanical properties

Table 3 presents the data results of the mechanical properties after the preloading protocol and the mechanical test by low tensile fracture at room temperature.

The data results of the mechanical tensile tests obtained are shown as experimental curves in Figures 6, 7, and 8 below.

The analysis of these curves shows a slight decrease in the resistance of the material as a function of the quantity of absorbed hydrogen represented by the loading duration, as Figure 6 shows. This is in agreement with the work carried out by various researchers who stipulate that hydrogen, by diffusing in the atomic form in the material, regroups in the form of (H_2) gas to occupy the existing defects and consequently exerts internal pressures (Murakami & Matsunaga, 2006), which reduces resistance (Hamissi et al., 2016). Firstly, Subfigure 6 (a) represents a decrease sensitive to the values of the mechanical resistance stress strength (Rm) as a function of hydrogen pre-charging time in hours. In parallel, a comparison of these values with the reference sample which presents a significant value is greater ($Rm_{(Air)} > Rm_{(H)}$) of the order of $Rm_{(Air)}$: 686±7.03 MPa to $Rm_{(H)}$: 532±4.44 MPa or the mechanical resistance passes through a minimum value of the order of $Rm_{(H)}$: 515±5.25 MPa, see Table 3. Secondly, a behavior expected by a yield strength (Re) in (MPa) as a function of the level of number of hours of

hydrogen preloaded, which represents a progressive reduction at this yield compared to the initial $Re_{(Air),}$ is of the order of $Re_{(Air)}$: 589±1.79 MPa to $Re_{(H)}$: 286±6.24 MPa, up to the duration of 13hours or this yield strength passes through less significant values of the order of $Re_{(H)}$: 191±9.82 MPa, as Subfigure 6 (b) shows. According to the two parameters of the variation of the mechanical resistance, stress strength $Rm_{(H)}$ and yield strength $Re_{(H)}$ in (MPa) undergo drops and progressive reductions compared to the initial $Re_{(Air)}$ value.

Table 3 – Mechanical characteristics of AISI304 after electrochemically-hydrogen preloading

Data results of tensile strength after preloading of hydrogen							
N° Specimens	Hydrogen Loaded	Stress strength, [TS]	Yield strength, [YS]	Failure strength, [FR]	Elongation percentage	Reduction percentage	Hardness (N/mm^2)
	in (hours)	Rm, MPa	Re, MPa	Rr, MPa	A, %	Z, %	$HRV_{(30)}$
As-delivered	Uncharged	686±7.03	589±1.79	414±1.12	41.5	78.8	227
Specimen.1	1 hour	532±4.44	286±6.24	302±5.47	58.2	79.7	166
Specimen.2	2 hours	553±3.43	254±7.77	334±3.94	57.7	78.6	172
Specimen.3	3 hours	553±3.43	246±8.15	336±2.42	56.5	79.7	172
Specimen.4	4 hours	549±3.63	238±8.63	350±3.18	61.3	81.9	171
Specimen.5	5 hours	541±4.01	238±8.53	342±3.56	58.2	80.8	168
Specimen.6	6 hours	551±0.24	238±8.53	358±2.80	59.6	80.8	172
Specimen.7	7 hours	545±3.82	230±8.91	358±2.80	57.9	80.8	170
Specimen.8	8 hours	551±3.53	238±8.53	350±2.80	58	80.8	172
Specimen.9	9 hours	541±4.01	230±8.91	358±2.80	57.8	80.8	166
Specimen.10	10 hours	543±3.91	230±8.91	334±3.94	69.4	82.9	169
Specimen.11	11 hours	525±4.77	230±8.91	350±3.18	57.1	80.8	165
Specimen.12	12 hours	515±5.25	222±9.29	342±6.60	64.5	81.9	158
Specimen.13	13 hours	515±5.25	191±9.82	350±3.18	57.8	80.8	158

The result is that this type of AISI304 steel studied is fragile under the effect of the industrial conditions adopted (Robertson et al., 2015; Cauwels et al., 2019) and in tests in the presence of the aggressive environment, the solution used is (H_2SO_4) acid at 0.05M with nitrogen bubbling (El Hilali et al., 1999) and different loading times in hours. Thus the value of the density of the applied polarization is 100 mA/cm^2 in order to carry the internal microcracks induced by the influence of these mechanical properties due to the absorption of charged hydrogen, as Subfigure 9 (b) shows. The yield strength (Re) and the failure strength (Rr) decrease, as

Figure 6 shows, with the increase in the tempering temperature due to the mobility and movement of carbon atoms towards preferential sites, the decrease in carbon concentration in the martensite quenched due to the diffusion of carbon atoms in cementite, and the decrease in dislocation density and lowering of hardening (Bhadeshia & Honeycombe, 2006).

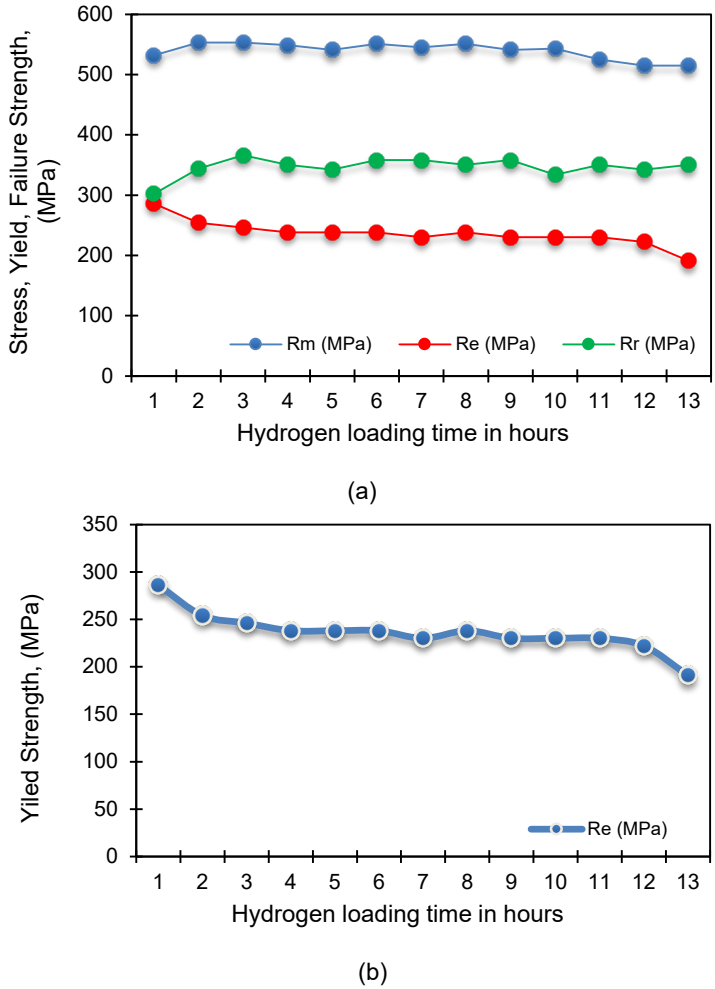

Figure 6 – (a) Variation of the resistance of stress strength, Rm, yield strength, Re and failure strength, Rr, and (b) the yield strength of AISI304 steel with loading duration in hydrogen medium sulfuric acid (H_2SO_4)

Plasticity variation

Figure 7 shows the variation of the plasticity properties for the steel studies, which is improved by the hydrogen preloading conditions in order to undergo a light increase in percentage reduction Z (%) compared to the reference $Z_{(Air)}$ (78.5 %) to $Z_{(H)}$ (79.7 %) in order to reach a value that becomes stable throughout the level in hours, which is $Z_{(H)}$ - 80.8 %. This leads to a variation in the percentage elongation A (%) , which increases relative to the reference condition from $A_{(Air)}$ - 41.5 % to $A_{(H)}$ - 58.2 % until it stabilizes at a plasticity value of $A_{(H)}$ of 57.8 %, as Table 3 shows. We also note that, in general, the variation in the plasticity values of the ($Z\%_{(Air)} < Z\%_{(H)}$), ($A\%_{(Air)} < A\%_{(H)}$) steel studied at the maxima increases significantly and remains almost constant throughout the hydrogen time loading stage in hours due to the duration and the sets of heat treatments of tempering at 700°C (El Hilali et al., 1999) and thus the use of the protocol immersion in succession following the cycle applied by cold quenching at -196°C (Prieto & Tuckart, 2017; Amar, 2023).

The experimental results obtained show that the plasticity indicators, ZH% and AH%, increase in the presence of hydrogen compared to the unloaded specimen, Z(Air)%, A(Air)%, in its delivery state and without heat treatment. This increase is directly correlated to the maximum number of dips during cryogenic quenching cycles at -196°C. Furthermore, this observed improvement in the plasticity indicators is attributed to the initial grain refinement, similarly to the results in the work (G. Prieto & Tuckart., 2017), which contributes to reduce the surface porosity of the studied AISI304 steel.

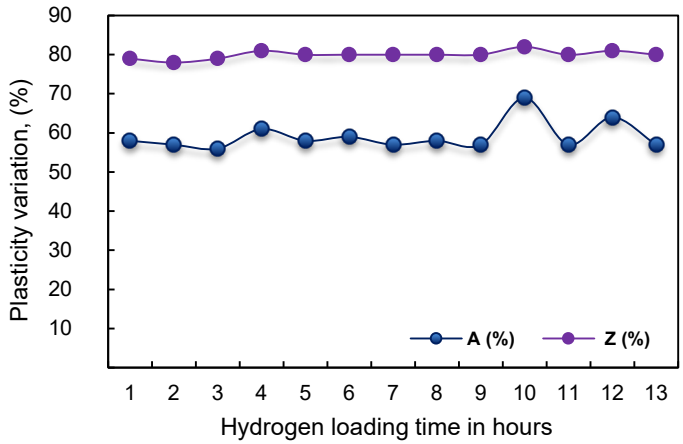

Figure 7 – Plasticity variation against hydrogen loading time

Hardness

Figure 8 shows the results of the evolution of hardness which undergoes a change in the level of loading time in hours. We noticed ($HRV_{(Air)} > HRV_{(H)}$) that the reference specimen presents the greatest value in $HRV_{(Air)}$ of the order of 227 N/mm^2 in relation to other test specimens which are pre-loaded during different hydrogen cathodic charging times of the order of $HRV_{(H)}$ of 166 N/mm^2. Where the hardness passes through a minimum value, HRV hardness ($HRV_{(H)}$) is of the order of 158 N/mm^2, as Table 3 shows.

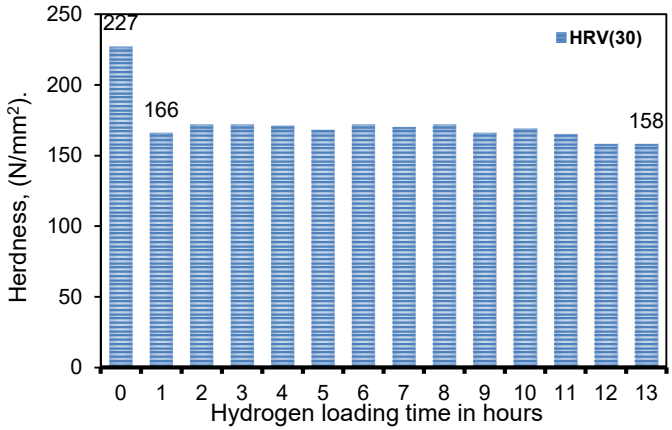

Figure 8 – Evolution hardness HRV versus hydrogen loading time

The AISI304 austenitic steel (quenched/tempered) possesses a martensitic structure after the previous heat treatments. Its structure can be embrittled by hydrogen (HE), which may manifest as transgranular facies characterized by an initiation site (inclusions) known as "fish eye". This type of defect can be highlighted during mechanical stress through tensile fracture tests. The results in a decrease in elongation at fractures and necking are shown in Subfigure 9 (b). It is a consequence of hydrogen enrichment at inclusions, grain boundaries, and micro-cavities, as well as carbide precipitations (trapping). These interfaces can be embrittled in the presence of hydrogen due to an inclusionary state, a precipitation state, segregation of chemical species, and residual austenite.

States of specimen faces

The study investigates the microstructure and fracture characteristics of AISI304 steel through various mechanical tests. Tensile tests conducted

in the air serve as a baseline, revealing the specimen crude state without any heat treatments, as Subfigure 9 (a) shows. In contrast, the tests performed in the hydrogen environment for 13 hours, following quenching at 1050°C and tempering at 700°C, show significant internal cracking along the edges of the cylindrical specimen (Subfigure 9 (b)) (Aurélie Laureys et al., 2020). This damage is attributed to a high concentration of absorbed hydrogen which adversely affects the matrix integrity under industrial conditions. The findings highlight the detrimental impact of hydrogen exposure on the mechanical properties of AISI304 steel. The diffusion and penetration of hydrogen molecules, particularly in the form of (H_2), are more pronounced in the austenitic phase (γ) of metals compared to the ferritic phase (α), even at room temperature (Frappart et al., 2011). This phenomenon leads to a significant deterioration of the metal's mechanical properties under various mechanical stresses during application. The observations regarding AISI304 steel, which was mechanically deformed and subjected to tensile loading, reveal a heightened sensitivity to crack initiation (Subfigure 9 (b)), with numerous inclusions present on the surface of the hydrogen-loaded samples. The deformed samples show an increased concentration of dislocation tangles at the interface with the matrix, resulting in localized hydrogen accumulation that promotes crack formation. Additionally, the presence of mico-voids (Subfigure 11 (b)), further accelerates the hydrogen embrittlement mechanism. The high number of inclusions in the material (Subfigure 10 (b)), along with the initiation of cracks at the grain boundaries and near these inclusions, suggests that they may act as nucleation points for hydrogen-induced cracks.

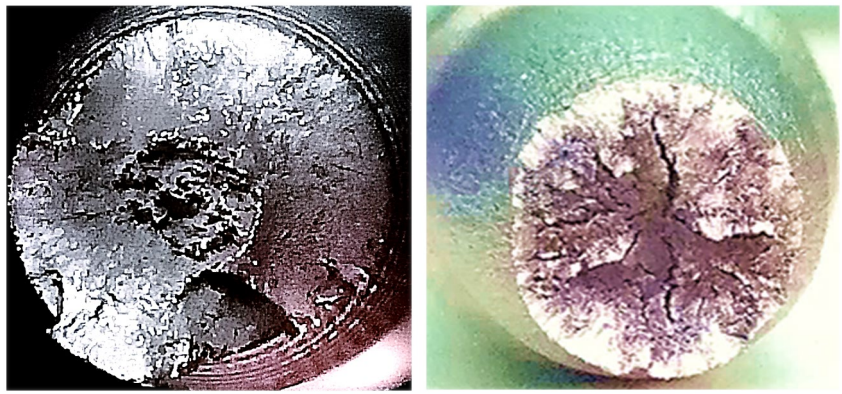

(a) (b)

Figure 9 – Specimen faces after mechanical fracture at tensile testing: (a) crude state faces, and (b) propagation of cracking faces, after the hydrogen pre-loaded state of 13hours

This results in a localized increase in hydrogen molecule concentration at the interface of the test specimen, promoting the onset of cracks. Additionally, a greater number of voids are present, which also accelerates the hydrogen embrittlement mechanism (H.E.M). Since the number of inclusions in the studied material is very high and initiatory cracks have also been found on the grain boundaries and near inclusions (Subfigure 10 (b)), they could also serve as nucleation points and voids for cracks induced by hydrogen.

Microstructures evolutions

For this, we carried out mechanical polishing and chemical attack with the 10% solution of oxalic acid ($C_2H_2O_4$), including the composition of 10 grams of oxalic acid in 100 millilitres of distilled water with an attack duration of 15 to 40 seconds under a voltage of 6 volts to reveal the microstructures represented in Subfigures 10 (a) and 10 (b) by optical microscopic (OM) reference Leica DM4-GMBH. Subfigure 10 (a) represents the microstructural analysis of the sample in the rough state without heat treatment. It can be seen that the microstructure is composed of several austenite platelets that are homogeneous with each other, with the total absence of precipitates, carbides, inclusions and microcavities. The corresponding microstructures, as Subfigure 10 (b) and Subfigure 11 (b) show, in the condition of austenitic and tempered AISI304 steel, followed by hydrogen charging for 13 hours, show a transformation to the martensitic (M) structure composed of several platelets with a lath-like interior bearing a high density of carbide precipitates and inclusions at the grain boundaries. Using the optical microscopy (OM) technique, an observation of the microstructure of the sample pre-loaded with hydrogen for a duration of 13 hours has revealed a dark area on the matrix near the inclusion known as the optical dark area (ODA), commonly referred to as "fish-eye" defect (Subfigure 12 (b)), similarly to the research conducted by (Murakami & Matsunaga, 2006). Based on these observations, it is noted that the growth in the number of ODAs is not attributed to the application of mechanical fracture solicitations by tensile loading but rather induced by the effect of the high mobility and rapid propagation of diffusible hydrogen (H) localized within interstitial sites, and microstructural defects trapped along the ODA-included zone.

On the other hand, the number of inclusions, as defects, is consistently incoherent with the matrix and serves as high-energy trapping

sites. In the regions where there were few inclusions, hydrogen appeared to weaken the grain boundaries, particularly at the interface between inclusions and the matrix. That led to embrittlement of the studied material without a change in the rupture mode, which continued to be ductile. The same evolution observed by scanning electron microscopy (SEM) (Subfigure 11 (b)) shows a high density and different sizes of ODA zones which are increased and closely spaced among themselves and with carbide precipitates at grain boundaries, depending on the adopted industrial conditions that promote hydrogen loading: the aggressive environment containing dihydrogen, a high density of the applied current, and the hydrogen content diffused with respect to loading durations in hours.

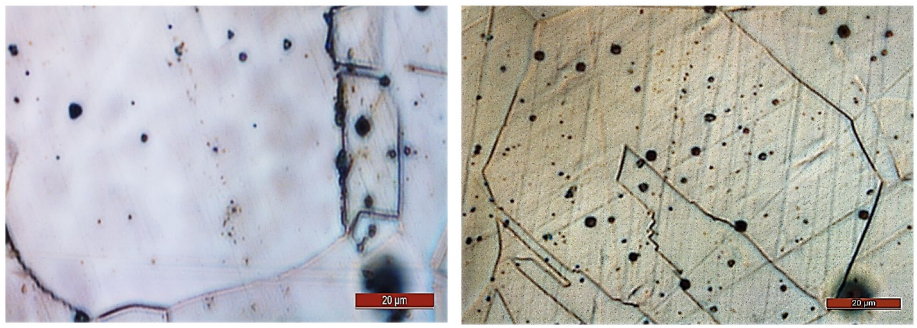

(a) (b)

Figure 10 – (a) Optical microscope (OM) images of the rough microstructure of the stainless steel studied (x20µm), and (b) the microstructure of the AISI304 steel pre-loaded with hydrogen, presented around ODA inclusions and a large density of carbide precipitates, small and medium-sized (x20µm).

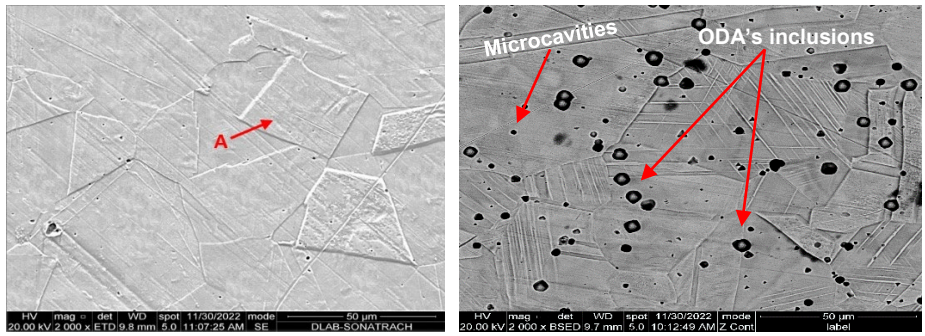

(a) (b)

Figure 11 – (a) Scanning electron microscope (SEM) image of the rough microstructure of AISI304 austenitic stainless steel (x50μm), and (b) the optical dark areas of steel loaded with hydrogen presented around ODA inclusions (fish eye), microcavities and large carbide precipitates in the grain boundaries (x50μm)

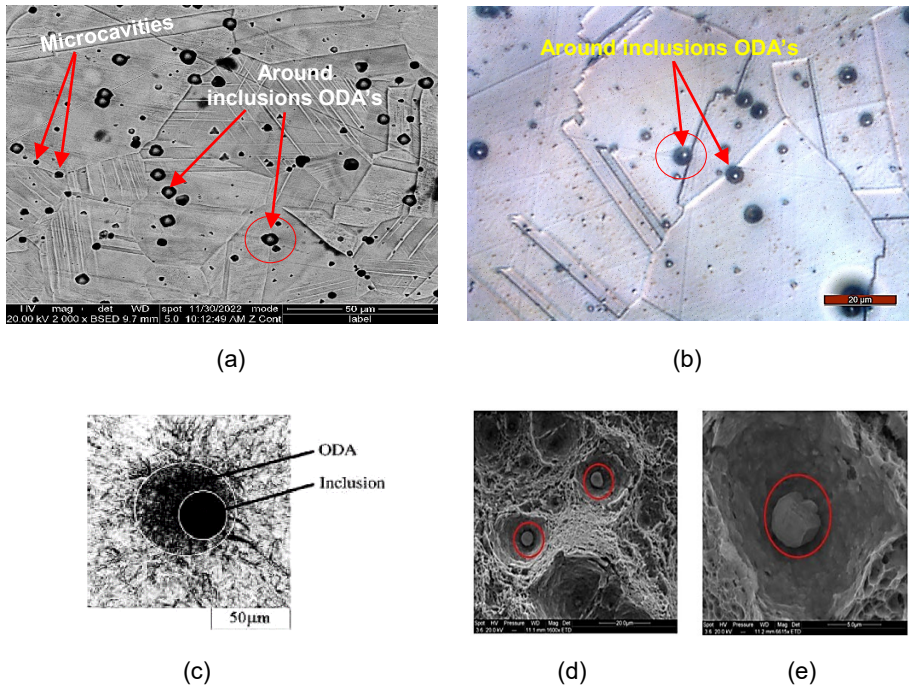

Figure 12 – (a) Scanning electron microscope (SEM) image of the optical dark areas (ODAs) of the AISI304 steel pre-loaded with hydrogen for 13hours, presents micro-cavities and the ODAs around the inclusions (fish eye) (x50μm). (b) The optical microscope (OM) image of the AISI304 steel pre-loaded with hydrogen for 13 hours presents the ODAs around the inclusions (fish eye) (x20μm). (c) The optical micrograph of the fracture origin (JIS SCM435, σ = 561 MPa, Nf = 1.1x10^8) with the optical dark area (ODA) around the inclusion. (Murakami et al., 2006) (x50μm). (d) and (e) The scanning electron microscope (SEM) image of the inclusions in the QTM9 alloy (Murakami et al., 2013) (x20 μm) and (x5 μm)

Under the influence of deformation constraints, the hydrogen pre-loaded into the studied material, as a function of loading durations in hours, will be transported by dislocations to the area of maximum stress plasticity. The accumulation of hydrogen in defects leads to the formation of cracks. The formation of molecules along a row of adjacent hydrogen atoms causes the anchoring of dislocations. At the same time, a fragile zone is

created, where maximum stress develops, reducing the resistance to rupture of the zone and leading to the creation of micro-cracks (Lo et al., 2009). The coalescence of these micro-cracks under the effect of high pressure from hydrogen molecules into a large crack causes the displacement and advancement of this crack. Carbide precipitations at grain boundaries (Lee & Lee, 1987; Aurélie Laureys et al., 2020) or the presence of high-density carbides in various forms of carbide precipitates (Laureys et al., 2018), due to the penetration of the hydrogen molecule (H_2), form which is called a "fish eye" defect, as Subfigure 11 (b), Subfigure 12 (a) and Subfigure 12 (b) show, validated by the work of (Murakami & Matsunaga, 2006), as Subfigures 12 (c), 2 (d), and (e) show (Murakami et al., 2013). In parallel, these small coherent and/or semi-coherent precipitates are associated with low-energy traps. However, they can trap a large amount of hydrogen, while incoherent precipitates are associated with high-energy traps that trap very little hydrogen (Subfigure 10 (b)) (Frappart et al., 2011).

Scanning electron microscope (SEM) analysis

A reference Scanning Electron Microscopy (SEM) Quanta FEG650 (accelerating voltage at 20.00Kv, spot size of 5.0nm) in combination with Energy Dispersive X-ray Analysis (EDXA), for the observation of fracture surfaces on cylindrical specimens, has revealed large inclusionary zones where the number of these inclusions represents privileged sites for the initiation of internal cracks in the mechanism of hydrogen-induced cracking (HIC) (Jin et al., 2010). That is particularly true for the HIC phenomenon. The nature of these ODA (Optical Dark Area) inclusions (Jin et al., 2010) is characterized by their shapes, sizes, numbers, and distribution state, which are their main characteristics. These characteristics have a significant influence on the cracking process in the presence of hydrogen molecules (H_2). The most harmful inclusions are coarse and closely spaced elongated inclusions (Murakami et al., 2013), as shown in Subfigures 12 (a) and (b). This results in a fracture surface where the metallic matrix is less ductile, and micro-cavities that appear at the particle interfaces can act as internal cracks. If the stress intensity factor exceeds the toughness of the material under study, crack propagation then leads to sudden fracture, which is highly brittle, as depicted in Subfigure 9 (b).

The ODAs around the inclusions observed in Subfigure 10 (b) and Subfigure 11 (b) play a significant role in the damage to the studied material. Indeed, the deformation incompatibility between the inclusions and the matrix can lead to local stresses that favour either inclusion fracture or interface decohesion. If the metallic matrix surrounding the

inclusions is ductile, the microcavities created during plastic deformation subsequently grow and ultimately lead to final fracture, typically through the process of coalescence, as depicted in Subfigure 12 (c) (Murakami & Matsunaga, 2006).

In this case, it can be concluded that the influence of hydrogen loading of AISI304 material is indeed significant for tensile rupture, especially when the surface of the fracture face of the sample, quenched/tempered and subsequently loaded for a prolonged duration of 13 hours, exhibits numerous internal cracks in all directions (Subfigure 9 (b)). In parallel, the microstructure matrix observed by SEM represents zones formed by several microcavity holes (Subfigure 11 (b)). This is where carbide precipitates at grain boundaries come into play, exerting their effects by accelerating hydrogen trapping.

The SEM ODA observation represents an intelligent quantitative analysis of the elemental composition of the material studied by EDAX, showing significant changes following the thermal treatments applied and the hydrogen loading process. A significant reduction in the percentages of the key elements is observed compared to the unloaded specimen (in as-delivered condition). Specifically, the carbon content is 6.46% by weight, iron 60.14% by weight, nickel 6.31% by weight, chromium 15.22% by weight, and sulphur 0.76% by weight. In addition, the typical spectral analysis representing the characteristic peaks of the identified elements of a sample preloaded with hydrogen shows the total absence of the elements of aluminium and molybdenum in this treated material. These results are supported by visual representations of the data in Figures 13 and 14, and the reference tables, Tables 4 and 5 in particular. Overall, the results show a significant change in the elemental composition of the material as a result of the electrolytic loading process under the industrial conditions adopted.

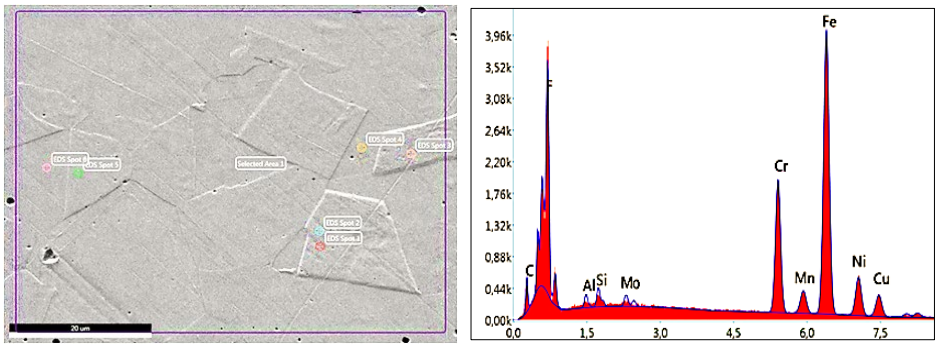

(a) (b)

Figure 13 – (a) Scanning electron microscope (SEM) microstructure (as-delivered condition) of AISI304 stainless steel (x20μm); and (b) Energy-Dispersive X-ray Analysis (EDXA) microanalysis of the elemental composition of AISI304 steel in crude state

Intelligent quantitative results before electrochemically-induced hydrogen loading

The data presented in Table 4 summarise the intelligent quantitative results, expressed in weight percent (%). These results were obtained under as-delivered conditions prior to the implementation of electrochemically induced hydrogen conditions.

Table 4 – Intelligent quantitative results of AISI304 in crude state before electrochemical hydrogen loading

Intelligent quantitative results				
Element	**% mass**	**% atomic**	**Total Intensity**	**Error %**
C K	7.64	25.67	121.29	12.75
F K	4.19	8.89	278.13	11.33
AlK	0.58	0.87	51.09	15.74
SiK	0.69	0.99	82.02	10.66
MoK	0.46	0.57	61.86	12.37
CrK	16.08	12.47	1491.38	3.55
MnK	1.42	1.04	101.55	10.10
FeK	61.71	44.56	3694.93	2.47
NiK	6.53	4.49	286.49	5.34
CuK	0.70	0.44	25.35	22.95

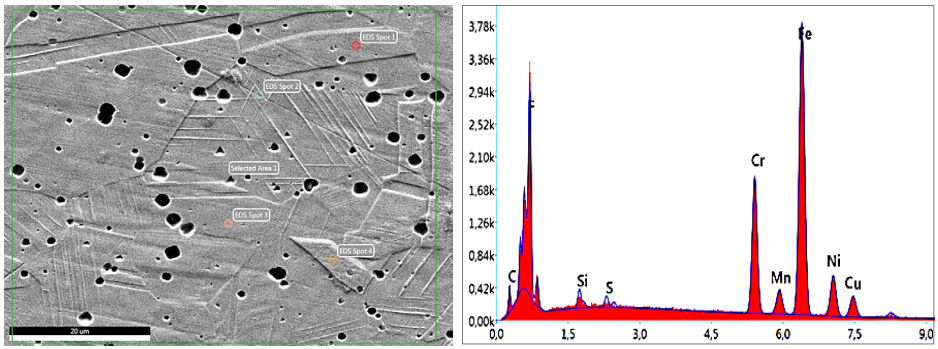

(a) (b)

Figure 14 – (a) Scanning electron microscope (SEM) image of the microstructure of the AISI304 stainless steel specimen after 13 hours of electrochemical hydrogen charging (x20μm), and (b) Energy-Dispersive X-ray Analysis (EDXA) microanalysis indicating the ODAs around the inclusions contained in AISI304 steel

Intelligent quantitative results after electrochemical hydrogen preloading

The initial Intelligent quantitative results expressed in wt (%) of the matrix composition after electrochemical hydrogen preloading are detailed in Table 5.

Table 5 – Intelligent quantitative results in wt (%) after hydrogen preloading

Intelligent quantitative results				
Element	**% mass**	**% atomic**	**Total Intensity**	**Error %**
C K	6.46	22.39	93.18	13.07
F K	4.38	9.82	272.59	11.30
SiK	0.66	0.98	71.44	11.39
S K	0.76	0.66	62.76	12.30
CrK	15.22	12.99	1371.09	3.58
MnK	1.22	1.15	98.95	10.64
FeK	60.14	47.07	3436.50	2.48
NiK	6.31	4.51	252.83	5.70
CuK	0.65	0.43	21.6	29.69

The analysis of Figures 13 and 14 reveals a significant result concerning the presence of sulphur in the materials examined. Specifically, the raw structure shows no sulphur content, whereas the ODA microanalysis indicates the emergence of sulphur (S).

This presence of sulphur is critical because it can react with hydrogen to produce hydrogen sulphide (H_2S). The formation of H_2S is linked to the development of hydrogen embrittlement (HE) in AISI304 stainless steel. Consequently, sulphur is identified as a harmful element that adversely affects the material's resistance to hydrogen embrittlement, highlighting its detrimental impact on the integrity of the steel.

Conclusion

This experimental study investigates the influence of hydrogen induced by the electrochemically-hydrogen preloading process on AISI304 stainless steel ductility, tensile strength, and fracture behavior. Based on the experimental results and analysis using optical microscopy (OM), X-ray diffraction (XRD), and scanning electron microscopy (SEM), the conclusions are drawn as follows:

The variation in the mechanical stress strength (Rm), yield (Re), and failure (Rr) of AISI304 austenitic stainless steel decreases significantly with the increase in the duration time in hours of hydrogen preloading. That can be explained by the fact that hydrogen, diffusing into the atomic lattice of the steel in the form (H), causes weakening of the metallic bond which causes the resistance to decrease until the material breaks.

The increase in the tempering temperature leads to a decrease in the variation in mechanical strength: (Rm), (Re) and the (Rr) with an increase in ductility A (%), Z (%).

The effects caused by the hydrogen embrittlement (HE) phenomenon on AISI304 stainless steel are characterized by a decrease in its ductility, which sometimes undergoes a sudden embrittlement.

Heat treatments and electrolytic hydrogen charging can significantly improve the plasticity of AISI304 austenitic stainless steel.

In cathodic loading, the conditions involved (charging time in hours, high current density, high acid concentration) can lead to a substantial difference in hydrogen concentration between the surface and the core of the internal matrix structure.

All second-phase particles (γ) residual, carbide precipitates, inclusions of small, medium, or large size, as well as interfaces and interphases, can be considered as inclusions. Their mechanical properties and hydrogen transport and segregation mechanisms differ from those of the matrix, particularly in the case where the structure is martensitic. That can be explained by the fact that hydrogen diffusing into steel creates a pseudo-martensitic transformation.

Optical Dark Areas(ODAs) surrounding inclusions manifest as black spots, corresponding to regions of hydrogen accumulation either in the molecular form (H_2) or combined with sulphur in the form H_2S. These two gases are responsible for the HE phenomenon in AISI304 austenitic stainless steel.

Symbols and abbreviations

Rm: Tensile strength, [TS], (MPa)

Re: Yield strength, [YS], (MPa)
Rr: Failure strength, [FS], (MPa)
A: Percentage elongations, in (%)
Z: Percentage reduction, (striction), in (%)
HRV (30): Hardness vickers, in (N/mm^2)
έ: Nominal speed, in (mm/min)
E: Young's modulus, in (MPa)
υ: Poisson's modulus
γ: Austenitic phase (A)
α: Ferritic phase (F)
M: Martensitic structure (M)
A : Austenitic structure
ODA: Optical dark area

References

Amar, A. 2023. The Effect of cryogenic heat treatments on the mechanical behavior of hydrogen filled steels. *International Journal of Advanced Sicentific Research and Innovation (IJASRI) Egypt.* Available at: https://www.academia.edu/121805278/The_Effect_of_cryogenic_heat_treatments_on_the_mechanical_behavior_of_hydrogen_filled_steels [11 August 2024].

Amar Abboub, Ahmed Aboura, Khaled Benmahdi, Mohamed Sadoun, Mokhtar Belkacem, Djameleddine Semsoum, "Mechanical behaviour of austenitic stainless steel loaded in the aqueous solution of H2SO4 during tensile testing", *Vojnotehnički glasnik/Military Technical Courier*, 2024, Vol. 72, Issus 4, P.P 1992-2011, Available at: https://doi.org/10.5937/vojtehg72-49964

Aurélie Laureys, Margot Pinson, Lisa Claeys, Tim Deseranno, Tom Depover, & Kim Verbeken. 2020. Initiation of hydrogen induced cracks at secondary phase particles. *Frattura ed Integrità Strutturale*, 14(52): 113–127. Available at: https://www.fracturae.com/index.php/fis/article/view/2710 [8 August 2024].

Bach, A.-C. 2018. *Etude du piégeage de l'hydrogène dans un acier inoxydable austénitique dans le cadre de la corrosion sous contrainte assistée par l'irradiation*.

BARRALIS, J., CASTEX, L. & MAEDER, G. 1999. Précontraintes et traitements superficiels. *Précontraintes et traitements superficiels*, MD1(M1180): M1180.1 (51).

Bhadeshia, H.K.D.H. & Honeycombe, R.W.K. 2006. *Steels: microstructure and properties*. 3rd ed. Amsterdam ; Boston: Elsevier, Butterworth-Heinemann.

Blanchard, R., Pelissier, J. & Pluchery, M. 1960. Effets de l'hydrogene sur les caracteristiques de rupture par traction d'aciers inoxydables. *Journal of Nuclear Materials*, 2(3): 216–224. Available at: https://www.sciencedirect.com/science/article/pii/0022311560900568 [8 August 2024].

Brass, A.-M., Chêne, J. & Coudreuse, L. 2000. Fragilisation des aciers par l'hydrogène : étude et prévention. *Corrosion Vieillissement*. Available at: https://www.techniques-ingenieur.fr/doi/10.51257/a/v2/m175 [9 July 2024].

Cauwels, M., Claeys, L., Depover, T. & Verbeken, K. 2019. The hydrogen embrittlement sensitivity of duplex stainless steel with different phase fractions evaluated by in-situ mechanical testing. *Frattura ed Integrità Strutturale*, 14(51): 449–458. Available at: https://www.fracturae.com/index.php/fis/article/view/2666 [8 August 2024].

Chêne, J. 2009. L'hydrogène dans les matériaux métalliques en relation avec les interactions plasticité-environnement. In *PlastOx 2007 - Mécanismes et Mécanique des Interactions Plasticité - Environnement*. PlastOx 2007 - Mécanismes et Mécanique des Interactions Plasticité - Environnement. Argelès-sur-Mer, France: EDP Sciences: 131–145. http://plastox.edpsciences.org/10.1051/ptox/2009010 [9 July 2024].

Colombié, M. 2008. *Matériaux métalliques*. 2e éd. Paris: Dunod.

Creus, P.J. 2013 DIFFUSION AND SEGREGATION OF HYDROGEN IN MARTENSITIC AISI 5135 : INFLUENCE OF BAKING TIME AT 20°C ON THE HYDROGEN DISTRIBUTION AND EMBRITTLEMENT.

Cunat, P.-J. 2000. Aciers inoxydables - Propriétés. Résistance à la corrosion. *Étude et propriétés des métaux*. Available at: https://www.techniques-ingenieur.fr/doi/10.51257/a/v1/m4541 [8 August 2024].

Depover, T., Pérez Escobar, D., Wallaert, E., Zermout, Z. & Verbeken, K. 2014. Effect of hydrogen charging on the mechanical properties of advanced high strength steels. *International Journal of Hydrogen Energy*, 39(9): 4647–4656. Available at: https://www.sciencedirect.com/science/article/pii/S0360319913031820 [10 July 2024].

DIN TASCHENBUCH 19. 1975. DIN-Taschenbuch 19. Materialprüfnormen für metallische Werkstoffe 1. Available at: https://www.ingenieur-buch.de/din-taschenbuch-19-materialprufnormen-fur-metallische-werkstoffe-1.html [10 July 2024].

El Hilali, F., Habashi, M. & Mohsine, A. 1999. Comportement mécanique de l'acier inoxydable martensitique 17-4 PH en corrosion sous contrainte et à la fragilisation par l'hydrogéne environnemental. *Annales de Chimie Science des Matériaux*, 24(3): 169–194. Available at: https://www.sciencedirect.com/science/article/pii/S0151910799800440 [9 August 2024].

Frappart, S., Oudriss, A., Feaugas, X., Creus, J., Bouhattate, J., Thébault, F., Delattre, L. & Marchebois, H. 2011. Hydrogen trapping in martensitic steel investigated using electrochemical permeation and thermal desorption spectroscopy. *Scripta Materialia*, 65(10): 859–862. Available at: https://linkinghub.elsevier.com/retrieve/pii/S1359646211004416 [8 August 2024].

Grimault, B., Chauveau, E., Gaillet, L., Drissi-Habti, M., Chaussadent, T. & Mantel, M. 2012. Comportement d'aciers inoxydables à hautes caractéristiques mécaniques vis-à-vis de la corrosion par piqûre et de la fragilisation par

hydrogène. *Matériaux & Techniques*, 100(2): 113–125. http://www.mattech-journal.org/10.1051/mattech/2012008 [9 July 2024].

Hamissi, C., Lakhdari, A., Aboura, A. & Seddak, M. 2016. Hydrogénation des vis en acier 35B2 lors du décapage acide. *Revue des matériaux et énergies renouvelables*, 1(1): 1–7. Available at: https://www.asjp.cerist.dz/en/article/67672 [9 August 2024].

He, J., Han, G., Fukuyama, S. & Yokogawa, K. 1999. Tensile behaviour of duplex stainless steel at low temperatures. *Materials Science and Technology*, 15(8): 909–920. Available at: https://journals.sagepub.com/doi/full/10.1179/026708399101506715 [9 July 2024].

Iacoviello, F. 1995. V - Fragilisation par l'hydrogène de l'acier inoxydable duplex Z2CND2205 chargé en hydrogène à 200°C. *Matériaux & Techniques*, 83: 48–50. http://www.mattech-journal.org/10.1051/mattech/199583120048s [9 July 2024].

Jin, T.Y., Liu, Z.Y. & Cheng, Y.F. 2010. Effect of non-metallic inclusions on hydrogen-induced cracking of API5L X100 steel. *International Journal of Hydrogen Energy*, 35(15): 8014–8021. Available at: https://linkinghub.elsevier.com/retrieve/pii/S0360319910010591 [27 December 2024].

Laureys, A., Claeys, L., De Seranno, T., Depover, T., Van Den Eeckhout, E., Petrov, R. & Verbeken, K. 2018. The role of titanium and vanadium based precipitates on hydrogen induced degradation of ferritic materials. *Materials Characterization*, 144: 22–34. Available at: https://linkinghub.elsevier.com/retrieve/pii/S1044580318310386 [8 August 2024].

Lee, J.-L. & Lee, J.-Y. 1987. The effect of lattice defects induced by cathodic hydrogen charging on the apparent diffusivity of hydrogen in pure iron. *Journal of Materials Science*, 22(11): 3939–3948. http://link.springer.com/10.1007/BF01133343 [8 August 2024].

Lo, K.H., Shek, C.H. & Lai, J.K.L. 2009. Recent developments in stainless steels. *Materials Science and Engineering: R: Reports*, 65(4–6): 39–104. Available at: https://linkinghub.elsevier.com/retrieve/pii/S0927796X09000461 [8 August 2024].

Ly, C. 2009. *Caractérisation d'aciers à très haute limite d'élasticité vis-à-vis de la fragilisation par l'hydrogène*.

Lynch, S. 2012. Hydrogen embrittlement phenomena and mechanisms. *Corrosion Reviews*, 30(3–4). Available at: https://www.degruyter.com/document/doi/10.1515/corrrev-2012-0502/html [8 August 2024].

Murakami, Y., Kanezaki, T. & Sofronis, P. 2013. Hydrogen embrittlement of high strength steels: Determination of the threshold stress intensity for small cracks nucleating at nonmetallic inclusions. *Engineering Fracture Mechanics*, 97: 227–243. Available at: https://linkinghub.elsevier.com/retrieve/pii/S0013794412004377 [8 August 2024].

Murakami, Y. & Matsunaga, H. 2006. The effect of hydrogen on fatigue properties of steels used for fuel cell system. *International Journal of Fatigue*, 28(11): 1509–1520. Available at: https://linkinghub.elsevier.com/retrieve/pii/S0142112306001009 [8 August 2024].

Na Li, Wei Wang, Qimin liang, Effect of hydrogen embritllement and non-metallic inclusions on tensile fracture properties of 55CrSi spring steel, Mater, Res. Express 7 046520. Available at: https://iopscience.iop.org/article/10.1088/2053-1591/ab8b19/pdf

Prieto, G. & Tuckart, W.R. 2017. Influence of Cryogenic Treatments on the Wear Behavior of AISI 420 Martensitic Stainless Steel. *Journal of Materials Engineering and Performance*, 26(11): 5262–5271. http://link.springer.com/10.1007/s11665-017-2986-y [8 August 2024].

Pundt A. & Kirchheim R., Hydrogen in metals : Microstructural aspects, Annu. Rev. Mater. Res. 36, 555–608, 2006. Available at: https://doi.org/10.1146/ANNUREV.MATSCI.36.090804.094451

Robertson, I.M., Sofronis, P., Nagao, A., Martin, M.L., Wang, S., Gross, D.W. & Nygren, K.E. 2015. Hydrogen Embrittlement Understood. *Metallurgical and Materials Transactions A*, 46(6): 2323–2341. Available at: https://link.springer.com/10.1007/s11661-015-2836-1 [9 July 2024].

Sales, D.G. 2015. *Etude des mécanismes d'endommagement d'aciers martensitiques associés au SSC (Sulphide Stress Cracking)*. Available at: https://theses.hal.science/tel-03091976

.

Утицај електролитичког оптерећења водоником на механичка својства и микроструктуру аустенитног нерђајућег челика AISI 304

Амар Абуба[а], **аутор за преписку**, *Ахмед*Абура [б], *Халед Бенмахди*[а], *Мохамед* Садун[а], *Мохамед* Букелеф[а]

[а] Универзитет Мустафа Стамбули, Факултет наука и технологије, Одсек за машинство, Маскара, Народна Демократска Република Алжир,

[б] Универзитет Ахмед Забана, Факултет наука и технологије ,

ОБЛАСТ:материјали
КАТЕГОРИЈА (ТИП) ЧЛАНКА: оригинални научни рад

Сажетак:

Увод/циљ: Водонична крхкост (HE) у знатној мери умањује механичка својства аустенитних нерђајућих челика чиме ограничава њихову ефикасност у различитим применама. У раду се испитује утицај изложености електролитичком водонику на механичке карактеристике и микроструктуру широко заступљеног аустенитног нерђајућег челика AISI 304.

Методе: Затезне епрувете пречника 8 мм произведене су машинском обрадом и подвргнуте оптерећењу електролитичким водоником у различитом трајању у стакленој комори са 0,05 M

сумпорне киселине (H_2SO_4). Механичка испитивања су вршена на кидалици универзалног типа 83431 фирме „Карл Франк GmbH". Епрувете су микроскопски испитане помоћу оптичког микроскопа (OM), дифракције X зрака (XRD) и скенирајуће електронске микроскопије (SEM). У процесу експерименталне карактеризације израђене су цилиндричне епрувете које су затим подвргнуте термичкој обради (аустенизацији), од каљења до отпуштања, као и циклусу накнадне изложености хладноћи на -196°C у трајању од 35 минута.

Предоптерећење водоником изведено је електрохемијским путем – за различита времена оптерећења у сатима.

Резултати: Резултати су показали да се утицај водоничне кртости на нерђајући челик AISI 304 огледа у смањењу дуктилности и понекад у наглој кртости. Ова појава је конзистентно уочена и у радовима других аутора који су указали на губитак дуктилности услед мартензитне трансформације аустенита проузроковане деформацијом и дифузијом водоника.

Закључак: Честице друге фазе – карбидни преципитати, инклузије малих, средњих или великих димензија, интерфејсови и међуфазе могу се сматрати инклузијама. Њихова механичка својства и транспорт водоника, као и механизми сегрегације, разликују се од оних који одликују матрицу, нарочито у мартензитним структурама. Уочавање оптички тамне области (optical dark area – ODA) и црних тачака указује на то да је водоник концентрисан или у молекуларном облику H_2 или комбинован са сумпором у облику H_2S.

Кључне речи: нерђајући челик AISI 304, термичка обрада, механичка својства, оптерећење водоником, водонична кртост, микроструктура

Paper received on: 16.01.2025.
Manuscript corrections submitted on:06.05.2025.
Paper accepted for publishing on: 27.05.2025.

Comparative study of two different zeolites BEA and ZSM-5 exchanged by copper and iron via the oxidation of phenol by hydrogen peroxide

Fatiha Talhaoui[a], *Fatiha* Hamidi[b], *Fransisco* Medina[c]

[a] Mohamed Boudiaf University of Science and Technology, Faculty of Chemistry, Laboratory of Functional and Nanostructured Ecomaterials, Oran, Algeria.
e-mail: talhaoui.fatiha@live.com, **corresponding author**,
ORCID iD: https://orcid.org/0000-0001-8708-0717

[b] Mohamed Boudiaf University of Science and Technology, Faculty of Chemistry, Laboratory of Functional and Nanostructured Ecomaterials, Oran, Algeria.
e-mail: fatiha.hamidi@univ-usto.dz
ORCID iD: https://orcid.org/0009-0000-2216-8195

[c] Chemical Engineering Department, Rovira I Vigili University, Avda dels Països Catalans, 26, 43007, Tarragona, Spain
e-mail: francesc.medina@urv.cat
ORCID iD: https://orcid.org/0000-0002-3111-1542

https://doi.org/10.5937/vojtehg73-57849

FIELD: materials, chemical technology
ARTICLE TYPE: original scientific paper

Abstract:

Introduction/Purpose: Water pollution by organic compounds such as phenol poses a major environmental risk. This study aims to compare the catalytic efficiency of ZSM-5 and BEA zeolites, doped with iron (Fe) and copper (Cu), for the wet oxidation of phenol using hydrogen peroxide (H_2O_2).

Method: BEA and ZSM-5 zeolites were synthesized via hydrothermal methods, then ion-exchanged to incorporate Cu^{2+} and Fe^{2+}. The catalysts were characterized using XRD, FTIR, SEM, and XPS. Phenol oxidation was carried out at 80 °C in aqueous medium with an H_2O_2/phenol molar ratio ranging from 10:1 to 15:1. The reaction products were analyzed by HPLC.

Results: The crystalline structures of the zeolites were maintained after ion exchange. The metals were well dispersed on the surface. Fe-BEA and Fe-ZSM-5 catalysts showed the highest activity (up to 99% conversion), followed by Cu-BEA (88%) and Cu-ZSM-5 (68%). The pure zeolites exhibited low activity (<10%). The optimal H_2O_2/phenol ratio was 14:1. Fe-BEA proved to be the most effective, combining high activity with enhanced diffusion within the pores.

Conclusion: Iron-exchanged zeolites, particularly Fe-BEA, are highly effective catalysts for phenol oxidation in aqueous media, outperforming both copper-doped and pure forms. The porous structure and the nature of the metal are key factors determining catalytic performance.

*K*eywords: ZSM-5, B*EA, hydrogen peroxide, phenol oxidation, heterogeneous catalysis*

Introduction

Water pollution is a major threat to our health, to the environment and also to life, due to the strong industrialization which releases various toxic pollutants into the environment. Phenol is one of the most common forms of toxic chemical pollutants due to its frequency in waste water from various industries such as petrochemical (Alattar et al, 2024), pharmaceutical (Keshri & Dutt, 2021), stationery (Mohd, 2022), plastic (Shirvani et al, 2025), and agrifood (Said et al, 2021) .

Various technologies of treatments are used for the removal of phenol; the choice of treatment depends on the level of phenol concentration, ease of control, reliability and effectiveness of the treatment (Sun et al, 2025; Peng et al, 2023; Zhang et al, 2025; Liu et al, 2021; Khader et al, 2024).

Wet oxidation based on solid catalysts is one of the methods used for the treatment of organic effluents, when their concentrations are too low to be incinerated and too high for biological treatment (Mumtaz et al, 2024; Pan et al, 2025; Chen et al, 2025; Thomsen et al, 2022). Therefore, researchers have studied the catalytic activity of various types of catalysts in oxidation, which uses hydrogen peroxide under mild conditions (Broekman & Deuss, 2024; Cao et al, 2025).

Heterogeneous zeolite catalysts have high activity in oxidation reactions (Tian et al, 2024; Jiang et al, 2025). This efficiency depends considerably on the chemical composition, the method of preparation and the nature of metal species dispersed on the catalyst (Martins et al, 2022 ; Shaida et al, 2023; Toloza-Blanco et al, 2024; Dou, 2025).

Previous studies have reported that the oxidation of phenol by hydrogen peroxide on zeolite-based catalysts was influenced by several factors such as pH, temperature, nature of metallic species, and method of preparation (Jiang et al, 2017; Aziz et al, 2016; Liu et al, 2021; Saputera et al, 2021; Villegas et al, 2024).

The zeolites of types Y, BEA and ZSM-5 have wide industrial applications (Kumar et al, 2024; Ávila et al, 2024; Diallo et al, 2016; Zang et al, 2023; Wu et al, 2020; Liu et al, 2021; Lee et al, 2018; Liu et al, 2023).

These zeolites have particular and interesting catalytic properties, uniform microporous structure with a pore size perfectly calibrated (zeolites with large and medium pores), a large specific surface area, high acidity and high thermal stability.

Zeolites also have the property of great adaptability, while the sizes of these pores make zeolites potentially suitable for adsorption and conversion of large molecules with large applications in phenol oxidation reactions (Bania & Deka, 2013; Xie et al, 2017; Ghaffari et al, 2019; Nguyen & Carreon, 2022).

As far as the objective is concerned, the current study is the first of such research available in the open literature on the comparison between the two zeolites, BEA and ZSM-5, exchanged by copper and iron via the oxidation of phenols.

The main objective of this work is to carry out a comparative study between the catalytic performances of materials based on ZSM-5 and BEA zeolites doped with copper and iron prepared by cation exchange in phenol oxidation by hydrogen peroxide.

Experimental

Materials

The chemicals used in this research study are as follows: fumed silica (99%, Cab-oil), silica gel 60 (Merck), sodium aluminate (purchased from Reidel-Haën), tetraethylammonium hydroxide TEAOH (20%, Fluka), tetrapropylammonium bromide (TPA-Br, 99%, Merck), sodium hydroxide (NaOH; 98%), ammonium chloride (Sigma Aldrich), iron (II) chloride (Sigma Aldrich), copper (II) chloride (Sigma Aldrich), and phenol (Flucka, 99%). Throughout all experiments, demineralized water was used.

Synthesis of zeolites

Synthesis of BEA zeolites

A quantity of sodium-aluminate was added into an aqueous solution containing demineralized water and TEAOH under stirring at room temperature. The fumed silica was added delicately with vigorous stirring. The reaction mixture, containing a molar ratio of 2.07 Na_2O: 20 TEA_2O: Al_2O_3: 110 SiO_2: 1550 H_2O was subjected to stirring for 4 hours at room temperature.

The mixture was then crystallized in Teflon-lined stainless-steel autoclave at 150 °C for 3 days. The solid and liquid phases were separated

by centrifugation; the recovered solids were washed several times with distilled water, then dried at 80 °C and calcined at 550 °C for 8 hours.

Synthesis of ZSM-5

The ZSM-5 zeolite was synthesized from a solution of molar composition: $NaAlO_2$: 100 SiO_2: 12.5 Na_2O:25 TPABr 1100 H_2O. Tetrapropylammonium bromide is introduced in an alkaline solution of aluminate prepared in our laboratory from aluminum hydroxide. After obtaining a clear solution, the silica gel was added slowly in order to avoid the formation of lumps. The mixture formed was homogenized at room temperature under stirring for 4 hours before the hydrothermal treatment, then sealed in a stainless-steel autoclave. Hydrothermal crystallization was carried out at a temperature of 150 °C for two days. The solid recovered by filtration was washed several times with demineralized water, then dried overnight at 80 °C. Then, the product was calcined at 550°C for 8 hours.

Preparation of catalysts

Once the BEA and ZSM-5 zeolites were synthesized, and before copper and iron were incorporated, a first ion exchange step with ammonium chloride 0.01 mol was performed to replace the Na^+ cations present in the zeolite network by NH_4^+. Usually, this treatment is used to generate the acidic form of zeolites by thermal degradation of ammonium. The zeolite produced was subjected to calcination for 5 hours.

Chloride solutions were prepared by the introduction of copper chloride ($CuCl_2$) and iron chloride ($FeCl_2$) salts into closed glass reactors containing deionized water under agitation for a few minutes to complete the homogenization of solutions.

Then, the adequate amount of solid (HBEA or HZSM-5) was introduced in the reactor. The amount of solid was generally 1 g of solid in 100 cm^3 of 0.01 mol exchange solution. The ion exchange experiments were carried out at room temperature with stirring. The reaction time was set at 24 hours. The catalysts obtained are recovered by filtration, washing with demineralized water and drying overnight at 80 °C.

Characterizations

The solids prepared by ion exchange with copper and iron were characterized by X-ray diffraction (XRD) using a PHILIPS PW1710 diffractometer (copper tube lk. A: = 1.54060). The surface morphology of catalysts was examined using a scanning electron microscope (SEM) (FEG Quanta 200F FEI / Phillips). The Fourier transform infrared (FTIR)

spectroscopy analyses were carried out on a Nicolet FTIR 320 spectrophotometer in the range 4000 and 400 cm^{-1}. X-ray photoelectron spectroscopy (XPS) was performed using a Thermofisher ESCALAB 250 system with Al K-alpha radiation. The spectra acquired were analyzed by the XPS peak software.

Oxidation of phenol

The catalytic tests were carried out in a three-chamber flask, equipped with a water condenser, a thermometer and a magnetic stirrer. This bottle was placed in an oil bath and heated to 80°C under stirring at 500 rpm (Valkaj et al, 2011).

The reaction was carried out by dissolving 0.094 g of phenol in 100 cm^3 of water and transferred into a flask containing 0.01 g of catalyst. Once the reaction mixture had reached the desired temperature, hydrogen peroxide H_2O_2 (0.1 mol) was added dropwise into the reactor under stirring for 3 hours.

The samples taken during the reaction were filtered through 0.2 µm nylon membranes to analyze the reaction mixture. The concentration of phenol and its conversion products were analyzed by high performance liquid chromatography (HPLC).

Results and discussion

Characterization of catalyst

X-ray diffraction

The crystal structures of the prepared catalysts were verified by XRD analysis. Figure 1 represent the XRD spectra of the parent zeolites and their forms exchanged by the transition metals (iron and copper).

The comparison of these spectra revealed that all the distinctive lines of the BEA and ZSM-5 zeolites were observed after the cationic exchange, suggesting that the crystalline structure of both zeolites was preserved (Chen et al, 2024; Sazama et al, 2020; Gabrienko et al, 2025).

The BEA zeolite catalyst diffractograms shown in Figure 1 were characterized by a mixture of broad and subtle lines. This indicated the presence of a disordered structure formed by the intergrowth of two polytypes A and B as previously reported by Camblor et al. (1996).

All these catalysts revealed the same diffraction peaks that resemble those of the BEA zeolite at 7.8 ° and 22.5 (IZA International Zeolite Association, 2018). At the same time, the different lines of the zeolite catalysts ZSM-5 observed in Figure 1 exhibited the same peaks in the

range of 2θ = 7–9 ° and 23–25 ° which are corresponding to the standard phase of the ZSM-5 zeolite (Treacy & Higgins, 2007).

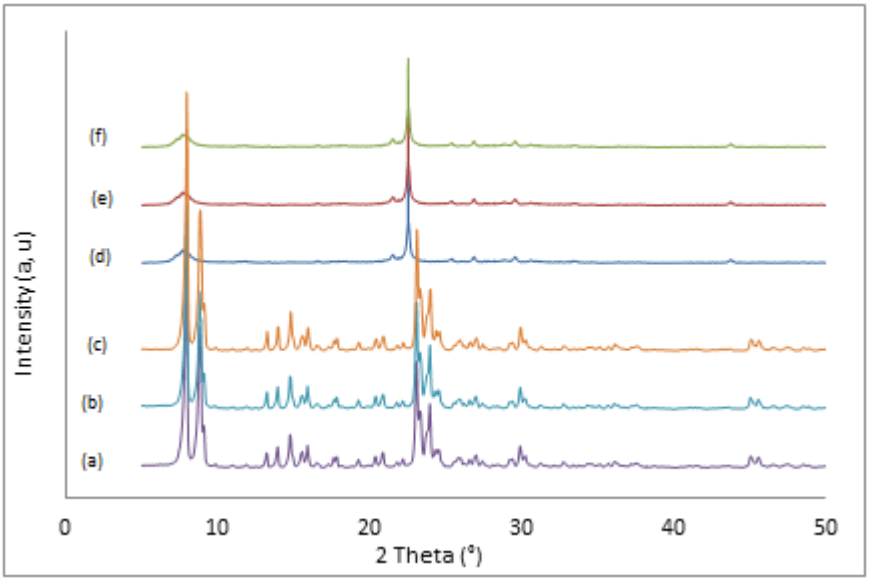

Figure 1- XRD patterns of ZSM-5 (a), Cu-ZSM-5 (b), Fe-ZSM-5 (c), BEA (d), Cu-BEA (e), and Fe-BEA (f) catalysts

In addition, no characteristic diffraction peak of copper and iron oxide (2θ approximately 35.5) was observed by XRD analysis in the modified samples (Ji et al, 2014; Sobuś et al, 2021), meaning that these two cations are entered into the interior of the zeolite, or they were highly dispersed on the surface of the zeolite (Song et al, 2016; Ren et al, 2019). Also, it can be suggested that the concentrations of Fe and Cu ions were below the XRD limits.

Thus, the intensities of each zeolite were reduced after the dispersion of metals Fe or Cu; this is due to the dispersion of iron or copper in ZSM-5 and BEA zeolites with X-rays absorption and the reduction of crystal degree of crystallinity (Sun et al, 2016).

Infrared spectroscopy

The fundamental vibration bands that characterize BEA and ZSM-5 zeolites lattice were observed in the range of 400-2000 cm^{-1}. The comparison of the BEA zeolite catalyst spectrum exchanged with copper and iron with those of zeolites synthesized (Figure 2) revealed the

presence of bands related to the characteristic vibrations of theBEA zeolite (Lin et al, 2020).

The absorption bands at 529-547 cm^{-1} and 433-434 cm^{-1} were due to the double cycles (D6R) and deformation of the internal bond Si -O in the SiO_4 tetrahedron.

The ratio of band intensities at 500 and 400 cm^{-1} was often used as an indicator of zeolite crystallinity (Coudurier et al, 1982). The samples exhibited a ratio ranged from 0.7 to 0.8 indicating the presence of high crystallinity materials. According to the literature (Bok et al, 1981, pp. 38505-38514), the ratio of bands was 0.8 for all BEA zeolites.

The bands at 1064-1076 cm^{-1} were due to the asymmetric elongation vibrations of internal links of TO_4 patterns. The vibration bands of symmetrical elongation at 628.76 cm^{-1} were attributed to the internal Si-O-Al bond, while the frequencies at 1226 cm^{-1} and 797-798 cm^{-1} were due to the bonds of the primary structural units.

The infrared spectra of ZSM-5 zeolites obtained before and after ion exchange with iron and copper shown in Figure 2 exhibited the characteristic bands of the ZSM-5 zeolite.

Therefore, the bands that appeared at 545.73-546.44 cm^{-1} were related to the vibrations of the secondary structural units (5-1) of an MFI zeolite.

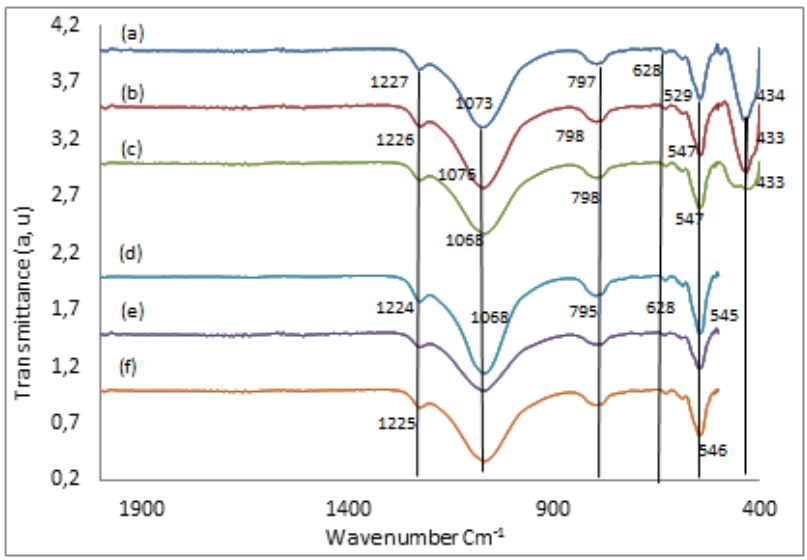

Figure 2- FTIR spectra of the samples: BEA (a), Fe-BEA (b), Cu-BEA (c), ZSM-5 (d), Fe-ZSM-5 (e), and Cu-ZSM-5 (f)

The asymmetric elongation vibration band at 1067.82-1068.86 cm^{-1} and the symmetrical elongation vibration band at 628.4-628.87 cm^{-1} were attributed to the internal bonds of Si-O-Al. The bands at the frequencies of 795.42-596.47 cm^{-1} and 1224.53-1225.10 cm^{-1} were due to the bonds of the primary structural units. The shifting of the bands was attributed to the exchange of hydrogen cations for cations of copper and iron.

Scanning electron microscope (SEM)

The morphology of the catalysts was examined using a scanning electron microscope (SEM). The images of different BEA and ZSM-5 catalysts are shown in Figure 3.

As reported, the crystal morphology of the iron and copper doped BEA zeolites revealed a large number of crystals with assemblages of very small crystals of the BEA zeolite.

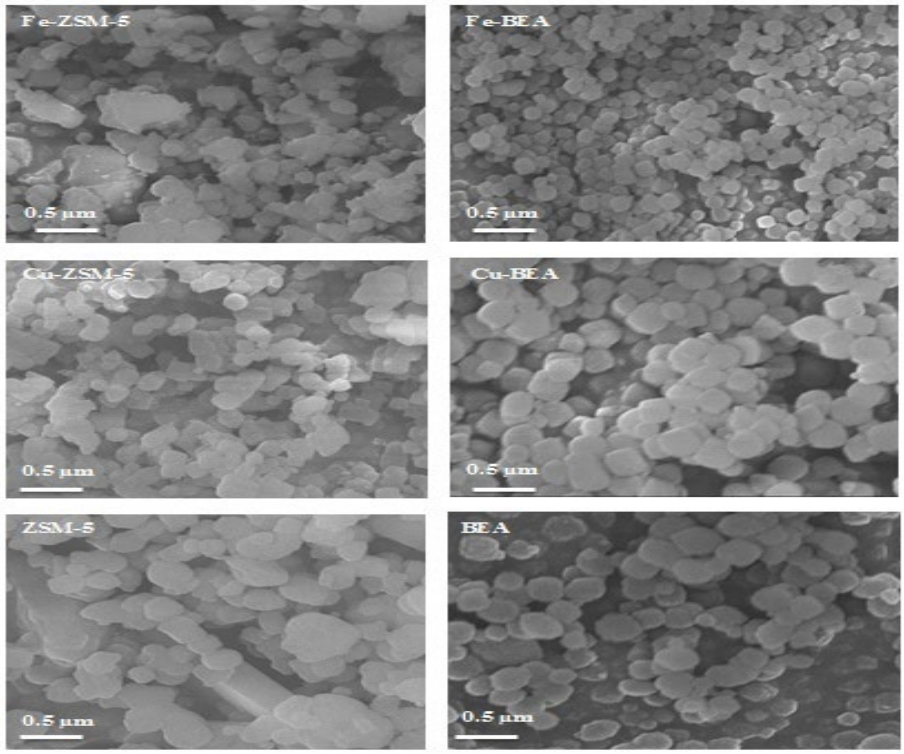

Figure 3- Scanning electron microscopy (SEM) images of BEA, Cu-BEA, Fe-BEA, ZSM-5, Cu-ZSM-5, and Fe-ZSM-5

The uniform shape and particle size were slightly greater than those of the parent zeolite. In fact, during the ion exchange process, the transition metals are distributed or doped on the parent zeolites.

Based on the images of different crystallite ZSM-5 zeolites, the images showed an agglomeration of small, medium-sized crystals of the order of 0.5 µm with a shape characteristic of the ZSM-5 zeolite. The particle size distribution and the morphology of the Cu-ZSM-5 and Fe-ZSM-5 catalysts are approximately the same as those of the parent ZSM-5 zeolite with no significant change in morphology. Furthermore, the modified products inherit the morphology of the parent zeolite after the ion exchange step.

X-ray photoelectron spectroscopy (XPS)

The chemical composition and the coordination between metal and M-zeolite (Fe or Cu) zeolite were identified by XPS analysis. The spectrums are depicted in Figure 4.

As shown in Figure 4.a, the spectra confirmed the presence of metal Fe in the modified zeolites, the presence of binding energy around 711.88-712 and 724.68-725.18 eV correspond to Fe 2p (3 / 2) and Fe 2p (1 / 2) (He et al, 2020), respectively, which are bound to Fe $^{2+}$ ions (Lin et al, 2018).

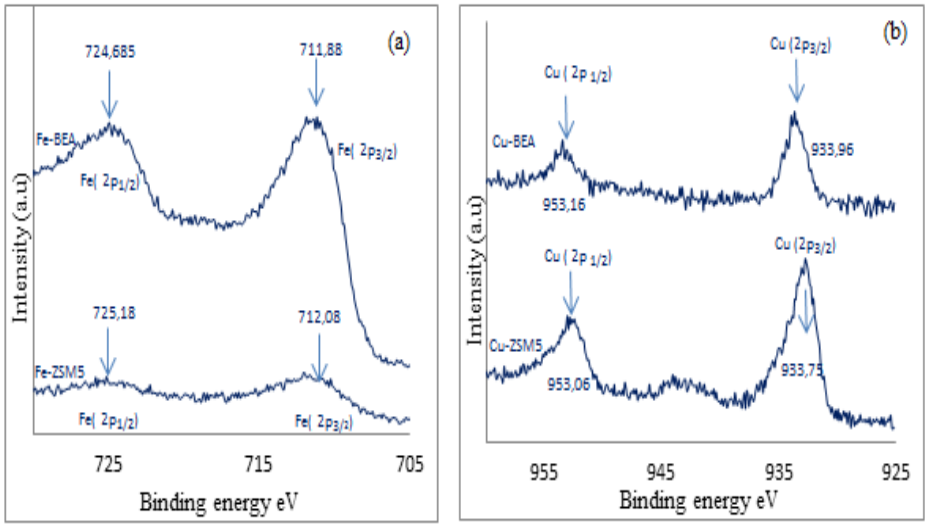

Figure 4 - X-ray photoelectron (XPS) spectra of modified zeolites (a) Fe 2p and (b) Cu 2p

The decrease in the peak intensities of Fe 2p indicated that the decline of iron species on the ZSM-5 zeolite surface might be due to ion

exchange causing the iron species found on the surface to become embedded inside the zeolite.

As shown in Figure 4.b, the XPS spectra of metal Cu confirmed its presence in the zeolites exchanged with narrow regions Cu 2p.

According to the literature (Wang et al, 2019), a binding energy of 932.5-952.3 eV corresponds to Cu 2p (3/2) and Cu 2p (1/2) attributed to Cu^{+} species, while peaks Cu 2p (3/2) and Cu 2p (1/2) located at 933.7 ± 0.2 eV and 953.7 ± 0.2 eV, were attributed to the Cu^{2+} species.

The Cu 2P (3/2) and Cu 2P (1/2) peaks shown in Figure 4.b and located at binding energies 933.7 ± 0.2 eV and 953.2 ± 0.2 eV are the essential characteristics of Cu^{2+} species.

Catalytic activity

Oxidant effect

A preliminary series of experiments was carried out to examine the behavior of zeolites containing iron, copper, and pure zeolites to distinguish the effect of adsorption and reaction.

Table 1- Conversion of phenol on zeolites: BEA, Cu-BEA, Fe-BEA, ZSM-5, Cu-ZSM-5, and Cu-ZSM-5) with and without oxidant (T = 80°C, Cc Ph= 0.01 mol/l, Cc H_2O_2 = 0.10 mol/l, mcat = 0.10 g/l, and pH = 4.2).

	Phenol + H_2O_2	ZSM5	ZSM5 + H_2O_2	Cu-ZSM5	Cu-ZSM-5 + H_2O_2	Fe-ZSM5	Fe-ZSM-5 + H_2O_2
X Ph %	35.7	6.36	29.38	9.69	68.03	6.16	98.1
	Phenol + H_2O_2	BEA	BEA + H_2O_2	Cu-BEA	Cu-BEA + H_2O_2	Fe-BEA	Fe-BEA + H_2O_2
X Ph %	35.7	6.98	30.31	8.45	88.61	7.33	99.3

At a temperature of 353 K under the conditions explained in the experimental section after 180 min of reaction, the results of these experiments are shown in Table 1.

During the evaluation of the prepared catalysts, a preliminary experiment showed that phenol can be oxidized by hydrogen peroxide in the absence of catalyst. The percentage of conversion was 35% after 3 h of reaction.

As shown in Table 1, the experiments performed with pure zeolites produced a conversion rate of 7% for the BEA zeolite and 6% for the ZSM-

5 zeolite in the absence of hydrogen peroxide as an oxidant. The results were quite similar to those of the zeolites doped with iron and copper with a slight difference between the pure BEA and ZSM-5 catalysts and the doped catalysts.

The results mentioned that the majority of removal phenol was carried out by adsorption while the percentage of removal by oxidation was almost negligible. Hence, the removal rate of phenol does not exceed 10%.

On the other hand, in the presence of H_2O_2, BEA and ZSM-5 catalysts exchanged with iron and copper are more active, with a conversion rate of 99% for Fe-BEA catalyst, 98% for Fe-ZSM-5 catalyst, 88% for the Cu-BEA catalyst, and 68% for the Cu-ZSM-5 catalyst.

This can be attributed to the limitation of diffusion of molecules into the pores.

Interestingly, phenol was removed more easily by the Fe-zeolite than that of Cu-zeolite catalysts, indicating the diffusion of phenol in the pores of the iron-doped zeolites rather than that of the doped zeolites of copper. This can be attributed to the thermodynamic properties and in particular to the electrochemical properties of iron compared to copper (Alejandre et al, 2000).

The molecular sizes of hydrogen peroxide and phenol are listed in Table 2 (Atoguchi et al, 2004).

The comparison between the data in Table 2 and the pore dimensions of the BEA and ZSM-5 zeolites mentioned that hydrogen peroxide and phenol can diffuse more easily in the pores of the BEA zeolite than that in the pores of the ZSM-5 zeolite.

Table 2 - Molecular size of phenol and hydrogen peroxide

Molecule	a, nm	b, nm	c, nm
Phenol	0.4792	0.4908	0.5090
H_2O_2	0.2476	0.2476	0.361

It can be suggested that zeolite catalysts containing iron and copper are active for the oxidation reaction of phenol by hydrogen peroxide.

Another suggestion is that the difference in catalyst activity is caused by the difference in the activity of zeolites. The redox properties of transition metal cations such as iron and copper species promoted the production of hydroxyl groups in the presence of hydrogen peroxide.

In addition, it is assumed that the zeolite acidity can influence the conversion of hydrogen peroxide, i.e., the highest rate of the formation of hydroxyl radicals is obtained with zeolites having a greater acidity (Bahranowski et al).

Effect of the molar ratio H_2O_2: phenol

The concentration of hydrogen peroxide plays an important role in the stability of a catalyst in the oxidation reaction. The final conversion values after 180 min of degradation of phenol at different molar ratios (H_2O_2: phenol) are given in Table 3.

Table 3 - Effect of the molar ratio H2O2: Phenol on the conversion of phenol on BEA and ZSM-5 catalysts exchanged with iron and copper at T = 80 ° C and pH = 4.2

	Conversion rate (%)		
	H_2O_2: Phenol 10 :1	H_2O_2: Phenol 14 :1	H_2O_2: Phenol 15 :1
Cu-ZSM-5	68,03	71,43	75,81
Cu-BEA	88,61	96,96	93,36
Fe-ZSM-5	98.1	99,01	99,09
Fe-BEA	99.3	99,7	99,54

As shown in Table 3, the oxidation of phenol was carried out using zeolite-based catalysts exchanged with iron and copper, employing three different H_2O_2: phenol molar ratios (10, 14, and 15). Increasing the H_2O_2: phenol molar ratio from 10:1 to 14:1 led to a significant improvement in the phenol conversion rate for all catalysts. This enhancement is attributed to the greater availability of hydrogen peroxide, which promotes the generation of hydroxyl radicals (HO•)—highly reactive species capable of effectively degrading phenol molecules. However, when the ratio reaches 15:1, a stagnation or slight decrease in performance is observed for certain catalysts (e.g., Cu-BEA). This phenomenon is explained by the formation of hydroperoxyl radicals (OOH•), which are less reactive than HO• and result from excess H_2O_2 (Equation 2). Subsequently, OH• radicals are

scavenged by OOH• and transformed into H_2O and O_2 according to Equation 3.

- Catalyst + $H_2O_2 \rightarrow$ OH• (1)
- OH• + $H_2O_2 \rightarrow$ OOH• + H_2O (2)
- OOH• + OH• $\rightarrow$ O_2 + H_2O (3)

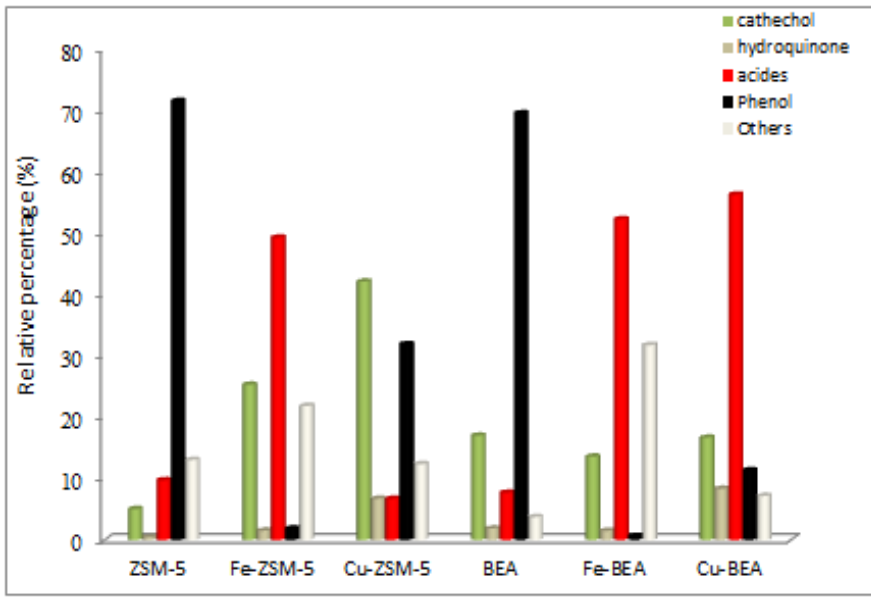

Figure 5-Distribution of by-products on catalysts based on M+/zeolites (T = 80°C, Cc Ph= 0.01 mol/l, Cc H_2O_2 = 0.10 mol/l, mcat = 0.10 g/l, and pH = 4.2)

The iron-doped catalysts (Fe-ZSM-5 and Fe-BEA) exhibit the highest conversion rates (up to 99.7%). This is due to the superior redox activity of iron for activating H_2O_2 and its strong ability to generate hydroxyl radicals. The BEA structure offers better diffusion than ZSM-5; however, even within the more restrictive ZSM-5 framework, iron remains highly active. The copper-doped catalysts (Cu-ZSM-5 and Cu-BEA) show lower performance compared to iron-based catalysts. Nonetheless, Cu-BEA outperforms Cu-ZSM-5, thanks to its more open porous structure that facilitates easier diffusion of reactants. However, copper is less efficient than iron in generating HO• species. It is well known that the catalytic oxidation of phenol in the liquid phase by hydrogen peroxide is a highly complex process, involving a series of parallel and consecutive reactions, with a wide range of intermediates and final products. These include aromatic compounds such as benzoquinone, hydroquinone, catechol,

carboxylic acids (acetic, maleic, oxalic, and fumaric acids), and other oxygenated compounds like aldehydes and ketones. At the beginning of the oxidation process, phenol can react with radicals generated from the decomposition of H_2O_2. The reaction medium initially turns dark brown due to the formation of by-products such as hydroquinone and catechol. Later, the solution becomes clear, indicating the formation of various acids and CO_2, as reported by Taran et al. (2018) and Devard et al. (2019)

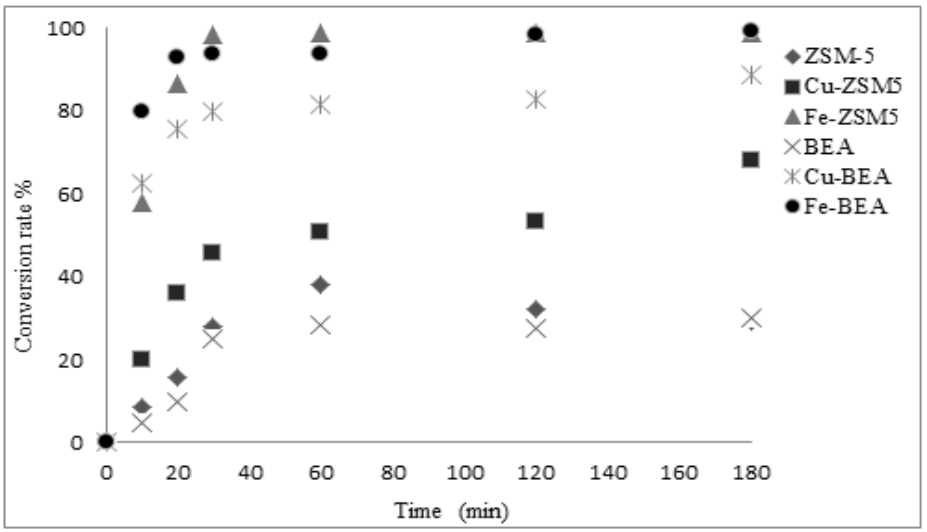

Figure 6 - Conversion of phenol as a function of time on pure catalysts and M + -zeolite catalysts (T = 80°C, CcPh= 0.01 mol/l, Cc H_2O_2 = 0.10 mol/l, mcat = 0.10 g/l, and pH = 4.2)

As depicted in Figure 6, the Fe-zeolite catalysts showed maximum activity with a conversion rate of 55% in the first 10 minutes and over 98% after 3 hours. The pure zeolite catalysts had a conversion rate of less than 10% during the first 10 minutes and it reached 30% after 3 hours.

On the other hand, the Cu-BEA catalyst showed an average catalytic efficiency with a rate of conversion of 62% in the first 10 minutes and 88% after 3 hours, while the Cu catalyst ZSM-5 showed minimal catalytic efficiency with a rate of conversion of 20% within the first 10 minutes and 68% after 3 hours.

Catalytic tests showed the catalytic activity of the Fe-BEA catalyst with a phenol conversion of 99%, which is very considerable compared to the other catalysts prepared.

The rapid decrease in the concentration of phenol can be explained by its adsorption on the catalyst. It is evident that zeolites doped with transit metals increased the conversion of phenol more than five times at the initial stage of the process.

According to this study, the BEA zeolite exhibited excellent results via the oxidation of phenol due to its structure with large pores and cavities resulting from the interconnection of its channels, the dimensions of pores being (6.4 - 7.6) Å2 along the axis [001] and (4.5 - 5.5 Å) along the axis [100]), at their high specific surface area (≥. 400 m^2 / g) (Selvam, 2003; Zhou et al, 2019), and its ion exchange capacity via transition metals.

Conclusion

The objective of this study was the wet oxidation of phenol with hydrogen peroxide on heterogeneous catalysts containing iron and copper under mild conditions.

The X-ray diffraction spectra indicated that the most of prepared zeolite catalysts exchanged with copper or iron exhibited diffraction peaks similar to those of pure zeolites. Then, the crystal structure was preserved during cation exchange for all catalysts based on exchanged zeolites.

Infrared, SEM, and XPS analyses confirmed the good dispersion of metals within the zeolite structure and the stability of the active phases on the catalyst surface. These characterizations also provided better insight into the interaction between the metals and the zeolitic support.

It can be concluded that all catalysts based on BEA and ZSM-5 zeolites doped with iron and copper are potentially active, in comparison with catalysts based on pure zeolites. They demonstrated high stability in aqueous media and are therefore suitable for use without causing metal pollution issues.

Regarding catalytic activity, phenol conversion rates reached approximately 70–90% for the ZSM-5 exchanged with copper and iron, while the doped BEA zeolites showed even higher conversions of 90–99%. In contrast, the pure zeolites exhibited significantly lower conversion rates, below 35%, thus confirming the beneficial effect of introducing transition metals, which are therefore favorable to be used without causing problems of metal pollution.

The efficiency of phenol oxidation strongly depends on two key factors:

- ✓ The H_2O_2: phenol ratio, a moderate excess of oxidant enhances conversion up to an optimal threshold.

- ✓ The nature of the metal cation, iron promotes the formation of oxidizing radicals more effectively than copper.

The most efficient combination is achieved with the Fe-BEA catalyst, which combines high catalytic activity with a porous structure that ensures optimal diffusion of reactants.

References

Alattar, S.A., Sukkar, K.A. & Alsaffar. M.A. 2024. Phenol removal from wastewater in petroleum refineries by managing flow characteristics and nanocatalyst in ozonized bubble column. *Journal of Petroleum Chemistry*, 159, pp.159-169. Available at: https://doi.org/10.1134/S0965544124020117

Alejandre, A., Medina, F., Rodriguez, X., Salagre, P. & Sueiras, J. E. 2000. Preparation and activity of copper, nickel and copper-nickel-al mixed oxides via hydrotalcite-like precursors for the oxidation of phenol aqueous solutions. *Journal of Studies in Surface Science and Catalysis*, 130, pp. 1763-1768. Available at: https://doi.org/10.1016/S0167-2991(00)80456-5

Atoguchi, T., Kanougi, T., Yamamoto, T. & Yao, S. 2004. Phenol oxidation into catechol and hydroquinone over H-MFI, H-MOR, H-USY and H-BEA in the presence of ketone. *Journal of Molecular Catalysis A: Chemical*, 220(2), pp.183-187. Available at: https://doi.org/10.1016/j.molcata.2003.10.026

Ávila, M.I., Alonso-Doncel, M.M., Briones, L., Gómez-Pozuelo, J., Escola, J.M., Serrano, D.P., Peral, A. & Botas, J.A. 2024. Catalytic upgrading of lignin-derived bio-oils over ion-exchanged H-ZSM-5 and H-beta zeolites. *Journal of Catalysis Today*, 427, p.114419. Available at : https://doi.org/10.1016/j.cattod.2023.114419

Aziz, A., Park, H., Kim, S. & Kim, K. S. 2016. Phenol and ammonium removal by using Fe-ZSM-5 synthesized by ammonium citrate iron source. *International Journal of Environmental Science and Technology*, 13, pp.2805–2816. Available at: https://doi.org/10.1007/s13762-016-1107-z

Bahranowski, K., Dula, R., Gasior, M., Łabanowska, M., Michalik, A., Vartikian, L. A. & Serwicka, E. M. 2001. Oxidation of aromatic hydrocarbons with hydrogen peroxide over Zn, Cu, Al-layered double hydroxides. *Journal of Applied clay science*, 18(1-2), pp.93-101. Available at: https://doi.org/10.1016/S0169-1317(00)00033-8

Bania, K. K. & Deka, R. C. 2013. Zeolite-y encapsulated metal picolinato complexes as catalyst for oxidation of phenol with hydrogen peroxide. *Journal of Physical Chemistry C*, 117(22), pp.11663-11678. Available at: https://doi.org/10.1021/jp402439x

Bok, T. O., Andriako, E. P., Knyazeva, E. E. & Ivanova, I.I. 2020. Engineering of zeolite BEA crystal size and morphology via seed-directed steam assisted conversion. *Journal of Rsc Advances* , 10 (63), 38505-38514. Available at: https://doi.org/10.1039/D0RA07610D

Broekman, J. O. P. & Deuss, P. J. 2024. Insights into the benign, selective catalytic oxidation of HMF to HMFCA in water using $[Mn^{IV}_2 (\mu\text{-}O)_3 (tmtacn)_2]^{2+}$ and Hydrogen Peroxide. *Journal of Organometallics*, *43*(11), pp.1264-1275. Available at: https://doi.org/10.1021/acs.organomet.4c00109

Camblor, M.A., Corma, A. & Valencia, S. 1996. Spontaneous nucleation and growth of pure silica zeolite-β free of connectivity defects. *Journal of Chemical Communications*, 20, pp.2365-2366. Available at: https://doi.org/10.1039/CC9960002365

Cao, K., Yang, F., Wan, H., Duan, X., Shi, J. & Sun, Z. 2025. A selective oxidative depolymerization of larch lignin to ethyl vanillate by multifunctional catalysts combining alkaline ionic liquid and polyoxometalates with hydrogen peroxide. *International Journal of Biological Macromolecules*, 295, p.139642. Available at: https://doi.org/10.1016/j.ijbiomac.2025.139642

Coudurier, G., Naccache, C. & Vedrine, J.C. 1982. Uses of IR spectroscopy in identifying ZSM zeolite structure. *Journal of the Chemical Society, Chemical Communications*, 24, pp.1413–1415. Available at: https://doi.org/10.1039/C39820001413

Chen, X., Zhou, S., Wang, L., Zhang, C., Gao, S., Yu, D., Cheng, Y., Xiaoqiang, V., Yu, X. & Zhao, Z. 2024. Facile preparation of Fe-Beta zeolite-supported transition metal oxide catalysts and their catalytic performance for the simultaneous removal of NOx and soot. *Chinese Journal of Chemical Engineering*, 76, pp.10-20. Available at: https://doi.org/10.1016/j.cjche.2024.07.016

Chen, Z., Meng, G., Han, Z., Li, H., Chi, S., Hu, G. & Zhao, X. 2025. Interfacial anchoring cobalt species mediated advanced oxidation: Degradation performance and mechanism of organic pollutants. *Journal of Colloid and Interface Science*, *679*, pp.67-78. Available at: https://doi.org/10.1016/j.jcis.2024.10.097

Devard, A., Brussino, P., Marchesini, F. A. & Ulla, M. A. 2019. Cu (5%)/Al_2O_3 catalytic performance on the phenol wet oxidation with H_2O_2: Influence of the calcination temperature. *Journal of Environmental Chemical Engineering*, 7(4), p.103201. Available at: https://doi.org/10.1016/j.jece.2019.103201

Diallo, M. M., Mijoin, J., Laforge, S. & Pouilloux, Y. 2016. Preparation of Fe-BEA zeolites by isomorphous substitution for oxidehydration of glycerol to acrylic acid. *Journal of Catalysis Communications*, 79, pp. 58-62. Available at: https://doi.org/10.1016/j.catcom.2016.03.003

Dou, X., Yan, T., Li, W., Zhu, C., Chen, T., Lo, B. T. W., Xiao,H. & Liu, L. 2025. Structure–reactivity relationship of zeolite-confined Rh catalysts for hydroformylation of linear α-olefins. *Journal of the American Chemical Society*, 147 (3), pp. 2726–2736. Available at: https://doi.org/10.1021/jacs.4c15445

Gabrienko, A. A., Kolganov, A. A., Yashnik, S. A., Kriventsov, V. V. & Stepanov, A. G. 2025. Methane to methanol transformation on Cu^{2+}/H-ZSM-5 zeolite. characterization of copper state and mechanism of the reaction. *Chemistry–A European Journal*, 31(10), e202403167. Available at: https://doi.org/10.1002/chem.202403167

Ghaffari, Y., Gupta, N. K., Bae, J. & Kim, K. S. 2019. Heterogeneous catalytic performance and stability of iron-loaded ZSM-5, zeolite-A, and silica for phenol

degradation: a microscopic and spectroscopic approach. *Journal of Catalysts*, *9*(10), p.859. Available at: https://doi.org/10.3390/catal9100859

He, Y., Lin, H., Luo, M., Liu, J., Dong, Y. & Li, B. 2020. Highly efficient remediation of groundwater co-contaminated with Cr (VI) and nitrate by using nano-Fe/Pd bimetal-loaded zeolite: process product and interaction mechanism. *Journal of Environmental Pollution*, 263, p.114479. Available at: https://doi.org/10.1016/j.envpol.2020.114479

Hunt, J.P. & Taube, H. 1952. The photochemical decomposition of hydrogen peroxide. *Journal of the American Chemical Society*, 74(23), pp.5999–6002. Available at: https://doi.org/10.1021/ja01143a052

IZA International Zeolite Association. 2018. *Database of Zeolite Structures*. [online] Available at: https://www.iza-structure.org/databases/ [Accessed : le 27 April 2025]

Ji, F., Li, C., Liu, Y. & Liu, P. 2014. Heterogeneous activation of peroxymonosulfate by Cu/ZSM5 for decolorization of Rhodamine B. *Journal of Separation and Purification Technology* , 135 , pp.1-6. Available at: https://doi.org/10.1016/j.seppur.2014.07.050

Jiang, S., Zhang, H., Yan, Y. & Zhang, X. 2017. Preparation and characterization of porous Fe-Cu mixed oxides modified ZSM-5 coating/PSSF for continuous degradation of phenol wastewater. *Journal of Microporous and Mesoporous Materials*, 240, pp.108-116. Available at : https://doi.org/10.1016/j.micromeso.2016.11.020

Jiang, Y., Yu, T., Zeng, S. & Luo, W. 2025. Direct and selective oxidation of methane into methanol over Cu/Fe-containing zeolites. *Journal of Molecular Catalysis*, 571, p.114721. Available at: https://doi.org/10.1016/j.mcat.2024.114721

Keshri, V. & Dutt, KR. 2021. Inhibitory effect of phenolic and flavonoidal content of H. indicum root extract on 1,1-diphenyl-2-picrylhydrazyl radicals. *Research Journal of Pharmaceutical and Technology*, 14(1), pp.235-238. Available at: 10.5958/0974-360X.2021.00041.X

Khader, E. H., Khudhur, R. H., Mohammed, T. J., Mahdy, O. S., Sabri, A. A., Mahmood, A. S. & Albayari, T. M. 2024. Evaluation of adsorption treatment method for removal of phenol and acetone from industrial wastewater. *Journal of Desalination and Water Treatment*, 317, p.100091. Available at: https://doi.org/10.1016/j.dwt.2024.100091

Kumar, N. D. & Swaminathan, M. 2024. Review on hierarchically porous BEA and ZSM-5 zeolites and Its industrial catalytic applications. *Journal of ES Materials & Manufacturing*, 24, p.1151. Available at: https://doi.org/10.30919/esmm1151

Lee, K. X., Tsilomelekis, G. & Valla, J. A. 2018. Removal of benzothiophene and dibenzothiophene from hydrocarbon fuels using CuCe mesoporous Y zeolites in the presence of aromatics. *Journal of Applied Catalysis B: Environmental*, 234, pp.130-142. Available at: https://doi.org/10.1016/j.apcatb.2018.04.022

Lin, Q., Feng, X., Zhang, H., Lin, C., Liu, S., Xu, H. & Chen, Y. 2018. Hydrothermal deactivation over CuFe/BEA for NH3-SCR. *Journal of industrial and engineering chemistry*, 65, pp.40-50. Available at: https://doi.org/10.1016/j.jiec.2018.04.009

Lin, Q., Liu, S., Xu, S., Liu, J., Xu, H., Chen, Y. & Dan, Y. 2020. Fabricate surface structure-stabilized Cu/BEA with hydrothermal-resistant via si-deposition for NOx abatement. *Journal of Molecular Catalysis*, 495, p.111153. Available at: https://doi.org/10.1016/j.mcat.2020.111153

Liu, H., Kim, G. E., Hong, C. O., Song, Y. C., Lee, W. K., Liu, D., Jang, S.H. & Park, Y. K. 2021. Treatment of phenol wastewater using nitrogen-doped magnetic mesoporous hollow carbon. *Journal of Chemiosphere*, 271, p.129595. Available at: https://doi.org/10.1016/j.chemosphere.2021.129595

Liu, T., Wang, H., Hu, Z. & Wei, F. 2021. Highly efficient adsorption of thiol compounds by ZSM-5 zeolites: Governing mechanisms. *Journal of Microporous and Mesoporous Materials*, *316*, p.110968. Available at: https://doi.org/10.1016/j.micromeso.2021.110968

Liu, Y., Lu, H. & Wang, G. 2021. Preparation of CuO/HZSM-5 catalyst based on fly ash and its catalytic wet air oxidation of phenol, quinoline and indole. *Journal of Materials Research Express*, 8(1), p.015503. Available at: https://doi.org/10.1088/2053-1591/abd6a4

Liu, Y., Osta, E. H., Poryvaev, A. S., Fedin, M. V., Longo, A., Nefedov, A. & Kosinov, N. 2023. Direct conversion of methane to zeolite-templated carbons, light hydrocarbons, and hydrogen. *Journal of Carbon*, 201, pp.535-541. Available at: https://doi.org/10.1016/j.carbon.2022.09.050

Martins, A., Nunes, N., Carvalho, A. P. & Martins, L. M. 2022. Zeolites and related materials as catalyst supports hydrocarbon oxidation reactions. *Journal of Catalysts*, 12 (2), p.154. Available at: https://doi.org/10.3390/catal12020154

Mohd, A. 2022. Presence of phenol in wastewater effluent and its removal: an overview. *International Journal of Environmental Analytical Chemistry*, 102(6), pp.1362-1384. Available at: https://doi.org/10.1080/03067319.2020.1738412

Mumtaz, H., Werle, S. & Sobek, S. 2024. A waste wet oxidation technique as a solution for chemical production and resource recovery in Poland. *Journal of Clean Technologies and Environmental Policy*, 26(5), pp.1363-1382. Available at: https://doi.org/10.1007/s10098-023-02520-4

Nguyen, H. M. & Carreon, M. L. 2022. Non-thermal plasma-assisted deconstruction of high-density polyethylene to hydrogen and light hydrocarbons over hollow ZSM-5 microspheres. *Journal of ACS Sustainable Chemistry & Engineering*, 10(29), pp. 9480-9491.

Available at: https://doi.org/10.1021/acssuschemeng.2c01959

Pan, C., Zhang, Q., Zhang, W., Bao, J., Dai, G., Liu, S.& Lan, J. 2025. Wet scrubbing coupled with advanced oxidation process for removal of chlorobenzene: A study of performance and mechanisms. *Journal of Environmental Research*, 268, p.120779.

Available at: https://doi.org/10.1016/j.envres.2025.120779

Peng, J., Zhou, P., Zhou, H., Huang, B., Sun, M., He, CS., Zhang, H., Ao, Z., Liu, W. & Lai, B. 2023. Removal of phenols by highly active periodate on carbon nanotubes: A mechanistic investigation. *Journal of Environmental Science & Technology*, 57(29), pp.10804–10815.

Available at: https://doi.org/10.1021/acs.est.2c08266

Ren, T. I. A. N., WANG, S. Y., LIAN, C. S., Xu, W. U., Xia, A. N. & XIE, X. M. 2019. Synthesis of the hierarchical Fe-substituted porous HBeta zeolite and the exploration of its catalytic performance. *Journal of Fuel Chemistry and Technology*, 47(12), pp.1476-1485. Available at: https://doi.org/10.1016/S1872-5813(19)30059-3

Said, K. A. M., Ismail, A. F., Karim, Z. A., Abdullah, M. S. & Hafeez, A. 2021. A review of technologies for the phenolic compounds recovery and phenol removal from wastewater. *Process Safety and Environmental Protection*, *151*, pp. 257-289. Available at: https://doi.org/10.1016/j.psep.2021.05.015

Saputera, W. H., Putrie, A. S., Esmailpour, A. A., Sasongko, D., Suendo, V. & Mukti, R. R. 2021. Technology advances in phenol removals: Current progress and future perspectives. *Journal of Catalysts*, 11(8), p.998. Available at: https://doi.org/10.3390/catal11080998

Sazama, P., Moravkova, J., Sklenak, S., Vondrova, A., Tabor, E., Sadovska, G. & Pilar, R. 2020. Effect of the nuclearity and coordination of Cu and Fe sites in β zeolites on the oxidation of hydrocarbons. *Journal of ACS Catalysis*, 10(7), pp.3984-4002. Available at: https://doi.org/10.1021/acscatal.9b05431

Selvam, T., Bandarapu, B., Mabande, G. T. P., Toufar, H. & Schwieger, W. 2003. Hydrothermal transformation of a layered sodium silicate, kanemite, into zeolite Beta (BEA). *Journal of Microporous and Mesoporous Materials*, 64(1-3), 41-50. Available at: https://doi.org/10.1016/S1387-1811(03)00508-0

Shaida, M. A., Verma, S., Talukdar, S., Kumar, N., Mahtab, M. S., Naushad, M. & Farooqi, I. H. 2023. Critical analysis of the role of various iron-based heterogeneous catalysts for advanced oxidation processes: A state of the art review. *Journal of Molecular Liquids*, 374, p.121259. Available at: https://doi.org/10.1016/j.molliq.2023.121259

Shirvani, M., Zhang, T., Gu, Y. & Hosseini-Sarvari, M. 2025. Sorghum grain as a bio-template: Emerging, cost-effective, and metal-free synthesis of C-doped g-C_3N_4 for photo-degradation of antibiotic, bisphenol A (BPA), and phenol under solar light irradiation. *Journal of Environmental Science and Pollution Research*, 32(4), pp.2036-2054. Available at: https://doi.org/10.1007/s11356-024-35868-1

Sobuś, N. & Czekaj, I. 2021. Comparison of synthetic and natural zeolite catalysts' behavior in the production of lactic acid and ethyl lactate from biomass-derived dihydroxyacetone. *Journal of Catalysts*, 11(8), p.1006. Available at: https://doi.org/10.3390/catal11081006

Song, S., Wu, G., Dai, W., Guan, N. & Li, L. 2016. Al-free Fe-beta as a robust catalyst for selective reduction of nitric oxide by ammonia. *Journal of Catalysis Science & Technology*, 6(23), pp.8325–8335. Available at: https://doi.org/10.1039/C6CY02124G

Sun, H., Li, J., Zhang, Y., Zhuang, L., Zhou, Z., Ren, Y., Xu, X., He, J. & Xue, Y. 2025. Treatment of high concentration phenol wastewater by low-frequency ultrasonic cavitation and long-term pilot scale study. *Journal of Chemosphere*, 370, p.143937. Available at: https://doi.org/10.1016/j.chemosphere.2024.143937

Sun, L., Zhang, X., Chen, L., Zhao, B., Yang, S. & Xie, X. 2016. Comparison of catalytic fast pyrolysis of biomass to aromatic hydrocarbons over ZSM-5 and Fe/ZSM-5

catalysts. *Journal of Analytical and Applied Pyrolysis*, 121, pp.342–346. Available at: https://doi.org/10.1016/j.jaap.2016.08.015

Taran, O.P., Zagoruiko, A.N., Yashnik, S.A., Ayusheev, A.B., Pestunov, A.V., Prosvirin, I.P., Prihodko, R.V., Goncharuk, V.V. & Parmon, V.N. 2018. Wet peroxide oxidation of phenol over carbon/zeolite catalysts: Kinetics and diffusion study in batch and flow reactors. *Journal of Environmental Chemical Engineering,* 6(2), pp.2551–2560. Available at: https://doi.org/10.1016/j.jece.2018.03.017

Thomsen, L. B. S., Anastasakis, K. & Biller, P. 2022. Wet oxidation of aqueous phase from hydrothermal liquefaction of sewage sludge. *Journal of Water research*, *209*, p.117863. Available at: https://doi.org/10.1016/j.watres.2021.117863

Tian, K., Pan, J., Liu, Y., Wang, P., Zhong, M., Dong, Y. & Wang, M. 2024. Fe-ZSM-5 zeolite catalyst for heterogeneous Fenton oxidation of 1, 4-dioxane: effect of Si/Al ratios and contributions of reactive oxygen species. *Journal of Environmental Science and Pollution Research* , *31* (13), pp.19738-19752. Available at: https://doi.org/10.1007/s11356-024-32287-0

Toloza-Blanco, L., Góra-Marek, K., Tarach, K. A., Sobalska, J., Martínez-Triguero, J., Plá-Hernandez, A. & Palomares, A. E. 2024. Catalytic oxidation of volatile organic compounds with Mn-zeolites. *Journal of Catalysis Today*, 432, p.114570. Available at: https://doi.org/10.1016/j.cattod.2024.114570

Treacy, M.M.J. & Higgins, J.B. 2007. *Collection of Simulated XRD Powder Patterns for Zeolites* (5th ed.). Amsterdam: Elsevier. Available at: https://doi.org/10.1016/B978-0-444-53067-7.X5470-7

Valkaj, K. M., Wittine, O., Margeta, K., Granato, T., Katović, A. & Zrnčević, S. 2011. Phenol oxidation with hydrogen peroxide using Cu/ZSM5 and Cu/Y5 catalysts. *Polish Journal of Chemical Technology*, *13*(3), pp.28-36. Available at: https://doi.org/10.2478/v10026-011-0033-6

Villegas, V. A. R., Ramirez, J. I. D. L., Perez-Sicairos, S., Yocupicio-Gaxiola, R. I., González-Torres, V. & Petranovskii, V. 2024. Catalyst for lactose hydrolysis based on zeolite Y modified with Fe species by ultrasound treatment. *Journal of Environmental Advances*, *15*, p.100475. Available at: https://doi.org/10.1016/j.envadv.2023.100475

Wang, H., Xu, R., Jin, Y. & Zhang, R. 2019. Zeolite structure effects on Cu active center, SCR performance and stability of Cu-zeolite catalysts. *Journal of Catalysis Today*, 327, pp.295-307. Available at: https://doi.org/10.1016/j.cattod.2018.04.035

Wu, Y., Zhang, H. & Yan. Y. 2020. Effect of copper ion-exchange on catalytic wet peroxide oxidation of phenol over ZSM-5 membrane. *Journal of Environmental Management*, 270, p.110907. Available at: https://doi.org/10.1016/j.jenvman.2020.110907

Xie, J., Zhuang, W., Yan, N., Du, Y., Xi, S., Zhang, W., Tang, J., Zhou, Y. & Wang, J. 2017. Directly synthesized V-containing BEA zeolite: Acid-oxidation bifunctional catalyst enhancing C-alkylation selectivity in liquid-phase methylation

of phenol. *Chemical engineering journal*, 328, pp.1031-1042. Available at: https://doi.org/10.1016/j.cej.2017.07.100

Zang, J., Yu, H., Liu, G., Hong, M., Liu, J. & Chen, T. 2023. Research progress on modifications of zeolite Y for improved catalytic properties. *Journal of Inorganics*, 11(1), p.22. Available at: https://doi.org/10.3390/inorganics11010022

Zhang, J., Shao, S., Guo, Q., Duan, X., Liu, Y. & Jiao, W. 2025. Co-removal of phenol and Cr (VI) by high gravity coupled heterogeneous catalytic ozonation-adsorption. *Journal of Separation and Purification Technology*, 358(Part A), p.130297. Available at: https://doi.org/10.1016/j.chemosphere.2024.143937

Zhou, X., Wang, M., Yan, D., Li, Q. & Chen, H. 2019. Synthesis and performance of high efficient diesel oxidation catalyst based on active metal species-modified porous zeolite BEA. *Journal of Catalysis*, 379, 138-146. Available at: https://doi.org/10.1016/j.jcat.2019.09.029

Компаративна студија два различита зеолита, BEA и ZSM-5, модификована бакром и гвожђем током оксидације фенола водоник-пероксидом

Фатиха Талхауи[а], **аутор за преписку**, *Фатиха* Хамиди[а], *Франсиско* Медина[б]

[а] Универзитет наука и технологије „Мухамед Будијаф", Хемијски факултет, Лабораторија функционалних и наноструктурираних екоматеријала, Оран, Алжир.

[б] Катедра за хемијско инжењерство, Универзитет „Ровира и Виргили", Авингуда делс Паисос Каталанс, 26, 43007, Тарагона, Шпанија.

ОБЛАСТ: материјали, хемијска технологија
ВРСТА ЧЛАНКА: оригинални научни рад

Резиме:

Увод/циљ: Загађење воде органским једињењима као што је фенол представља значајан еколошки ризик. Циљ овог истраживања био је да се упореди каталитичка ефикасност зеолита ZSM-5 и BEA, модификованих гвожђем (Fe) и бакром (Cu), у мокројоксидацији фенола коришћењем водоник-пероксида (H_2O_2).

Метод: Зеолити BEA и ZSM-5 синтетисани су хидротермалним методама, а затим подвргнути јонској размени ради уношења Cu^{2+} и Fe^{2+}. Катализатори су окарактерисани техникама XRD, FTIR, SEM и XPS. Оксидација фенола извођена је на 80°C у воденој средини, са моларним односом H_2O_2/фенол између 10:1 и 15:1. Реакциони производи анализирани су методом HPLC.

Резултати: Кристална структура зеолита очувана је након јонске размене. Метали су били равномерно распоређени на површини. Катализатори Fe-BEA и Fe-ZSM-5 показали су највећу активност (до 99% конверзије), затим Cu-BEA (88%) и Cu-ZSM-5 (68%). Чисти зеолити показали су ниску активност (<10%). Оптималан однос

H_2O_2/фенол био је 14:1. Fe-BEA се показао као најефикаснији катализатор, комбинујући високу активност и бољу дифузију у порама.

Закључак: Зеолити модификовани гвожђем, посебно Fe-BEA, представљају веома ефикасне катализаторе за оксидацију фенола у воденој средини, надмашујући како узорке модификоване бакром, тако и чисте зеолите. Порозност структуре и природа метала кључни су фактори који одређују каталитичке перформансе.

Кључне речи: ZSM-5, BEA, водоник-пероксид, оксидација фенола, хетерогена катализа

Paper received on: 28.03.2025.
Manuscript corrections submitted on:03.04.2025.
Paper accepted for publishing on: 04.05.2025.

REVIEW PAPERS

Command and control information systems for military applications

Branislav M. Todorović[a], *Zoran* Vasić[b], *Andrija* Ostojić[c], *Saša* Sretenov[d], *Aleksandar* Kopta[e], *Aleksandar* Lazović[f], *Lazar* Paunović[g], *Veljko* Đilas[h], *Miloš* Delić[i], *Mirko* Delić[j]

[a] SEDEC, Belgrade, Republic of Serbia
e-mail: b.todoro@eunet.rs, **corresponding author,**
ORCID iD: https://orcid.org/0000-0003-1932-8332

[b] SEDEC, Belgrade, Republic of Serbia
e-mail: zoran.vasic@sedec.rs ,
ORCID iD: https://orcid.org/0009-0001-7743-2210

[c] SEDEC, Belgrade, Republic of Serbia
e-mail: software.engineer@sedec.rs,
ORCID iD: https://orcid.org/0009-0007-1318-0898

[d] COMARS, Belgrade, Republic of Serbia
e-mail: ceo@comars.com,
ORCID iD: https://orcid.org/0009-0009-5134-3816

[e] COMARS, Belgrade, Republic of Serbia
e-mail: akopta@gmail.com,
ORCID iD: https://orcid.org/0009-0006-5660-4534

[f] COMARS, Belgrade, Republic of Serbia
e-mail: aca.lazovic@gmail.com,
ORCID iD: https://orcid.org/0000-0002-4581-0459

[g] OPTERA, Belgrade, Republic of Serbia
e-mail: lazar.paunovic@optera.rs,
ORCID iD: https://orcid.org/0009-0005-7945-4674

[h] OPTERA, Belgrade, Republic of Serbia
e-mail: veljko.djilas@optera.rs,
ORCID iD: https://orcid.org/0009-0005-2983-8709

[i] MAŠINOTEHNIKA, Belgrade, Republic of Serbia
e-mail: delicm96@gmail.com,
ORCID iD: https://orcid.org/0009-0007-0598-7894

[j] MAŠINOTEHNIKA, Belgrade, Republic of Serbia
e-mail: delicmirko@gmail.com,

ORCID iD: https://orcid.org/0009-0009-5543-1848

https://doi.org/10.5937/vojtehg73-59336

FIELD: Information technologies
ARTICLE TYPE: Review paper

Abstract:

Introduction/purpose: A command and control information system (C2IS) is a technical system designed to provide decision makers with the information they need to plan, coordinate, and manage operations. It consists of hardware and software, and includes a specialized set of tools and processes that aim to ensure the timely and accurate flow of information. C2IS can be intended for military applications, public safety, and corporate management. The paper presents the historical development of military C2IS. Examples of modern C2IS of some technologically advanced countries are given, such as the USA (NATO), the Russian Federation, the People's Republic of China, India, the United Kingdom, France and Israel.

Methods: This article is a review of 60+ references relating to the historical development of military C2IS, as well as modern C2IS of some technologically advanced countries.

Results: Based on cited references, this article summarizes the historical development of C2IS for military applications, and presents a brief overview of the modern C2IS of seven technologically advanced countries.

Conclusion: Command and control information systems are widely used in modern militaries. Their development began in the mid-20th century. Over the past 80 years, C2IS have evolved from the manually operated systems of the 1940s to the modern systems that are driven by artificial intelligence (AI) today. The era of modern C2IS began in the 1990s. Since then, the focus has been on decentralization and autonomous decision making, efficient data management, and cybersecurity. In recent years, the central focus has been on the integration of AI into C2IS.

Key words: defense technologies, command and control information systems, informatics, telecommunications

Introduction

Command and control theory separates the art of *command and control* (C2) from technical systems that support C2. A technical system, which consists of hardware and software and supports C2 by providing decission makers (commanders) with the necessary information to make decisions, is called a *command and control information system* (C2IS).

For years it was thought that the qualities of commanders and their ideas are more important to a general theory of command and control than are qualities of their technical hardware and software systems. In an age of almost unlimited technical capabilities, commanders are increasingly faced with the problem of too much information, not too little. In this regard, technical systems that perform acquiring, filtering, correlating, and fusing information have become extremely important. Understanding which information is the most important for decision making is now a major issue in the design of C2 information system (Builder et al, 1999).

Rather than thinking of C2 as a static set of defined activities that take place, the modern concept views C2 as a socio-technical capability that must continuously evolve to respond to the scale and complexity of the challenges likely to be faced in the future operating environment (Ellis et al, 2024).

C2IS consists of hardware and software, and involves a specialized set of tools and processes designed to provide accurate and secure information to decision makers for planning, coordinating, and managing operations. The applications of C2IS can be very diverse. They include, but are not limited to:

- Military applications,
- Public safety and security, and
- Corporate management.

In this article, the focus will be on the use of C2IS in military applications. In that sense, C2IS can be defined as a military system designed for retrieval, storage, exchange, processing and visualization of tactical data in order to provide effective decision-making support to commanders.

There is no straightforward definition of C2, reflecting debates about the term's scope and relevance in the contemporary operating environment. At the most basic level, C2 can be broken down into its two constituent elements (Black et al, 2024):

- Command: the authority given to an individual in the armed forces for the direction, coordination and control of military forces, and
- Control: the authority held by a commander over part of the activities of subordinate or other organisations, not otherwise under his/her command, which includes responsibility for implementing orders or directives.

The usage of new C2-related buzzwords reflects the fact that 'words move money', and that new terminology can help provide new funding for defence projects (Black et al, 2024).

Since control requires the ability to communicate, and usually depends on computers, in technical literature the acronyms C3 (*command, control and communications*) or C4 (*command, control, communications and computers*) are also encountered.

Furthermore, since the role of the C2 information system is to provide decision support, in technical literature the term *command information and decision support system* (CIDSS) is also used.

Finally, the examples of jargon include, but are certainly not limited to: C3I (*command, control, communications and intelligence*), C4ISR (command, control, communications, computers, intelligence, surveillance and reconnaissance), C4ISTAR (which adds target acquisition), C5ISR (which adds cyber), and even C6ISR (which also includes combat systems).

Although different terms are used for essentially the same concept, the authors of this paper have chosen to use the term *command and control information system* and the corresponding acronym C2 *information system*, i.e. C2IS, in the rest of this article.

Since C2IS is a highly sensitive military system, in most cases the exact technical details are not publicly available. However, some sources provide credible data based on military doctrine and expert analysis.

There is no C2IS that integrates all types, branches and services of military forces. As a rule, the existing systems are designed for one type: the Army, the Navy or the Air Force, or for some specific branches or services. A special problem is defining the requirements that C2IS needs to fulfill. In technical literature, one can find a statement that „we have the situation where defining Army C2IS requirements is perhaps more difficult than building the systems to meet those requirements" (Kroening, 1986). So, one can say that a military C2IS is composed of multiple interconnected subsystems focused on a specific type, branch or service.

The term C2IS is often equated with the term *integrated combat system* (ICS), but there is a significant difference between the two. The aim of C2IS is to process battlefield data to help commanders make strategic and tactical decisions, as well as coordination in military operations. On the other hand, the aim of ICS is to execute combat missions by integrating sensors, C2, and weapons. In other words, an ICS often incorporates C2IS functions, but extends beyond to include actual combat execution.

In the text which follows, the history of military C2IS development and some modern military C2IS will be considered.

History of military C2IS development

The development of command and control information systems (C2IS) for military applications began in the mid-20th century, evolving from early command and control (C2) concepts used in World War II.

The British integrated air defence system in World War II, known as the Dowding System after the Air Chief Marshal Hugh Dowding (1882-1970), is considered to be the first C2IS. This system included code-breakers, radar stations, observers, searchlights, barrage balloons, anti-aircraft guns, and fighter planes. Working together through a combined operations centre, these various elements ensured that the German Air Force could be better tracked and intercepted (Cartwright, 2024). The Dowding System is considered to be a C2IS, although it has elements of an ICS because it contains aircraft guns.

The Semi-Automatic Ground Environment (SAGE) system was the first USA air defense C2IS developed by the Lincoln Laboratory of the Massachusetts Institute of Technology (MIT) (Freeman, 1995). SAGE was a system of large computers and associated network equipment that coordinated data from many radar locations and processed them to produce a unified image of airspace over a wide area. The processing power behind SAGE was supplied by the largest discrete component-based computer ever built, the AN/FSQ-7, manufactured by IBM (IBM History, 2025). SAGE was operating in this role from the late 1950s into the 1980s.

During the 1960s, a major confrontation between the two superpowers occured, leading to an exhausting arms race. New types of weapons and military equipment were being developed at a high rate. Microelectronics and, based on it, telecommunications and computing equipment were developing especially quickly, which in turn became a powerful platform for the development of C2IS for weapons control.

During the 1960s, the USA and NATO began integrating digital computers into C2IS. The Tactical Fire Direction System (TACFIRE) was a computer based system for support of USA Army artillery units (Salisbury, 1979).

The Tactical Air Control System (TACS) is the USA Air Force's C2IS for planning, coordinating, and managing air operations in support of joint and combined operations. It integrates various ground, airborne, and space-based assets to ensure effective air support for military operations.

A version of TACS, a so-called distributed TACS, consists solely of ground-based C2 nodes separated by hundreds of kilometers. Erlang analysis yielded a message queuing time of 20 seconds and 97% voice channel availability (Bausch, 1987). TACS is a roofing system whose origins date back to the 1940s and continues to evolve with new AI-driven battle management, improved multi-domain operations, and enhanced connectivity with space and cyber warfare assets.

In the late 1960s, the USA and NATO began developing digital systems like JTIDS (Joint Tactical Information Distribution System) and AWACS (Airborne Warning and Control System) (Brick and Ellersick, 1980).

The JTIDS project was initiated with an advanced planning study sponsored by the USA Air Force Electronic Systems Division and conducted by the MITRE Corporation in 1967. JTIDS is an L band (1 to 2 GHz) Distributed Time Division Multiple Access (DTDMA) radio network used to support data communications needs, mainly for air and missile defense. It produces a spread spectrum signal using Frequency-Shift Keying (FSK) and Phase-Shift Keying (PSK) to spread radiated power over a wider range of frequencies than conventional radio transmissions. This reduces susceptibility to noise, jamming, and interception (Fried, 1978; Golliday, 1985; Roetzheim, 1987; Wang et al, 2005).

The JTIDS project underwent several phases of development and implementation. By the 1990s, it was largely operational and widely deployed across USA and NATO forces.

At the beginning of 2000s, JTIDS was succeeded by the Multifunctional Information Distribution System (MIDS) which provided smaller, more efficient, and interoperable terminals. So, while JTIDS itself was not officially finished, its role was gradually phased out in favor of MIDS (Collins Aerospace, 2025).

AWACS is an airborne C2 platform designed for surveillance, battle management, and airspace control. It provides real-time intelligence, tracking, and coordination of air operations.

The Tactical Air Control System (TACS), the Joint Tactical Information Distribution System (JTIDS), and the Airborne Warning and Control System (AWACS) are all key components of the USA Air Force's C2 network. They work together to provide real-time situational awareness, air and space management, and secure communication to provide commanders with effective decision-making support.

Soviet C2 information systems were specialized military systems designed to provide situational awareness and facilitate communication, coordination and decision making across different types, branches and

services of the Soviet armed forces. These systems were crucial for both conventional and nuclear warfare (Donnelly, 1976).

ASUV (Автоматизированная система управления войсками - Automated troop control system) was the first Soviet C2 information system introduced in 1960s. It was a semi-automated C2IS similar to its Western counterpart SAGE. ASUV was designed to support decision making and coordination of forces, including tank formations and frontal aviation management. It consisted of subsystems for managing the Army, the Air Force, the Air Defense, and the Rear Management (Sterling, 1985; Военное обозрение, 2013).

Later, in the 1970s and 1980s, the Soviet Union developed its own digital computer-based C2 information system. In comparison to NATO's systems, Soviet's systems are more centralized, less advanced in computing and have a stronger focus on a strategic-level C2IS rather than tactical digitalization. They allow real-time tracking of threats across the ex-Warsaw Pact nations and enhance rapid decision making in specific types and branches, such as (Sterling, 1985; Военное обозрение, 2013; Herspring, 1990; Военное обозрение, 2012):

- Manevr[1] (Манёвр) – C2 information system for ground forces at operational-tactical levels,
- Vozdukh (Воздух) – air defense C2 information system, integrated with radar networks,
- Legend (Легенда) – naval surveillance and targeting C2 information system,
- Signal (Сигнал) – C2 information system for strategic missile forces,
- Kazbek (Казбек) – high-level nuclear C2 information system, linked to the Cheget briefcase carried by the Soviet leadership, and
- Cheget (Чегет) – C2 information system used to authorize nuclear strikes.

Soviet C2ISs use landlines, radio, and satellite communications to ensure redundancy in case of NATO strikes, as well as hardened underground bunkers and mobile command centers. They are highly centralized with decision making concentrated in the General Staff (Генеральный штаб) and the Ministry of Defense (Министерство обороны СССР).

[1] Sometimes, non-Russian sources may mistranslate or misinterpret "Manevr" as "Maneuver".

The Soviet C2 doctrine emphasized deception (маскировка) to confuse adversaries and heavy use of electronic warfare (EW) to disrupt NATO communications (Ivanov et al, 1977).

Modern military C2IS

For the past 80 years, C2IS development has evolved from manually operated systems in 1940s to AI-driven, real-time, networked battle management systems today.

It can be said that the era of modern C2IS began in 1990s. Since that time, the focus has been on multi-domain operations, decentralization and autonomous decision making, efficient data management, and cybersecurity. Fort he last few years, the central focus has been on the integration of AI into C2 information systems.

USA and NATO

NATO's primary Joint Command and Control (JC2) information system is crucial for ensuring interoperability and military coordination among the NATO member states, enabling them to operate effectively in joint operations. The new USA military intiative Joint All-Domain Command and Control (JADC2) information system aims to enhance this capability of real-time data exchange by integrating sensors and systems from all military types, branches and services. AI enables new and unimagined possibilities for the C2IS. An analytic framework for identifying and developing AI command and control applications for modern warfare is presented in (Lingel et al, 2020). The authors examine and recommend opportunities for applying AI and automation to deliberate planning for JADC2.

Information from all domains (land, sea, air, space, and cyberspace) is processed in a unified JADC2 network, using cloud computing, big data analytics and AI to improve situational awareness and accelerate decisions (Deptula, 2022).

The development of the JADC2 information system involves multiple contracts awarded by the U.S. Department of Defense (DoD) to various companies. Each of these contracts has a ceiling value of $950 million, structured as indefinite-delivery/indefinite-quantity (IDIQ) agreements. This structure allows the DoD to issue task orders up to the specified ceiling during the term of the contract. Notable recipients of these contracts include Aptima, Science Applications International Corp. (SAIC) and Oceus (Aptima, 2025; Businessware, 2020; Businessware, 2022).

Given that multiple companies have been awarded these $950 million ceiling contracts, the cumulative potential investment in the JADC2 development is significant. However, the exact total expenditure depends on the specific task orders issued and executed under each contract, which may vary and not necessarily reach the maximum ceiling. Therefore, while the awarded contracts suggest a significant financial commitment to JADC2, the precise total cost of its development remains variable and contingent upon future DoD decisions and budget allocations. In fiscal year 2024, the DoD requested $1,8 billion for AI and $1,4 billion for the JADC2 initiatives (Harper, 2023).

JADC2 consists of several subsystems, such as:

- LC2IS (Land C2 Information System),
- MC2IS (Maritime C2 Information System),
- AC2IS (Air C2 Information System),
- Space C2IS (Space C2 Information System),
- Cybersecurity C2IS (Cybersecurity C2 Information System), and
- LOGFAS (Logistics Functional Area Services) – Logistics planning and managing system.

The development cost of LOGFAS is not explicitly detailed in open sources. However, a related modernized version, the Logistics Functional Services (LOG FS), which aims to replace LOGFAS, was initially allocated €30 million. This budget is expected to increase due to the additional requirements and approval processes (Pecina and Dufek, 2016; Pecina and Husak, 2018).

The NATO Integrated Air and Missile Defence System (NATINAMDS**)** is NATO's overarching C2 framework for coordinating air and missile defence across allied European nations. It ensures a unified approach to detecting, tracking, and countering airborne threats, including aircraft, cruise missiles, and ballistic missiles (NATO IAMD, 2025).

FBCB2 (Force XXI Battle Command Brigade-and-Below)[2] is the USA and NATO tactical C2 information system to provide real-time situational awareness, digital C2, and friendly force tracking at the brigade level and below, introduced in the late 1990s. It provides ground forces, armored vehicles, aviation, and joint forces with a unified picture of the

[2] The Force XXI Battle Command Brigade-and-Below (FBCB2) and Blue Force Tracker (BFT) are closely related systems, with BFT being a satellite-based extension of the FBCB2 program (Army Programs FBCB2/BFT, 2025).

battlefield (Army Programs FBCB2, 2025). Since 2015, FBCB2 has been upgraded to the JBC-P (Joint Battle Command-Platform) with improved interfaces, faster satellite connectivity, and cybersecurity enhancements. The development of the JBC-P began in 2010. The combined planned development and procurement funding for the JBC-P program through fiscal year 2018 was approximately $824 million (Studylib.net, 2014).

The Nett Warrior system is a soldier-level situational awareness C2 information system, designed to enhance infantry with real-time digital battlefield data (Nett Warrior, 2015). It is part of the Integrated Tactical Network (ITN) and serves a similar role to Russian Strelets.

The AN/MLQ-44 is a tactical EW system used by the USA Army. Electronic intelligence (ELINT) platforms are designed to intercept electromagnetic signals for radio communications (Hitchens and Valasek, 2006).

Russian Federation

The Russian Armed Forces employ a mix of Soviet legacy and modern digital C2 systems to support their military operations, including space, electronic, and cyber warfare. These systems are designed to enhance situational awareness and coordinate military multi-domain operations at the strategic, operational, and tactical levels (Poulsen and Staun (eds.), 2021).

The Russian strategic-level C2 information system is Akatsiya-M (Акация-М). It serves as the backbone of the Russian C2 information system which integrates data from all domains (land, sea, air, space, and cyberspace) and supports automated decision making and real-time coordination of military operations for the Russian General Staff and high-level military command centers (McDermott, 2019-a; McDermott, 2019-b). It is used for strategic missile forces.

Another strategic-level C2 information system is Kazbek (Казбек**)** – the nuclear command and control system, linked to the Cheget briefcase.

Andromeda-D (Андромеда-Д) is a C2 information system developed for Russian Airborne Troops (VDV – Воздушно-десантные войска)**.** It integrates satellites, drones, radio communications, and radio reconnaissance into a single network for real-time troop and artillery situational awareness and operational coordination. Andromeda-D is a critical system of Russia's airborne warfare strategy (Withington, 2025; McDermott, 2019-a).

ESU TZ (Единая Система Управления Тактического Звена) is a tactical-level C2 information system for the brigade level and below. It supports mechanized and infantry units with real-time battlefield data

from drones, and uses AI for decision support and automated targeting. ESU TZ is integrated with EW units. This system is similar to NATO's FBCB2 (Live Journal, 2025).

Polyana-D4M (Поляна-Д4М) is a C2 information system developed for Russian Aerospace Forces[3] (Воздушно-Космические Силы), which is a branch of the Russian Armed Forces combining air and space capabilities. It provides real-time situational awareness from satellites and radar systems, coordinates the work of various air defense systems, such as Buk-M3, Pantsir-S1, S-300, S-400, S-500 missile defense systems, and integrates air force units with early warning systems for missile defense (Dbpedia.org, 2025; Poulsen and Staun (eds.), 2021).

Strelets (Стрелец) is a soldier-level situational awareness system for infantry. It provides GPS-based navigation, secure communication, and targeting assistance. Strelets is used by Russian Special Forces (Силы специального назначения - Спецназ) and mechanized infantry.

Borisoglebsk-2 (Борисоглебск-2) is an EW system aimed to disrupt enemy's C2 capabilities. It jams communications, satellite navigation (GPS, GLONASS, Galileo), and radar signals in the frequency range from 1.5 MHz to 2 GHz. The Krasukha-4 (Красукха-4) is specialized to jam airborne early warning radars (AWACS), drones and satellite communication links (Uppal, 2024).

The RuNet (Рунет) is the Russian sovereign internet infrastructure that reduces dependence on the global system and provides resilience to cyberattacks or external disconnection. It ensures military communications remain operational if the global internet is cut off.

People's Republic of China

The People's Liberation Army (PLA) has been actively developing and integrating advanced C2 information systems to enhance its military capabilities (Scobell and Kamphausen, 2007). The PLA has undergone many changes since Xi Jinping became general secretary of the Communist Party of China in 2013. Efforts at modernising the PLA have been conducted in earnest for the past 10 years through the overhaul of the organisation and the introduction of latest technologies to make it battle-ready. These systems integrate advanced AI, big data, satellite networks, and cyber capabilities (Bommakanti and Amjad, 2023; Alsaied, 2023). However, for security reasons, detailed technical specifications remain classified. There are no widely known or publicly confirmed

[3] On August 1, 2015, the Russian Air Forces and the Russian Aerospace Defence Forces were merged to form the Russian Aerospace Forces.

Chinese military C2 systems in authoritative defense publications or PLA documentation.

According to DeepSeek, Qin Tian and Jian Bing are two distinct strategic-level Chinese military satellite C2 information systems, each serving different roles in the PLA space and reconnaissance infrastructure. The difference between the Qin Tian and Jian Bing C2 information systems lies in their respective applications and operational frameworks. Qin Tian is designed to provide situational awareness, facilitate decision making, and enable centralized control over operations. Jian Bing refers to a different kind of C2 systems, more focused on surveillance, reconnaissance, and cybersecurity of digital infrastructure.

Zhong Jun is a tactical-level C2 system for the brigade level. Using AI, this system integrates signals received from drones and EW warnings.

According to (Demarest, 2023), China is developing its own version of JADC2 to counter the USA.

India

The Indian Integrated Defence Staff released the first-ever public joint doctrine for the Indian Armed Forces (JDIAF-2017) in April 2017. Within this doctrinary document, “C2 is underpinned by a philosophy of centralised intent and decentralized managing” (Rej, A. and Joshi, S. 2018).

Indian military C2 systems are used to plan, coordinate, manage, and control operations across all domains: land, air, sea, space, and cyber. These systems are critical for ensuring situational awareness**,** decision making, and operational effectiveness in both peacetime and wartime scenarios. In the last few years, research efforts have been focused on integrating AI, cyber technology, and quantum technology into the Indian Armed Forces (Pant and Bommakanti, 2023).

The Integrated Strategic Command System (ISCS) is a critical component of the Indian nuclear C2 infrastructure, ensuring the secure and effective management of its strategic forces. It is designed to facilitate decision making at the highest levels of government and military leadership while maintaining strict control over nuclear assets (Borja and Ramana, 2020).

The Integrated Air Command and Control System (IACCS) is a sophisticated network linking radars, AWACS, ground stations, and fighter aircraft. It provides real-time situational awareness and rapid response capability, and acts as the backbone of the Indian air defense command network (IndraStra Global, 2015; BEL C4ISS. 2025).

The Naval Command Control Communication Intelligence (NC3I) network is an interconnected coastal command and control system capable of collecting data from coastal radars, ships, submarines, aircraft, and satellites in Gurgaon, a city just outside the capital city of Delhi. The Indian Navy has also constructed multiple communication centres for transmitting messages in the VLF bandwidth to its submarines (Pandit, 2014a; Pandit, 2014b).

The Command Information and Decision Support System (CIDSS) is a C2 system to support tactical decision making**,** which offers real-time data sharing and battlefield visualization. It interconnects various units within systems like artillery, logistics, and electronic warfare (BEL CIDSS, 2025).

The Battlefield Surveillance System (BSS) is a mobile C2 system capable of integrating data from drones**,** sensors, and reconnaissance units, processing and fusing them. In that way, it enhances situational awareness on the battlefield and aids the commander in decision making, particularly in border areas (BEL BSS, 2025).

United Kingdom

The United Kingdom (UK) uses advanced C2 systems across all its military forces to ensure effective planning, coordination, and managing of operations. These systems integrate intelligence, surveillance, communications, and data processing to support joint and multi-domain operations. The UK's military C2 systems are evolving towards greater integration, automation and multi-domain operations to ensure the UK remains a key player in NATO.

The UK's strategic military C2 information systems are evolving to meet complex and diverse threats, particularly in air and missile defense, space, and joint operations.

GUARDIAN is a new C2IS designed to protect against aerial threats by linking radars and radios across the UK and NATO to provide a real-time air picture. It supports rapid decision making and fighter jet deployment to intercept or escort suspicious aircraft. GUARDIAN was developed with IBM and has been operational since 2022 (DE&S, 2022).

Also, the UK is developing the Borealis space system to protect military satellites by providing timely, interoperable information to commanders, enhancing space domain awareness (Borealis, 2025).

The UK military uses several tactical C2 systems designed to enhance situational awareness, force tracking, and communication at the tactical level.

The BAE Tactical Command and Control (TC2) system enables real-time tracking of vehicles and soldiers throughout the chain of command, providing a comprehensive operational picture. It improves situational awareness and enables forces to communicate operational intelligence up and down the chain of command (BAE TC2, 2025).

LETacCIS (Land Environment Tactical Communication and Information Systems) is a UK Army programme aimed at delivering the next generation of C4I information systems to support land environment operations, enhancing connectivity and information sharing at the tactical level (LETacCIS, 2023; BattleSpace, 2023).

France

The French military employs sophisticated and evolving C2 systems across its armed forces, integrating air, land, naval, and space domains. These systems emphasize interoperability, resilience, and modernization to meet contemporary operational demands.

SCCOA (Système de Commandement et de Conduite des Opérations Aérospatiales) is a networked C2 system integrating radar, AWACS, and ground-based assets for real-time situational awareness (RDN, 2025).

SICF (Système d'Information pour le Commandement des Forces) is a C2 information system in service with land forces at tactical levels from the headquarters to the brigade. SIA (Système d'information des Armées) is a unified C2 system for the Army and the Navy. SICF and SIA are produced by Thales (Thales, 2016).

Israel

Israeli military C2 systems are highly advanced and integral to its defense operations across multiple domains.

Tirat Ha'Agam (Castle of the Lake) is the primary C2 system used at the General Headquarters level, providing a real-time, comprehensive battle picture for decision makers. It supports operational processes from routine actions to total war scenarios and is designed for stationary use with robust IT infrastructure integration. The system has been under continuous development since the late 1990s (IsraelDefense, 2016).

The Citron Tree and the Golden Almond are C2 systems which integrate data from multiple sensors to create a unified aerial threat picture and coordinate interceptors against ballistic missiles, rockets, drones, and aircraft. They employ advanced algorithms and AI to optimize target tracking and interception (Elbit, 2024).

The Orion Handheld C2 system consists of thousands of smartphone-like ruggedized terminals that have been delivered to infantry units to replace paper maps with a digital geographic information system (GIS). They offer 3D imagery of the battlespace and improve situational awareness and planning at the tactical level (Janes, 2022).

Conclusion

A command and control information system (C2IS) is a technical system designed to provide decision makers with the information they need to plan, coordinate, and manage operations. It integrates data from various sources, processes it, and presents it in a way that helps decision makers (commanders) effectively plan, coordinate and manage operations. C2IS can be intended for military applications, public safety, and corporate management. This article focuses on C2IS for military applications. The development of military C2IS began in the mid-20th century. Over the past 80 years, C2IS have evolved from manually operated systems of the 1940s to modern systems driven by artificial intelligence today. The era of modern C2IS can be said to have begun in the 1990s. Since then, the focus has been on decentralization and autonomous decision making, efficient data management, and cybersecurity. In recent years, the central focus has been on the integration of AI into C2IS.

References

Builder, C.H., Bankes, S.C. and Nordin, R. 1999. *Command Concepts – A Theory Derived from the Practice of Command and Control*, RAND Corporation, Santa Monica (CA). ISBN 0-8330-2450-7 [online]. Available at: https://www.rand.org/content/dam/rand/pubs/monograph_reports/2006/MR775.pdf [Accessed: 10 February 2025].

Ellis, C., Lucas, R., Fawkes, B., Robson, M., Brown, A., Keedwell, E. and Black, J. 2024. *Command and Control in the Future*, RAND Europe, Cambridge (UK) [online]. Available at: https://assets.publishing.service.gov.uk/media/669e455049b9c0597fdb01bd/Paper_3_Conceptualising_C2_as_a_Capability_Final.pdf [Accessed: 10 February 2025].

Black, J., Lucas, R., Kennedy, J., Hughes, M. and Fine, H. 2024. *Command and Control in the Future*, RAND Europe, Cambridge (UK) [online]. Available at: https://assets.publishing.service.gov.uk/media/65c4dde79c5b7f0012951b35/Command_Control_Future_C2_Complexity.pdf [Accessed: 10 February 2025].

Kroening, D.W. 1986. Army Command and Control Information Systems Requirements Definition, *IEEE Transactions on Systems, Man, and Cybernetics*, 16(6), pp. 974-979. Available at: https://doi.org/10.1109/TSMC.1986.4309015.

Cartwright, M. 2024. Dowding System, *World History Encyclopedia* [online]. Available at: https://www.worldhistory.org/Dowding_System/ [Accessed: 10 February 2025].

Freeman, E.C. (Editor). 1995. *Technology in the National Interest*, MIT Lincoln Laboratory, Lexington (MA) [online]. Available at: https://www.ll.mit.edu/about/history/sage-semi-automatic-ground-environment-air-defense-system [Accessed: 10 February 2025].

IBM History. 2025. *SAGE* [online]. Available at: https://www.ibm.com/history/sage [Accessed: 10 February 2025].

Salisbury, A.B. 1979. TACFIRE: A case history of a weapon system software development, *Journal of Systems and Software*, 1, pp.155-175. Available at: https://doi.org/10.1016/0164-1212(79)90015-3.

Bausch, F. A. 1987. Distributed TACS Communications, *Proc. of IEEE Military Communications Conference (MILCOM),* Washington (DC), pp. 0796-8000. Available at: https://doi.org/10.1109/MILCOM.1987.4795326.

Brick, D. and Ellersick, F. 1980. Future Air Force Tactical Communications, *IEEE Transactions on Communications*, 28(9), pp. 1551-1572. Available at: https://doi.org/10.1109/TCOM.1980.1094859.

Fried, W. R. 1978. Principles and Simulation of JTIDS Relative Navigation, *IEEE Transactions on Aerospace and Electronic Systems*, 14(1), pp. 76-84. Available at: https://doi.org/10.1109/TAES.1978.308581.

Golliday, C. 1985. Data Link Communications in Tactical Air Command and Control Systems, *IEEE Journal on Selected Areas in Communications*, 3(5), pp. 779-791. Available at: https://doi.org/10.1109/JSAC.1985.1146251.

Roetzheim, W. H. 1987. JTIDS Dynamic Net Management, *Proc. of IEEE Military Communications Conference (MILCOM),* Washington (DC), pp. 13-18. Available at: https://doi.org/10.1109/MILCOM.1987.4795150.

Wang, H., Kuang, J., Wang, Z. and Xu, H. 2005. Transmission performance evaluation of JTIDS, *Proc of IEEE Military Communications Conference (MILCOM)*, Atlantic City (NJ) pp. 2264-2268. Available at: https://doi.org/10.1109/MILCOM.2005.1606006.

Collins Aerospace. 2025 [online]. Available at: https://www.collinsaerospace.com/what-we-do/industries/military-and-defense/communications/tactical-data-links/multifunctional-information-distribution-system [Accessed: 17 February 2025].

Donnelly, C. 1976. *The Soviet War Machine: An Encyclopedia of Russian Military Equipment and Strategy,* Chartwell Books, New York, ISBN 978-0890090848.

Sterling, M.J. 1985. Soviet Reactions to NATO's Emerging Technologies for Deep Attack, RAND Note N-2294-AF [online]. Available at: https://www.rand.org/content/dam/rand/pubs/notes/2009/N2294.pdf [Accessed: 17 February 2025].

Военное обозрение. 2013. Концепция автоматизированной системы управления боем [online]. Available at: https://topwar.ru/33550-koncepciy-avtomatizirovannoy-sistemy-upravleniya-boevymi-deystviyami.html [Accessed: 17 February 2025].

Herspring, D.R. 1990. The Soviet High Command, 1967-1989, Princeton University Press, ISBN 978-0691633428.

Военное обозрение. 2012. Манёвр – первая советская АСУВ поля боя [online]. Available at: https://topwar.ru/19414-manevr-pervaya-sovetskaya-asuv-polya-boya.html [Accessed: 17 February 2025].

Ivanov, D.A, Savelyev, V.P. and Shemanskiy, P.V. 1977. *Fundamentals of Tactical Command and Control: A Soviet View* (translation from Russian), Soviet Military Thought, Moscow [online]. Available at: https://apps.dtic.mil/sti/tr/pdf/ADA141119.pdf [Accessed: 17 February 2025].

Lingel, S., Hagen, J., Hastings, E., Lee, M., Sargent, M., Walsh, M., Zhang, L.A. & Blancett, D. 2020. Joint All-Domain Command and Control for Modern Warfare, *RAND Corporation*, Santa Monica (CA). ISBN: 978-1-9774-0514-2 [online]. Available at: https://www.rand.org/pubs/research_reports/RR4408z1.html [Accessed: 17 February 2025].

Deptula, D. 2022. Making joint all domain command and control a reality, *War on the Rocks* [online]. Available at: https://warontherocks.com/2022/12/making-joint-all-demand-command-and-control-a-reality/ [Accessed: 24 February 2025].

Aptima, 2025 [online]. Available at: https://www.aptima.com/aptima-awarded-id-iq-contract-with-950-million-ceiling-to-enable-joint-all-domain-command-and-control-jadc2/?utm [Accessed: 24 February 2025].

Businesswire. 2020 [online]. Available at: https://www.businesswire.com/news/home/20200804005364/en/SAIC-to-Partner-with-U.S.-Air-Force-on-Joint-All-Domain-Command-and-Control-under-Multiple-Award-950-Million-Advanced-Battle-Management-System-Contract?utm [Accessed: 24 February 2025].

Businesswire. 2022 [online]. Available at: https://www.businesswire.com/news/home/20220926005136/en/Oceus-Awarded-to-the-Advanced-Battle-Management-System-IDIQ-to-Enable-Joint-All-Domain-Command-and-Control-JADC2?utm [Accessed: 24 February 2025].

Harper, J. 2023. Pentagon requesting more than $3B for AI and JADC2, *DefenseCoop* [online]. Available at: https://defensescoop.com/2023/03/13/pentagon-requesting-more-than-3b-for-ai-jadc2/?utm [Accessed: 24 February 2025].

Pecina, M. and Dufek, R. 2016. Use of LOGFAS tools in logistics planning in NATO, *Revista Academiei Fortelor Terestre*, 2(82), pp. 120-126 [online]. Available at: https://www.armyacademy.ro/reviste/rev2_2016/Pecina.pdf [Accessed: 24 February 2025].

Pecina, M. and Husak, J. 2018. Application of the new NATO logistics system, *Land Forces Academy Review,* 23(2), pp. 121-127, Available at: https://doi.org/10.2478/raft-2018-0014.

NATO IAMD. 2025 [online]. Available at: https://www.nato.int/cps/en/natohq/topics_8206.htm [Accessed: 3 March 2025].

Army Programs FBCB2. 2025 [online]. Available at: https://www.dote.osd.mil/Portals/97/pub/reports/FY2011/army/2011fbcb2.pdf?ver=2019 [Accessed: 3 March 2025].

Studylib.net. 2014 [online]. Available at: https://studylib.net/doc/10878983/unclassified [Accessed: 3 March 2025].

Army Programs FBCB2/BFT. 2025 [online]. Available at: https://www.globalsecurity.org/military/library/budget/fy2005/dot-e/army/2005fbcb2.pdf [Accessed: 10 March 2025].

Nett Warrior IOT&E Report. 2015 [online]. Available at: https://www.esd.whs.mil/Portals/54/Documents/FOID/Reading%20Room/Science_and_Technology/16-F-0250_(REPORT)_Nett_Warrior_IOT&E_Report.pdf [Accessed: 10 March 2025].

Hitchens, T. and Valasek, T. 2006. The security dimension of European collective efforts in space. In: *SIPRI Yearbook 2006: Armaments, Disarmament and International Security* [online]. Available at: https://www.sipri.org/sites/default/files/YB06%20565%2011.pdf [Accessed: 10 March 2025].

Poulsen, N.B. and Staun. J. (eds.). 2021. *Russia's Military Might – A Portrait of its Armed Forces,* Djøf Publishing, København [online]. Available at: https://www.fak.dk/globalassets/fak/dokumenter/publikationer/-russias-military-might-.pdf [Accessed: 17 March 2025].

McDermott, R. 2019-a. Russian Military Introduces New Automated Command-and-Control Systems, *Eurasia Daily Monitor,* 16(86) [online]. Available at: https://jamestown.org/program/russian-military-introduces-new-automated-command-and-control-systems/?utm [Accessed: 17 March 2025].

McDermott, R. 2019-b. Moscow Showcases Breakthrough in Automated Command and Control, *Eurasia Daily Monitor,* 16(164) [online]. Available at: https://jamestown.org/program/moscow-showcases-breakthrough-in-automated-command-and-control/?utm [Accessed: 17 March 2025].

Withington, T. 2025. Of Strelets and Andromeda, *Armada International* [online]. Available at: https://www.armadainternational.com/2025/01/russian-land-forces-tactical-and-operational-command-and-control-milcom/?utm [Accessed: 17 March 2025].

Live Journal. 2025. Единая система управления тактического звена [online]. Available at: https://ru-artillery.livejournal.com/550096.html [Accessed: 17 March 2025].

Dbpedia.org. 2025 [online]. Available at: https://dbpedia.org/page/Russian_Space_Forces [Accessed: 17 March 2025].

Uppal, R. 2024. Russia's Electronic Warfare Dominance: A Comprehensive Overview, *International Defense, Securuty & Technology* [online]. Available at:

https://idstch.com/geopolitics/russias-electronic-warfare-dominance-a-comprehensive-overview/ [Accessed: 17 March 2025].

Scobell, A. and Kamphausen, R. 2007. *Right Sizing the People's Liberation Army: Exploring the Contours of China's Military*, USAWC Press [online]. Available at: https://press.armywarcollege.edu/cgi/viewcontent.cgi?article=1021&context=monographs [Accessed: 24 March 2025].

Bommakanti, K. and Amjad H. 2023. *China's military modernisation: recent trends,* Observer Research Foundation (ORF), New Delhi (India) [online]. Available at: https://www.zbw.eu/econis-archiv/bitstream/11159/654398/1/1845125193_0.pdf [Accessed: 24 March 2025].

Alsaied, J. 2023. The People's Liberation Army's Command and Contol Affects the Future of Out-of-Area Operations, *Journal of Indo-Pacific Affairs*, 6(2), pp. 145-153 [online]. Available at: https://www.airuniversity.af.edu/JIPA/Display/Article/3371571/the-peoples-liberation-armys-command-and-control-affects-the-future-of-out-of-a/ [Accessed: 24 March 2025].

Demarest, C. 2023. China developing own version of JADC2 to counter US, *c4isrnet* [online]. Available at: https://www.c4isrnet.com/battlefield-tech/it-networks/2023/01/05/china-developing-own-version-of-jadc2-to-counter-us/ [Accessed: 24 March 2025].

Rej, A. and Joshi, S. 2018. *India's Joint Doctrine: A Lost Opportunity,* Observer Research Foundation (ORF), New Delhi (India). ISBN: 978-93-87407-49-7 [online]. Available at: https://www.orfonline.org/public/uploads/posts/pdf/20240812130129.pdf [Accessed: 31 March 2025].

Pant, H.V. and Bommakanti, K. 2023. *Towards the Integration of Emerging Technologies in India's Armed Forces,* Observer Research Foundation (ORF), New Delhi (India) [online]. Available at: https://www.orfonline.org/public/uploads/posts/pdf/20240610150049.pdf [Accessed: 31 March 2025].

Borja, L.J. and Ramana, M.V. 2020. Command and Control of India's Nuclear Arsenal, *Journal for Peace and Nuclear Disarmament*, 3(1), pp. 1-20. Available at: https://doi.org/10.1080/25751654.2020.1760021 [Accessed: 31 March 2025].

IndraStra Global. 2015. India's Integrated Air Command & Control System (IACCS): A NCW Milestone [online]. Available at: https://www.indrastra.com/2015/09/ANALYSIS-IACCS-257.html?utm_source=chatgpt.com [Accessed: 31 March 2025].

BEL C4ISS. 2025 [online]. Available at: https://bel-india.in/product/c4is-trinetra-command-control-solution-for-integrated-air-defence-operations/ [Accessed: 31 March 2025].

Pandit, R. 2014a. Naval Intelligence Network Launch Tomorrow. *The Times of India*, November 21, 2014 [online]. Available at:

https://timesofindia.indiatimes.com/india/Naval-intelligence-network-launch-tomorrow/articleshow/45237364.cms [Accessed: 31 March 2025].

Pandit, R. 2014b. Navy Gets New Facility to Communicate with Nuclear Submarines Prowling Underwater." *The Times of India*, July 31, 2014 [online]. Available at: https://timesofindia.indiatimes.com/india/Navy-gets-new-facility-to-communicate-with-nuclear-submarines-prowling-underwater/articleshow/39371121.cms [Accessed: 31 March 2025].

BEL CIDSS. 2025 [online]. Available at: https://bel-india.in/product/command-information-and-decision-support-system-cidss/ [Accessed: 31 March 2025].

BEL BSS. 2025 [online]. Available at: https://bel-india.in/product/battlefield-surveillance-system-bss/ [Accessed: 31 March 2025].

DE&S. 2022 [online]. Available at: https://des.mod.uk/guardian-air-command-control-system/ [Accessed: 7 April 2025].

Borealis. 2025 [online]. Available at: https://www.gov.uk/government/news/new-uk-made-space-system-to-help-protect-military-satellites?utm [Accessed: 7 April 2025].

BAE TC2. 2025 [online]. Available at: https://www.baesystems.com/en/product/tactical-command-and-control [Accessed: 7 April 2025].

LETacCIS. 2023 [online]. Available at: https://www.gov.uk/guidance/le-taccis-programme [Accessed: 7 April 2025].

BattleSpace. 2023 [online]. Available at: https://battle-updates.com/update/trinity-breathes-life-into-morpheus/ [Accessed: 7 April 2025].

RDN. 2025 [online]. Available at: https://www.defnat.com/e-RDN/vue-article-cahier.php?carticle=1233 [Accessed: 7 April 2025].

Thales. 2016 [online]. Available at: https://www.thalesgroup.com/en/worldwide/press-release/thales-provide-first-interoperable-command-information-system-french-army [Accessed: 14 April 2025].

IsraelDefense. 2016 [online]. Available at: https://www.israeldefense.co.il/en/node/22310 [Accessed: 14 April 2025].

Elbit. 2024 [online]. Available at: https://www.elbitsystems.com/blog/the-science-behind-our-air-defense [Accessed: 14 April 2025].

Janes. 2022 [online]. Available at: https://www.janes.com/osint-insights/defence-news/c4isr/idf-using-thousands-of-orion-handheld-c2-systems [Accessed: 14 April 2025].

Командно-контролни информациони системи за војне примене

Бранислав М. Тодоровић[а], **аутор за преписку**, *Зоран* Васић[а], *Андрија* Остојић[а], *Саша* Сретенов[б], *Александар* Копта[б], *Александар* Лазовић[б], *Лазар* Пауновић[в], *Вељко* Ђилас[в], *Милош* Делић[г], *Мирко* Делић[г]

[а] SEDEC, Београд, Република Србија

[б] COMARS, Београд, Република Србија

[в] OPTERA, Београд, Република Србија
[г] MAŠINOTEHNIKA, Београд, Република Србија

ОБЛАСТ: информационе технологије
ВРСТА ЧЛАНКА: прегледни рад

Сажетак:

Увод/циљ: Командно-контролни информациони систем (ККИС) јесте технички систем дизајниран да обезбеди потребне информације доносиоцима одлука за планирање, координацију и управљање операцијама. Састоји се од хардвера и софтвера, а укључује специјализовани скуп алата и процеса, који имају за циљ да обезбеде благовремен и тачан проток информација. Може бити намењен за војну примену, јавну безбедност и корпоративно управљање. У раду је представљен историјски развој војних ККИС. Наведени су примери модерних ККИС неких технолошки развијених земаља, као што су САД (НАТО), Руска Федерација, НР Кина, Индија, Велика Британија, Француска и Израел.

Методе: Овај чланак је преглед 60+ референци које се односе на историјски развој војних ККИС, као и на модерне ККИС неких технолошки развијених земаља.

Резултати: На основу наведених референци, у раду је сумиран историјски развој ККИС за војну примену, и представљен кратак преглед модерних ККИС седам технолошки развијених земаља.

Закључак: Командно-контролни информациони системи се увелико користе у савременим војскама. Њихов развој започео је средином 20. века. Током протеклих 80 година ККИС су еволуирали од ручно управљаних система из 1940-их до модерних система који су данас вођени вештачком интелигенцијом. Ера модерних ККИС почиње 1990-их, од када је фокус на децентрализацији и аутономном доношењу одлука, ефикасном управљању подацима и сајбер безбедности. Последњих неколико година централни фокус је интеграција вештачке интелигенције у ККИС.

Кључне речи: одбрамбене технологије, командно-контролни информациони системи, информатика, телекомуникације

Paper received on: 06.06.2025.
Manuscript corrections submitted on:11.06.2025.
Paper accepted for publishing on: 31.07.2025.

Barriers and opportunities to innovation in the Malaysian Army: a multilevel approach

Mohd Aman Armawai[a], *Imaduddin* Abidin[b], *Puteri* Fadzline Muhamad Tamyez[c]

[a] University of Malaysia Pahang Al-Sultan Abdullah, Faculty of Industrial Management, Lebuh Persiaran Tun Khalil Yaakob, Kuantan, Pahang, Malaysia + *4 Woksyop Briged, Kem Batu 10,* Kuantan Pahang
e-mail: aman8x8@gmail.com, **corresponding author**,
ORCID iD: https://orcid.org/0009-0006-4353-4960

[b] University of Malaysia Pahang Al-Sultan Abdullah, Faculty of Industrial Management, Lebuh Persiaran Tun Khalil Yaakob, 26300, Kuantan, Pahang, Malaysia
e-mail: imaduddin@umpsa.edu.my,
ORCID iD: https://orcid.org/0000-0002-5087-2152

[c] University of Malaysia Pahang Al-Sultan Abdullah, Faculty of Industrial Management, Lebuh Persiaran Tun Khalil Yaakob, 26300, Kuantan, Pahang, Malaysia
e-mail: fadzline@umpsa.edu.my,
ORCID iD: https://orcid.org/0000-0002-2251-2707

https://doi.org/10.5937/vojtehg73-57765

FIELD: military science
ARTICLE TYPE: review paper

Abstract:

Introduction/Purpose: This study is to explore the barriers and opportunities to innovation within the Malaysian Army at the individual, team, and organizational levels, addressing a critical gap in military innovation research.

Methods: An interpretative phenomenological approach is employed with qualitative data derived from 15 in-depth interviews with military officers and other ranks who have consistently contributed to innovation efforts within the Malaysian Armed Forces.

Results: The results revealed that innovation barriers exist across three levels: seven themes were identified at the individual level, six at the team level, and four at the organizational level. These findings underscore the multifaceted nature of innovation challenges in structured military environments.

Conclusions: The paper highlights the interconnectivity of these barriers and the necessity of a holistic understanding to foster innovation effectively within the Malaysian Army.

Key words: innovation, barriers to innovation, ecosystem, armed forces, military, Malaysian army

Introduction

Innovation is pertinent to all organisations, and through innovation, creative thinking and new ideas can be introduced to solve issues in organisations. This can be seen from various security aspects in several issues such as national security and advanced military technology. Thus, strategies are essential to protect a nation's sovereignty and deter potential threats. Innovation ensures that a country's military can effectively respond to evolving threats and maintain a strategic advantage over adversaries.

Military innovation is closely tied to a country's security development, with organisations like the North Atlantic Treaty Organisation (NATO) that have supported science and innovation for more than 70 years. Major powers such as the United States and China have heavily invested in science and technology. For instance, the U.S. National Security Commission's 2023 report the highlights of the growing role of artificial intelligence (AI) across various domains, particularly in space, cyber, and information operations, where AI helps manage and analyse large amounts of data. AI enhances situational awareness, predicts outcomes, and supports military planning by simulating scenarios. As new threats like cyber warfare, drone attacks, and asymmetric warfare emerge, military forces must innovate continuously to develop both defensive and offensive capabilities. AI also transforms threats, creating new ones and enabling adversaries to exploit vulnerabilities (Dale F. Reding Álvaro Martín Blanco Angelo De Lucia Col Laura A. Regan, USAF, 2023)

Additionally, the military has been an early adopter of virtual reality (VR) technology, using it to address traditional training challenges such as high costs and the disparity between training environments and actual battlefields (Khaled Osmani and Detlef Schulz, 2024). VR provides an immersive and realistic experience, replicating stimuli that are difficult to recreate in real life while offering a safe training space that reduces the risk of injury and equipment damage. Similarly, unmanned aerial vehicles (UAVs) are increasingly used in modern defence strategies for roles such as intelligence, surveillance, reconnaissance (ISR), target acquisition, and combat strikes, offering remote operations in high-risk environments and minimizing human risk through advanced avionics and autonomous capabilities(Khaled Osmani and Detlef Schulz, 2024). Technological superiority also drives military innovation and technological advancements that can be adapted for civilian use. Technologies such as the internet, GPS, and radar were initially developed for military purposes and later revolutionized civilian life (Bidwell and Macdonald, 2018)

Barriers to innovation in the military

Scholars have shown a growing interest in barriers to innovation growth. For example, an empirical study by Gogoi (2021) found the importance of addressing issues about emotional blocks, such as fear of making mistakes and lack of trust, and structural blocks (associated with an individual's preferences for physical surroundings, dealing with distractions, use of personal space, and need for privacy). More importantly, studies have approached barriers to innovation growth in various ways, employing different concepts with similar meanings. For example, innovation barriers are associated with specific constraints such as institutional constraints (Hartono & Kusumawardhani, 2019), and leadership (Yusof et al., 2022).

Few studies, however, have explored barriers related to multiple levels of barriers and how the dynamics of these barriers inhibit innovation. To improve innovation, it is crucial to explore the full spectrum of barriers experienced by the Malaysian Armed Forces (MAF) innovators from the Malaysian Army. Given the innovation ecosystem weaknesses the defence industry faces in developing countries, studies of innovation barriers to growth may yield important insights, as advocated by scholars (Ismail & Johnson, 2021). Various strategies at the sectoral level will be implemented to strengthen the ecosystem to increase productivity, including uplifting research, development, commercialization and innovation (R&D&C&I) in new technology and improving access to financing in supporting innovation and skills development (The Government of Malaysia, 2021). Thus, we seek to address the central research question: What hinders the innovation growth of the armed forces in a developing country?

This study was conducted in Malaysia, an ideal context for the Malaysian Army (MA) as one of the branches services in the Malaysian Armed Forces (MAF). The MAF is a military institution in Malaysia that is responsible for protecting and defending the sovereignty and security of national interests in all domains. The MA is responsible for land forces domain security and consists of 16 Corps and Regiments that play a role in combat, combat support and combat service support. Every corps has its primary role and task to ensure that military operations are successfully executed. Based on Rusu (2023), in the military organization context, its culture is shaped by the unique requirements and needs of military operations as well as the history, traditions and values of military institutions. Yusof *et al.* (2022) stated two specific external and internal barriers and challenges to public sector innovation in Malaysia.

Building upon the organisational psychology field of research, a multilevel framework is foundational to understanding how individuals behave within complex organisations. Applying a multilevel framework to innovation growth in military institutions could provide important insights into the barriers experienced by Malaysian Army innovators. The multilevel framework maintains that individual, team and organisational factors influence innovative behaviours. A qualitative research design was used, namely, interpretative phenomenology analysis (IPA). IPA is useful for topics with limited research and less explored variables. IPA is a qualitative analysis technique that uses phenomenology, hermeneutics and ideography to explore a concept by attending to individuals' unique experiences (Smith and Osborn, 2008). To obtain rich data from different perspectives, we conducted interviews with MA officers and other ranks who have experience with consistent roles as innovators for the MA. The present study is divided into five sections: introduction, literature review, methodology, results, discussion, and conclusions.

Methodology

Ijebor (2019) and Rosen (1991) emphasize the importance of innovation for military organizations to address evolving threats and challenges, driving advancements in weapons, communications, and surveillance technologies. Weiss (2018) demonstrates some examples of the development of military innovation in the 20th century, such as intercontinental ballistic missiles, robots and drones to enhance operational efficiency. Thus, based on several crucial factors in military innovation, a qualitative method is employed to obtain detailed descriptions of the barriers and potential opportunities for innovation. The interviews were conducted with innovators who are experienced in innovative activities and have been involved in military innovation competitions.

These informants come from MA or land forces officers and other ranks. In-depth semi-structured interviews were conducted to gain insights into the lived experiences of MA innovators. The semi-structured interviews took place in person using an interview protocol. Morse *et al.* (2002) stated that the sample for a qualitative study is at least 6 and Creswell (2024) suggested that the sample size should be between 5 to 25 participants. For this research, we identified 15 interviewees, and we maintained the privacy and safety of the informants during all interviews. Despite reaching saturation at a small sample size, the study's sample size enabled it to explore the research issues in-depth as the researchers

believe that the selected participants are the true representation or the reflection of the study's entire population due to the common characteristics of the informants - participants. We tend to employ non-probability sampling as carefully chosen informants will generate robust and in-depth information (Smith, Flowers and Larkin, 2009). In capturing a phenomenon, information-rich cases are significant for deriving detailed information (Patton, 2002) from the selected participants; therefore, the purposive sampling technique has been used to explore military innovation behaviour in the MA.

Table 1: Interview questions

No	*Questions*
1.	*Do you do any innovation? (Rosen,1991; Ijebor, 2019; Wies, 2018)*
2.	*What are the barriers to your innovation? (Scaliza et al., 2022)*
3.	*Do you think military culture helps or hinders you from doing innovation? (Rusu, 2023)*
4.	*What are other factors that impact you in innovating? (Scaliza et al., 2022)*
5.	*How to overcome the barriers to innovation? (Yusof et al., 2022)*

All interviews were audio-recorded and ranged in duration from 30 minutes to 50 minutes. The audio recordings of all interviews were transcribed verbatim and translated into English from the Malay language. The translations were kept as literal as possible, except where minor modifications were necessary to preserve the conversational style and meaning (Nikander, 2008). To increase trustworthiness in data collection and data analysis, we conducted member checking and peer debriefing sessions among the research team members to review the emerging codes and themes.

The data (written accounts and transcripts) was analysed with thematic template analysis (TTA) (Brooks et al., 2015; King, 2012; Langdridge, 2007). TTA is one of the version styles included in the broad category of qualitative approaches to classical theme analysis (Brooks *et al.*, 2015). TTA was used instead of Braun & Clarke (2006) thematic analysis approach due to its usage of a priori themes and emphasis on establishing a balance between adaptability and coding hierarchical structure. The data could reveal meanings or motives from the informants' lived experiences. Prior themes were viewed as preliminary and vulnerable to reinterpretation and removal if they did not fit the informants' experiential assertions. The streamlined-codes-to-theory process by Saldana (2013) guided the data's themes, categories, and coding. The process involved four stages: decontextualising data into meaning units,

compressing meaning units into everyday words, categorising condensed meaning units, and assembling categories into final themes. ATLAS.ti version 24 was utilised to facilitate the procedure.

Results

Table 2 shows the demographic profile of the key informants who belong to military personnel consisting of officers and other ranks with experience in military service or experience as innovators in the MA. There are five officers and ten other ranks, which gives 15 informants. Most of them work in the units in Kuantan, Pahang. The selected officers are very experienced in innovation competitions in the MA, the MAF, the ministries at the national level and currently serve as strategic and innovation directorss. A participant with military experience was identified as whoever from military personnel completed their basic training and specialised training (basic military course and basic corps development course).

The duration of a basic military course is about 1 to 2 years of service in a military organisation. Most of the informants from other ranks hold the Sijil Pelajaran Malaysia (SPM) or the Sijil Kemahiran Malaysia (SKM) education certificate or they graduated from secondary education and vocational institutions, while officers have completed tertiary education to master and PhD levels. Out of the 15 informants, 3 of them received innovation awards in a range of 3 to 31 awards at the ministry level and the national level. Figure 1 resulted from the interview data coding in Table 3**.** The process involved four stages: decontextualising data into meaning units, compressing meaning units into everyday words, categorising condensed meaning units, and assembling categories into final themes. ATLAS.ti software version 24 was utilised to facilitate the procedure.

Individual-level barriers: internal elements

Internal elements in individual-level barriers consist of 4 codes, namely, a comfort zone, which is resistance to change, weak mentality in the innovation process, fear of mistakes in innovation, and lack of new ideas due to the advanced technology required. The personality development of military officers and subordinates is normally based on basic military training that has been outlined by the combat school. They will grow to advance military training suited to their role and task corps where they join in. The military training is to change their mindset and teach them military culture towards being a person who will be responsible for the security and sovereignty of the country.

Table 2: Informants' demographic profile

ID Code	Experience in the Military (Years)	Department	Nature of Position	Education Level	Number of Innovation Awards
A1	28	Army Inspectorate Department	Strategic & Innovation	PhD	10
A2	29	Army Logistics Command HQ – EME Gp	EME Gp	Master	3
A3	38	Veteran Army Officer (2023)	Retired in 2023	SKM	31
A4	11	Bde Wksp	Officer	Degree	-
A5	20	Bde Wksp Officer	Officer	Degree	-
B1	19	Bde Wksp – Armament Wing	Engineering Tech Class 2	SKM	-
B2	20	Bde Wksp – Storage Wing	Logistics	SKM	-
B3	20	Bde Wksp – Electronic Wing	Engineering Tech Class 2	SKM	-
B4	16	Bde Wksp – Armament Wing	Engineering Tech Class 2	SKM	-
B5	10	Bde Wksp – Recovery Wing	Recovery Tech	SPM	-
B6	13	Bde Wksp – Automotive Wing	Tech Class 1	SKM	-
B7	8	Bde Wksp – Automotive Wing	Tech Class 1	SKM	-
B8	4	Bde Wksp – A & G Wing	Welder	SPM	-
B9	1	Bde Wksp – A & G Wing	Welder	SPM	-
B10	1	Bde Wksp – Armament Wing	Armament	SPM	-

They are also trained in referring to the military doctrines on combat matters, technology, intelligence, etc. They are also trained through lessons learned from the history of past successes and defeats to learn war techniques and tactics. This lesson does not happen in a short period but sometimes requires 5 years of staged training. That is why some officers and subordinates have rigid thinking or resistance to change due to worries about facing failure in innovation.

"...After that, resistance to change, we want to train/change to the direction of innovation is difficult because there is still 'old school thinking'."– A2

"…. he is afraid to try something new "Do you want to do something new? It's difficult, sir if you're new"– A3.

"Actually, we work in that organisation (workplace). That is the challenge. Either the head of the organisation or among the staff. That's why when I attend the workshop, I see that a member/team involved, if he is not strong in terms of his mentality or he does not have support, he will withdraw."– A3.

Weak mentality in the innovation process: officers and other ranks have been trained with tough and rugged military training that tested mental and physical endurance, especially in the phase of training which emulates being a prisoner by an enemy. However, the mental strength to prepare innovative work including writing papers and producing innovative products requires a tough mentality due to the process taking up from 6 months to a year to complete. This forces them to use extra time outside their primary work.

Individual-level barriers: external elements

There are 3 codes for external elements - time constraints, a lack of practical training, and a lack of exposure to new technology. In terms of time constraints, both for military officers and other ranks, time to perform the main task is highly necessary. For example, the role of REME Corps in the MA is responsibility for maintenance and repair of all types of equipment and vehicles in MA units. The primary task is maintaining and updating vehicles and equipment documents before and after repair work. At the same time, additional tasks are required to be accomplished, such as auditing matters, admin inspection, organizing meetings, organizing ceremonies, contributing as executors in military exercises or operations, etc. Based on a pack of commitment to various tasks, the need for time to innovate regularly and systematically is not addressed well.

"The third constraint on time was work constraints to other tasks. So, for me, my time is only on Saturdays and Sundays, that's when I want to innovate." – A1.

"….in terms of time (time constraint). Like us as soldiers, again we as technicians and so on. We have our primary work, right? That's why, if you look at it, there are a lot of technical innovations from the technical teams." – A3.

"The challenge for me is time. This innovation is a secondary task. So, even the primary task/duty has become a workload to complete." - B2, B3.

Barriers to innovation

We identified three levels of innovation barriers which ranged from individual to organisational barriers. Table 3 shows the three levels of barriers. Exposure to how the process of innovation occurs both in writing innovation papers and in producing innovation products needs to be explained to every officer and other ranks. Usually, only innovation teams are trained and get actual exposure to innovation due to the replacement of an appointment (posting out) innovation team needed to set up for newcomers to join. However, exposure only applies to those who have been selected for innovation teams, and it is not comprehensive. In the digitalization era, the military is also exposed to emerging technologies with artificial intelligence (AI), big data banks, military Internet of Things, autonomous systems, etc., which requires a deeper knowledge of writing innovation papers.

"Our soldiers are less exposed to advanced technology knowledge. For example, right now, we are moving towards industry 4.0/5.0. So, human tasks want to be transferred to robots and robots control machines. So, we must keep up with the technology and we have to have exposure using AI, using the latest technology in security matters" - A3.

In terms of a lack of generating new ideas, it is a challenge to innovate when the ideas obtained still use mechanical systems and do not involve current technology such as AI, autonomous systems, and the Internet of Things. Ideas that have the 'wow' factor are hard to explore in advanced technology and need group discussion and brainstorming.

"*So far, the challenge is to find new ideas, which is more useful today. Looking for something suitable for current use and in line with IR 5.0." – B2, B3.*

Team-level barriers: internal elements

Internal elements consist of four codes which are: difficulty to find team members interested in innovation, less skilled members, difficulty to get cooperation, and lack of motivation.

"The challenge that I face is to find capable team members. Because now we are towards industry 5.0. When we compare to today's soldiers and soldiers who are at my level age most of them do not know much about robotics and are not exposed. Their times are also different from today's soldiers"-A3.

In the code 'difficulty to get cooperation' while developing an innovation team, there is also 'difficulty in obtaining cooperation' - this is due to several things. Firstly, team members are formed of new members or new soldiers with 5 years of working experience who have no exposure and experience in innovation. They are willing to listen to and follow the instructions first rather than anticipate the project. Secondly, there is a lack of or less interest in innovation due to the need to give more commitment and time to the preparation of innovation projects. Thirdly, cooperation in terms of poor innovation knowledge and fear of trying something new results in being inert to think critically.

"Both in terms of group cooperation. Because everyone has their own primary and secondary tasks/ are busy. So that cooperation is difficult to realize." – A1.

"...I asked other members of the team, but he didn't know what project he was doing. He does not focus on the team's effort and only the team leader innovates and gives the idea and direction." – A3.

The lack of skilled team members meant that most of team members had the same level of knowledge and had never been involved in any innovation project or design project during their service in the army or other institutions and organisations. Knowledge and skill to innovate have a great impact on producing an innovation project, especially when brainstorming, shortening innovation meeting time and preparing innovation papers.

"...Then another thing, we lack skilled team members to develop projects." – A3

A lack of motivation is related to a lack of knowledge and a feeling that innovation is difficult. For example, the preparation of an innovation paper and a product is a long process lasting from 6 months up to a year due to obtaining related documentation. Long duration will affect commitment and pose challenges such as family problems, personal problems, and even financial problems of the project as well. The motivation of group members or individuals can be boosted by giving awards to those team members performing well in team cooperation, by enhancing their innovation knowledge when sending them to innovation courses and by encouraging them to enjoy innovation culture.

"*The factor that I see, from my point in my innovation team is motivation. Motivation to team members. Leadership is not a problem because I am a leader. So, there is no issue. Only the motivation for the team members..." - A2,*

"Innovation is difficult" - B1, B2

As far as innovation team members who have no direct exposure to an innovation process are concerned, they will be surprised by the long duration of an innovation process and will need a lot of patience for the first time of involvement. Some members have no courses or exposure to innovation due to limited course allocations and because an innovation project needs to be completed within a certain period given by superiors. This causes weak motivation due to a lack of knowledge and creates a feeling that innovation is difficult.

"Only motivation for the team members, and I also see that few of the team members do not know innovation."- A2,

Team-level barriers: external elements

The external elements consist of 3 codes: plagiarized innovation products, financial constraints on when to start, and patent innovations.

"But I have seen our project, has been plagiarized by another institution. It was already at the competition or after we were at the national level, I don't remember. But as I told you, this project started before 2010. So, when we go to the roadshow, we bring this thing to the roadshow, that's when people imitate/plagiarize, people take pictures and so on. That's what's important about that patent." – A2.

"The challenge that I faced in innovation was preparing a project paper. We make project paper. Before we create a product, we must create a project paper first and we keep it, when I initially created this work, we didn't have a patent. So, the project has been plagiarized/imitated by others, that's the problem I'm facing, and this is happening in our service (MA)." – A3.

Another external element is the financial constraint in producing a product or a patent. When starting an innovative product, it is necessary to have finances due to the incompleteness of the product to be innovated. Products to be innovated almost from ground zero and from second-hand goods need supporting equipment to be paid for. Sometimes, a new product that needs to be innovated requires minor or major modifications first, before being combined with supporting equipment, which also requires financial funds. Some of used products that have been selected for innovation are worn out and damaged, so the cost of repairing needs to be considered as the first financial challenge before completing an innovative product.

"For me, the main challenge is in terms of financial/money, because this innovation requires money and cannot use used/discarded items because not all discarded items can be used properly. We need to buy quality items to develop, to make projects. In terms of security, it's the

same, if we take discarded items we have no guarantee from a safety point of view, but the items we buy/original are better, more guaranteed, and better quality. So, the challenge is money/finance" -A1.

In terms of financial constraints on patenting, innovations that have won certain awards at an MA organisation, a ministry and at the national level should be patented to avoid any plagiarism from other agencies because the production of innovative products can be sold and used commercially in the market. However, patenting a product is quite expensive. For example, a patent for an innovation paper is about RM 5,000, a patent for a product is RM 10,000 and a patent for a brand is RM 30,000. However, the cost of a particular patent will change from time to time. This is a big challenge in patent finance allocation. Nevertheless, it is beneficial to avoid copying from others or any form of plagiarism.

"But to make a patent, you need money. For all costs, we must see what kind of patent we want to overcome. Otherwise, people will steal our projects, physical projects and so on." - A2.

"Financially, it's a bit lacking, sir. The reason for innovation is to save costs. But if you want to make that product free from plagiarism, you must have a patent as well. It costs money to start." – B2, B3.

Organisational-level barriers

Organisational-level barriers consist of innovation competition issues, innovation exposure not reaching the lower level of subordinates, no support for commercialization, hindrance by military culture, and the application of old tools. There is a need to cultivate innovation in the MA. Although the culture of innovation can produce many innovators, innovation should happen comprehensively for every individual in the organisation because everyone faces problems and challenges in their work that need to be solved with innovation that saves cost, time and energy.

Thus, participating in competitions is not sufficient. All instructions and guidelines to innovate competitively have been issued by superiors. However, there are still barriers to innovating in the MA. MAF's culture of innovation should be parallel with innovation culture at the national level. The cultivation of innovation should be seen from various angles to increase its success.

"The third is a challenge from the superiors. Although superiors are there to give a little encouragement/support, this competition is not a 100% per cent culture for this soldier's work." – A2.

There is no denying that exposure to the innovation work process in the competition is only focused on innovation leaders and team members.

They will be sent to improve their innovation knowledge by attending courses or seminars, through awards if they win and other advantages.

If the encouragement is not comprehensive, only innovation team members will commit themselves to completing papers and producing innovative products while those who are not involved in teams will not participate in the work to gain knowledge. In addition, such work needs to be done outside the main working hours or after the primary task is done. This will create a culture that is not healthy for innovation in the organisation.

"When I ask random questions, I think almost 80 percent of them do not understand what I'm asking. I asked about the competition, they didn't know. I asked why you didn't know. They answered, "I don't know about your innovation", that's his thinking (don't know). We want everyone to know. In the army, our Chief of Army (COA) was issued a directive to encourage innovation. If you look at it, he has outlined innovation, but that thing may not reach the bottom (subordinate). That's what happened in the MA. I emphasized. It's also happened to MAF and the Ministry level as well." – A3.

Thus, this shows that there is less support for commercialization. The requirement for the commercialization of innovations can be considered as: (1) market research, (2) product development, (3) product pricing, (4) marketing plan, (5) distribution, (6) licenses and permits, (7) customer service, (8) financial management, and (9) sales team. This is the challenge in military or public service to work on until achieving commercialization. That is why the process of commercialization needs the attention of the MA.

"Then, the other one that I want to inform is, in terms of continuity challenges. Challenges in terms of the continuity of this product, when we have made innovative product like our product Spider Wheel Carrier until at national level. But there is no end state, it is not commercialized. So, why not commercialise? There is an issue why soldiers don't want to use it for what?" - A2.

The repair tools are still 'old school' and do not follow the latest technology, which may be due to the fact that technology is developing too quickly, or the organisation is still not ready to deal with technological changes. For example, military vehicles have begun to enter military service with various electronic modules and sensors, while the inspection method still uses the old approach of cannibalising or testing with good components borrowed from other vehicles. The way to resolve this is to use a computerized inspection or scan tool to identify the root cause of

Table 3: Identification of multilevel barriers to innovation

Level of Barrier to Innovation	Codes	A1	A2	A3	A4	A5	B1	B2	B3
Individual									
External elements	Time constraint	+		+	+	+	+	+	+
	Lack of practical training			+					
	Lack of advanced technology exposure			+					+
Internal elements	Resistance to change		+	+			+		
	In a comfort zone			+			+		+
	Afraid to make mistakes in innovation			+	+				+
	Lack of new ideas					+	+	+	+
Team									
Internal elements	Lack of interested team members	+		+	+	+			
	Lack of expert and experienced team members		+	+					
	Hard to get cooperation among team members	+		+	+				
External elements	Financial constraints to patent the innovations		+	+					
	Financial constraints to develop innovations	+	+	+	+	+	+		
	Plagiarism on the innovation		+	+					
Organisation	Innovation competitions are not sufficient to cultivate an innovation culture in the military		+	+					
	Innovation exposure does not reach the lower subordinate		+	+					
	No support towards commercialization innovation product		+	+					
	Military culture hinders innovation in the military					+	+		
	Still used old equipment/ technology			+		+	+		

Level of Barrier to Innovation	Codes	B4	B5	B6	B7	B8	B9	B10
Individual								
External elements	*Time constraint*	+		+	+	+	+	+
	Lack of practical training					+		+
	Lack of advanced technology exposure					+		+
Internal elements	*Resistance to change*		+					
	In a comfort zone							
	Afraid to make mistakes in innovation			+				
	Lack of new ideas	+	+		+	+		+
Team								
Internal elements	*Lack of interested team members*							
	Lack of expert and experienced team members		+					
	Difficult to get cooperation among team members	+						
External elements	*Financial constraints to patent the innovation*		+					
	Financial constraints to develop the innovation	+	+	+				+
	Plagiarism on innovation		+					
Organisation	*Innovation competitions are not sufficient to cultivate an innovation culture*		+					
	Innovation exposure does not reach the lower subordinate.		+	+				
	No support towards commercialization of the innovation		+					+
	Military culture hinders innovation in the military							
	Still used old equipment/technology			+				

some damage or malfunction. This situation requires innovative ways for resolving it.

"…the second in terms of equipment. The available equipment is difficult for us to obtain. So, I always think how we want to make the work easier, make it easier for our technicians to carry out the work." – A3.

"Now our soldiers are not directly exposed to innovation and technology towards the outside world and remain with the existing culture." – B2, B5.

Military culture restricts innovation seen in terms of the essential work of the military which requires selflessness. It requires sacrifice and time for which military personnel must always be ready 24 hours a day for the security duty of defending the country. This primary task covers operations, training, administration, logistics, etc. to ensure the smooth running of military operations. They also work with limited human resources; in addition, family management responsibility is important for those who have a family. When added to innovation projects that require preparing paperwork with proofing documents and producing products, it is seen as a military culture that does not support innovation culture even though the instructions and guidelines of innovation competitions have been issued by superiors.

"Hindering sir. Among the barriers is a commitment to primary duty and military activity." – B2, B3.

Discussion

The study reveals that MA innovation in the Malaysian Armed Forces (MAF) aligns with national requirements and promotes a competitive innovation culture at various levels. The government and ministry support in fostering this innovation culture aligns with the industry's needs in the digitalization era. The study explores barriers to innovation in the MA at individual, team, and organizational levels, highlighting that communication, lack of ideas, constraint resources, military culture, etc. (Figure 1) will hinder MA innovation.

Additionally, team-level challenges include concerns about product plagiarism, limitations on available team members, a lack of financial support for initial product development, insufficient innovation knowledge among members, and inadequate teamwork support. These challenges are similar to the challenges from the government study on innovation in the public sector (Srirahayu et al., 2023; Hashim, 2021; Retkoceri & Kurteshi, 2018; Cinar et al., 2019; (Yusof et al., 2022). The same issues persist regarding organizational challenges in competition: there is

insufficient development of an innovation culture, lower level employees are not adequately exposed to innovative practices, support for commercialization is inadequate, military culture impedes innovation, and obsolete equipment remains in use.

The sustainability of innovative behaviours among MA officers can be enhanced by overcoming team-level barriers such as concerns about product plagiarism which restrict the participation of interested team members and impede financial support for initial product development. Furthermore, there is a lack of innovation knowledge among team members, and collaboration is often limited due to the usual structure of MA innovators working as a team. The MA should address barriers to military innovation through open innovation, design thinking, dedicated units, improved communication, resource allocation, and fostering innovation culture by the top-down approach.

Communication: team and organisation level

Military innovation faces communication barriers due to hierarchical structures. Higher-level orders lack context, leading to misunderstandings and disconnected teams. Lower-ranking personnel may hesitate to share ideas due to fear or cultural norms, resulting in missed opportunities.

Military culture: individual, team, and organisation level

Military innovation faces cultural barriers, including individual resistance, rigid hierarchies, and bureaucracy. Malaysia's leadership encourages innovation through competitions despite these challenges, as it encourages creativity and adapts to changing organizational structures, despite the risk-averse mindset prevalent in the military.

Establishment of units' innovation department: team and organisation level

Military units often face barriers to idea development due to rigid hierarchies and discipline, which discourage lower-ranking personnel from voicing new ideas. Establishing innovation departments can foster a culture of creativity by dedicating time and resources to idea development.

Approach to design thinking and open innovation method: team and organisational level

Military innovation can be accelerated by combining open innovation and design thinking. Open innovation involves sharing ideas beyond traditional boundaries, while design thinking involves end users early in

the process. This approach overcomes barriers like hierarchies and risk aversion, fostering a culture of openness and collaboration.

Specific allocation for initial development product from MAF R&D effort: team and organisational level

Financial constraints in early innovation stages can hinder progress, especially in resource-limited organizations. A lack of funding restricts access to resources, skilled personnel, and advanced technologies, leading to project delays and lower-quality outcomes. Allocating specific funding from higher authorities can alleviate financial pressures, enhance patent acquisition likelihood, and strengthen the innovation ecosystem.

CONCLUSION

This is the first qualitative study to explore the barriers and potential interventions or opportunities for innovation in the MAF and subsequently related to the defence industry in Malaysia. A primary strength of the study was the inclusion of both team leaders and members who are currently active in innovation activities and participate in innovation competitions. This allows for a comprehensive understanding of both perspectives. The study highlights that MAF's military innovation aligns with national requirements, but the challenges such as proactivity, collaboration, resource availability, and communication persist. Addressing these can enhance capabilities, particularly in enhancing military equipment and service efficiency in the digital era.

However, the study had some limitations. All informants who participated in the interviews were self-reported. However, member checking was conducted during the data collection. Furthermore, the study informants were limited to those who actively participated in innovation competitions, which potentially excluded non-participants in innovation competitions that might give insights into barriers towards innovation. Future research should include these stakeholders to capture the full spectrum of perspectives better. More importantly, a more in-depth study of this issue is to be carried out concerning innovative work behaviour.

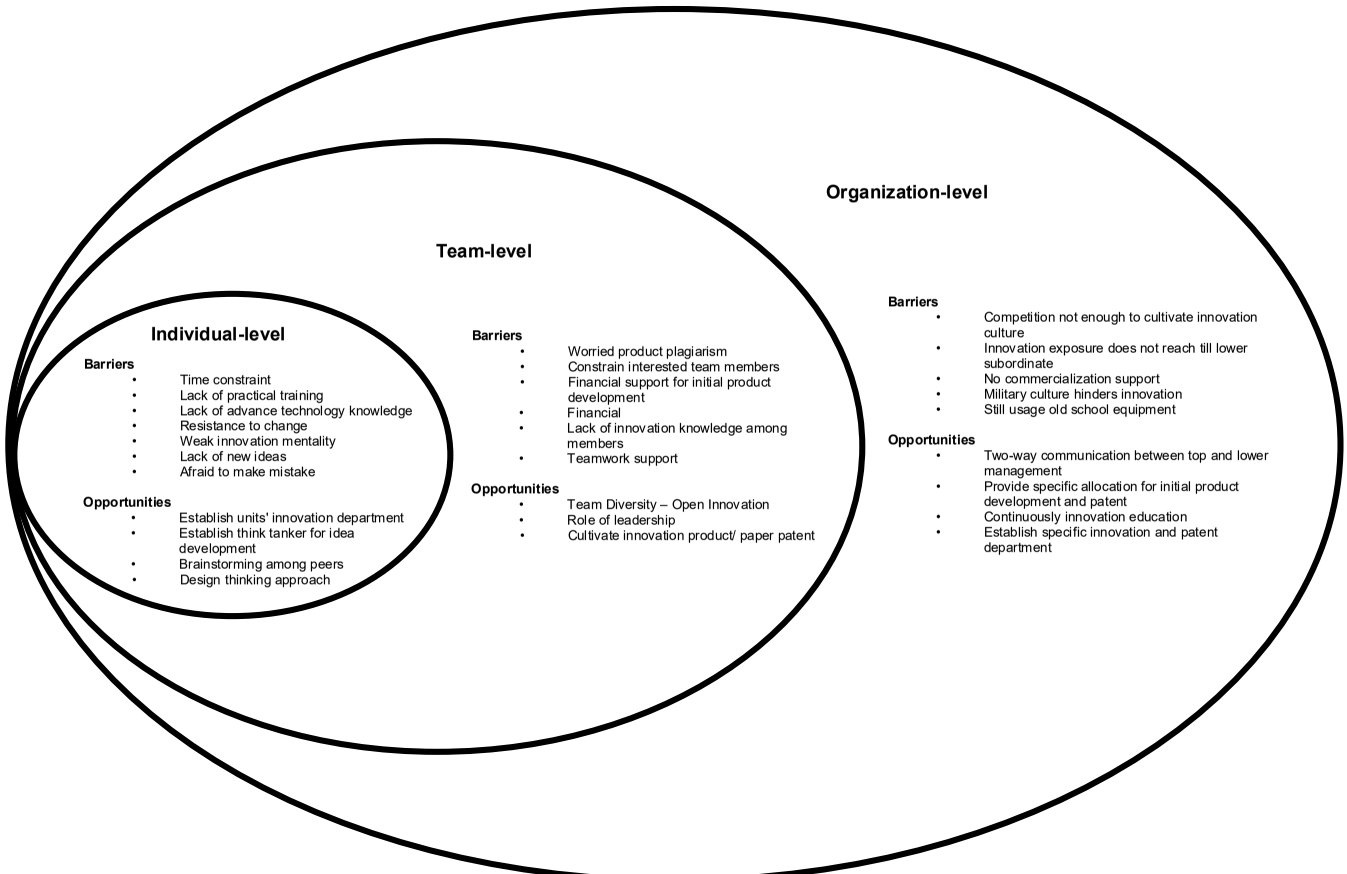

Figure 1 - Overview of individual, team and organisational level barriers and opportunities for innovation

References

Bidwell, C.A. and Macdonald, B.W. (2018) *Emerging Disruptive Technologies and Their Potential Threat to Strategic Stability and National Security* [online]. https://fas.org/wp-content/uploads/media/FAS-Emerging-Technologies-Report.pdf [Accessed on: 14 January 2025].

Braun, V. and Clarke, V. (2006) 'Using thematic analysis in psychology', *Qualitative Research in Psychology*, 3(2), pp. 77–101. Available at: https://doi.org/10.1191/1478088706qp063oa

Brooks, J. *et al.* (2015) 'The Utility of Template Analysis in Qualitative Psychology Research', *Qualitative Research in Psychology*, 12(2), pp. 202–222. Available at: https://doi.org/10.1080/14780887.2014.955224

Cinar, E., Trott, P. and Simms, C. (2019) 'A systematic review of barriers to public sector innovation process', *Public Management Review*, 21(2), pp. 264–290. Available at: https://doi.org/10.1080/14719037.2018.1473477

Creswell, J.W. (2024) *Educational Research: Planning, conducting, and evaluating quantitative and qualitative research*, *Educational Principles and Practice in Veterinary Medicine*. Available at: https://doi.org/10.1002/9781119852865.ch17

Dale F. Reding Álvaro Martín Blanco Angelo De Lucia Col Laura A. Regan, USAF, P.D.B. (2023) *Science & Technology Trends 2023-2043 Across the Physical, Biological, and Information Domains NATO Science & Technology Organization : Part 2*, *NATO Science & Technology Organization*.

Hartono, A., & Kusumawardhani, R. (2019). Innovation Barriers and Their Impact on Innovation: Evidence from Indonesian Manufacturing Firms. Global Business Review, 20(5), 1196–1213. https: doi.org/10.1177/0972150918801647

Hashim, K.L. (2021) 'Enhancing Innovative Work Behaviour of Malaysian Public Sector Employees', *Malaysian Journal of Social Sciences and Humanities (MJSSH)*, 6(2), pp. 253–265. Available at: https://doi.org/10.47405/mjssh.v6i2.665

Ijebor, C. (2019) 'The Role Of Artificial Intelligence In Facilitating Military Innovation.', *Journal of Military & Strategic Studies*, 20(1), pp. 234–261 [online]. Available at: https://jmss.org/article/view/69495/53641%0Ahttp://search.ebscohost.com/login.aspx?direct=true&db=tsh&AN=140914996&lang=pl&site=ehost-live [Accessed: 14 February 2025].

Ismail & Johnson (2021) 'Operating as a Social Enterprise within Resource and Institutional Constraints', *Entrepreneurship Research Journal*, 11(1), pp. 1–17. Available at: https://doi.org/10.1515/erj-2017-0120

Johnny Saldana (2013) *The Coding Manual for Qualitative Researchers (3rd edition)*, *Qualitative Research in Organizations and Management: An International Journal*. Available at: https://doi.org/10.1108/qrom-08-2016-1408

Khaled Osmani and Detlef Schulz (2024) 'Comprehensive Investigation of Unmanned Aerial Vehicles', *MDPI* [Preprint].

King, N. (2012) 'Doing Template Analysis', in, pp. 426–450. Available at: https://doi.org/10.4135/9781526435620.n24

Langdridge, D. (2007) 'Phenomenological Psychology: Theory, Research and Method'.

Morse, J.M. *et al.* (2002) 'Verification Strategies for Establishing Reliability and Validity in Qualitative Research', *International Journal of Qualitative Methods*, 1(2), pp. 13–22. Available at: https://doi.org/10.1177/160940690200100202

Nikander, P. (2008) 'Working with transcripts and translated data', *Qualitative Research in Psychology*, 5(3), pp. 225–231. Available at: https://doi.org/10.1080/14780880802314346

Patton, M.Q. (2002) 'Two Decades of Developments in Qualitative Inquiry: A Personal, Experiential Perspective', *Qualitative Social Work*, 1(3), pp. 261–283. Available at: https://doi.org/10.1177/1473325002001003636

Retkoceri, B. and Kurteshi, R. (2018) 'Barriers to innovation in services and manufacturing firms: The case of Kosovo', *HOLISTICA – Journal of Business and Public Administration*, 9(2), pp. 73–94. Available at: https://doi.org/10.2478/hjbpa-2018-0013

Rosen, S.P. (1991) *Winning the Next War: Innovation and the Modern Military*. Cornell University Press (Cornell studies in security affairs) [online]. Available at: https://books.google.com.my/books?id=ncLRUf-q-XYC [Accessed: 21 January 2019]

Rusu, M.-L. (2023) 'The Military Organization – A Culture of Innovation', *Land Forces Academy Review*, 28(2), pp. 126–135. Available at: https://doi.org/10.2478/raft-2023-0016

Scaliza, J.A.A. *et al.* (2022) 'Relationships among organizational culture, open innovation, innovative ecosystems, and performance of firms: Evidence from an emerging economy context', *Journal of Business Research*, 140, pp. 264–279. Available at: https://doi.org/https://doi.org/10.1016/j.jbusres.2021.10.065

Smith, J.A., Flowers, P. and Larkin, M. (2009) 'Interpretative Phenomenological Analysis: Theory, Method and Research', *QMiP Bulletin*, 1(10), pp. 44–46. Available at: https://doi.org/10.53841/bpsqmip.2010.1.10.44

Smith, J.A. and Osborn, M. (2008) 'Interpretative Phenomenological Analysis', in *Doing Social Psychology Research*, pp. 229–254. Available at: https://doi.org/10.1002/9780470776278.ch10

Srirahayu, D.P., Ekowati, D. and Sridadi, A.R. (2023) 'Innovative work behavior in public organizations: A systematic literature review', *Heliyon*, 9(2), p. e13557. Available at: https://doi.org/10.1016/j.heliyon.2023.e13557

The Government of Malaysia (2021) *Twelfth Malaysia Plan 2021-2025: A Prosperous, Inclusive, Sustainable Malaysia*, *Directorate General Economic Planning Unit* [online]. Available at: https://rmke12.epu.gov.my/bm [Accessed: 24 February 2025].

Weiss, M. (2018) 'How to become a first mover? Mechanisms of military innovation and the development of drones', *European Journal of International Security*, 3, pp. 1–24. Available at: https://doi.org/10.1017/eis.2017.15

Yusof, N.A.M. *et al.* (2022) 'Challenges and Barriers in Public Services Innovations in Malaysia', *STI Policy and Management Journal*, 7(1), pp. 47–61. Available at: https://doi.org/10.14203/stipm.2022.326

Препреке и могућности за иновације у малезијској војсци: приступ на више нивоа

Мод Аман Армаваи, **аутор за преписку**, *Имадудин* Абидин,
Путери Фадзлине Мухамад Тамјез
Универзитет Малезије „Паханг Ал-Султан Абдулах", Факултет за индустријски менаџмент, Лебух Периаран Тун Калил Јакоб, Куантан, Паханг, Малезија

Област: војне науке
Категорија (врста) чланка: прегледни рад

Сажетак:

Увод/циљ: Испитују се препреке, као и могућности за иновације у Војсци Малезије на појединачном, тимском и организационом нивоу, чиме се приступа решавању критичног недостатка истраживања иновација у Војсци.
Методологија: Примењен је интерпретативни феноменолошки приступ уз помоћ квалитативних података добијених из петнаест аналитичких интервјуа са припадницима Војске Мелезије који носе официрске и друге чинове и редовно доприносе раду на иновацијама унутар оружаних снага Малезије.
Резултати: Истраживање је показало да препреке иновацијама постоје на три нивоа; седам тема је идентификовано на појединачном нивоу, шест на нивоу тима и четири на нивоу организације. Овакви налази истичу вишеслојну природу иновационих изазова у структурираним војним срединама.
Закључак: Наглашава се међусобна повезаност препрека иновацијама, као и неопходност холистичког разумевања ради ефикасног афирмисања иновација у Војсци Малезије.

Кључне речи: иновација, препреке иновацијама, екосистем, оружане снаге, војска, Војска Малезије

Paper received on: 22.03.2025.
Manuscript corrections submitted on:11.04.2025.
Paper accepted for publishing on: 27.05.2025.

Vučković, D., SAVREMENO NAORUŽANJE I VOJNA OPREMA / MODERN WEAPONS AND MILITARY EQUIPMENT, pp.1553-1562

Распоређивање нове руске обалске артиљерије *A-222M Bereg*[1]

Руски државни медији су потврдили испоруку унапређеног обалског артиљеријског система *A-222M Bereg* руској Пацифичкој флоти. То представља значајан корак у модернизацији руских поморских одбрамбених способности на Далеком истоку, у складу са текућом стратегијом Москве да ојача своје присуство дуж стратешких приобалних коридора и спорних поморских зона.

Визуелно поређење оригиналног обалског артиљеријског система A-222 Bereg (130 мм) и недавно модернизоване варијанте A-222M топом калибра 152 мм, продуженим дометом од 50 км и интеграцијом прецизно вођене муниције Краснопољ.

Систем *A-222M Bereg* је напредна верзија совјетског *A-222 Bereg,* самоходног обалског артиљеријског топа калибра 130 мм, развијеног осамдесетих година. Првобитно замишљен као артиљеријски систем за брзо реаговање на брзе поморске циљеве, систем *Bereg* је дизајниран да пружи мобилну подршку са великом брзином ватре како би заштитио

[1] *Defense News Army 2025 8 May, 2025*

простране обале Русије, посебно у уским мореузима и критичним приобалним уским тачкама.

Наслеђени систем *А-222 Bereg,* изграђен на шасији *МАЗ-543* 8х8, имао је аутоматски топ калибра 130 мм и компјутеризовани систем за управљање ватром, способан да дејствује на циљеве удаљене до 22 километра. Био је опремљен радаром и електрооптичким нишанским уређајем како би се обезбедило аутономно откривање, праћење и ангажовање у борби против поморских претњи. Батерија се обично састојала од једног командног возила, шест возила наоружаних топовима и јединицама за подршку, које су заједно радиле на стварању интегрисаног мобилног одбрамбеног кишобрана против површинских бродова и десантних пловила.

Новопредстављени *А-222М Bereg* представља значајно унапређење. Иако задржава основу мобилности и обалске ватрене моћи, замењује застарели топ од 130 мм топом од 152 мм, постављеним на модернизованој шасији *МАЗ-543М*. Ова промена продужава његов максимални ефективни домет на 50 км – више него удвостручујући оригинални капацитет. Поред тога, укључивање вођеног артиљеријског пројектила *Краснополъ* додатно побољшава прецизност и смртоносност система. Граната *Краснополъ*, вођена ласерским сноповима или беспилотним летелицама, позната је по својој способности да погоди и статичне и мобилне циљеве великом прецизношћу. Иако се обично користи за копнене циљеве, њена употреба у контексту обалске одбране отвара нове оперативне могућности, бришући границе између артиљерије и прецизно вођених ракета.

Усвајање вођене артиљеријске гранате *Краснополъ* у оквиру система *А-222М Bereg* знатно побољшава његову тактичку свестраност. За разлику од стандардних невођених граната које прате фиксне балистичке путање, *Краснополъ* је прецизно вођена муниција (PGM) опремљена инерцијалним навигационим системом и полуактивним ласерским трагачем. То омогућава вођеној гранати да прилагоди курс током лета и да се усмери на циљеве осветљене ласером. Резултат је оружје које нуди високу вероватноћу поготка првом гранатом, смањујући трошкове муниције и логистичко оптерећење, што је посебно важно за удаљена распоређивања дуж руске пацифичке обале.
Штавише, *Краснополъ* омогућава ангажовање брзих или малих поморских циљева, као што су патролни бродови који развијају брзину до 100 чворова. Његова способност прецизног удара драстично минимизира колатералну штету, нарочито у хибридним конфликтним окружењима или у близини цивилне инфраструктуре. То чини систем *А-222М* посебно погодним за операције у уским мореузима, архипелазима и приобалним зонама које се налазе на већем делу источне поморске границе Русије.
Брзо време распоређивања *А-222М* (достиже спремност за паљбу за само 5 мин)– и велика брзина паљбе чине га идеалном контрамером против

изненадних амфибијских искрцавања или поморских упада. Возило за командовање и контролу које је интегрисано у систем користи напредне радарске и електрооптичке системе за праћење и одређивање циљева, обезбеђујући ефикасну координацију међу јединицама за паљбу и побољшавајући сазнање о ситуацији.
Ова најновија испорука Пацифичкој флоти има значајну стратешку тежину. Руска Пацифичка флота, са седиштем у Владивостоку, задужена је за одбрану источне поморске границе Русије. Њене одговорности укључују обезбеђивање виталних морских комуникационих линија, заштиту економских интереса, као што су рибарство и приобална енергетска инфраструктура, и обезбеђивање војне готовости у регионима близу америчких и савезничких снага стационираних у Пацифику. Са порастом тензија око контроле над северним морским путем и повећањем војне активности у близини Јапана, Кореје и Тајвана, модернизација обалских артиљеријских средстава има кључну улогу у ширем војном положају Русије.

Поред традиционалних одбрамбених дужности, Пацифичка флота служи као платформа за пројекцију моћи у азијско-пацифичком региону, често учествујући у заједничким вежбама са Кином и другим стратешким партнерима. Интеграција система попут *A-222M* додатно повећава способност флоте да подржи операције комбинованих оружја дуж источне обале Русије и спорних поморских зона.

Може се закључити да увођење *A-222M Bereg* у активну службу илуструје посвећеност Русије јачању њених асиметричних поморских ратних способности. Како се приобални региони све више оспоравају на глобалном нивоу, мобилни високопрецизни артиљеријски системи попут *A-222M* представљају исплативу и снажну линију одбране против конвенционалних поморских претњи и тактика хибридног ратовања.

Драган М. Вучковић (*Dragan* M. Vučković),
e-mail: draganvuckovic64@gmail.com,
ORCID iD: https://orcid.org/0000-0003-1620-5601

Удар са велике удаљености – *AIM-174B*[2]

Америчка морнарица је први пут јавно представила своју ракету ваздух-ваздух дугог домета *AIM-174B* током годишњег Дана пријатељства који се одржава у ваздухопловној бази Маринског корпуса (MCAS) Ивакуни, заједничкој америчко-јапанској војној бази. Циљ је био да се ојачају везе између америчких снага и локалне јапанске заједницеи обезбеди стратешко окружење, што је значајан корак у интеграцији ударних система дугог домета у арсенал америчке морнарице са носача авиона.

Ракета ваздух-ваздух AIM-174B је веома дугог домета, изведена из ракете земља-ваздух RIM-174 SM-6 (*Standard ERAM*).

Посетиоци су могли да виде *F/A-18F Super Hornet* из ескадриле VFA-102, са носача авиона (CVW-5), постављеног поред ловца *F-35C Lightning II* из *VFA-147*. *Super Hornet* је био наоружан са две инертне тренажне ракете *CATM-174B,* постављене на његовим унутрашњим носачима, поред спољашњег резервоара за гориво на средишњој линији. Иако није изложена бојева муниција, било је то прво познато јавно приказивање ракете од њеног оперативног распоређивања у јулу 2024. године.
Развијена у компанији *Raytheon* за америчку морнарицу, *AIM-174B* је ракета ваздух-ваздух веома дугог домета изведена из ракете земља-ваздух *RIM-174 SM-6 (Standard ERAM).* Описана је као „конфигурација лансирања из

[2] *Defense News Army 2025 12 May, 2025*

ваздуха" ракете *SM-6*, задржавајући структурни дизајн ракете *RIM-174*, али без бустера на чврсто гориво MK72, што омогућава интеграцију са ловцима *F/A-18E/F Super Hornet* — јединим авионом тренутно сертификованим за ношење те ракете. Масе приближно 860 кг и дужине 4,7 м, ракета *AIM-174B* задржава погон на чврсто гориво, бојеву главу са фрагментацијом експлозије од 64 кг и системе за навођење који комбинују инерцијалну навигацију са активним и полуактивним радарским самонавођењем. Може достићи брзине до 3,5 маха, са минималним потврђеним дометом од 130 наутичких миља (око 240 км), иако незваничне процене сугеришу знатно већи домет, посебно када се лансира на великој висини и великом брзином.

Ракета *AIM-174B* је пројектована тако да се супротстави изазовима које представљају ракете дугог домета које су поставиле Кина и Русија, као што су *PL-21* и *R-37M*. Главна мисија ракете је да дејствује на велике, значајне циљеве у ваздушном простору као што су радарске летеће платформе и авиони, платформе за пуњење горивом или средства за електронско ратовање која делују иза линија фронта. Способна да користи профиле лета у подигнутим положајима који достижу висине изнад 30.000 м, ракета проширује способност америчке морнарице да спречи напад из ваздушног простора у спорним поморским регионима. Иако је првенствено намењена за пресретање у ваздушном простору, њена првобитна улога као морничке ракете сугерише потенцијалне секундарне функције, укључујући ангажовање против поморских или балистичких циљева, доприносећи њеној оперативној флексибилности усред растућих претњи дугог домета.

Од 2018. године, америчка морнарица спроводи испитивања за прилагођавање *SM-6* за лансирање из ваздушног простора. Прототипови су примећени на ловцима бомбардерима *Super Hornet* из пробних ескадрила VX-31 и VX-9 већ 2021. године, али је оперативна интеграција убрзана тек 2024. године. Ракета је први пут виђена на платформи *VFA-192* „Златни змајеви" на ловцима *F/A-18E Super Hornet,* током вежбе *RIMPAC 2024* на Хавајима. У септембру те године, појавиле су се фотографије авиона *VX-9* који носи комплет од четири ракете *AIM-174B*, заједно са ракетама *AIM-120*, *AIM-9X* и инфрацрвеним системом за претрагу и праћење (*IRST) ASG-34A,* интегрисаним у модификованом резервоару за гориво, што говори о напредним конфигурацијама вишенаменског терета.

Иако ракети *AIM-174B,* лансираној из ваздушног простора, недостаје бустер *MK72* који се користи у верзијама лансираним са бродова, њено распоређивање са брзих авиона на великим висинама вероватно јој омогућава да надмаши перформансе свог морничког еквивалента. Ова способност позиционира *AIM-174B* као једно од оружја ваздух-ваздух са највећим дометом које је икада користила америчка морнарица, попуњавајући празнину насталу након што је ракета *AIM-54 Phoenix* повучена из употребе 2004. године, а коју је претходно носио *F-14 Tomcat*.

Ракета AIM-174B је пројектована да се супротстави ракетама дугог домета које користе Кина и Русија, као што су PL-21 и R-37M.

Интеграција ракете на ловце носача авиона *USS George Washington* указује на њено оперативно присуство у распоређеним снагама широм Индо-Пацифика. Једина стално распоређена ваздухопловна ескадрила америчке морнарице CVW-5 делује из Јокосуке у Јапану – региона од стратешког значаја с обзиром на све веће војне капацитете Кине и растуће тензије у Јужном кинеском мору. У овом окружењу, капацитет ангажовања на великим даљинама сматра се неопходним, посебно као одговор на системе као што су кинеске ракете *PL-15* и *PL-21*, које наводно достижу домет од 200 до 300 километара. Ракета *AIM-174B* могућност ангажовања авиона за надзор, командовање и танкере пре него што могу да угрозе америчке снаге.

Заједничко приказивање ловаца *F/A-18F* и *F-35C* током Дана пријатељства у граду Ивакуни потврдило је оперативну комплементарност између платформи. Иако *F-35C* не може интерно да носи ракету *AIM-174B* због своје величине, може да служи као напредни сензорски чвор у оквиру концепта умрежене интегрисане контроле ватре противваздухопловног дејства (NIFC-CA Networked Integrated Fire Control – Counter Air), одређујући циљеве за ракете лансиране са авиона *Super Hornet* уз одржавање прикривености.
Чини се да јавно приказивање ракете упућује поруку савезницима и потенцијалним противницима, јер наглашава развој ударних способности

америчке морнарице. Приказивањем система током јавног догађаја, америчка морнарица појачава позицију одвраћања кроз транспарентност и подржава ширу стратегију пројектовања моћи широм индо-пацифичког региона. Након што је достигла почетну оперативну способност (IOC) у јулу 2024. године на броду *CVW-2 USS Carl Vinson*, ракета *AIM-174B* сада се вероватно шире распоређује у америчкој флоти. Дизајн ракете, заснован на провереној бродској противваздухопловној ракети *SM-6*, омогућава додатне мисије, укључујући одбрану од бродова и ракета, иако његова главна функција остаје ваздушна надмоћ на великим даљинама.

Развој ракете је напредовао упоредо са развојем заједничке напредне тактичке ракете *AIM-260 (JATM),* за коју се очекује да ће имати већи домет и компатибилност унутрашњег носача са *F-35.* Међутим, пошто ракета *AIM-260* још није оперативна, чини се да *AIM-174B* испуњава хитну потребу за прилагођавањем постојећег и тестираног система како би се премостио тренутни јаз у односу на оперативне могућности руских и кинеских ракета ваздух-ваздух.

Прво јавно представљање ракете *AIM-174B* у Јапану означава значајну прекретницу у развоју могућности америчке морнарице. Адаптиран од проверене морнаричке ракете, овај нови систем обнавља капацитет система дугог домета за дејство у ваздушном простору авиона са носача авиона, што је кључна предност у огромном оперативном подручју Пацифика. Овим откривањем америчка морнарица показује своју намеру да осујети нове претње, истовремено јачајући одвраћање и координацију са регионалним савезницима.

Драган М. Вучковић (*Dragan* M. Vučković),
e-mail: draganvuckovic64@gmail.com,
ORCID iD: https://orcid.org/0000-0003-1620-5601

Нова руска ракета ваздух-ваздух KS-172[3]

Руска Уједињена ваздухопловна корпорација (УАК) значајно је подигла улоге у области ваздушне одбране надоградњом свог култног пресретача *MiG-31* интеграцијом новог ракетног система дугог домета *KS-172*. Првобитно развијен током хладног рата за пресретање стратешких бомбардера надзвучним брзинама и на великим висинама, *MiG-31* сада улази у нову фазу еволуције, која би могла редефинисати концепт ваздушне доминације дугог домета. У ери када су брзо време реакције и супериорне могућности одбрана одлучујуће, обновљена моћ *MiG-31* представља велики технолошки и стратешки пробој. Овај развој долази у време ескалације глобалних тензија, повећане војне конкуренције у областима великих висина и поновног фокуса на пресретање претњи наоружањем следеће генерације.

Према речима руског војног стручњака Константина Сивкова, KS-172 надмашује R-37 по компактности, а истовремено нуди импресиван домет од преко 400 километара.

Ловац пресретач *MiG-31*, развијен у руском ваздухопловном гиганту УАК, остаје један од најбржих оперативних војних авиона на свету, способан за брзине до 2,83 маха и висине преко 20.000 метара. Опремљен је моћним фазним радарским системом Заслон-М, који може истовремено да прати 24

[3] Defense News Aerospace 202519 May, 2025

циља и да дејствује на осам. Пројектован за пресретање на великим даљинама, авион је првобитно био наоружан ракетом R-33, са дометом до 300 км, а касније ракетом R-37M са дометом од 150 до 400 км. Међутим, увођење KS-172 представља већу убојитост дејства. Према речима руског војног стручњака Константина Сивкова, KS-172 надмашује R-37M по компактности, а истовремено има импозантан домет од преко 400 километара. Ова ракета драматично проширује домет дејства *MiG-31*, омогућавајући му да погоди стратешке циљеве попут авиона *AWACS*, танкера за допуну горивом у ваздушном простору и стелт платформи пре него што стигну у зону ефикасног дејства. Ловац *MiG-31*, који се у НАТО-у назива „Foxhound", развијен је седамдесетих година као наследник пресретача *MiG-25*. Био је то први совјетски авион са фазираном радарском решетком и остаје једна од ретких платформи посебно израђених за пресретање циљева велике брзине и висине, као што су крстареће ракете, извиђачки авиони и бомбардери. Током деценија, платформа је прошла кроз неколико фаза модернизације, посебно варијанте *MiG-31BM* и *MiG-31 K*, при чему је ова друга прилагођена за ношење хиперсоничне ракете *Kinzhal*. Пројекат ракете *KS-172*, који се у почетку суочавао са паузама у развоју и недостатком буџетских средстава, сада се поново појавио као део ширег руског напора да побољша своје ваздухопловно одвраћање.

За разлику од западних еквивалената, попут америчког *AIM-120D* или кинеског *PL-15*, домет ракете *KS-172* драматично се истиче. Док *AIM-120D* нуди максимални домет од око 160–180 км, а *PL-15* чак до 300 км, домет ракете *KS-172* од 400 км сврстава је у посебну категорију. Компактност ракете, како је приметио Сивков, омогућава већу флексибилност носивости и потенцијално чак и вишенаменско распоређивање на другим платформама. Историјски гледано, слични ракетни системи веома дугог домета, као што је индијска верзија *KS-172* или рани совјетски покушаји, били су ограничени у погледу тежине, вођења и погона. Недавни напредак у минијатуризацији руских ракета и ефикасности погона сада осварује *MiG-31* неупоредивим дометом првог удара у ваздушном простору.

Оперативно распоређивање ловца *MiG-31* са ракетама *KS-172* носи велике импликације, како на регионалну, тако и на глобалну динамику ваздухопловних снага. Са геополитичке перспективе, то јача руске капацитете за спречавање приступа/ускраћивање зоне (A2/AD) над огромним ваздушним просторима као што су Арктик, Источна Европа и Пацифик. Са војног аспекта, то намеће значајне ризике за западна ваздушна средства, укључујући *JSTARS, AWACS* и танкере, који су кључни за оперативну координацију и пројекцију моћи. Ракета *KS-172* омогућава Русији да угрози ова средства са дистанце, компликујући ваздухопловно планирање НАТО-а и САД и потенцијално одвраћајући операције раног уласка у спорне зоне. Тако *MiG-31* еволуира од брзог пресретача у стратешки ваздушни снајпер.

Пресретач *MiG-31*, застарела реликвија хладног рата, трансформише се у једног од најмоћнијих ваздухопловних пресретача 21. века захваљујући интеграцији ракете *KC-172*. Овом надоградњом платформа не само да добија проширени домет већ и нову улогу у стратешком одвраћању и мисијама првог удара за обезбеђивање ваздухопловне надмоћи. У свету где контрола неба често одређује исход модерних сукоба, еволуција ловца *MiG-31* је више од технолошког ажурирања; то је јасан сигнал руске намере да одржи доминацију у ваздухопловној одбрани и ускрати непријатељским снагама могућност неометаног маневрисања. Докле год *MiG-31* лети са *KS-172* под својим крилима, остаће једна од најопаснијих ваздухопловних претњи које постоје.

Драган М. Вучковић (*Dragan* M. Vučković),
e-mail: draganvuckovic64@gmail.com,
ORCID iD: https://orcid.org/0000-0003-1620-5601

CALL FOR PAPERS AND INSTRUCTIONS FOR AUTHORS

ПОЗИВ И УПУТСТВО АУТОРИМА

CALL FOR PAPERS AND ARTICLE FORMATTING INSTRUCTIONS

The instructions to authors about the article preparation for publication in the *Military Technical Courier* are based on the Regulations on categorization and ranking of scientific journals of the Ministry of Education, Science and Technological Development of the Republic of Serbia (Official Gazette of the Republic of Serbia, No 159/20). This Regulations aims at improving the quality of national journals and raising the level of their compliance with the international system of scientific information exchange.

The Military Technical Courier / Vojnotehnički glasnik (www.vtg.mod.gov.rs/index-e.html, втг.мо.упр.срб, ISSN 0042-8469 – print issue, e-ISSN 2217-4753 – online, UDC 623+355/359, DOI: 10.5937/VojnotehnickiGlasnik; https://doi.org/10.5937/VojnotehnickiGlasnik), is an peer-reviewed scientific journal.

The owners of the journal are the Ministry of Defence of the Republic of Serbia and the Serbian Armed Forces. The publisher and financier of the *Military Technical Courier* is the University of Defence in Belgrade (Military Academy).

The program of the journal is based on the annual classification of journals performed by a relevant Ministry as well as on its indexing in international indexing databases.

The journal covers scientific and professional fields within the educational-scientific field of **Natural-Mathematical Sciences**, as well as within the educational-scientific field of **Technical-Technological Sciences**, and especially the field of **defense sciences and technologies**. It publishes theoretical and practical achievements leading to professional development of all members of Serbian, regional and international academic communities as well as members of the military and ministries of defence in particular. It publishes papers with balanced coverage of analytical, experimental, and applied research as well as numerical simulations from various disciplines. The material published is of high quality and relevance, written in a manner that makes it accessible to a wider readership. The journal welcomes papers reporting original theoretical and/or practice-oriented research as well as extended versions of already published conference papers. Manuscripts for publication are selected through a double-blind peer-review process to validate their originality, relevance, and readability. This being so, the objective is not only to keep the quality of published papers high but also to provide a timely, thorough, and balanced review process.

The editorial policy of the *Military Technical Courier* is based on the COPE Core Practices, common COPE, DOAJ, OASPA and WAME Principles of Transparency and Best Practice in Scholarly Publishing as well as on the best accepted practices in scientific publishing. The Military Technical Courier has been a COPE (Committee on Publication Ethics) member since 2nd May 2018 and a member of OASPA (Open Access Scholarly Publishers Association) since 27th November 2015.

The Ministry of Science, Technological Development and Innovation of the Republic of Serbia classified the *Military Technical Courier* for the year 2024, on December 13, 2024

- **on the list of periodicals for computer sciences,**
  category: reputed national journal **(M51)**,
- **on the list of periodicals for electronics, telecommunications and IT,**
  category: reputed national journal **(M51)**,
- **on the list of periodicals for mechanical engineering,**
  category: reputed national journal **(M51)**,

– on the list of periodicals for materials and chemical technology,
category: national journal of international importance **(M24)**.

The approved lists of national periodicals for the year 2024 can be viewed on the website of the *Military Technical Courier*, page *Journal categorization*.

More detailed information can be found on the website of the Ministry of Education, Science and Technological Development of the Republic of Serbia.

The information on the categorization can be also found on the website of KOBSON (Consortium of Libraries of Serbia for Unified Acquisition).

The periodical is categorized in compliance with the Regulations on categorization and ranking of scientific journals of the Ministry of Education, Science and Technological Development of the Republic of Serbia (Official Gazette of the Republic of Serbia, No 159/20). More detailed information can be found on the website of the Ministry of Education, Science and Technological Development.

The journal is in the Serbian Citation Index – SCIndex (data base of national scientific journals), in the Scientific Information System Redalyc, and in the Russian Index of Science Citation/Российский индекс научного цитирования (RINC/РИНЦ) and is constantly monitored depending on the impact within the bases themselves. More detailed information can be viewed on the website of the *Military Technical Courier*, page *Journal indexing*.

The *Military Technical Courier*, in terms of its content, offers the possibility of open access (DIAMOND OPEN ACCESS) and applies the Creative Commons Attribution (CC BY) licence on copyright. The copyright details can be found on the *Copyright notice and Self-archiving policy* page of the journal's website.

Manuscripts are submitted online, through the electronic editing system ASSISTANT, developed by the Center for Evaluation in Education and Science – CEON.

The access and the registration are through the *Military Technical Courier* site http://www.vtg.mod.gov.rs/index-e.html, on the page *ASSISTANT* or the page *SCINDEKS* or directly through the link (aseestant.ceon.rs/index.php/vtg).

The detailed instructions about the registration for the service are on the website http://www.vtg.mod.gov.rs/index-e.html, on the page *Instructions for ASSISTANT*.

All authors submitting a manuscript for publishing in the *Military Technical Courier* should register for an ORCID ID following the instructions on the web page *Registration for an ORCID identifier*.

The *Military Technical Courier* publishes articles in English, using Arial and a font size of 11pt with Single Spacing.

The procedures of article preparation, writing and editing should be in accordance with the *Publication ethics statement* (http://www.vtg.mod.gov.rs/publication-ethics-statement.html).

The article should contain an abstract with keywords, introduction (motivation for the work), body (adequate overview of the representative work in the field, a clear statement of the novelty in the presented research, suitable theoretical background, one or more examples to demonstrate and discuss the presented ideas), conclusion, and references (without heading and subheading enumeration). The article length should not normally exceed 16 pages of the A4 paper format with single spacing, up to a maximum of 24 pages with references and supplementary material included.

The article should be formatted following the instructions in the Article Form which can be downloaded from website page *Article form*.

Title

The title should be informative. It is in both Journal's and author's best interest to use terms suitable for indexing and word search. If there are no such terms in the title, the author is strongly advised to add a subtitle.

Letterhead title

The letterhead title is given at a top of each page for easier identification of article copies in an electronic form in particular. It contains the author's surname and first name initial (for multiple authors add "et al"), article title, journal title and collation (year, volume, issue, first and last page). The journal and article titles can be given in a shortened form.

Author's name

Full name(s) of author(s) should be used. It is advisable to give the middle initial. Names are given in their original form (with diacritic signs if in Serbian).

Author's affiliation

The full official name and seat of the author's affiliation is given, possibly with the name of the institution where the research was carried out. For organizations with complex structures, give the whole hierarchy (for example, University of Defence in Belgrade, Military Academy, Department for Military Electronic Systems). At least one organization in the hierarchy must be a legal entity. When some of multiple authors have the same affiliation, it must be clearly stated, by special signs or in other way, which department exactly they are affiliated with. The affiliation follows the author's name. The function and title are not given.

Contact details

The postal addresses or the e-mail addresses of the authors are given in the first page.

Type of articles

Classification of articles is a duty of the editorial staff and is of special importance. Referees and the members of the editorial staff, or section editors, can propose a category, but the editor-in-chief has the sole responsibility for their classification.

The *Military Technical Courier* publishes scientific articles.

Scientific articles:

– Original scientific papers (giving the previously unpublished results of the author's own research based on scientific methods);

– Review papers (giving an original, detailed and critical view of a research problem or an area to which the author has made a contribution demonstrated by self-citation);

– Short communications or Preliminary communications (original scientific full papers but shorter or of a preliminary character);

– Scientific commentaries or discussions (discussions on a particular scientific topic, based exclusively on scientific argumentation) and opinion pieces.

Exceptionally, in particular areas, a scientific paper in the Journal can be in a form of a monograph or a critical edition of scientific data (historical, archival, lexicographic, bibliographic, data survey, etc.) which were unknown or hardly accessible for scientific research.

Papers classified as scientific must have at least two positive reviews.

If the journal contains non-scientific contributions as well, the section with scientific papers should be clearly denoted in the first part of the Journal.

Short communications are usually 4-7 pages long, research articles and case studies 10-14 pages, while reviews can be longer. Page number limits are not strict and, with appropriate reasoning, submitted manuscripts can also be longer or shorter. If extended versions of previously published conference papers are submitted, Editors will check if sufficient new material has been added to meet the journal standards and to qualify such manuscripts for the review process. The added material must not have been previously published. New results are desired but not necessarily required; however, submissions should contain expansions of key ideas, examples, elaborations, etc. of conference papers.

Language

The language of the article should be in English. The grammar and style of the article should be of good quality. The systematized text should be without abbreviations (except standard ones). All measurements must be in SI units. The sequence of formulae is denoted in Arabic numerals in parentheses on the right-hand side.

Abstract and summary

An abstract is a concise informative presentation of the article content for fast and accurate evaluation of its relevance. It contains the terms often used for indexing and article search. A 100- to 250-word abstract has the following parts: introduction/purpose of the research, methods, results and conclusion.

Keywords

Keywords are terms or phrases showing adequately the article content for indexing and search purposes. They should be allocated heaving in mind widely accepted international sources (index, dictionary or thesaurus), such as the Web of Science keyword list for science in general. The higher their usage frequency is, the better. Up to 10 keywords immediately follow the abstract and the summary, in respective languages. For this purpose, the ASSISTANT system uses a special tool KWASS for the automatic extraction of key words from disciplinary thesauruses/dictionaries by choice and the routine for their selection, i.e. acceptance or rejection by author and/or editor.

Article acceptance date

The date of the reception of the article, the dates of submitted corrections in the manuscript (optional) and the date when the Editorial Board accepted the article for publication are all given in a chronological order at the end of the article.

Acknowledgements

The name and the number of the project or programme within which the article was realised is given in a separate note at the bottom of the first page together with the name of the institution which financially supported the project or programme.

Article preliminary version

If an article preliminary version has appeared previously at a meeting in a form of an oral presentation (under the same or similar title), this should be stated in a separate note at the bottom of the first page. An article published previously cannot be published in the *Military Technical Courier* even under a similar title or in a changed form.

Tables and illustrations

All the captions should be in the original language as well as in English, together with the texts in illustrations if possible. Tables are typed in the same style as the text and are denoted by Arabic numerals at the top. Photographs and drawings, placed appropriately in the text, should be clear, precise and suitable for reproduction. Drawings should be created in Word or Corel.

For figures and graphs, proper data plot is recommended i.e. using a data analysis program such as Excel, Matlab, Origin, SigmaPlot, etc. It is not recommended to use a screen capture of a data acquisition program as a figure or a graph.

Citation in the text

Citation in the text must be uniform. The *Military Technical Courier* applies the Harvard Referencing System given in the Harvard Style Manual. When citing sources within your paper, i.e. for in-text references of the works listed at the end of the paper, place the year of publication of the work in parentheses and optionally the number of the page(s) after the author's name, e.g. (Petrovic, 2012, pp.10-12). A detailed guide on citing, with examples, can be found on *Military Technical Courier* website on the page *Instructions for Harvard Style Manual*. In-text citations should follow its guidelines. For checking in-text citations, the ASSISTANT system uses a special tool CiteMatcher to find out quotes left out within papers and in reference lists.

Footnotes

Footnotes are given at the bottom of the page with the text they refer to. They can contain less relevant details, additional explanations or used sources (e.g. scientific material, manuals). They cannot replace the cited literature.

Reference list (Literature)

The cited literature encompasses bibliographic sources such as articles and monographs and is given in a separate section in a form of a reference list. References are not translated to the language of the article.

In compiling the reference list and bibliography, the *Military Technical Courier* applies the Harvard System – Harvard Style Manual. All bibliography items should be listed alphabetically by author's name, without numeration. A detailed guide for listing references, with examples, can be found on *Military Technical Courier* website on the page *Instructions for Harvard Style Manual*. Reference lists at the end of papers should follow its guidelines. In journal evaluation systems, non-standard, insufficient or inconsequent citation is considered to be a sufficient cause for denying the scientific status to a journal.

Authorship Statement

The Authorship statement, submitted together with the paper, states authors' individual contributions to the creation of the paper. In this statement, the authors also confirm that they followed the guidelines given in *the Call for papers* and the *Publication ethics and malpractice statement of the journal*.

All articles are peer reviewed.

The list of referees of the *Military Technical Courier* can be viewed at website page *List of referees*. The article review process is described on the *Peer Review Process* page of the website.

Editorial Team

Address of the Editorial Office:
Vojnotehnički glasnik / Military Technical Courier
Veljka Lukića Kurjaka 33
11042 Belgrade, Republic of Serbia
e-mail: vojnotehnicki.glasnik@mod.gov.rs, tel.: +381 11 3603 260, +381 66 8700 123

ПОЗИВ И УПУТСТВО АУТОРИМА О НАЧИНУ ПРИПРЕМЕ ЧЛАНКА

Упутство ауторима о начину припреме чланка за објављивање у *Војнотехничком гласнику* урађено је на основу Правилника о категоризацији и рангирању научних часописа Министарства просвете, науке и технолошког развоја Републике Србије ("Службени гласник РС", број 159/20). Примена овог Правилника првенствено служи унапређењу квалитета домаћих часописа и њиховог потпунијег укључивања у међународни систем размене научних информација.

Војнотехнички гласник / Vojnotehnički glasnik / Military Technical Courier (втг.мо.упр.срб, www.vtg.mod.gov.rs, ISSN 0042-8469 – штампано издање, e-ISSN 2217-4753 – online, UDC 623+355/359, DOI: 10.5937/VojnotehnickiGlasnik; https://doi.org/10.5937/VojnotehnickiGlasnik), јесте рецензирани научни часопис.

Власници часописа су Министарство одбране Републике Србије и Војска Србије. Издавач и финансијер часописа је Универзитет одбране у Београду (Војна академија).

Програмска оријентација часописа заснива се на годишњој категоризацији часописа, коју врши надлежно државно министарство у одређеним областима, као и на његовом индексирању у међународним индексним базама.

Часопис обухвата научне, односно стручне области у оквиру образовно-научног поља **природно-математичких наука**, као и у оквиру образовно-научног поља **техничко-технолошких наука**, а нарочито области **одбрамбених наука и технологија**. Објављује теоријска и практична достигнућа која доприносе усавршавању свих припадника српске, регионалне и међународне академске заједнице, а посебно припадника војски и министарстава одбране. Публикује радове са уравнотеженим извештавањем о аналитичким, експерименталним и примењеним истраживањима, као и нумеричким симулацијама, обухватајући различите дисциплине. Објављени материјали су високог квалитета и релевантности, написани на начин који их чини доступним широкој читалачкој публици. Сви радови који извештавају о оригиналним теоријским и/или практично оријентисаним истраживањима или проширеним верзијама већ објављених радова са конференција су добродошли. Радови за објављивање одабиру се двоструко слепим поступком рецензије како би се осигурала оригиналност, релевантност и читљивост. Притом циљ није само да се квалитет објављених радова одржи високим већ и да се обезбеди правовремени, темељни и уравнотежени поступак рецензије.

Уређивачка политика *Војнотехничког гласника* заснива се на препорукама Одбора за етичност у издаваштву (COPE Core Practices) и заједничким принципима транспарентности и најбоље праксе у издаваштву COPE, DOAJ, OASPA и WAME, као и на најбољим прихваћеним праксама у научном издаваштву. *Војнотехнички гласник* је члан COPE (Committee on Publication Ethics) од 2. маја 2018. године и члан OASPA (Open Access Scholarly Publishers Association) од од 27. новембра 2015. године.

Министарство науке, технолошког развоја и иновација Републике Србије утврдило је дана 13. 12. 2024. године категоризацију *Војнотехничког гласника*, за 2024. годину:

– на листи часописа за рачунарске науке:
категорија врхунски часопис националног значаја **(M51)**,

– на листи часописа за електронику, телекомуникације и информационе технологије:
категорија врхунски часопис националног значаја **(M51)**,

– на листи часописа за машинство:

категорија врхунски часопис националног значаја **(М51)**,

– на листи часописа за материјале и хемијске технологије:
категорија национални часопис међународног значаја **(М24)**.

Усвојене листе домаћих часописа за 2024. годину могу се видети на сајту *Војнотехничког гласника*, страница *Категоризација часописа*.

Детаљније информације могу се пронаћи и на сајту Министарства просвете, науке и технолошког развоја Републике Србије.

Подаци о категоризацији могу се пратити и на сајту КОБСОН-а (Конзорцијум библиотека Србије за обједињену набавку).

Категоризација часописа извршена је према Правилнику о категоризацији и рангирању научних часописа Министарства просвете, науке и технолошког развоја Републике Србије ("Службени гласник РС", број 159/20).

Часопис се прати у контексту Српског цитатног индекса – СЦиндекс (база података домаћих научних часописа), Научно-информационог система Redalyc и Руског индекса научног цитирања (РИНЦ). Подвргнут је сталном вредновању (мониторингу) у зависности од утицајности (импакта) у самим базама. Детаљи о индексирању могу се видети на сајту *Војнотехничког гласника*, страница *Индексирање часописа*.

Војнотехнички гласник, у погледу свог садржаја, пружа могућност отвореног приступа (DIAMOND OPEN ACCESS) и примењује Creative Commons (CC BY) одредбе о ауторским правима. Детаљи о ауторским правима могу се видети на сајту часописа, страница *Ауторска права и политика самоархивирања*.

Радови се предају путем онлајн система за електронско уређивање АСИСТЕНТ, који је развио Центар за евалуацију у образовању и науци (ЦЕОН).

Приступ и регистрација за сервис врше се на сајту www.vtg.mod.gov.rs, преко странице *АСИСТЕНТ* или *СЦИНДЕКС*, односно директно на линку aseestant.ceon.rs/index.php/vtg.

Детаљно упутство о регистрацији и пријави за сервис налази се на сајту www.vtg.mod.gov.rs, страница *Упутство за АСИСТЕНТ*.

Потребно је да се сви аутори који подносе рукопис за објављивање у *Војнотехничком гласнику* региструју у регистар ORCID (Open Researcher and Contributor ID), према упутству на страници сајта *Регистрација за добијање ORCID идентификационе шифре*.

Војнотехнички гласник објављује чланке на енглеском језику (arial, величина слова 11 pt, проред Single).

Поступак припреме, писања и уређивања чланка треба да буде у сагласности са *Изјавом о етичком поступању* (http://www.vtg.mod.gov.rs/izjava-o-etickom-postupanju.html).

Чланак треба да садржи сажетак са кључним речима, увод (мотивацију за рад), разраду (адекватан преглед репрезентативности рада у његовој области, јасну изјаву о новини у представљеном истраживању, одговарајућу теоријску позадину, један или више примера за демонстрирање и дискусију о представљеним идејама), закључак и литературу (без нумерације наслова и поднаслова). Обим чланка треба да буде до једног ауторског табака (16 страница формата А4 са проредом Single), а највише 24 странице.

Чланак треба да буде написан на обрасцу за писање чланка, који се у електронској форми може преузети са сајта на страници *Образац за писање чланка*.

Наслов

Наслов треба да одражава тему чланка. У интересу је часописа и аутора да се користе речи прикладне за индексирање и претраживање. Ако таквих речи нема у наслову, пожељно је да се придода и поднаслов.

Текући наслов

Текући наслов се исписује са стране сваке странице чланка ради лакше идентификације, посебно копија чланака у електронском облику. Садржи презиме и иницијал имена аутора (ако аутора има више, преостали се означавају са „et al.“ или „и др.“), наслове рада и часописа и колацију (година, волумен, свеска, почетна и завршна страница). Наслови часописа и чланка могу се дати у скраћеном облику.

Име аутора

Наводи се пуно име и презиме (свих) аутора. Веома је пожељно да се наведу и средња слова аутора. Имена и презимена домаћих аутора увек се исписују у оригиналном облику (са српским дијакритичким знаковима), независно од језика на којем је написан рад.

Назив установе аутора (афилијација)

Наводи се пун (званични) назив и седиште установе у којој је аутор запослен, а евентуално и назив установе у којој је аутор обавио истраживање. У сложеним организацијама наводи се укупна хијерархија (нпр. Универзитет одбране у Београду, Војна академија, Катедра природно-математичких наука). Бар једна организација у хијерархији мора бити правно лице. Ако аутора има више, а неки потичу из исте установе, мора се, посебним ознакама или на други начин, назначити из које од наведених установа потиче сваки од наведених аутора. Афилијација се исписује непосредно након имена аутора. Функција и звање аутора се не наводе.

Контакт подаци

Адреса или е-адреса свих аутора даје се поред имена и презимена аутора.

Категорија (тип) чланка

Категоризација чланака обавеза је уредништва и од посебне је важности. Категорију чланка могу предлагати рецензенти и чланови уредништва, односно уредници рубрика, али одговорност за категоризацију сноси искључиво главни уредник.

Војнотехнички гласник објављује научне чланке.

Научни чланак је:

– оригиналан научни рад (рад у којем се износе претходно необјављени резултати сопствених истраживања научним методом);

– прегледни рад (рад који садржи оригиналан, детаљан и критички приказ истраживачког проблема или подручја у којем је аутор остварио одређени допринос, видљив на основу аутоцитата);

– кратко или претходно саопштење (оригинални научни рад пуног формата, али мањег обима или прелиминарног карактера);

– научна критика, односно полемика (расправа на одређену научну тему, заснована искључиво на научној аргументацији) и осврти.

Изузетно, у неким областима, научни рад у часопису може имати облик монографске студије, као и критичког издања научне грађе (историјско-архивске,

лексикографске, библиографске, прегледа података и сл.), дотад непознате или недовољно приступачне за научна истраживања.

Радови класификовани као научни морају имати бар две позитивне рецензије.

Ако се у часопису објављују и прилози ваннаучног карактера, научни чланци треба да буду груписани и јасно издвојени у првом делу свеске.

Пожељно је да обим кратких саопштења буде 4 до 7 страница, научних чланака и студија случаја 10 до 14 страница, док прегледни радови могу бити и дужи. Број страница није строго ограничен и, уз одговарајуће образложење, пријављени чланци такође могу бити дужи или краћи.

Ако су радови који су претходно објављени на конференцији проширени, уредници ће проверити да ли је додато довољно новог материјала који испуњава стандарде часописа и квалификује поднесак за поступак рецензије. Додати материјал не сме бити претходно објављен. Нови резултати нису нужно потребни, али су пожељни. Међутим, поднесак треба да садржи проширене кључне идеје, примере, разраде, итд., који су претходно били садржани у поднеску са конференције.

Језик рада

Језик рада треба да буде енглески.

Текст мора бити језички и стилски дотеран, систематизован, без скраћеница (осим стандардних). Све физичке величине морају бити изражене у Међународном систему мерних јединица – SI. Редослед образаца (формула) означава се редним бројевима, са десне стране у округлим заградама.

Сажетак

Сажетак јесте кратак информативан приказ садржаја чланка који читаоцу омогућава да брзо и тачно оцени његову релевантност. У интересу је уредништава и аутора да сажетак садржи термине који се често користе за индексирање и претрагу чланака. Саставни делови сажетка су увод/циљ истраживања, методи, резултати и закључак. Сажетак треба да има од 100 до 250 речи и треба да се налази између заглавља (наслов, имена аутора и др.) и кључних речи, након којих следи текст чланка.

Кључне речи

Кључне речи су термини или фразе које адекватно представљају садржај чланка за потребе индексирања и претраживања. Треба их додељивати ослањајући се на неки међународни извор (попис, речник или тезаурус) који је најшире прихваћен или унутар дате научне области. За нпр. науку уопште, то је листа кључних речи Web of Science. Број кључних речи не може бити већи од 10, а у интересу је уредништва и аутора да учесталост њихове употребе буде што већа. У чланку се пишу непосредно након сажетка.

Систем АСИСТЕНТ у ту сврху користи специјалну алатку KWASS: аутоматско екстраховање кључних речи из дисциплинарних тезауруса/речника по избору и рутине за њихов одабир, тј. прихватање односно одбацивање од стране аутора и/или уредника.

Датум прихватања чланка

Датум када је уредништво примило чланак, датум када је уредништво коначно прихватило чланак за објављивање, као и датуми када су у међувремену достављене евентуалне исправке рукописа наводе се хронолошким редоследом, на сталном месту, по правилу на крају чланка.

Захвалница

Назив и број пројекта, односно назив програма у оквиру којег је чланак настао, као и назив институције која је финансирала пројекат или програм, наводи се у посебној напомени на сталном месту, по правилу при дну прве стране чланка.

Претходне верзије рада

Ако је чланак у претходној верзији био изложен на скупу у виду усменог саопштења (под истим или сличним насловом), податак о томе треба да буде наведен у посебној напомени, по правилу при дну прве стране чланка. Рад који је већ објављен у неком часопису не може се објавити у *Војнотехничком гласнику* (прештампати), ни под сличним насловом и измењеном облику.

Табеларни и графички прикази

Пожељно је да наслови свих приказа, а по могућству и текстуални садржај, буду дати двојезично, на језику рада и на енглеском језику.

Табеле се пишу на исти начин као и текст, а означавају се редним бројевима са горње стране. Фотографије и цртежи треба да буду јасни, прегледни и погодни за репродукцију. Цртеже треба радити у програму word или corel. Фотографије и цртеже треба поставити на жељено место у тексту.

За слике и графиконе не сме се користити снимак са екрана рачунара програма за прикупљање података. У самом тексту чланка препоручује се употреба слика и графикона непосредно из програма за анализу података (као што су Excel, Matlab, Origin, SigmaPlot и други).

Навођење (цитирање) у тексту

Начин позивања на изворе у оквиру чланка мора бити једнообразан.

Војнотехнички гласник за референцирање (цитирање и навођење литературе) примењује Харвардски систем референци, односно Харвардски приручник за стил (Harvard Referencing System, Harvard Style Manual). У самом тексту, у обичним заградама, на месту на којем се врши позивање, односно цитирање литературе набројане на крају чланка, обавезно у обичној загради написати презиме цитираног аутора, годину издања публикације из које цитирате и, евентуално, број страница. Нпр. (Petrović, 2012, pp.10–12).

Детаљно упутство о начину цитирања, са примерима, дато је на страници сајта *Упутство за Харвардски приручник за стил*. Потребно је да се позивање на литературу у тексту уради у складу са поменутим упутством.

Систем АСИСТЕНТ у сврху контроле навођења (цитирања) у тексту користи специјалну алатку CiteMatcher: откривање изостављених цитата у тексту рада и у попису референци.

Напомене (фусноте)

Напомене се дају при дну стране на којој се налази текст на који се односе. Могу садржати мање важне детаље, допунска објашњења, назнаке о коришћеним изворима (на пример, научној грађи, приручницима), али не могу бити замена за цитирану литературу.

Листа референци (литература)

Цитирана литература обухвата, по правилу, библиографске изворе (чланке, монографије и сл.) и даје се искључиво у засебном одељку чланка, у виду листе

референци. Референце се не преводе на језик рада и набрајају се у посебном одељку на крају чланка.

Војнотехнички гласник, као начин исписа литературе, примењује Харвардски систем референци, односно Харвардски приручник за стил (Harvard Referencing System, Harvard Style Manual).

Литература се обавезно пише на латиничном писму и набраја по абецедном редоследу, наводећи најпре презимена аутора, без нумерације.

Детаљно упутство о начину пописа референци, са примерима, дато је на страници сајта *Упутство за Харвардски приручник за стил*. Потребно је да се попис литературе на крају чланка уради у складу са поменутим упутством.

Нестандардно, непотпуно или недоследно навођење литературе у системима вредновања часописа сматра се довољним разлогом за оспоравање научног статуса часописа.

Систем АСИСТЕНТ у сврху контроле правилног исписа листе референци користи специјалну алатку RefFormatter: контрола обликовања референци у складу са Харвардским приручником за стил.

Изјава о ауторству

Поред чланка доставља се *Изјава о ауторству* у којој аутори наводе свој појединачни допринос у изради чланка. Такође, у тој изјави потврђују да су чланак урадили у складу са *Позивом и упутством ауторима* и *Изјавом о етичком поступању часописа*.

Сви радови подлежу стручној рецензији.

Списак рецензената *Војнотехничког гласника* може се видети на страници сајта *Списак рецензената*. Процес рецензирања објашњен је на страници сајта *Рецензентски поступак*.

Уредништво

Адреса редакције:
Војнотехнички гласник
Вељка Лукића Курјака 33
11042 Београд
e-mail: vojnotehnicki.glasnik@mod.gov.rs.
тел: војни 40-260 (011/3603-260), 066/8700-123

Graphic design editor
Marija Marić, e-mail: marija.maric@mod.gov.rs

Proofreader
Dobrila Miletić, e-mail: miletic.dobrila@gmail.com

English translation and polishing
Jasna Višnjić, e-mail: jasnavisnjic@yahoo.com

CIP – Catalogisation in the publication
National Library of Serbia, Belgrade

623+355/359

ВОЈНОТЕХНИЧКИ гласник : научни часопис Министарства одбране и Војске Србије = Военно-технический вестник : научный журнал Министерства обороны и Вооружённых сил Республики Сербия = Military Technical Courier : scientific Journal of the Ministry of Defence and the Serbian Armed Forces / главни и одговорни уредник Драган Памучар. - Год. 1, бр. 1 (1. јан. 1953)- . - Београд : Универзитет одбране у Београду, Војна академија, 1953- (Београд : Војна штампарија). - 23 cm

Тромесечно. - Текст на срп., рус. и енгл. језику. - Друго издање на другом медијуму: Vojnotehnički glasnik (Online) = ISSN 2217-4753
ISSN 0042-8469 = Војнотехнички гласник
COBISS.SR-ID 4423938

Price: 600.00 RSD

Printed in 100 copies

According to the Opinion of the Ministry of Science and Technological Development No 413-00-1201/2001-01 of 12th September 2001, the *Military Technical Courier* is a publication of special interest for science.

UDC: National Library of Serbia, Belgrade

Address: Vojnotehnički glasnik/Military Technical Courier,
Veljka Lukića Kurjaka 33, 11042 Belgrade, Republic of Serbia

https://www.scopus.com/sourceid/21101207440
http://www.vtg.mod.gov.rs/index-e.html
http://aseestant.ceon.rs/index.php/vtg/issue/current
http://scindeks.nb.rs/journaldetails.aspx?issn=0042-8469
https://www.redalyc.org/revista.oa?id=6617
http://elibrary.ru/title_about.asp?id=53280
https://doaj.org/toc/2217-4753

Military Technical Courier has entered into an electronic licensing relationship with EBSCO Publishing. The full text of *Military Technical Courier* can be found on EBSCO Publishing's databases.

e-mail: vojnotehnicki.glasnik@mod.gov.rs, X: @MilTechCourier
Subscription to print edition: e-mail: vojnotehnicki.glasnik@mod.gov.rs; Tel. +381 66 87 00 123.

The journal is published quarterly.

The first printed issue of the *Military Technical Courier* appeared on 1st January 1953.
The first electronic edition of the *Military Technical Courier* on the Internet appeared on 1st January 2011.

Printed by Vojna štamparija – Belgrade, Resavska 40b, e-mail: vojna.stamparija@mod.gov.rs

Ликовно-графички уредник
Марија Марић, e-mail: marija.maric@mod.gov.rs

Лектор
Добрила Милетић, e-mail: miletic.dobrila@gmail.com

Превод на енглески
Јасна Вишњић, e-mail: jasnavisnjic@yahoo.com

CIP – Каталогизација у публикацији
Народна библиотека Србије, Београд

623+355/359

ВОЈНОТЕХНИЧКИ гласник : научни часопис Министарства одбране и Војске Србије = Военно-технический вестник : научный журнал Министерства обороны и Вооружённых сил Республики Сербия = Military Technical Courier : scientific Journal of the Ministry of Defence and the Serbian Armed Forces / главни и одговорни уредник Драган Памучар. - Год. 1, бр. 1 (1. јан. 1953)- . - Београд : Универзитет одбране у Београду, Војна академија, 1953- (Београд : Војна штампарија). - 23 cm

Тромесечно. - Текст на срп., рус. и енгл. језику. - Друго издање на другом медијуму: Vojnotehnički glasnik (Online) = ISSN 2217-4753
ISSN 0042-8469 = Војнотехнички гласник
COBISS.SR-ID 4423938

Цена: 600,00 динара

Тираж: 100 примерака

На основу мишљења Министарства за науку, технологију и развој Републике Србије, број 413-00-1201/2001-01 од 12. 9. 2001. године, часопис „Војнотехнички гласник“ је публикација од посебног интереса за науку.

УДК: Народна библиотека Србије, Београд

Адреса редакције: Војнотехнички гласник,
Вељка Лукића Курјака 33, 11042 Београд

https://www.scopus.com/sourceid/21101207440
http://www.vtg.mod.gov.rs
http://aseestant.ceon.rs/index.php/vtg/issue/current
http://scindeks.nb.rs/journaldetails.aspx?issn=0042-8469
https://www.redalyc.org/revista.oa?id=6617
http://elibrary.ru/title_about.asp?id=53280
https://doaj.org/toc/2217-4753

Војнотехнички гласник је лиценциран код EBSCO Publishing-a.
Комплетан текст *Војнотехничког гласника* доступан је у базама података EBSCO Publishing-a.

e-mail: vojnotehnicki.glasnik@mod.gov.rs; X: @MilTechCourier

Претплата на штампано издање: e-mail: vojnotehnicki.glasnik@mod.gov.rs; тел. 066/87-00-123.

Часопис излази тромесечно.

Први штампани број *Војнотехничког гласника* објављен је 1. 1. 1953. године.

Прво електронско издање *Војнотехничког гласника* на Интернету објављено је 1. 1. 2011. г.

Штампа: Војна штампарија – Београд, Ресавска 40б, e-mail: vojna.stamparija@mod.gov.rs


ОД 1953.
73
ГОДИНА
ВТГ

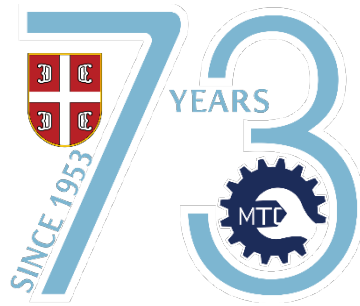
SINCE 1953
73
YEARS
MTC